July 2007
Research Report: UCPRC-RR-2007-09

Reflective Cracking Study: Second-Level Analysis Report

Authors:
D. Jones, B.Tsai, P. Ullidtz, R. Wu, J. Harvey, and C. Monismith

Partnered Pavement Research Program (PPRC) Contract Strategic Plan Element 4.10:
Development of Improved Rehabilitation Designs for Reflective Cracking

PREPARED FOR:

California Department of Transportation
Division of Research and Innovation
Office of Roadway Research

PREPARED BY:

University of California
Pavement Research Center
UC Davis, UC Berkeley

DOCUMENT RETRIEVAL PAGE		**Research Report: UCPRC-RR-2007-09**
Title: Reflective Cracking Study: Second-Level Analysis Report		
Authors: D. Jones, B. Tsai, P. Ullidtz, R Wu, J. Harvey and C. Monismith		
Prepared for: Caltrans	**FHWA No:** CA091073J	**Date:** July 2007
Contract No: 65A0172	**Client Reference No:** SPE 4.10	**Status:** Stage 6, Approved Version

Abstract:

This report follows a series of seven first-level Heavy Vehicle Simulator (HVS) testing reports, two laboratory reports on shear and fatigue testing, a forensic investigation report, and a report on the backcalculation of deflection measurements, all of which document an investigation undertaken to validate Caltrans overlay strategies for the rehabilitation of cracked asphalt concrete. It presents the findings from a detailed analysis of the laboratory fatigue and shear results, and a series of simulations using *CalME* mechanistic-empirical design software and continuum damage mechanics implemented using a finite element method.

The work was conducted by the University of California Pavement Research Center (UCPRC) as part of Partnered Pavement Research Center Strategic Plan Item 4.10: "Development of Improved Rehabilitation Designs for Reflective Cracking." This work was originally requested by the Caltrans/Industry Rubber Asphalt Concrete Task Group (RACTG) to compare the performance of one set of examples of thin overlays of cracked asphalt pavement containing different types of binders modified with recycled tire rubber. This work, included as Appendix H of the Rubber Modified Binder Pilot Projects Review prepared by the RACTG is part of a more comprehensive work plan prepared by the Task Group that included evaluation of pilot projects and construction and monitoring of field test sections (undertaken by Caltrans).

The objective of this UCPRC project will be met after completion of the following four tasks:

1. Develop improved mechanistic models of reflective cracking in California,
2. Calibrate and verify these models using laboratory and HVS testing,
3. Evaluate the most effective strategies for reflective cracking, and
4. Provide recommendations for reflective cracking strategies.

This report addresses all the tasks and consists of six main chapters. Chapter 2 provides an overview of the HVS testing program for the study. Chapter 3 summarizes a second-level analysis of the laboratory fatigue and shear test results. Chapter 4 discusses mechanistic-empirical modeling and simulations of the HVS results using *CalME* software, which is currently being developed for Caltrans by the UCPRC. Chapter 5 discusses modeling and simulations using continuum damage mechanics implemented using finite-element models. Chapter 6 lists key findings of the study, and provides recommendations for implementation.

Keywords:

Reflective cracking, overlay, modified binder, HVS test, MB Road, forensic investigation

Related documents:

UCPRC-WP-2003-01, UCPRC-RR-2005-03, RR-2006-04, RR-2006-05, RR-2006-06, RR-2006-07, RR-2006-08, RR-2006-11, RR-2006-12, RR-2007-04, RR-2007-05, RR-2007-08

Signatures:

D. Jones 1st Author	J Harvey Technical Review	D. Spinner Editor	J. Harvey Principal Investigator	M Samadian Caltrans Contract Manager

DISCLAIMER

The contents of this report reflect the views of the authors who are responsible for the facts and accuracy of the data presented herein. The contents do not necessarily reflect the official views or policies of the State of California or the Federal Highway Administration. This report does not constitute a standard, specification, or regulation.

PROJECT OBJECTIVES

The objective of this project is to develop improved rehabilitation designs for reflective cracking for California.

This objective will be met after completion of four tasks identified by the Caltrans/Industry Rubber Asphalt Concrete Task Group (RACTG):

1. Develop improved mechanistic models of reflective cracking in California,
2. Calibrate and verify these models using laboratory and HVS testing,
3. Evaluate the most effective strategies for reflective cracking, and
4. Provide recommendations for reflective cracking strategies

This document addresses all these tasks.

ACKNOWLEDGEMENTS

The University of California Pavement Research Center acknowledges the assistance of the Rubber Pavements Association, Valero Energy Corporation, and Paramount Petroleum which contributed funds and asphalt binders for the construction of the Heavy Vehicle Simulator test track discussed in this study.

REFLECTIVE CRACKING STUDY REPORTS

The reports prepared during the reflective cracking study document data from construction, Heavy Vehicle Simulator (HVS) tests, laboratory tests, and subsequent analyses. These include a series of first- and second-level analysis reports and two summary reports. On completion of the study this suite of documents will include:

1. Reflective Cracking Study: Summary of Construction Activities, Phase 1 HVS testing and Overlay Construction (UCPRC-RR-2005-03).
2. Reflective Cracking Study: First-level Report on the HVS Rutting Experiment (UCPRC-RR-2007-06).
3. Reflective Cracking Study: First-level Report on HVS Testing on Section 590RF — 90 mm MB4-G Overlay (UCPRC-RR-2006-04).
4. Reflective Cracking Study: First-level Report on HVS Testing on Section 589RF — 45 mm MB4-G Overlay (UCPRC-RR-2006-05).
5. Reflective Cracking Study: First-level Report on HVS Testing on Section 587RF — 45 mm RAC-G Overlay (UCPRC-RR-2006-06).
6. Reflective Cracking Study: First-level Report on HVS Testing on Section 588RF — 90 mm AR4000-D Overlay (UCPRC-RR-2006-07).
7. Reflective Cracking Study: First-level Report on HVS Testing on Section 586RF — 45 mm MB15-G Overlay (UCPRC-RR-2006-12).
8. Reflective Cracking Study: First-level Report on HVS Testing on Section 591RF — 45 mm MAC15-G Overlay (UCPRC-RR-2007-04).
9. Reflective Cracking Study: HVS Test Section Forensic Report (UCPRC-RR-2007-05).
10. Reflective Cracking Study: First-level Report on Laboratory Fatigue Testing (UCPRC-RR-2006-08).
11. Reflective Cracking Study: First-level Report on Laboratory Shear Testing (UCPRC-RR-2006-11).
12. Reflective Cracking Study: Backcalculation of FWD Data from HVS Test Sections (UCPRC-RR-2007-08).
13. Reflective Cracking Study: Second-level Analysis Report (UCPRC-RR-2007-09).
14. Reflective Cracking Study: Summary Report (UCPRC-SR-2007-01). Detailed summary report.
15. Reflective Cracking Study: Summary Report (UCPRC-SR-2007-03). Four-page summary report.

CONVERSION FACTORS

SI* (MODERN METRIC) CONVERSION FACTORS				
APPROXIMATE CONVERSIONS TO SI UNITS				
Symbol	**Convert From**	**Multiply By**	**Convert To**	**Symbol**
LENGTH				
in	inches	25.4	millimeters	mm
ft	feet	0.305	meters	m
AREA				
in^2	square inches	645.2	square millimeters	mm^2
ft^2	square feet	0.093	square meters	m2
VOLUME				
ft^3	cubic feet	0.028	cubic meters	m^3
MASS				
lb	pounds	0.454	kilograms	kg
TEMPERATURE (exact degrees)				
°F	Fahrenheit	5 (F-32)/9 or (F-32)/1.8	Celsius	C
FORCE and PRESSURE or STRESS				
lbf	poundforce	4.45	newtons	N
lbf/in^2	poundforce/square inch	6.89	kilopascals	kPa
APPROXIMATE CONVERSIONS FROM SI UNITS				
Symbol	**Convert From**	**Multiply By**	**Convert To**	**Symbol**
LENGTH				
mm	millimeters	0.039	inches	in
m	meters	3.28	feet	ft
AREA				
mm^2	square millimeters	0.0016	square inches	in^2
m^2	square meters	10.764	square feet	ft^2
VOLUME				
m^3	cubic meters	35.314	cubic feet	ft^3
MASS				
kg	kilograms	2.202	pounds	lb
TEMPERATURE (exact degrees)				
C	Celsius	1.8C+32	Fahrenheit	F
FORCE and PRESSURE or STRESS				
N	newtons	0.225	poundforce	lbf
kPa	kilopascals	0.145	poundforce/square inch	lbf/in^2

*SI is the symbol for the International System of Units. Appropriate rounding should be made to comply with Section 4 of ASTM E380. (Revised March 2003)

GLOSSARY OF TERMS

av	Percent air-void content
binder	Binder types including AR4000, ARB, MB4, MB15, and MAC15
comp	Compaction including FMFC, FMLC, and LMLC
cond	Conditioning, either aging or non-aging
grad	Gradation
FMFC	Field-mixed field-compacted
FMLC	Field-mixed laboratory-compacted
LMLC	Laboratory-mixed laboratory-compacted
$\ln\alpha_1$ and β_1	Intercept and slope of Stage I of a three-stage fatigue/shear Weibull curve
$\ln\alpha_2$ and β_2	Intercept and slope of Stage II of a three-stage fatigue/shear Weibull curve
$\ln\alpha_3$ and β_3	Intercept and slope of Stage III of a three-stage fatigue/shear Weibull curve
ln*G*	Initial resilient shear modulus (MPa) in natural logarithm
ln*kcy5*	Permanent shear strain after 5,000 loading cycles
$\ln n_1$	Separation point between Stage I and Stage II of a three-stage fatigue/shear Weibull curve
$\ln n_2$	Separation point between Stage II and Stage III of a three-stage fatigue/shear Weibull curve
ln*Nf*	Traditional fatigue life (repetitions at 50 percent loss of initial stiffness) in natural logarithm
ln*pct5*	Cycles to 5 percent permanent shear strain (in natural logarithm)
ln*stif*	Initial stiffness (MPa) in natural logarithm
lnstn	Strain level in natural logarithm
lnsts	Stress level (kPa) in natural logarithm
pa	Phase angle
PSS	Permanent shear strain
RSS	Residual sum of squares
SR	Stiffness ratio
srn_1	Stage I stiffness ratio in a three-stage fatigue Weibull curve
srn_2	Stage II stiffness ratio in a three-stage fatigue Weibull curve
temp	Temperature in °C
γ_1	Parameter that determines the degree of slope change from Stage I to Stage II of a three-stage fatigue/shear Weibull curve
γ_2	Parameter that determines the degree of slope change from Stage II to Stage III of a three-stage fatigue/shear Weibull curve

EXECUTIVE SUMMARY

This report follows a series of seven first-level Heavy Vehicle Simulator (HVS) testing reports, two laboratory reports on shear and fatigue testing, a forensic investigation report, and a report on the backcalculation of deflection measurements, all of which document an investigation undertaken to validate Caltrans overlay strategies for the rehabilitation of cracked asphalt concrete. The report presents the findings from a detailed analysis of the laboratory fatigue and shear results, and a series of simulations using *CalME* mechanistic-empirical design software and continuum damage mechanics implemented using a finite element method.

The work was conducted by the University of California Pavement Research Center (UCPRC) as part of Partnered Pavement Research Center Strategic Plan Item 4.10: "Development of Improved Rehabilitation Designs for Reflective Cracking." This work was originally requested by the Caltrans/Industry Rubber Asphalt Concrete Task Group (RACTG), to compare the performance of one set of examples of thin overlays of cracked asphalt pavement that contain different types of binders modified with recycled tire rubber. This work, included as Appendix H of the "Rubber Modified Binder Pilot Projects Review" prepared by the RACTG is part of a more comprehensive work plan prepared by the Task Group that included evaluation of pilot projects and construction and monitoring of field test sections (undertaken by Caltrans).

The objective of this UCPRC project will be met after completion of the following four tasks:

1. Develop improved mechanistic models of reflective cracking in California;
2. Calibrate and verify these models using laboratory and HVS testing;
3. Evaluate the most effective strategies for reflective cracking; and
4. Provide recommendations for reflective cracking overlay strategies.

This report addresses all the tasks and consists of six main chapters. Chapter 2 provides an overview of the HVS testing program for the study. Chapter 3 summarizes a second-level analysis of the laboratory fatigue and shear test results. Chapter 4 discusses mechanistic-empirical modeling and simulations of the HVS results using *CalME* software, which is currently being developed for Caltrans by the UCPRC. Chapter 5 discusses modeling and simulations using continuum damage mechanics implemented using finite element models. Chapter 6 lists key findings of the study and provides recommendations for implementation.

Five binders were assessed during the study, including MB4, MB4 with minimum 15 percent recycled tire rubber, MAC15TR with minimum 15 percent recycled tire rubber (all terminal blended), asphalt rubber

binder (ARB), and AR4000 (approximately equivalent to PG64-16). The asphalt rubber (field blended) and AR4000 binders were included for control purposes.

The following conclusions are drawn from the results of this study, organized by the study objectives agreed to by the RACTG and documented in the project work plan at the beginning of the study. All of these conclusions are based on an experiment design set that includes one example of each binder at one binder content.

Objective 1: Develop Improved Mechanistic Models of Reflective Cracking in California

Two sets of mechanistic-empirical models were developed for reflective cracking as part of this study:

- One set of models is based on the use of layer elastic theory, and has been incorporated into the mechanistic-empirical pavement design and analysis software, *CalME (*final calculations were made using Version December-2007. Version 1.0 will be delivered to Caltrans in June 2008 when documentation is completed). *CalME* is being developed under the technical supervision of a Caltrans technical working group under the direction of the Division of Design, and is intended to be used as a design and analysis tool by Caltrans engineers and their consultants.
- The second set of models, which does not have a formal name and is not intended as a full-scale design tool by Caltrans, is based on the finite element method and continuum damage mechanics. It is a more sophisticated method that provides greater insight into the crack propagation process and local (under the wheel) versus global (away from the wheel) damage than does the use of layer elastic theory. However, this model requires faster computation than can currently be accommodated in a design and analysis method to be used in practice. The findings from comparison of the results of modeling individual crack propagation with these models are being used to enhance the reflective cracking models used in *CalME*.

Objective 2: Calibrate and Validate Mechanistic Models Using Laboratory and HVS Testing

Results from a comprehensive HVS study (during which more than 15 million load repetitions equating to about 400 million Equivalent Standard Axle Loads were applied), and a comprehensive laboratory study (during which about 400 Repeated Simple Shear and Flexural Fatigue Beam tests were completed), were used together with results from other studies to calibrate and verify the models discussed above. Conclusions for this objective include:

- Both mechanistic-empirical models described in Objective 1 were calibrated and validated using the laboratory and HVS data generated in this study, as well as several data sets from other HVS tests and test tracks. The calibrations resulted in models that predicted the performance of the sections in terms of calculated versus measured deflections, changes in stiffnesses, and ranking of

reflective cracking performance. The overall approaches were validated when it was shown that use of the same calibrated coefficients across all the different tests sections resulted in a good match between predicted performance and measured performance.

- It was found during calibration that bonding was a significant variable in predicting actual performance of several HVS test sections, where forensic evidence showed that layers had become unbonded. The reason for the debonding is uncertain because a tack coat was applied. This conclusion emphasizes the need for continued use and improvement of effective bonding strategies. It also emphasizes the need for mechanistic-empirical analysis methods to explicitly consider the extent of bonding.
- The methods of characterizing the fatigue damage process in the mechanistic-empirical design models developed in this project were successful in predicting the performance of mixes with modified and rubberized binders. The fatigue damage curve characterization of laboratory data and the incremental-recursive damage updating approach successfully modeled the significantly better crack propagation resistance of these mixes. In particular, the modified binder mixes tended to have laboratory fatigue damage curves that showed a decreasing rate of damage during propagation, whereas the conventional AR4000 dense-graded mix had an increasing damage rate during the propagation phase. This is a significant improvement over traditional mechanistic-empirical analysis approaches, which tended to underpredict the reflective cracking performance of these mixes.
- A forensic investigation of the HVS rutting tests showed that most of the shear deformation actually occurred in the underlying asphalt concrete layer and not in the overlays, although the ranking of the total HVS rutting followed the laboratory shear deformation resistance test results of the overlay mixes. The mechanistic-empirical models for rutting of the asphalt layers predicted the overall rutting performance ranking of each section, but did not fully capture the distribution of rutting between the overlay and the underlying asphalt layers. It is not clear whether the relative lack of aging and trafficking of the underlying asphalt layers (light car traffic and fewer than five delivery trucks per day at the HVS test site over three years) before placing the overlay influenced this behavior. It is also not clear whether this phenomenon occurs with in-service pavements, where longer loading periods, lighter traffic loads, and more years of age-hardening in the underlying asphalt layers differentiate them from HVS tests. These HVS results and model predictions suggest the need for forensic investigation of several rutted field pavements with thin rubberized and modified binder mixes.

Objective 3: Evaluate the Most Effective Strategies for Reflective Cracking

A more detailed analysis of the laboratory results and a series of simulations with the calibrated mechanistic-empirical models were used to evaluate which strategies had the best reflective cracking performance. Conclusions for this objective include:

- Second-level analysis of the fatigue and shear laboratory test data using three-stage Weibull analysis identified significant differences in the crack initiation and propagation performance, and the shear deformation resistance of the different mixes under various conditions. The performance with respect to fatigue and shear were combined using similar parameters into a single plot. This approach can be used in the future by designers in the consideration of relative risk of fatigue and shear, and in considering the effects of aging and gradation. This is an improvement on past strategies which do not always optimize both shear and fatigue performance aspects for a given application.
- Although the shear test results correlated well with the observed rutting performance under the HVS, the results showed the importance of using mechanistic-empirical analysis to develop rutting and cracking performance estimates that consider the overlay material as well as its interaction with the rest of the pavement structure, instead of using only laboratory data.
- The results from controlled-deformation fatigue beam testing used in this project were also found to match the results of reflective cracking of thin overlays for the structures tested by the HVS. However, the ranking of fatigue beam test results and predicted or actual field performance of thicker overlays and/or different pavement structures may differ because of the interaction of the overlay with the pavement structure.
- The results of a limited exploratory laboratory experiment (included in the approved work plan) using modified binders in dense-graded mixes indicate that these mixes have lower cracking resistance, higher stiffness, and better rutting resistance compared to mixes with the same binders but using gap-gradation. This suggests that, apart from their use in thin reflective cracking overlays, the modified binders also hold promise for use in thicker structural overlays and new pavements. Mechanistic-empirical simulations for dense-graded modified binder mixes showed superior cracking resistance but poorer rutting resistance than conventional DGAC (now called hot-mix asphalt [HMA]).

Objective 4: Provide Recommendations for Reflective Cracking Overlay Strategies

Findings of the more detailed analysis of the laboratory shear and fatigue results, and the simulations with the calibrated models were used to prepare recommendations for reflective cracking studies. Conclusions for this objective include:

- Overall, the results indicate that, with respect to reflective cracking, when the half-thickness modified binder mixes assessed in this study were used as thin overlays on cracked pavement they provide better performance than the full-thickness, conventional dense-graded asphalt concrete (HMA). This is demonstrated by the absence of reflective cracking on the half-thickness modified binder overlays, despite their being subjected to over a million more HVS repetitions than that required to crack the full-thickness AR4000-D overlay. The half-thickness RAC-G mix did not perform as well as the modified mixes, but still showed superior reflective cracking performance compared with the full-thickness AR4000-D, confirming results from previous HVS studies performed for Caltrans by the UCPRC.
- The re-analysis of the HVS fatigue test results using uniform underlying conditions, as opposed to the actual underlying conditions (which varied between HVS test sections) used during calibration, showed that the reflective cracking resistance of the modified and rubberized mixes in half-thickness overlays remained significantly better than that of the conventional dense-graded asphalt concrete full-thickness overlay. This was found to be true using both mechanistic-empirical analysis approaches (*CalME* and continuum damage mechanics models).
- Re-analysis of the HVS rutting test results using uniform underlying conditions indicates that there is a faster rutting of the asphalt layers when the modified mixes are used with slow traffic in hot climates. Performance should be assessed in pilot projects before wider use is considered under these conditions.
- Overall, the results indicate that the modified binder mixes (regardless of half or full thickness) assessed in this study have a greater risk of asphalt rutting under slow, heavy loads and hot conditions compared to the full-thickness, conventional dense-graded asphalt concrete (HMA) overlay. The modified binder mix designs were performed using the same Hveem Stabilometer procedure used for RAC-G mixes. It is not known to what extent the rutting performance would have been improved, and conversely if the reflective cracking performance would have been effected by using a different method that selected lower design binder contents.

Recommendations

The following recommendations with regard to the establishment of pilot projects are made based on the conclusions presented above:

- There is sufficient evidence from this study that a number of production-level pilot projects should be constructed using mixes with modified binders.
- Control mixes should be included in the pilot projects.
- Mixes used in the pilot projects should be subjected to laboratory testing and analysis of the type (reduced experiment design) used in this research project. This testing and analysis is needed to

identify the range of performance for these mix types, which could not be measured with the one binder example in this study.

- The initial pilot projects with modified binder mixes should not be placed in locations with very hot climates and/or high traffic counts of slow, heavy trucks.
- The pilot projects should be monitored following the Pavement Preservation Study Technical Advisory Guide (PPSTAG [UCPRC-GL-2005-01]).

The following recommendations with regard to the testing and analysis are made based on the conclusions presented above:

- New mixes developed for reflective cracking, with either new gradations or new binders, should be evaluated with the laboratory testing and analysis techniques and the mechanistic-empirical analysis models developed in this study. Based on the available research and performance data, additional HVS testing is not warranted before constructing and evaluating pilot projects, unless there is uncertainty from the modeling results for these new mixes.
- Laboratory investigation, additional analysis, and HVS validation is recommended to improve mix design procedures for rubberized and modified-binder mixes. The mixes used in this study were designed using the Hveem Stabilometer with criteria (e.g., gradation) that were not consistent between mixes with conventional binders and mixes with rubberized and modified binders.
- Additional laboratory and modeling studies and HVS tests are also warranted to better assess the risk of rutting using mixes with these binders in thicker overlays, hot climates, and under slow, heavy loads, and the effects of changes to the mix design on reducing that risk.

TABLE OF CONTENTS

GLOSSARY OF TERMS ..... **v**
EXECUTIVE SUMMARY ..... **vii**
LIST OF TABLES ..... **xix**
LIST OF FIGURES ..... **xxi**
1. INTRODUCTION **1**
1.1. Objectives 1
1.2. Overall Project Organization 1
1.3. Structure and Content of this Report 4
1.4. Measurement Units 4
2. HEAVY VEHICLE SIMULATOR TEST DETAILS **5**
2.1. Phase 2 Experiment Layout 5
2.2. Underlying Pavement Design 5
2.3. Summary of Testing on the Underlying Layer 8
2.4. Overlay Design 10
2.5. Summary of Phase 2 HVS Testing 12
2.5.1 Test Section Failure Criteria 12
2.5.2 Environmental Conditions 12
2.5.3 Test Duration 13
2.5.4 Loading Program 13
3. LABORATORY FATIGUE AND SHEAR TESTING **15**
3.1. Introduction 15
3.1.1 Overall Approach 15
3.1.2 Experimental Designs 16
3.2. Introduction to Weibull Characterization of Test Results 16
3.2.1 Definition of Three-Stage Weibull Curve for Fatigue 16
3.2.2 Definition of Three-Stage Weibull Curve for Shear 23
3.2.3 Types of Weibull Curves 25
3.3. Tree-Based Regression Modeling for Three-Stage Fatigue Weibull Parameters 28
3.3.1 Introduction 28
3.3.2 Fitting with a Tree-Based Model: An Example 29
3.4. Weibull Parameters and Fatigue Performance 33
3.4.1 Weibull Curves of Modified Binder Fatigue Results 33
3.4.2 Tree-Based Regression/Category Modeling 35

3.4.3 Summary Boxplots for Fatigue 38
3.5. Weibull Parameters and Shear Performance 45
3.5.1 Weibull Curves of Modified Binder Shear Results 45
3.5.2 Tree-Based Regression Modeling 45
3.5.3 Summary Boxplots for Shear 49
3.6. Laboratory Two-Stage Weibull Fatigue Integrated Equations 56
3.6.1 Equation Development Methodology 57
3.6.2 Equations from Temperature Effect Data 59
3.6.3 Equations from Gradation Effect Data 64
3.7. Fatigue and Shear Performance Comparison 64
3.7.1 Comparison of Fatigue and Shear Data Using Traditional Parameters 64
3.7.2 Weibull Parameters Identifying Fatigue Performance 67
3.7.3 Weibull Parameters Identifying Shear Performance 69
3.8. Rationale for Selecting the $\ln\alpha_3/\beta_3$ and $\ln\alpha_2/\beta_2$ Parameters 71
3.9. Findings and Discussion 75
3.9.1 Use of Three-Stage Weibull Analysis to Characterize Fatigue and Shear Tests 75
3.9.2 Most Appropriate Parameters Identifying Fatigue and Shear Performance 76
3.9.3 Comparison of Fatigue and Shear Performance 76
4. MECHANISTIC-EMPIRICAL PERFORMANCE SIMULATIONS 81
4.1. Introduction to Simulations 81
4.2. Introduction to Simulations with *CalME* 83
4.3. Data and Methodology for Simulations Using Actual Conditions 83
4.3.1 Data 84
4.3.2 Methodology 84
4.4. *CalME* Models 85
4.4.1 Asphalt Concrete Master Curve 85
4.4.2 Stiffness of Unbound Layers 87
4.4.3 Strain Over Existing Crack 88
4.4.4 Fatigue Damage of Asphalt 89
4.4.5 Relationship Between Damage and Cracking 90
4.4.6 Fatigue Damage of Recycled Aggregate Base 93
4.4.7 Permanent Deformation of Asphalt 95
4.4.8 Permanent Deformation of Unbound Layers 96
4.4.9 Time Hardening 96
4.5. Analysis of Frequency Sweep Tests for Input to Simulations 97

4.6. Analysis of Falling Weight Deflectometer (FWD) Tests for Input to Simulations 99
4.6.1 FWD Results Before Overlay Construction 99
4.6.2 FWD Results After Overlay Construction 104
4.7. Fatigue Test to Characterize Asphalt Damage in Simulations 108
4.8. Shear Tests 111
4.9. Simulation of Original Pavement Structure (Actual Conditions) 114
4.9.1 RSD Response 116
4.9.2 MDD Response 116
4.9.3 Damage 116
4.9.4 Surface Permanent Deformation 116
4.9.5 MDD Permanent Deformation 116
4.10. Simulation of Overlaid Sections (Actual Conditions): Rutting Study 129
4.10.1 Temperatures 129
4.10.2 MDD Response 129
4.10.3 Surface Permanent Deformation 130
4.10.4 In-Depth Permanent Deformation 130
4.11. Simulation of Overlaid Sections (Actual Conditions): Reflective Cracking Study 133
4.11.1 RSD Response 133
4.11.2 MDD Response 134
4.11.3 Damage 134
4.11.4 Surface Permanent Deformation 134
4.11.5 MDD Permanent Deformation 134
4.12. Summary of All Simulations Using Actual Conditions 139
4.12.1 Response 139
4.12.2 Fatigue of Asphalt Concrete Layers 143
4.12.3 Permanent Deformation 147
4.13. Simulation of Overlaid Sections (Uniform Conditions): Rutting Study 151
4.14. Simulation of Overlaid Sections (Uniform Conditions): Reflective Cracking Study 152
4.15. Extrapolation to Field Conditions and Sensitivity Analyses 154
4.15.1 Methodology 154
4.15.2 Parameters for Different Groups of Simulations 156
4.16. Simulation Results 157
4.16.1 FMLC Mix Reflective Cracking Performance in Different Climate Zones 157
4.16.2 FMLC Mix Rutting Performance in Different Climate Zones 160
4.16.3 LMLC Mix Reflective Cracking Performance in Overlays at 20°C 161

4.16.4 LMLC Mix Rutting Performance in Overlays at 20°C 164
5. CONTINUUM DAMAGE MECHANICS SIMULATIONS 167
5.1. Introduction 167
5.2. Development of CDM Model Inputs 168
5.2.1 Pavement Structure, Environment, and Loading 168
5.2.2 Underlying DGAC Crack Spacing and Width 168
5.2.3 Backcalculation of Base and Subgrade Moduli 169
5.2.4 Asphalt Layer Characterization 171
5.2.5 Damage Evolution Parameters 177
5.3. Simulation Procedure 178
5.3.1 FEM Model 179
5.3.2 Considerations for FEM Model Use 181
5.4. First-Stage Simulation Results 183
5.4.1 Comparison Between Observed and Predicted Reflective Cracking Life 183
5.4.2 Crack Propagation History Plots 183
5.4.3 Summary of Simulation Results 186
5.5. Second-Stage Simulations and Ranking of Cracking Performance 186
5.5.1 Methodology 186
5.5.2 Simulation Results 187
5.6. Extrapolation to Field Conditions and Sensitivity Analyses 189
5.6.1 Methodology 189
5.6.2 Parameters for Different Groups of Simulations 190
5.7. Simulation Results 192
5.7.1 FMLC Mix Performance in Different Climate Zones 192
5.7.2 LMLC Mix Performance in Overlays at 20°C 197
5.8. Summary and Observations 200
5.8.1 Simulation of HVS Test Sections 200
5.8.2 General Simulations 200
6. CONCLUSIONS AND RECOMMENDATIONS 203
6.1. Conclusions 203
Objective 1: Develop Improved Mechanistic Models of Reflective Cracking 203
Objective 2: Calibrate and Validate Mechanistic Models 204
Objective 3: Evaluate the Most Effective Strategies for Reflective Cracking 205
Objective 4: Provide Recommendations for Reflective Cracking Overlay Strategies ... 206
6.2. Recommendations 207

Pilot Projects 207
Testing and Analysis 207
7. REFERENCES 209
APPENDIX A. LABORATORY FATIGUE AND SHEAR 214
A.1. Tree Structure for Predicting Initial Stiffness 214
A.2. Weibull Curves of Modified Binder Fatigue Results 215
A.3. Pruned Dendograms for Laboratory Fatigue Results 241
A.4. Weibull Curves of Modified Binder Shear Results 243
A.5. Pruned Dendograms for Laboratory Shear Results 269
A.6. Fatigue and Shear Equations from Temperature Effect Data 271
A.7. Fatigue and Shear Equations from Gradation Effect Data 282
APPENDIX B. MECHANISTIC EMPIRICAL PERFORMANCE SIMULATIONS 288
B.1. Simulation of Overlaid Sections: Rutting Study 288
B.2. Simulation of Overlaid Sections (Actual Conditions): Reflective Cracking Study 288
APPENDIX C. CONTINUUM DAMAGE MECHANICS SIMULATIONS 314
C.1. Regression Parameters for Base and Subgrade Stiffness Degradation 314
C.2. Backcalculated Initial Stiffness for Underlying Asphalt Concrete Layer 315

LIST OF TABLES

Table 2.1: Summary of Testing on the Underlying DGAC Layer 8
Table 2.2: Design versus Actual Binder Contents....10
Table 2.3: Air-Void Contents....12
Table 2.4: Pavement Temperatures at 50-mm Depth During Phase 2 HVS Trafficking 13
Table 2.5: Test Duration for Phase 2 HVS Testing....13
Table 2.6: Summary of HVS Loading Program....14
Table 3.1: Experimental Design for Fatigue Laboratory Testing....17
Table 3.2: Experimental Design for Laboratory Shear Testing (RSST-CH)....18
Table 3.3: Summary of Shape Counts for Each Mix Type for Fatigue....36
Table 3.4: Summary of the 1st-, 2nd-, and 3rd-Level Covariates for Fatigue Tree Modeling....38
Table 3.5: Summary of Shape Counts for Each Mix Type for Shear....47
Table 3.6: Summary of the 1st, 2nd, and 3rd-Level Covariates for Shear Tree Modeling....49
Table 3.7: Two-Stage Weibull Fatigue Integrated Equations Using Temperature Effect Data 60
Table 3.8: Laboratory Two-Stage Weibull Shear Integrated Equations Using Temperature Effect Data 62
Table 3.9: Two-Stage Weibull Fatigue Integrated Equations Using Gradation Effect Data....65
Table 3.10: Laboratory Two-Stage Weibull Shear Integrated Equations Using Gradation Effect Data....66
Table 3.11: Summary of Parameters Identifying Fatigue and Shear Performance 76
Table 3.12: Summary of the Covariates for Parameters that Identify Performance....79
Table 4.1: Master Curve Parameters for Test Track Asphalt Concrete Materials....99
Table 4.2: Backcalculated Moduli Before and After HVS Testing....104
Table 4.3: Moduli Before and After HVS Testing 105
Table 4.4: Damage Calculated from Backcalculated Moduli....105
Table 4.5: Fatigue Parameters from Laboratory Testing....108
Table 4.6: Permanent Deformation Parameters for Asphalt Concrete 114
Table 4.7: Moduli of Original Structure Before and After HVS Loading....115
Table 4.8: Moduli from Simulation of Rutting Study 129
Table 4.9: Moduli Before and After HVS Experiment. 133
Table 4.10: Initial Deflections as Calculated by *CalME* and Measured by RSD and MDDs 139
Table 4.11: Terminal Deflections as Calculated by *CalME* and Measured by RSD and MDDs 141
Table 4.12: Overall Permanent Deformation from *CalME* and as Measured 147
Table 4.13: Final Deformation of Top MDD Module from *CalME* Simulation and as Measured 149
Table 4.14: Calculated Compression of Asphalt Concrete Layers....150
Table 4.15: Underlying Structure for Ranking of Overlays 152

Table 4.16: Ranking of Overlays after Increasing Damage 153
Table 4.17: Factors Considered in the Extrapolation and Sensitivity Analyses.....155
Table 4.18: Common Variables for the Reference Simulation Case.....156
Table 4.19: Variations of variables considered for Group A1 156
Table 4.20: Variations of Variables Considered for Group B1.....157
Table 5.1: Number of Cracks Counted on the Underlying DGAC Layer 168
Table 5.2: Crack Spacing at Different Locations on the Underlying DGAC Layer.....169
Table 5.3: Loading Frequencies for Different Load Levels and Section Thickness 173
Table 5.4: Aging Ratio for Different HVS Sections at Start of HVS Trafficking.....175
Table 5.5: Pavement Temperatures and Load Repetitions for the First Five RSD Data Collections.....175
Table 5.6: Overlay Layer Moduli for the First Five RSD Data Collections.....175
Table 5.7: Layer Moduli for Underlying DGAC at 20°C at Trafficking Speed.....176
Table 5.8: Layer Moduli for Overlays at 20°C at Trafficking Speed.....176
Table 5.9: Adjusted Factors for Asphalt Concrete Stiffness 177
Table 5.10: Damage Evolution Parameters for Different Aspahlt Concrete Overlay Mixes 178
Table 5.11: Reflective Cracking Life for Different HVS Sections 183
Table 5.12: Variable Inputs Used in Stage 2 Simulations.....187
Table 5.13: Fixed Inputs Used in Stage 2 Simulations.....187
Table 5.14: Ranking of Reflective Cracking Performance of Asphalt Concrete Mixes.....189
Table 5.15: Factors Considered in the Extrapolation and Sensitivity Analyses.....189
Table 5.16: Common Variables for the Reference Simulation Case.....191
Table 5.17: Variations of Variables Considered for Group A1.....191
Table 5.18: Variations of Variables Considered for Group B1.....191

LIST OF FIGURES

Figure 1.1: Timeline for the Reflective Cracking Study. 3
Figure 2.1: Layout of the Reflective Cracking Study test track. 6
Figure 2.2: Pavement design for Reflective Cracking Study experiment (design and actual). 7
Figure 2.3: Cracking patterns and rut depths on Sections 567RF through 573RF after Phase 1. 9
Figure 2.5: Gradation for AR4000-D overlay. 11
Figure 2.6: Gradation for modified binder overlays. 11
Figure 3.1: Three-stage Weibull curve. 20
Figure 3.2: Parameter estimation of a three-stage Weibull equation. 22
Figure 3.3: Definition of a shear Weibull curve in three stages. 24
Figure 3.4: Example of three-stage shear Weibull-fitted curves of various mix types. 24
Figure 3.5: Schematic plots of various shapes of fatigue stiffness deterioration curves. 25
Figure 3.6: Schematic plots of various shapes of RSST permanent shear strain accumulation curves.....26
Figure 3.7: Three-stage Weibull equation for a flexural controlled-deformation fatigue test. 27
Figure 3.8: Using three-stage Weibull equations to describe damage (*PSS*) in a repeated shear test. 28
Figure 3.9: Dendrogram with split rules of initial stiffness (ln*stif*). 29
Figure 3.10: Examples of residual plots of initial stiffness. 31
Figure 3.11: Examples of residual plots of permanent strain. 31
Figure 3.12: Typical dendogram representations. 32
Figure 3.13: Pruned dendrogram of initial stiffness (ln*stif*). 33
Figure 3.14: Typical Weibull curves for Reflective Cracking Study mixes. 34
Figure 3.15: Summary boxplots of fatigue life (ln*Nf*). 39
Figure 3.16: Summary boxplots of the fatigue three-stage Weibull parameter $\ln\alpha_1$. 40
Figure 3.17: Summary boxplots of the fatigue three-stage Weibull parameter β_1. 41
Figure 3.18: Summary boxplots of the fatigue three-stage Weibull parameter $\ln\alpha_2$. 41
Figure 3.19: Summary boxplots of the fatigue three-stage Weibull parameter β_2. 42
Figure 3.20: Summary boxplots of the fatigue three-stage Weibull parameter $\ln\alpha_3$. 42
Figure 3.21: Summary boxplots of the fatigue three-stage Weibull parameter $\ln\beta_3$. 43
Figure 3.22: Summary boxplots of the fatigue three-stage Weibull parameter $\ln(\beta_3/\beta_2)$. 43
Figure 3.23: Summary boxplots of the fatigue three-stage Weibull parameter $sign(\gamma_1)\ln(|\gamma_1|)$. 44
Figure 3.24: Summary boxplots of the fatigue three-stage Weibull parameter $sign(\gamma_2)\ln(|\gamma_2|)$. 44
Figure 3.25: Summary boxplots of the fatigue three-stage Weibull parameter $SR@n_2$. 45
Figure 3.26: Summary boxplots of permanent shear strain (ln*pct5*). 50
Figure 3.27: Summary boxplots of the shear three-stage Weibull parameter: $\ln\alpha_1$. 51

Figure 3.28: Summary boxplots of the shear three-stage Weibull parameter: β_1. 51
Figure 3.29: Summary boxplots of the shear three-stage Weibull parameter: lnα_2. 52
Figure 3.30: Summary boxplots of the shear three-stage Weibull parameter: β_2 52
Figure 3.31: Summary boxplots of the shear three-stage Weibull parameter: lnα_3. 53
Figure 3.32: Summary boxplots of the shear three-stage Weibull parameter:β_3. 54
Figure 3.33: Summary boxplots of the shear three-stage Weibull parameter: ln(β_3/β_2). 54
Figure 3.34: Summary boxplots of the shear three-stage Weibull parameter: $sign(\gamma_1)$ln(|γ_1|). 55
Figure 3.35: Summary boxplots of the shear three-stage Weibull parameter: $sign(\gamma_2)$ln(|γ_2|). 55
Figure 3.36: Summary boxplots of the shear three-stage Weibull parameter: $pss@n_2$. 56
Figure 3.37: Fatigue versus shear performance of various mix types and testing conditions. 67
Figure 3.38: Fatigue life (ln*Nf*) contour plot in terms of ln(β_3/β_2) and lnα_2/β_2. 68
Figure 3.39: Fatigue life (ln*Nf*) contour plot in terms of lnα_3/β_3 and lnα_2/β_2.....69
Figure 3.40: Permanent shear strain (ln*pct5*) contour plot in terms of β_3 and lnα_3. 70
Figure 3.41: Permanent shear strain (ln*pct5*) contour plot in terms of ln(β_3/β_2) and lnα_3/β_3. 71
Figure 3.42: Permanent shear strain (ln*pct5*) contour plot in terms of $ln\alpha_3/\beta_3$ and lnα_2/β_2.....72
Figure 3.43: Schematic interpretation between lnα_3/β_3 and ln*pct5*/ln*Nf*.....74
Figure 3.44: Summary boxplots of stiffness reduction at Stage I and II separation points. 75
Figure 3.45: Summary boxplots of permanent shear strain at Stage I and II separation points. 75
Figure 3.46: Identification of fatigue performance from lnα_3/β_3 and lnα_2/β_2 parameters. 77
Figure 3.47: Identification of shear performance from lnα_3/β_3 and lnα_2/β_2 parameters. 78
Figure 3.48: Pruned dendrograms of fatigue and shear three-stage Weibull parameters. 79
Figure 4.1: Relative decrease in modulus as a function of damage, for E_{min} = 100 MPa. 90
Figure 4.2: Crack initiation with S-shaped curve. 91
Figure 4.3: Cracking model compared to terminal cracking at WesTrack. 92
Figure 4.4: Example of master curve fitted to frequency sweep data. 97
Figure 4.5: Comparison of moduli versus temperature for different asphalt concrete materials. 98
Figure 4.6: Backcalculated moduli from center line, before overlay. 100
Figure 4.7: Relative modulus as a function of normal strain from triaxial tests. 101
Figure 4.8: Backcalculated DGAC moduli compared to frequency sweep master curve. 102
Figure 4.9: Backcalculated modulus of aggregate base compared to Equation 4.27. 102
Figure 4.10: Subgrade modulus as a function of bending resistance. 103
Figure 4.11: Backcalculated moduli for original pavement layers, versus time. 104
Figure 4.12: Moduli of underlying DGAC before and after overlay.....106
Figure 4.13: Moduli of AR4000-D overlay, from frequency sweep tests and FWD backcalculation. 106

Figure 4.14: Moduli of RAC-G, from frequency sweep tests and FWD backcalculation.....106
Figure 4.15: Moduli of MB4-G, from frequency sweep tests and FWD backcalculation.....106
Figure 4.16: Moduli of MB15-G, from frequency sweep tests and FWD backcalculation.....107
Figure 4.17: Moduli of MAC15-G, from frequency sweep tests and FWD backcalculation.....107
Figure 4.18: Calculated and measured stiffness ratio for the underlying DGAC.....109
Figure 4.19: Calculated and measured stiffness ratio for the AR4000-D overlay.....109
Figure 4.20: Calculated and measured stiffness ratio for the RAC-G overlay.....109
Figure 4.21: Calculated and measured stiffness ratio for the MB4-G overlay.....109
Figure 4.22: Calculated and measured stiffness ratio for the MB15-G overlay.....110
Figure 4.23: Calculated and measured stiffness ratio for the MAC15-G overlay.....110
Figure 4.24: Example of damage versus load repetitions, for 20°C and 500 µstrain.....111
Figure 4.25: Normalized strain versus load applications for underlying DGAC.....112
Figure 4.26: Normalized strain versus load applications for AR4000-D overlay.....112
Figure 4.27: Normalized strain versus load applications for RAC-G overlay.....112
Figure 4.28: Normalized strain versus load applications for MB15-G overlay.....112
Figure 4.29: Normalized strain versus load applications for MB4-G overlay.....113
Figure 4.30: Normalized strain versus load applications for MAC15-G overlay.....113
Figure 4.31: Comparison of down rut (mm) versus load repetitions for test track AC mixes.....114
Figure 4.32: 567RF, measured (RSD) and calculated surface deflection.....117
Figure 4.33: 568RF, measured (RSD) and calculated surface deflection.....117
Figure 4.34: 568RFa, measured (RSD) and calculated surface deflection.....117
Figure 4.35: 569RFb, measured (RSD) and calculated surface deflection.....117
Figure 4.36: 571RF, measured (RSD) and calculated surface deflection.....118
Figure 4.37: 572RF, measured (RSD) and calculated surface deflection.....118
Figure 4.38: 573RF, measured (RSD) and calculated surface deflection.....118
Figure 4.39: 567RF, measured and calculated deflection at upper MDD.....119
Figure 4.40: 567RF, resilient compression of upper AB layers.....119
Figure 4.41: 567RF, measured and calculated deflection of lower subgrade.....119
Figure 4.42: 569RFb, measured and calculated deflection at upper MDD.....119
Figure 4.43: 569RFb, resilient compression of AB layers plus upper subgrade.....120
Figure 4.44: 569RFb, measured and calculated deflection of subgrade.....120
Figure 4.45: 571RF, measured and calculated deflection at upper MDD.....120
Figure 4.46: 571RF, resilient compression of AB layers plus upper subgrade.....120
Figure 4.47: 571RF, measured and calculated deflection of subgrade.....121

Figure 4.48: 567RF, damage and cracking. 121
Figure 4.49: 568RF, damage and cracking. 121
Figure 4.50: 569RFa, damage and cracking. 122
Figure 4.51: 569RFb, damage and cracking. 122
Figure 4.52: 571RF, damage and cracking. 122
Figure 4.53: 572RF, damage and cracking. 122
Figure 4.54: 573RF, damage and cracking. 123
Figure 4.55: 567RF, measured and calculated down rut 123
Figure 4.56: 568RF, measured and calculated down rut. 123
Figure 4.57: 569RFa, measured and calculated down rut. 124
Figure 4.58: 569RFb, measured and calculated down rut. 124
Figure 4.59: 571RF, measured and calculated down rut. 124
Figure 4.60: 572RF, measured and calculated down rut. 124
Figure 4.61: 573RF, measured and calculated down rut. 125
Figure 4.62: 567RF, measured and calculated permanent deformation at upper MDD. 125
Figure 4.63: 567RF, measured and calculated permanent deformation of upper AB layers. 125
Figure 4.64: 567RF, measured and calculated permanent deformation of lower subgrade. 126
Figure 4.65: 569RFb, measured and calculated permanent deformation at top MDD. 126
Figure 4.66: 569RFb, measured and calculated permanent compression of upper AB layers. 126
Figure 4.67: 569RFb, measured and calculated permanent compression of lower AB layers. 126
Figure 4.68: 569RFb, measured and calculated permanent compression of AB layers. 127
Figure 4.69: 569RFb, measured and calculated permanent deformation of subgrade. 127
Figure 4.70: 571RF, measured and calculated permanent deformation of top MDD 127
Figure 4.71: 571RF, measured and calculated permanent compression of AB layers. 127
Figure 4.72: 571RF, measured and calculated permanent deformation at top of subgrade. 128
Figure 4.73: 580RF, measured and calculated down rut. 131
Figure 4.74: 581RF, measured and calculated down rut. 131
Figure 4.75: 582RF, measured and calculated down rut. 131
Figure 4.76: 583RF, measured and calculated down rut. 131
Figure 4.77: 584RF, measured and calculated down rut. 132
Figure 4.78: 585RF, measured and calculated down rut. 132
Figure 4.79: 586RF, calculated damage and observed cracking. 135
Figure 4.80: 587RF, calculated damage and observed cracking. 135
Figure 4.81: 588RFa, calculated damage and observed cracking. 135

Figure 4.82: 588RFb, calculated damage and observed cracking. 135
Figure 4.83: 589RF, calculated damage and observed cracking. 136
Figure 4.84: 590RF, calculated damage and observed cracking. 136
Figure 4.85: 591RF, calculated damage and observed cracking. 136
Figure 4.86: 586RF, measured and calculated down rut. 137
Figure 4.87: 587RF, measured and calculated down rut. 137
Figure 4.88: 588RFa, measured and calculated down rut. 137
Figure 4.89: 588RFb, measured and calculated down rut. 137
Figure 4.90: 589RF, measured and calculated down rut. 138
Figure 4.91: 590RF, measured and calculated down rut. 138
Figure 4.92: 591RF, measured and calculated down rut. 138
Figure 4.93: Calculated initial deflections compared to measured values. 140
Figure 4.94: Calculated deflections at end of HVS experiment compared to measured values.....140
Figure 4.95: Increase in deflection during HVS experiments, as simulated and measured. 141
Figure 4.96: Logarithm of measured deflection versus calculated deflection of top MDD module. 142
Figure 4.97: Logarithm of terminal moduli, FWD tests versus simulation with *CalME*. 143
Figure 4.98: Observed cracking versus damage calculated by *CalME*. 143
Figure 4.99: Observed reflective cracking versus damage calculated using modified parameters. 144
Figure 4.100: Predicted versus observed reflective cracking, using modified parameters.....145
Figure 4.101: Observed cracking versus calculated fatigue damage of overlay. 146
Figure 4.102: Observed cracking versus fatigue damage calculated using modified parameters. 146
Figure 4.103: Predicted versus observed reflective cracking 147
Figure 4.104: Final down rut versus calculated overall permanent deformation. 148
Figure 4.105: Average of all measured down ruts compared to calculated values. 148
Figure 4.106: Measured final permanent deformation of top MDD versus calculated value. 149
Figure 4.107: Measured final compression of AC from profile and MDD versus calculated value. 151
Figure 4.108: Rutting simulation with uniform conditions. 152
Figure 4.109: Simulated damage for identical testing conditions. 154
Figure 4.110: Design plot of relative reflective cracking life with FMLC mixes. 158
Figure 4.111: Relative reflective cracking performance of FMLC mixes, grouped by climate zone. 159
Figure 4.112: Relative reflective cracking performance of FMLC mixes, grouped by thickness.....159
Figure 4.113: Relative reflective cracking performance of FMLC mixes, grouped by TI for 10 years.....159
Figure 4.114: Relative reflective cracking performance of FMLC mixes, grouped by traffic speed.....159
Figure 4.115: Design plot of relative rutting life with FMLC mixes. 160

Figure 4.116: Relative rutting performance of FMLC mixes, grouped by climate zone. 162
Figure 4.117: Relative rutting performance of FMLC mixes, grouped by overlay thickness. 162
Figure 4.118: Relative rutting performance of FMLC mixes, grouped by TI for 10 years. 162
Figure 4.119: Relative rutting performance of FMLC mixes, grouped by traffic speed. 162
Figure 4.120: Design plot of relative reflective cracking life with LMLC mixes at 20°C. 163
Figure 4.121: Relative reflective cracking performance of LMLC, grouped by overlay thickness 164
Figure 4.122: Relative reflective cracking performance of LMLC, grouped by traffic speed 164
Figure 4.123: Design plot of relative rutting life with LMLC mixes at 20°C 165
Figure 4.124: Relative rutting performance of LMLC, grouped by overlay thickness 166
Figure 4.125: Relative rutting performance of LMLC, grouped by traffic speed 166
Figure 5.1: Comparison of average fitted aggregate base stiffness for the HVS sections.....170
Figure 5.2: Comparison of average fitted upper 400 mm subgrade stiffness for the HVS sections.....170
Figure 5.3: Comparison of lower 5,600 mm backcalculated subgrade stiffness for the HVS sections.....171
Figure 5.4: Overall FEM mesh for a typical HVS simulation. 179
Figure 5.5: Close-up view (1) of the FEM mesh shown in Figure 5.4. 180
Figure 5.6: Close-up view (1) of the FEM mesh shown in Figure 5.5. 180
Figure 5.7: Surface deflection corresponding to different transverse HVS wheel locations.....182
Figure 5.8: Evolution of crack tip height with load repetitions for Section 587RF (RAC-G). 184
Figure 5.9: Evolution of crack tip height with load repetitions for Section 588RF (AR4000-D). 184
Figure 5.10: Evolution of crack tip height with load repetitions for Section 589RF (45mm MB4-G). 185
Figure 5.11: Evolution of crack tip height with load repetitions for Section 590RF (90mm MB4-G). 185
Figure 5.12: Evolution of crack tip height with load repetitions for Section 591RF (MAC15-G). 186
Figure 5.13: Effects of overlay thickness on reflective cracking life for different mixes. 188
Figure 5.14: Effects of base stiffness on reflective cracking life for different AC mixes. 188
Figure 5.15: Design plot of reflective cracking life for AC-over-AC overlays with FMLC mixes. 192
Figure 5.16: Design plot of reflective cracking life for AC-over-PCC overlays with FMLC mixes. 193
Figure 5.17: Performance of FMLC mixes in AC-over-AC overlays, grouped by climate zone.....195
Figure 5.18: Performance of FMLC mixes in AC-over-PCC overlays, grouped by climate zone.....195
Figure 5.19: Performance of FMLC mixes in AC-over-AC overlays, grouped by overlay thickness. 195
Figure 5.20: Performance of FMLC mixes in AC-over-PCC overlays, grouped by overlay thickness. 195
Figure 5.21: Performance of FMLC mixes in AC-over-AC overlays, grouped by TI for 10 years. 196
Figure 5.22: Performance of FMLC mixes in AC-over-PCC overlays, grouped by TI for 10 years. 196
Figure 5.23: Performance of FMLC mixes in AC–over-AC overlays, grouped by traffic speed. 196
Figure 5.24: Performance of FMLC mixes in AC-over-PCC overlays, grouped by traffic speed. 196

Figure 5.25: Design plot of reflective cracking life for AC-over-AC overlays with LMLC mixes. 197
Figure 5.26: Design plot of reflective cracking life for AC-over-PCC overlays with LMLC mixes. 197
Figure 5.27: Performance of LMLC mixes in AC-over-AC overlays, grouped by overlay thickness. 199
Figure 5.28: Performance of LMLC mixes in AC–over-PCC overlays, grouped by overlay thickness. 199
Figure 5.29: Performance of LMLC mixes in AC-over-AC overlays, grouped by traffic speed. 199
Figure 5.30: Performance of LMLC mixes in AC-over-PCC overlays, grouped by traffic speed. 199

1. INTRODUCTION

1.1. Objectives

The second-level analysis presented in this report is part of Partnered Pavement Research Center Strategic Plan Element 4.10 (PPRC SPE 4.10) being undertaken for the California Department of Transportation (Caltrans) by the University of California Pavement Research Center (UCPRC). The objective of the study is to evaluate the reflective cracking performance of asphalt binder mixes used in overlays for rehabilitating cracked asphalt concrete pavements in California. The study includes mixes modified with rubber and polymers, and it will develop tests, analysis methods, and design procedures for mitigating reflective cracking in overlays. This work is part of a larger study on modified binder (MB) mixes being carried out under the guidance of the Caltrans Pavement Standards Team (PST) (1) that includes laboratory and accelerated pavement testing using the Heavy Vehicle Simulator (carried out by the UCPRC), and the construction and monitoring of field test sections (carried out by Caltrans).

1.2. Overall Project Organization

This UCPRC project is a comprehensive study, carried out in three phases, involving the following primary elements (2):

- Phase 1
  - The construction of a test pavement and subsequent overlays;
  - Six separate Heavy Vehicle Simulator (HVS) tests to crack the pavement structure;
  - Placing of six different overlays on the cracked pavement;
- Phase 2
  - Six HVS tests that assessed the susceptibility of the overlays to high-temperature rutting (Phase 2a);
  - Six HVS tests to determine the low-temperature reflective cracking performance of the overlays (Phase 2b);
  - Laboratory shear and fatigue testing of the various hot-mix asphalts (Phase 2c);
  - Falling Weight Deflectometer (FWD) testing of the test pavement before and after construction and before and after each HVS test;
  - Forensic evaluation of each HVS test section;

- Phase 3
  - Performance modeling and simulation of the various mixes using models calibrated with data from the primary elements listed above.
  -

Phase 1

In this phase, a conventional dense-graded asphalt concrete (DGAC) test pavement was constructed at the Richmond Field Station (RFS) in the summer of 2001. The pavement was divided into six cells, and within each cell a section of the pavement was trafficked with the HVS until the pavement failed by either fatigue(2.5 m/m^2 [0.76 ft/ft^2]) or rutting (12.5 mm [0.5 in]). This period of testing began in the summer of 2001 and was concluded in the spring of 2003. In June 2003 each test cell was overlaid with either conventional DGAC or asphalt concrete with modified binders as follows:

- Full-thickness (90 mm) AR4000-D dense-graded asphalt concrete overlay, included as a control for performance comparison purposes (AR-4000 is approximately equivalent to a PG64-16 performance grade binder);
- Full-thickness (90 mm) MB4-G gap-graded overlay;
- Half-thickness (45 mm) rubberized asphalt concrete gap-graded overlay (RAC-G), included as a control for performance comparison purposes;
- Half-thickness (45 mm) MB4-G gap-graded overlay;
- Half-thickness (45 mm) MB4-G gap-graded overlay with minimum 15 percent recycled tire rubber (MB15-G), and
- Half-thickness (45 mm) MAC15-G gap-graded overlay with minimum 15 percent recycled tire rubber.

The conventional overlay was designed using the current (2003) Caltrans overlay design process. The various modified overlays were either full (90 mm) or half thickness (45 mm). Mixes were designed by Caltrans. The overlays were constructed in one day.

Phase 2

Phase 2 included high-temperature rutting and low-temperature reflective cracking testing with the HVS as well as laboratory shear and fatigue testing. The rutting tests were started and completed in the fall of 2003. For these tests, the HVS was placed above a section of the underlying pavement that had not been trafficked during Phase 1. A reflective cracking test was next conducted on each overlay from the winter of 2003-2004 to the summer of 2007. For these tests, the HVS was positioned precisely on top of the

sections of failed pavement from the Phase 1 HVS tests to investigate the extent and rate of crack propagation through the overlay.

In conjunction with Phase 2 HVS testing, a full suite of laboratory testing, including shear and fatigue testing, was carried out on field-mixed, field-compacted (FMFC); field-mixed, laboratory-compacted (FMLC); and laboratory-mixed, laboratory-compacted (LMLC) specimens.

Phase 3

Phase 3 entailed a second-level analysis carried out on completion of HVS and laboratory testing (the focus of this report). This included extensive analysis and characterization of the mix fatigue and mix shear data, backcalculation of the FWD data, performance modeling of each HVS test, and a detailed series of pavement simulations carried out using the combined data.

An overview of the project timeline is shown in Figure 1.1.

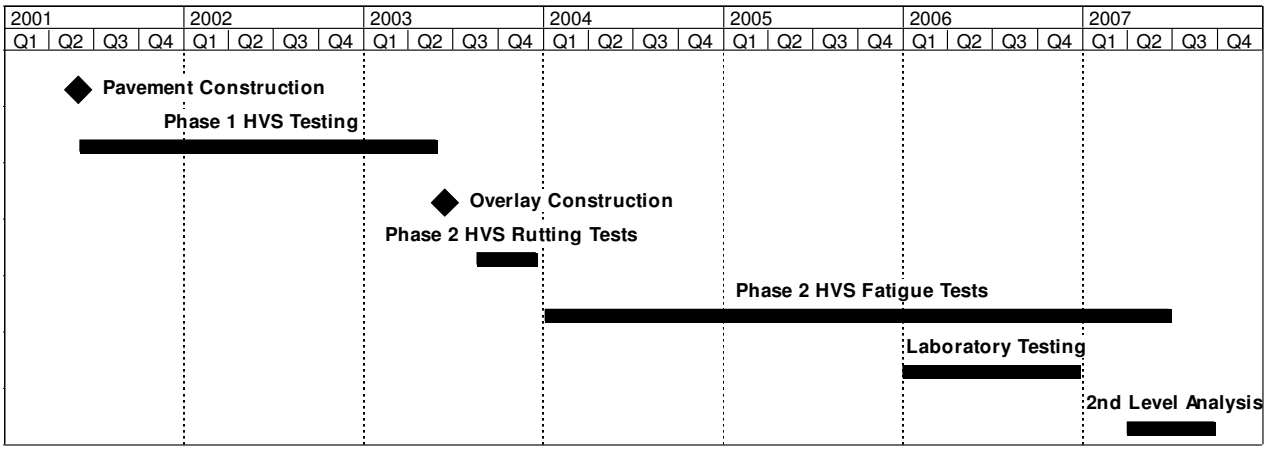

Figure 1.1: Timeline for the Reflective Cracking Study.

Reports

The reports prepared during the reflective cracking study document data from construction, HVS tests, laboratory tests, and subsequent analyses. These include a series of first- and second-level analysis reports and two summary reports. On completion of the study this suite of documents will include:

- One first-level report covering the initial pavement construction, the six initial HVS tests, and the overlay construction (Phase 1);
- One first-level report covering the six Phase 2 rutting tests (but offering no detailed explanations or conclusions on the performance of the pavements);
- Six first-level reports, each of which covers a single Phase 2 reflective cracking test (containing summaries and trends of the measured environmental conditions, pavement responses, and

pavement performance but offering no detailed explanations or conclusions on the performance of the pavement);

- One first-level report covering laboratory shear testing;
- One first-level report covering laboratory fatigue testing;
- One report summarizing the HVS test section forensic investigation;
- One report summarizing the backcalculation analysis of deflection tests,
- One second-level analysis report detailing the characterization of shear and fatigue data, pavement modeling analysis, comparisons of the various overlays, and simulations using various scenarios (Phase 3), and
- One four-page summary report capturing the entire study's conclusions and one longer, more detailed summary report that covers the findings and conclusions from the research conducted by the UCPRC.

1.3. Structure and Content of this Report

This report presents the results of a second-level analysis of HVS and laboratory results and is organized as follows:

- Chapter 2 contains a brief description of the HVS and laboratory test programs.
- Chapter 3 presents findings of the second-level analysis of laboratory fatigue and shear test results.
- Chapter 4 summarizes the findings of mechanistic-empirical performance simulations.
- Chapter 5 summarizes the findings of continuum damage mechanics simulations.
- Chapter 6 provides conclusions and recommendations.

1.4. Measurement Units

Metric units have always been used in the design and layout of HVS test tracks, all the measurements and data storage, and all associated laboratory testing at the eight HVS facilities worldwide (as well as all other international accelerated pavement testing facilities). Use of the metric system facilitates consistency in analysis, reporting, and data sharing.

In this report, metric and English units (provided in parentheses after the metric units) are used in the Executive Summary, Chapters 1 and 2, and the Conclusion. In keeping with convention, only metric units are used in Chapters 3, 4, and 5. A conversion table is provided on Page iv at the beginning of this report.

2. HEAVY VEHICLE SIMULATOR TEST DETAILS

2.1. Phase 2 Experiment Layout

Twelve test sections (six rutting and six reflective cracking) were constructed as part of the second phase of the study, as follows (Figure 2.1):

1. Sections 580RF and 586RF: Half-thickness (45 mm) MB4 gap-graded overlay with minimum 15 percent recycled tire rubber (referred to as "MB15-G" in this report);
2. Sections 581RF and 587RF: Half-thickness (45 mm) rubberized asphalt concrete gap-graded (RAC-G) overlay;
3. Sections 582RF and 588RF: Full-thickness (90 mm) AR4000 dense-graded asphalt concrete overlay (designed using CTM356 and referred to as "AR4000-D" in this report);
4. Sections 583RF and 589RF: Half-thickness (45 mm) MB4 gap-graded overlay (referred to as "45 mm MB4-G" in this report);
5. Sections 584RF and 590RF: Full-thickness (90 mm) MB4 gap-graded overlay (referred to as "90 mm MB4-G" in this report), and
6. Sections 585RF and 591RF: Half-thickness (45 mm) MAC15TR gap-graded overlay with minimum 15 percent recycled tire rubber (referred to as "MAC15-G" in this report).

2.2. Underlying Pavement Design

The pavement for the first phase of HVS trafficking was designed according to the Caltrans Highway Design Manual Chapter 600 using the computer program *NEWCON90.* Design thickness was based on a tested subgrade R-value of 5 and a Traffic Index of 7 (~121,000 ESALs) (3).

The pavement design for the test road and the as-built pavement structure for each section (580RF through 591RF) are illustrated in Figure 2.2. As-built thicknesses were determined from cores removed from the edge of the sections.

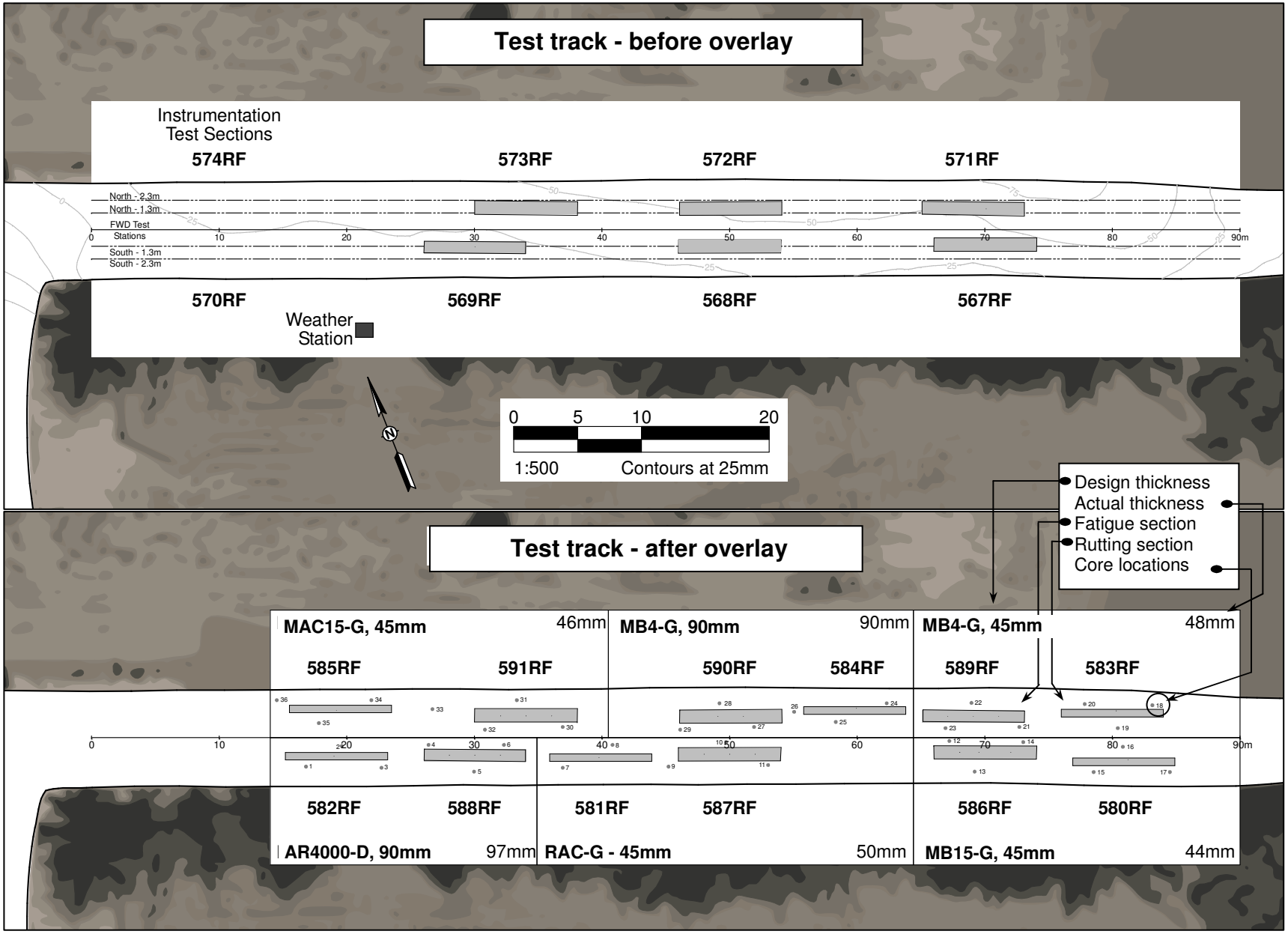

Figure 2.1: Layout of the Reflective Cracking Study test track.

Design	580RF/586RF	581RF/587RF	582RF/588RF	583RF/589RF	584RF/590RF	585RF/591RF
Overlay (45 or 90 mm)	MB15-G (46 mm)	RAC-G (50 mm)	AR4000-D (94 mm)	MB4-G (48 mm)	MB4-G (91 mm)	MAC15-G (45 mm)
DGAC (90 mm)	DGAC (81 mm)	DGAC (81 mm)	DGAC (93 mm)	DGAC (77 mm)	DGAC (88 mm)	DGAC (110 mm)
Class 2 Aggregate Base (410 mm)	Class 2 Aggregate Base (398 mm)	Class 2 Aggregate Base (398 mm)	Class 2 Aggregate Base (369 mm)	Class 2 Aggregate Base (372 mm)	Class 2 Aggregate Base (352 mm)	Class 2 Aggregate Base (411 mm)
Clay subgrade (semi-infinite)	Clay subgrade (semi-infinite)	Clay subgrade (semi-infinite)	Clay subgrade (semi-infinite)	Clay subgrade (semi-infinite)	Clay subgrade (semi-infinite)	Clay subgrade (semi-infinite)

Figure 2.2: Pavement design for Reflective Cracking Study experiment (design and actual).

The existing subgrade was ripped and reworked to a depth of 200 mm (4 in) so that the optimum moisture content and the maximum wet density met the specification per Caltrans Test Method, CTM 216. The average maximum wet density of the subgrade was 2,180 kg/m^3 (136 pcf). The average relative compaction of the subgrade was 97 percent (3).

The aggregate base was constructed to meet the Caltrans compaction requirements for aggregate base Class 2 using CTM 231 nuclear density testing. The average maximum wet density of the base determined according to CTM 216 was 2,200 kg/m^3 (137 pcf). The average relative compaction was 98 percent.

The DGAC layer consisted of a dense-graded asphalt concrete (DGAC) with AR-4000 binder (approximately equivalent to a PG64-16 performance grade binder) and aggregate gradation limits following Caltrans 19-mm (0.75 in) maximum size coarse gradation (3). The target asphalt content was 5.0 percent by mass of aggregate, while actual contents varied between 4.34 and 5.69 percent. Nuclear density measurements and extracted cores were used to determine a preliminary as-built mean air-void content of 9.1 percent with a standard deviation of 1.8 percent. The based was primed before placing the asphalt concrete.

2.3. Summary of Testing on the Underlying Layer

Phase 1 trafficking took place between December 21, 2001, and March 25, 2003, and is summarized in Table 2.1. Figure 2.3 presents the final cracking patterns of each section after testing.

Table 2.1: Summary of Testing on the Underlying DGAC Layer

Section	Start Date	End Date	Repetitions	Wheel Load (kN)	Wheel	Tire Pressure (kPa)	Direction
567RF	12/21/01	01/07/02	78,500	60[1]	Dual	720[2]	Bi
568RF	01/14/02	02/12/02	377,556	60	Dual	720	Bi
569RF	03/25/03	04/11/03	217,116	60	Dual	720	Bi
571RF	07/12/02	10/02/02	1,101,553	60	Dual	720	Bi
572RF	01/23/03	03/12/03	537,074	60	Dual	720	Bi
573RF	03/18/02	03/08/02	983,982	60	Dual	720	Bi

[1] 13,500 lb
[2] 104 psi

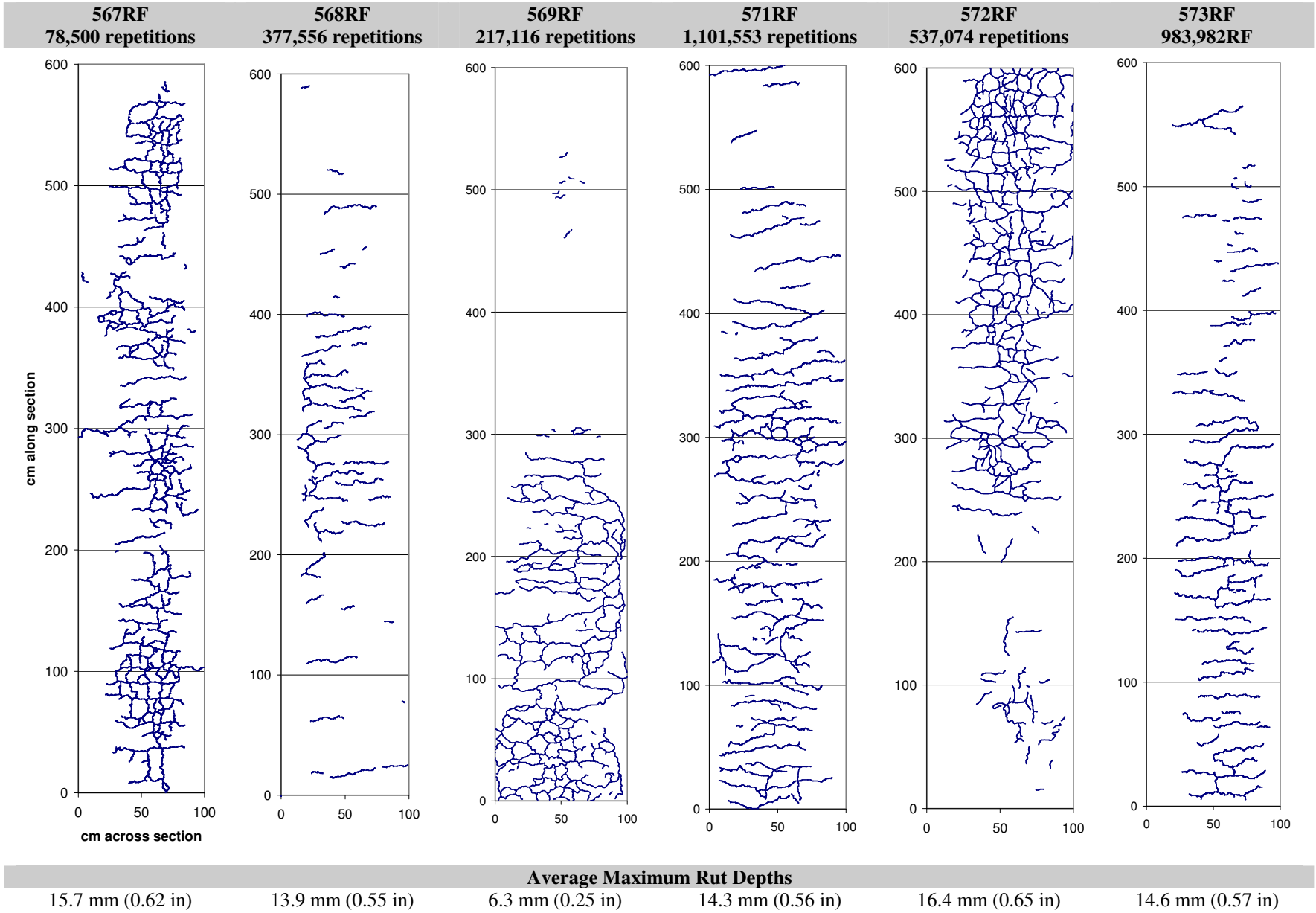

Figure 2.3: Cracking patterns and rut depths on Sections 567RF through 573RF after Phase 1.

2.4. Overlay Design

The overlay thickness for the experiment was determined according to Caltrans Test Method CTM 356 using Falling Weight Deflectometer data from the Phase 1 experiment.

Laboratory testing was carried out by Caltrans and UCPRC on samples collected during construction to determine actual binder properties, binder content, aggregate gradation, and air-void content. The binders met requirements, based on testing performed by Caltrans. The average ignition-extracted binder contents of the various layers, corrected for aggregate ignition and compared to the design binder content, are listed in Table 2.2. For each section, actual binder contents were higher than design contents. It is not clear whether this is a function of the test or contractor error.

Table 2.2: Design versus Actual Binder Contents

Section	Mix	Binder Content (%)	
		Design	Actual
580RF and 586RF	MB15-G	7.1	7.52
581RF and 587RF	RAC-G	8.0	8.49
582RF and 588RF	AR4000-D	5.0	6.13
583RF and 589RF	MB4-G (45 mm)	7.2	7.77
584RF and 590RF	MB4-G (90 mm)	7.2	7.77
585RF and 591RF	MAC15-G	7.4	7.55

The aggregate gradations for the dense- and gap-graded mixes generally met Caltrans specifications for 19.0 mm (0.75 in.) maximum size coarse and gap gradations respectively, with specifics for each section detailed below. Gradations are illustrated in Figure 2.5 (AR4000-D) and Figure 2.6 (modified binders).

- 580RF and 586RF (MB15-G): Material passing the 6.35 mm (1/4 in), 9.5 mm (3/8 mm), 12.5 mm (1/2 in), and 19.0 mm (3/4 in) sieves was on the lower envelope limit (Figure 2.6).
- 581RF and 587RF (RAC-G): Material passing the 0.3 mm (#50), 0.6 mm (#30), and 2.36 mm (#8) sieves was on the upper envelope limit (Figure 2.6).
- 582RF and 588RF (AR4000-D): Material passing the 0.6 mm (#30), 2.36 mm (#8), and 4.75 mm (#4) sieves was on the upper envelope limit (Figure 2.5).
- 583RF and 589RF (45 mm MB4-G): Material passing the 6.35 mm (1/4 in) and 9.5 mm (3/8 in) sieves was on the lower envelope limit (Figure 2.6).
- 584RF and 590RF (90 mm MB4-G): Material passing the 6.35 mm (1/4 in) and 9.5 mm (3/8 in) sieves was on the lower envelope limit (Figure 2.6).
- 585RF and 591RF (MAC15-G): Material passing the 0.6 mm (#30), 9.5 mm (3/8 in), 12.5 mm (1/2 in), and 19.0 mm (3/4 in) sieves was on the upper envelope limit, while material passing the 2.36 mm (#8), 4.75 mm (#4), and 6.35 mm (1/4 in) sieves was outside the upper limit (Figure 2.6).

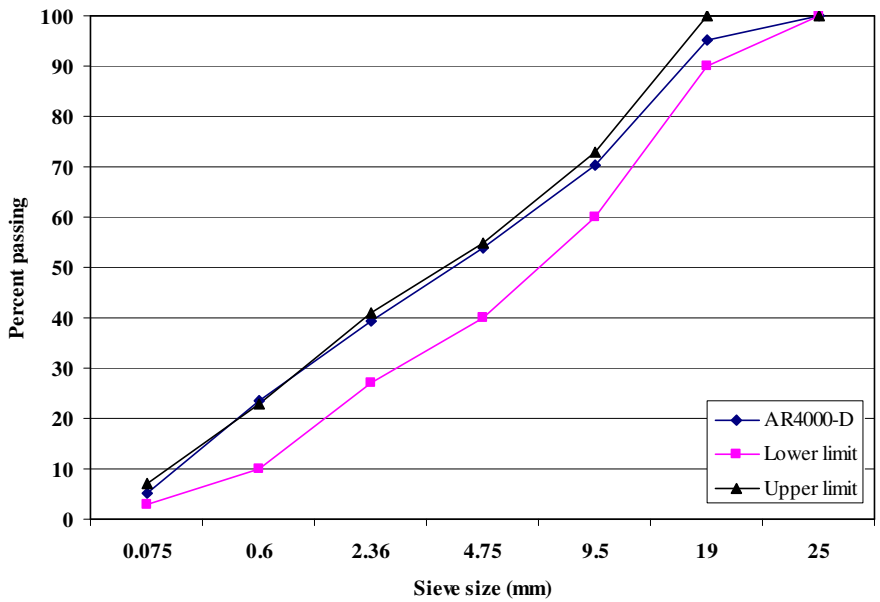

Figure 2.5: Gradation for AR4000-D overlay.

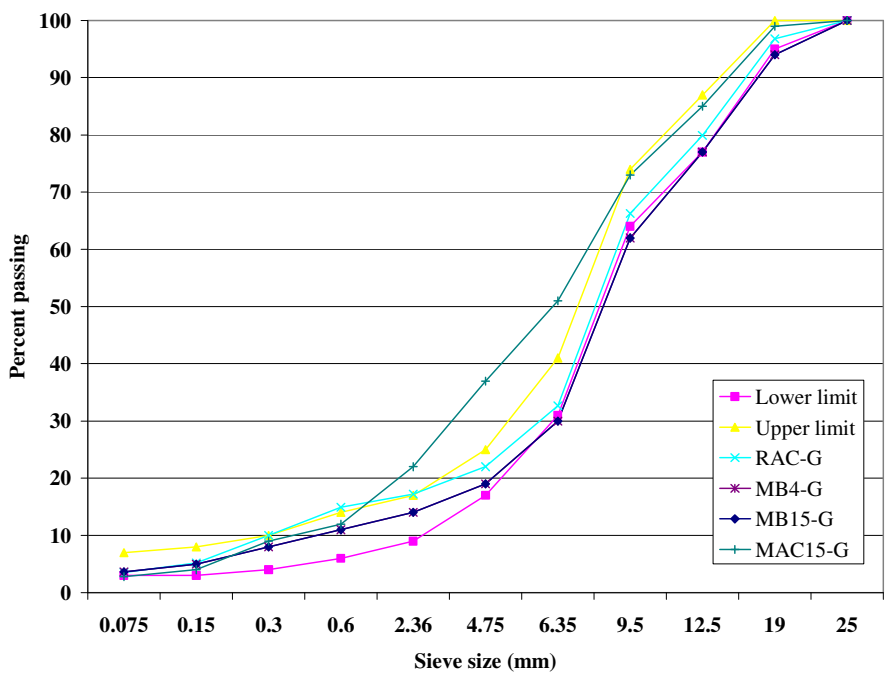

Figure 2.6: Gradation for modified binder overlays.

The overlays were placed on the same day, within a few hours of each other. A tack coat was applied prior to placement. The 90 mm layers were placed in two lifts of 45 mm and a tack coat was applied between lifts. The preliminary as-built air-void contents for each section, based on cores taken outside of the HVS sections prior to HVS testing, together with the air-void contents from each section after trafficking are listed in Table 2.3.

Table 2.3: Air-Void Contents

Section	Mix	Air-Void Content (%)	
		Average for Section	Standard Deviation
580RF and 586RF	MB15-G	5.1	1.7
581RF and 587RF	RAC-G	8.8	1.3
582RF and 588RF	AR4000-D	7.1	1.5
583RF and 589RF	MB4-G (45 mm)	6.5	0.6
584RF and 590RF	MB4-G (90 mm)	6.5	0.6
585RF and 591RF	MAC15-G	4.9	1.0

2.5. Summary of Phase 2 HVS Testing

Phase 2 HVS testing is discussed in a series of first-level analysis reports (4-12) and a forensic investigation report (13).

2.5.1 Test Section Failure Criteria

Failure criteria for HVS testing were set as follows:

- Rutting study:
  - Maximum surface rut depth of 12.5 mm (0.5 in) or more
- Reflective cracking study:
  - Cracking density of 2.5 m/m^2 (0.76 ft/ft^2) or more, and/or
  - Maximum surface rut depth of 12.5 mm (0.5 in) or more.

2.5.2 Environmental Conditions

In the rutting study, the pavement surface temperature was maintained at 50°C±4°C (122°F±7°F) in order to assess the susceptibility of the mixes to early rutting under typical pavement temperatures. In the reflective cracking study, the pavement surface temperature was maintained at 20°C±4°C (68°F±7°F) for the first one million repetitions to minimize rutting in the asphalt concrete and to accelerate fatigue damage. Thereafter, the pavement surface temperature was reduced to 15°C±4°C (59°F±7°F) to further accelerate fatigue damage. A temperature control chamber (14) was used to maintain the test temperatures. A summary of actual pavement temperatures during the test is provided in Table 2.4.

The pavement surface received no direct rainfall as it was protected by the temperature control chamber. The sections were tested during both wet and dry seasons and hence water infiltration into the pavement from the side drains and through the raised groundwater table was possible at certain stages of the testing.

Table 2.4: Pavement Temperatures at 50-mm Depth During Phase 2 HVS Trafficking

Section	Mix	Stage 1		Stage 2	
		Duration (Million Reps)	Temperature* (°C)	Duration (Million Reps)	Temperature* (°C)
586RF	MB15-G	0 to 1.0	19.5 (1.3)	1.0 to completion	15.5 (0.6)
587RF	RAC-G	0 to 1.0	18.5 (1.7)	1.0 to completion	16.9 (0.6)
588RF	AR4000-D	0 to 1.0	14.5 (1.5)	1.0 to completion	14.0 (1.2)
589RF	MB4-G (45 mm)	0 to 1.0	21.4 (0.8)	1.0 to completion	15.3 (1.4)
590RF	MB4-G (90 mm)	0 to completion	20.7 (1.1)	-	-
591RF	MAC15-G	0 to 1.0	19.9 (1.3)	1.0 to completion	15.3 (1.4)

* Average temperature and (standard deviation)

2.5.3 Test Duration

HVS trafficking on each section was initiated and completed as shown in Table 2.5.

Table 2.5: Test Duration for Phase 2 HVS Testing

Phase	Section	Mix	Start Date	Finish Date	Repetitions
Rutting	580RF	MB15-G	09/29/03	10/01/03	2,000
	581RF	RAC-G	09/15/03	09/19/03	7,600
	582RF	AR4000-D	09/04/03	09/09/03	18,564
	583RF	MB4-G (45 mm)	12/08/03	12/16/03	15,000
	584RF	MB4-G (90 mm)	11/13/03	11/26/03	34,800
	585RF	MAC15-G	10/10/03	10/20/03	3,000
Reflective cracking	586RF	MB15-G	05/25/06	11/21/06	2,492,387
	587RF	RAC-G	03/15/05	10/10/05	2,024,793
	588RF	AR4000-D	11/02/05	04/11/06	1,410,000
	589RF	MB4-G (45 mm)	06/23/04	02/08/05	2,086,004
	590RF	MB4-G (90 mm)	01/13/04	06/16/04	1,981,365
	591RF	MAC15-G	01/10/07	06/25/07	2,554,335

2.5.4 Loading Program

The HVS loading program for each section is summarized in Table 2.6. Test configurations were as follows:

- In the rutting tests, all trafficking was carried out with a dual-wheel configuration, using radial truck tires (Goodyear G159 - 11R22.5- steel belted radial) inflated to a pressure of 720 kPa (104 psi), in a channelized, unidirectional loading mode.
- In the reflective cracking tests, all trafficking was carried out with a dual-wheel configuration, using radial truck tires (Goodyear G159 - 11R22.5- steel belted radial) inflated to a pressure of 720 kPa (104 psi), in a bidirectional loading mode. Lateral wander over the one-meter width of the test section was programmed to simulate traffic wander on a typical highway lane.

Table 2.6: Summary of HVS Loading Program

Phase	Section	Start Repetition	Total Repetitions	Wheel Load (kN)		ESALs	Traffic Index
				Planned	Actual*		
Rutting	580RF	Full test	2,000	40	60	11,000	N/A
	581RF		7,600			42,000	N/A
	582RF		18,564			102,000	N/A
	583RF		15,000			83,000	N/A
	584RF		34,800			191,000	N/A
	585RF		3,000			17,000	N/A
Reflective cracking	586RF (MB15-G)	0 215,000 410,000 1,000,001	2,492,387	40 60 80 100	60 90 80 100	88 million	15
	587RF (RAC-G)	0 215,000 410,000 1,000,001	2,024,793	40 60 80 100	60 90 80 100	66 million	15
	588RF (AR4000-D)	0 215,000 410,000 1,000,001	1,410,000	40 60 80 100	60 90 80 100	37 million	14
	589RF (45 mm MB4-G)	0 215,000 407,197 1,002,000	2,086,004	40 60 80 100	60 90 80 100	69 million	15
	590RF** (90 mm MB4-G)	0 1,071,004 1,439,898 1,629,058	1,981,365	40 60 80 100	60 90 80 100	37 million	14
	591RF (MAC15-G)	0 215,000 410,000 1,000,001	2,554,335	40 60 80 100	60 90 80 100	91 million	15

* The loading program differs from the original test plan due to an incorrect hydraulic control system setup on loads less than 65 kN in the Phase 1 experiment. The loading pattern from the Phase 1 experiment was thus retained to facilitate comparisons of performance between all tests in the Reflective Cracking Study.

** 590RF was the first HVS test on the overlays, and the 60 kN loading pattern was retained for an extended period to prevent excessive initial deformation (rutting) of the newly constructed overlay.

40 kN - 9,000 lb 60 kN - 13,500 lb 80 kN - 18,000 lb 90 kN - 20,200 lb 100 kN - 22,500 lb

3. LABORATORY FATIGUE AND SHEAR TESTING

3.1. Introduction

The first-level laboratory fatigue and shear analyses (11,12) applied conventional analytical procedures to characterize and rank fatigue and shear performance of mixes with five binder types, namely AR4000, ARB (Asphalt Rubber Binder), MAC15, MB15, and MB4, while they were subjected to various effects including temperature, air-void content, aging, compaction, and gradation.

The main objective of this second-level analysis of the laboratory data was to compare the performance of the mixes with the five binders using the approaches and information gathered from assessments of the:

- Stiffness deterioration process (or fatigue damage process) of a flexural controlled-deformation fatigue test of the mixes using a three-stage Weibull approach;
- Most appropriate parameters that identify fatigue performance, specifically the fatigue damage process used in comparing fatigue performance of different mixes in the future;
- Permanent shear strain (PSS) accumulation processes of a controlled-load repetitive simple shear test with constant height (RSST-CH) of test results applied in the first level analysis using a three-stage Weibull approach, and
- Most appropriate parameters that identify rutting performance used in comparing rutting performance of different mixes in the future.

3.1.1 Overall Approach

For fatigue studies, the three-stage Weibull curve is defined by plotting ln(-ln*SR*) against ln*n*, where *SR* is the stiffness ratio and *n* the number of load repetitions. In the rutting studies, ln(-ln*PSS*) is plotted against ln*n*, where *PSS* is the permanent shear strain and *n* the number of load repetitions. Each test is fit with a three-stage Weibull curve using a genetic algorithm to obtain optimized Weibull parameters. These parameters are then analyzed using various statistical tools including:

- Summary boxplots, to compare the Weibull parameters of the different mixes;
- Tree-based regression/category modeling, to explore the data structure of the Weibull parameters;
- Pruned-tree modeling, to simplify the tree structures for presentation, and
- Regression analysis, to develop integrated Weibull equations to simulate fatigue and shear performance.

In addition to the three-stage Weibull analysis, the traditional parameter of fatigue life, 50 Percent Loss of Initial Stiffness (ln*Nf*), was compared with the traditional rutting performance parameter, repetitions to 5 Percent Permanent Shear Strain (ln*pct5*), for each binder type, based on the effect of temperature, air-void content, aging, and gradation. Several other parameters were inspected using performance contour plots and corresponding density functions to determine which provided the best indication of overall performance in the laboratory tests.

3.1.2 Experimental Designs

The experimental designs for laboratory fatigue and shear testing are summarized in Tables 3.1 and 3.2. Partial factorials were used in both studies to accommodate time and funding constraints. It should be noted that in the fatigue study all testing apart from that for temperature effect was conducted at one temperature, namely 20°C, while in the shear study all testing apart from that for temperature effect was conducted at one stress level, namely 70 kPa.

3.2. Introduction to Weibull Characterization of Test Results

Characterizing laboratory test results such as those from flexural fatigue tests and repeated shear tests by using Weibull curves has considerable advantages over characterizing them with the traditional approach (used in the first level analysis reports), which defines the test result based on one point in the damage process of the test, i.e., 50 Percent Loss of Stiffness (for fatigue) and Repetitions to 5 Percent Permanent Strain (for shear). For example, the Weibull approach for fatigue tests:

- Includes all stages of the damage process and crack development, including initiation and propagation.
- Permits comparison of each stage between different mixes, particularly when analyzing rubber- and polymer-modified mixes, which often have significantly different crack propagation performance compared with conventional mixes.

3.2.1 Definition of Three-Stage Weibull Curve for Fatigue

A three-stage Weibull fatigue curve is a three-stage stiffness deterioration curve representing flexural fatigue damage formulated by the Weibull distribution function.

Table 3.1: Experimental Design for Fatigue Laboratory Testing

Type of Fatigue Study	Compaction	Condition	Binder Type	Grading	Design AC (%)	Air Void (%)	Temp. (°C)	Strain (micro strain)	Replicates	Total Runs
Temperature Effect (90)	FMLC	None	AR4000	DG	5.0	6 ± 0.5	10, 20, 30	400, 700	3	18
			ARB	GG	8.0					18
			MAC15		7.4					18
			MB15		7.1					18
			MB4		7.2					18
Air-Void Content Effect (30) (Compared to Temperature Effect Specimens at 20°C)	FMLC	None	AR4000	DG	5.0	9 ± 1	20	400, 700	3	6
			ARB	GG	8.0					6
			MAC15		7.4					6
			MB15		7.1					6
			MB4		7.2					6
Aging Effect (20) (Compared to Temperature Effect Specimens at 20°C)	FMLC	Aging	AR4000	DG	5.0	6 ± 0.5	20	400, 700	2	4
			ARB	GG	8.0					4
			MAC15		7.4					4
			MB15		7.1					4
			MB4		7.2					4
Compaction Effect (20) (Compared to Temperature Effect Specimens at 20 C)	LMLC	None	AR4000	DG	5.0	6 ± 0.5	20	400, 700	2	4
			ARB	GG	8.0					4
			MAC15		7.4					4
			MB15		7.1					4
			MB4		7.2					4
Gradation Effect (12) (Compared to Compaction Effect LMLC specimens)	LMLC	None	MAC15	DG	6.0	6 ± 0.5	20	400, 700	2	4
			MB15		6.0					4
			MB4		6.3					4
FMLC — Field-mixed, laboratory compacted LMLC — Laboratory-mixed, laboratory compacted				DG — dense-graded GG — gap-graded						

Table 3.2: Experimental Design for Laboratory Shear Testing (RSST-CH)

Type of Shear Study	Compaction	Condition	Binder Type	Grading	Design AC (%)	Air-Void (%)	Temp (°C)	Stress (kPa)	Replicates	Total Runs
Temperature Effect (90)	FMLC	None	AR4000	DG	5.0	6 ± 0.5	45, 55	70, 100, 130	3	18
			ARB	GG	8.0					18
			MAC15		7.4					18
			MB15		7.1					18
			MB4		7.2					18
Air-Void Content Effect (20) (Compared to Temperature Effect Specimens at 45°C, 70 kPa)	FMLC	None	AR4000	DG	5.0	9 ± 1	45, 55	70	2	4
			ARB	GG	8.0					4
			MAC15		7.4					4
			MB15		7.1					4
			MB4		7.2					4
Aging Effect (20) (Compared to Temperature Effect Specimens at 45°C, 70 kPa)	FMLC	Aging	AR4000	DG	5.0	6 ± 0.5	45, 55	70	2	4
			ARB	GG	8.0					4
			MAC15		7.4					4
			MB15		7.1					4
			MB4		7.2					4
Compaction Effect (21) (Compared to Temperature Effect Specimens at 45°C, 70 kPa)	FMFC	Field Aged and Trafficked	AR4000	DG	5.0	6.3 ± 0.8	45	70	3	3
			MB4	GG	7.2					3
	LMLC	None	AR4000	DG	5.0	6 ± 0.5	45	70	3	3
			ARB	GG	8.0					3
			MAC15		7.4					3
			MB15		7.1					3
			MB4		7.2					3
Gradation Effect (9) (Compared to compaction effect LMLC specimens)	LMLC	None	MAC15	DG	6.0	6 ± 0.5	45	70	3	3
			MB15		6.0					3
			MB4		6.3					3

FMLC — Field-mixed, laboratory compacted
FMFC — Field-mixed, field compacted (cores from HVS test track)
LMLC — Laboratory-mixed, laboratory compact

DG — dense-graded
GG — gap-graded

The stiffness ratio (*SR*) at repetition *n*, which is defined as the ratio of stiffness at repetition *n* relative to the initial stiffness (determined after 50 repetitions), is utilized as an index for characterizing the fatigue damage or stiffness deterioration processes. The use of stiffness ratio has several advantages as an index, including:

- Stiffness is easy to measure both in the laboratory and in the field, and
- Stiffness is often utilized as an input for layered-elastic programs for pavement analysis, thus making it useful for programming fatigue performance simulations.

The stiffness deterioration curve obtained from the flexural controlled-deformation fatigue test, especially in the crack initiation phase, can be adequately expressed as a two-parameter, one-stage Weibull distribution function with the following form (Equation 3.1):

$$SR = \exp(-\alpha\, n^{\beta}) \text{ or } \ln(-\ln SR) = \ln\alpha + \beta \ln n \qquad \textbf{(3.1)}$$

where SR = the stiffness ratio,

n = loading repetitions,

α, β = the experiment-determined coefficients.

The one-stage Weibull equation does not appear to represent the damage process when:

- The fatigue test has a prolonged initial phase;
- The fatigue tests are conducted beyond a certain stiffness ratio threshold (such as the 50 Percent Reduction in Stiffness criterion) at which time the fatigue cracks start to propagate or at which time the fatigue damage slows down, as seen in certain mixes with modified binders.

Therefore, to describe the stiffness deterioration process in all three stages, an alternative function is necessary. One of the approaches that serves this purpose is the application of the two-stage Weibull distribution function suggested by Jiang (15), with extension to a three-stage Weibull distribution function (16). This extended distribution function has the following form:

$$\begin{cases} SR_1 = \exp\left(-\alpha_1 \cdot n^{\beta_1}\right), & 0 \le n < n_1 \\ SR_2 = \exp\left(-\alpha_2 \cdot (n-\gamma_1)^{\beta_2}\right), & n_1 \le n < n_2 \\ SR_3 = \exp\left(-\alpha_3 \cdot (n-\gamma_2)^{\beta_3}\right), & n_2 \le n < \infty \end{cases} \qquad \textbf{(3.2)}$$

That is,

$$\begin{cases} \ln\left(-\ln SR_1\right) = ln\alpha_1 + \beta_1 lnn, & 0 \le n < n_1 \\ \ln\left(-\ln SR_2\right) = \ln\alpha_2 + \beta_2 \ln(n-\gamma_1), & n_1 \le n < n_2 \\ \ln\left(-\ln SR_3\right) = \ln\alpha_3 + \beta_3 \ln(n-\gamma_2), & n_2 \le n < \infty \end{cases} \qquad \textbf{(3.3)}$$

The equation consists of ten parameters, namely α_1, α_2, α_3, β_1, β_2, β_3, γ_1, γ_2, n_1, and n_2 (Figure 3.1), and needs to comply with the following continuity conditions:

$$SR_1 = SR_2,\ when\ n = n_1 \tag{3.4}$$

$$\frac{\partial SR_1}{\partial n} = \frac{\partial SR_2}{\partial n},\ when\ n = n_1 \tag{3.5}$$

$$SR_2 = SR_3,\ when\ n = n_2 \tag{3.6}$$

$$\frac{\partial SR_2}{\partial n} = \frac{\partial SR_3}{\partial n},\ when\ n = n_2 \tag{3.7}$$

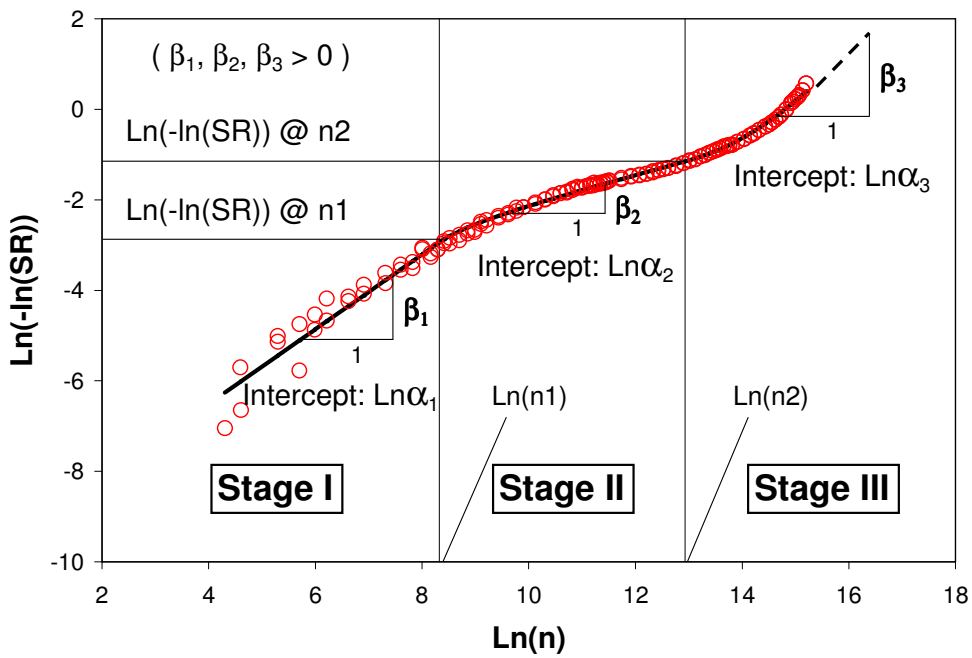

Figure 3.1: Three-stage Weibull curve.
Stage I: Heating and reaching of temperature equilibrium under initial repetitions; Stage II: Crack initiation developing; and Stage III: Crack propagating.

With a series of mathematical manipulations, for the given values α_1, α_2, α_3, β_1, β_2, and β_3, the four parameters n_1, γ_1, n_2, and γ_2 can be calculated sequentially as follows:

$$n_1 = \left[\frac{\alpha_2}{\alpha_1} \cdot \left(\frac{\beta_2}{\beta_1} \right)^{\beta_2} \right]^{\frac{1}{\beta_1 - \beta_2}} \tag{3.8}$$

$$\Rightarrow \gamma_1 = \left(1 - \frac{\beta_2}{\beta_1} \right) \cdot n_1 \tag{3.9}$$

$$\Rightarrow n_2 = \gamma_1 + \left[\frac{\alpha_3}{\alpha_2} \cdot \left(\frac{\beta_3}{\beta_2} \right)^{\beta_3} \right]^{\frac{1}{\beta_2 - \beta_3}} \tag{3.10}$$

$$\Rightarrow \gamma_2 = \left(1 - \frac{\beta_3}{\beta_2} \right) \cdot n_2 + \frac{\beta_3}{\beta_2} \cdot \gamma_1 \tag{3.11}$$

To fit the values of the parameters for a three-stage Weibull equation to a flexural controlled-deformation fatigue test using the Genetic Algorithm (GA), it is necessary to resolve the six fundamental parameters, α_1, β_1, α_2, β_2, α_3, and β_3. The parameters and fitness functions are defined following the GA procedure outlined by Tsai, et al. (17), as follows:

- Parameters: Weibull parameters $\ln\alpha_1$, $\ln\alpha_2$, $\ln\alpha_3$, β_1, β_2, and β_3
- Fitness functions: $RSS = \sum (y_i - \hat{y}_i)^2 = \min.$

  where: RSS is the residual sum of squares

  γ_1, is the measured $\ln(-\ln SR)$

  $\hat{y}_i$ is the fitted $\ln\left(-\ln \hat{SR}\right)$

The GA procedures for this problem include the following:

1. Specify empirically the ranges of parameters, $\ln\alpha_1$, $\ln\alpha_2$, $\ln\alpha_3$, β_1, β_2, and β_3.
2. Define a gene, which is a set of these six parameters that are generated randomly using the uniform distribution constrained by their specified ranges.
3. For each gene in a gene pool, calculate the derivative quantities, n_1, γ_1, n_2, and γ_2 and then evaluate the fitness function.
4. Rank the genes according to fitness, mate the ranked genes, abandon the bad genes, and then replace the discarded genes with new genes.
5. Repeat Steps 2 through Step 4 until the specified number of generations is reached. A systematic method for determining the initial estimate for the three-stage Weibull fitting is used. Figure 3.2(a) provides an example of a plot $\ln(-\ln(SR))$ against $\ln(n)$ for a field-mixed, laboratory-compacted (FMLC) AR4000-D mix with 8.6 percent air-void content tested at 10 Hz, 20°C, and 200 microstrain. The following steps are required to determine the parameters for the three-stage Weibull equation:
   - Obtain an initial parameter estimate with an *Excel*® spreadsheet.
   - Find the asymptotic regression lines for both Stages I and III and the regression line for Stage II in the plot of $\ln(-\ln(SR))$ against $\ln(n)$. These intercepts and slopes of linear regression lines are the initial estimates of $\ln\alpha_1$, $\ln\alpha_2$, $\ln\alpha_3$, β_1, β_2, and β_3 (Figure 3.2[b]).

- Use Equation 3.4 to calculate the n_1 and insert it into Equation 3.5 to obtain γ_1 and into Equations 3.6 and 3.7 to obtain parameters n_2 and γ_2.
- Plot the fitting result with the real data and change the values of the parameters if modification is necessary (Figure 3.2[c]).
- Fit with the genetic algorithm using an appropriate (e.g., *FORTRAN)* program (Figure 3.2[d])

The three-stage Weibull equation generally provides a satisfactory fitting, especially for Stage I, the reaching of temperature equilibrium under the initial repetitions, and Stage II, the crack initiation stage.

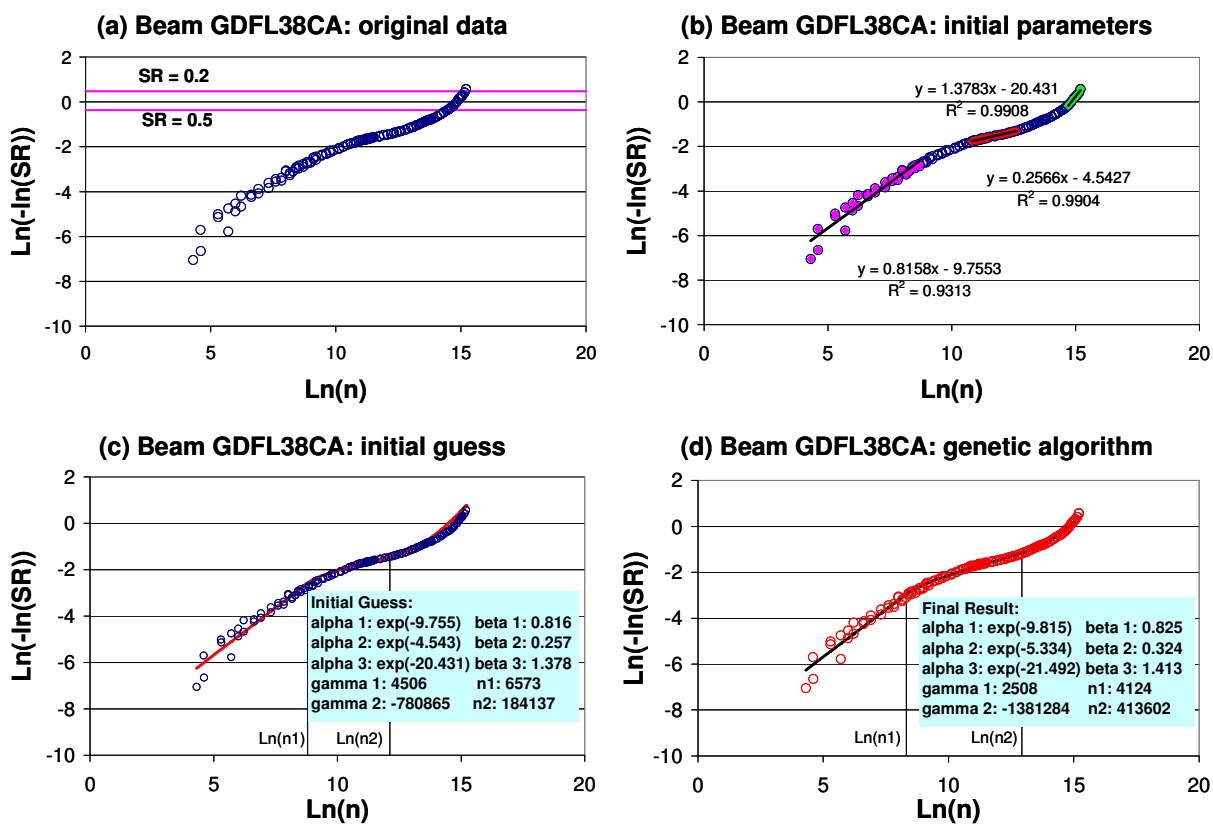

Figure 3.2: Parameter estimation of a three-stage Weibull equation.
(a) Original data, (b) initial parameters for $\ln\alpha_1$, $\ln\alpha_2$, $\ln\alpha_3$, β_1, β_2, and $\beta 3$,
(c) initial estimate, and (d) fitting with genetic algorithm.

In summary, the fatigue Weibull curve is fundamentally defined by six parameters, β_1, β_2, *and* β_3, $\ln\alpha_1$, $\ln\alpha_2$, and $\ln\alpha_3$, which are slopes and intercepts associated with different stages. The other four parameters, n_1, n_2, γ_1 and γ_2 can be derived from the six parameters. The parameter properties of the fatigue Weibull curves can be summarized as follows:

β_1, β_2, and $\beta_3 > 0$

$\ln\alpha_1$, $\ln\alpha_2$, and $\ln\alpha_3 < 0$

$$\begin{cases} \beta_2 < \beta_1 \text{ if and only if } \gamma_1 > 0 \\ \beta_2 > \beta_1 \text{ if and only if } \gamma_1 < 0 \end{cases}$$

$$\begin{cases} \beta_3 < \beta_2 \text{ if and only if } \gamma_2 > 0 \text{ (i.e., crack propagation has been suppressed)} \\ \beta_3 > \beta_2 \text{ if and only if } \gamma_2 < 0 \text{ (i.e., crack propagation occurs in stage III)} \end{cases}$$

It should be noted that Stage III is designated as the crack propagation stage, although mixes with modified binders often do not exhibit much crack propagation due to a very slow rate of fatigue damage.

3.2.2 Definition of Three-Stage Weibull Curve for Shear

The definition of a three-stage Weibull curve for shear is very similar to the definition of that for fatigue, except that Permanent Shear Strain (*PSS*) is utilized as the response variable to characterize the mix's rutting performance. The shear Weibull curve is generally a mirror image of a fatigue Weibull curve along the x-axis. The three-stage shear Weibull curve is defined in the following:

$$\begin{cases} PSS_1 = \exp\left(-\alpha_1 \cdot n^{\beta_1}\right), & 0 \le n < n_1 \\ PSS_2 = \exp\left(-\alpha_2 \cdot (n-\gamma_1)^{\beta_2}\right), & n_1 \le n < n_2 \\ PSS_3 = \exp\left(-\alpha_3 \cdot (n-\gamma_2)^{\beta_3}\right), & n_2 \le n < \infty \end{cases} \quad \textbf{(3.12)}$$

That is,

$$\begin{cases} \ln\left(-\ln PSS_1\right) = \ln\alpha_1 + \beta_1 \ln n, & 0 \le n < n_1 \\ \ln\left(-\ln PSS_2\right) = \ln\alpha_2 + \beta_2 \ln(n-\gamma_1), & n_1 \le n < n_2 \\ \ln\left(-\ln PSS_3\right) = \ln\alpha_3 + \beta_3 \ln(n-\gamma_2), & n_2 \le n < \infty \end{cases} \quad \textbf{(3.13)}$$

The equation consists of the same ten parameters (Figure 3.3) and needs to comply with the following continuity conditions:

$$PSS_1 = PSS_2, \text{ when } n = n_1 \quad \textbf{(3.14)}$$

$$\frac{\partial PSS_1}{\partial n} = \frac{\partial PSS_2}{\partial n}, \text{ when } n = n_1 \quad \textbf{(3.15)}$$

$$PSS_2 = PSS_3, \text{ when } n = n_2 \quad \textbf{(3.16)}$$

$$\frac{\partial PSS_2}{\partial n} = \frac{\partial PSS_3}{\partial n}, \text{ when } n = n_2 \quad \textbf{(3.17)}$$

The same Genetic Algorithm (GA) used in the fitting of a fatigue Weibull curve can also be applied to resolve the six fundamental parameters that define a three-stage shear Weibull curve, with the equation

providing a satisfactory fitting. As an example, Figure 3.4 illustrates the fitting results for shear tests at 45°C and 100 kPa for various field-mixed, laboratory-compacted (FMLC) mixes.

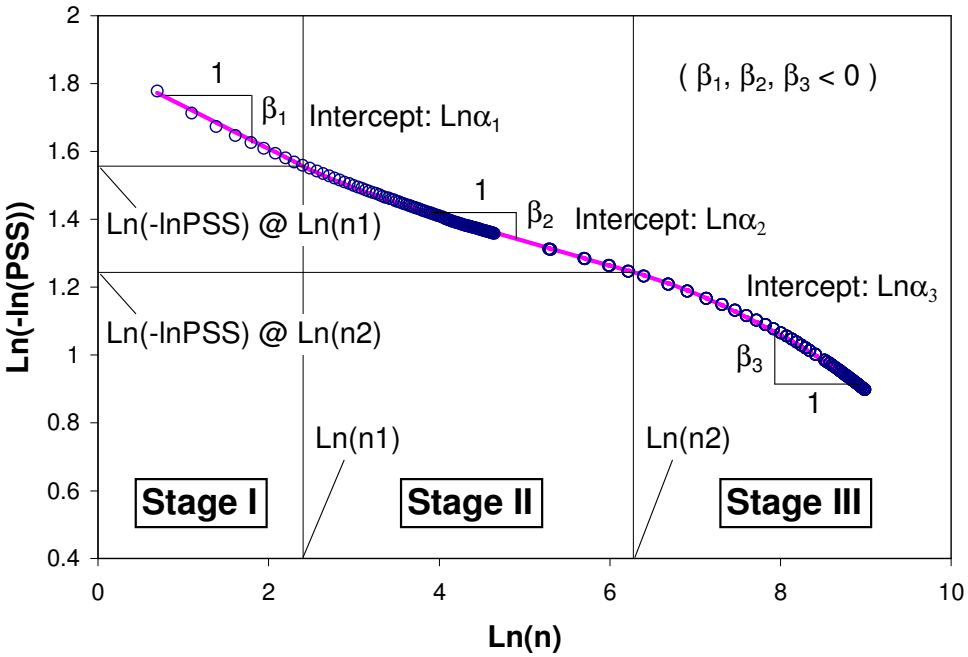

Figure 3.3: Definition of a shear Weibull curve in three stages.

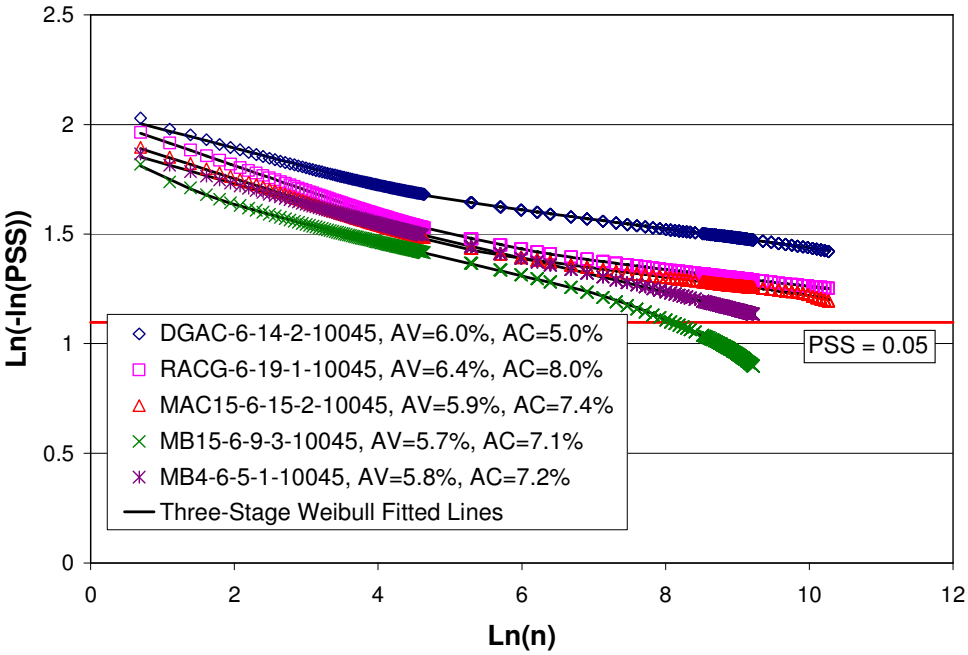

Figure 3.4: Example of three-stage shear Weibull-fitted curves of various mix types.
(FMLC, Temp = 45°C, Load = 100 kPa)

The parameter properties of the shear Weibull curves can be summarized in the following:

$\beta_1, \beta_2, \beta_3 < 0$

$\ln\alpha_1$, $\ln\alpha_2$, and $\ln\alpha_3 > 0$

$$\begin{cases} |\beta_2| < |\beta_1| \ \textit{if and only if} \ \gamma_1 > 0 \\ |\beta_2| > |\beta_1| \ \textit{if and only if} \ \gamma_1 < 0 \end{cases}$$

$$\begin{cases} |\beta_3| < |\beta_2| \ \textit{if and only if} \ \gamma_2 > 0 \ \textit{(i.e., retarded shear damage at stage III)} \\ |\beta_3| > |\beta_2| \ \textit{if and only if} \ \gamma_2 < 0 \ \textit{(i.e., accelerated shear damage at stage III)} \end{cases}$$

3.2.3 Types of Weibull Curves

Based on the laboratory test data, four general shapes of fatigue and shear Weibull curves can be categorized, as shown in Figures 3.5 and 3.6. Curve shape is used as a factor response variable (four factor levels) in tree-based modeling, which permits analysis at more than two levels.

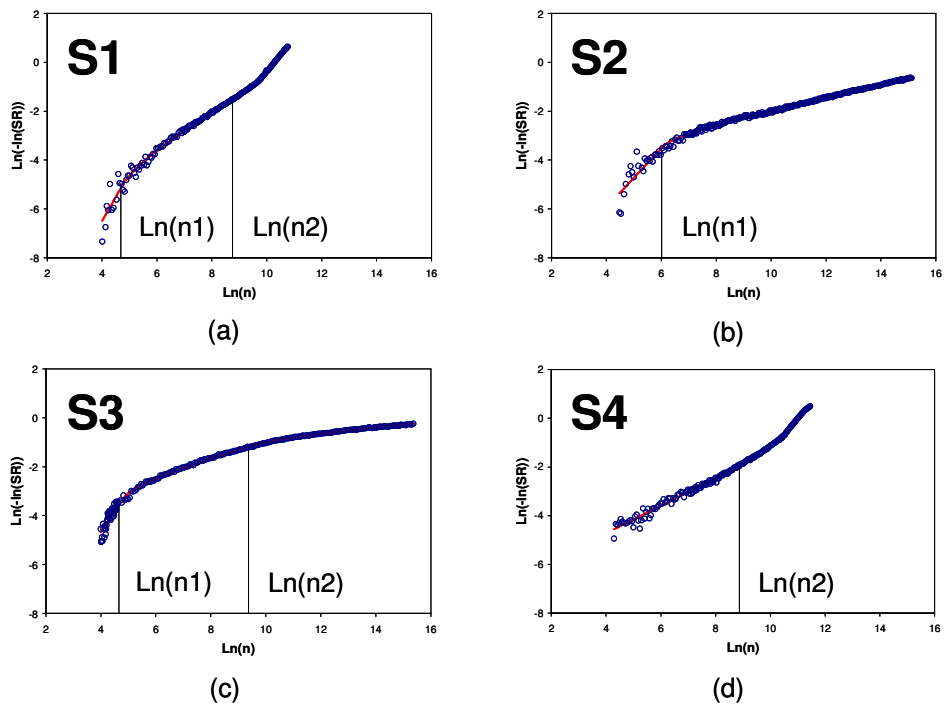

Figure 3.5: Schematic plots of various shapes of fatigue stiffness deterioration curves.
(a) Shape S_1, (b) shape S_2, (c) shape S_3, and (d) shape S_4.

In Figure 3.5, the typical fatigue Weibull curve for conventional asphalt mixes with crack initiation and crack propagation is shown in shape S_1. Shape S_2 is a curve with no clear transition between Stage II and Stage III ($\beta_2 = \beta_3$). Shape S_3 illustrates the retarded fatigue damage at Stage III ($\beta_3 > \beta_2$) typical of rubber- and polymer-modified mixes, while shape S_4 resembles the shape S_1, but without a clear stage transition between Stages I and II.

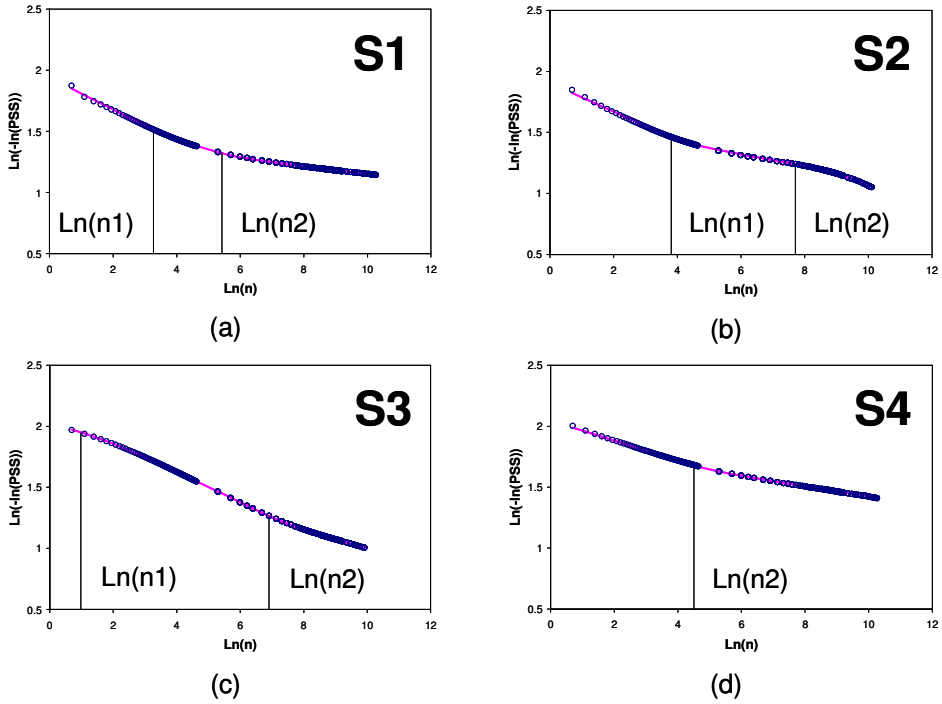

Figure 3.6: Schematic plots of various shapes of RSST permanent shear strain accumulation curves
(a) Shape S_1, (b) shape S_2, (c) shape S_3, and (d) shape S_4.

Figure 3.7 plots the fatigue test result in terms of Weibull curves and stiffness ratio against load repetitions in a linear scale for three cases. The figure demonstrates the necessity of using three-stage Weibull equations to describe a flexural controlled-deformation fatigue test. As depicted, if the test results are fitted only by the Stage II parameters, the fatigue life for $\beta_3 < \beta_2$ and $\beta_3 > \beta_2$ will be under- and overestimated respectively. Similarly, Figure 3.8 plots the shear test result in terms of Weibull curves and the permanent shear strain against load repetitions. If the test result is fitted only by the Stage II parameters, the Cycles to 5 Percent Permanent Shear Strain for $|\beta_3|<|\beta_2|$ and $|\beta_3|>|\beta_2|$will be under- and overestimated respectively.

The stages in the Weibull curve for repeated shear tests are not identified with names, unlike the initiation and propagation stages in the fatigue curve. The various stages in shear deformation are controlled by hardening processes in the mix under repeated shear loading at constant height.

In Figure 3.6, the typical shear Weibull curve for accelerated shear damage ($|\beta_3|>|\beta_2|$) at Stage III represents shape S_2, which occurred at a frequency of 84 tests out of 177 tests. Shape S_1 was the second most common shape (75 tests out of 177 tests), representing retarded shear damage ($|\beta_3|<|\beta_2|$) at Stage III (i.e., the permanent shear strain accumulation rate of Stage III is less than that of Stage II). Shape S_3

appears as a reverse s-shaped curve with retarded shear damage at Stage III. Shape S_4 resembles shape S_1 but without stage transition between Stage I and II (i.e., $|\beta_1|=|\beta_2|$).

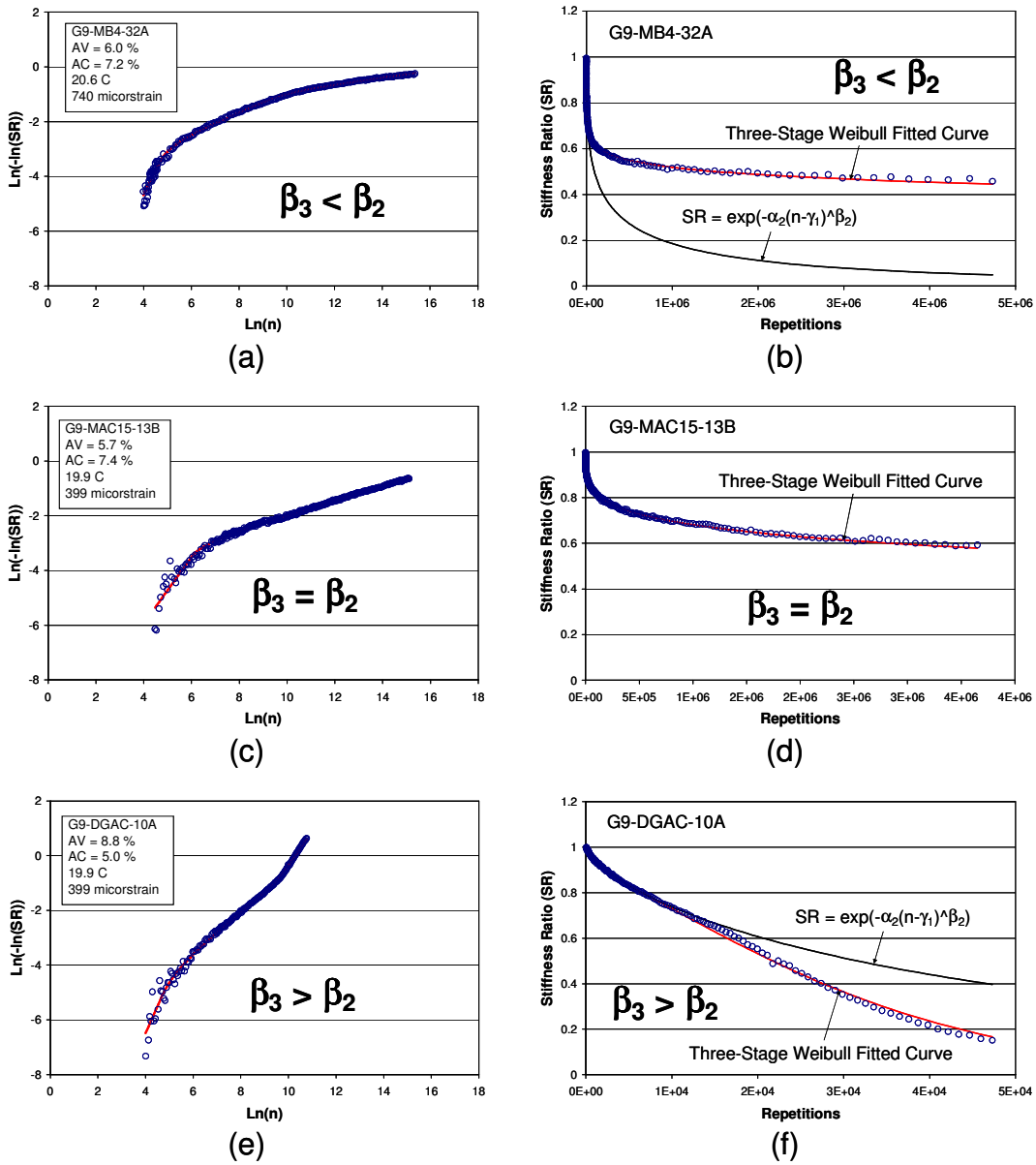

Figure 3.7: Three-stage Weibull equation for a flexural controlled-deformation fatigue test.

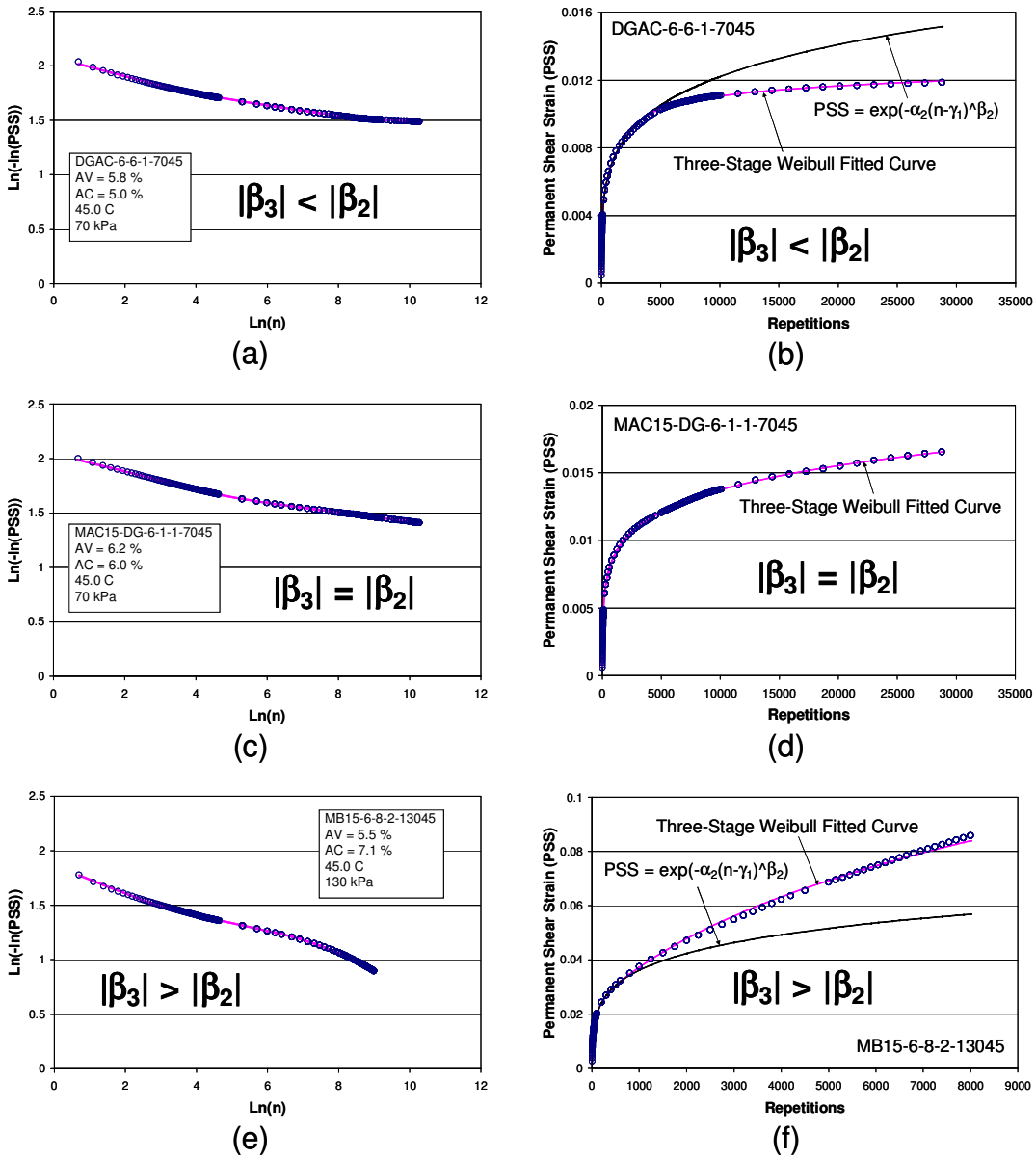

Figure 3.8: Using three-stage Weibull equations to describe damage (*PSS*) in a repeated shear test.

3.3. Tree-Based Regression Modeling for Three-Stage Fatigue Weibull Parameters

3.3.1 Introduction

Tree-based modeling, which was developed by Breiman et al. (18) in the early 1980s, is a technique to explore and evaluate appropriate data structures. Tree-based models provide an alternative not only to the linear and additive models for regression problems, but also to the linear logistic and additive logistic models for classification problems.

Tree-based models are fitted based on a binary recursive partitioning algorithm applied to a data set until it is successively split into increasingly homogeneous subsets. The response variables and covariates can be either a factor or numeric; accordingly, the trees are named classification or regression trees. The tree-based model is an appropriate means of analysis for factor response variables at more than two levels.

3.3.2 Fitting with a Tree-Based Model: An Example

To explain the tree-based model more clearly, the full data set of laboratory fatigue results (172 tests) is used in the following demonstration example. The response variable is the natural logarithm of initial stiffness (ln*stif*) and the covariates utilized are binder type (*binder*), percent air-void content (*av*), gradation (*grad*), conditioning (either aging or non-aging) (*cond*), compaction (*comp*), temperature in °C (*temp*), and strain level in natural logarithm (ln*stn*). Numeric response and a mix of factorial and numerical covariates are included.

Figure 3.9 is a dendrogram used to display a tree-based model relating initial stiffness to its associated covariates. It should be noted that the strain level and air-void content covariate was not sufficiently significant to include in the model. Similarly, oven aging was excluded from the comparable exercise using the shear data. In order to predict initial stiffness, the path from the top node of the tree, known as the root, is followed to a terminal node, known as a leaf, according to the rules, known as splits, at the interior nodes.

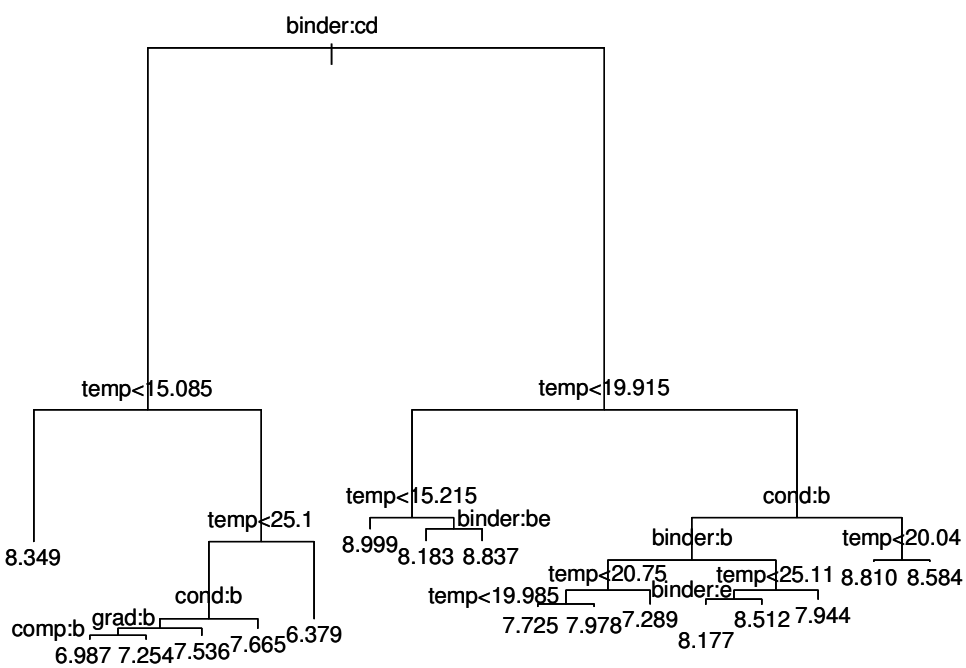

Figure 3.9: Dendrogram with split rules of initial stiffness (ln*stif*).

The split rules have formats such as *binder:cd*, *cond:b*, or *temp<15.085*. The binder category covariate has five levels and conditioning has two levels as listed in alphabetical order as follows:

```
> levels(xalltree$binder)
[1] "ar4000" "mac15"  "mb15"   "mb4"    "rac"
      (a)      (b)      (c)      (d)      (e)
> levels(xalltree$cond)
[1] "aging" "none"
      (a)     (b)
> levels(xalltree$comp)
[1] "fmlc" "lmlc"
      (a)    (b)
> levels(xalltree$grad)
[1] "dg" "gg"
     (a)  (b)
>
```

The *binder:cd* at root representing the MB15-G (c) and MB4-G (d) mixes will take the left path; the *cond:b*, representing the no-aging also takes the left path. As depicted, the left path has to be taken if the split rule is satisfied regardless of whether the split rules contain a category or a numerical covariate. The entire tree structure for predicting initial stiffness (ln*stif*) is provided in Appendix A.

Tree-based models can be analyzed through residual plots similar to the approach used for linear regression modeling. Examples for fatigue (initial stiffness) and shear (Cycles to 5 Percent Permanent Shear Strain) are shown in Figures 3.10 and 3.11, respectively. Figures 3.10(a) and 3.11(a) plot the residuals against fitted values and show no strong patterns. Figures 3.10(b) and 3.11(b) are normal probability plots of residuals, which are close to the line. Figure 3.10(c) presents a histogram with one mode (peak value) and a slightly unsymmetrical shape of residual distribution which is slightly skewed to the right, while Figure 3.11(c) presents a histogram with one mode (peak value) and a symmetrical bell shape of residual distribution. Figures 3.10(b) and 3.10(c) show possible outliers in the data set, while none of the plots in Figure 3.11 indicate outliers. The plots suggest that the modeling is appropriate.

The tree-based modeling suggested the following results for the fatigue analysis example, all of which are expected:

- According to the dendrogram, the lowest stiffness (~ exp(6.379) = 590 MPa) occurred at a temperature of 30°C for MB15-G and MB4-G mixes, while the highest average stiffness (~ exp(8.999) = 8,100 MPa) was measured at a temperature of 10°C for the AR4000-D, RAC-G, and MAC15-G mixes.
- Viewed from the vertical distance between nodes, the binder covariate was the most significant covariate determining stiffness. Temperature was the next most significant covariate.
- Aging generally increased the stiffnesses for all five mixes.

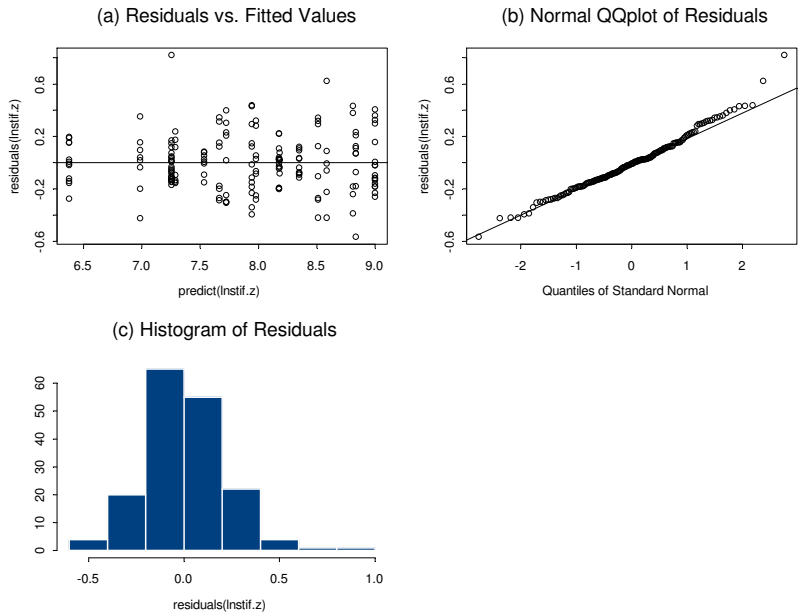

Figure 3.10: Examples of residual plots of initial stiffness.
(a) Residuals versus fitted values of ln*stif* tree model; (b) normal probability plot of residuals of ln*stif* tree model; (c) histogram of residuals of ln*stif* tree model.

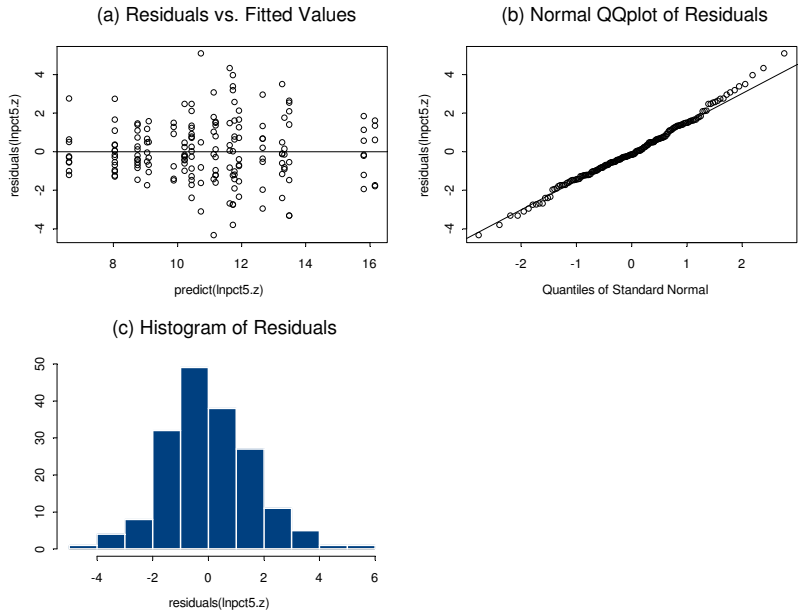

Figure 3.11: Examples of residual plots of permanent strain.
(a) The histogram of residuals of ln*pct5* tree model; (b) the normal probability plot of residuals of ln*pct5* tree model; (c) the residuals versus fitted values of ln*pct5* tree model.

For the analysis of shear, a similar exercise revealed that:

- The lowest number of Cycles to 5 Percent Permanent Shear Strain (~ exp(6.63) = 757) occurred at a temperature of 55°C and a stress level of 130 kPa for MAC15-G, MB15-G, and MB4-G mixes.

The highest number of Cycles to 5 Percent Permanent Shear Strain (~ exp(16.16) = 10 million) occurred at a temperature of 45°C and air-void content of less than 5.8 percent for the AR4000-D and MAC15-G mixes.

- Temperature was the most significant covariate determining permanent shear strain (ln*pct5*). The binder and stress covariates were the next most significant.

The vertical position of a node pair in a dendrogram is a function of the importance of the parent split. In certain cases, the long-distance dendrograms render it difficult to clearly display the split rules on the nodes. Hence, if a complex tree is encountered, the dendrogram can be presented in two ways:

- The original dendrogram without split rules as shown in Figure 3.12(a), and
- The dendrogram with split rules but at a uniform distance among nodes (Figure 3.12[b]).

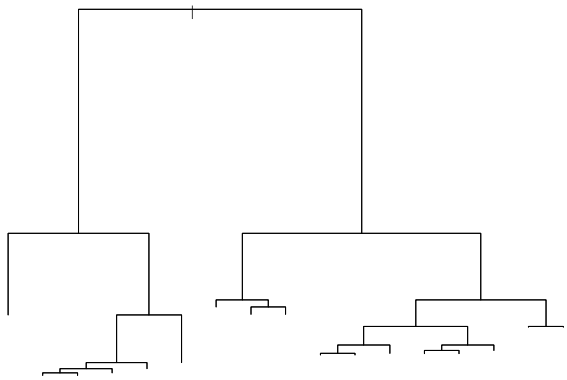

(a)

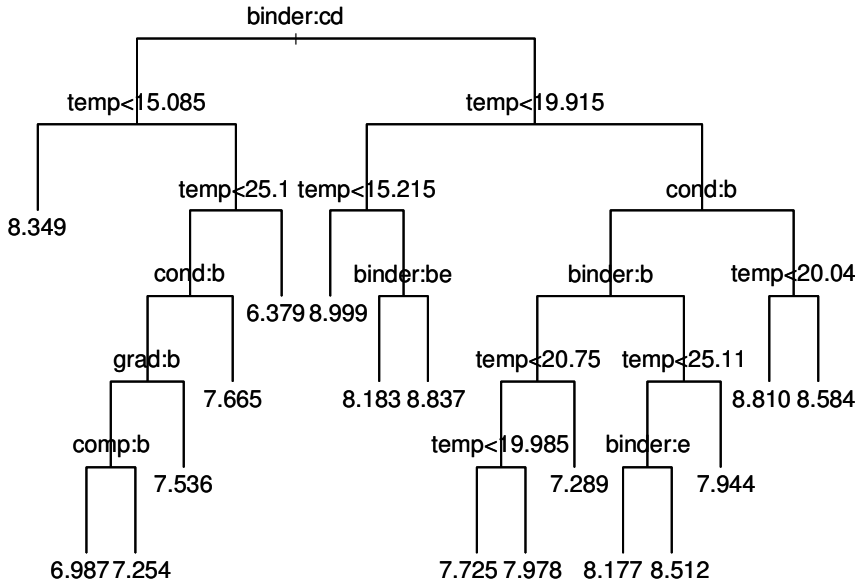

(b)

Figure 3.12: Typical dendogram representations.
(a) Dendrogram without split rules of initial stiffness (ln*stif*);
(b) dendrogram with split rules of ln*stif*, and without vertical distance reference.

Pruning the tree is sometimes necessary if a parsimonious description of the data structure is required. However, simplification of the tree should not sacrifice goodness-of-fit. The pruned dendrogram of initial stiffness is shown in Figure 3.13.

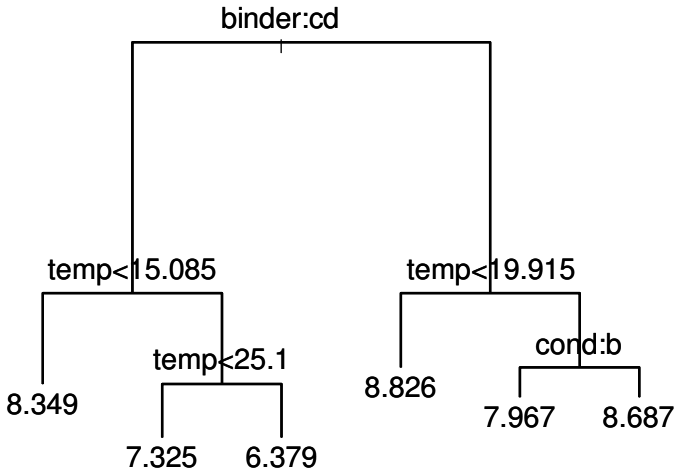

Figure 3.13: Pruned dendrogram of initial stiffness (ln*stif*).

3.4. Weibull Parameters and Fatigue Performance

3.4.1 Weibull Curves of Modified Binder Fatigue Results

The laboratory fatigue test results and associated Weibull-fitted curves are presented in Tables A.1 to A.9 and Figures A.1 to A.33 in Appendix A.

The selected Weibull curves provided in Figure 3.14 show that different deterioration patterns were obtained for the different mixes, especially at Stage III. As can be seen in Figure 3.14, the typical AR4000-D mix has an S_1 shape, with an accelerated damage rate in the propagation stage (Stage III), resulting in the mix reaching 10 percent of its original stiffness (0.10 SR) before all other mix types. The RAC-G mix has an S_2 shape with a greatly reduced propagation rate compared with the AR4000-D. The other three mixes (MB4-G, MB15-G, and MAC15-G) all have typical S_3 shapes, with crack propagation slowing on the curve with continuing repetitions, to the extent that they may never lose 90 percent of the initial stiffness (0.1 SR) under the testing conditions. Generally, the fitting of a three-stage Weibull equation to the results is satisfactory.

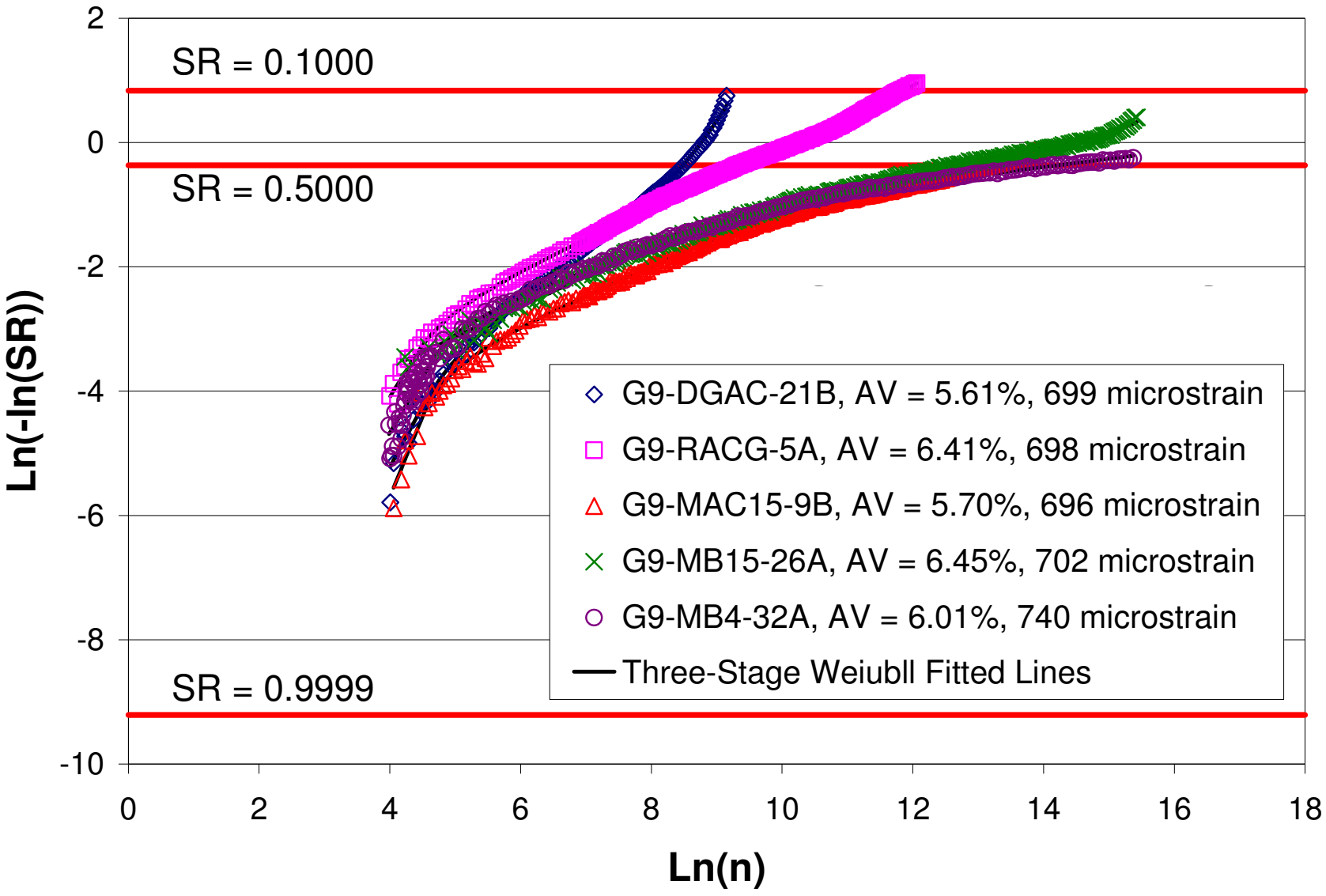

Figure 3.14: Typical Weibull curves for Reflective Cracking Study mixes.
20°C and 700 microstrain.

3.4.2 Tree-Based Regression/Category Modeling

The following Weibull parameters, response variables, and factor levels were considered in the tree-based regression and category modeling phase of the analysis:

- Weibull parameters investigated (defined in Figure 3.3):
  - $\ln\alpha_1$, β_1, $\ln n_1$, $sign(\gamma_1)\ln(|\gamma_1|)$, $\ln\alpha_2$, β_2, $\ln n_2$, $sign(\gamma_2)\ln(|\gamma 2|)$, $\ln\alpha_3$, β_3, srn_1 and srn_2.
- Fatigue response variables investigated:
  - Initial stiffness (ln*stif*), phase angle (*pa*), fatigue life (ln*Nf*), and Weibull curve shape (*shape*).
- Factor levels investigated:
  - Binder type (*binder*): (a) AR4000 (b) MAC15 (c) MB15 (d) MB4, and (e) ARB
  - Compaction (*comp*): (a) FMLC and (c) LMLC
  - Conditioning (*cond*): (a) aging and (b) none
  - Gradation (*grad*): (a) DG and (b) GG

Pruned dendrograms for the laboratory fatigue results are presented in Figure A.34 in Appendix A. Only the pruned trees with three (or more) levels are shown. The full dendrogram, the printed full tree structure, and the residual analysis are not included. A summary of pertinent findings follows:

- **Initial Stiffness (ln*stif*)**

  The initial stiffness is defined as the stiffness at the 50th load repetition. The ln*stif* is highly correlated with the phase angle and can be regarded as an index of mix rheology.
  - The initial stiffnesses of the MB4-G and MB15-G mixes are mainly a function of temperature.
  - Aging begins to have an effect on initial stiffness at intermediate and high temperatures. The initial stiffness of the AR4000-D, MAC15-G, and RAC-G mixes is not influenced by aging at low temperatures.
- **Phase Angle (*pa*)**

  The phase angle is the initial phase angle at the 50th load repetition. The *pa* is highly correlated with the ln*stif* and thus also provides an index of the mix rheology.
  - At low temperature, no apparent difference of phase angles was noted for the five mixes.
  - At intermediate and high temperatures, the phase angles of MB15-G and MB4-G mixes are higher than those of the AR4000-D, MAC15-G, and RAC-G mixes.
  - The average phase angle of the MB15-G and MB4-G mixes could be as high as 57.6 degrees.
- **Fatigue Life (ln*Nf*)**

  The conventional definition of fatigue life is the accumulated load repetitions until a 50 percent reduction of the initial stiffness is reached. The ln*Nf* is a conventional performance index that reflects the fatigue-resistant capacity of asphalt mixes.

- As expected for mixes with modified binders, the binder type had a larger influence than strain level, and becomes the most significant factor affecting fatigue life.

- **Shape (*shape*)**
- The shapes of Weibull fatigue curves are defined in Figure 3.1. This category variable classifies the mix stiffness deterioration process with emphasis on whether the crack propagation occurs in Stage III. Shapes S_1 and S_3 are the dominant shapes as shown in Table 3.3. The predominance of S_1 decreases and the predominance of S_3 increases in the order of AR4000, ARB, MAC15, MB15, and MB4.
  - The shape of the fatigue Weibull curves are mainly determined by binder type, followed by temperature.

Table 3.3: Summary of Shape Counts for Each Mix Type for Fatigue.

Binder	Shape			
	S_1	S_2	S_3	S_4
AR4000	**27**	0	2	3
ARB	**23**	1	8	0
MAC15	**22**	4	10	0
MB15	12	6	**18**	0
MB4	1	0	**35**	0
∑	*85*	*11*	*73*	*3*

- **Stage I Intercept and Slope ($\ln\alpha_1$, β_1, and $\ln n_1$)**

  The definitions of these Stage I parameters are shown in Figure 3.1. They indicate the fatigue damage rate and duration at Stage I.
  - The pruned dendrograms show that $\ln\alpha 1$ and β_1 are not sensitive to binder type. The same observation is made from the summary boxplots.

- ***sign*(γ_1)ln(|γ_1|)**

  Equation 3.9 defines γ_1. The magnitude of γ_1 indicates the degree of slope change from Stage I to Stage II.
  - The positive values of γ_1 for all the mix types indicate that $\beta_2 < \beta_1$. Binder type and strain level have the most influence in determining the γ_1 value.

- **Stage II Intercept and Slope ($\ln\alpha_2$, and β_2)**

  These two parameters indicate the fatigue damage rate at Stage II. Increasing values of β_2 are associated with faster development of fatigue damage in the crack initiation stage.
  - These two parameters are highly negative-correlated with a correlation -0.9. The pruned dendrograms show that the binder type is far more significant than other factors such as strain level, temperature, and air-void content.

- **Stage II/III Separation Point (lnn_2)**
  - At a strain level of 700 microstrain, the separation points between the initiation and propagation stages of AR4000-D and MB4-G mixes are mainly affected by gradation type, with the average n_2 value of the gap gradation (~ exp(9.256) = 10,470) greater than that of the dense gradation (~ exp(7.709) = 2,228).
  - For the MAC15-G, MB15-G, and RAC-G mixes, at strain level of 700 microstrain, the lnn_2 values are mainly affected by air-void content. A larger air-void content ($av > 6.4$ percent) resulted in a larger average n_2 value (~ exp(10.57) = 38,950) compared with the average n_2 (~ exp(9.45) = 12,700) obtained with a lower air-void content.
  - At strain level of 400 microstrain, the lnn_2 values are determined by the sensitivity to temperature of each mix.
- ***sign*(γ_2)ln(|γ_2|)**

  Equation 3.11 defines γ_2. The magnitude of γ_2 indicates the degree of slope change from Stage II to Stage III.
  - Based on the premise that if $\gamma_2 > 0$, then fatigue damage in Stage III appears retarded, indicating little crack propagation, and if $\gamma_2 < 0$, then crack propagation develops in Stage III, the dendrogram shows that the MB4-G mixes consistently exhibit retarded fatigue damage regardless of the testing conditions.
  - The AR4000-D mixes always developed crack propagation.
  - The RAC-G, MAC15-G, and MB15-G mixes presented retarded fatigue damage only at 30°C. At temperatures other than 30°C, crack propagation will occur.
- **Stage III Intercept and Slope (lnα_3 and β_3)**

  These two parameters indicate the fatigue damage rate at Stage III. If $\beta_3 > \beta_2$, then crack propagation occurs in Stage III. If $\beta_3 < \beta_2$, then crack propagation has been suppressed in Stage III.
  - These two parameters are also highly negative-correlated with a correlation -0.97 and mainly determined by binder type.
- **Stage I Stiffness Ratio (srn_1)**

  The srn_1 indicates the fatigue damage that has been accumulated at the end of Stage I.
  - Generally, the reductions of stiffness ratios for the mixes are no more than six percent at the end of Stage I.
- **Stage II Stiffness Ratio (srn_2)**

  The srn_2 indicates the fatigue damage that has been accumulated at the end of Stage II.

- The average stiffness ratio value at n_2 could be as high as 0.87 at 10°C and 400 microstrain for all mixes, and could be as low as 0.43 at 10°C and 700 microstrain for AR4000-D, MB15-G, and RAC-G mixes.

Table 3.4 summarizes the first three levels of significant covariates for the conventional response variables and the three-stage Weibull parameters of fatigue testing results. The following observations are noted from the table:

- Binder type followed by strain level, temperature, and air void content are generally the most significant factors influencing fatigue performance and defining the shape of the fatigue Weibull curve.
- At Stage I of the fatigue Weibull curve, the stiffness deterioration depends on the strain level rather than the binder type, whereas at Stages II and III the stiffness deterioration is mainly dependent on the binder type.

Table 3.4: Summary of the 1st-, 2nd-, and 3rd-Level Covariates for Fatigue Tree Modeling

Parameters	1st Level	2nd Level	3rd Level
ln*stif*	*binder*	*temp*	*temp, cond*
pa	*temp*	*binder*	*temp*
ln*Nf*	*binder*	ln*stn*	*binder, temp*
$\ln\alpha_1$	ln*stn*	ln*stn*	*binder, grad, temp*
β_1	ln*stn*	ln*stn, binder*	*temp, grad,* ln*stn*
$\ln n_1$	ln*stn*	*grad,* ln*stn*	*temp, binder*
$sign(\gamma_1)\ln(\lvert\gamma_1\rvert)$	*binder*	ln*stn*	*av, binder, temp*
$\ln\alpha_2$	*binder*	*temp*	*av, binder*
β_2	*binder*	ln*stn, av*	*binder*
$\ln n_2$	*binder*	ln*stn*	*temp, grad, av*
$sign(\gamma_2)\ln(\lvert\gamma_2\rvert)$	*binder*	*temp*	*binder*
$\ln\alpha_3$	*binder*	ln*stn, temp*	*binder, av*
β_3	*binder*	*temp,* ln*stn*	*binder, av, grad*
srn_1	*binder*	*temp, binder*	*temp, av,* ln*stn*
srn_2	ln*stn*	*temp, binder*	*binder, temp, av*
shape	*binder*	*av, binder*	*temp*

3.4.3 Summary Boxplots for Fatigue

Based on the findings summarized in Table 3.4, summary boxplots for fatigue can be categorized according to mix type. Each mix type is subcategorized with strain levels and temperatures. The summary boxplots of the Weibull parameters inspected include: $\ln\alpha_1$, β_1, $\ln\alpha_2$, β_2, $\ln\alpha_3$, β_3, $\ln(\beta_3/\beta_2)$ $sign(\gamma_1)\ln(\lvert\gamma_1\rvert)$, $sign(\gamma_2)\ln(\lvert\gamma_2\rvert)$, and $SR@n_2$. In addition to these parameters, the summary boxplots of fatigue life (ln*Nf* [SR = 0.5]) based on the results of all 172 fatigue tests are presented.

The γ_1 and γ_2 parameters are expressed as $sign(\gamma_1)\ln(\lvert\gamma_1\rvert)$ and $\mathrm{sign}(\gamma_2)\ln(\lvert\gamma_2\rvert)$ in order to preserve the sign, which determines the shape of the Weibull curve, and to perform a natural logarithm transformation to

limit the effect of variation of the values of γ_1 and γ_2 in a linear scale. The larger the magnitudes of $|\gamma_1|$ and $|\gamma_2|$ values, the sharper the stage transition. The $\ln(\beta_3/\beta_2)$ parameter is used to inspect the transition from Stage II to Stage III as follows:

If $\beta_3 > \beta_2$, then $\ln(\beta_3/\beta_2) > 0$; this indicates significant crack propagation and is related to an S_1 shape (Figure 3.5);

If $\beta_3 < \beta_2$, then $\ln(\beta_3/\beta_2) < 0$; this indicates little or no crack propagation and is related to an S_3 shape;

If $\beta_3 = \beta_2$, then $\ln(\beta_3/\beta_2) = 0$; this indicates reduced crack propagation related to an S_2 shape.

The summary boxplots of fatigue life (ln*Nf* [SR = 0.5]) in Figure 3.15 illustrates that, as expected, fatigue life increases as temperature increases and strain level decreases. The ranking of fatigue life, from best to worst, for the mixes tested followed the order, MB4-G > MAC15-G > MB15-G > RAC-G > AR4000-D.

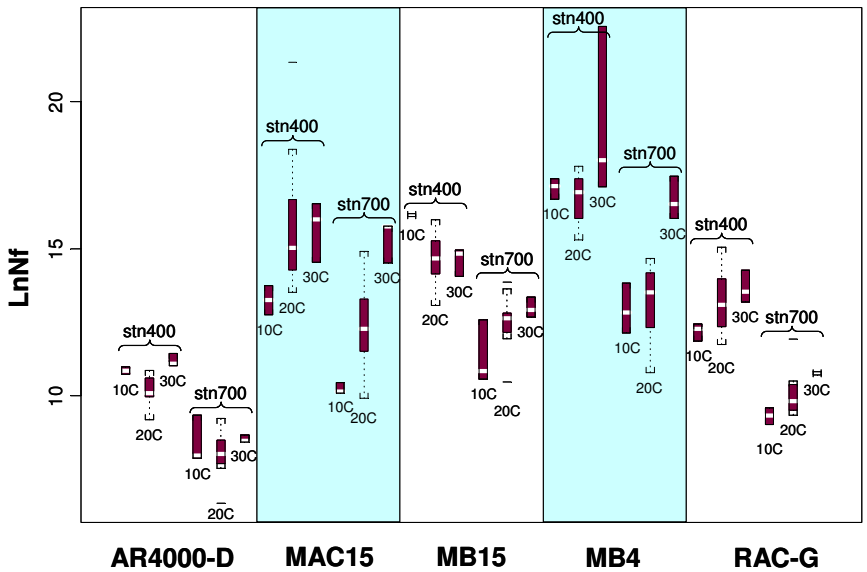

Figure 3.15: Summary boxplots of fatigue life (ln*Nf*).
(stn400 = 400 µstrain, stn700 = 700 µstrain)

Comparing the boxplots in Figures 3.16 and 3.17 reveals that the intercepts and slopes at Stage I are mainly dependent on temperature and strain level rather than on mix type. The higher strain levels and temperatures result in steeper slopes which are associated with more negative intercepts. However, the slopes and intercepts at Stage II and III in Figures 3.18 through 3.21 indicate that these values are affected by mix type more than by strain level and temperature and that the fundamental parameters, $\ln\alpha_2$, β_2, $\ln\alpha_3$, and β_3, at Stage II and III might be more useful for characterizing fatigue performance of the various mixes. Further discussion regarding the parameters that best identify fatigue performance is provided in Section 3.7. Figures 3.20 through 3.23 also show that:

- The intercepts $\ln\alpha_2$ and $\ln\alpha_3$ appear to be mix- and temperature-dependent rather than strain-dependent;
- For each mix, lower strain levels and higher temperatures generally result in smaller Stage II slope (β_2) values that correspond to larger Stage II intercept ($\ln\alpha_2$) values, and
- The trends observed in Stage II are also apparent at Stage III; with the exception of the AR4000-D mixes, which have an opposite trend when compared with the other four mixes.

In the summary boxplots of $\ln(\beta_3/\beta_2)$ (Figure 3.22), the following observations are made:

- MB4-G mixes always present retarded fatigue damage at Stage III, indicating no crack propagation;
- For the RAC-G and MAC15-G mixes, retarded fatigue damage only occurs at 30°C regardless of strain level;
- For the MB15-G mixes, crack propagation occurs only at 10°C;
- For the AR4000-D mixes, crack propagation always develops at Stage III, and
- For the MAC15-G mixes, the variations of $\ln(\beta_3/\beta_2)$ values at 20°C are relatively large compared with the other four mixes. This suggests that the MAC15-G mixes are more susceptible to the effects of the air-void content, aging, compaction, and gradation effects, which were all tested at 20°C (excluding tests for temperature effect).

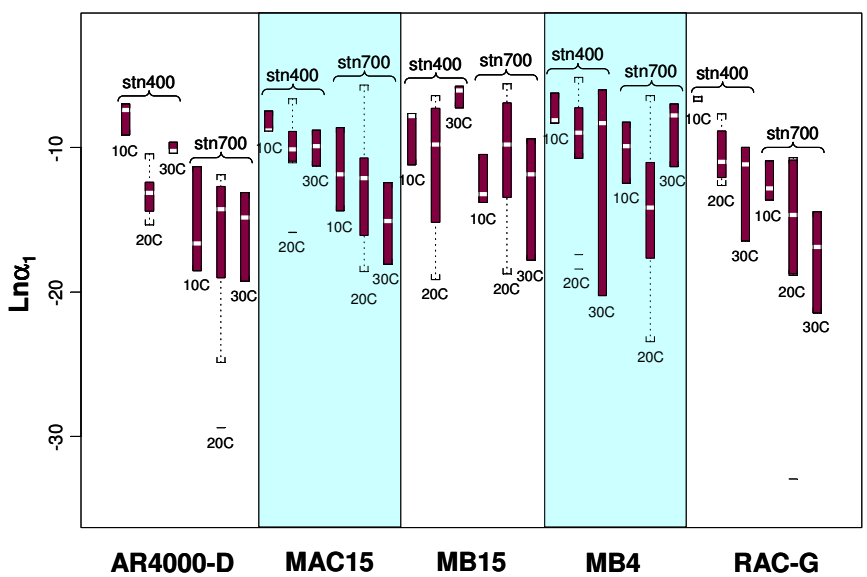

Figure 3.16: Summary boxplots of the fatigue three-stage Weibull parameter $\ln\alpha_1$.

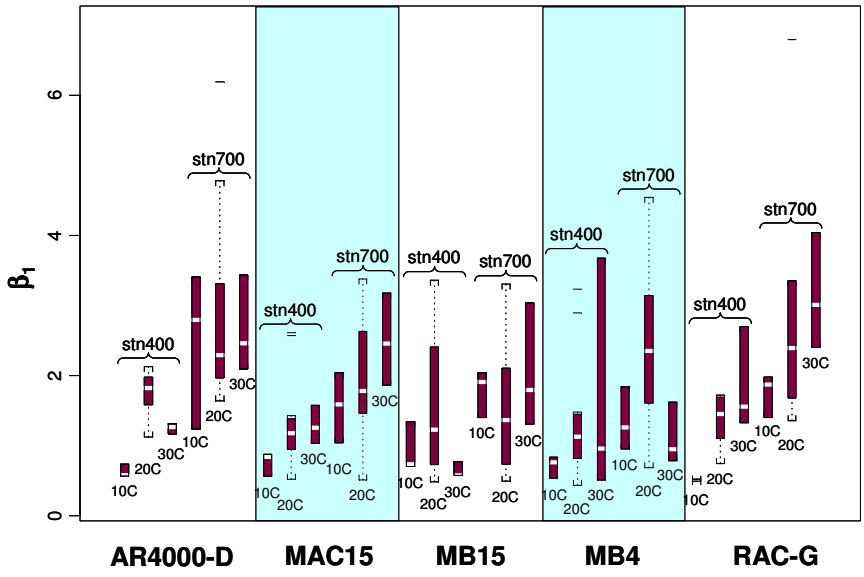

Figure 3.17: Summary boxplots of the fatigue three-stage Weibull parameter β_1.

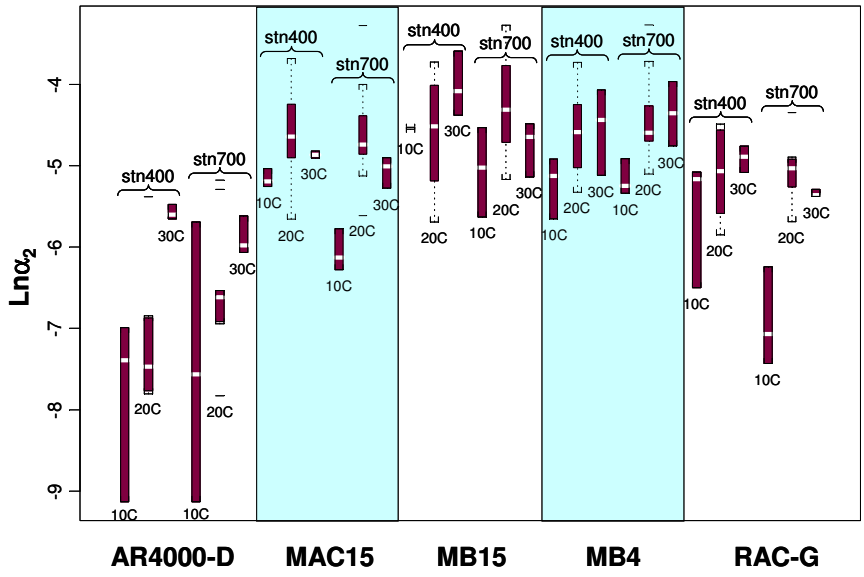

Figure 3.18: Summary boxplots of the fatigue three-stage Weibull parameter $\ln\alpha_2$.

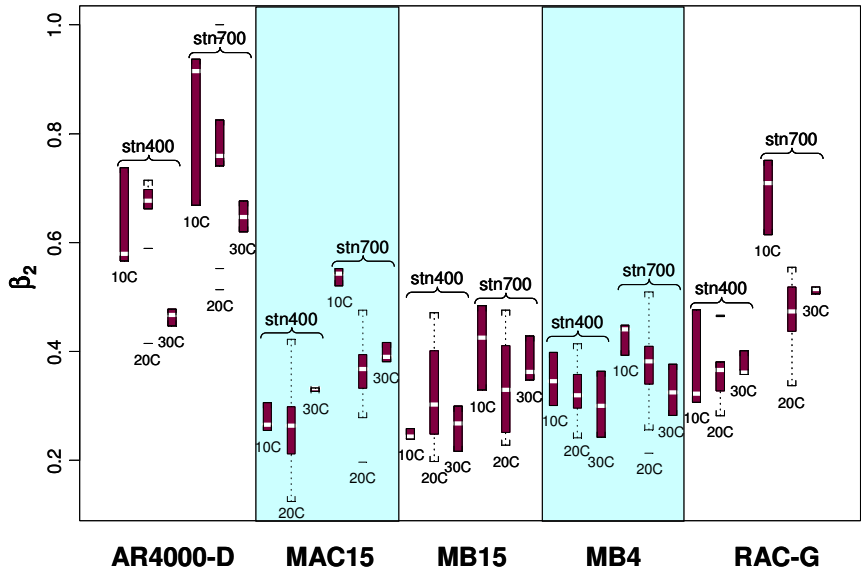

Figure 3.19: Summary boxplots of the fatigue three-stage Weibull parameter β_2.

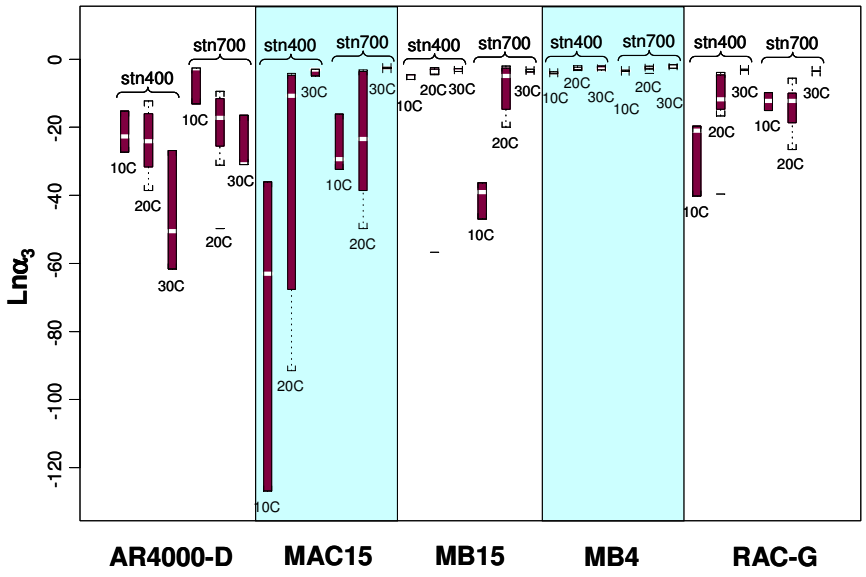

Figure 3.20: Summary boxplots of the fatigue three-stage Weibull parameter $\ln\alpha_3$.

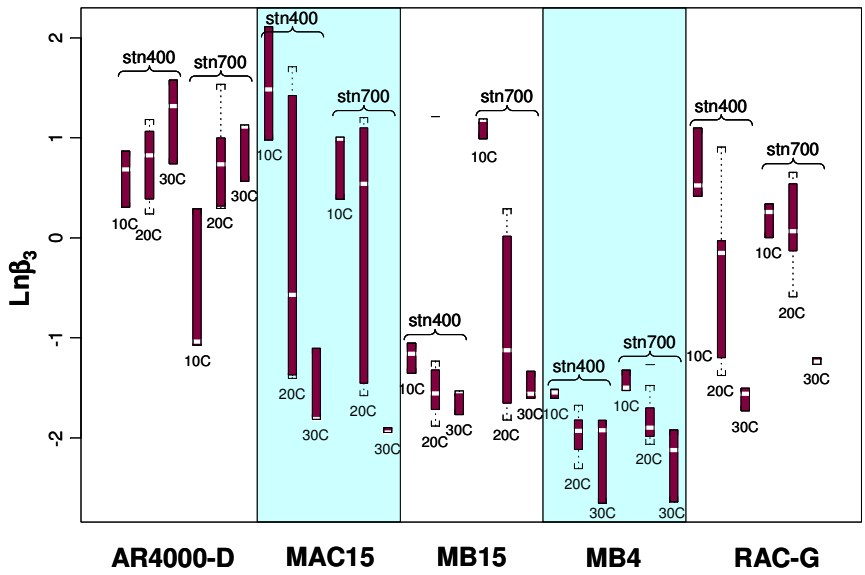

Figure 3.21: Summary boxplots of the fatigue three-stage Weibull parameter lnβ_3.

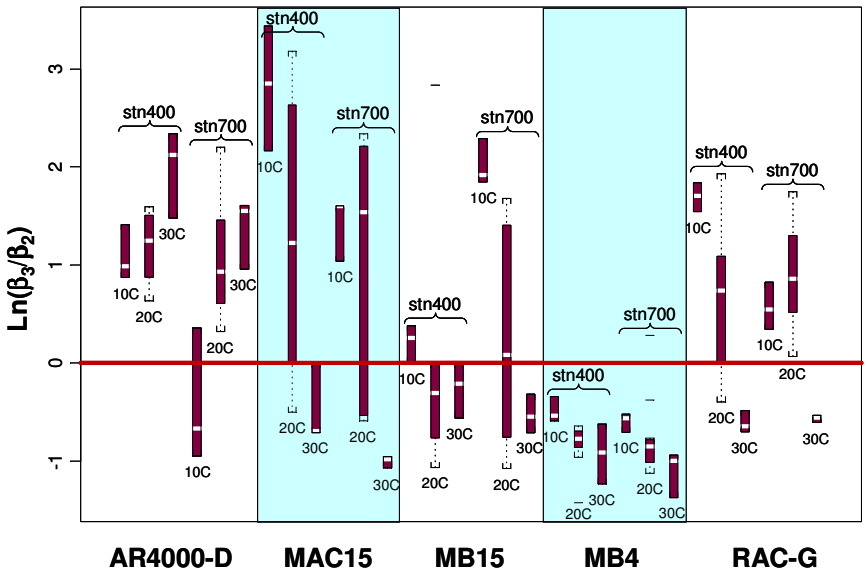

Figure 3.22: Summary boxplots of the fatigue three-stage Weibull parameter ln(β_3/β_2).

The summary boxplots of $sign(\gamma_1)\ln(|\gamma_1|)$ in Figure 3.23 show that:

- The γ_1 values are positive for all five mixes; and
- The effect of binder/mix type on $sign(\gamma_1)\ln(|\gamma_1|)$ is barely perceived.

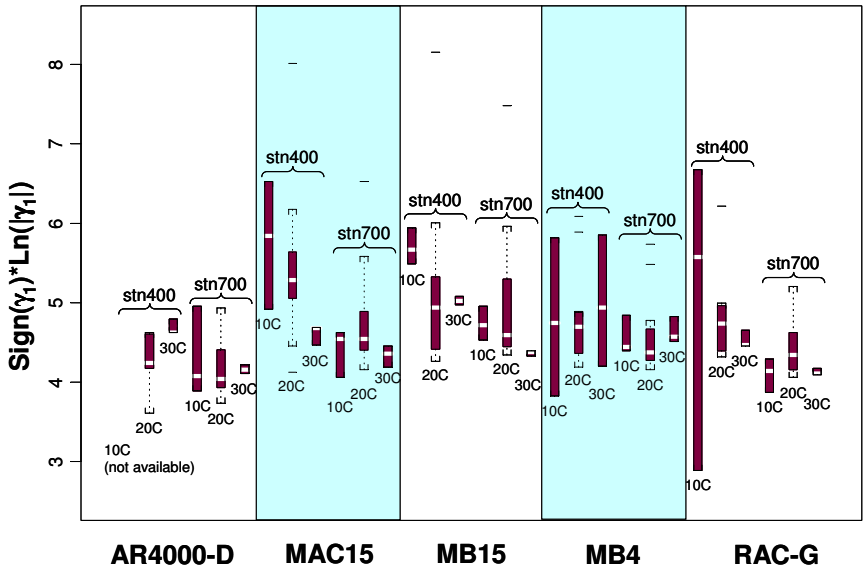

Figure 3.23: Summary boxplots of the fatigue three-stage Weibull parameter *sign*(γ_1)ln(|γ_1|).

The *sign*(γ_2)ln(|γ_2|) summary boxplots (Figure 3.24) provide the same stage transition information as the ln(β_3/β_2) summary boxplots.

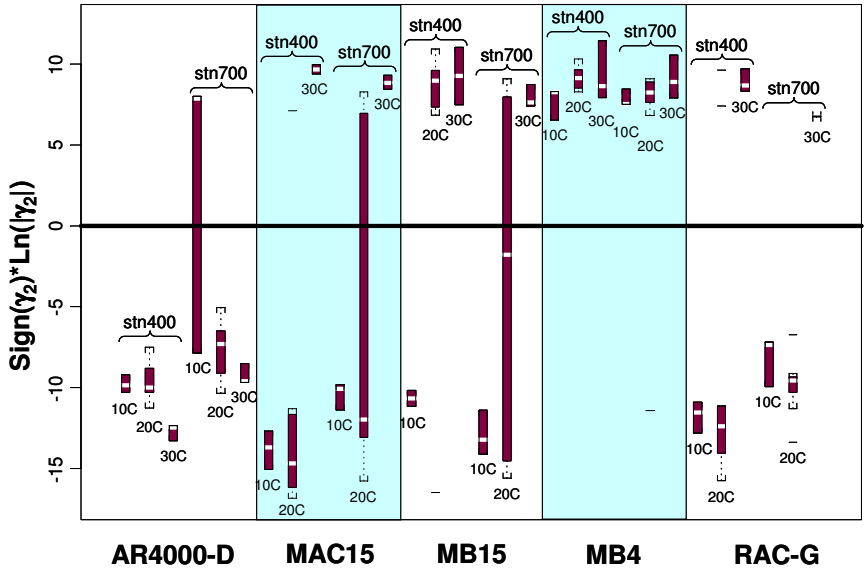

Figure 3.24: Summary boxplots of the fatigue three-stage Weibull parameter *sign*(γ_2)ln(|γ_2|).

The summary boxplots of stiffness ratio ($SR@n_2$) in Figure 3.25 show that, with the exception of a few tests, stiffness ratio values are all greater than 0.5. This implies that, regardless of mix type, the transition from Stage II to Stage III (initiation to propagation) occurs before the failure criterion of conventional definition of fatigue life, defined as 50 Percent Loss of Initial Stiffness (SR = 0.5).

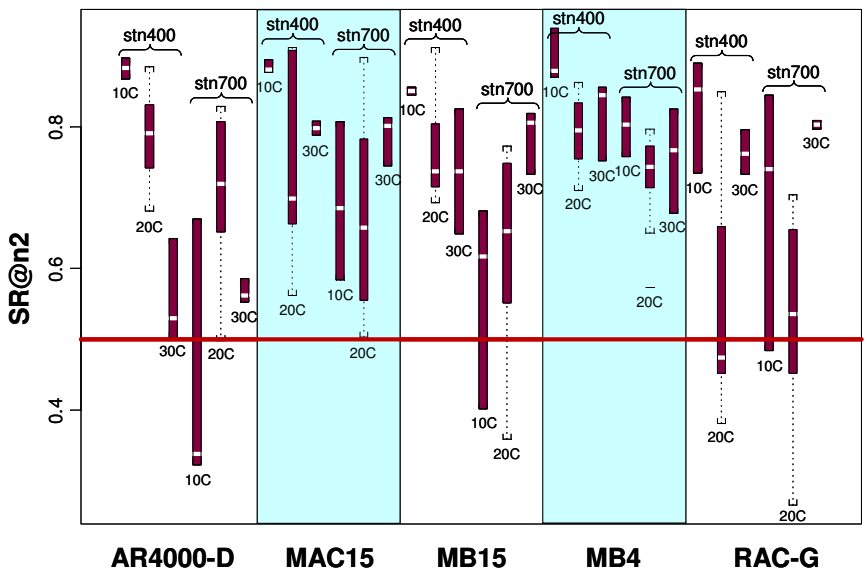

Figure 3.25: Summary boxplots of the fatigue three-stage Weibull parameter $SR@n_2$.

3.5. Weibull Parameters and Shear Performance

3.5.1 Weibull Curves of Modified Binder Shear Results

The laboratory shear test results and associated Weibull-fitted curves are presented in Tables A.10 to A.18 and Figures A.35 to A.67 in Appendix A.

3.5.2 Tree-Based Regression Modeling

The following Weibull parameters, response variables, and factor levels were considered in the tree-based regression and category modeling phase of the analysis of the Repeated Simple Shear Test at Constant Height (RSST-CH) results:

- Shear Weibull parameters:
  - $\ln\alpha_1$, β_1, $\ln n_1$, $sign(\gamma_1)\ln(|\gamma_1|)$, $\ln\alpha_2$, β_2, $\ln n_2$, $sign(\gamma_2)\ln(|\gamma_2|)$, $\ln pssn_1$, and $\ln pssn_2$.
- Shear response variables:
  - $\ln G$, $\ln pct5$, $\ln kcyc5$, and the shapes of Weibull curves, shape, are also inspected.
- Factor levels investigated:
  - Binder type (*binder*): (a) AR4000 (b) MAC15 (c) MB15 (d) MB4, and (e) ARB
  - Compaction (*comp*): (a) FMFC (b) FMLC, and (c) LMLC
  - Conditioning (*cond*): (a) aging and (b) none
  - Gradation (*grad*): (a) DG and (b) GG

Pruned dendrograms for the laboratory shear results are presented in Figure A.68 in Appendix A. Only the pruned trees with three (or more) levels are shown. The full dendrogram, the printed full tree structure, and the residual analysis are not included. Pertinent findings include:

- **Resilient Shear Modulus (ln*G*)**

  The initial resilient shear modulus is defined as the maximum shear stress divided by the maximum shear strain at the 100th cycle when subjected to a pulse loading followed by a rest period. The ln*G* can be regarded as an index of the initial shear-resistance capacity of the mix.

  - The values of ln*G* can be separated into two groups based on mix type: (1) MAC15-G, MB15-G, and MB4-G mixes with an average value of 74 MPa (not shown in the dendrogram) and (2) AR4000-D and RAC-G mixes with an average value of 166 MPa (not shown in the dendrogram).
  - On average, the initial resilient shear moduli of AR4000-D and RAC-G mixes is about twice the magnitude of the MAC15-G, MB15-G, and MB4-G mixes. No apparent within-group differences were perceived at 55°C for each mix type.

- **Cycles to 5 Percent Permanent Shear Strain (ln*pct5*)**

  The ln*pct5* is a conventional performance index that reflects the rutting resistance capacity of an asphalt mix. Low accumulated permanent shear strains relate to better rutting performance of the asphalt mix.

  - The AR4000-D and MAC15-G mixes had the highest average Cycles to 5 Percent Permanent Shear Strain of around 10 million, which occurred at a temperature 45°C and air-void content of less than 5.75 percent.
  - The MAC15-G, MB15-G, and MB4-G mixes at 55°C and stress levels of 100 kPa and 130 kPa had the lowest average Cycles to 5 Percent Permanent Shear Strain of about 1,540.

- **Accumulated Permanent Shear Strain at 5,000 Cycles (ln*kcyc5*)**

  The ln*kcyc5* is also a performance index used to assess the rutting resistance capacity of asphalt mixes. Small accumulated permanent shear strains at 5,000 cycles relate to better rutting performance.

  - The data can be separated into two groups based on gradation (1) dense-graded with an average value of 3.4 percent Permanent Shear Strain, and (2) gap-graded with an average value of 2.0 percent Permanent Shear Strain. This implies that the conventional AR4000-D mixes and modified binder dense-graded mixes perform better than the gap-graded RAC, MAC15, MB15, and MB4 mixes.
  - The largest accumulated Permanent Shear Sstrain at 5,000 Cycles (~exp(-2.712) = 0.066), occurred at stress levels of 100 kPa and 130 kPa for the MB15 gap-graded mixes.

- ***shape* and *sign*(γ_2)ln(|γ_2|)**

  The *shape* parameter (as defined in Figure 3.6) qualitatively categorizes the shape of a three-stage Weibull shear curve, while the *sign* parameter is a quantitative expression of the Stage III curve, showing either accelerated or retarded shear damage. Shape types S_1 and S_2 are dominant as shown in Table 3.5. In this study, the AR4000-D mix has either an S_1 or S_2 shape, while the RAC-G and MAC15-G mixes are identical in terms of the shape counts. The MB4-G and MB15-G mixes are dominated by an S_2 shape (faster accumulated permanent shear strain at Stage III).

Table 3.5: Summary of Shape Counts for Each Mix Type for Shear

Binder	Shape			
	S_1	S_2	S_3	S_4
AR4000	15	15	1	3
ARB	23	10	3	0
MAC15	24	9	0	1
MB15	1	28	1	6
MB4	12	22	0	3
$\sum$	*75*	*84*	*5*	*13*

  - Given that $\gamma_2 > 0$ if and only if $|\beta_3|<|\beta_2|$, implies retarded shear damage at Stage III and that $\gamma_2 < 0$ if and only if $|\beta_3|>|\beta_2|$, implies accelerated shear damage at Stage III, the MB15-G mixes always present an S_2 shape, which indicates accelerated shear damage at Stage III.
  - At 55°C, the AR4000-D and MB4-G mixes also exhibit an S_2 shape. At other temperatures, the AR4000-D, MAC15-G, MB4-G, and RAC-G mixes have an S_1 shape.
  - The pruned dendrogram of *sign*(γ_2)ln(|γ_2|) presents similar information regarding Stage III of each mix type. The γ_2 values of the MB15-G mixes are always negative, which indicates the occurrence of accelerated shear damage at Stage III in all circumstances. The other four mixes exhibit retarded shear damage at 45°C and accelerated shear damage at 55°C.
  - As expected, higher stress levels equate to increased shear damage.

- **Stage I Intercept and Slope (lnα_1 and β_1)**

  The lnα_1 and β_1 are the intercept and slope of the asymptotic line of a three-stage shear Weibull curve at Stage I. Increasing negative values of β_1 indicate faster accumulation of permanent shear strain.

  - Ideally, it is expected that smaller intercepts (intercepts of a three-stage shear Weibull curve are all positive) and flatter slopes (slopes of a three-stage shear Weibull curve are all negative) in each stage result in better rutting performance.
  - In the pruned dendrogram of lnα_1, the smallest intercept is 1.8 at 55°C and stress levels of 100 kPa and 130 kPa for the MAC15-G, MB15-G, and MB4-G mixes.
  - The flattest slope of β_1 (-0.0944) was recorded at stress levels of 70 kPa and 100 kPa for the field-mixed, laboratory-compacted AR4000-D and RAC-G mixes. Occurrences of both the

smallest intercept and the flattest slope were not recorded for any mix, which was verified by the low correlation (0.18) between $\ln\alpha_1$ and β_1.

- **Stage II Intercept and Slope ($\ln\alpha_2$ and β_2)**

  The $\ln\alpha_2$ and β_2 are the intercept and slope of the regression line of a three-stage shear Weibull curve at Stage II. Increasing negative values of β_2 indicate faster accumulation of permanent shear strain at Stage II.

  - The mix properties, specifically gradation and air-void content, replace mix type as the most significant factors affecting the $\ln\alpha_2$ and β_2 parameters (i.e., the shape of Stage II) respectively.

- **Stage III Intercept and Slope ($\ln\alpha_3$ and β_3)**

  The $\ln\alpha_3$ and β_3 are the intercept and slope of the asymptotic line of a three-stage shear Weibull curve at Stage III. Increasing negative values of β_3 relative to the value of β_2 indicates increasingly accelerated shear damage.

  - The intercept and slope of Stage III are highly negative correlated with a correlation -0.89.
  - In both pruned dendrograms, the MB15-G mixes have the largest average intercept (2.398) and the steepest average slope (-0.1711) at stress levels of 100 kPa and 130 kPa. This suggests that the MB15-G mixes might have poor rutting performance.

- **Separation Points ($\ln n_1$, $\ln n_2$) and their Corresponding Accumulated Permanent Shear Strain ($\ln pssn_1$, $\ln pssn_2$)**

  The separation point is the end of one stage and the start of the curve transition to the next stage. Separation points and their corresponding accumulated permanent shear strains are used to understand the permanent shear strain accumulation process of the various mix types.

  - The $\ln n_1$ and $\ln n_2$ represent the separation points from Stage I to Stage II and from Stage II to Stage III, respectively. The accumulated permanent shear strains in natural logarithm corresponding to these points are designated as $\ln pssn_1$ and $\ln pssn_2$ respectively.
  - The pruned dendrogram of $\ln n_1$ shows that the values of $\ln n_1$ range from 2.433 (i.e., $n_1 \cong 11$) to 4.092 (i.e., $n_1 \cong 60$).
  - The pruned dendrogram of $\ln pssn_1$ indicates that the accumulated permanent shear strains range from 0.3 percent up to 1.1 percent.
  - For the transition from Stage II to Stage III, the dendrograms of $\ln n_2$ and $\ln pssn_2$ indicate that (1) the values of n_2 are from 198 up to 1,469 cycles and (2) the accumulated permanent shear strains range from 0.8 percent to 3.1 percent (i.e., the transition from Stage II to Stage III occurred long before the failure criterion of RSST testing, namely 5 Percent Permanent Shear Strain). Accordingly, the choice of Stages II and III of a three-stage RSST Weibull curve to

represent the shear damage process is considered appropriate with a minimum loss of accuracy.

- **Air-Void Content**
  - Air-void content is the most significant covariate in the pruned dendrogram of Stage II slope (β_2).
  - As expected, lower air-void contents result in improved rutting performance.

Table 3.6 summarizes the first three levels of significant covariates for the conventional response variables and the three-stage Weibull parameters of shear testing results. The following points are noted from the table:

- Binder/mix type, stress level, and temperature are the most significant factors influencing rutting performance and defining the shape of the shear Weibull curve.
- At Stage II of the shear Weibull curve, the accumulation of permanent shear strain depends on gradation type and air-void content rather than the binder/mix type or stress level.
- Air-void content (i.e., level of compaction) influences various parameters at different levels of the dendrograms, which reinforces the need for critical control of compaction in all construction projects.

Table 3.6: Summary of the 1st, 2nd, and 3rd-Level Covariates for Shear Tree Modeling

Parameters	1st Level	2nd Level	3rd Level
$\ln G$	*binder*	*temp*	*binder, comp*
$\ln pct5$	*temp*	*binder, sts*	*sts, av, binder*
$\ln kcyc5$	*grad*	*temp, sts*	*comp, av, binder*
$\ln \alpha_1$	*binder*	*temp*	*binder, sts, comp*
β_1	*sts*	*binder*	*grad, comp, av*
$\ln n_1$	*sts*	*binder*	*av, cond, temp*
$sign(\gamma_1)\ln(\lvert\gamma_1\rvert)$	*binder*	*temp, av*	*av, binder, sts*
$\ln \alpha_2$	*grad*	*temp, sts*	*binder, av*
β_2	*av*	*sts, binder*	*sts, binder, temp*
$\ln n_2$	*binder*	*grad, sts*	*av, binder*
$sign(\gamma_2)\ln(\lvert\gamma_2\rvert)$	*binder*	*temp*	*sts*
$\ln \alpha_3$	*binder*	*sts*	*grad, binder, av*
β_3	*sts*	*binder*	*av, temp*
$\ln pssn_1$	*grad*	*comp, temp*	*binder*
$\ln pssn_2$	*grad*	*comp, sts*	*temp, binder*
shape	*binder*	*sts, temp*	*av, binder*

3.5.3 Summary Boxplots for Shear

Based on the findings summarized in Table 3.6, shear performance is primarily affected by mix type, temperature, and stress level. Summary boxplots for shear performance, like those for fatigue, are categorized by mix type, each of which is subcategorized by temperature and stress level. The summary boxplots of the Weibull parameters inspected include: $\ln\alpha_1$, β_1, $\ln\alpha_2$, β_2, $\ln\alpha_3$, β_3, $\ln(\beta_3/\beta_2)$, $sign(\gamma_1)\ln(\lvert\gamma_1\rvert)$,

sign(γ_2)ln(|γ_2|), and $PSS@n_2$. In addition to these parameters, the summary boxplots of permanent shear strain (ln*pct5* [PSS = 5 percent]), based on the results of all 177 shear tests, are also presented.

Figure 3.26 provides an overview of the Cycles to 5 Percent Permanent Shear Strain in natural logarithm (ln*pct5*) of shear testing results in terms of binder type, temperature, and stress level. Observations from these boxplots include:

- Permanent shear strain increases with increasing stress levels and temperatures, as expected.
- The ranking of rutting performance, from best to worst, generally follows the order AR4000-D > MAC15-G > RAC-G > MB4-G > MB15-G.
- The differences between MAC15-G and RAC-G mixes are minimal.
- The MAC15-G mixes perform better at 45°C and worse at 55°C when compared with RAC-G mixes.
- The MB4-G mixes appear to have the least testing variation compared with the other mixes, while the MAC15-G mixes appear to have the largest testing variation. This suggests that the performance of MB4-G mixes might be more consistent and predictable under field conditions.

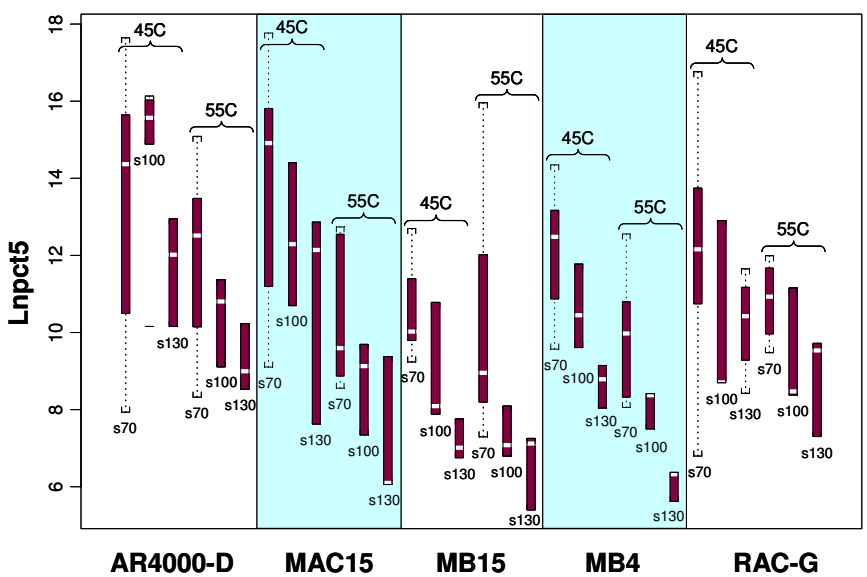

Figure 3.26: Summary boxplots of permanent shear strain (ln*pct5*).
(s70, s100, and s140 are the test stress levels of 70 kPa, 100 kPa, and 130 kPa)

In the summary boxplots representing Stage I intercepts (lnα_1) (Figure 3.27), the pattern and ranking of the mixes is similar to the boxplots of permanent shear strain (Figure 3.26). The correlation (0.61) between ln*pct5* and lnα_1 verifies the similarity.

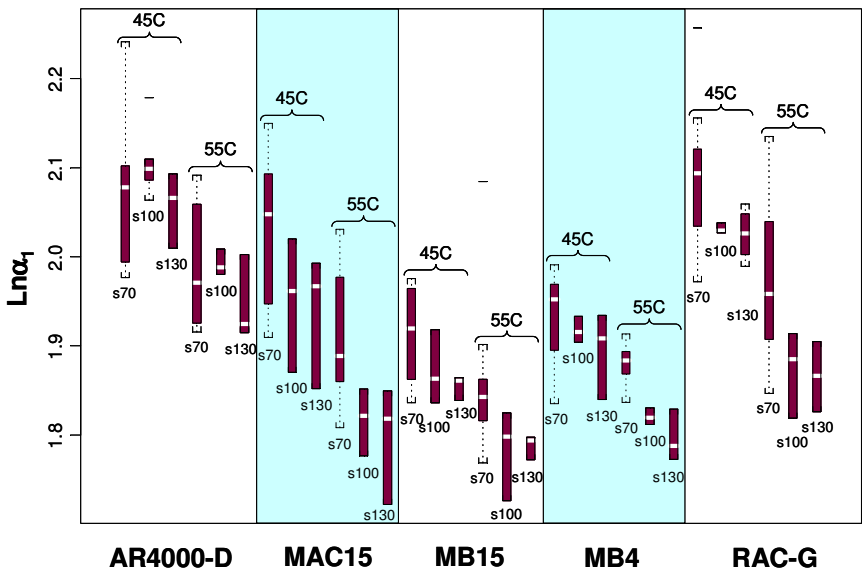

Figure 3.27: Summary boxplots of the shear three-stage Weibull parameter: lnα_1.

From the summary boxplots of Stage I slope (β_1) (Figure 3.28), it is apparent that higher stress levels equate to larger values of $|\beta_1|$ (i.e., steeper slope in Stage I). Temperature does not appear to have an effect within the same mix type, and it is difficult to detect the differences between the various mix types.

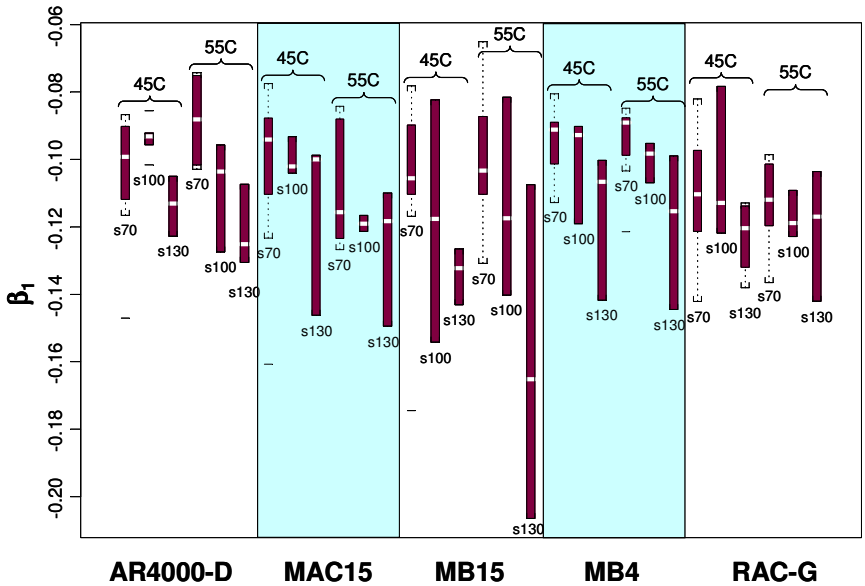

Figure 3.28: Summary boxplots of the shear three-stage Weibull parameter: β_1.

The summary boxplots of the Stage II intercept (lnα_2) shown in Figure 3.29 indicate that the effect of stress level is significant for the MAC15-G and RAC-G mixes; but has no apparent stress effect on the MB15-G and MB4-G mixes. The correlation of the Stage II intercept (lnα_2) and slope ($|\beta_2|$) is 0.46, which

borders on rejection of the statement that the combination of low values of $\ln\alpha_2$ and $|\beta_2|$ in the shear Weibull curve will indicate good rutting performance.

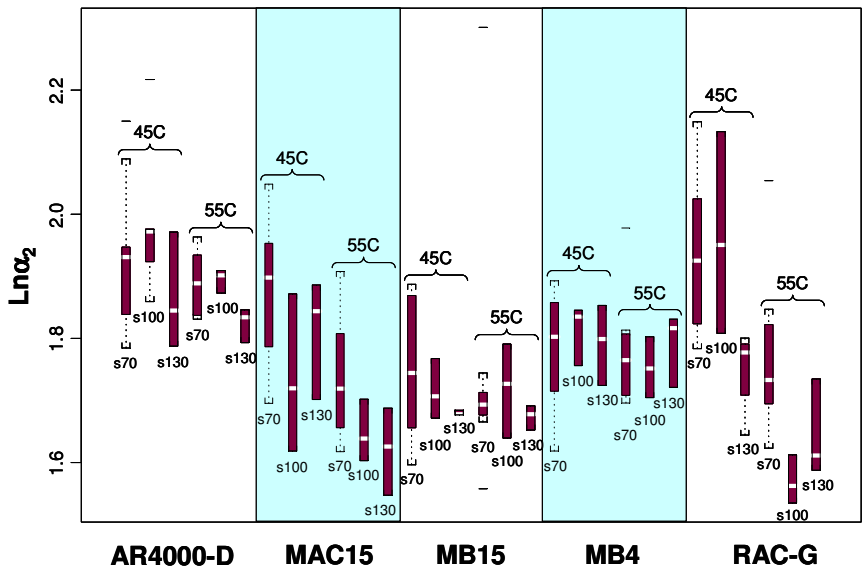

Figure 3.29: Summary boxplots of the shear three-stage Weibull parameter: $\ln\alpha_2$.

The summary boxplots of Stage II slope (β_2) (Figure 3.30) show that:

- Stress effect is apparent for all mix types.
- Higher stress levels generally lead to larger $|\beta_2|$ values, except in the RAC-G mixes.
- Both $\ln\alpha_1$ and β_2 parameters are clearly affected by binder/mix type.

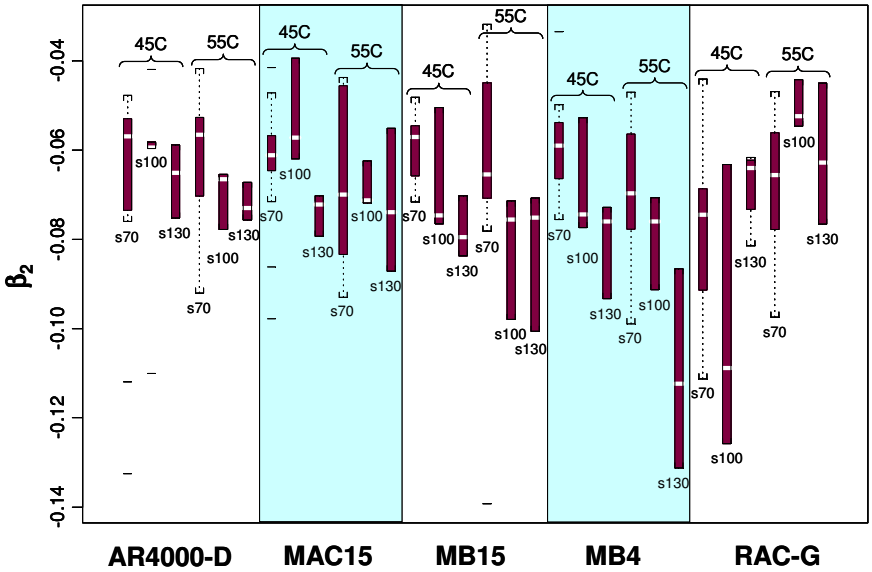

Figure 3.30: Summary boxplots of the shear three-stage Weibull parameter: β_2

Figures 3.31 and 3.32 are the respective summary boxplots of the Stage III intercept ($\ln\alpha_3$) and slope (β_3) and indicate that:

- The value of $\ln\alpha_3$ increases as stress level increases, which contradicts the observations from the Stage II intercept ($\ln\alpha_2$).
- The effect of binder/mix type on $\ln\alpha_3$ is obvious.
- The effect of stress level on the Stage III slope (β_3) parameter is dominant compared to the effects of mix type and temperature. The variation of β_3 is also greater than that of β_2.
- The $\ln\alpha_3$ and $|\beta_3|$ parameters are highly positive-correlated with a correlation of 0.89 (i.e., larger values of $|\beta_3|$ correspond to larger values of $\ln\alpha_3$).

The parameter $\ln(\beta_3/\beta_2)$ is used to characterize whether Stage III of a shear Weibull curve reflects accelerated or retarded shear damage. The β_3 and β_2 parameters on the curve are negative; hence, if $\ln(\beta_3/\beta_2) > 0$, then $|\beta_3| > |\beta_2|$ (indicating accelerated shear damage at Stage III) and if $\ln(\beta_3/\beta_2) < 0$, then $|\beta_3| < |\beta_2|$, (indicating retarded shear damage at Stage III). The summary boxplot of $\ln(\beta_3/\beta_2)$ (Figure 3.33) indicates that:

- Accelerated shear damage at Stage III is most likely to occur when the mix is subjected to high stress levels and high temperatures.

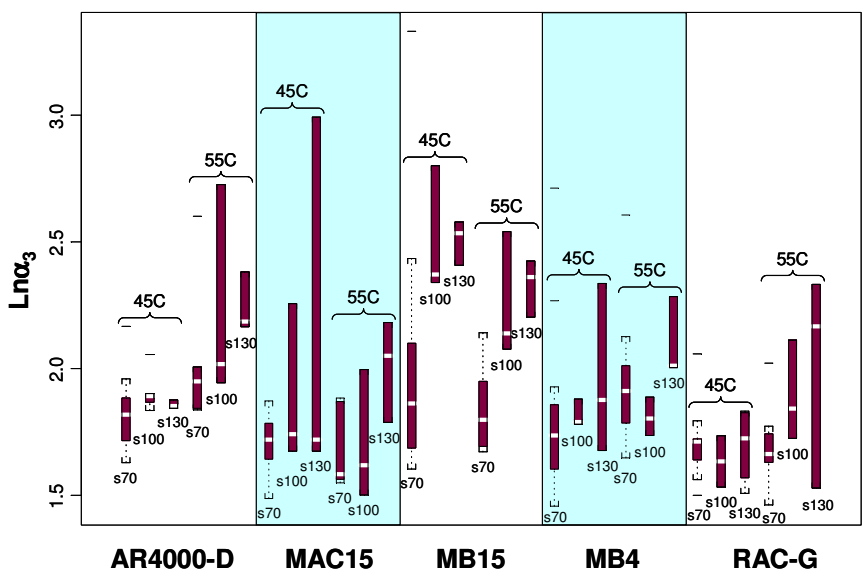

Figure 3.31: Summary boxplots of the shear three-stage Weibull parameter: $\ln\alpha_3$.

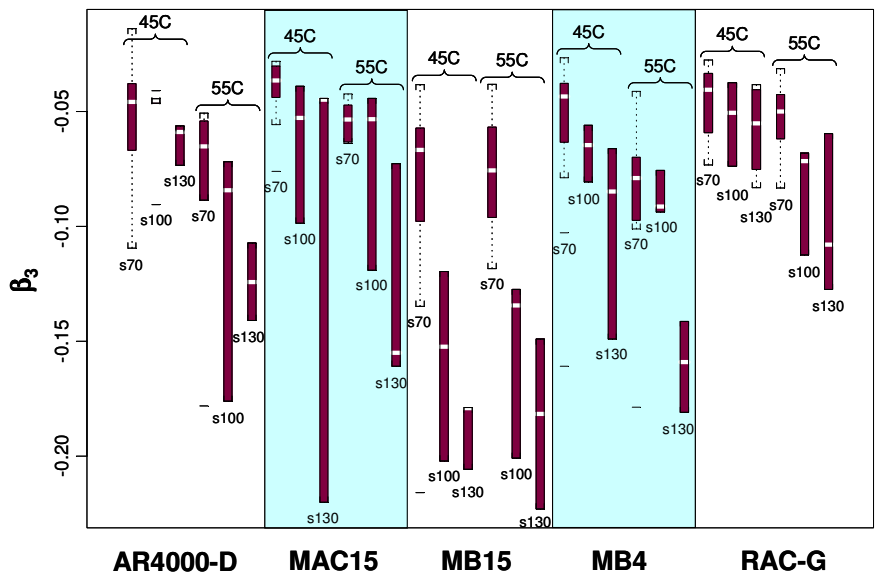

Figure 3.32: Summary boxplots of the shear three-stage Weibull parameter:β_3.

- The values of $\ln(\beta_3/\beta_2)$ of the MB15-G mixes are all greater than zero, which implies that these mixes are prone to accelerated shear damage in all circumstances;
- The boxplots of MAC15-G mixes show that the boxes always cross the zero line except at two extreme testing conditions, namely 45°C/70 kPa and 55°C/130 kPa, indicating some inconsistency in the performance of this mix.

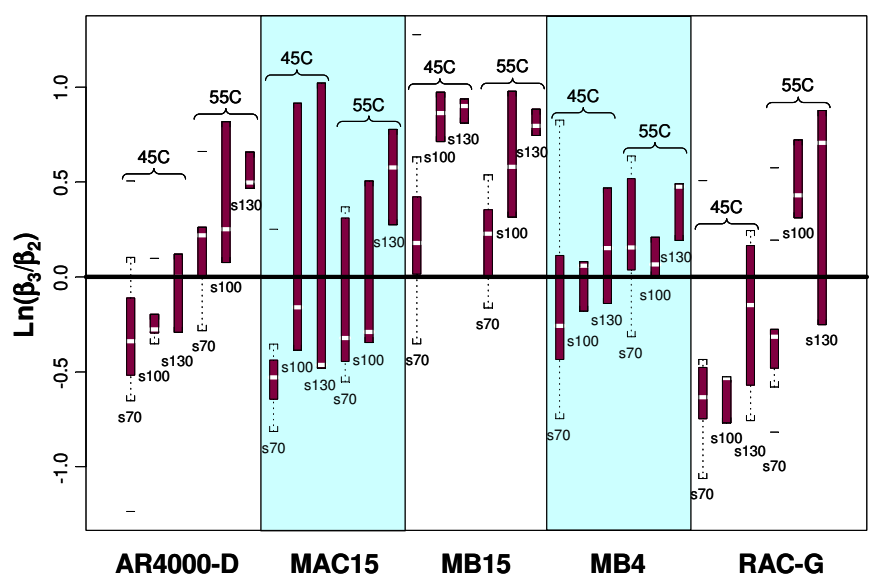

Figure 3.33: Summary boxplots of the shear three-stage Weibull parameter: $\ln(\beta_3/\beta_2)$.

The summary boxplots of $sign(\gamma_1)\ln(|\gamma_1|)$ in Figure 3.34 reveal that:

- All the values of $sign(\gamma_1)\ln(|\gamma_1|)$ are greater than zero (i.e., $|\beta_2| < |\beta_1|$);

- The higher the stress level the smaller the value of γ_1 (i.e., $|\beta_2|$ is close to $|\beta_1|$), and
- Temperature effect is minimal within the same mix type.

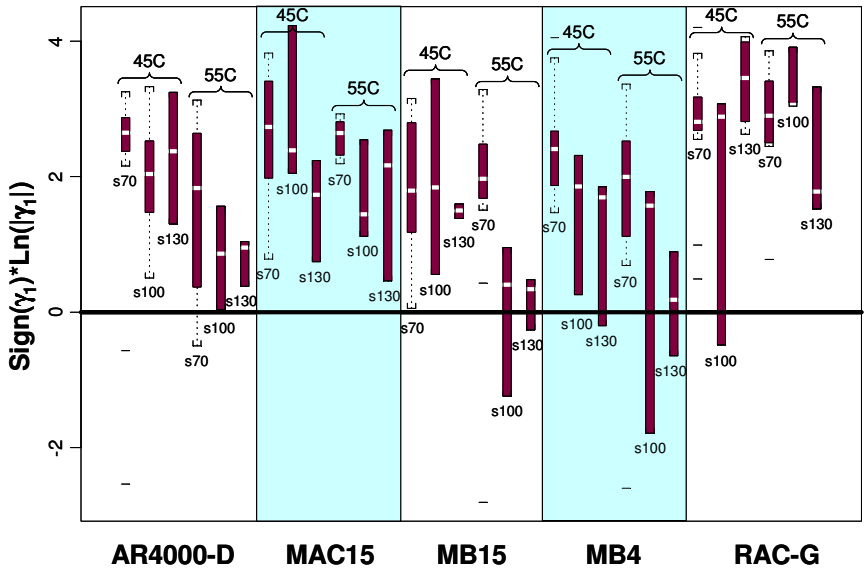

Figure 3.34: Summary boxplots of the shear three-stage Weibull parameter: *sign*(γ_1)ln($|\gamma_1|$).

The summary boxplots of sign(γ_2)ln($|\gamma_2|$) in Figure 3.35 generally provide the same information as the summary boxplots of ln(β_3/β_2), which characterize whether Stage III shear damage is accelerated or retarded. The larger the magnitude of $|\gamma_2|$, the sharper the transition from Stage II to Stage III.

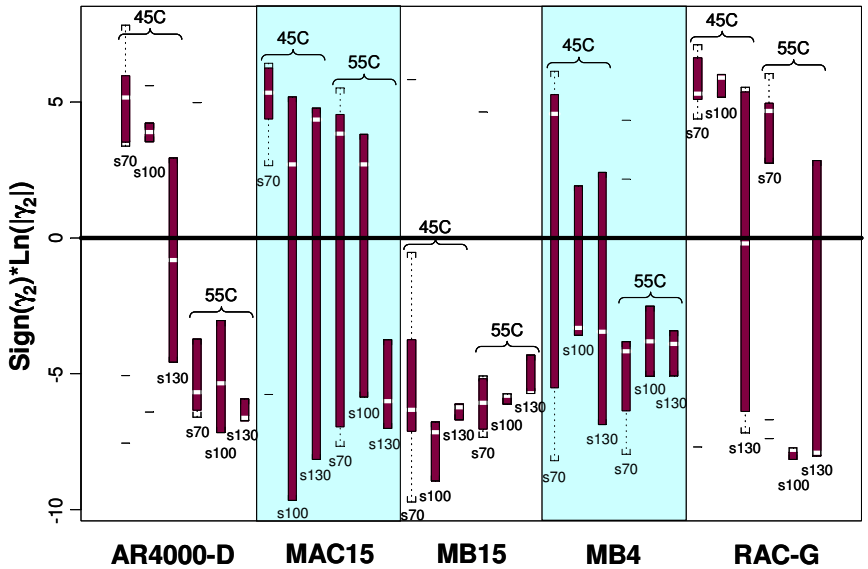

Figure 3.35: Summary boxplots of the shear three-stage Weibull parameter: *sign*(γ_2)ln($|\gamma_2|$).

In the summary boxplots (Figure 3.36) of accumulated permanent shear strain at the transition between Stage II and III ($PSS@n_2$):

- The values of $PSS@n_2$ for each mix type are all less than 5 Percent Permanent Shear Strain; indicating that the application of a three-stage Weibull equation to results from the Repeated Simple Shear Test at Constant Height test is appropriate.
- The values of $PSS@n_2$ appear to be affected first by mix type then by stress level. Temperature presents no apparent effect.

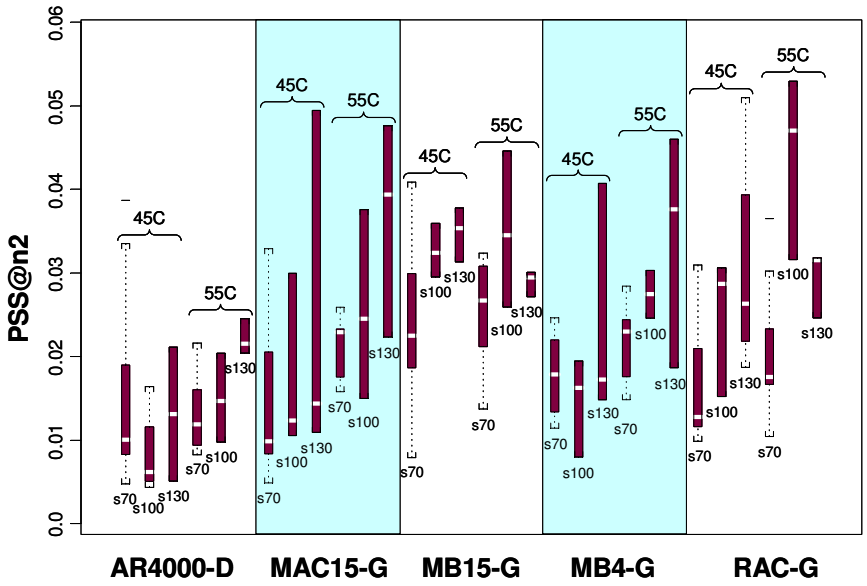

Figure 3.36: Summary boxplots of the shear three-stage Weibull parameter: $pss@n_2$.

3.6. Laboratory Two-Stage Weibull Fatigue Integrated Equations

Integrated Weibull equations are used for recursive (dynamic) simulation of fatigue and rutting under field conditions, with the fatigue and/or shear damage of the field mix per repetition being functions of the temperature of the mix and tensile strain (for fatigue) and shear stress (for shear) caused by the load, as well as the mix design.

Based on the results in the preceding sections, the fitting of a three-stage Weibull equation to flexural controlled-deformation fatigue and shear test results appears reasonable and appropriate in all circumstances. The intercepts ($\ln\alpha_1$, $\ln\alpha_2$, and $\ln\alpha_3$,) and slopes (β_1, β_2, and β_3) are the six fundamental Weibull parameters that determine the three-stage Weibull curve representing the stiffness deterioration (or fatigue damage) and permanent shear strain accumulation (rutting damage) processes. These processes were found to be dependent on different strains (for fatigue), stresses (for shear), temperatures,

and the construction quality or mix design variables of gradation, air-void content, and binder content. Therefore, the six fundamental Weibull parameters are essentially functions of these variables and integrated equations should represent all these various test situations.

3.6.1 Equation Development Methodology

To develop laboratory two-stage Weibull fatigue integrated equations, only Stage II and Stage III of each test are considered. The covariates used to construct the two-stage Weibull fatigue integrated equations are temperature, strain, air-void content, and load repetitions. For shear, strain is substituted with stress. The following methodology is used in the development of the equations.

Firstly, the following one-stage fatigue Weibull equation is considered:

Fatigue: $$SR = \exp\left(-\alpha \cdot n^{\beta}\right) \quad \textbf{(3.12a)}$$

Shear: $$PSS = \exp\left(-\alpha \cdot n^{\beta}\right) \quad \textbf{(3.12b)}$$

Taking the natural logarithm of both sides twice:

Fatigue: $$\ln\left(-\ln SR\right) = \ln\alpha + \beta \cdot \ln n \quad \textbf{(3.13a)}$$

Shear: $$\ln\left(-\ln PSS\right) = \ln\alpha + \beta \cdot \ln n \quad \textbf{(3.13b)}$$

From this, a three-term interaction full model can be expressed as follows:

Fatigue:

$$\begin{aligned}\ln\left(-\ln SR\right) = {} & C_0 + C_1 av + C_2 temp + C_3 \ln stn + C_4 \ln n + C_5 av \cdot temp \\ & + C_6 av \cdot \ln stn + C_7 av \cdot \ln n + C_8 temp \cdot \ln stn + C_9 temp \cdot \ln n \\ & + C_{10} \ln stn \cdot \ln n + C_{11} av \cdot \ln stn \cdot \ln n + C_{12} av \cdot temp \cdot \ln stn \\ & + C_{13} av \cdot temp \cdot \ln n + C_{14} temp \cdot \ln stn \cdot \ln n\end{aligned} \quad \textbf{(3.14a)}$$

Shear:

$$\begin{aligned}\ln\left(-\ln PSS\right) = {} & C_0 + C_1 av + C_2 temp + C_3 \ln sts + C_4 \ln n + C_5 av \cdot temp \\ & + C_6 av \cdot \ln stn + C_7 av \cdot \ln n + C_8 temp \cdot \ln sts + C_9 temp \cdot \ln n \\ & + C_{10} \ln sts \cdot \ln n + C_{11} av \cdot \ln sts \cdot \ln n + C_{12} av \cdot temp \cdot \ln sts \\ & + C_{13} av \cdot temp \cdot \ln n + C_{14} temp \cdot \ln sts \cdot \ln n\end{aligned} \quad \textbf{(3.14b)}$$

The terms associated with $\ln n$ are then collected giving:

Fatigue:

$$\begin{aligned}\beta \ln n = {} & C_4 \ln n + C_7 av \cdot \ln n + C_9 temp \cdot \ln n + C_{10} \ln stn \cdot \ln n + C_{11} av \cdot \ln stn \cdot \ln n \\ & + C_{13} av \cdot temp \cdot \ln n + C_{14} temp \cdot \ln stn \cdot \ln n\end{aligned} \quad \textbf{(3.15a)}$$

Shear:

$$\begin{aligned}\beta \ln n = {} & C_4 \ln n + C_7 av \cdot \ln n + C_9 temp \cdot \ln n + C_{10} \ln sts \cdot \ln n \\ & + C_{11} av \cdot \ln sts \cdot \ln n + C_{13} av \cdot temp \cdot \ln n + C_{14} temp \cdot \ln sts \cdot \ln n\end{aligned} \quad \textbf{(3.15b)}$$

Dividing both sides by ln$n$:

Fatigue:

$$\beta = C_4 + C_7 av + C_9 temp + C_{10} \ln stn + C_{11} av \cdot \ln stn + C_{13} av \cdot temp + C_{14} temp \cdot \ln stn \quad \textbf{(3.16a)}$$

Shear:

$$\beta = C_4 + C_7 av + C_9 temp + C_{10} \ln sts + C_{11} av \cdot \ln sts + C_{13} av \cdot temp + C_{14} temp \cdot \ln sts \quad \textbf{(3.16b)}$$

The remaining terms are used to construct the intercept term lnα as follows:

Fatigue:

$$\begin{aligned} \ln\alpha = {} & C_0 + C_1 av + C_2 temp + C_3 \ln stn + C_5 av \cdot temp + C_6 av \cdot \ln stn \\ & + C_8 temp \cdot \ln stn + C_{12} av \cdot temp \cdot \ln stn \end{aligned} \quad \textbf{(3.17a)}$$

Shear:

$$\begin{aligned} \ln\alpha = {} & C_0 + C_1 av + C_2 temp + C_3 \ln sts + C_5 av \cdot temp \\ & + C_6 av \cdot \ln sts + C_8 temp \cdot \ln sts + C_{12} av \cdot temp \cdot \ln sts \end{aligned} \quad \textbf{(3.17b)}$$

Taking the antilog:

Fatigue:

$$\alpha = \exp\left(\begin{aligned} & C_0 + C_1 av + C_2 temp + C_3 \ln stn + C_5 av \cdot temp + C_6 av \cdot \ln stn \\ & + C_8 temp \cdot \ln stn + C_{12} av \cdot temp \cdot \ln stn \end{aligned} \right) \quad \textbf{(3.18a)}$$

Shear:

$$\alpha = \exp\left(\begin{aligned} & C_0 + C_1 av + C_2 temp + C_3 \ln sts + C_5 av \cdot temp + C_6 av \cdot \ln sts \\ & + C_8 temp \cdot \ln sts + C_{12} av \cdot temp \cdot \ln sts \end{aligned} \right) \quad \textbf{(3.18b)}$$

Each single test is then fitted with a three-stage Weibull equation from which the two-stage separation points n_1 and n_2 are determined. The ln(-lnSR) or ln(-lnPSS) and ln$n$ data points and the associated testing variables of every test are collected and compared with the specified model using a regular regression analysis to find the integrated Stage II equations. Note that the Stage II equation shifts the real time axis (or repetitions) with a γ_1 value. If $\hat{n} = n - \gamma_1$, then the plot of ln(-lnSR) or ln(-lnPSS) versus $\ln\hat{n}$ should be a straight line. Therefore, the repetition at Stage II has to be subtracted by γ_1 before conducting the linear regression analysis.

The same approach and model specification can be applied to determine the integrated equation at Stage III. The repetition at Stage III of each test has to be subtracted by γ_2.

In this analysis, only the temperature effect data of the five mixes and the gradation effect data of three mixes (MB4-G, MB15-G, and MAC15-G), as shown in the experiment design (Tables 3.1 and 3.2), were utilized to develop the laboratory two-stage Weibull fatigue and shear integrated equations. It should be noted that, when laboratory Weibull fatigue integrated equations are used to predict field performance, a

correction factor is still required to account for differences in boundary conditions between laboratory specimens and full-scale in-service pavements.

3.6.2 Equations from Temperature Effect Data

As listed in Table 3.1, the temperature effect data used to develop the laboratory two-stage Weibull integrated equations include:

- Fatigue
  - Five mix types (AR4000-D, RAC-G, MAC15-G, MB15-G, and MB4-G);
  - Three temperatures (10°C, 20°C, and 30°C), and
  - Two strain levels (400 and 700 microstrain).
- Shear
  - Five mix types (AR4000-D, RAC-G, MAC15-G, MB15-G, and MB4-G);
  - Two temperatures (45°C and 55°C), and
  - Three stress levels (70, 100, and 130 kPa).
- All data were used to develop the model and no data were retained for model verification.

The regression results of Stages II and III for each mix type are tabulated in Tables 3.7 (fatigue) and 3.8 (shear).

<u>Fatigue</u>

Figures A.69 to A.73 in Appendix A illustrate the fitting results using the laboratory two-stage Weibull fatigue integrated equations for AR4000-D, MAC15-G, MB15-G, MB4-G, and RAC-G mixes respectively. The integrated equations generally show the main trends of the fatigue damage process and provide reasonable fitting results. For fatigue testing, the MB4-G mixes had the highest R-squared values of Stages II and III, while the MAC15-G had the lowest R-squared values at Stage III. However, the crack propagation occurring at Stage III of the AR4000-D and MAC15-G mixes is difficult to fit with the integrated equations.

<u>Shear</u>

Figures A.74 to A.78 in Appendix A illustrate the fitting results using the laboratory two-stage Weibull shear integrated equations for AR4000-D, MAC15-G, MB15-G, MB4-G, and RAC-G mixes respectively. As with fatigue, the integrated equations generally show the main trends of the permanent shear strain accumulation process and provide reasonable fitting results. For shear testing, MB4-G mixes had the highest R-squared values of Stages II and III and MB15-G mixes the lowest.

Table 3.7: Two-Stage Weibull Fatigue Integrated Equations Using Temperature Effect Data

Item	Coefficient	Mix Types					
		MAC15-G		MB15-G		MB4-G	
		Stage II	Stage III	Stage II	Stage III	Stage II	Stage III
const	C_0	-53.77755000	45.000130000	-40.18087000	-40.86237000	22.88748000	-56.97284000
av	C_1	5.50806000	-3.790545000	5.91769500	7.69241800	-3.41458200	10.61930000
temp	C_2	0.42741710	-0.877528000	2.67713500	-0.21578160	-0.21978310	5.11981900
ln*stn*	C_3	-6.02652900	7.072415000	-4.34326500	-3.89949800	3.10638700	-6.80867200
ln*n*	C_4	8.78514500	0.848726900	2.07246100	1.21186200	0.23369050	1.98043000
av,·temp	C_5	-0.01043845	-0.011769690	-0.46566460	-0.04617474	0.00855356	-0.87339120
av,·ln*stn*	C_6	0.67074330	-0.583372400	0.73288530	0.83817160	-0.33853350	1.37632200
av,·ln*n*	C_7	-0.63816470	0.00000000	0.00000000	-0.05167970	0.09654296	-0.10081770
temp,·ln*stn*	C_8	0.04551279	-0.133716700	0.33528530	-0.06623466	-0.02681144	0.65275400
temp,·ln*n*	C_9	-0.11576130	-0.004541231	-0.02746738	0.001324984	-0.00326125	-0.09479084
ln*stn,*·ln*n*	C_{10}	1.10696200	0.073926760	0.23027770	0.09761946	0.04801055	0.14994040
av,·ln*stn,*·ln*n*	C_{11}	-0.08355119	0.00000000	0.00000000	0.00000000	0.00000000	0.00000000
av,·temp,·ln*stn*	C_{12}	0.00000000	0.00000000	-0.05931348	0.00000000	0.00000000	-0.11261190
av,·temp,·ln*n*	C_{13}	0.00000000	0.00000000	0.00000000	0.00000000	0.00000000	0.00551789
temp,·lnstn,·ln*n*	C_{14}	-0.01527260	0.00000000	-0.00334353	0.00000000	0.00000000	-0.00775068
R2		0.97	0.65	0.97	0.85	0.96	0.93

Table 3.7: Two-Stage Weibull Fatigue Integrated Equations Using Temperature Effect Data *(continued)*

Item	Coefficient	Mix Types			
		AR4000-D		RAC-G	
		Stage II	Stage III	Stage II	Stage III
const	C_0	427.42160000	745.74170000	38.30612000	9.32955700
av	C_1	-62.95922000	-56.19954000	-7.87022900	2.47855400
temp	C_2	-12.30349000	-29.97154000	-0.10719380	-0.37055420
ln*stn*	C_3	59.93669000	111.02000000	5.78764300	4.59419800
ln*n*	C_4	-20.73830000	-26.53032000	-4.72430400	3.58736500
av, ·temp	C_5	1.69355000	1.73884300	0.00751533	-0.11494880
av,·ln*stn*	C_6	-8.70301400	-9.11180400	-1.01782900	0.00000000
av,·ln*n*	C_7	3.19181200	-1.18925600	1.30461100	-0.27158760
temp,·ln*stn*	C_8	-1.70770600	-4.23098000	-0.01456926	-0.17171730
temp,·ln*n*	C_9	0.06105140	1.52401300	-0.02121171	-0.09660989
ln*stn,*·ln*n*	C_{10}	-3.16888400	-4.65610000	-0.67281900	0.14320360
av,·ln*stn*,·ln*n*	C_{11}	0.47558920	0.00000000	0.16893250	0.00000000
av, temp,·ln*stn*	C_{12}	0.23536440	0.26369880	0.00000000	0.00000000
av, temp,·ln*n*	C_{13}	0.01425653	0.02684279	0.00000000	0.01263612
temp, ·lnstn, ·ln*n*	C_{14}	0.02061669	0.22826070	-0.00238881	0.00000000
R^2		0.94	0.72	0.98	0.85

Table 3.8: Laboratory Two-Stage Weibull Shear Integrated Equations Using Temperature Effect Data

Item	Coefficient	Mix Types					
		MAC15-G		MB15-G		MB4-G	
		Stage II	Stage III	Stage II	Stage III	Stage II	Stage III
const	C_0	-152.28520000	39.25815000	6.73109700	-199.06630000	-1.08985900	13.49739000
av	C_1	26.70734000	-8.35726800	-0.56089030	28.35580000	0.36868410	-4.63420300
temp	C_2	3.23961400	-0.30905310	-0.06858246	2.57885000	0.06581096	-0.48719540
ln*sts*	C_3	34.35092000	-2.20299600	-0.51050640	34.68025000	0.23497480	-3.15099200
ln*n*	C_4	-0.24692890	-4.90307500	-0.05796839	18.04529000	0.12360040	3.20167100
av, ·temp	C_5	-0.55628900	0.09983803	0.00813821	-0.32663610	-0.00786988	0.14027550
*av,·*ln*sts*	C_6	-5.88812800	0.89503670	0.02736067	-4.65914300	0.00000000	1.11115600
av, ·ln*n*	C_7	0.00000000	1.14569000	0.00000000	-2.35860200	0.00863518	-0.23271080
temp, ·ln*sts*	C_8	-0.71946270	-0.07265415	0.00376373	-0.37225750	-0.00589514	0.11772420
temp, ·ln*n*	C_9	0.00313412	0.03617961	0.00000000	-0.19464310	-0.00091239	-0.03678063
ln*sts*,·ln*n*	C_{10}	0.00638769	0.32122320	0.00000000	-2.75434100	-0.04474705	-0.70174950
av, ·ln*sts,* ·ln*n*	C_{11}	0.00000000	-0.13165800	0.00000000	0.31293540	0.00000000	0.05153891
av, ·temp, ·ln*sts*	C_{12}	0.12222190	0.00000000	0.00000000	0.03918020	0.00000000	-0.03254697
av, ·temp, ·ln*n*	C_{13}	0.00000000	-0.01300050	0.00000000	0.01952211	0.00000000	0.00000000
*temp,·*ln*sts,* ·ln*n*	C_{14}	0.00000000	0.00978649	0.00000000	0.01729624	0.00000000	0.00768121
R^2		0.90	0.84	0.76	0.57	0.97	0.92

Table 3.8: Laboratory Two-Stage Weibull Shear Integrated Equations Using Temperature Effect *(continued)*

Item	Coefficient	Mix Types			
		AR4000-D		RAC-G	
		Stage II	Stage III	Stage II	Stage III
const	C_0	-1.33472800	217.97000000	16.81258000	18.63981000
av	C_1	0.57320920	-37.04035000	-0.59414140	-1.90115700
temp	C_2	0.03827847	-4.04320500	-0.17122420	-0.22023500
ln*sts*	C_3	0.38781380	-46.28002000	-3.46666800	-2.26476700
ln*n*	C_4	0.06645535	-1.84949800	-0.14532950	-0.47142820
av, ·temp	C_5	-0.00688036	0.69065200	-0.00428085	0.02249325
av,·ln*sts*	C_6	-0.06590134	7.91656300	0.20936260	0.19028140
av, ·ln*n*	C_7	0.01688064	0.36216790	-0.03070482	0.06442946
temp, ·ln*sts*	C_8	0.00000000	0.85964560	0.03714547	0.01620826
temp, ·ln*n*	C_9	-0.00178949	0.04291182	0.00242055	0.00902497
ln*sts*,·ln*n*	C_{10}	-0.03172248	-0.05351421	0.03005671	0.00781635
av, ·ln*sts,* ·ln*n*	C_{11}	0.00000000	0.00000000	0.00000000	0.00000000
av, ·temp, ·ln*sts*	C_{12}	0.00000000	-0.14648520	0.00000000	0.00000000
av, ·temp, ·ln*n*	C_{13}	0.00000000	-0.00763623	0.00000000	-0.00147065
temp,·ln*sts,* ·ln*n*	C_{14}	0.00000000	0.00000000	0.00000000	0.00000000
R^2		0.88	0.82	0.89	0.54

3.6.3 Equations from Gradation Effect Data

This analysis was undertaken to evaluate whether dense-graded mixes with MB4, MB15, and MAC15 binders retained the good fatigue-resistance capacity of gap-graded mixes with these binders, but with improved rutting resistance. A limited set of data from the gradation effect experiment were used to establish the laboratory two-stage Weibull fatigue and shear integrated equations.

Tables 3.9 (fatigue) and 3.10 (shear) list the regression results of Stages II and III for the MB4-D, MB15-D, and MAC15-D mixes. The fitting results, as plotted in Figures A.79 to A.81 (fatigue) and Figures A.82 to A.84 (shear) in Appendix A were generally satisfactory for all mixes.

3.7. Fatigue and Shear Performance Comparison

3.7.1 Comparison of Fatigue and Shear Data Using Traditional Parameters

Laboratory fatigue and shear performance test results cannot be directly compared given the differences in the nature of the tests. Instead, the mean values of fatigue life and Cycles to 5 Percent Permanent Shear Strain of the various effect groups were compared. The effect-groups discussed below include temperature, air-void content, aging, and gradation.

Figure 3.37 illustrates the use of a vector diagram to compare fatigue and shear performance using the natural logarithms of the traditional fatigue and shear test parameters of 50 Percent Loss of Initial Stiffness ($\ln N_f$) and Repetitions to 5 Percent Permanent Shear Strain ($\ln pct5$), respectively, for various effect-groups for each mix type. The background arrow points in the direction of materials with both better fatigue and shear performance. Observations from this diagram include:

- Increasing air-void content generally reduced both the fatigue and shear performance for all five mix types, as expected.
- Aging had differing effects on the various mixes:
  - It improved shear resistance and reduced fatigue performance for the AR4000-D, MB4, and MB15-G mixes as expected.
  - For the MAC15-G mixes, fatigue and shear resistance diminished with aging effect.
  - For the RAC-G mixes, aging improved fatigue performance marginally and slightly reduced shear resistance.
- Dense-graded MAC15 and MB15 mixes had better shear performance than the gap-graded mixes, but poorer fatigue-resistance. The dense-graded MB4 mixes had poorer fatigue- and shear-resistance compared to the gap-graded MB4 mixes. The extent of this tradeoff can be assessed for each mix in the vector diagrams.

Table 3.9: Two-Stage Weibull Fatigue Integrated Equations Using Gradation Effect Data

Item	Coefficient	Mix Types					
		MAC15-D		MB15-D		MB4-D	
		Stage II	Stage III	Stage II	Stage III	Stage II	Stage III
const	C_0	-4055.81200000	-9339.97800000	35.36408000	33.97827000	-11.38856000	49.95085000
av	C_1	678.09220000	1762.09220000	-5.52654800	-4.65233000	0.00000000	-9.45259900
temp	C_2	205.68340000	0.00000000	0.00000000	0.00000000	0.00000000	0.00000000
ln*stn*	C_3	-547.10890000	-1337.61400000	6.13045000	5.39829600	-0.89267740	6.94289500
ln*n*	C_4	3.42089400	937.27660000	1.01393000	0.13862120	2.24495000	1.18659000
av,·temp	C_5	-34.56455000	0.00000000	0.00000000	0.00000000	0.00000000	0.00000000
av,·ln*stn*	C_6	91.4005600	251.64920000	-0.87083660	-0.70134570	0.00000000	-1.24806800
av,·ln*n*	C_7	-0.28707310	-171.71090000	-0.10739190	-0.01731518	0.00000000	-0.03270903
temp,·ln*stn*	C_8	27.86587000	0.00000000	0.00000000	0.00000000	0.00000000	0.00000000
temp,·ln*n*	C_9	0.09440960	0.00000000	0.00000000	0.00000000	0.00000000	0.00000000
ln*stn,*·ln*n*	C_{10}	0.42922950	133.35120000	0.00000000	-0.02085901	0.24549320	0.10927420
av,·ln*stn,*·ln*n*	C_{11}	0.00000000	-24.39271000	0.00000000	0.00000000	0.00000000	0.00000000
av,·temp,·ln*stn*	C_{12}	-4.67369900	0.00000000	0.00000000	0.00000000	0.00000000	0.00000000
av,·temp,·ln*n*	C_{13}	0.00000000	0.00000000	0.00000000	0.00000000	0.00000000	0.00000000
temp,·lnstn,·ln*n*	C_{14}	0.00000000	0.00000000	0.00000000	0.00000000	0.00000000	0.00000000
R^2		0.99	0.94	0.99	0.99	0.98	0.99

Table 3.10: Laboratory Two-Stage Weibull Shear Integrated Equations Using Gradation Effect Data

Item	Coefficient	Mix Types					
		MAC15-D		MB15-D		MB4-D	
		Stage II	Stage III	Stage II	Stage III	Stage II	Stage III
const	C_0	44.36049000	-4.29064900	51.90478000	60.99952000	19.21360000	68.20344000
av	C_1	-6.99395200	0.90735900	-8.20396000	-13.48568000	-3.31531000	-8.33512900
temp	C_2	0.00000000	0.00000000	0.00000000	0.00000000	0.00000000	0.00000000
ln*sts*	C_3	-8.94704200	1.65675700	-10.81793000	-16.68616000	-3.89966900	-13.82772000
ln*n*	C_4	-0.71647990	-0.26338750	-0.95391320	4.69091400	0.11140270	-3.01453700
av, ·temp	C_5	0.00000000	0.00000000	0.00000000	0.00000000	0.00000000	0.00000000
av,·ln*sts*	C_6	1.48186400	-0.24890540	1.77781400	3.65039700	0.74938690	1.66327600
av, ·ln*n*	C_7	0.14533840	0.02205515	0.14203750	-0.23231350	0.03334438	0.15375660
temp, ·ln*sts*	C_8	0.00000000	0.00000000	0.00000000	0.00000000	0.00000000	0.00000000
temp, ·ln*n*	C_9	0.00000000	0.00000000	0.00000000	0.00000000	0.00000000	0.00000000
ln*sts*,·ln*n*	C_{10}	-0.06118177	0.02064384	0.00000000	-0.80358600	-0.08827740	0.47813610
av, ·ln*sts,* ·ln*n*	C_{11}	0.00000000	0.00000000	0.00000000	0.00000000	0.00000000	0.00000000
av, ·temp, ·ln*sts*	C_{12}	0.00000000	0.00000000	0.00000000	0.00000000	0.00000000	0.00000000
av, ·temp, ·ln*n*	C_{13}	0.00000000	0.00000000	0.00000000	0.00000000	0.00000000	0.00000000
temp, ·ln*sts,* ·ln*n*	C_{14}	0.00000000	0.00000000	0.00000000	0.00000000	0.00000000	0.00000000
R^2		0.99	0.96	0.96	0.91	0.99	0.74

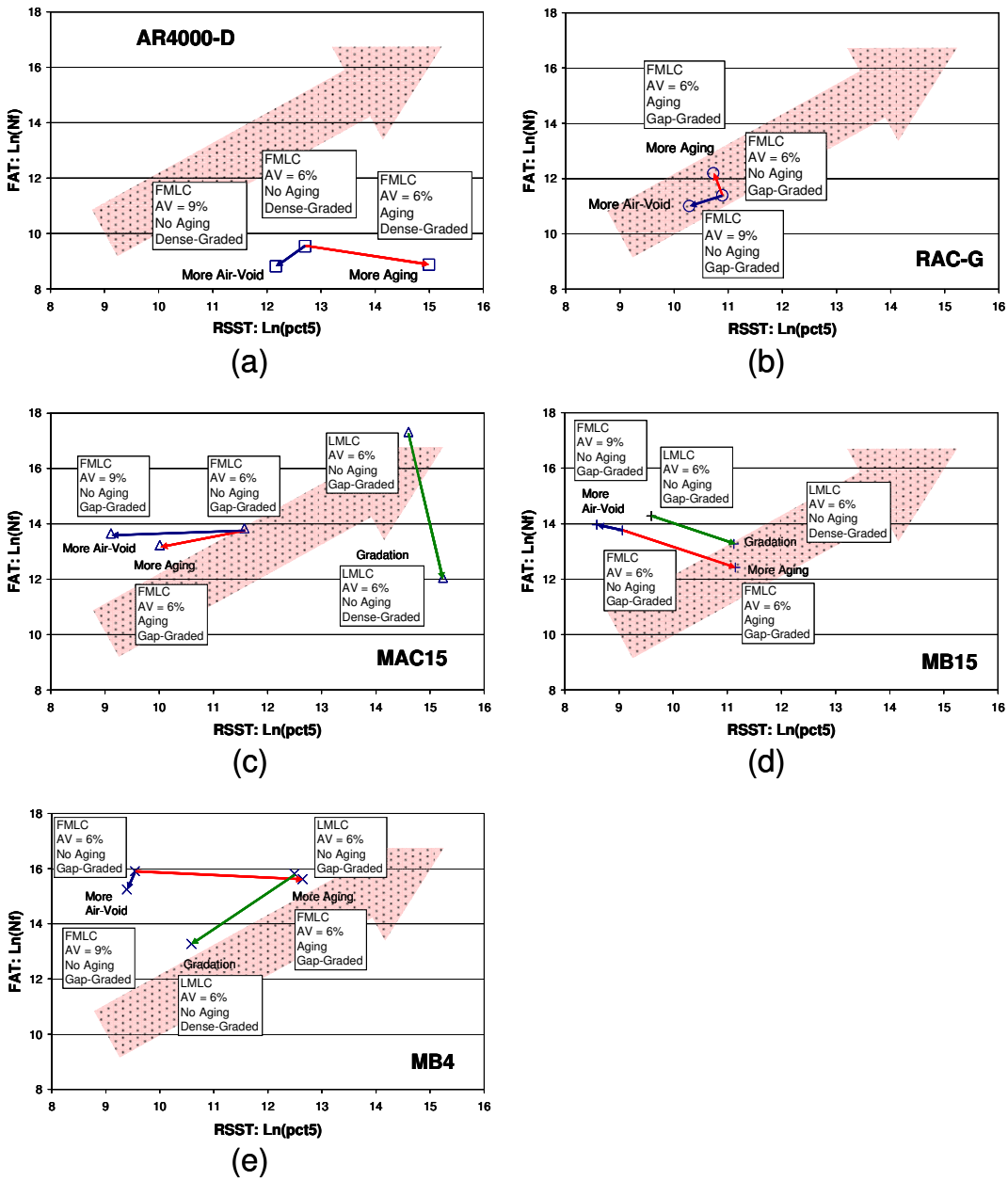

Figure 3.37: Fatigue versus shear performance of various mix types and testing conditions.
(Note: background arrow indicates direction of both improved fatigue and shear performance)

3.7.2 Weibull Parameters Identifying Fatigue Performance

As noted, the traditional fatigue life parameter is defined as the number of load repetitions at which a specimen mix reaches 50 percent stiffness reduction ($\ln N_f$). However, asphalt mixes with modified binders rarely reach this point in a reasonable testing period. Consequently, results have to be extrapolated to obtain the fatigue life. Even more importantly, this parameter does not reflect the much better crack propagation properties of these mixes, as illustrated previously in Figure 3.14. In three-stage Weibull analyses, the fundamental Weibull parameters are process-oriented parameters by definition and

therefore more appropriate for predicting fatigue life of modified binder mixes and for considering the entire damage process including initiation and propagation.

Two combinations of fatigue Weibull parameters to be considered in place of the traditional parameters for identifying fatigue performance are discussed below.

- **Fatigue Life (ln*Nf*) vs. ln(β_3/β_2) vs. lnα_2/β_2**
  - The ln(β_3/β_2) parameter indicates whether or not crack propagation occurs in the third stage of the Weibull curve, based on the following rules:
    - If ln(β_3/β_2) > 0, i.e., $|\beta_3| > |\beta_2|$, then crack propagation occurs at third stage.
    - If ln(β_3/β_2) ≤ 0, then no crack propagation develops in the third stage.
  - The lnα_2 and β_2 parameters are the intercept and slope at Stage II which is recognized as a critical stage in fatigue analysis. The rationale of choosing the lnα_2/β_2 parameter is discussed in Section 3.8. More negative values of lnα_2/β_2 indicate improved fatigue life.
  - Figure 3.38 is the performance contour plot of fatigue life (ln*Nf*) in terms of ln(β_3/β_2) and lnα_2/β_2 with their corresponding density functions. For each mix, the mean position of the density function is presented in the density plot. Ideally, a good parameter is expected to have a symmetrical bell-shape density function with one mode. In the performance contour plot, it is apparent that the data are separated into two groups by the zero line, resulting in a two-mode density function.

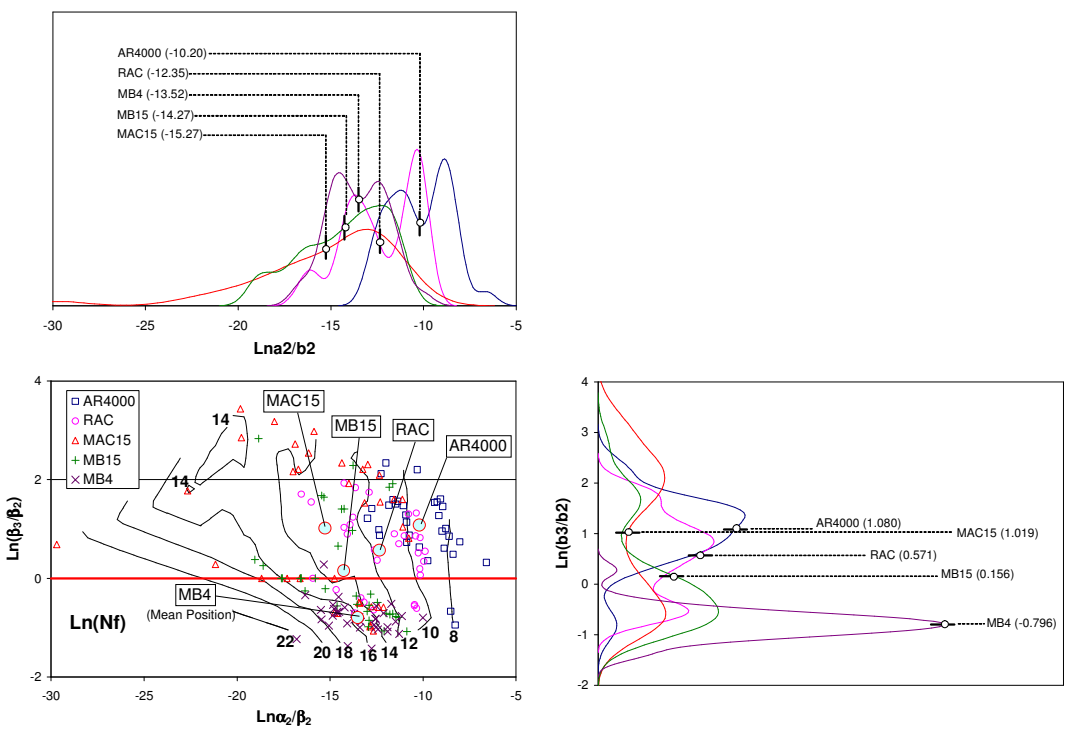

Figure 3.38: Fatigue life (ln*Nf*) contour plot in terms of ln(β_3/β_2) and lnα_2/β_2.
(Corresponding density functions shown in the bottom-right and top-left respectively)

- **Fatigue Life (ln*Nf*) vs. lnα_3/β_3 vs. lnα_2/β_2**
  - The lnα_3/β_3 and lnα_2/β_2 parameters are derived from the fundamental Stage II and III Weibull parameters. The performance contour plot in Figure 3.39 presents a simple contour pattern, with contour lines of fatigue life (ln*Nf*) evenly spaced, and increasingly negative values of lnα_3/β_3 and lnα_2/β_2, indicating improved fatigue life. The density plots of lnα_3/β_3 and lnα_2/β_2 show that, with the exception of RAC-G mixes, the shapes of the density functions are acceptable despite not having a symmetrical bell shape with one mode.

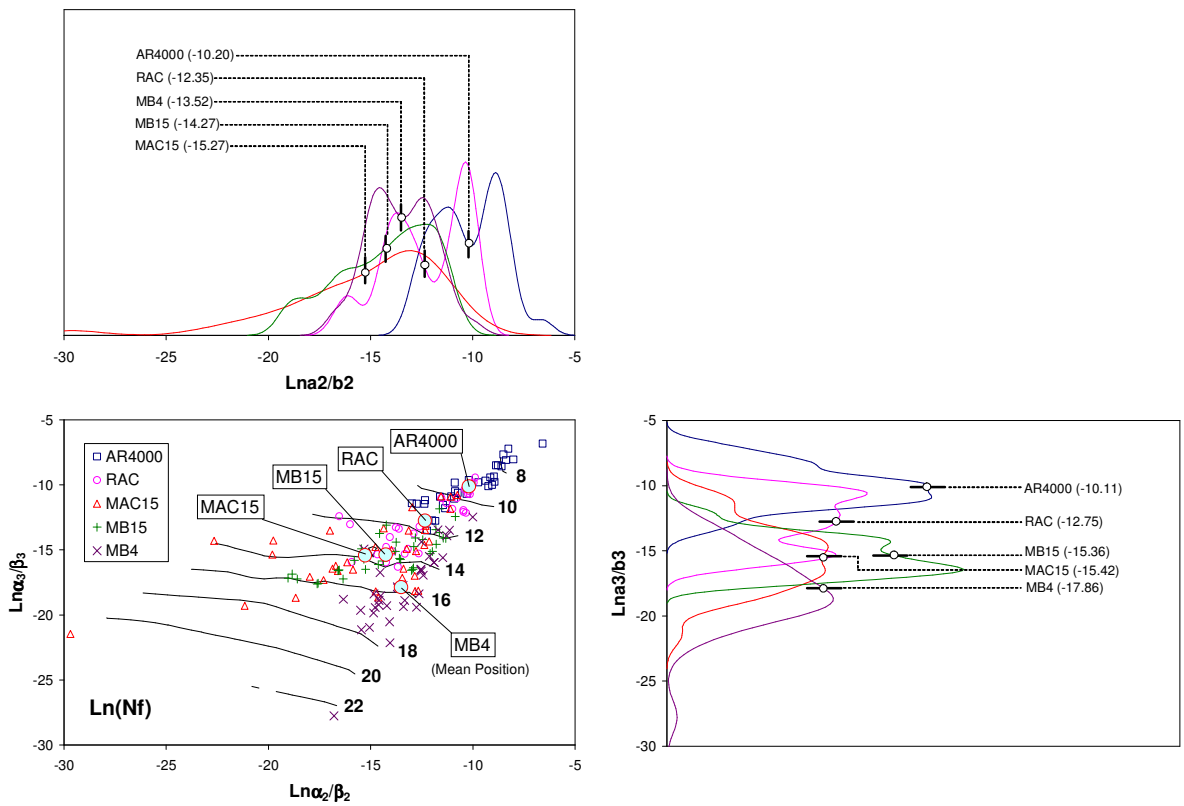

Figure 3.39: Fatigue life (ln*Nf*) contour plot in terms of lnα_3/β_3 and lnα_2/β_2.
(Corresponding density functions shown in the bottom-right and top-left respectively)

3.7.3 Weibull Parameters Identifying Shear Performance

Shear performance is conventionally measured as the load cycles when the material reaches five percent permanent shear strain with the controlled-load Repeated Simple Shear Test at Constant Hheight (RSST-CH). As with fatigue testing, this point could not be reached within a reasonable testing time period for many of the modified binder mixes and extrapolation, with a risk of increased uncertainty, is necessary. The use of process-oriented Weibull parameters to identify the shear performance appears to be more appropriate than the traditional parameters for this test of rutting performance.

Three combinations of shear Weibull parameters for identifying shear performance are discussed below:

- **Permanent Shear Strain (ln*pct5*) vs. β_3 vs. lnα_3**
  - The fundamental Weibull parameters in Stage III are selected because it is recognized that shear performance is most influenced in this stage. Figure 3.40 illustrates the performance contour plot of shear strain (ln*pct5*) in terms of β_3 and lnα_3. Lower values of β_3 and lnα_3 indicate better rutting performance. The contour lines are parallel with increasing values associated with decreasing intervals between contour lines. Density functions are all skewed to the right (i.e., unevenly distributed data points) when presented in terms of β_3 and lnα_3.

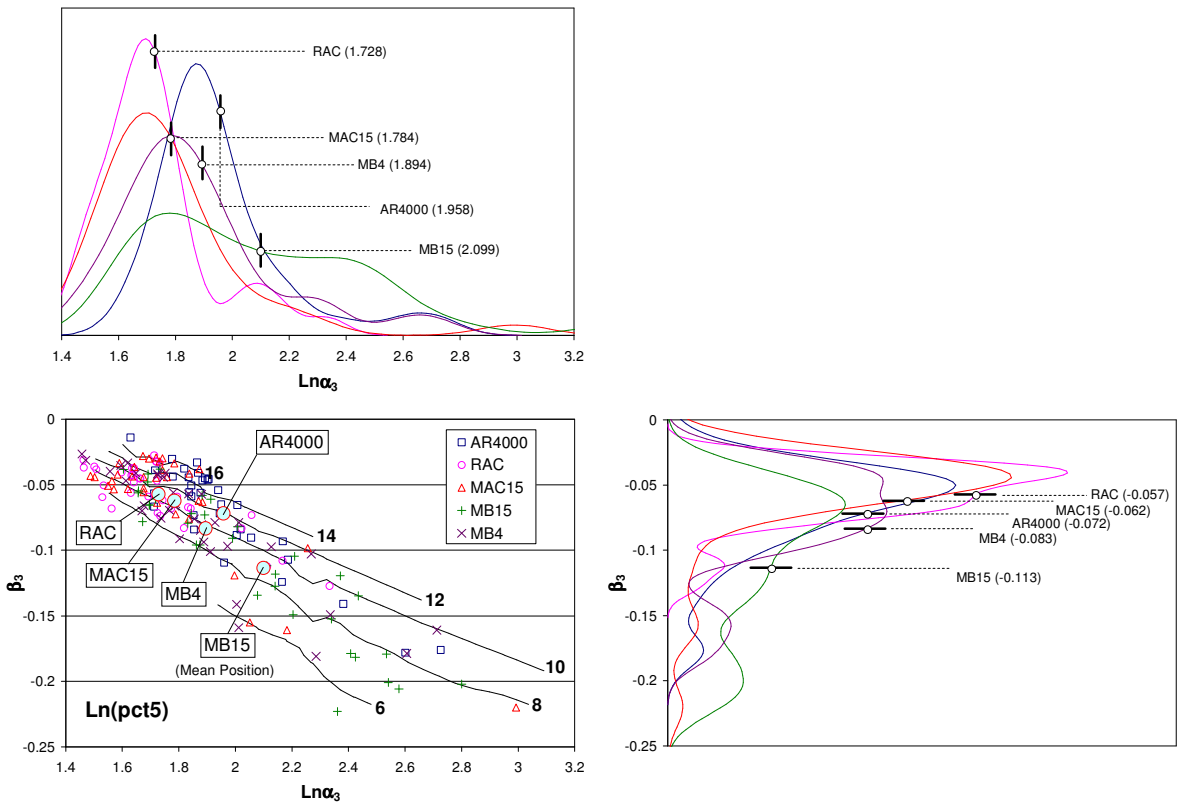

Figure 3.40: Permanent shear strain (ln*pct5*) contour plot in terms of β_3 and lnα_3.
(Corresponding density functions are shown in the bottom-right and top-left respectively.)

- **Permanent Shear Strain (ln*pct5*) vs. ln(β_3/β_2) vs. lnα_3/β_3**
  - The Stage III lnα_3 and β_3 parameters are highly negative-correlated (correlation of -0.89) compared to the Stage II lnα_2 and β_2 parameters (correlation of -0.46), which supports the use of Stage III parameters in predicting shear performance. Lower values of ln(β_3/β_2) and lower values of ln(α_3/β_3) indicate better shear performance. The associated density plots of lnα_3/β_3 show no obvious two-mode distributions. The performance contour plot (Figure 3.41) of permanent shear strain (ln*pct5*) against lnα_3/β_3 in combination with ln(β_3/β_2) presents a radiated pattern originating from the top-right corner of the figure, with contour line values increasing from right to left. The pattern is similar to the fatigue performance contour plot in

terms of $\ln(\beta_3/\beta_2)$ and $\ln\alpha_2/\beta_2$ but with opposite results with respect to the zero line. Unlike the fatigue performance contour plot of $\ln(\beta_3/\beta_2)$ and $\ln\alpha_2/\beta_2$, there are no obvious two-mode density functions for each mix type.

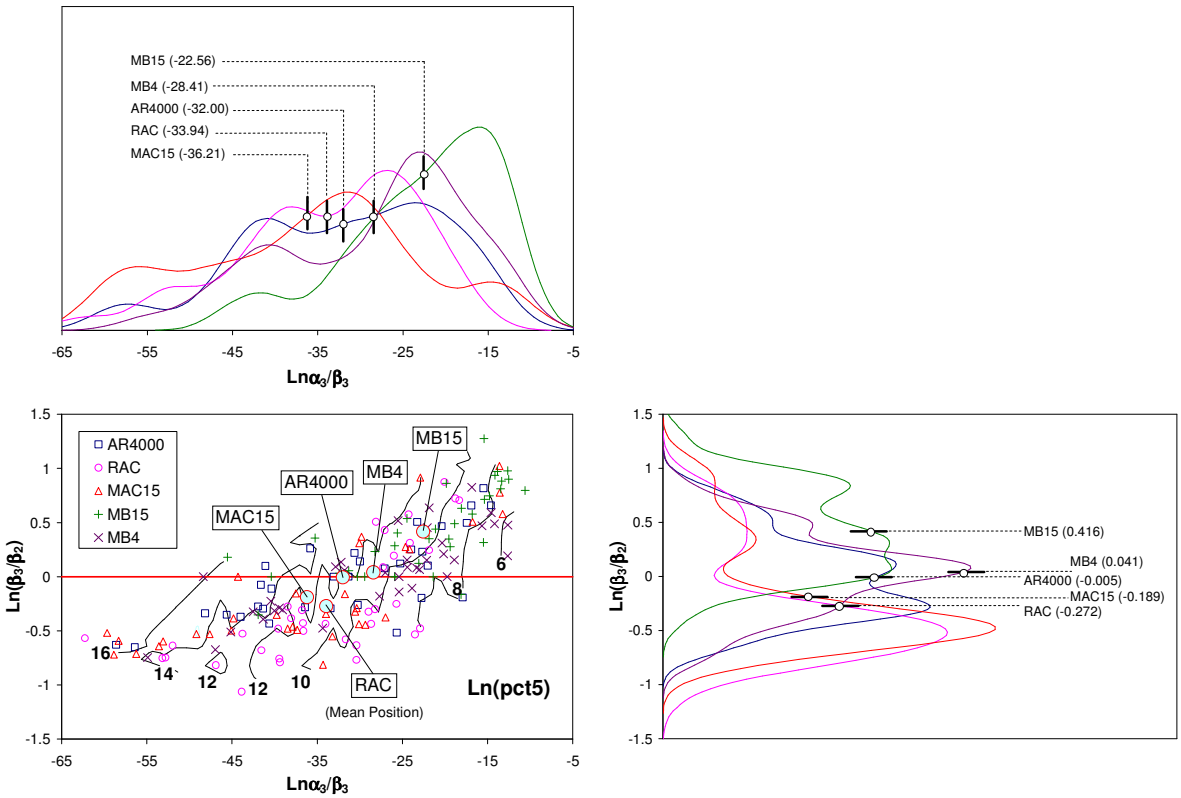

Figure 3.41: Permanent shear strain (ln*pct5*) contour plot in terms of $\ln(\beta_3/\beta_2)$ and $\ln\alpha_3/\beta_3$.
(Corresponding density functions are shown in the bottom-right and top-left respectively.)

- **Permanent shear strain (ln*pct5*) vs. $\ln\alpha_3/\beta_3$ vs. $\ln\alpha_2/\beta_2$**
  - The $\ln\alpha_3/\beta_3$ and $\ln\alpha_2/\beta_2$ parameters generate almost the same pattern (Figure 3.42) as that of the fatigue performance contour plot (Figure 3.39) using the same parameters. Lower values of both parameters indicate better shear performance. However, due to the larger variation in the shear test results, the contour line appears as a band rather than a clear line. The shapes of the density plots, although not as symmetrical, are considered acceptable. The use of the $\ln\alpha_3/\beta_3$ and $\ln\alpha_2/\beta_2$ parameters provides a consistent way of characterizing both fatigue and rutting performance of any asphalt concrete mix.

3.8. Rationale for Selecting the $\ln\alpha_3/\beta_3$ and $\ln\alpha_2/\beta_2$ Parameters

Based on the comparisons in Section 3.7.2 and 3.7.3 and further analysis, the parameters $\ln\alpha_3/\beta_3$ and $\ln\alpha_2/\beta_2$ are recommended for comparing fatigue and shear test results in place of the traditional

parameters. These parameters are recommended for use in vector plots considering fatigue and shear performance of different mixes together.

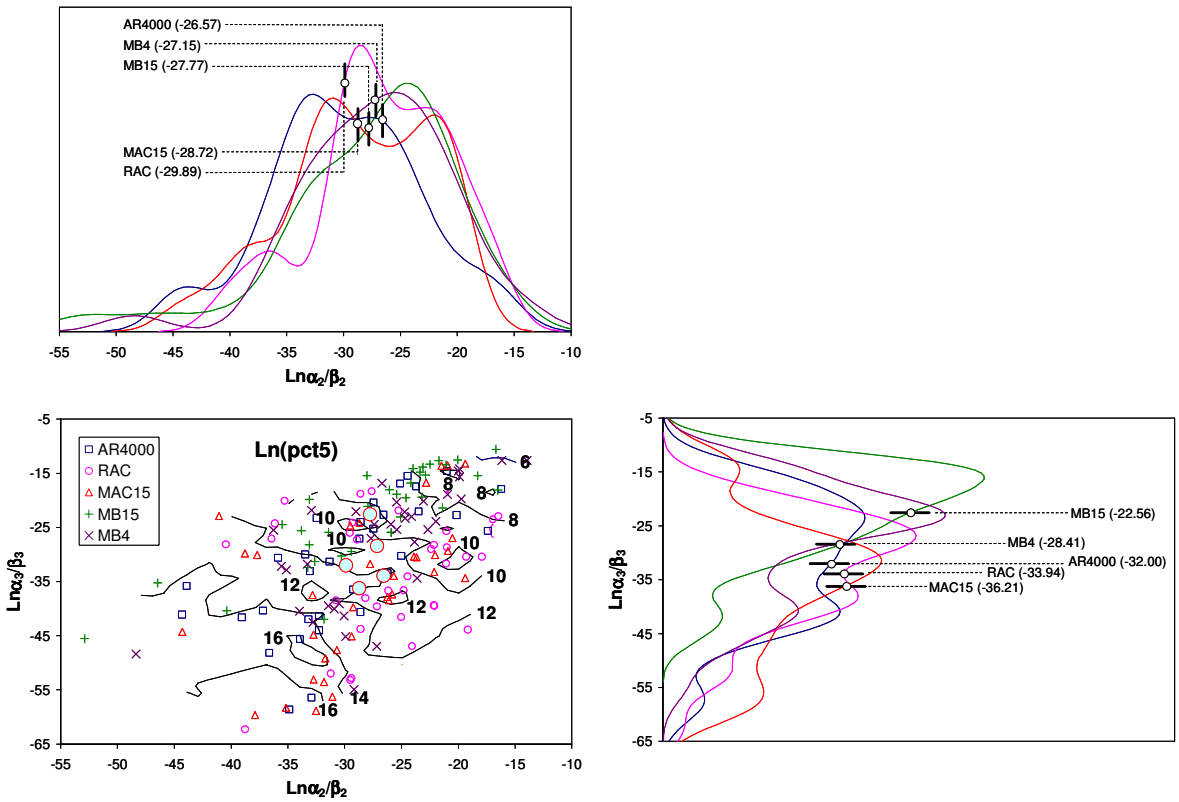

Figure 3.42: Permanent shear strain (ln*pct5*) contour plot in terms of $ln\alpha_3/\beta_3$ and $\ln\alpha_2/\beta_2$.
(Corresponding density functions are shown in the bottom-right and top-left respectively.)

The rationale for selecting $\ln\alpha_3/\beta_3$ and $\ln\alpha_2/\beta_2$ parameters to specify the fatigue and rutting performance of asphalt mixes is based on the hypothesis: "Stages II and III of a fatigue/shear Weibull curve are critical in determining the fatigue/rutting performance."

The following facts are provided to support the hypothesis:

- The average Stage I and II separation point (n_1) values were 164 and 23 repetitions for fatigue and shear test results, respectively, which are relatively small in comparison with the corresponding average Stage II and III separation point (n_2) values of 19,010 and 642 repetitions, respectively. Quantitatively, this shows that Stages II and III are more important than Stage I.
- Given that the intercepts and slopes of each stage ($\ln\alpha_1$, $\ln\alpha_2$, $\ln\alpha_3$, β_2, and β_3) can be used to determine the full Weibull curve and that Stages II and III dominate overall performance through the entire damage process of each test, then the parameters $\ln\alpha_2$, $\ln\alpha_3$, β_2, and β_3 should be considered as fundamental parameters.

The performance contour plots shown above explore various combinations of these four basic parameters at Stages II and III. Contour plots using the $\ln\alpha_3/\beta_3$ and $\ln\alpha_2/\beta_2$ parameters provide a consistent pattern for fatigue and shear, with increasingly negative values of $\ln\alpha_3/\beta_3$ and $\ln\alpha_2/\beta_2$ indicating better fatigue and shear performance. Figure 3.43, supported by Equations 3.19 through 3.22, illustrate two shear cases and two fatigue cases at Stage III verifying this statement. Sub-indices outside brackets indicate Mix 1 or Mix 2.

- **Case I (Shear):**

$$(\beta_3)_1 = (\beta_3)_2 < 0 \; ; \; (\ln\alpha_3)_1 > (\ln\alpha_3)_2 > 0$$

$$\Rightarrow \frac{(\ln\alpha_3)_1}{(\beta_3)_1} < \frac{(\ln\alpha_3)_2}{(\beta_3)_2} < 0 \quad \Leftrightarrow \quad (\ln pct5)_1 > (\ln pct5)_2$$

(3.19) (Fig 3.43[a])

- **Case II (Shear):**

$$(\ln\alpha_3)_1 = (\ln\alpha_3)_2 > 0 \; ; \; 0 > (\beta_3)_1 > (\beta_3)_2$$

$$\Rightarrow \frac{(\ln\alpha_3)_1}{(\beta_3)_1} < \frac{(\ln\alpha_3)_2}{(\beta_3)_2} < 0 \quad \Leftrightarrow \quad (\ln pct5)_1 > (\ln pct5)_2$$

(3.20) (Fig 3.43[b])

- **Case III (Fatigue):**

$$(\beta_3)_1 = (\beta_3)_2 > 0 \; ; \; 0 > (\ln\alpha_3)_1 > (\ln\alpha_3)_2$$

$$\Rightarrow \frac{(\ln\alpha_3)_2}{(\beta_3)_2} < \frac{(\ln\alpha_3)_1}{(\beta_3)_1} < 0 \quad \Leftrightarrow \quad (\ln Nf)_2 > (\ln Nf)_1$$

(3.21) (Fig 3.43[c])

- **Case IV (Fatigue):**

$$(\ln\alpha_3)_1 = (\ln\alpha_3)_2 < 0 \; ; \; (\beta_3)_1 > (\beta_3)_2 > 0$$

$$\Rightarrow \frac{(\ln\alpha_3)_2}{(\beta_3)_2} < \frac{(\ln\alpha_3)_1}{(\beta_3)_1} < 0 \quad \Leftrightarrow \quad (\ln Nf)_2 > (\ln Nf)_1$$

(3.22) (Fig 3.43[d])

Based on the observations from the summary boxplots (Figures 3.44 and 3.45) of stiffness ratios and accumulated permanent shear strains at the Stage I and Stage II separation points, it was found that:

- The deterioration of stiffness ratio and permanent shear strain at Stage I separation (n_1) is relatively small compared with the deterioration in Stages II and III.
- Although a partial factorial with consequent reduced number of tests was used, the stiffness ratio and accumulated permanent shear strain at Stage II separation (n_2) do not exceed the limits of 50 Percent Loss in Stiffness or Five Percent Permanent Shear Strain, further indicating suitability of

the fundamental Weibull parameters associated with Stages II and III for identifying fatigue and shear performance.

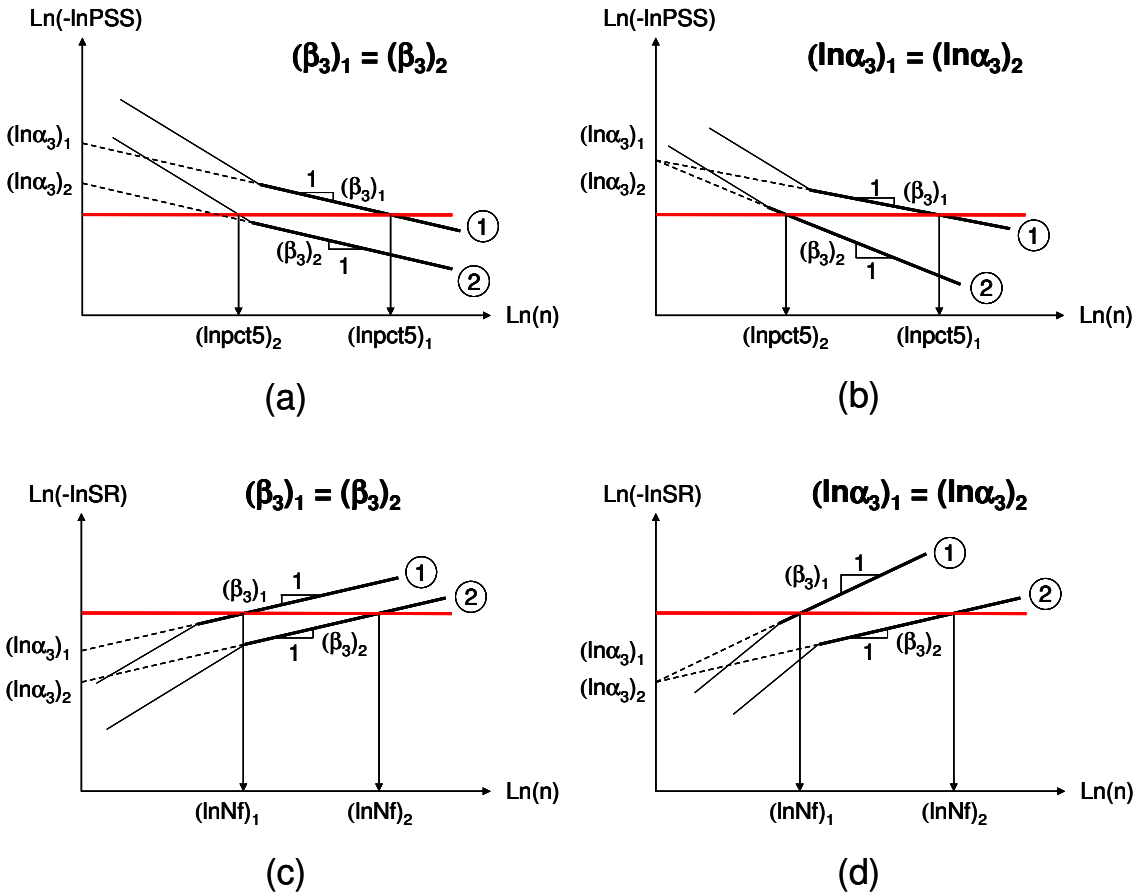

Figure 3.43: Schematic interpretation between lnα_3/β_3 and ln*pct5*/ln*Nf*.
(a) Case I (Shear): $(\beta3)1 = (\beta3)2 < 0$; $(\ln\alpha3)1 > (\ln\alpha3)2 > 0$;
(b) Case II (Shear): $(\ln\alpha3)1 = (\ln\alpha3)2 > 0$; $0 > (\beta3)1 > (\beta3)2$;
(c) Case III (Fatigue): $(\beta3)1 = (\beta3)2 > 0$; $0 > (\ln\alpha3)1 > (\ln\alpha3)2$;
(d) Case IV (Fatigue): $(\ln\alpha3)1 = (\ln\alpha3)2 < 0$; $(\beta3)1 = (\beta3)2 > 0$.

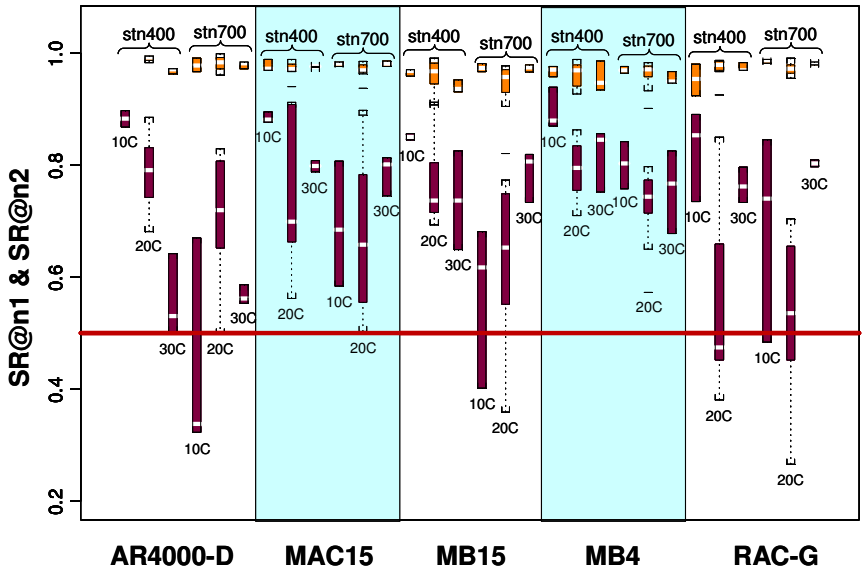

Figure 3.44: Summary boxplots of stiffness reduction at Stage I and II separation points.
($SR@n_1$ in grey and $SR@n_2$ in black).

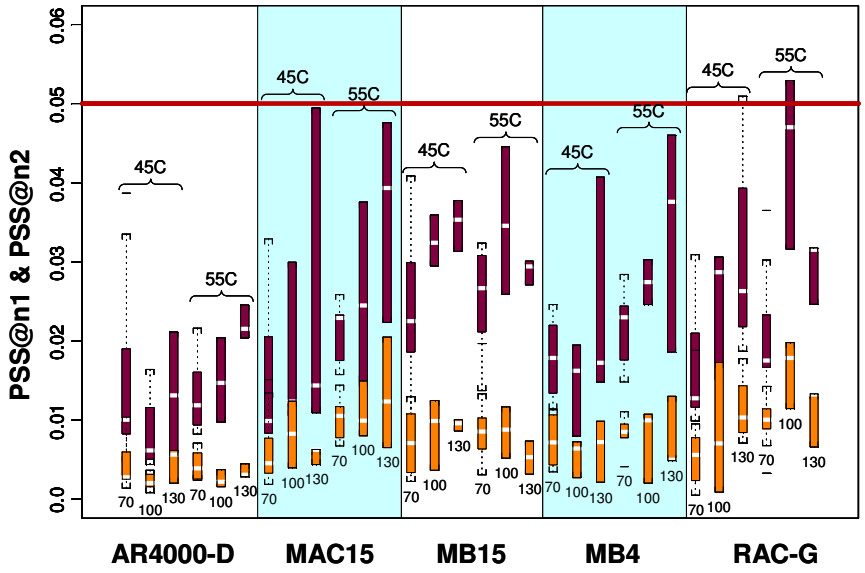

Figure 3.45: Summary boxplots of permanent shear strain at Stage I and II separation points.
($SR@n_1$ in grey and $SR@n_2$ in black.)

3.9. Findings and Discussion

3.9.1 Use of Three-Stage Weibull Analysis to Characterize Fatigue and Shear Tests

The fitting of flexural controlled-deformation fatigue test results with a three-stage Weibull equation appears promising. The three-stage Weibull equation is flexible and sufficiently precise to accommodate most fatigue damage curve shapes, while adequately characterizing fatigue performance in terms of the entire damage process. Conventional two-point fatigue life modeling considers only initial (50th load

repetitions) and end (50 percent stiffness reduction) points and neglects the fatigue damage process. For mixes using modified binders, the traditional parameter of 50 Percent Loss of Initial Stiffness does not capture the improved crack propagation resistance of rubber- and polymer-modified mixes that occurs after 50 Percent Loss of Stiffness. In addition, test duration to reach 50 percent stiffness reduction is very long and thus not feasible. Hence, to accurately characterize the fatigue performance of these mixes, the fatigue damage process is important. Occasionally there are problems fitting the transition from Stage II initiation to Stage III propagation. This is not common with unmodified mixes.

The fit of a controlled-load repetitive simple shear test with the three-stage Weibull equation is also satisfactory and provides an even better fit than that of a flexural controlled-deformation fatigue test, especially at Stage III.

3.9.2 Most Appropriate Parameters Identifying Fatigue and Shear Performance

Based on the findings of this study, the $\ln\alpha_2/\beta_2$ and $\ln\alpha_3/\beta_3$ parameters can be used for characterizing both fatigue and shear performance in a consistent way, with increasingly negative values corresponding to improved performance for both flexural fatigue tests and repeated shear tests. This can be summarized as follows (Table 3.11):

Table 3.11: Summary of Parameters Identifying Fatigue and Shear Performance

Test	Parameter	Indicator of	Interpretation
Fatigue	$\ln\alpha_2/\beta_2$	Crack initiation performance	Increasingly negative values = improved performance
	$\ln\alpha_3/\beta_3$	Crack propagation performance	Increasingly negative values = improved performance
Shear	$\ln\alpha_2/\beta_2$	Early trafficking performance	Increasingly negative values = improved performance
	$\ln\alpha_3/\beta_3$	Later trafficking performance	Increasingly negative values = improved performance

3.9.3 Comparison of Fatigue and Shear Performance

Vector performance plots are considered useful for comparing the fatigue and shear performance of each mix when they are subjected to the effects of aging, air-void content, and gradation. As expected, the plots show that mixes that perform well in fatigue do not perform well in shear and vice versa. Care needs to be taken when interpreting results from small data sets.

Figures 3.46 and 3.47 show the performance contour plots of fatigue and shear test results as well as the overall mean of each mix. The plots show that the contour line values appear to be a linear combination of the $\ln\alpha_3/\beta_3$ and $\ln\alpha_2/\beta_2$ parameters. Accordingly, the ranking of fatigue and shear performance, from best to worst is:

Fatigue		Shear	
1	MB4-G	1	MAC15-G
2	MAC15-G	2	AR4000-D
3	MB15-G	3	RAC-G
4	RAC-G	4	MB4-G
5	AR4000-D	5	MB15-G

In the ranking of shear performance, the mean positions of the MAC15-G, AR4000-D, and RAC-G mixes are very close with no apparent differences. The MB4-G and MB15-G mixes are also in the same contour band with the MB4-G mixes, appearing to perform slightly better than the MB15-G mixes.

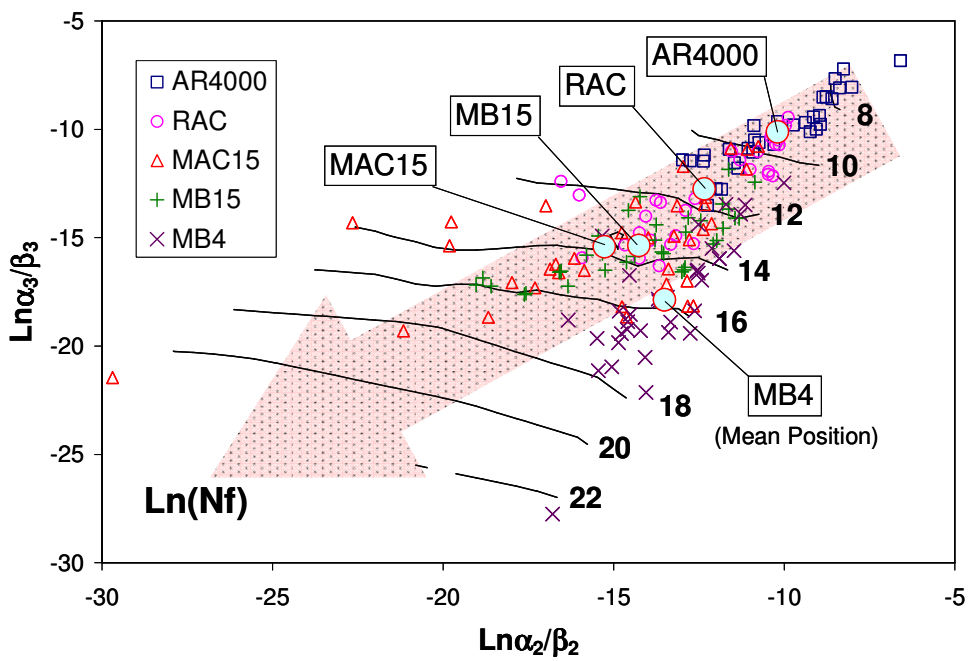

Figure 3.46: Identification of fatigue performance from lnα_3/β_3 and lnα_2/β_2 parameters.

One possible disadvantage of using lnα_3/β_3 and lnα_2/β_2 as the parameters to identify fatigue and shear performance is that independent testing variables such as temperature, stress/strain, and air-void content are embedded in the parameters, which can limit assessment of the influence of individual variables on material performance. The two parameters thus become functions of the independent testing variables, thereby potentially losing the connection between independent test variables and material performance.

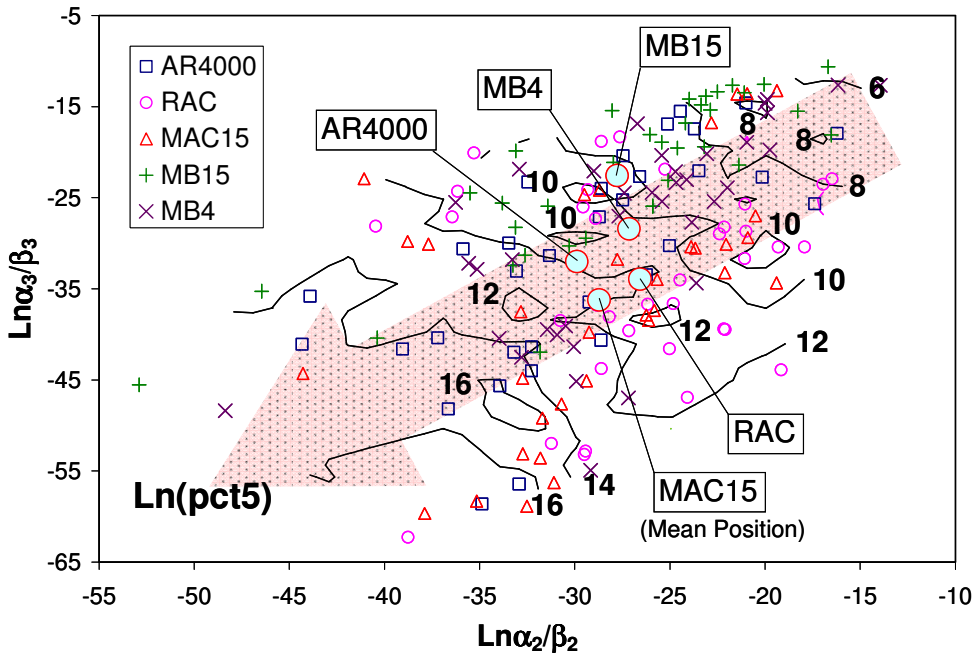

Figure 3.47: Identification of shear performance from lnα_3/β_3 and lnα_2/β_2 parameters.

Figure 3.48 shows the pruned dendrograms of lnα_3/β_3 and lnα_2/β_2 for fatigue and shear test results in this experiment. The following can be interpreted from the figure:

<u>Fatigue</u>

- The value of lnα_2/β_2 at Stage II of a fatigue Weibull curve is primarily affected by strain level, secondly by binder type, and then by air-void content and temperature.
- At Stage III, the values of lnα_3/β_3 are first determined by binder type and then by strain level.

<u>Shear</u>

- Stress level was the most significant factor affecting both values of lnα_2/β_2 and lnα_3/β_3.
  - At stress levels of 70 kPa and 100 kPa, the air-void content critically affects the values of lnα_2/β_2, with lower air-void contents resulting in increasingly improved shear performance as indicated by more negative values of lnα_2/β_2.
  - At a stress level of 130 kPa, binder type has the biggest influence on the values of lnα_2/β_2.
  - In Stage III, at a stress level of 70 kPa, the values of lnα_3/β_3 are mainly affected by temperature, with lower temperatures resulting in increasingly better performance as indicated by more negative values of lnα_3/β_3.
  - At stress levels of 100 kPa and 130 kPa, binder type has the biggest influence on lnα_3/β_3.

Table 3.12 summarizes the first-, second-, and third-level covariates (first level being most important) that affect the values of the lnα_2/β_2 and lnα_3/β_3 parameters for the fatigue and shear test results. The table

shows that strain level contributes most to crack initiation (Stage II), and that binder type contributes most to the shape of the crack propagation curve (Stage III). Stress level has the biggest influence on shear damage in both stages, with the effects of air-void content and temperature also contributing.

Table 3.12: Summary of the Covariates for Parameters that Identify Performance

(Note: importance is first level > second level > third level).

Performance Category	Parameters	1st Level	2nd Level	3rd Level
Fatigue	$\ln\alpha_2/\beta_2$ $\ln\alpha_3/\beta_3$	ln*stn* *binder*	*binder* ln*stn*	*temp, av, binder* *binder, temp*
Shear	$\ln\alpha_2/\beta_2$ $\ln\alpha_3/\beta_3$	*sts* *sts*	*av, binder* *temp, binder*	*binder, av, temp* *binder, av, temp*

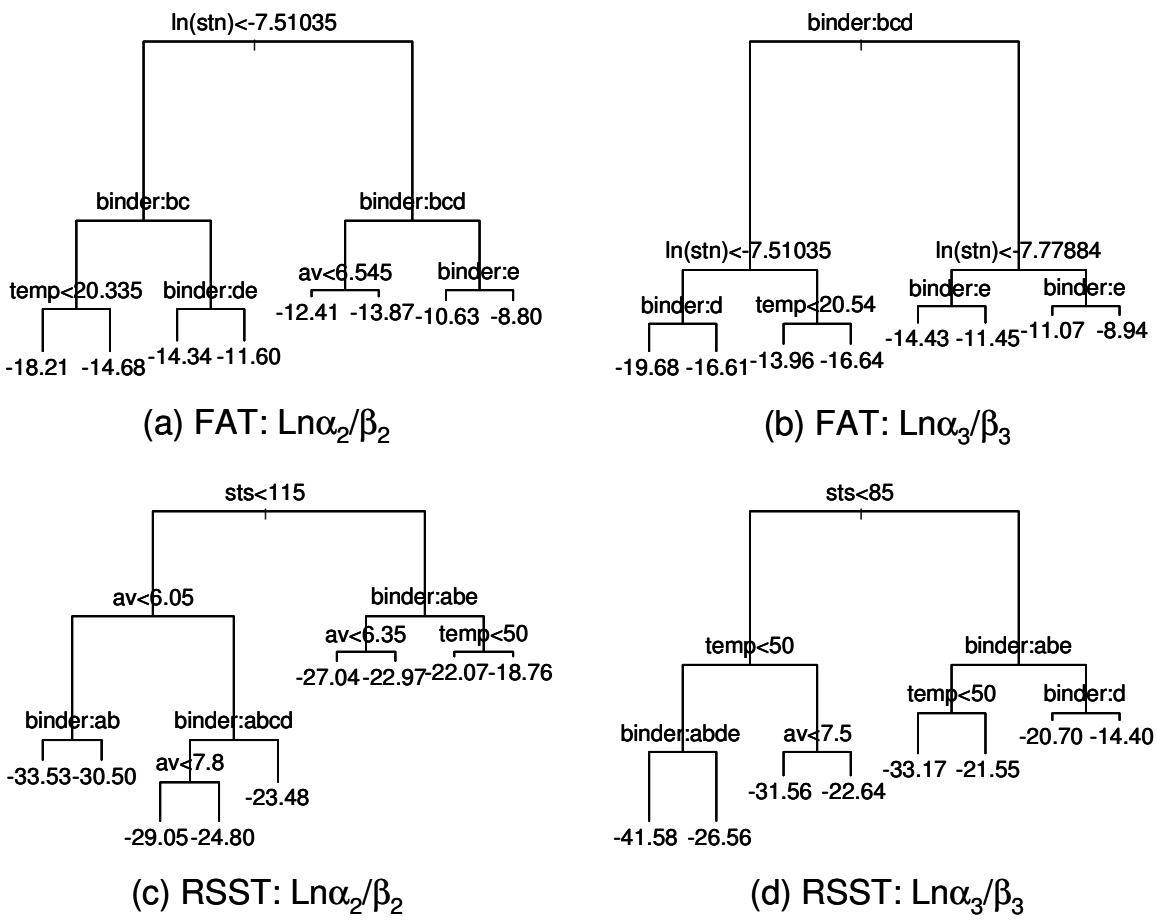

Figure 3.48: Pruned dendrograms of fatigue and shear three-stage Weibull parameters.

4. MECHANISTIC-EMPIRICAL PERFORMANCE SIMULATIONS

4.1. Introduction to Simulations

Long-Term Pavement Performance (LTPP) sections and Accelerated Pavement Testing (APT) have traditionally been used to understand pavement distress mechanisms, and to provide empirical performance data points for calibration of empirical or mechanistic-empirical design and analyses. An example is the use of the AASHO Road Test, carried out in the 1960s, to calibrate the current Caltrans flexible pavement design models.

All empirical design models and most mechanistic-empirical (ME) analysis models, including the models in the Mechanistic-Empirical Pavement Design Guide (M-E PDG), only use the end point of the LTPP data or the APT test (i.e., the "failure" state) for calibration. The data relating to the damage process leading to the failure are not used for calibration because the models do not completely replicate the process, and therefore the model will not fit the data points prior to the failure. An example is the M-E PDG asphalt fatigue models, which do not update the loss of stiffness of the mix (damage) leading to cracking during the calculation of damage from each load. This loss of stiffness during the fatigue process could have been obtained from the LTPP database used to calibrate the M-E PDG. This database contains deflection data collected (at great expense) at regular intervals each year since the sections were constructed. However, these data were not used because the models cannot use the data for calibration; therefore the process leading to the fatigue failure was assumed to be correct.

One of the advantages of using APT for developing improved mechanistic analysis models is that the sections are instrumented and the response of the pavement throughout the damage process can be measured. The pavement materials can also be thoroughly characterized in the laboratory. New analysis models are being developed by researchers that model the entire damage process, as well as the failure end-point. The UCPRC has developed such models for asphalt pavement distresses for Caltrans, which have been incorporated into two analysis packages:

- *CalME*, which includes models for fatigue damage (and its resultant cracking) of the asphalt concrete layers, and rutting of the asphalt and unbound layers. *CalME* uses layer-elastic type models for calculating most pavement response. Reflective cracking, which cannot be accurately calculated with layer models, is modeled with regression equations from finite element calculations, which are used to compute critical strains that cause reflective cracking in asphalt overlays placed on cracked or jointed pavement.

- A continuum damage mechanics (CDM) model for reflective cracking in asphalt overlays placed on cracked or jointed pavement. This model uses finite element analysis to calculate critical strains.

Both of these analysis packages use an "incremental-recursive" type analysis, meaning that damage is updated in the pavement after each set of loads, thus modeling the damage process from the beginning of loading to the final failure state of the pavement or to the cessation of loading if failure does not occur. APT data from the Heavy Vehicle Simulators and the WesTrack, NCAT, and MnRoad test tracks, together with data from Caltrans field sections, are being used to calibrate these models.

The *CalME* and continuum damage mechanics models provide much greater insight into the mechanisms of pavement damage, including the responses (deformations) of the different layers acting as a system under the combined effects of climate and traffic, and the damage that occurs because of those deformations. This insight is particularly important for modeling new materials and pavement structures for which the assumed responses and damage processes may not be correct, and which can be missed if only the failure data point at the end of the test is used for the calibration. An additional advantage of these models is that data from APT and LTPP sections that never demonstrate distress on the surface can be used for calibration of the models (e.g., some of the HVS test sections in the Reflective Cracking Study never exhibited surface cracking, but had measurable fatigue damage [loss of stiffness]).

Simulations with the *CalME* and CDM models were used for two purposes in this study:

- To simulate the HVS tests (presented in previous reports [11-17]) using uniform underlying support conditions, design thicknesses, and identical temperature conditions. These simulations were performed as a check on the results of the HVS test sections, which had some inevitable variability of testing conditions and deviations from the intended designs, to ensure that the conclusions did not change.
- To simulate the performance of other pavement structures functioning in different climate conditions. This permits extrapolation of the results of this project to a wider range of conditions, and provides Caltrans with preliminary conclusions for implementation of the results in the field.

This chapter presents the results of simulations of the HVS tests using the *CalME* models. Chapter 5 presents the results of simulations of the HVS tests using the CDM model. Chapter 6 presents the results of simulation of various pavement structures in different climate regions in California using *CalME* and CDM models.

4.2. Introduction to Simulations with *CalME*

This chapter presents simulations of the HVS tests on the Reflective Cracking Study test track using the California mechanistic-empirical design and analysis software *CalME*. The simulations are divided into six parts:

1. Simulation of the tests on the original pavement structure using actual (in-situ) conditions;
2. Simulation of the high-temperature rutting tests on the overlaid pavement structure using actual conditions;
3. Simulation of the moderate-temperature cracking tests on the overlaid pavement structure using actual conditions;
4. Simulation of the high-temperature rutting tests on the overlaid pavement structure using design thicknesses for the overlays and identical conditions of underlying pavement structure and temperature across all of the tests, and
5. Simulation of the moderate-temperature cracking tests on the overlaid pavement structure using design thicknesses for the overlays and identical conditions of underlying pavement structure and temperature across all of the tests.
6. Simulation of rutting and cracking for a hypothetical set of typical Caltrans structures and traffic conditions in different climate regions in the state.

The first three sets of simulations serve to validate the *CalME* models by comparing the calculated results from *CalME* models with the measured responses and performance. Simulations 4 and 5 provide objective ranking of the different asphalt overlays without the influence of underlying conditions, which varied in the actual HVS tests. The sixth set of simulations provide extrapolation of the HVS results to field conditions and an understanding of the sensitivity of the predicted performance of the different overlays. These results will be used to help make recommendations for implementation of the results of this project.

4.3. Data and Methodology for Simulations Using Actual Conditions

To perform the simulations using actual conditions, data from each HVS test, reported in a series of first-level analysis reports (4-9), were imported into a *CalME* database. The data comprised information on loads (time of application and load level), temperatures at different levels, Road Surface Deflectometer (RSD) results, Multi-depth Deflectometer (MDD) resilient and permanent deformations, and pavement profiles.

4.3.1 Data

The backcalculated layer moduli from the last Falling Weight Deflectometer (FWD) tests undertaken before commencement of HVS loading on each section were used as the initial asphalt concrete layer moduli (reference temperature of 20ºC). The master curve for the asphalt concrete layers was obtained from frequency sweep tests on beams in the laboratory, with the exception of the original DGAC layer where the master curve was based on FWD backcalculated moduli. The change in stiffness of the subgrade with changing stiffness of the pavement layers and with changing load level was obtained from FWD backcalculated values. These parameters were used with the layer-elastic response model *(LEAP)* to calculate stresses, strains, and deflections in the pavement structure. The strain in an overlay over an existing cracked asphalt concrete layer was calculated using a regression equation based on finite element method modeling.

4.3.2 Methodology

A number of models were used to predict the pavement performance, in terms of cracking and permanent deformation. Parameters for prediction of asphalt concrete damage were obtained from controlled strain fatigue tests on beams. Repeated Simple Shear Tests at Constant Height (RSST-CH) were used to determine the parameters for predicting permanent deformation in the asphalt concrete layers. A crushing model was developed for the lightly cemented base layer, consisting of recycled material with a high content of concrete. The model was based on a model developed for cement-treated bases (CTB) at an HVS-Nordic experiment (19). A model developed for subgrade materials in the Danish Road Testing Machine was used for permanent deformation of the unbound layers. Cracking at the pavement surface was calculated from the damage to the surface layer, using a model developed based on previous simulations of HVS tests and the FHWA WesTrack experiment in Nevada (20, 21), with parameters modified to suit the Reflective Cracking experiment.

An incremental-recursive process was used to simulate the performance of the test sections. A one-hour time increment was used for the HVS tests. For the first hour of the simulation the program reads the temperatures from the database and calculates the moduli for a constant wheel speed of 7.6 km/h. The number of loads during the first hour, as well as the load level and the tire pressure, are also read from the database. The modulus of the subgrade is adjusted to the stiffness of the pavement layers and to the load level. If the test has wheel wander, five different positions of the wheel are considered. For the first wheel position the stresses and strains at the center line of the test section are calculated (using *LEAP* for most responses and a reflective cracking model for strains in overlays on a cracked asphalt concrete layer) and used to determine the decrease in moduli and the increase in permanent deformation of each of the pavement layers. The output from these calculations are used, recursively, as input to the calculation for

the next wheel position. Because of the changes to moduli, response, damage, and permanent deformation a "time hardening" procedure is used. This procedure is explained later in this section.

The first step in the simulation ensures that the calculated pavement response is reasonably close to the actual pavement response during the test. The calculated pavement response is used to predict the pavement performance (damage and permanent deformation) and if this response is not reasonably correct it would be futile to use it for calibration of the performance models. In this study, response measurements included resilient MDD deflections and/or RSD deflections.

Once the resilient deflections are predicted with reasonable accuracy during the simulations, the performance models can be calibrated such that the permanent deformation of each layer, the decrease in layer moduli, and the observed surface cracking, are reasonably well predicted.

The different models used in *CalME* and the derivation of the input parameters from laboratory and in situ tests are briefly described in the following sections, as some details in the models have changed since publication of the calibration reports (20, 21).

4.4. *CalME* Models

The most important structural inputs to the mechanistic response models are layer thickness and the modulus of elasticity. Poisson's ratio is also an input value, and may be important particularly for normal strains. In the calculations described below a fixed value of 0.35 for the Poisson's ratio has been used.

The modulus of the asphalt materials varies with temperature, loading time, age, and damage. Aging is of little importance during an HVS test of relatively short duration and was not included in the simulations. The variation of modulus with temperature and loading time for intact asphalt materials is described through the master curve.

4.4.1 Asphalt Concrete Master Curve

CalME uses the same sigmoidal format of the master curve to determine the modulus versus reduced time as is used in the NCHRP 01-37 Mechanistic-Empirical Pavement Design Guide (M-E PDG) (Equation 4.1):

$$\log(E)=\delta+\frac{\alpha}{1+\exp(\beta+\gamma\log(tr))} \qquad \textbf{(4.1)}$$

where: E is the modulus in MPa,

tr is reduced time in seconds (sec),

α, β, γ, and δ are constants, and

logarithms are to base 10.

Reduced time as a function of loading time and viscosity of the binder is calculated from (Equation 4.2):

$$tr = lt \times \left(\frac{visc_{ref}}{visc} \right)^{aT} \tag{4.2}$$

where: lt is the loading time (in sec)

$viscref$ is the binder viscosity at the reference temperature,

$visc$ is the binder viscosity at the present temperature, and

aT is a constant.

Equation 4.1 may also be written in a simpler format as (Equation 4.3):

$$\log(E) = \delta + \frac{\alpha}{1 + \left(tr / tr^* \right)^{\gamma^1}} \tag{4.3}$$

where: $\gamma^1 = \gamma / \ln(10)$, and

$tr^* = \exp\left(-\beta / \gamma \times \ln(10) \right)$

With this format tr^* is reduced time corresponding to the inflection point of the master curve and γ' describes the change in the slope of the curve.

The binder viscosity (cPoise), as a function of temperature, is found from (Equation 4.4):

$$\log(\log(visccPoise)) = A + VTS^* \log(K) \tag{4.4}$$

where: K is the temperature (in °K), and

A and VTS are constants.

An alternative format of the master curve incorporating the viscosity can be written as follows (Equation 4.5):

$$\log(E) = \delta \frac{\alpha}{1 + \left(lt / tr^* \times \exp\left(\eta \times \left(K_{ref}^{VTS} - K^{VTS} \right) \right) \right)^{\gamma^1}} \tag{4.5}$$

where: $\eta = \ln(10) \times aT \times 10^A$

A, VTS, and K are defined in Equation 4.4, and

K_{ref} is the reference temperature in ºK.

The value of VTS ranges from -2.642 to -4.570, and is almost linearly correlated to the parameter A for all binders in the M-E PDG. It is relatively simple to fit a master curve within this range of VTS values by modifying VTS and η using the format in Equation 4.5. The type of binder selected (or the values of A and VTS) is not particularly important for modeling the changes in asphalt concrete modulus with temperature and loading time.

The same values of A (= 9.6307 with temperatures in ºK, 10.5254 with ºR) and VTS (= -3.5047) have been used for modeling the master curves of the different asphalt materials used in this study.

4.4.2 Stiffness of Unbound Layers

During calibration of the *CalME* models using data from the first 27 flexible HVS test sections and the 26 original WesTrack sections, it was found that the moduli of unbound materials could vary with the stiffness of the asphalt layers. This occurred both when the variation in stiffness was due to temperature variations and when it was due to fatigue damage to the asphalt. The change in stiffness was the opposite of what would be expected for granular layers due to the nonlinearity of the material. The following relationship is used to describe this stiffness variation as a function of confinement in the unbound layers (Equation 4.6):

$$E_n = E_{nref} \times \left(1 - \left(1 - S/S_{ref}\right) \times Stiffness\ factor\right), with$$
$$S = \left(\sum_{1}^{n-1} h_i \times \sqrt[3]{E_i}\right)^3 \qquad \textbf{(4.6)}$$

where: h_i is the thickness of layer i,

E_i is the modulus of layer i,

En_{ref} is the modulus of layer n at a bending stiffness $S = S_{ref}$, and

S_{ref} and *Stiffness factor* are constants.

The unbound layers for some of the HVS tests also showed the well-known nonlinearity of such materials, with the modulus of granular layers increasing with increasing bulk stress and the modulus of cohesive materials decreasing with increasing deviator stress. Due to the variation in modulus given by Equation 4.6, these nonlinearities had to be treated as functions of the wheel load rather than as functions of the stress condition (Equation 4.7):

$$E_P = \left(\frac{P}{40kN}\right)^{\alpha} \times E_{40kN} \qquad \textbf{(4.7)}$$

where: E_P is the modulus at wheel load P in kN,

$E_{40\,kN}$ is the modulus at a wheel load of 40 kN, and

α is a constant (positive for granular materials and negative for cohesive).

4.4.3 Strain Over Existing Crack

Reflective cracking damage was calculated using the method developed by Wu (22). In this method the tensile strain at the bottom of the overlay is estimated using a regression equation. The calculated tensile strain at the bottom of the overlay is used with the fatigue equation described in the next section to calculate reflective cracking damage in the asphalt layers.

The regression equation for tensile strain (in μstrain) at the bottom of the overlay is based on numerous finite element calculations, and assumes a dual wheel on a single axle (Equation 4.8):

$$\varepsilon=\alpha\times E_{an}^{\beta 1}\times E_{bn}^{\beta 2}\times(a1+b1\times\ln(LS_n))\times\exp(b2\times H_{an})\times(1+b3\times H_{un})\times(1+b4\times E_{un})\times\sigma_n \quad \textbf{(4.8)}$$

$$E_{an}=E_a/E_s \qquad E_{bn}=E_b/E_s \qquad E_{un}=E_u/E_s \qquad \sigma_n=\sigma_o/E_s$$

$$LS_n=LS/a \qquad H_{an}=H_a/H_a \qquad H_{un}=H_u/H_a$$

where: E_a is the modulus of the overlay,

H_a is the thickness of the overlay,

E_u is the modulus of the underlying layer,

H_u is the thickness of the underlying layer,

E_b is the modulus of the base/subbase,

E_s is the modulus of the subgrade,

LS is the crack spacing,

σ_o is the tire pressure, and

a is the radius of the loaded area for one wheel.

The units need to be consistent. The following constants were used:

α = 342650, $\beta 1$ = -0.73722, $\beta 2$ = -0.2645,

$a1$ = 0.88432, $b1$ = 0.15272, $b2$ = -0.21632, $b3$ = -0.061, and $b4$ = 0.018752.

The fatigue damage (i.e., the decrease in layer modulus) of the overlay was calculated using the strain at the bottom of the asphalt layers. This modulus was also used in Equation 4.8. The modulus of the intact material (i.e., between the cracks) was used for the underlying layer, E_u.

4.4.4 Fatigue Damage of Asphalt

The model for damaged asphalt has the format (Equation 4.9):

$$\log(E)=\delta+\frac{\alpha\times(1-\omega)}{1+\exp(\beta+\gamma\log(tr))} \quad \textbf{(4.9)}$$

where: the damage (ω), as a function of number of loads, strain, and modulus is calculated from Equation 4.10:

$$\omega=\left(\frac{MN}{MNp}\right)^{\alpha} \quad \textbf{(4.10)}$$

where: $MNp=A\times\left(\frac{\mu\varepsilon}{\mu\varepsilon_{ref}}\right)^{\beta}\times\left(\frac{E}{E_{ref}}\right)^{\gamma}\times\left(\frac{E_i}{E_{ref}}\right)^{\delta}$

E is the modulus of damaged material,

E_i is the modulus of intact material,

MN is the number of load repetitions in millions ($N/10^6$),

$\mu\varepsilon$ is the strain at the bottom of the asphalt layer in μstrain, and

α, β, γ, and δ are constants (that are not related to the constants in Equations 4.1 and 4.9).

The initial (intact) modulus (E_i) corresponds to a damage (ω) of zero and the minimum modulus ($E_{min} = 10^{\delta}$) to a damage of 1.

Equation 4.9 leads to the development of relations between moduli and damage (Equation 4.11):

$\log(E)-\delta=(\log(E_1)-\delta)\times(1-\omega)$, or

$\frac{E}{E_1}=\left(\frac{E_{\min}}{E_1}\right)$, or

$$\omega=\frac{\log\left(E/E_1\right)}{\log\left(E_{\min}/E_1\right)}=\frac{\ln(SR)}{\ln\left(E_{\min}/E_1\right)} \quad \textbf{(4.11)}$$

In other words, damage is sometimes defined as the relative decrease in modulus, $(E_i - E)/E_i = dE/E_i$ (e.g., the damage to the aggregate base layer in this report). The M-E PDG defines damage to the asphalt concrete both through Equation 4.9 and as the relative decrease in modulus, which is not possible. If damage is defined through Equation 4.9, then the relative decrease in modulus will depend on the minimum modulus (E_{min}) and on the initial modulus (E_i) which is a function of temperature and loading time. Some examples are shown in Figure 4.1 for E_{min} = 100 MPa and different values of E_i. A decrease in

modulus by 50 percent would correspond to damage between 0.15 and 0.30, depending on the initial modulus.

The power γ was set equal to $\beta/2$, making damage a function of the strain energy density (and reducing the number of parameters to be determined by one). As all of the reflective cracking HVS experiments were carried out at approximately 20ºC or 15°C, depending on the stage of the test, only fatigue tests at 20ºC were considered, with the parameter δ set to zero.

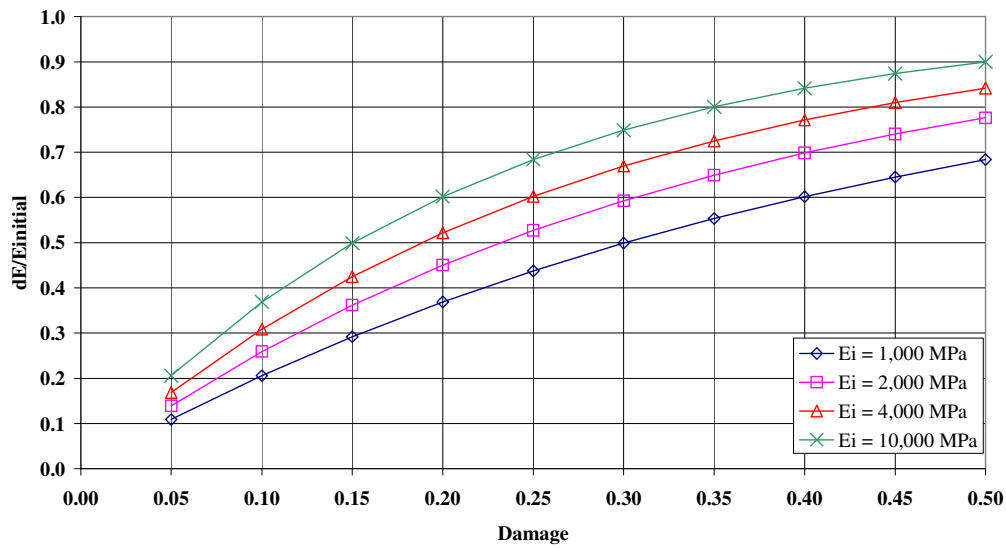

Figure 4.1: Relative decrease in modulus as a function of damage, for E_{min} = 100 MPa.

A shift factor of 3 was used between laboratory and HVS loading for new, undamaged material (i.e., three HVS load repetitions would correspond to one load repetition in the laboratory). This is the same shift factor used in previous simulations of HVS experiments. A shift factor of 0.6 was used for material that was previously cracked, again in accordance with previous practice.

4.4.5 Relationship Between Damage and Cracking

The number of loads to crack initiation was calculated or estimated for 17 HVS sections for which applicable data were available (20). Best-fit equations of the following form (Equation 4.12) were fitted to the data:

$$\omega_{initiation} = a\left(\frac{h_{AC}}{100\ mm}\right)^b \quad \text{and} \quad \omega = a\left(\frac{h_{AC}}{100mm}\right)^b \qquad \textbf{(4.12)}$$

where: $\omega_{initiation}$ is the damage at crack initiation,

ω_{2m/m^2} is the damage at 2.0 m/m^2 of cracking,

H_{AC} is the combined thickness of the asphalt concrete layers, and

a and b are intercepts.

The correlation coefficients were 0.76 and 0.82 after exclusion of the outliers and when uncertainties such as slip between asphalt layers, collapse of the asphalt treated permeable base (ATPB) layer during wet testing, and recementation of the base layer on the test track are taken into consideration. Section 569RF (underlying sections were numbered 567RF through 573RF) was considered as an outlier.

For practical purposes (i.e., to avoid damage larger than 1) an S-shaped curve for damage at crack initiation as a function of asphalt concrete thickness (Equation 4.13), shown in Figure 4.2, may be preferable:

$$\omega_{initiation} = \frac{1}{1+\left(\frac{h_{AC}}{250mm}\right)^{-2}} \tag{4.13}$$

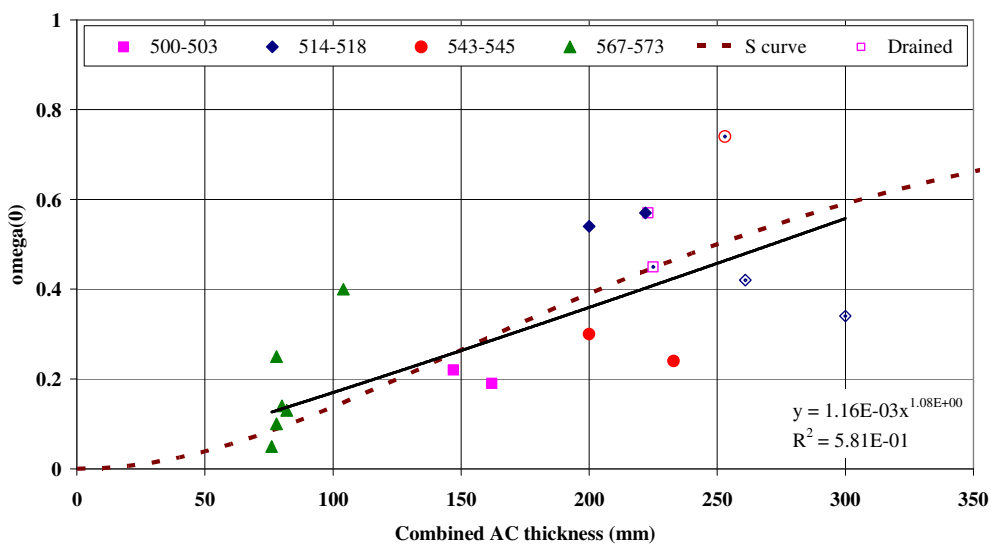

Figure 4.2: Crack initiation with S-shaped curve.

Using these equations on the WesTrack experiment mixes (21) would result in damage of 0.26 at crack initiation and of 0.35 at a crack density of 2.0 m/m^2. These values appear to be reasonable for the "Fine Superpave" mix and the "Fine Plus Superpave" mix (2.0 m/m^2 would correspond to 30 percent wheel track cracking using the WesTrack procedure in which the “area” of a crack is assumed to be crack length x 0.15 m^2). The calculated damage for the Coarse Superpave mix was much lower at crack initiation and would correspond to Equation 4.14 with the asphalt concrete thickness raised to -5 rather than to -2, as shown in Equation 4.13:

$$\omega_{initiation,coarsemix} = \frac{1}{1+\left(\frac{h_{AC}}{250mm}\right)^{-5}} \tag{4.14}$$

Cracking in percent of the wheelpath can be modeled using WesTrack data as a function of the calculated damage using an equation of the format (Equation 4.15):

$$Cr\% = \frac{100\%}{1+\left(\frac{\omega}{\omega_o}\right)^{\alpha}} \tag{4.15}$$

where: $Cr\%$ is the cracking in percent,

ω is the calculated damage, and

ω_o, and α are constants.

The fully drawn curves in Figure 4.3 were calculated from Equation 4.15 on the assumptions that crack initiation (Equations 4.14) would correspond to 5 percent cracking and that α was -8.

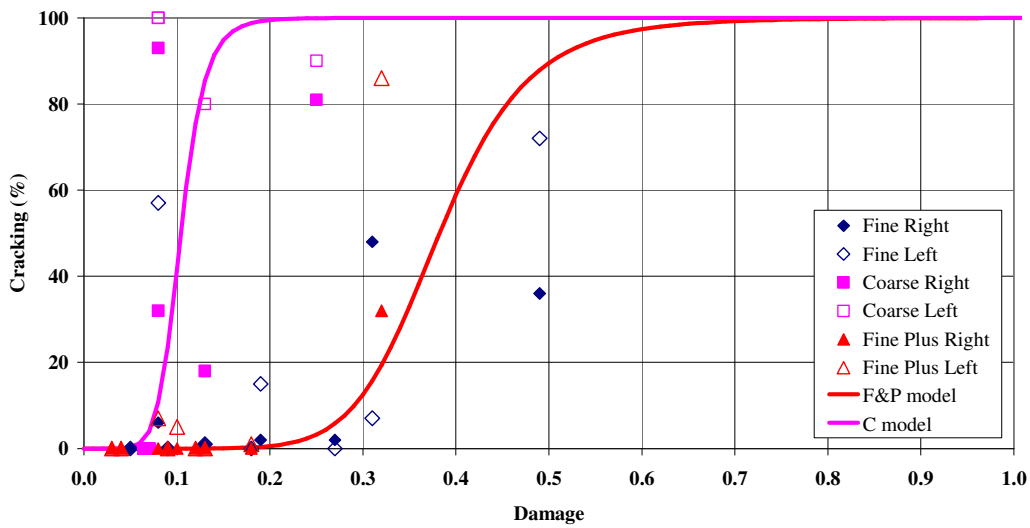

Figure 4.3: Cracking model compared to terminal cracking at WesTrack.

One of the WesTrack "Fine" mix sections (02FLM) had surprisingly good fatigue performance in the laboratory tests, considering that the binder content was low. Therefore the calculated damage is low even though the section had a considerable amount of cracking in the left wheelpath and some cracking in the right wheelpath. With the large difference between the performance in the right and left wheelpaths there is a possibility that the laboratory fatigue specimens were obtained from material that was not entirely representative of the section. The calculated damage may also have been underestimated at some of the sections with poor fatigue performance because the first series of FWD tests were carried out when the sections had already had a traffic load corresponding to 4,500 ESALs. Any damage caused by these loads is not included in the calculated damage.

Crack density in HVS tests can reach 8.0 to 9.0 m/m^2. This results in cracking of more than 100 percent using the WesTrack method of calculating cracking density. The crack area formula was therefore revised to crack length x 0.1 m^2 in order to provide more realistic results. Using the revised formula, a crack density of 10 m/m^2 would correspond to 100 percent cracking. Equation 4.15 can then be written in terms of cracking in m/m^2 as (Equation 4.16):

$$Cr\,m/m^2 = \frac{10}{1+\left(\frac{\omega}{\omega_o}\right)^{\alpha}} \qquad \textbf{(4.16)}$$

In the simulations in this report, Equations 4.13 and 4.16 were used to calculate the surface cracking as a function of the damage in the overlay. The thickness of all asphalt concrete layers was used for h_{AC}. Crack initiation was assumed to correspond to 0.5 m/m^2 cracking of the wheelpath and the value of α was first assumed to be -8. It was found that modified the parameters of Equations 4.15 and 4.16 resulted in a better fit to the measured data.

4.4.6 Fatigue Damage of Recycled Aggregate Base

The aggregate base of the test track consisted of predominantly recycled material with a high content of recycled portland cement concrete. The backcalculated moduli of the base layer showed a large increase with time, prior to loading, to values of more than 1,000 MPa. During HVS loading the modulus of the base deteriorated rapidly again. To accurately model the response during the HVS tests it was considered important to capture this decrease in modulus of the base during loading.

Initially, an incremental-recursive model developed for cement-treated base materials during an HVS-Nordic study in Sweden was used to simulate this decrease; an approach similar to that followed in earlier calibration studies (20). The model, developed by Busch (19), was based on six HVS tests on three different cement treated base materials, each with a replicate section. Two of the materials were based on a 16-mm maximum size gravel with target strengths (28 days, unconfined compressive) of 8 MPa and 4 MPa, respectively, and the third was based on an 8-mm maximum size sand with a target strength of 4 MPa. The cement content ranged from 60 kg/m^3 (approximately 2.5 percent by weight) to 100 kg/m^3 (approximately 3.0 percent by weight). Prior to cement stabilization, material grading was corrected with the addition of 330 kg/m^3 of limestone powder (approximately 12.5 percent by weight). The final incremental-recursive model developed during the Swedish study is described in Equation 4.17 (19):

$$\omega = \left(\frac{N}{10^6}\right)^{\alpha} x \left(\frac{\varepsilon}{\varepsilon_{REF}}\right)^{\beta} x\,(1-\omega)^{\gamma} \qquad \textbf{(4.17)}$$

where: N is the number of load repetitions, and

E is the maximum horizontal strain in the bottom of the stabilized layer

The constants used are:

$\alpha = 0.25$

$\beta = 0.25 + 0.90 \text{ x } (E_{INITIAL}/10{,}000 \text{ MPa})$

$\gamma = 0.5 + 0.90 \text{ x } (E_{INITIAL}/10{,}000 \text{ MPa})$

$\varepsilon = 45$ µstrain

The findings from the report (19) concluded that a central model is not always satisfactory for deterministic design purposes since some measure of safety is normally required. Typical Danish design models are based on 25 percent percentiles of E-moduli for the pavement layers (i.e., 75 percent of the initial E-moduli will be above the design values). If a similar line of reasoning is applied to the incremental-recursive model, it should predict values where only 25 percent of the measurements from the HVS sections fall below the prediction. This objective can be achieved by reducing the α value to 0.19.

The recycled base of the test track was a considerably weaker material than any of the materials used for development of the HVS-Nordic model. There was also some evidence from Dynamic Cone Penetrometer (DCP) testing that the modulus of the base was lower at the top than at the bottom of the layer, indicating that the upper region could have been subjected to crushing during compaction and/or HVS trafficking. The model was therefore changed to use the vertical stress at the top of the layer instead of the tensile strain at the bottom. The following damage function for the aggregate base was used (Equation 4.18):

$$\omega = MN^{\alpha} \times \left(\frac{\sigma_z}{\sigma_{ref}}\right)^{\beta} \times \left(\frac{E}{E_i}\right)^{\gamma} \qquad \textbf{(4.18)}$$

where: σ_z is the vertical, normal stress at the top of a layer,

σ_{ref} is a permissible stress,

E_i is the initial modulus of the material, and

α, β, and γ are calculated in the same way as for the HVS-Nordic model.

The initial modulus (E_i) was backcalculated from the last FWD test before the HVS experiment. The value of the permissible stress (σ_{ref}) was chosen such that the final modulus of the base would be close to the modulus determined for the base from the first FWD test after the HVS experiment, and such that the calculated RSD and MDD deflections would be close to the measured values. The base layer was originally constructed in three lifts and for the simulations it was subdivided into three layers. The model was used on each of the layers, resulting in the lowest modulus being at the top of the base. The model for decrease of the modulus of the base layer is not important in itself, but it is important for the response

calculated in the pavement structure. It is possible that different values of α, β, and γ could have resulted in a better fit to the measured response.

4.4.7 Permanent Deformation of Asphalt

A shear-based approach, developed by Deacon et al. (23), was used for predicting rutting (permanent deformation) of the asphalt layer, which is assumed to be controlled by shear deformation. The permanent, or inelastic, shear strain (γ_i) is determined as a function of the shear stress (τ), the elastic shear strain (γ_e), and the number of load repetitions from Repeated Simple Shear Tests at Constant Height (RSST-CH) in the laboratory. The best-fitting relationship for permanent shear strain for the materials used in the test track was found to be a gamma function (Equation 4.19). Similar functions were used in the analysis of previous HVS experiments.

$$\gamma^i = \exp\left(A + \alpha \times \left[1 - \exp\left(\frac{-\ln(N)}{\gamma}\right) \times \left(1 + \frac{\ln(N)}{\gamma}\right)\right]\right) \times \exp\left(\frac{\beta \times \tau}{\tau_{ref}}\right) \times \gamma^e \quad \textbf{(4.19)}$$

where: γ_e is the elastic shear strain,

τ is the shear stress,

N is the number of load repetitions,

τ_{ref} is a reference shear stress (0.1 MPa ≈ atmospheric pressure), and

A, α, β, and γ are constants determined from the RSST-CH.

The rut depth is calculated for the upper 100 mm of the asphalt concrete layers. The shear stress is calculated at a depth of 50 mm beneath the edge of the tire. For each of the layers within 100 mm of the surface the elastic shear strain (γ_e) is calculated from (Equation 4.20):

$$\gamma^e = \frac{\tau}{E_i / (1 + \nu_i)} \quad \textbf{(4.20)}$$

where: E_i is the modulus of layer i, and

ν_i is Poisson's ratio for layer i.

The permanent shear strain of each layer is calculated from Equation 4.20, and the permanent deformation is determined from the relationship between permanent deformation and permanent shear strain of layer i. (Equation 4.21):

$$dp_i = K \times h_i \times \gamma^i \quad \textbf{(4.21)}$$

where: h_i is the thickness of layer i (above a depth of 100 mm), and

K is a calibration constant.

The total rut depth (down rut) in the asphalt concrete is the sum of the permanent deformation of the layers within the top 100 mm of the asphalt concrete. A value of $K = 1.4$ was used for all simulations and all materials.

4.4.8 Permanent Deformation of Unbound Layers

Permanent deformation (dp) of the unbound materials is based on the vertical resilient strain at the top of the layer (μ_ε), and on the modulus of the material (E) (Equation 4.22):

$$dp,\ mm = A \times MN^{\alpha} \times \left(\frac{\mu\varepsilon}{\mu\varepsilon_{ref}} \right)^{\beta} \times \left(\frac{E}{E_{ref}} \right)^{\gamma} \tag{4.22}$$

The constants used were:

$\alpha = 0.333$, $\beta = 1.333$, $\gamma = 0.333$, $\mu\varepsilon_{ref} = 1{,}000$ µstrain, and $E_{ref} = 40$ MPa.

A value of $A = 1.1$ mm was used for the subgrade and $A = 0.3$ for the recycled base. (The subgrade parameters are based on a series of full-scale tests in the Danish Road Testing Machine, with a subgrade of Danish "Moraine Clay," which is classified as a "clayey, silty sand" (AASHTO classification A-4[0]) (20) All values for subgrade are the same as those used in previous simulations of HVS tests. However, a lower value of A was used for the base in this study, compared to 0.8 in previous studies, given that the self-cementing base attained moduli much higher than those typically obtained for granular base materials.

4.4.9 Time Hardening

The models described above are used in an incremental-recursive process. This means that the parameters on the right side of the equal-sign may change from increment to increment. The first step in the process is therefore to calculate the "effective" number of load applications that would have been required, with the present parameters, to produce the condition at the beginning of the increment. In the second step the new condition, at the end of the increment, is calculated for the "effective" number of load applications plus the number of applications during the increment. This must be repeated for each load and load position during the increment.

The method may be illustrated using Equation 4.22. If, for example, the permanent deformation of the subgrade was 2.0 mm at the start of the increment, the vertical strain calculated for the first wheel load at the first position was 800 µstrain, and the modulus was 60 MPa, then the effective number of load applications at the start of the increment may be found from (Equation 4.23):

$$MN_{eff} = \left[\frac{2}{1.1 \times \left(800/1000 \right)^{1.333} \times \left(60/40 \right)^{0.333}} \right]^{1/0.333} \tag{4.23}$$

If the number of repetitions of this load (in millions) at this position was *dMN* during the increment, then the permanent deformation after these load applications would be (Equation 4.24):

$$dp,mm = 1.1 \times \left(MN_{eff} + dMN \right)^{0.333} \times \left(800/1000 \right)^{1.333} \times \left(60/40 \right)^{0.333} \tag{4.24}$$

The process must be repeated recursively, using the output from each calculation as the input to the next, for all loads at each position before proceeding to the next time increment.

4.5. Analysis of Frequency Sweep Tests for Input to Simulations

Moduli of the asphalt concrete layers were determined from laboratory frequency sweep tests on prepared beams.

An example of a master curve (fully drawn line with no symbols) fitted to the frequency sweep data is shown in Figure 4.4 for the underlying DGAC layer of the test track. The legend for the frequency sweep data indicates the test temperature in °C. Results from shear (RSST-CH) frequency sweep tests and from fatigue tests (initial moduli) are shown for comparison.

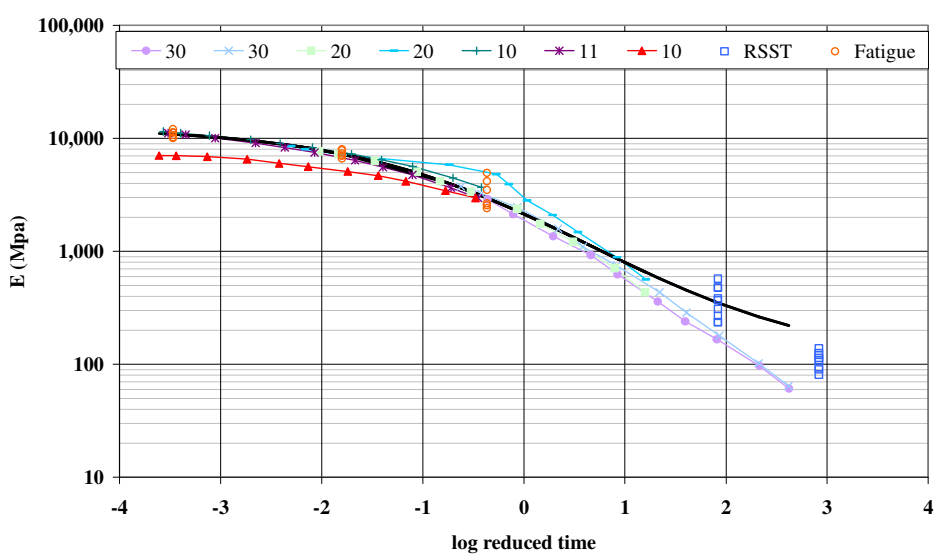

Figure 4.4: Example of master curve fitted to frequency sweep data.

For large values of reduced time (high temperature and/or long loading time) the test results are seen to deviate from the master curve. This is attributed to using 100 MPa as a minimum modulus (10^{δ} in Equation 4.1). The measured modulus may well be less than this value in the laboratory tests, but it is doubtful whether this would ever happen in an asphalt layer in a pavement. A value of 100 MPa is less than the modulus of the pure aggregate. Therefore this value was retained even though a lower minimum modulus would have given a better fit to the frequency sweep data.

Figure 4.5 compares the moduli versus temperature for the test track asphalt concrete materials at a loading time (creep test time) of 0.015 sec, corresponding approximately to the loading time of the FWD or to a frequency of 10 Hz. An approximate master curve for the underlying DGAC, determined from FWD backcalculated values, is also shown.

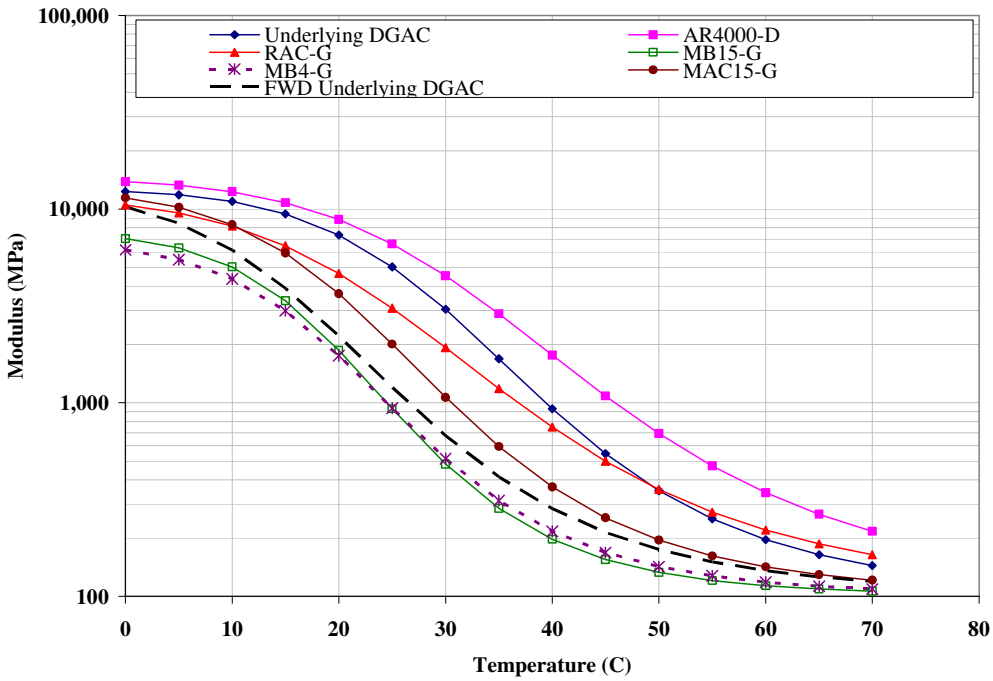

Figure 4.5: Comparison of moduli versus temperature for different asphalt concrete materials.

A summary of the master curve parameters are provided in Table 4.1. The table headings refer to the parameters of Equation 4.1. The modulus at the reference temperature (E_{ref}) and the maximum modulus ($E_{max} = 10^{(\delta + \alpha)}$) are in MPa. For all of the master curves, the minimum modulus ($E_{min} = 10^{\delta}$) was 100 MPa, the reference temperature (t_{ref}) was 20ºC, and the parameters describing the viscosity of the binder were A = 9.6307 (10.5254 if ºR is used) and VTS = -3.5047.

Table 4.1: Master Curve Parameters for Test Track Asphalt Concrete Materials

Material	β	γ	aT	E_{ref}	α	E_{max}
DGAC original	-0.5462	0.832	1.3369	7353	2.1035	12690
Overlays						
AR4000-D	-0.8040	0.7711	1.2330	8,832	2.1595	14,436
RAC-G	-0.2734	0.6360	1.3726	4,658	2.0661	11,643
MB15-G	0.9418	0.9192	1.3169	1,867	1.8808	7,600
MB4-G	0.9269	0.9190	1.2210	1,749	1.8303	6,765
MAC15-G	0.1988	0.6939	1.4913	3,658	2.1012	12,623
FWD original	0.7000	0.7000	1.3370	2,213	2.1004	12,600

4.6. Analysis of Falling Weight Deflectometer (FWD) Tests for Input to Simulations

FWD tests were carried out periodically on the test track, starting shortly after construction of the pavement (construction completed on 09/24/2001, first FWD test series on 10/03/2001). The testing was done along several lines of the pavement as well as more intensively at the sites that were selected for HVS testing. When the pavement was overlaid in June 2003, deflections on the centerline of the road, where no HVS testing took place, could no longer be measured due to differences in thickness between the different overlays.

CalBack was used to backcalculate the layer moduli, using Odemark-Boussinesq as the response model. The nonlinearity of the subgrade was determined from the two outermost geophones, except for a few tests where the outermost geophone was at 2,000 mm from the plate center, in which case this geophone was not used. In most instances, the genetic algorithm was used to obtain the closest possible fit to the measured deflections.

4.6.1 FWD Results Before Overlay Construction

The backcalculated moduli from the centerline, from tests done before the overlay, are shown in Figure 4.6, as a function of age in days after construction. The modulus of the DGAC was adjusted to 20ºC.

Given the variability in the base and asphalt concrete layer thicknesses, a thickness of 80 mm was assumed for the DGAC layer and 350 mm for the base. It is normally recommended that the modulus of the top layer not be backcalculated if its thickness is less than half the radius of the loading plate, or 75 mm in this case. With a thickness only a little above this limit, there is considerable uncertainty in the backcalculated values, particularly when the aggregate base layer hardens to a modulus similar to that of the DGAC as it is often problematic for the backcalculation procedure to distinguish between the moduli of two consecutive layers of similar stiffness.

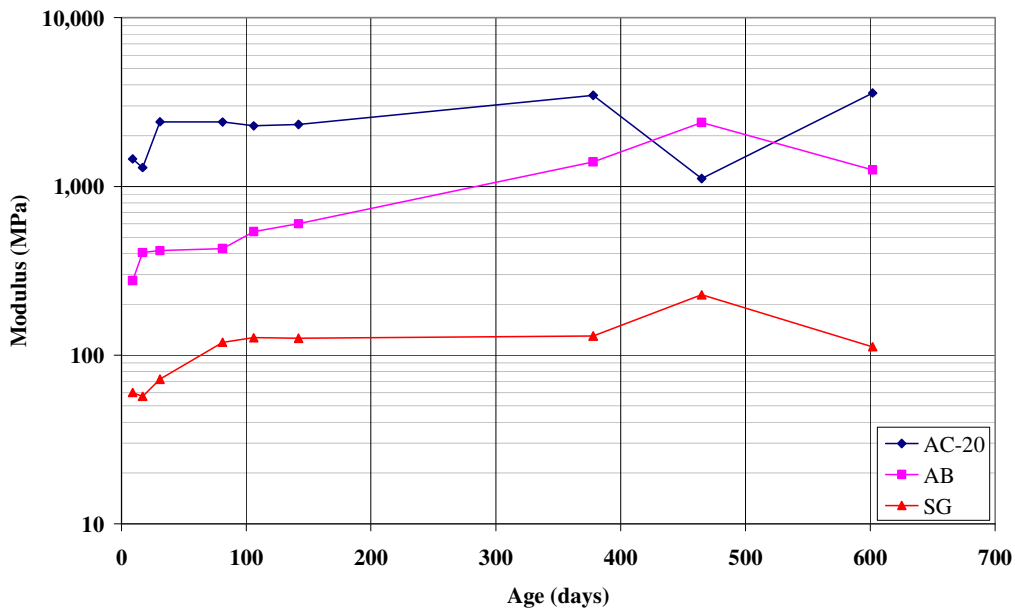

Figure 4.6: Backcalculated moduli from center line, before overlay.

The nonlinearity of the subgrade may add to these problems. In the backcalculation it is assumed to be a constant, but in reality it varies with the stress (or strain) on top of the subgrade, with a decreasing slope for decreasing stress level. The stress level on the subgrade varies both with temperature and with the hardening of the base layer.

Triaxial test results on subgrade samples from previous HVS experiments located close to the test track were used as seed values in the backcalculation. Figure 4.7, derived from Equation 4.25, shows the modulus determined from triaxial testing on soaked and saturated specimens versus the axial strain, in microstrain (μm/m).

$$E = \frac{E_{\max}}{1 + \left(\log(\varepsilon) / \log(300) \right)^3} \tag{4.25}$$

where: the maximum modulus (E_{max}) was assumed to be 150 MPa,
the strain (μ_ε) is in μm/m, and
the logarithms are to base 10.

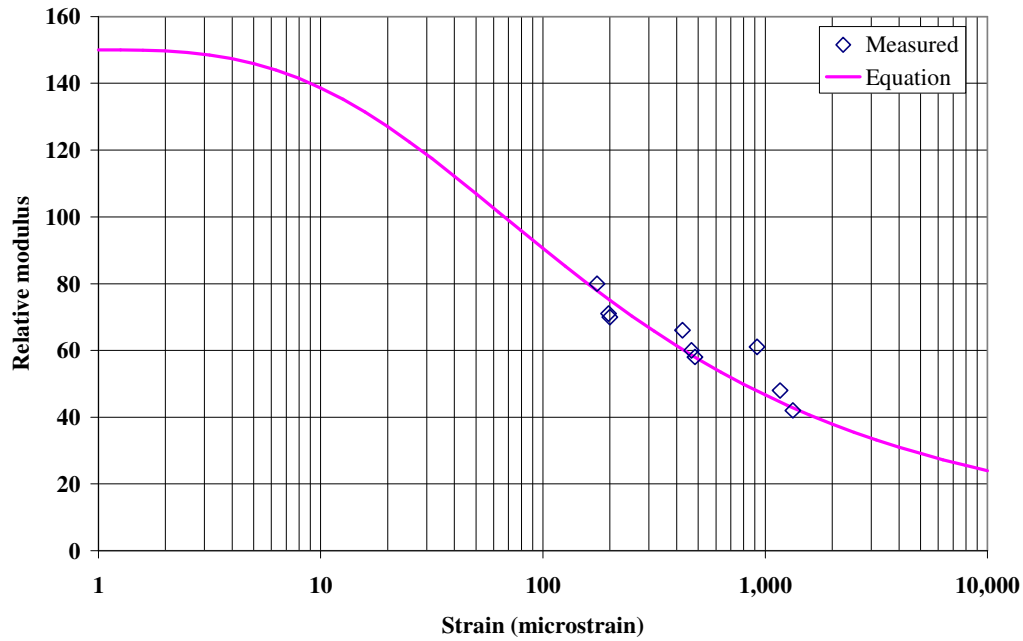

Figure 4.7: Relative modulus as a function of normal strain from triaxial tests.

An approximate value of the subgrade modulus from the same triaxial tests, as a function of the deviator stress, may also be found from (Equation 4.26):

$$E = 42.4MPa \times \left(\frac{\sigma_d}{0.1MPa} \right)^{-0.282} \tag{4.26}$$

where: σ_d is the deviator stress.

The agreement with measured values was not as good with Equation 4.26 as it was for Equation 4.25.

The FWD tests on Day 465 after construction were done at rather low temperatures (BELLS temperature for the DGAC was 11.9ºC on average). The asphalt modulus at this temperature was 2,640 MPa and the strain levels, from which the subgrade parameters were derived, were less than 20 µstrain. This may be part of the explanation for the high subgrade modulus (Figure 4.6), which was also associated with a low nonlinearity, for these tests. The preceding and following FWD test series were both at BELLS temperatures above 35ºC.

Figure 4.8 compares the backcalculated moduli, before overlay, from the center line and from HVS sections before loading, to the master curve from the frequency sweep testing. The alternative master curve based on FWD tests, for which the parameters are given as the last line in Table 4.1, is also shown. The FWD-derived master curve was used for the underlying DGAC layer in the *CalME* simulations.

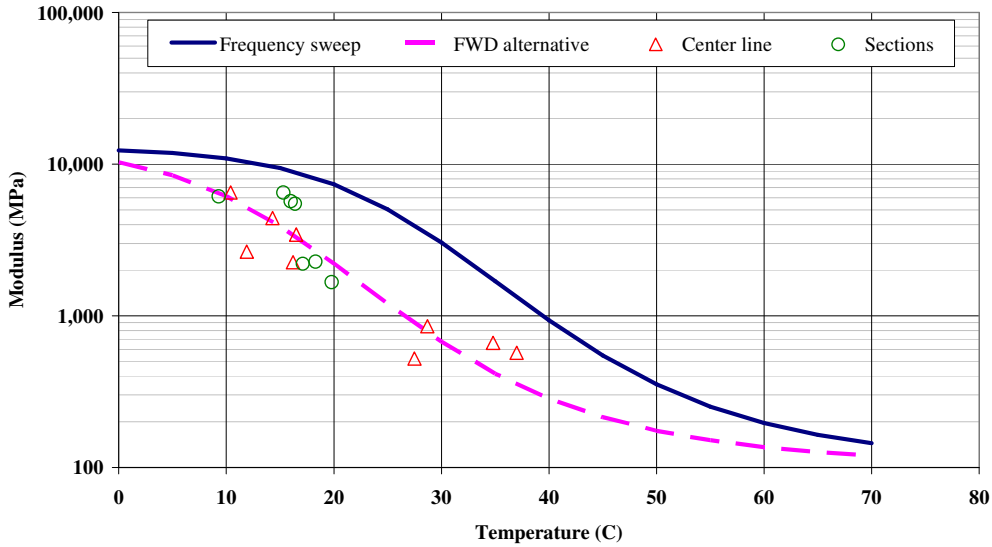

Figure 4.8: Backcalculated DGAC moduli compared to frequency sweep master curve.

The modulus of the aggregate base (E_{AB}) shows an increase with age, which can be described approximately with Equation 4.27:

$$E_{AB} = 800MPa \times (\ln(days + 200) - 5) \quad \textbf{(4.27)}$$

where: days are the number of days after construction.

The backcalculated moduli of the aggregate base are compared to Equation 4.27 in Figure 4.9.

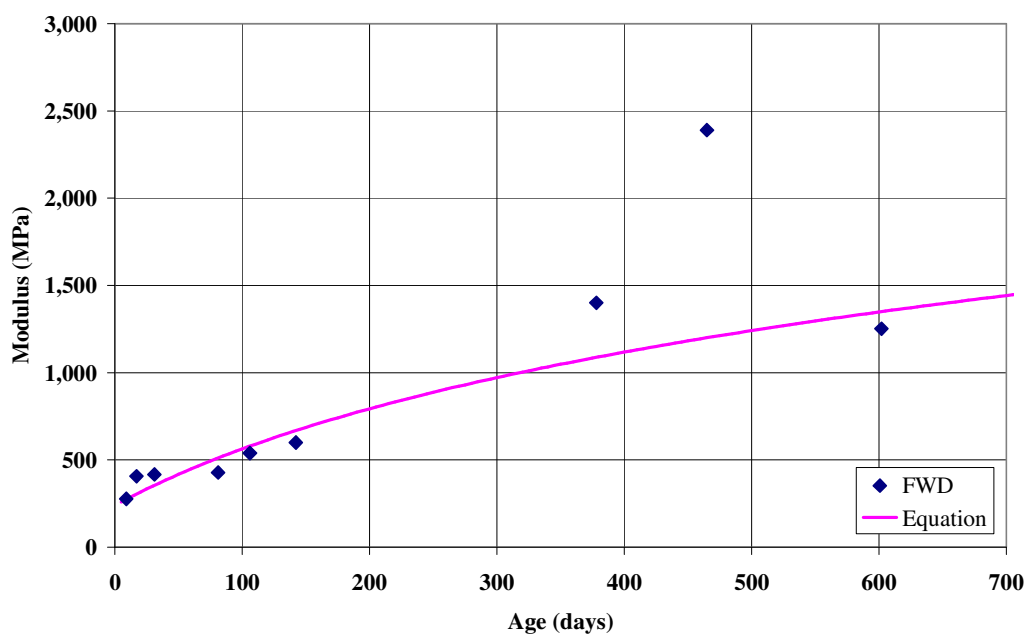

Figure 4.9: Backcalculated modulus of aggregate base compared to Equation 4.27.

The modulus of the subgrade was found to vary both with the bending resistance of the pavement layers and with the deviator stress in the material. As described previously in Section 4.4.2, these two effects must be treated separately. The effects from the bending resistance from the pavement layers were determined as shown in Equation 4.28 (corresponding to Equation 4.6):

$$E_{SG} = 77.8MPa \times \left(1 - \left(1 - S/S_{ref}\right) \times 0.51\right) \quad \textbf{(4.28)}$$

where: $$S/S_{ref} = \frac{\left(80 \times E_{AC}^{(1/3)} + 350 \times E_{AB}^{(1/3)}\right)^3}{3500^3}$$

The moduli determined from Equation 4.28 are compared to backcalculated values in Figure 4.10. A value of α = -0.3 was used for the subgrade nonlinearity given by Equation 4.7.

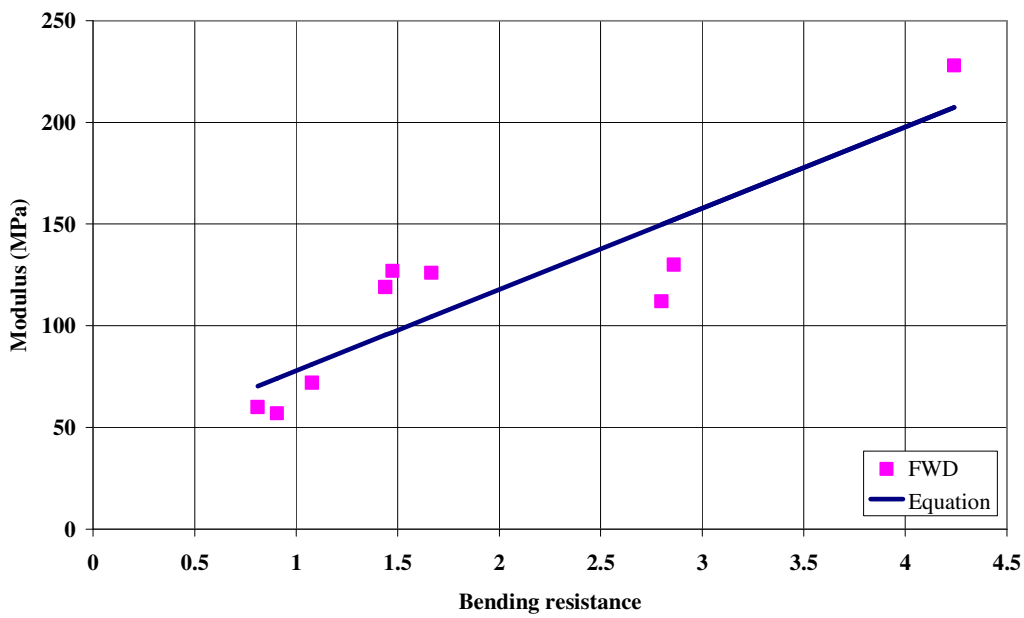

Figure 4.10: Subgrade modulus as a function of bending resistance.

The backcalculated moduli for the last FWD test series before an HVS experiment, and from the first FWD test series after the HVS experiment, are provided in Table 4.2. The moduli are given at a reference temperature of 20ºC. The modulus of the aggregate base shows a considerable decrease after HVS loading in all cases. The damage (ω) to the aggregate base varies from 0.7 to 0.95. It is likely that some of this damage in reality was due to damage to the asphalt concrete layer, but has been assigned to the base layer because of the uncertainty in the backcalculation of the modulus of the relatively thin asphalt concrete layer. There was a considerable amount of surface cracking at the end of the HVS tests and it is unlikely that the modulus of the asphalt concrete whould have remained essentially unchanged.

Table 4.2: Backcalculated Moduli Before and After HVS Testing

Section	Moduli Before HVS (MPa)			Moduli After HVS (MPa)		
	$E_{ac}(20)$	E_{ab}	E_{sg}	$E_{ac}(20)$	E_{ab}	E_{sg}
567RF	2,192	586	132	2,278	168	150
568RF	5,473	483	163	3,799	79	166
569RFa	3,451	1,680	185	5,618	227	66
569RFb	3,623	1,132	158	2,318	62	58
571RF	1,624	773	158	4,430	230	206
572RF	2,141	1,108	194	4,944	93	73
573RF	1,629	648	99	3,904	189	152

4.6.2 FWD Results After Overlay Construction

A fixed ratio was used between the moduli of the overlay and the underlying DGAC when backcalculating the moduli of the overlaid sections. For each FWD test series, the ratio was determined from the frequency sweep master curve for the overlay and the FWD master curve for the underlying DGAC layer, at the temperature of the FWD test series.

Figure 4.11 shows the backcalculated moduli for the original pavement layers versus time, both for the center line tests before overlay (i.e., before June 2003) and for the last FWD test series before HVS loading on the respective overlays (i.e., after June 2003). The aging model for the aggregate base (Equation 4.27) and the bending resistance model for subgrade (Equation 4.28) are shown as dotted lines for comparison. The subgrade model is seen to be quite good, whereas the aggregate base has not fully recovered from the HVS loading on the original pavements prior to overlay in all cases. It is still difficult to see any effects of the first HVS experiment on the modulus of the underlying DGAC layer. The modulus of the asphalt concrete layer appears to be either constant or slightly increasing.

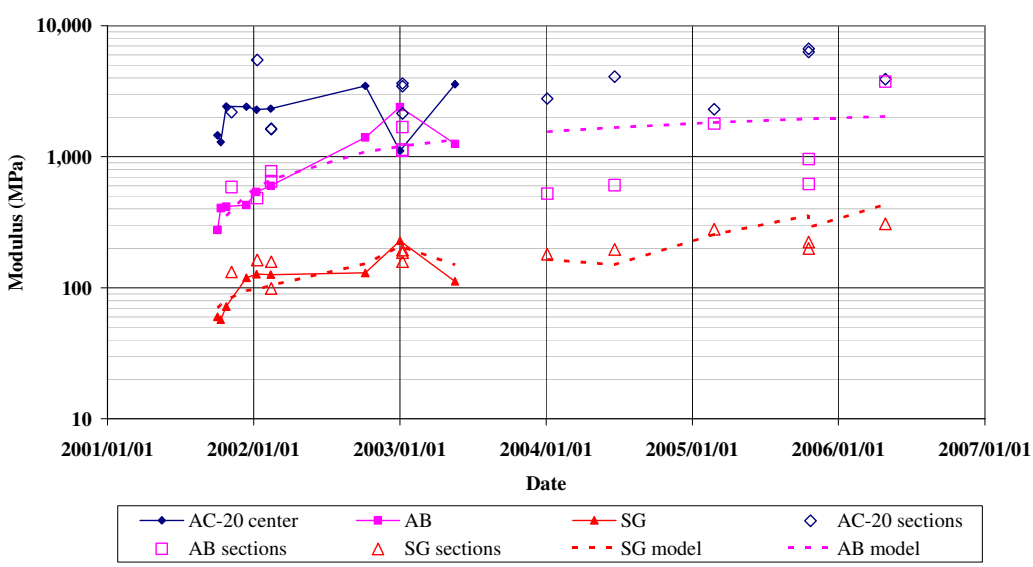

Figure 4.11: Backcalculated moduli for original pavement layers, versus time.

Figures 4.12 to 4.17 compare the backcalculated moduli of the asphalt layers to the master curve from laboratory frequency sweep tests versus the temperature in Celsius, at a loading time of 0.015 seconds (approximate loading time of the FWD, or a frequency of 10 Hz). The agreement between frequency sweep and backcalculated values is considered acceptable for the overlays, although the backcalculated values tend to be slightly higher than the frequency sweep moduli. This is the opposite tendency of what was observed for the underlying DGAC layer.

Table 4.3 shows the layer moduli at 20ºC for asphalt layers, backcalculated from the last FWD test series before an HVS experiment, and from the first FWD test series after the experiment.

Table 4.3: Moduli Before and After HVS Testing

Section		Moduli Before HVS (MPa)				Moduli After HVS (MPa)			
No.	Overlay	$E_{ovl}(20)$	$E_{ac}(20)$	E_{ab}	E_{sg}	$E_{ovl}(20)$	$E_{ac}(20)$	E_{ab}	E_{sg}
586RF	MB15-G	4,109	3,901	3,736	308	1,924	4,060	1,019	270
587RF	RAC-G	5,361	2,300	1,792	280	1,887	1,258	115	129
588RFa	AR4000-D	9,567	6,662	956	223	3,483	2,761	342	66
588RFb	AR4000-D	8,760	6,296	620	199	1,660	1,365	178	63
589RF	MB4-G	2,894	4,086	606	196	1,230	1,721	167	117
590RF	MB4-G	2,147	2,774	522	180	2,655	3,213	128	86
591RF	MAC15-G	6,280	3,581	1,750	211	3,410	2,703	199	50

The damage calculated from the backcalculated moduli (Table 4.4) shows that the overlay and the underlying DGAC endured approximately the same amount of damage, except in Experiment 590RF, where none of the layers were damaged. No cracking developed on this section. The aggregate base endured a large amount of damage, similar to that determined for Phase 1 testing on the underlying DGAC layer.

Table 4.4: Damage Calculated from Backcalculated Moduli

Section	Overlay	Overlay	Underlying DGAC	Aggregate Base
586RF	MB15-G	0.20	-0.01	0.73
587RF	RAC-G	0.26	0.19	0.94
588RFa	AR4000-D	0.22	0.21	0.64
588RFb	AR4000-D	0.37	0.37	0.71
589RF	MB4-G	0.25	0.23	0.72
590RF	MB4-G	-0.07	-0.04	0.75
591RF	MAC15-G	0.16	0.08	0.89

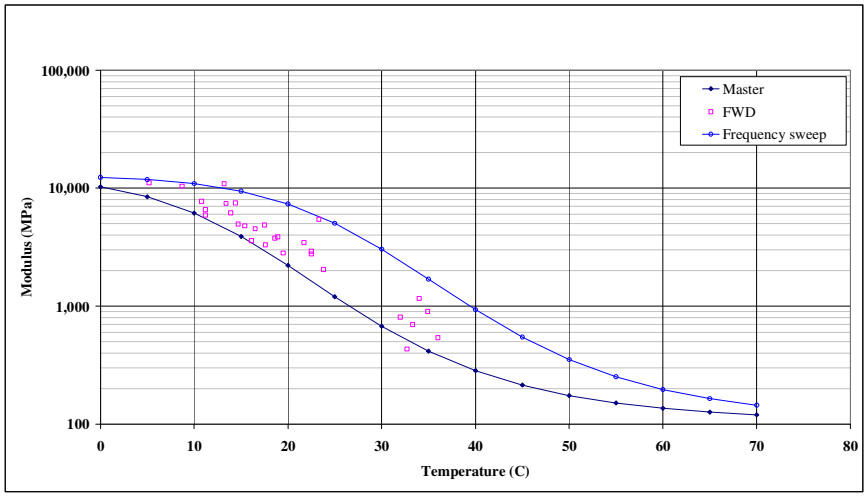

Figure 4.12: Moduli of underlying DGAC before and after overlay.

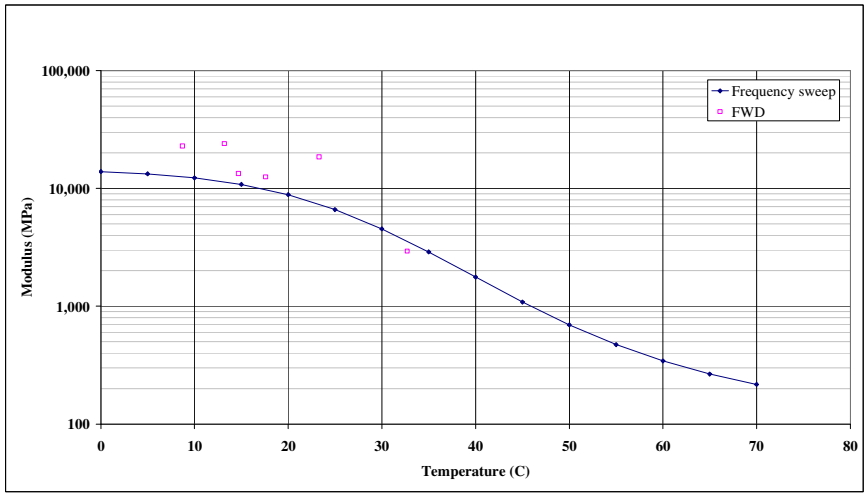

Figure 4.13: Moduli of AR4000-D overlay, from frequency sweep tests and FWD backcalculation.

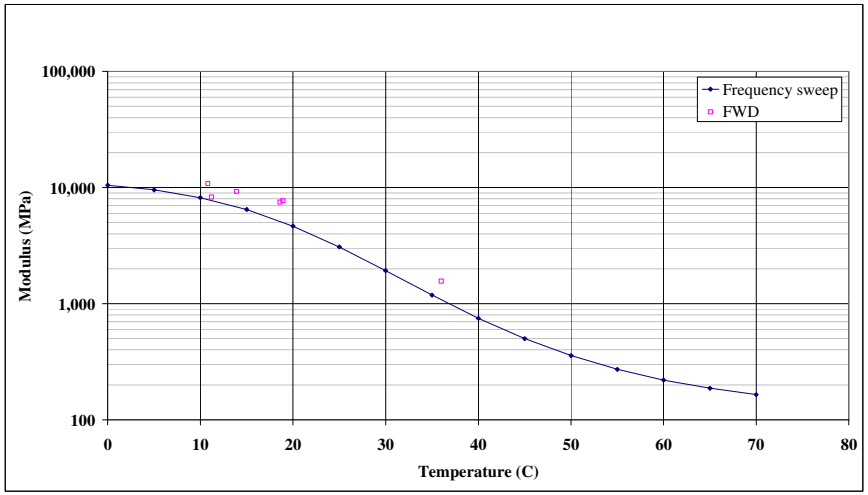

Figure 4.14: Moduli of RAC-G, from frequency sweep tests and FWD backcalculation.

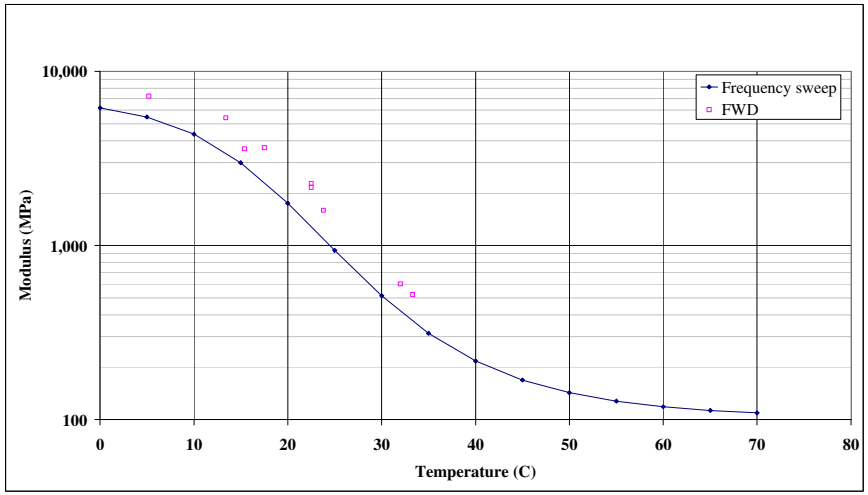

Figure 4.15: Moduli of MB4-G, from frequency sweep tests and FWD backcalculation.

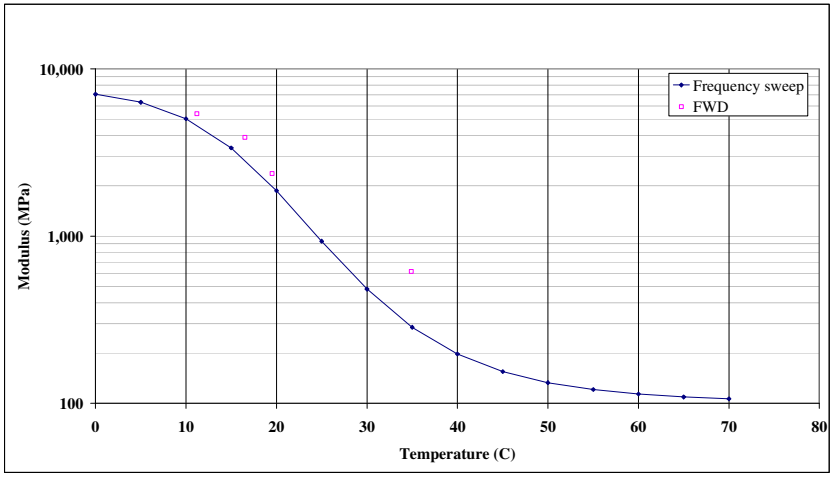

Figure 4.16: Moduli of MB15-G, from frequency sweep tests and FWD backcalculation.

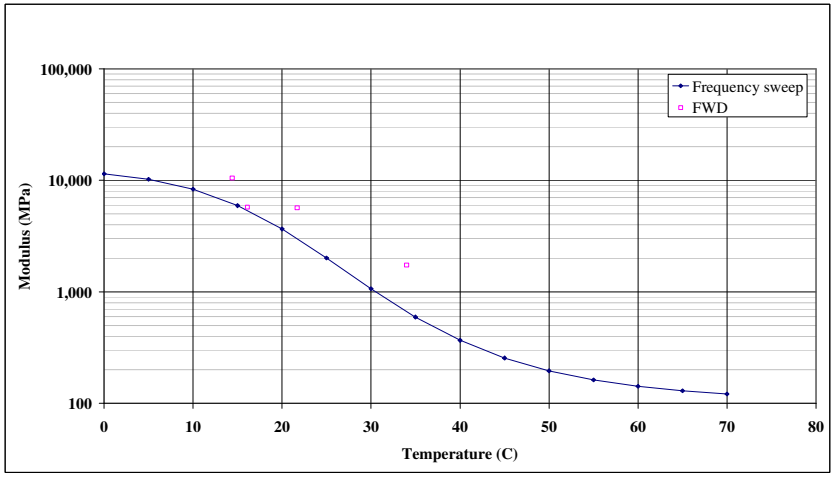

Figure 4.17: Moduli of MAC15-G, from frequency sweep tests and FWD backcalculation.

4.7. Fatigue Test to Characterize Asphalt Damage in Simulations

The laboratory fatigue beam tests at 20ºC were imported into spreadsheets and the parameters of Equation 4.10 were determined using Microsoft *Excel*® Solver. The minimum modulus was assumed to be 100 MPa. The Root Mean Square (RMS) difference between the measured and calculated stiffness ratio (ratio of the damaged modulus to the intact modulus) was minimized. The parameter γ was set equal to $\beta/2$ and δ was set to 0.

The measured and calculated stiffness ratios are shown for all of the asphalt concrete materials for the test track in Figures 4.18 to 4.23. The agreement between measured and calculated values is generally good down to a stiffness ratio of 0.5. A better agreement between measured and calculated values could have been obtained in some cases with a minimum modulus less than 100 MPa, but for an asphalt pavement layer it is probably not realistic to expect moduli lower than 100 MPa.

A summary of the fatigue parameters is given in Table 4.5.

Table 4.5: Fatigue Parameters from Laboratory Testing

Material	A	α	$\mu\varepsilon_{ref}$	β	E_{ref}	γ	δ
Underlying DGAC	45.34	0.7581	200	-4.421	3,000	-2.21	0
Overlays							
DGAC	7.1806	1.0328	200	-3.8638	3,000	-1.9319	0
RAC-G	153.6	0.4873	200	-5.1066	3,000	-2.5533	0
MB15-G	361.8	0.274	200	-4.6136	3,000	-2.3068	0
MB4-G	1,841	0.2272	200	-5.024	3,000	-2.512	0
MAC15-G	4,569	0.2614	200	-3.2517	3,000	-1.6258	0

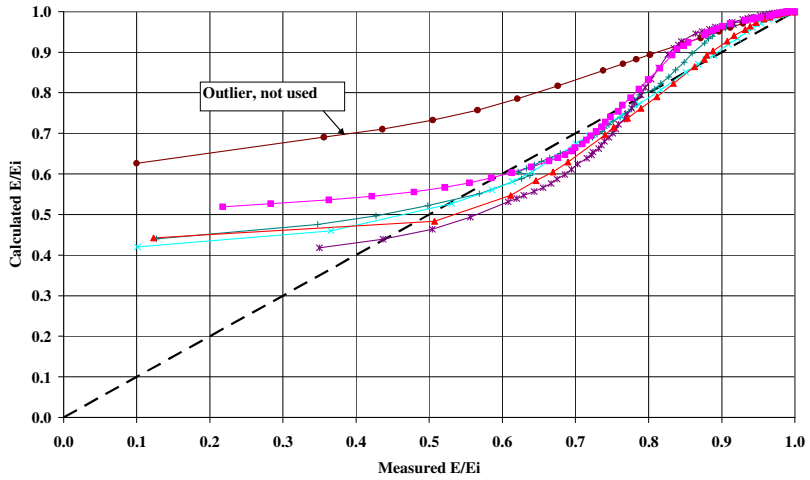

Figure 4.18: Calculated and measured stiffness ratio for the underlying DGAC.

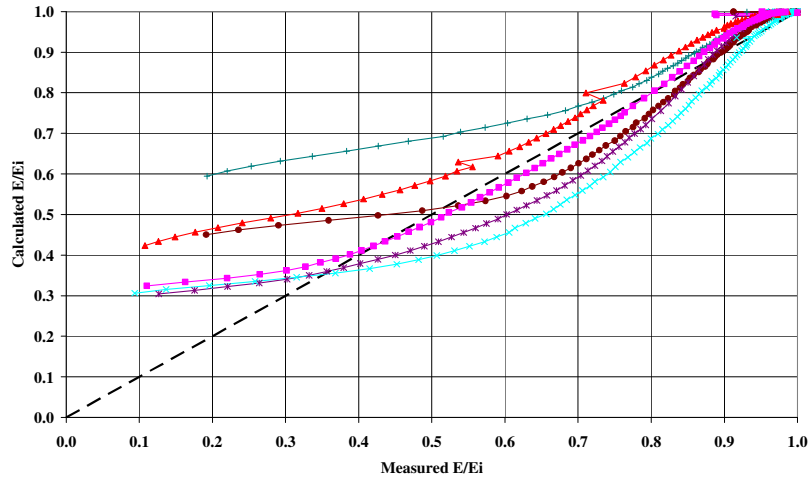

Figure 4.19: Calculated and measured stiffness ratio for the AR4000-D overlay.

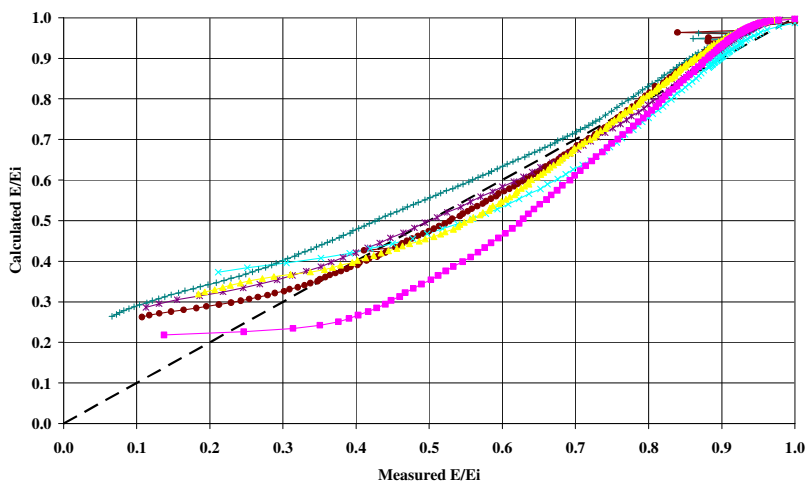

Figure 4.20: Calculated and measured stiffness ratio for the RAC-G overlay.

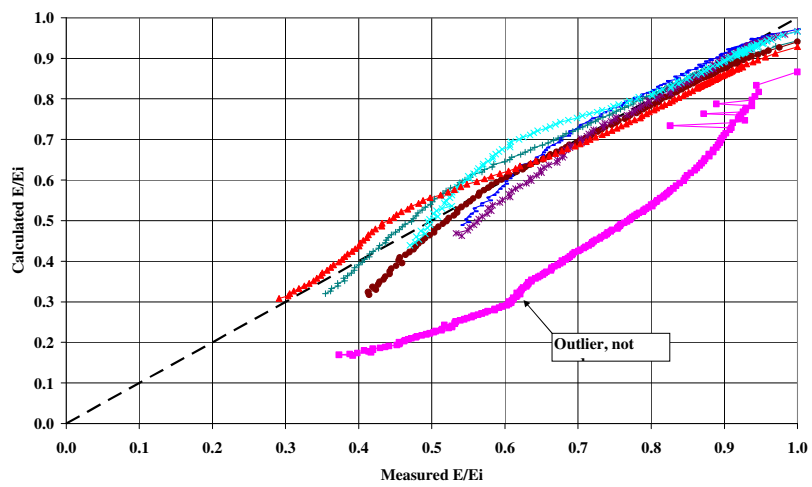

Figure 4.21: Calculated and measured stiffness ratio for the MB4-G overlay.

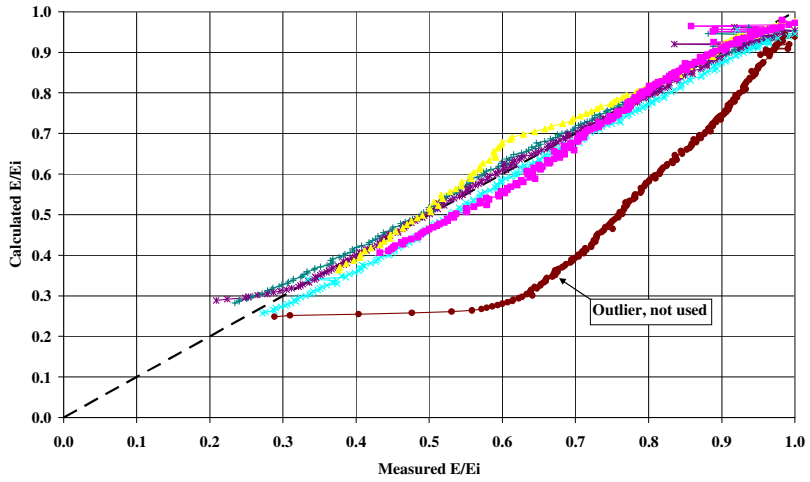

Figure 4.22: Calculated and measured stiffness ratio for the MB15-G overlay.

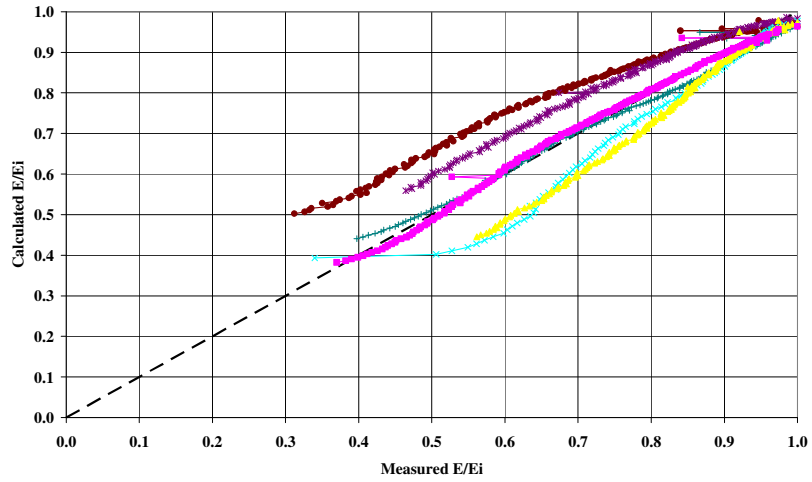

Figure 4.23: Calculated and measured stiffness ratio for the MAC15-G overlay.

Figure 4.24 compares the different materials at the reference temperature (20°C) and a constant strain of 500 µstrain for Equation 4.10 and the parameters in Table 4.5.

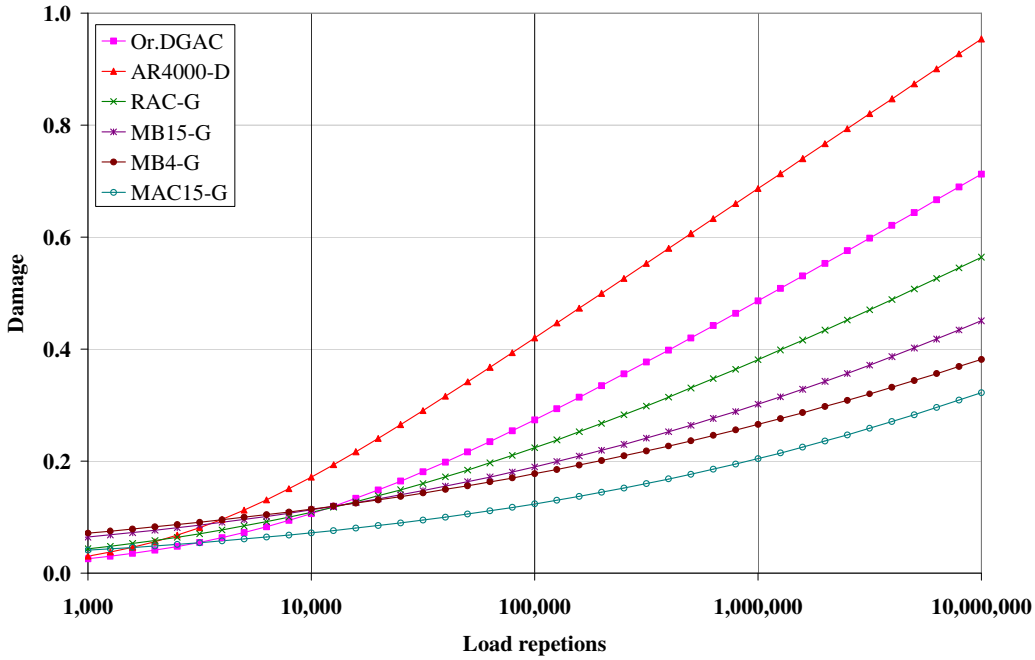

Figure 4.24: Example of damage versus load repetitions, for 20°C and 500 µstrain.

4.8. Shear Tests

The results of the shear (RSST-CH) tests were imported into *Excel*® spreadsheets and the parameters of Equation 4.19 were determined using Solver. The optimization was based on minimizing the difference between the natural logarithm of measured and calculated normalized strains. The normalized strains were calculated as (Equation 4.29):

$$normalized\,strain = \frac{\gamma^{i}}{\exp\left(\beta \times \tau / \tau_{ref}\right) \times \gamma^{e}} \tag{4.29}$$

The natural logarithm of the measured normalized strains versus the natural logarithm of the number of load applications is compared to the calculated values (depicted as "Model" in the legend) in Figures 4.25 to 4.30. The detail in the legend indicates the test temperature (in °C), the air-void content (in percent), and the method of specimen preparation (in this case, field-mixed, field-compacted [FMFC], indicating that specimens were obtained from cores).

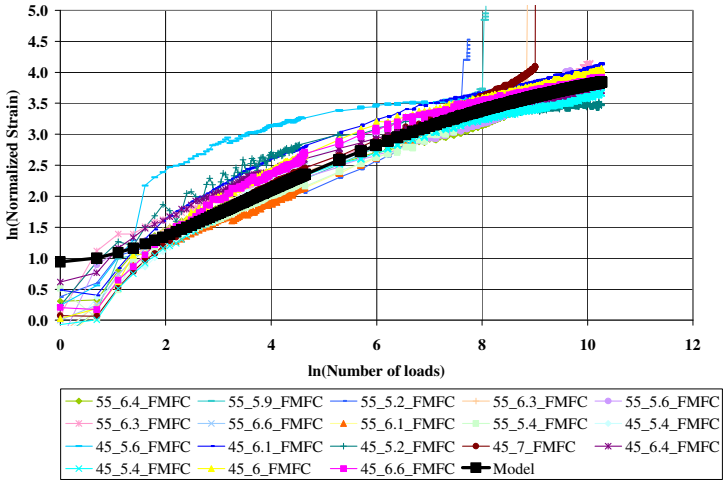

Figure 4.25: Normalized strain versus load applications for underlying DGAC.

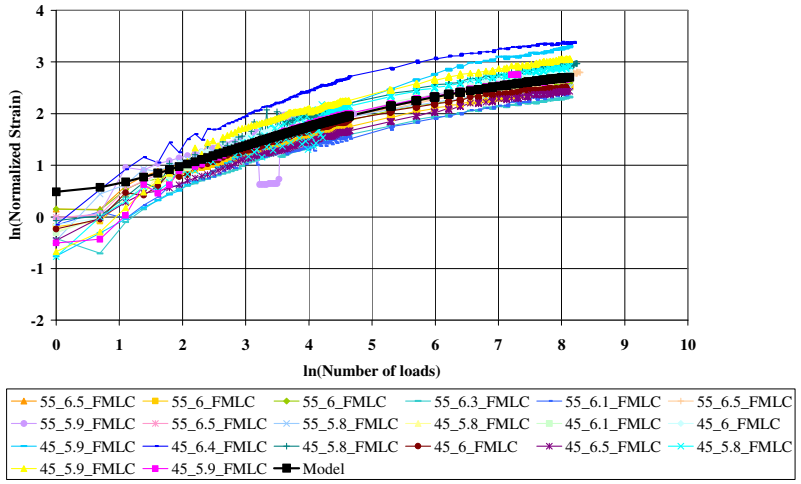

Figure 4.26: Normalized strain versus load applications for AR4000-D overlay.

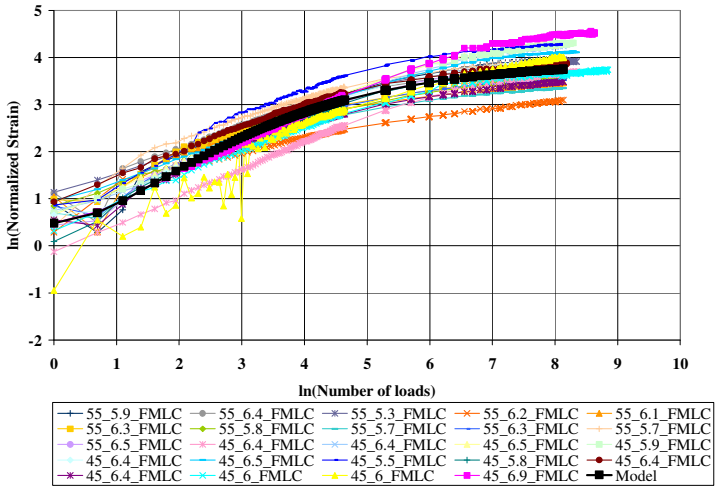

Figure 4.27: Normalized strain versus load applications for RAC-G overlay.

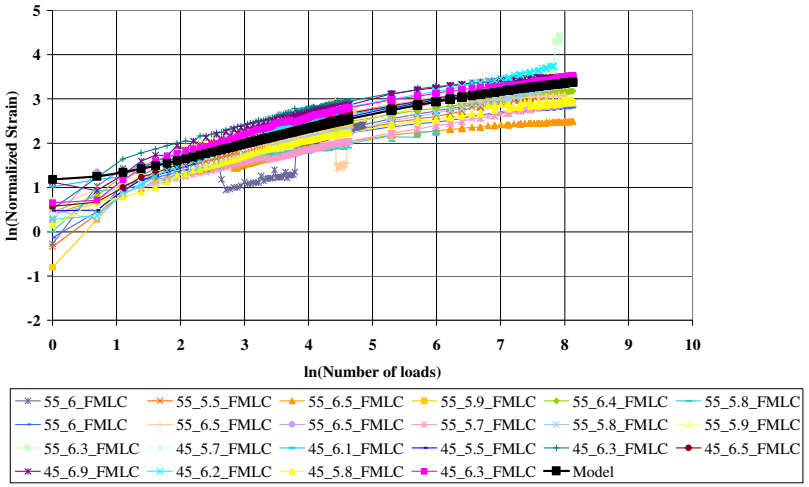

Figure 4.28: Normalized strain versus load applications for MB15-G overlay.

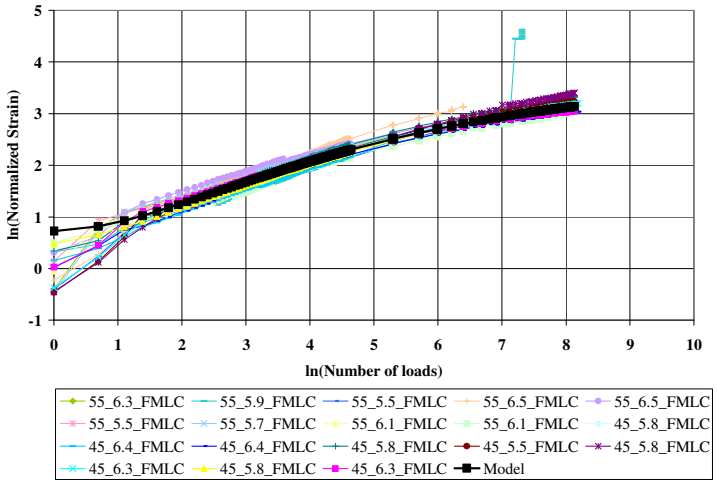

Figure 4.29: Normalized strain versus load applications for MB4-G overlay.

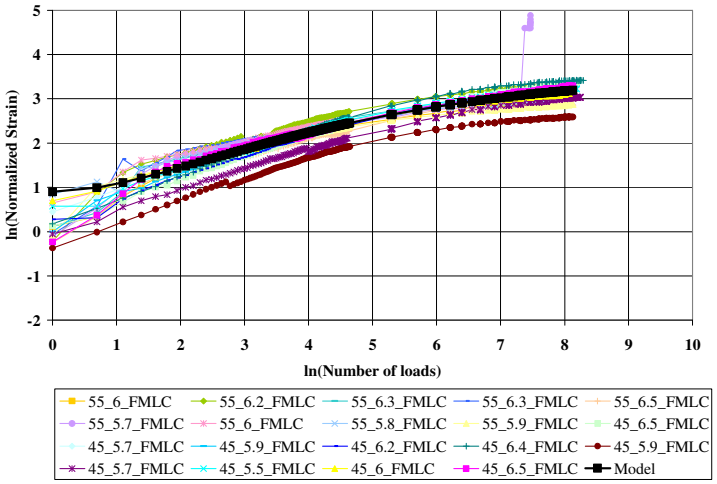

Figure 4.30: Normalized strain versus load applications for MAC15-G overlay.

A summary of the parameters of Equation 4.19 is provided in Table 4.6, for the different asphalt materials of the test track. It is noteworthy that the permanent deformation is a function of the shear stress in the DGAC layers only, except for a very small influence for MB4-G.

Table 4.6: Permanent Deformation Parameters for Asphalt Concrete

Material	A	A	τ_{ref}	β	γ
Underlying DGAC	0.9411	3.6452	0.1	0.2246	3.4646
Overlays					
AR4000-D	0.4867	2.6589	0.1	0.519	2.5068
RAC-G	0.4792	3.4280	0.1	0	1.6782
MB15-G	1.1795	2.8238	0.1	0	2.8442
MB4-G	0.7266	2.9315	0.1	0.03522	2.5801
MAC15-G	0.8996	2.6916	0.1	0	2.3948

Figure 4.31 compares the down rut (in mm) calculated for the different asphalt materials, assuming a shear stress of 0.1 MPa, a temperature of 50°C, and a loading time of 0.015 seconds. The master curve corresponding to the FWD tests was used for the underlying DGAC (Or.DGAC in the figure). This master curve was also used for the simulations of the HVS experiments, using *CalME*. It can be seen that the shear (RSST-CH) derived parameters for the underlying DGAC indicate a high propensity for rutting.

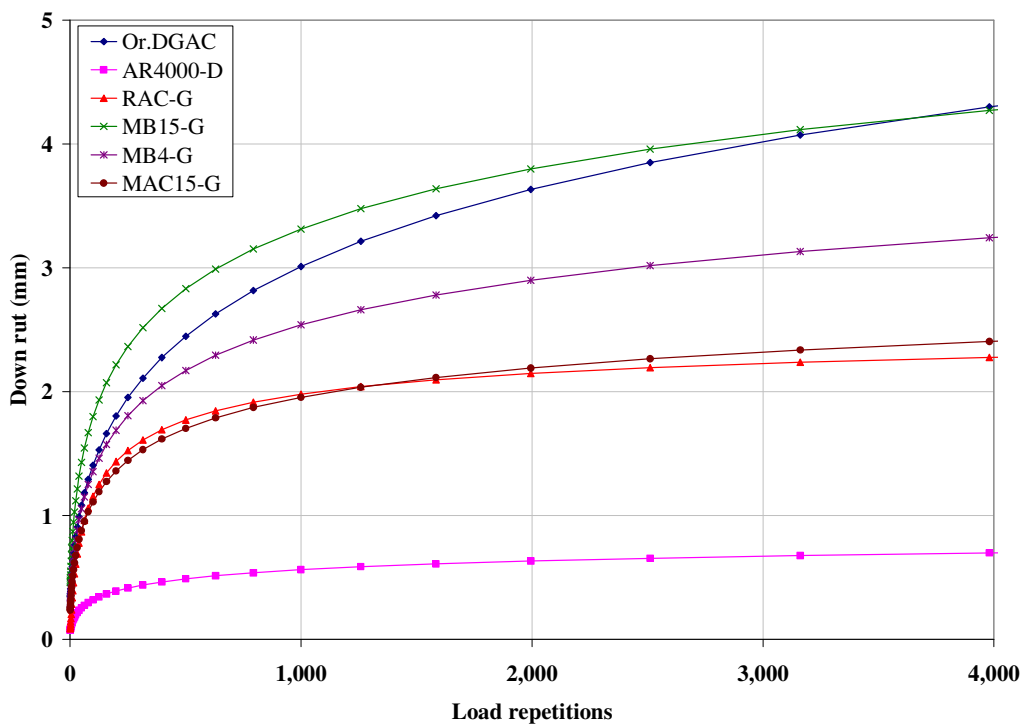

Figure 4.31: Comparison of down rut (mm) versus load repetitions for test track AC mixes.

4.9. Simulation of Original Pavement Structure (Actual Conditions)

The first step in the simulation is to ensure that the calculated response is reasonably similar to the measured response. The available response measurements for the reflective cracking experiment included

MDD and/or RSD deflections. In addition, the backcalculated moduli before and after the HVS experiment were used to evaluate the reasonableness of the simulations. FWD and backcalculated moduli before and after HVS testing for each section on the test track are summarized in Table 4.7. Moduli backcalculated from FWD tests before HVS loading were used as the initial values in the simulations ("initial" in Table 4.7), except where the FWD tests showed an increase in the backcalculated asphalt concrete value after loading ("terminal" in Table 4.7), in which case the latter value was used.

The first three columns in Table 4.7 show the moduli backcalculated for the pavement layers before (initial) and after (terminal) the HVS loading. The last five columns show the initial moduli used in *CalME* and the terminal moduli predicted by *CalME*. The base layer was split into three layers for the simulations with *CalME*, as explained earlier. The asphalt concrete moduli are given at the reference temperature of 20°C and a loading time of 0.015 sec (the approximate loading time of the FWD). The backcalculated values for the subgrade correspond to the FWD load and the asphalt concrete modulus adjusted to 20°C, whereas the subgrade modulus calculated by *CalME* is at a load level of 60 kN and the actual temperature recorded at the end of the experiment.

Section 569RF showed very large differences over the length of the section and was therefore split into two subsections, 569RFa and 569RFb, for the simulations. This split was carried to the overlaid sections 588RFa and 588RFb.

Table 4.7: Moduli of Original Structure Before and After HVS Loading

Layer	Moduli (MPa)							
	FWD			*CalME*				
	AC	AB	SG	AC	AB1	AB2	AB3	SG
567RF initial	2,192	586	132	2,278	586	586	586	132
567RF terminal	2,278	168	150	2,198	106	162	232	92
568RF initial	5,473	483	163	5,473	483	483	483	163
568RF terminal	3,799	79	166	2,137	53	92	142	84
569RFa initial	3,451	1,680	185	5,618	1,680	1,680	1,680	185
569RFa terminal	5,618	227	66	5,092	136	282	531	83
569RFb initial	3,623	1,132	158	3,623	1,132	1,132	1,132	158
569RFb terminal	2,318	62	58	2,398	57	116	252	67
571RF initial	1,624	773	158	4,430	773	773	773	158
571RF terminal	4,430	230	206	3,169	139	213	312	86
572RF initial	2,141	1,108	194	4,944	1,108	1,108	1,108	194
572RF terminal	4,944	93	73	1,924	57	110	242	72
573RF initial	1,629	648	99	3,904	648	648	648	99
573RF terminal	3,904	189	152	2,552	111	177	267	56
AC1 is overlay, AC2 is underlying DGAC, AB is aggregate base and SG is subgrade.								

No information was available on the damage propensity of the partially self-cementing aggregate base, so the permissible stress in Equation 4.18 was changed until the resulting response and moduli were reasonably close to measured values.

4.9.1 RSD Response

The measured and calculated RSD response as a function of the number of load applications is shown as screen captures from *CalME* in Figures 4.32 through 4.38. The first value shown ("RSD") is the measured value and the second ("Calc.") is the value calculated by *CalME*. The RSD deflections were measured at a number of locations within the test section, whereas the calculated values assume the section to be perfectly uniform. All of the comparisons are at a wheel load of 60 kN.

4.9.2 MDD Response

The measured surface deflection, resilient compression of the base layers, and deflection of the subgrade, are compared to values calculated by *CalME* in Figures 4.39 through 4.47 on those HVS sections with useable MDD results. The measured values has a legend "M" followed by the depth of the MDD module in mm or, for the compression of the base layers, by the depths of the first and second MDD module. In Figure 4.40, for example, "M90-330" indicates the resilient compression between the two MDDs at 90 mm and 330 mm. The similar calculated values have legend "C" (i.e., C90-330). All comparisons are at a wheel load of 60 kN.

4.9.3 Damage

The damage (ω) of the asphalt concrete layer is shown in Figures 4.48 through 4.54, as defined by Equation 4.9. The observed cracking, in m/m^2, is shown on the secondary y-axis.

4.9.4 Surface Permanent Deformation

The measured down rut is shown in Figures 4.55 through 4.61, with the mean, minimum, and maximum values within the central 6.0 m of the test sections, as a function of the number of load applications. They are compared to the value calculated by *CalME* ("Calc").

4.9.5 MDD Permanent Deformation

The permanent deformation at the upper MDD, the permanent compression of the aggregate base layers, and the permanent deformation of the subgrade are shown as functions of the number of load applications in Figures 4.62 through 4.72, for those sections with useable MDD results. The same legend-convention is used as for the resilient deflections. It should be noted that the upper MDD is approximately at the top of the aggregate base so that the permanent deformation of the asphalt concrete layer is excluded.

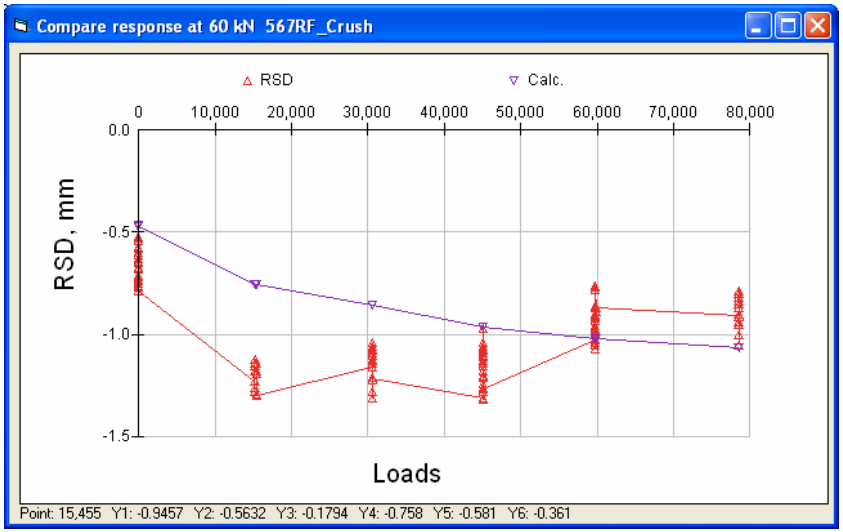

Figure 4.32: 567RF, measured (RSD) and calculated surface deflection.

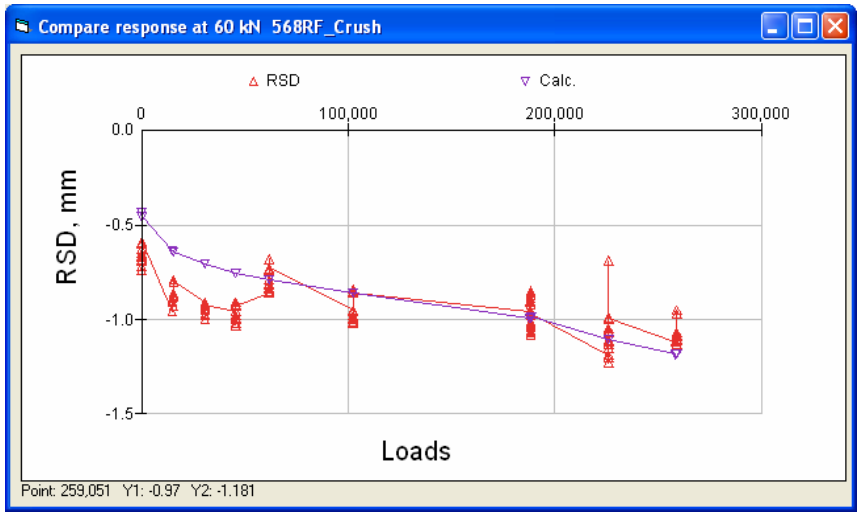

Figure 4.33: 568RF, measured (RSD) and calculated surface deflection.

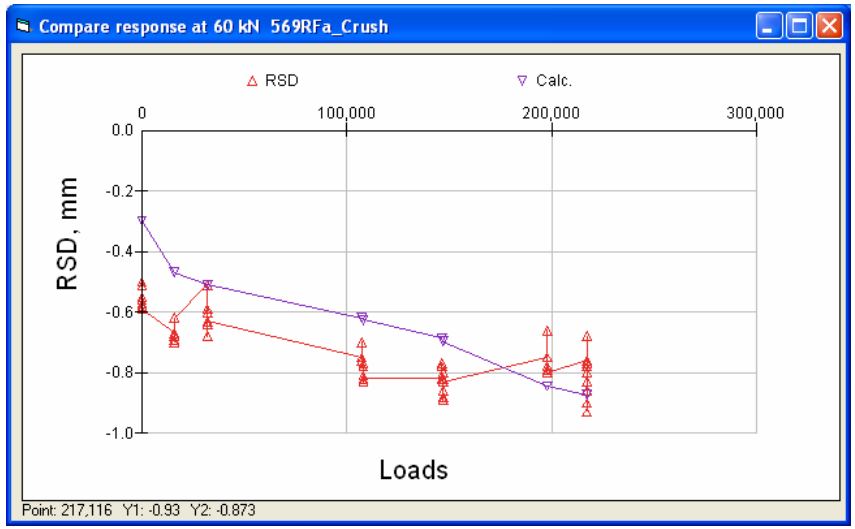

Figure 4.34: 568RFa, measured (RSD) and calculated surface deflection.

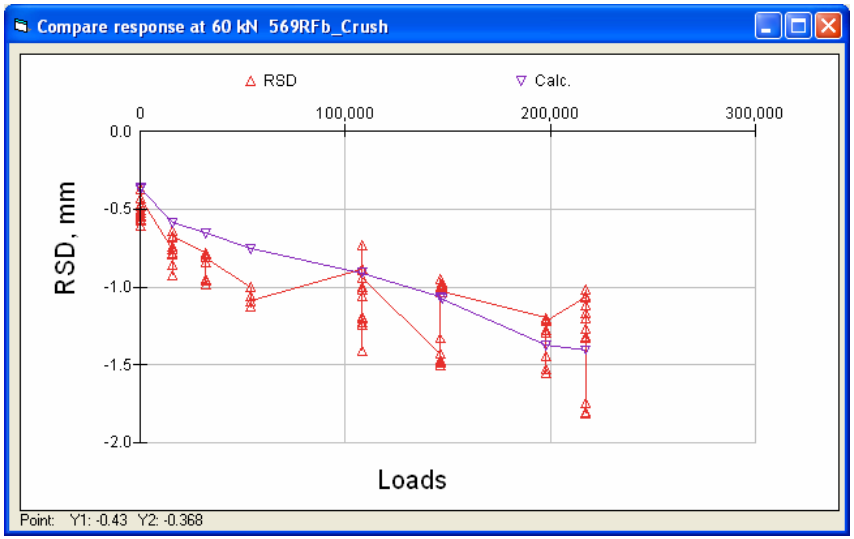

Figure 4.35: 569RFb, measured (RSD) and calculated surface deflection.

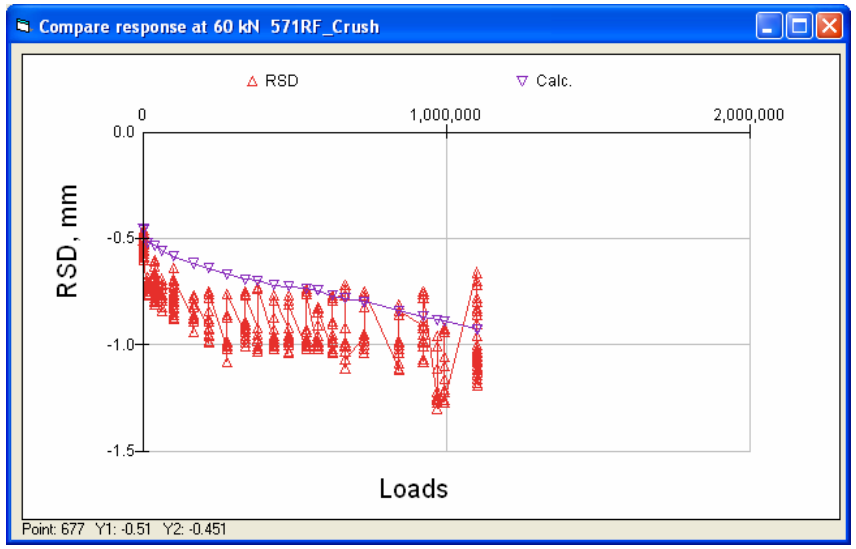

Figure 4.36: 571RF, measured (RSD) and calculated surface deflection.

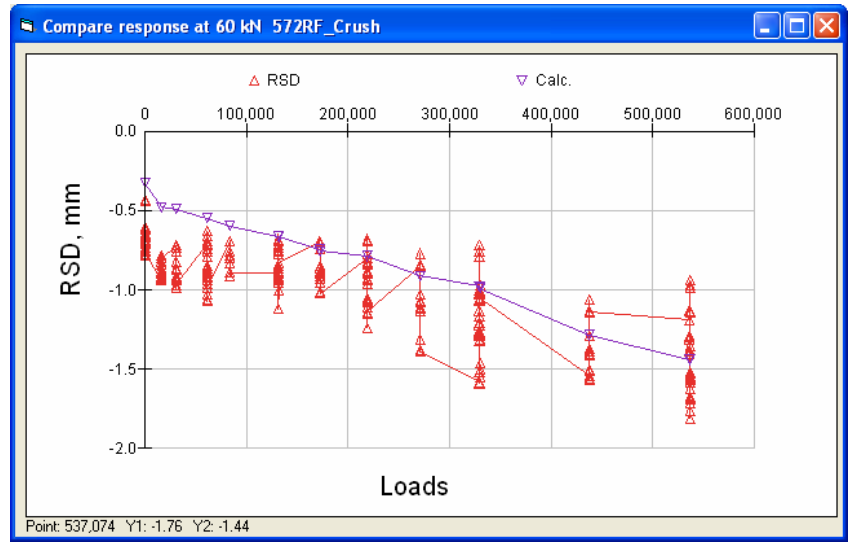

Figure 4.37: 572RF, measured (RSD) and calculated surface deflection.

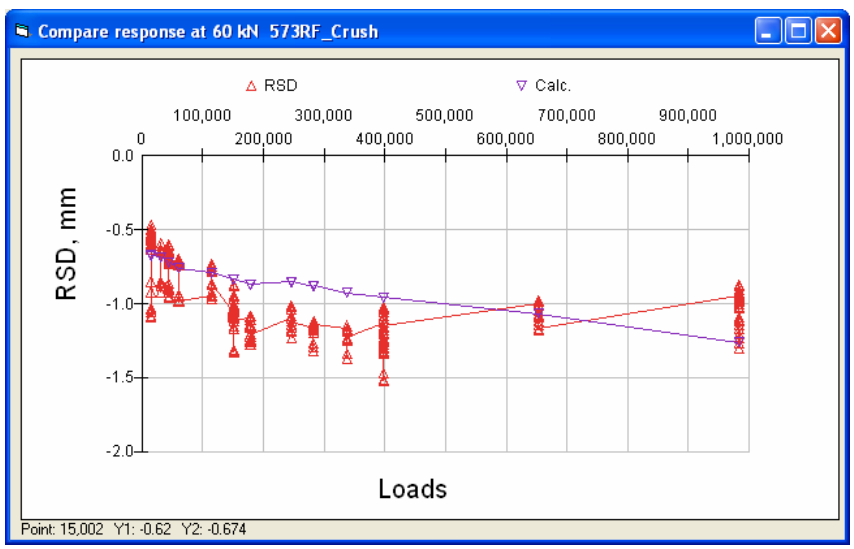

Figure 4.38: 573RF, measured (RSD) and calculated surface deflection.

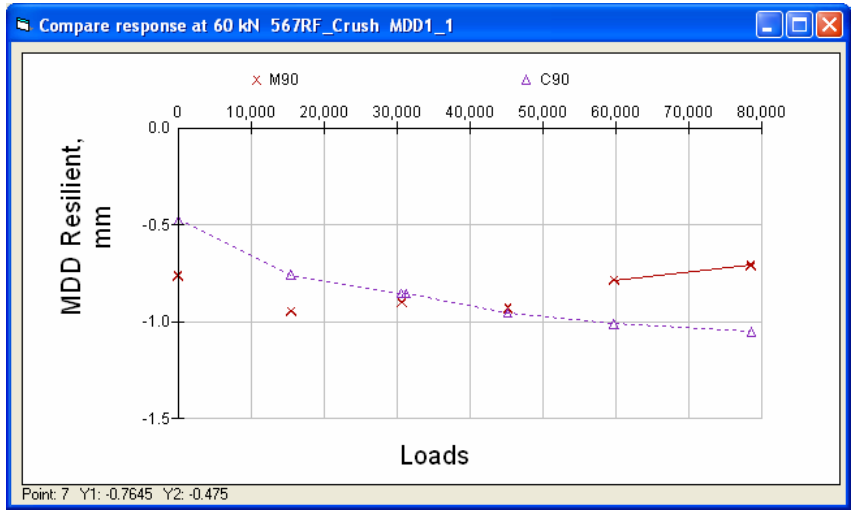

Figure 4.39: 567RF, measured and calculated deflection at upper MDD.

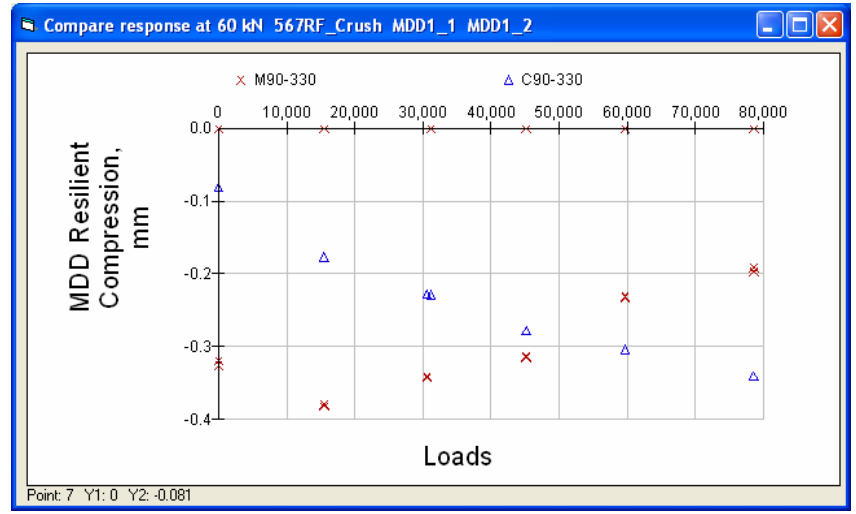

Figure 4.40: 567RF, resilient compression of upper AB layers.

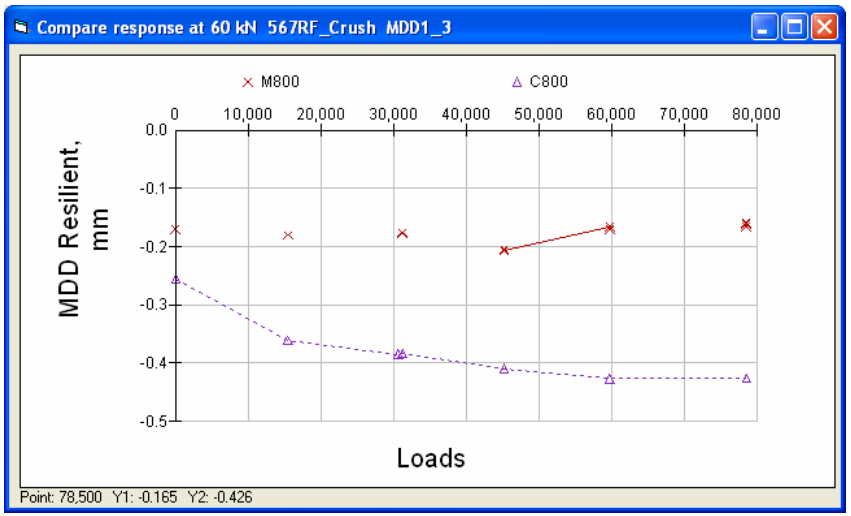

Figure 4.41: 567RF, measured and calculated deflection of lower subgrade.

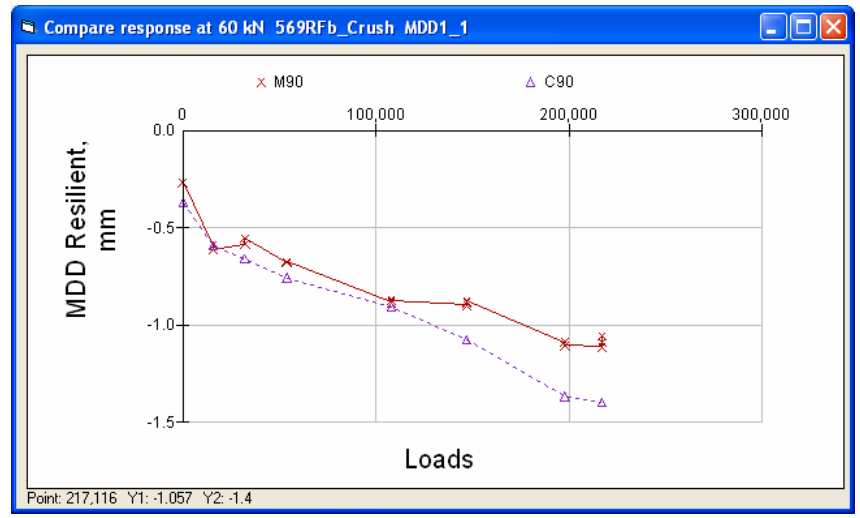

Figure 4.42: 569RFb, measured and calculated deflection at upper MDD.

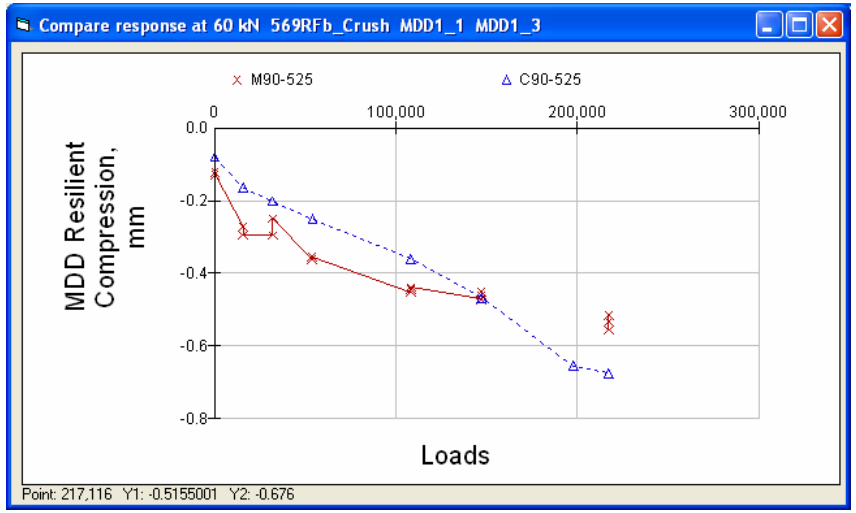

Figure 4.43: 569RFb, resilient compression of AB layers plus upper subgrade.

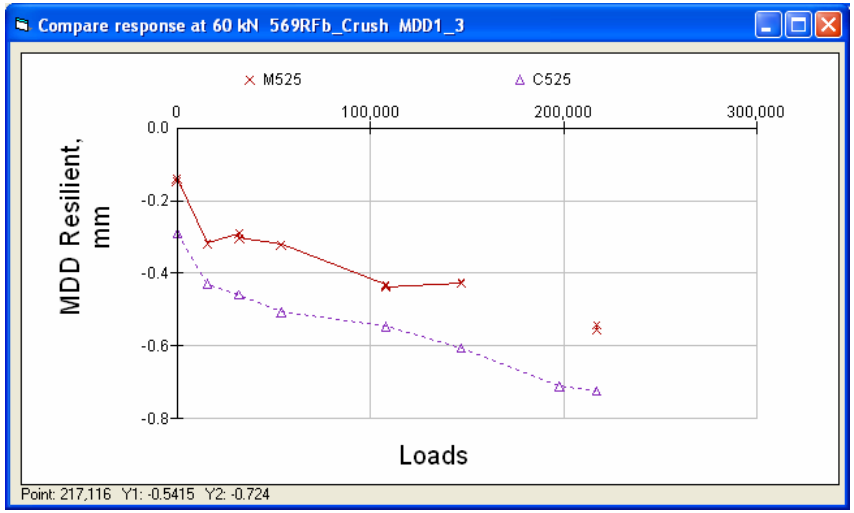

Figure 4.44: 569RFb, measured and calculated deflection of subgrade.

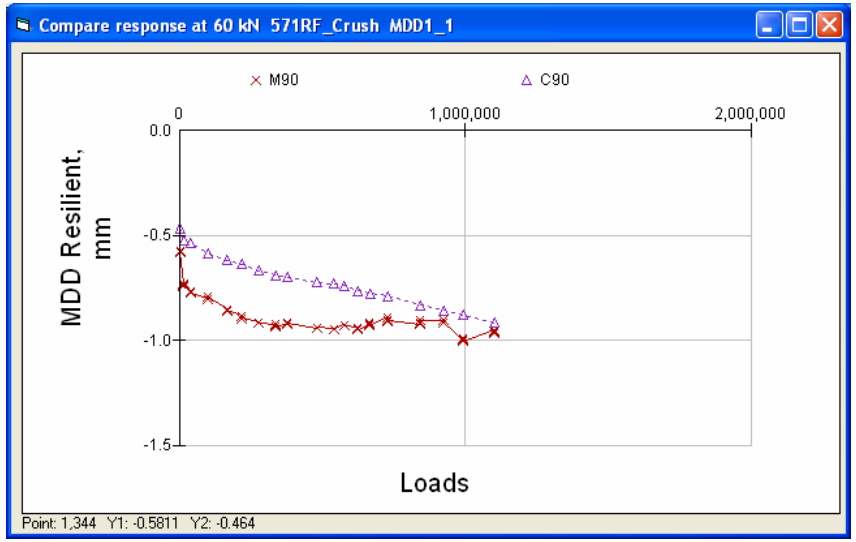

Figure 4.45: 571RF, measured and calculated deflection at upper MDD.

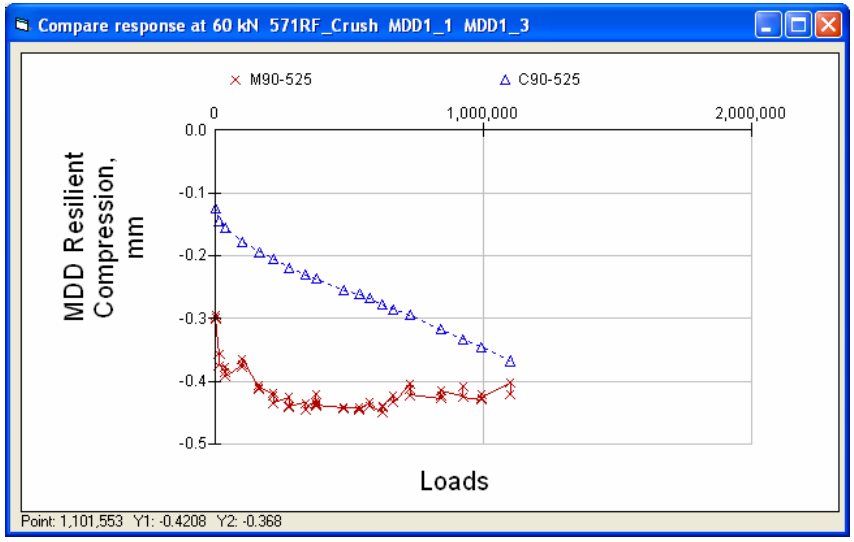

Figure 4.46: 571RF, resilient compression of AB layers plus upper subgrade.

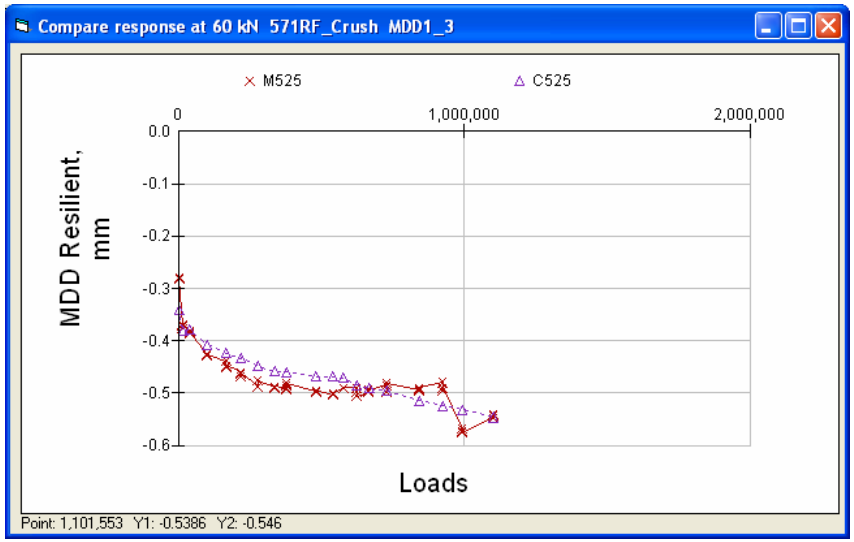

Figure 4.47: 571RF, measured and calculated deflection of subgrade.

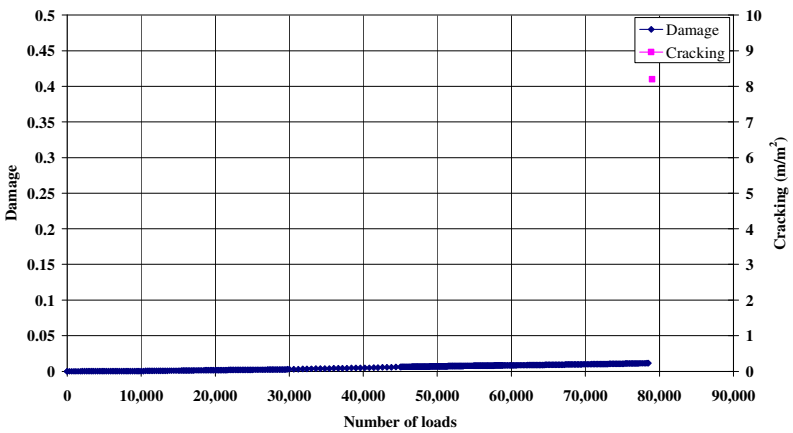

Figure 4.48: 567RF, damage and cracking.

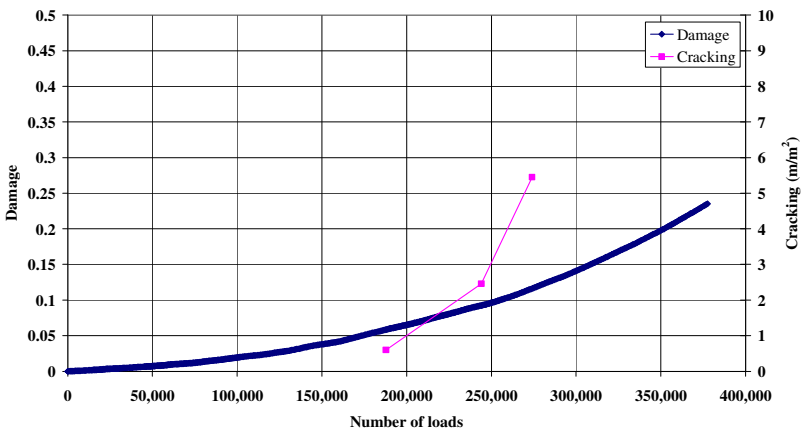

Figure 4.49: 568RF, damage and cracking.

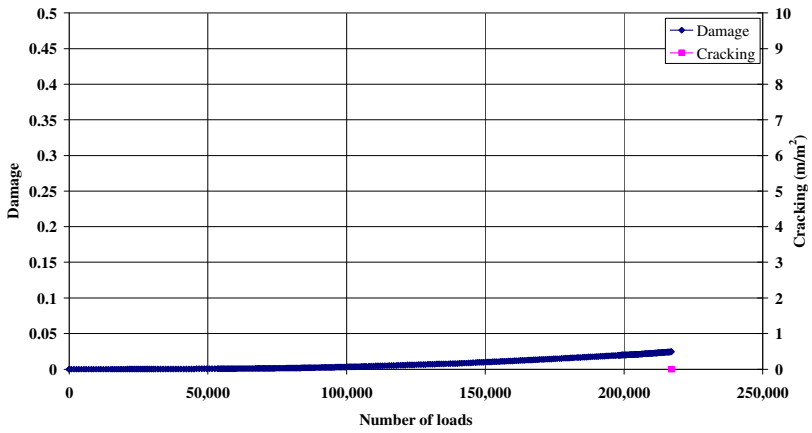

Figure 4.50: 569RFa, damage and cracking.

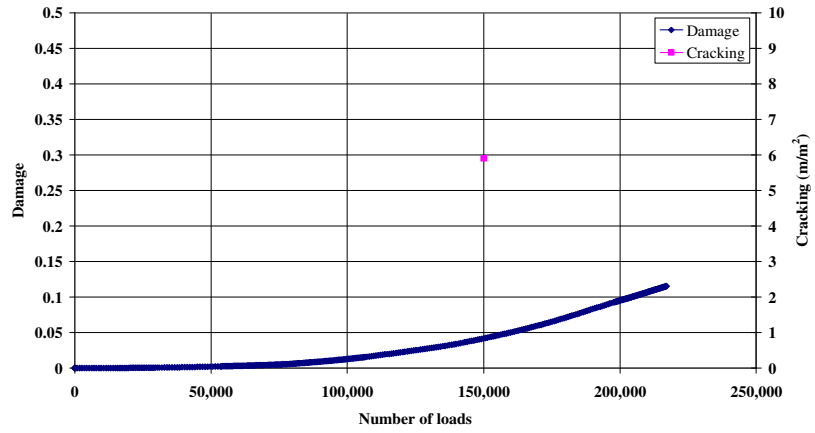

Figure 4.51: 569RFb, damage and cracking.

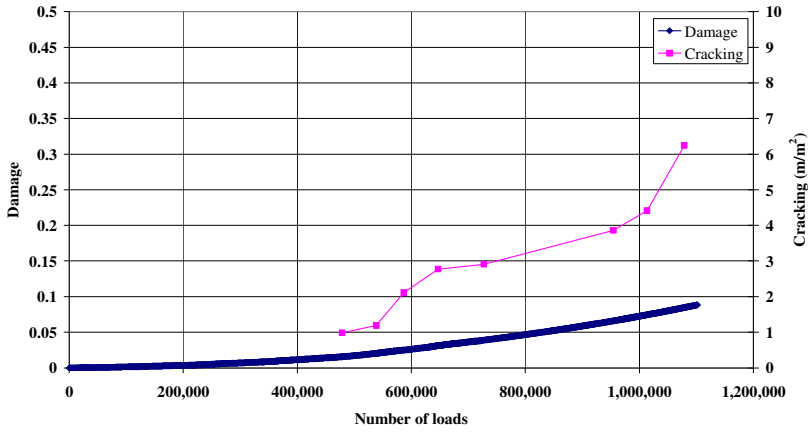

Figure 4.52: 571RF, damage and cracking.

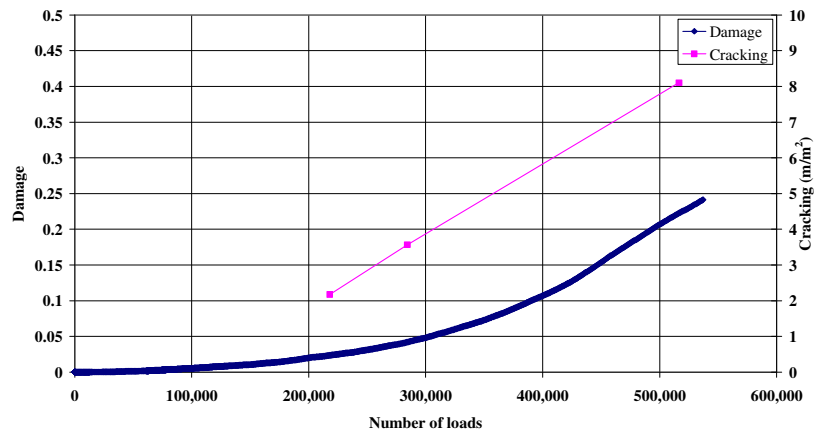

Figure 4.53: 572RF, damage and cracking.

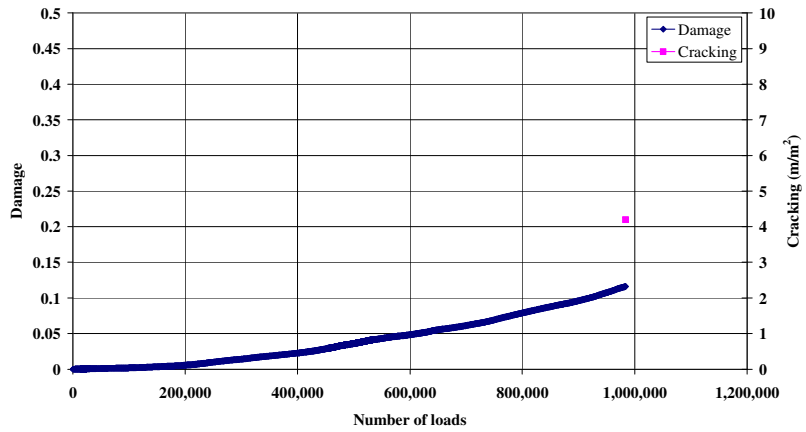

Figure 4.54: 573RF, damage and cracking.

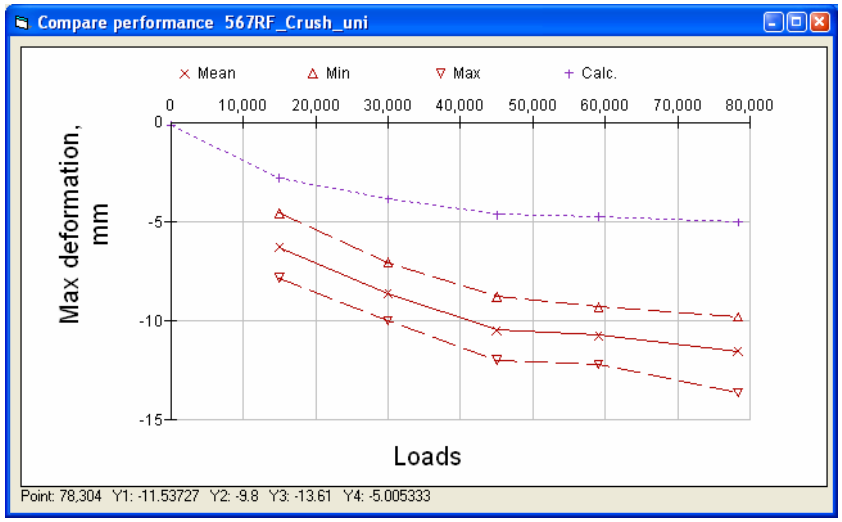

Figure 4.55: 567RF, measured and calculated down rut

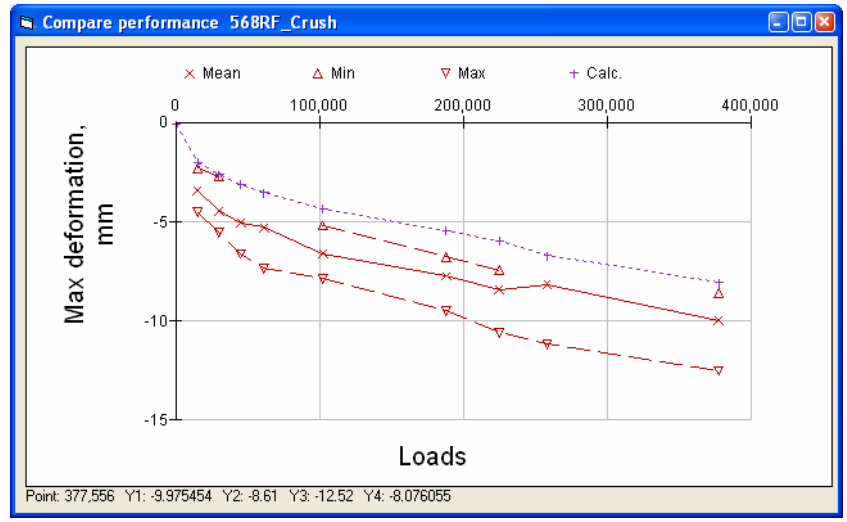

Figure 4.56: 568RF, measured and calculated down rut.

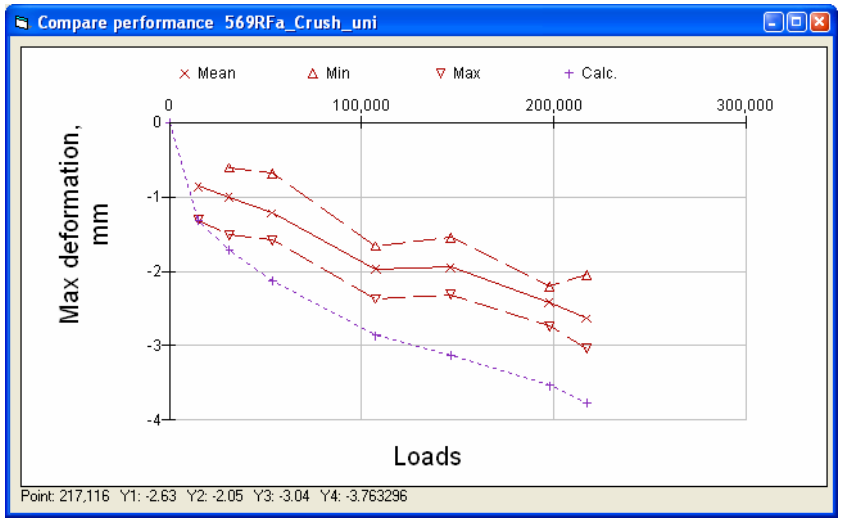

Figure 4.57: 569RFa, measured and calculated down rut.

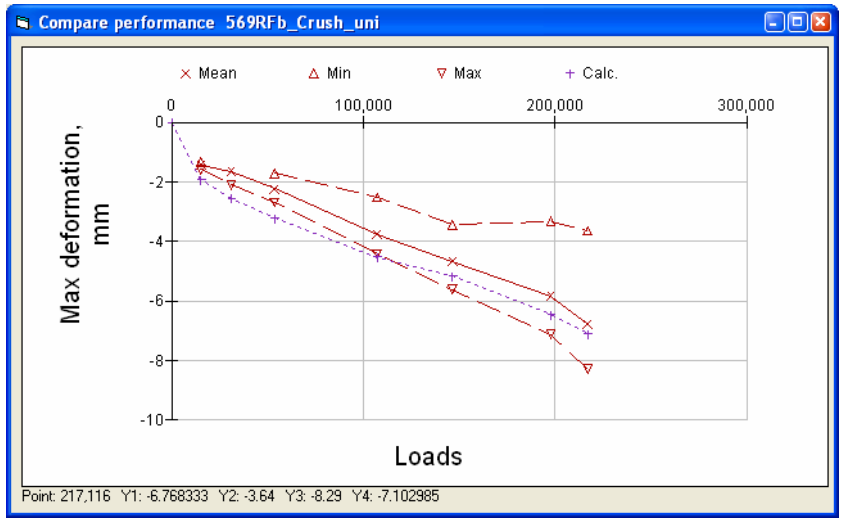

Figure 4.58: 569RFb, measured and calculated down rut.

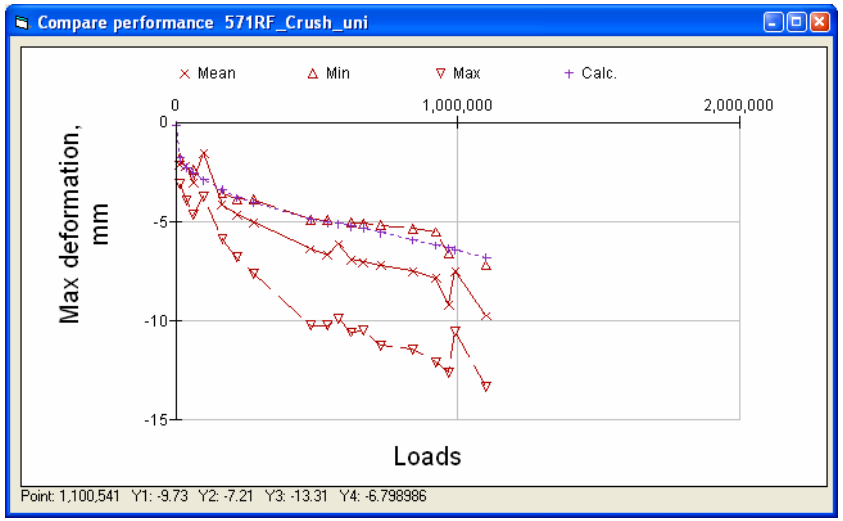

Figure 4.59: 571RF, measured and calculated down rut.

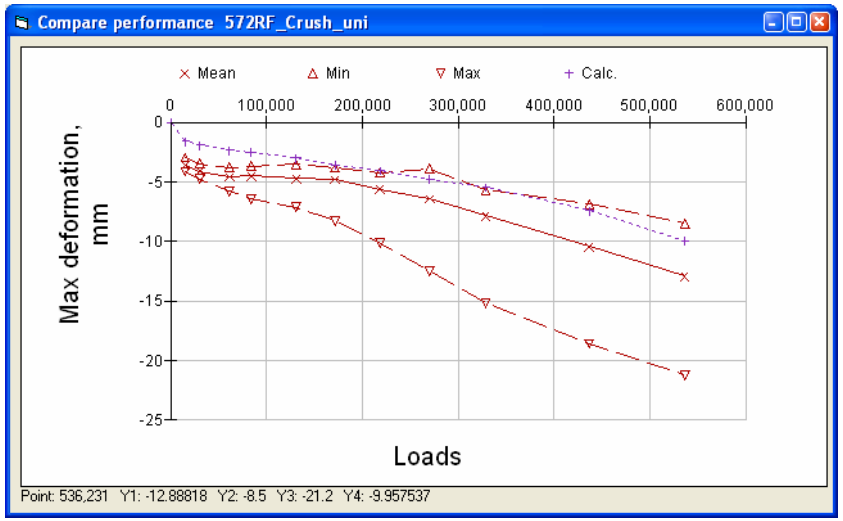

Figure 4.60: 572RF, measured and calculated down rut.

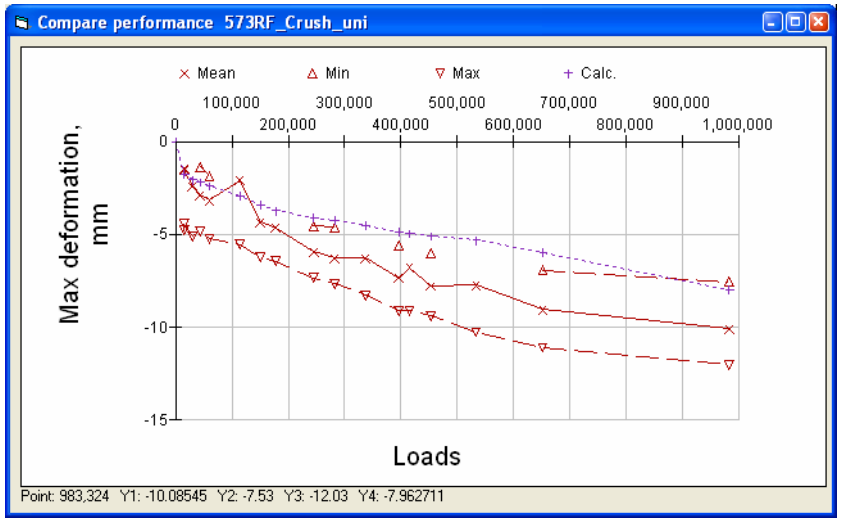

Figure 4.61: 573RF, measured and calculated down rut.

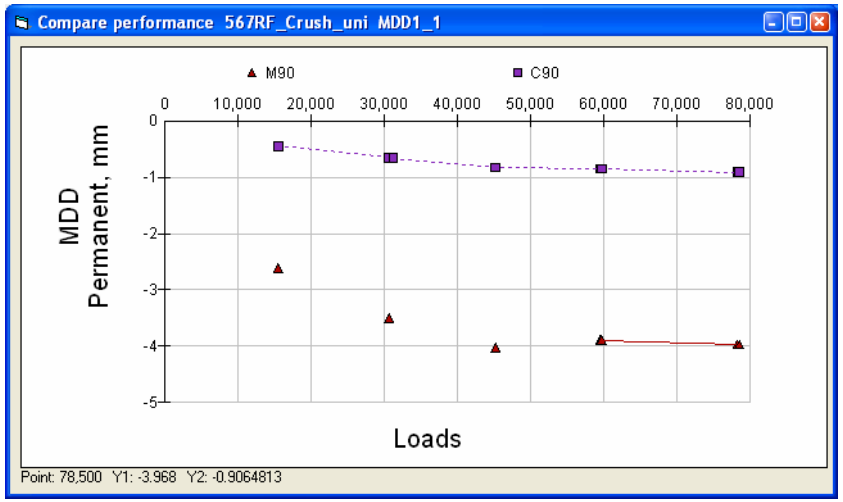

Figure 4.62: 567RF, measured and calculated permanent deformation at upper MDD.

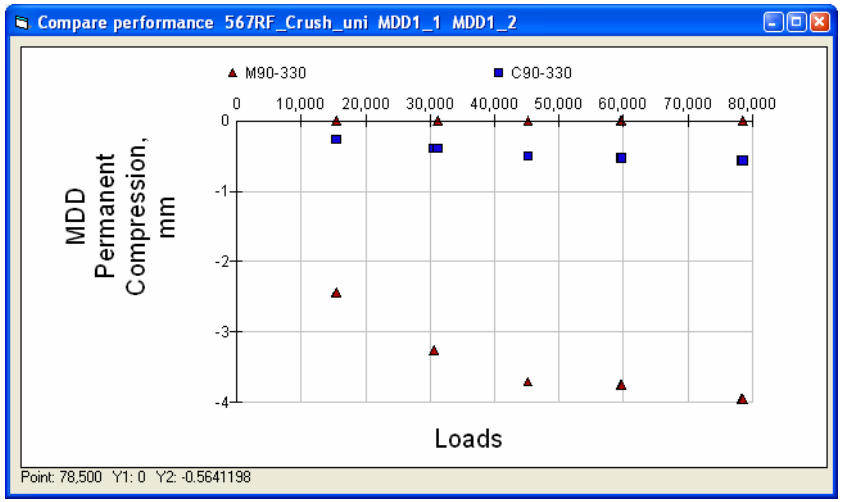

Figure 4.63: 567RF, measured and calculated permanent deformation of upper AB layers.

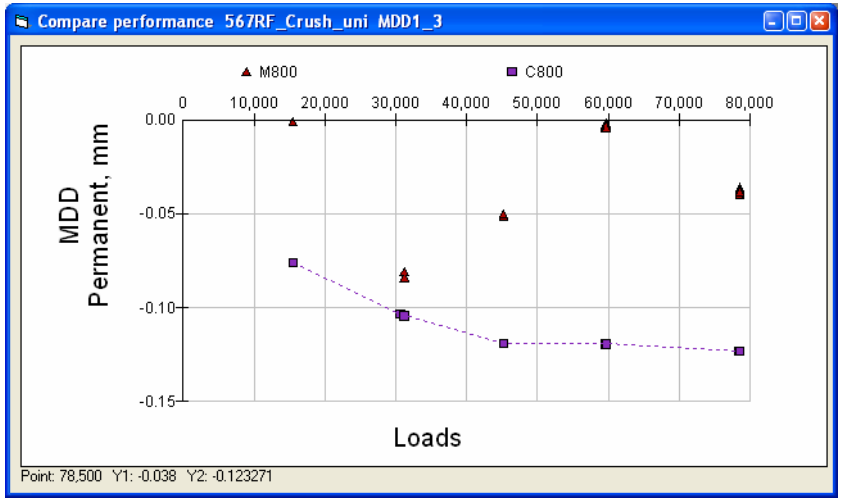

Figure 4.64: 567RF, measured and calculated permanent deformation of lower subgrade.

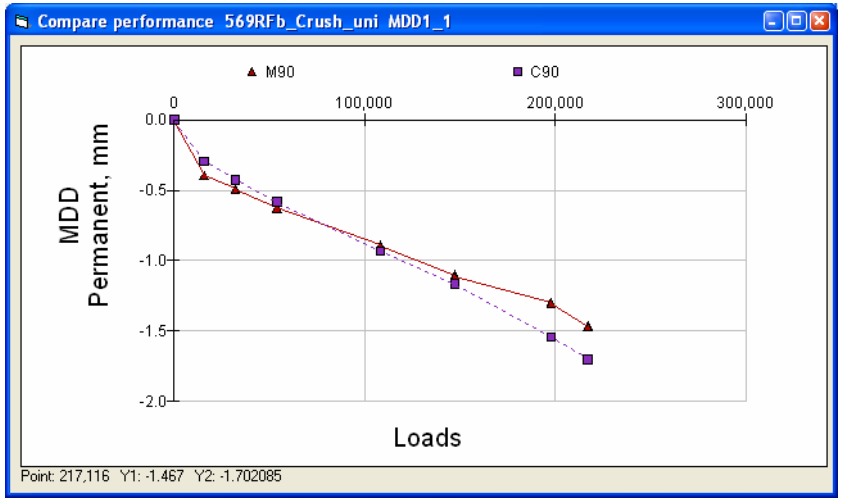

Figure 4.65: 569RFb, measured and calculated permanent deformation at top MDD.

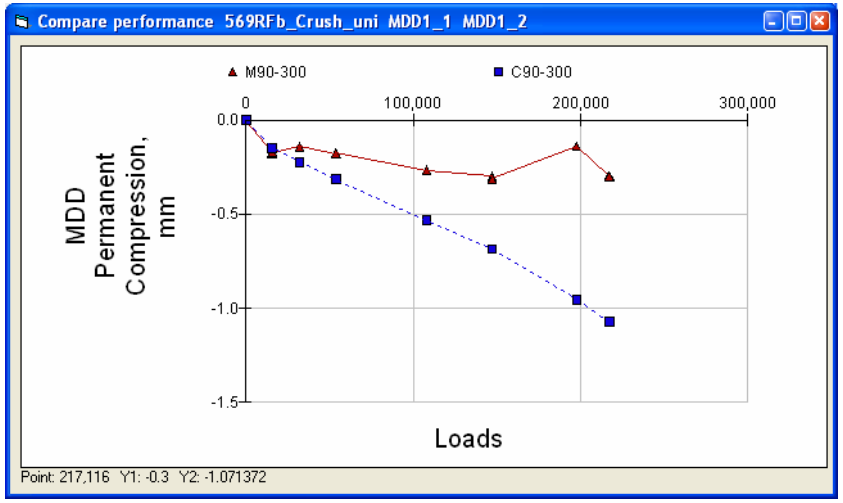

Figure 4.66: 569RFb, measured and calculated permanent compression of upper AB layers.

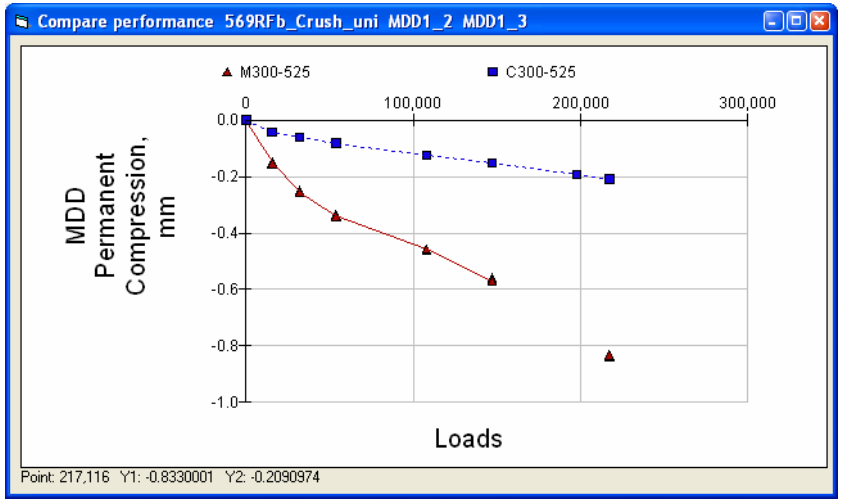

Figure 4.67: 569RFb, measured and calculated permanent compression of lower AB layers.

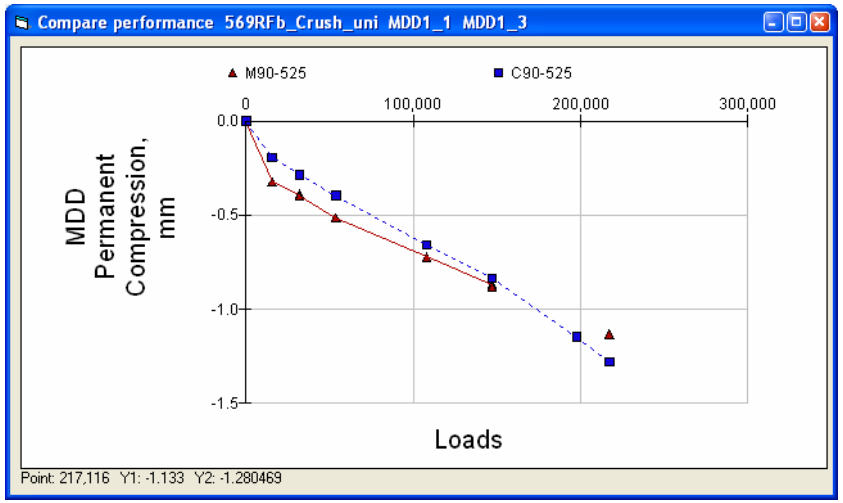

Figure 4.68: 569RFb, measured and calculated permanent compression of AB layers.

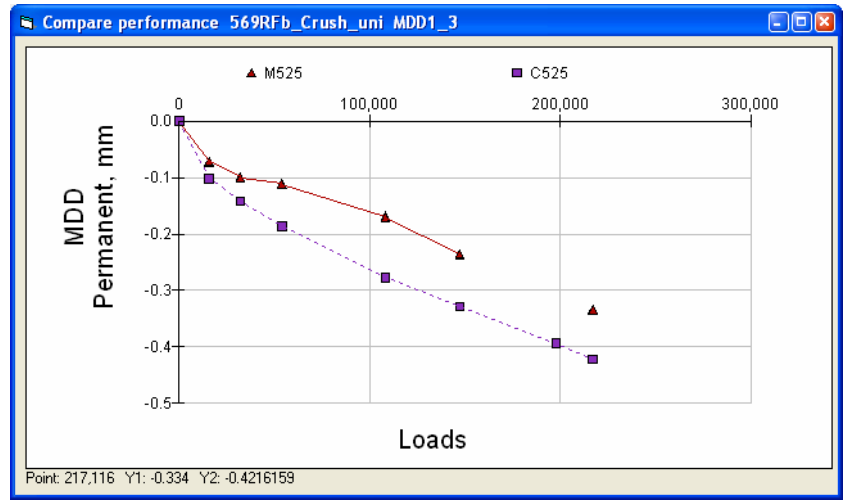

Figure 4.69: 569RFb, measured and calculated permanent deformation of subgrade.

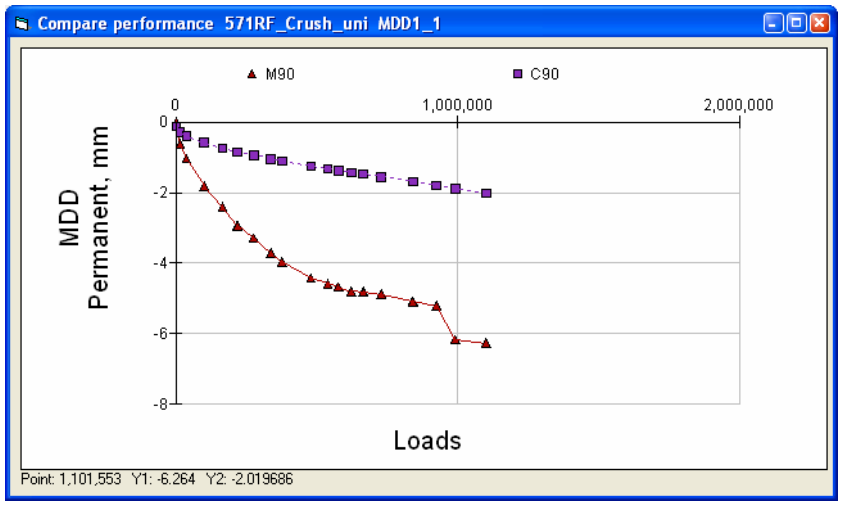

Figure 4.70: 571RF, measured and calculated permanent deformation of top MDD

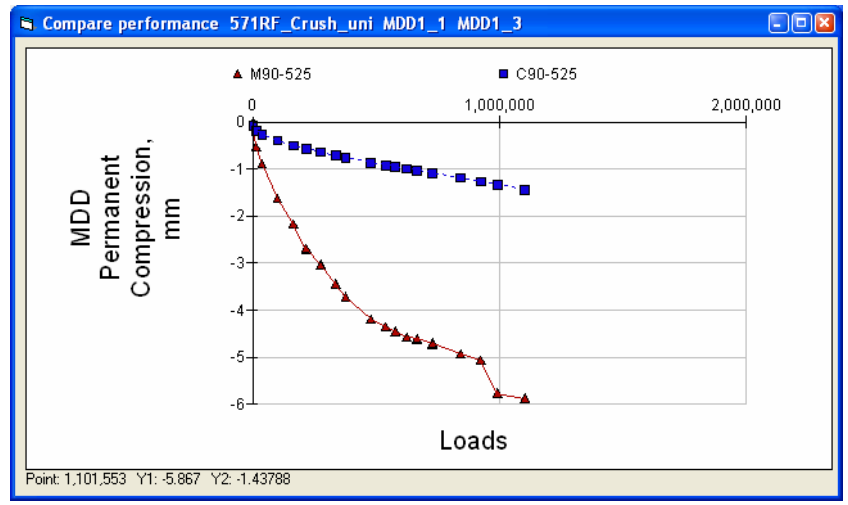

Figure 4.71: 571RF, measured and calculated permanent compression of AB layers.

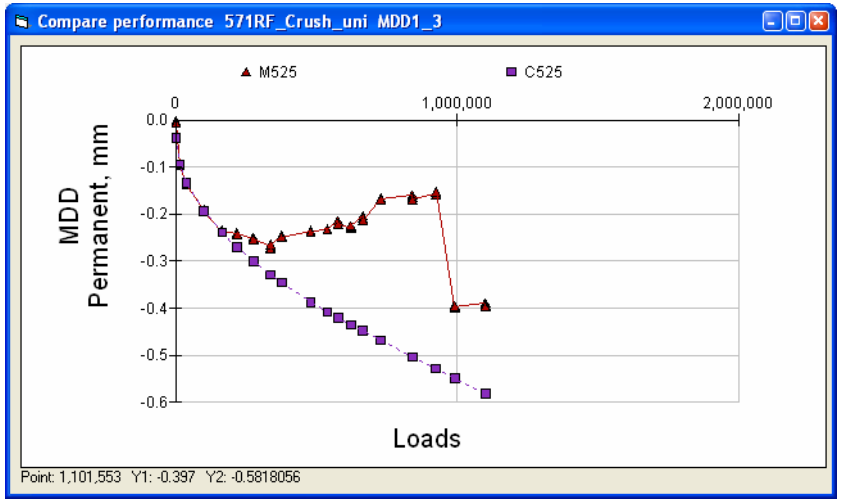

Figure 4.72: 571RF, measured and calculated permanent deformation at top of subgrade.

4.10. Simulation of Overlaid Sections (Actual Conditions): Rutting Study

FWD test results were not available directly on the sections used for the rutting study due to the nature of the deformation on the surface after HVS testing. The moduli were estimated from FWD tests on the sides of the section and from the initial MDD deflections at the start of the HVS experiments. A summary of the input moduli, in MPa ("initial"), is provided in Table 4.8.

Table 4.8: Moduli from Simulation of Rutting Study

Layer	Overlay	*CalME* Predicted Moduli (MPa)					
		AC1	AC2	AB1	AB2	AB3	SG
580RF initial	MB15-G	2,200	2,600	200	200	200	300
580RF terminal		2,098	2,598	146	154	161	171
581RF initial	RAC-G	6,000	3,000	600	600	600	80
581RF terminal		5,954	3,000	368	410	456	37
582RF initial	AR4000-D	10,000	2,500	300	300	300	250
582RF terminal		9,860	2,500	178	193	209	94
583RF initial	MB4-G	2,600	3,600	430	430	430	340
583RF terminal		2,397	3,599	236	267	295	160
584RF initial	MB4-G	2,600	3,200	250	250	250	300
584RF terminal		2,242	3,169	119	138	155	141
585RF initial	MAC15-G	2,500	3,000	200	200	200	300
585RF terminal		2,391	2,996	140	149	157	172
AC1 is overlay, AC2 is underlying DGAC, AB is aggregate base, and SG is subgrade.							

The "terminal" values calculated by *CalME* are also shown. It can be seen from Table 4.8 that there is very little damage to the asphalt layer (although it should be kept in mind that the damage function for the asphalt concrete was derived from laboratory testing at 20°C only). There is a significant decrease in the modulus of the aggregate base during the experiment. The subgrade moduli before and after the HVS experiment cannot be directly compared as the input value ("initial") is at a temperature of 20°C for the asphalt concrete, whereas the terminal modulus ("terminal") is at the actual temperature at the completion of the HVS experiment (approximately 50 C at 500 mm pavement depth).

4.10.1 Temperatures

The temperatures in the upper 100 mm of the pavement are shown in Figures B.1 through B.6, as a function of the number of load applications. The number in the legend indicates the depth of the thermocouple.

4.10.2 MDD Response

The resilient deflections measured with the MDD are shown in Figures B.7 through B.27 in Appendix B using the same legend convention as described in Section 4.9.2.

4.10.3 Surface Permanent Deformation

The measured down rut is shown in Figures 4.73 through 4.78 — with the mean (labeled "Right" in the screen captures), minimum, and maximum values within the central 6.0 m of the test sections — as a function of the number of load applications. Down rut measurements are compared to the value calculated by *CalME* ("Calc."). The results indicate that the model provided a satisfactory simulation of the measured rutting.

4.10.4 In-Depth Permanent Deformation

The permanent deformation at the upper MDD, the permanent compression of the aggregate base layers, and the permanent deformation of the subgrade are shown as functions of the number of load applications in Figures B.28 through B.45, for those sections with useable MDD results. The same legend-convention is used as for the resilient deflections. The figures indicate that the permanent deformation in the base was less than 1.0 mm and in the subgrade less than 0.1 mm.

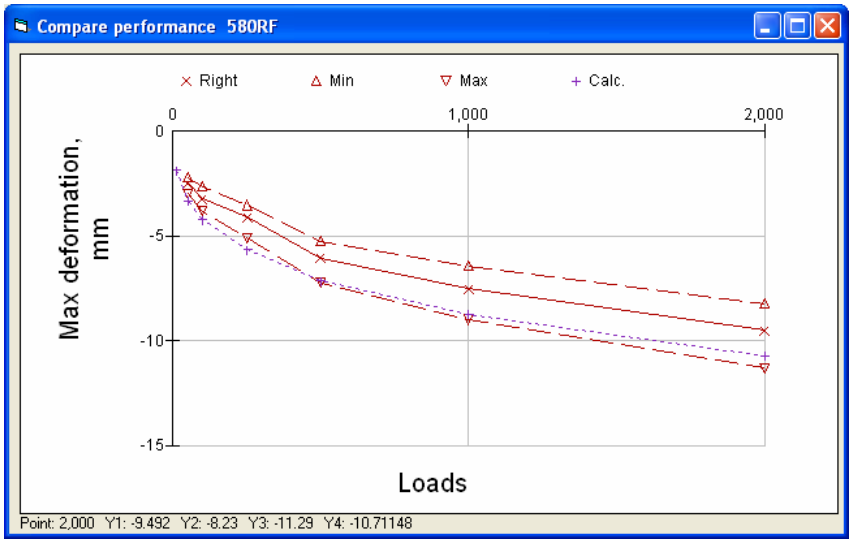

Figure 4.73: 580RF, measured and calculated down rut.

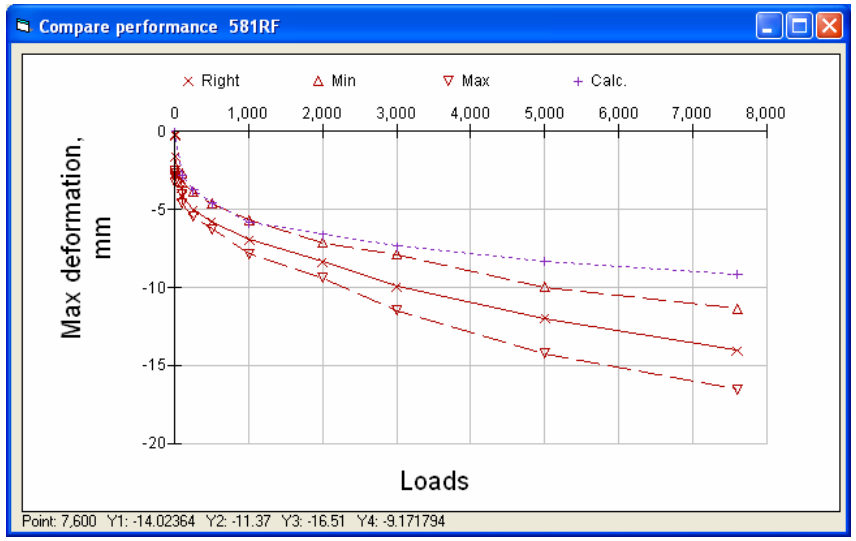

Figure 4.74: 581RF, measured and calculated down rut.

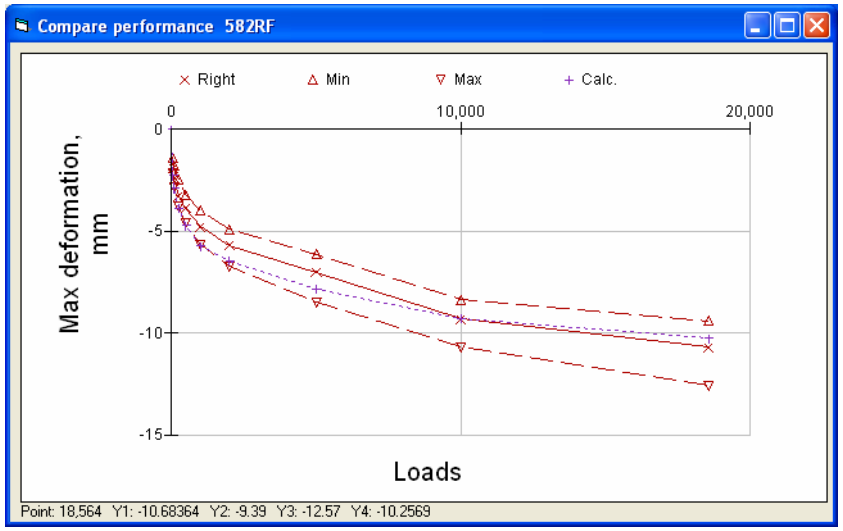

Figure 4.75: 582RF, measured and calculated down rut.

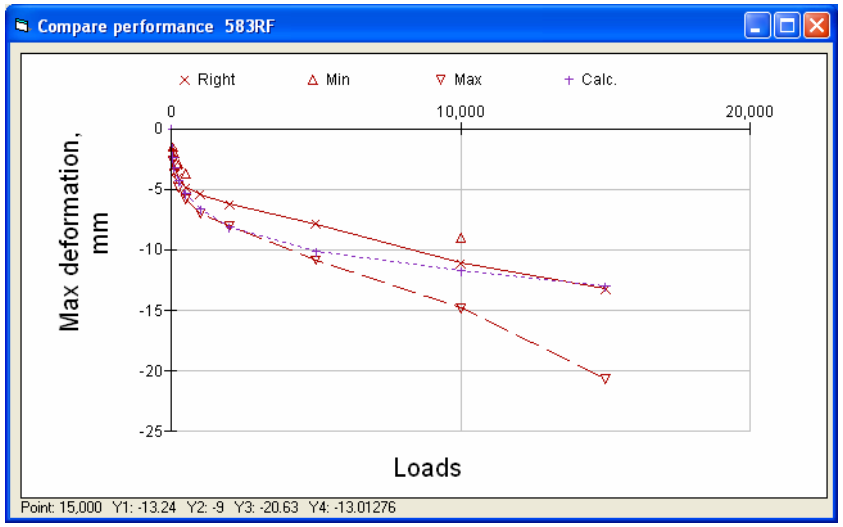

Figure 4.76: 583RF, measured and calculated down rut.

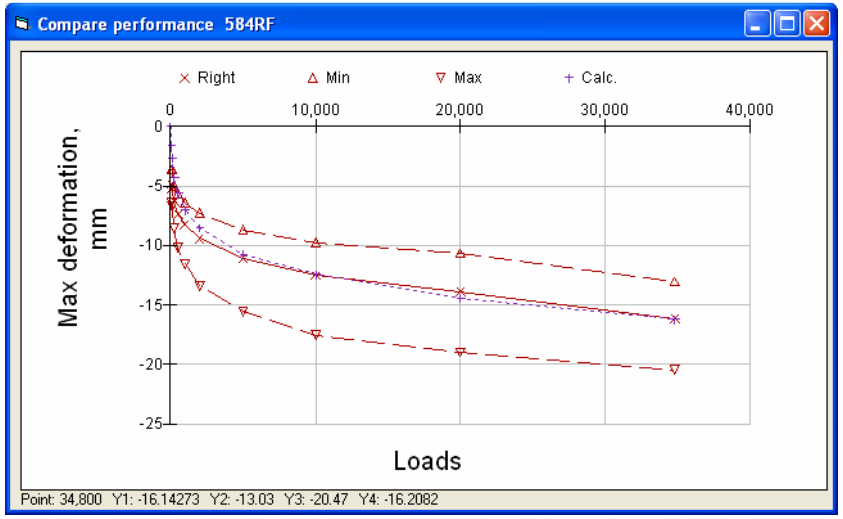

Figure 4.77: 584RF, measured and calculated down rut.

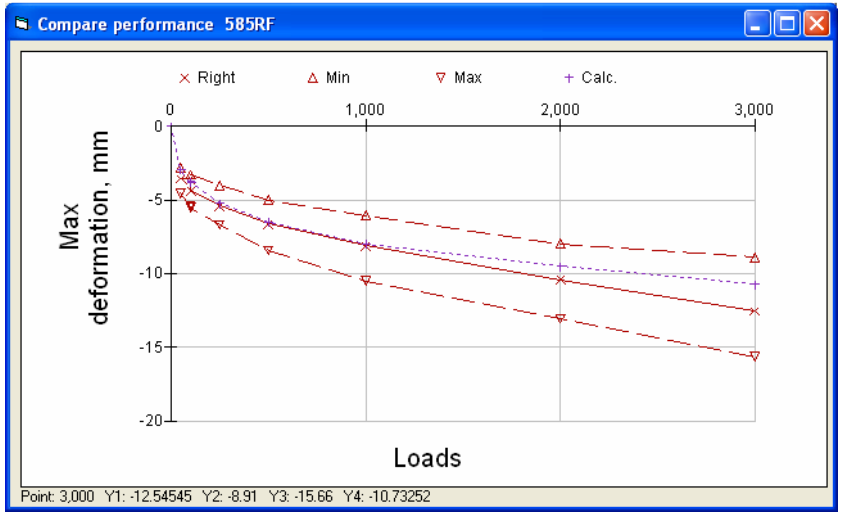

Figure 4.78: 585RF, measured and calculated down rut.

4.11. Simulation of Overlaid Sections (Actual Conditions): Reflective Cracking Study

Backcalculated layer moduli from the last FWD test before the HVS experiment were used as initial moduli in the *CalME* simulation. Table 4.9 presents a summary of the backcalculated layer moduli before HVS loading ("initial") and from the first FWD test after loading ("terminal"). In a single case, 590RF, an FWD test series was carried out in the middle of the experiment ("mid"). The corresponding moduli calculated by *CalME* are also provided.

Table 4.9: Moduli Before and After HVS Experiment.

Layer	Moduli (MPa)									
	FWD				*CalME*					
	AC1	AC2	AB	SG	AC1	AC2	AB1	AB2	AB3	SG
586RF initial	4,109	3,901	3,736	308	4,109	3,901	3,736	3,736	3,736	308
586RF terminal	1,924	4,060	1,019	270	2,724	3,611	567	966	1,684	175
587RF initial	5,361	2,300	1,792	280	5,361	2,300	1,792	1,792	1,792	280
587RF terminal	1,887	1,258	115	129	815	396	90	202	434	88
588RFa initial	9,567	6,662	956	223	9,567	6,662	956	956	956	223
588RFa terminal	3,483	2,761	342	66	2,026	4,144	265	338	443	82
588RFb initial	8,760	6,296	620	199	8,760	6,296	620	620	620	199
588RFb terminal	1,660	1,365	178	63	100	443	77	122	189	42
589RF initial	2,894	4,086	606	196	2,894	4,086	606	606	606	196
589RF terminal	1,230	1,721	167	117	859	347	111	158	220	97
590RF initial	2,147	2,774	522	180	2,147	2,774	522	522	522	180
590RF mid	1,478	1,964	195	89	1,518	2,379	168	205	248	122
590RF terminal	2,655	3,213	128	86	1,030	741	94	133	182	88
591RF initial	6,820	3,581	1,750	211	6,820	3,581	1,750	1,750	1,750	211
591RF terminal	3,410	2,703	199	50	2,886	592	145	292	547	86

AC1 is overlay, AC2 is underlying DGAC, AB is aggregate base, and SG is subgrade.

The forensic study (13) showed that Section 588RF (DGAC overlay) had severe slip between the overlay and the underlying DGAC. In simulating this section, full slip was assumed to have developed after a number of loads corresponding to one million ESALs. When calculating the strain over an existing crack from Equation 4.8, it was assumed that the crack spacing was 200 mm.

4.11.1 RSD Response

The measured and calculated RSD response as a function of the number of load applications is shown in Figures B.46 through B.52 in Appendix B. The first value shown ("RSD") is the measured value and the second ("Calc.") is the value calculated by *CalME*. The RSD deflections were measured at a number of locations within the test section, whereas the calculated values assume the section to be perfectly uniform. All of the comparisons are at a wheel load of 60 kN. The results indicate good agreement between measured and calculated deflections.

4.11.2 MDD Response

The measured surface deflection, resilient compression of the aggregate base layers, and deflection of the subgrade are compared to values calculated by *CalME* in Figures B.53 through B.69 in Appendix B on those HVS sections with useable MDD results. The measured values have a legend "M" followed by the depth of the MDD module in mm or, for the compression of the base layers, by the depths of the first and second MDD module. All comparisons are at a wheel load of 60 kN. The MDD resilient deflection results generally match the calculated values, although measured and calculated deflections in the aggregate base differ more than do measured and calculated deflections in other layers, or for the total pavement structure. Some problems were encountered with MDD measurements during wet periods.

4.11.3 Damage

The reflection damage (ω) of the asphalt concrete layer is shown in Figures 4.79 through 4.85, as defined by Equation 4.9. The observed cracking (in $m/m^{2)}$ is shown on the secondary y-axis.

4.11.4 Surface Permanent Deformation

The measured down rut is shown in screen captures in Figures 4.86 through 4.92 — with the mean, minimum, and maximum values within the central 6.0 m of the test sections — as a function of the number of load applications. They are compared to the value calculated by *CalME* ("Calc.").

4.11.5 MDD Permanent Deformation

For those sections with useable MDD results, the permanent deformation at the upper MDD, the permanent compression of the aggregate base layers, and the permanent deformation of the subgrade are shown as functions of the number of load applications in Figures B.70 through B.87 in Appendix B. The same legend-convention is used as for the resilient deflections.

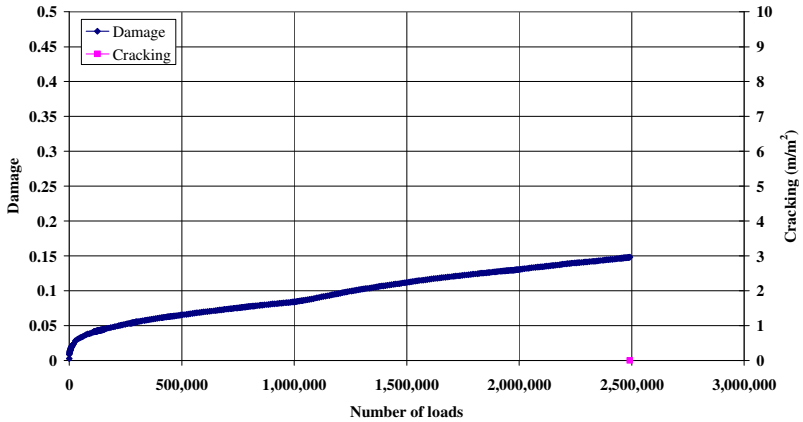

Figure 4.79: 586RF, calculated damage and observed cracking.

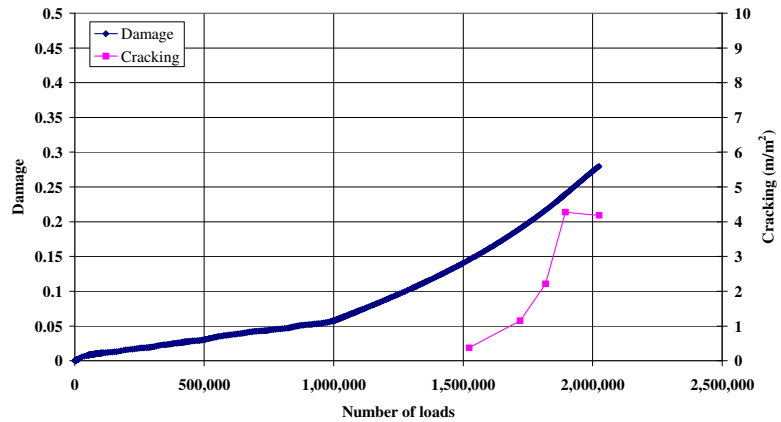

Figure 4.80: 587RF, calculated damage and observed cracking.

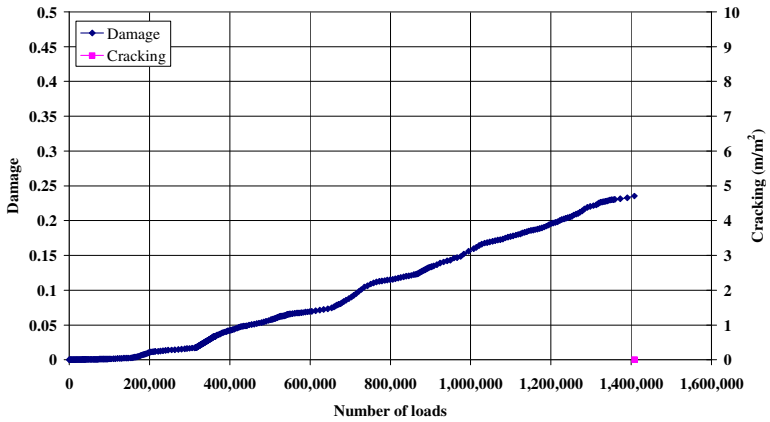

Figure 4.81: 588RFa, calculated damage and observed cracking.

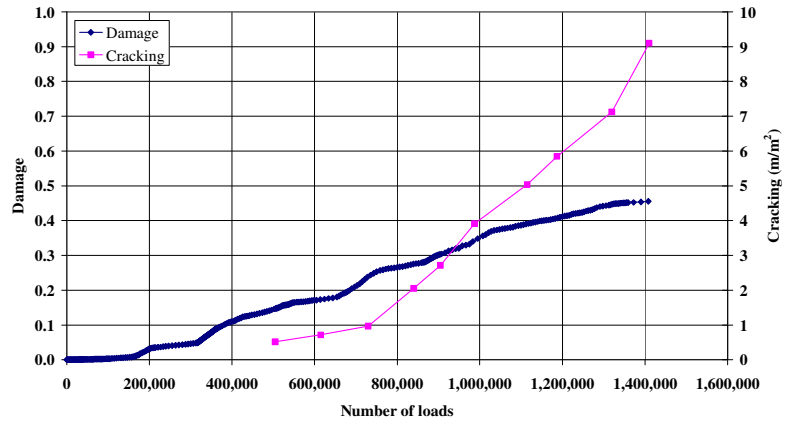

Figure 4.82: 588RFb, calculated damage and observed cracking.

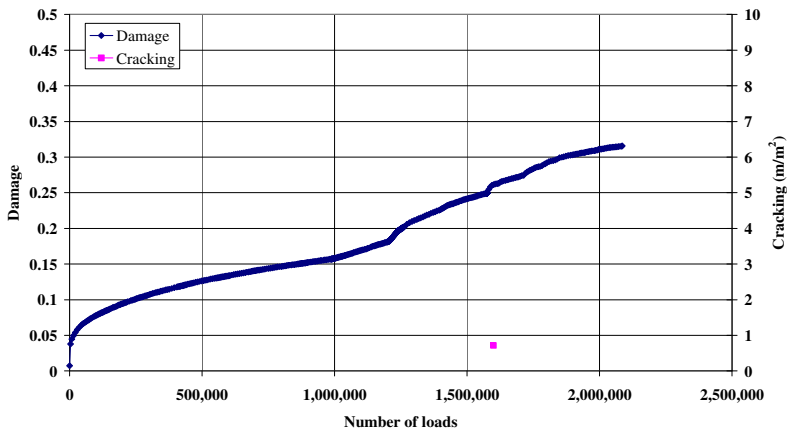

Figure 4.83: 589RF, calculated damage and observed cracking.

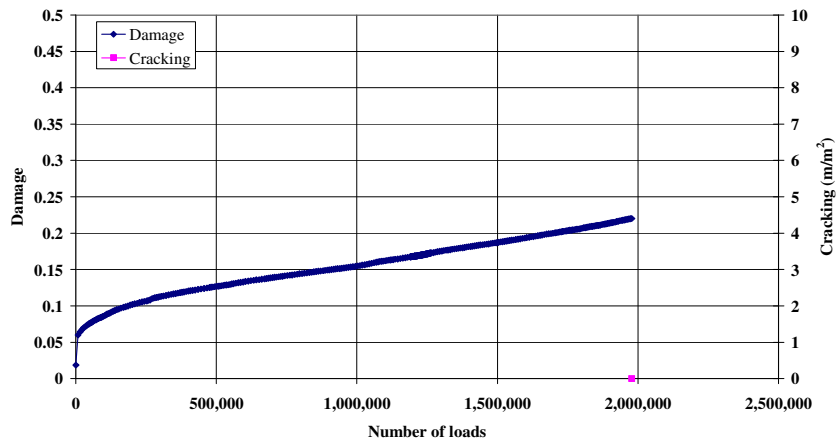

Figure 4.84: 590RF, calculated damage and observed cracking.

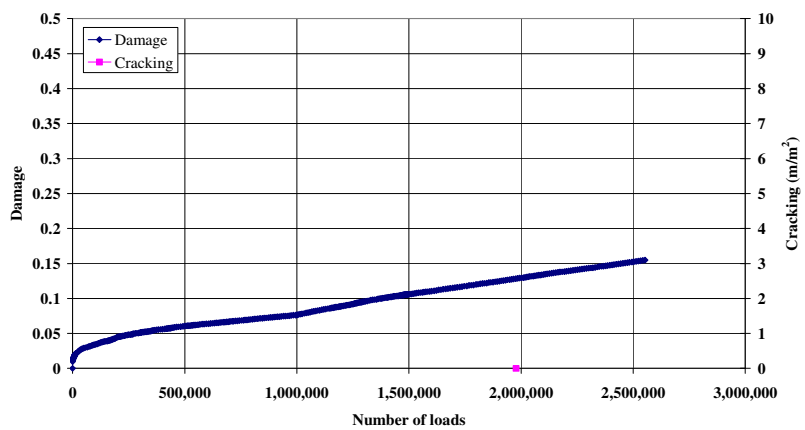

Figure 4.85: 591RF, calculated damage and observed cracking.

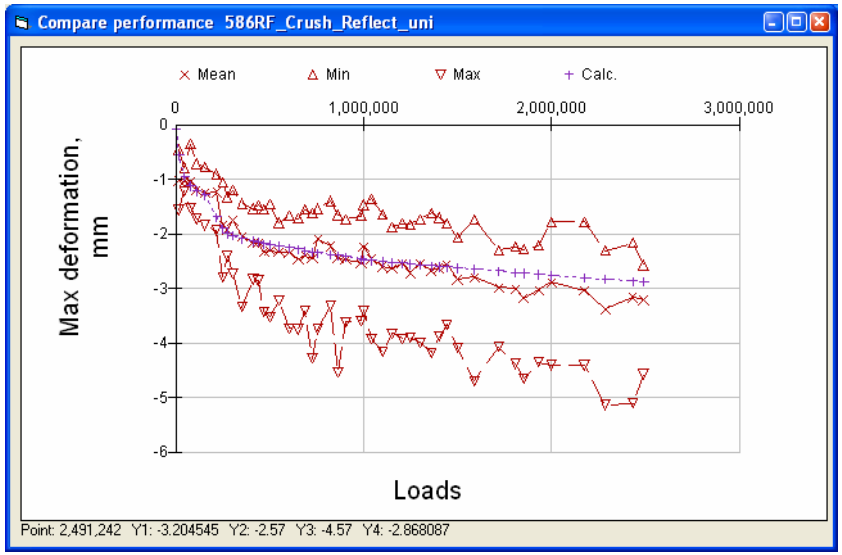

Figure 4.86: 586RF, measured and calculated down rut.

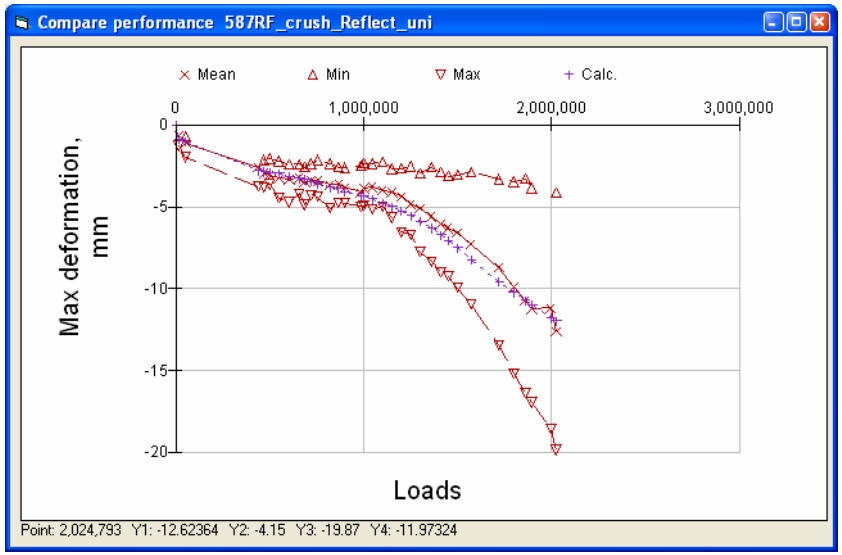

Figure 4.87: 587RF, measured and calculated down rut.

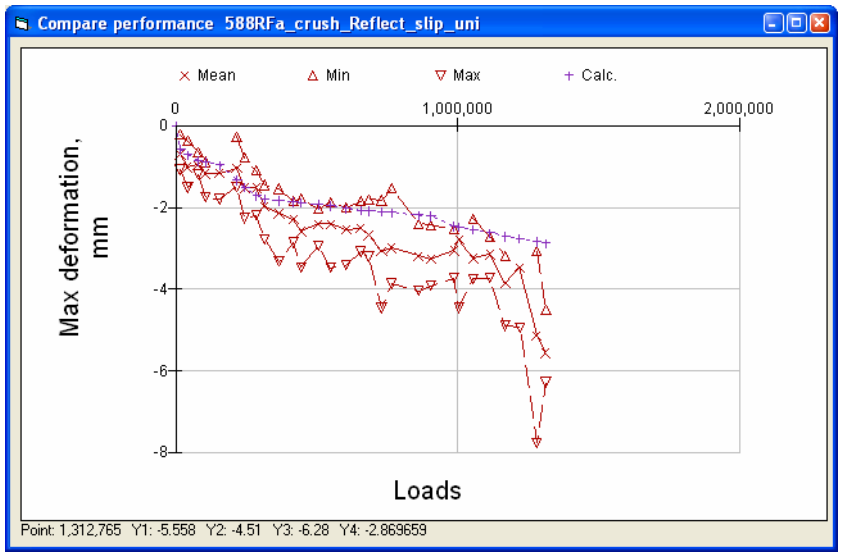

Figure 4.88: 588RFa, measured and calculated down rut.

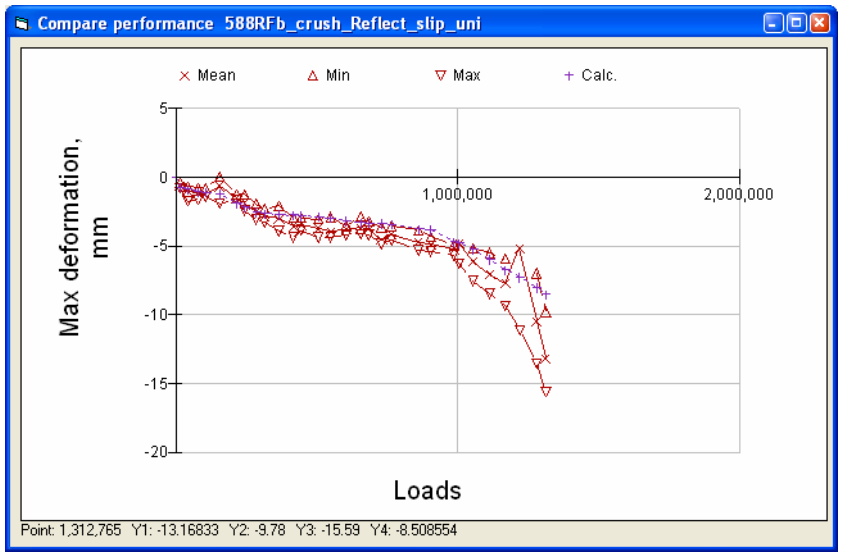

Figure 4.89: 588RFb, measured and calculated down rut.

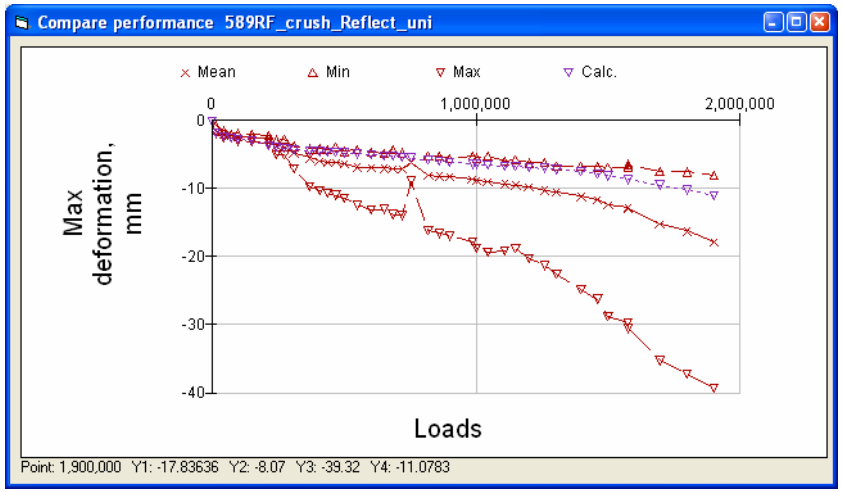

Figure 4.90: 589RF, measured and calculated down rut.

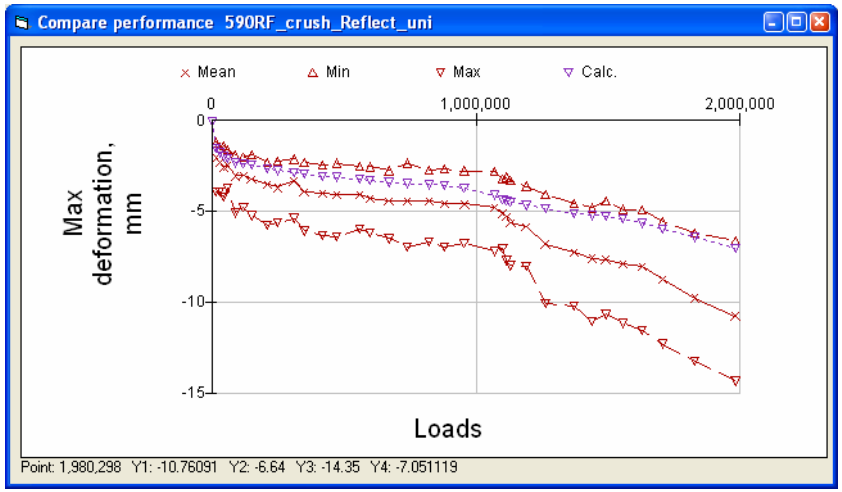

Figure 4.91: 590RF, measured and calculated down rut.

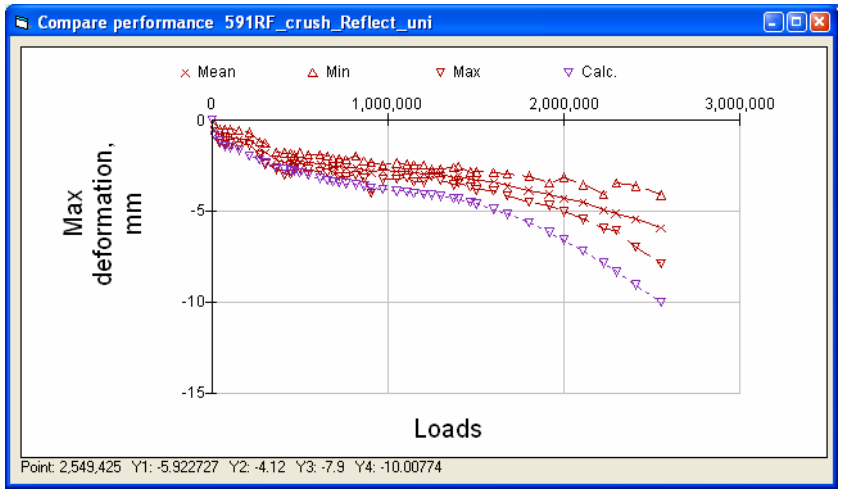

Figure 4.92: 591RF, measured and calculated down rut.

4.12. Summary of All Simulations Using Actual Conditions

4.12.1 Response

The moduli backcalculated from FWD tests were used as initial moduli in the simulations with *CalME*. The initial deflections measured with the RSD and the MDDs give an indication of the extent to which these moduli were representative of the materials under the slow moving wheel load. The FWD test is an impulse load with a duration of 25 to 30 milliseconds whereas the RSD and MDD deflections were measured between the dual wheels of the HVS at a very low speed of about 1.8 km/h. *CalME* adjusts the moduli to the temperature and loading time conditions of the HVS loads using the master curve for the asphalt and the bending stiffness for the subgrade. Differences between the deflections calculated by *CalME* and the measured values may be due to inaccuracies in the backcalculated moduli, insufficient transformations to the HVS loading conditions, incorrect measured values, or to deficiencies of the response model.

Table 4.10 and Figure 4.93 show the deflections as calculated by *CalME* and measured using the RSD and the MDDs for the initial loads during the HVS experiment. Where several measurements were recorded, either at different positions with the RSD or with different MDDs, the standard deviation (Std. Dev.) is also listed. Only deflections of the top MDD module are provided.

Table 4.10: Initial Deflections as Calculated by *CalME* and Measured by RSD and MDDs

Section		Initial Deflection (mm)					
		CalME	RSD		MDD		
No	Overlay		Mean	Std Dev	Depth	Mean	Std Dev
567RF	Underlying DGAC	0.465	0.623	0.071	90	0.764	-
568RF		0.433	0.661	0.046	-	-	-
569RFb		0.364	0.507	0.059	90	0.266	-
571RF		0.459	0.537	0.040	90	0.581	-
572RF		0.327	0.665	0.091	-	-	-
573RF		0.673	0.705	0.204	-	-	-
580RF	MB15-G	0.658	-	-	122	0.684	-
581RF	RAC-G	0.963	-	-	120	0.972	-
582RF	AR4000-D	0.640	-	-	195	0.633	-
583RF	MB4-G	0.442	-	-	132	0.470	-
584RF	MB4-G	0.564	-	-	158	0.751	-
585RF	MAC15-G	0.619	-	-	122	0.518	-
586RF	MB15-G	0.175	0.174	0.017	120-162	0.201	0.007
587RF	RAC-G	0.249	0.353	0.039	132	0.354	-
588RFb	AR4000-D	0.282	0.277	0.035	-	-	-
589RF	MB4-G	0.420	0.564	0.052	132	0.605	0.076
590RF	MB4-G	0.410	0.428	0.035	158	0.654	0.119
591RF	MAC15-G	0.331	0.282	0.018	120-125	0.294	0.014

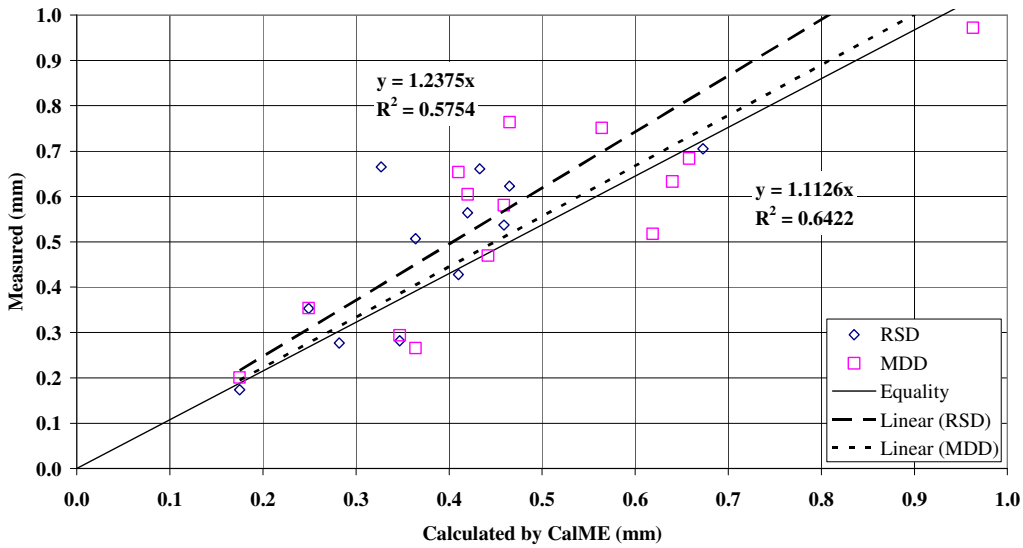

Figure 4.93: Calculated initial deflections compared to measured values.

The general trend of the deflections is correct but in most cases the measured deflections are larger than the deflections calculated by *CalME*. This is most pronounced at intermediate deflections. From the MDDs it appears that *CalME* underestimates the resilient compression of the aggregate base layer. This could be caused by the aggregate base modulus decreasing more rapidly than predicted by the damage model for the material. A more detailed study of the relationship between deflections and moduli under FWD loading and under the HVS rolling wheel loads is recommended. At the end of the HVS loading there was no systematic difference between the calculated and the measured deflections, as shown in Table 4.11 and Figure 4.94. The point marked "Outlier" in Figure 4.100 was not used in the regression analysis for the RSD deflections.

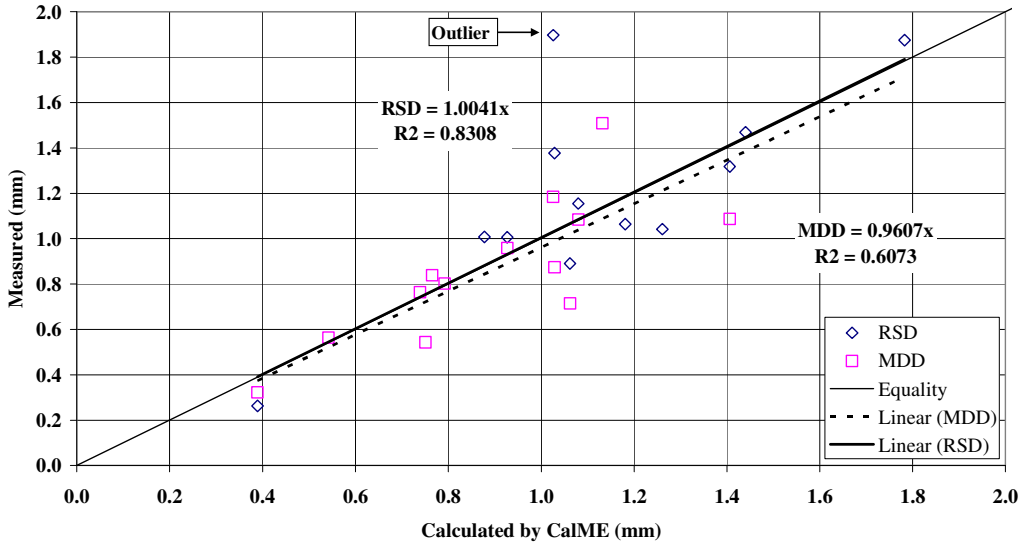

Figure 4.94: Calculated deflections at end of HVS experiment compared to measured values.

Table 4.11: Terminal Deflections as Calculated by *CalME* and Measured by RSD and MDDs

Section		Terminal Deflection (mm)					
		CalME	RSD		MDD		
No	Overlay		Mean	Std Dev	Depth	Mean	Std Dev
567RF	Underlying DGAC	1.062	0.890	0.074	90	0.715	-
568RF		1.181	1.064	0.060	-	-	-
569RFb		1.406	1.318	0.263	90	1.087	0.028
571RF		0.927	1.006	0.150	90	0.959	-
572RF		1.440	1.469	0.267	-	-	-
573RF		1.261	1.042	0.127	-	-	-
580RF	MB15-G	0.739	-	-	122	0.764	0.016
581RF	RAC-G	1.132	-	-	120	1.508	0.018
582RF	AR4000-D	0.765	-	-	195	0.838	0.033
583RF	MB4-G	0.542	-	-	132	0.564	0.009
584RF	MB4-G	0.792	-	-	158	0.802	0.035
585RF	MAC15-G	0.751	-	-	122	0.543	0.006
586RF	MB15-G	0.389	0.263	0.008	120-162	0.322	0.110
587RF	RAC-G	1.026	1.897	0.403	132	1.184	-
588RFb	AR4000-D	1.783	1.875	0.888	-	-	-
589RF	MB4-G	1.029	1.377	0.260	132	0.873	0.015
590RF	MB4-G	1.080	1.155	0.210	158	1.084	0.050
591RF	MAC15-G	0.878	0.878	1.008	120-125	0.934	0.075

The increase in deflection caused by the HVS loading ranges from about a factor of 1 (i.e., no increase), mostly for the rutting study, to a factor of more than 5, as shown in Figure 4.95. *CalME* tends to slightly overestimate the increase in deflection. The uncertainty on the measured values is illustrated by the difference between the deflections measured by the RSD and by the MDD, which in some cases is quite large. Some of this difference is due to the variability within the test section, where the RSD measurement is the average for a number of positions and the MDD measurement represents a single point.

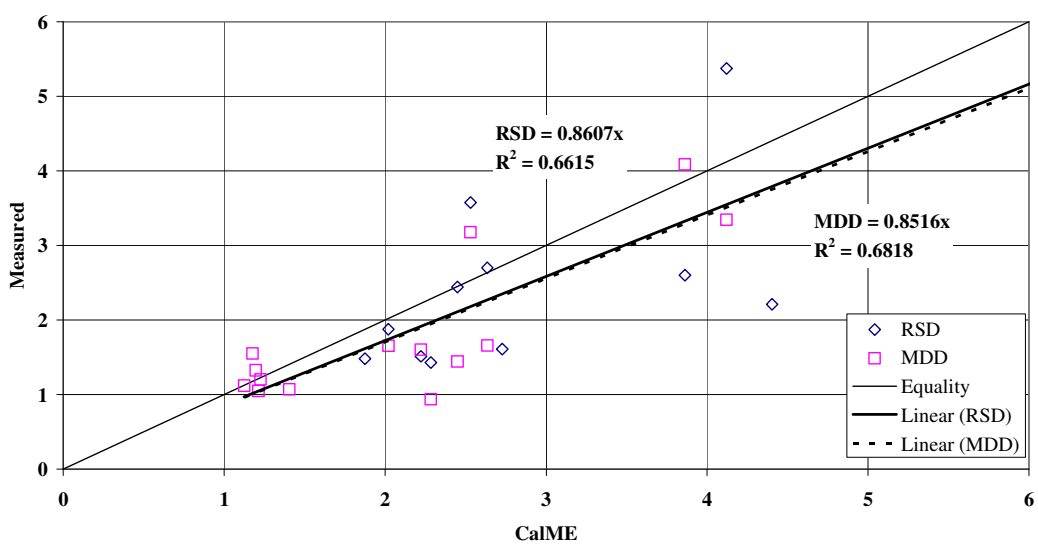

Figure 4.95: Increase in deflection during HVS experiments, as simulated and measured.

It appears that the initial moduli from FWD backcalculation may have been a little higher than the actual moduli under the HVS wheel load. The most likely explanation for this is that the aggregate base modulus was lower under the wheel load than under the FWD load, possibly due to a more rapid deterioration of the aggregate base layer than predicted. *CalME* then compensated for this by overestimating the increase in deflection during the HVS experiment. It is possible that a different model for the deterioration of the aggregate base under loading, or different parameter values in the model used, could have resulted in a better agreement. The differences between the calculated and the measured response, however, are not large compared to the variability between and even within the test sections.

The above comparisons show the initial and the terminal deflections only. The best impression of the agreement (or lack of agreement) between the measured and calculated values is obtained from the plots of deflections versus number of load repetitions given in the preceding sections and in Appendix B for the full length of the HVS experiment. A summary of all of the top MDD deflections is provided in Figure 4.96, which shows the logarithm of the measured deflection versus the logarithm of the calculated deflection.

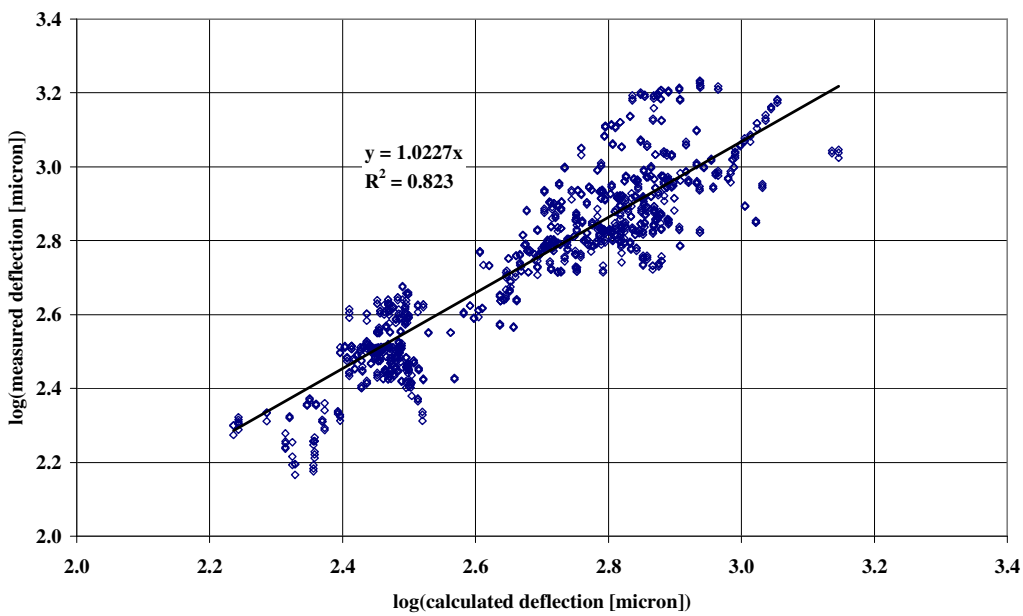

Figure 4.96: Logarithm of measured deflection versus calculated deflection of top MDD module.

Closely related to the change in response is the change in layer moduli. In Figure 4.97, the moduli backcalculated from the first FWD test series after the completion of each HVS test are compared to the terminal moduli from the simulation with *CalME*. The logarithm of the moduli is shown to illustrate the full range of moduli for all of the pavement layers. The simulated value is the average of the moduli of the three sublayers for the base layer.

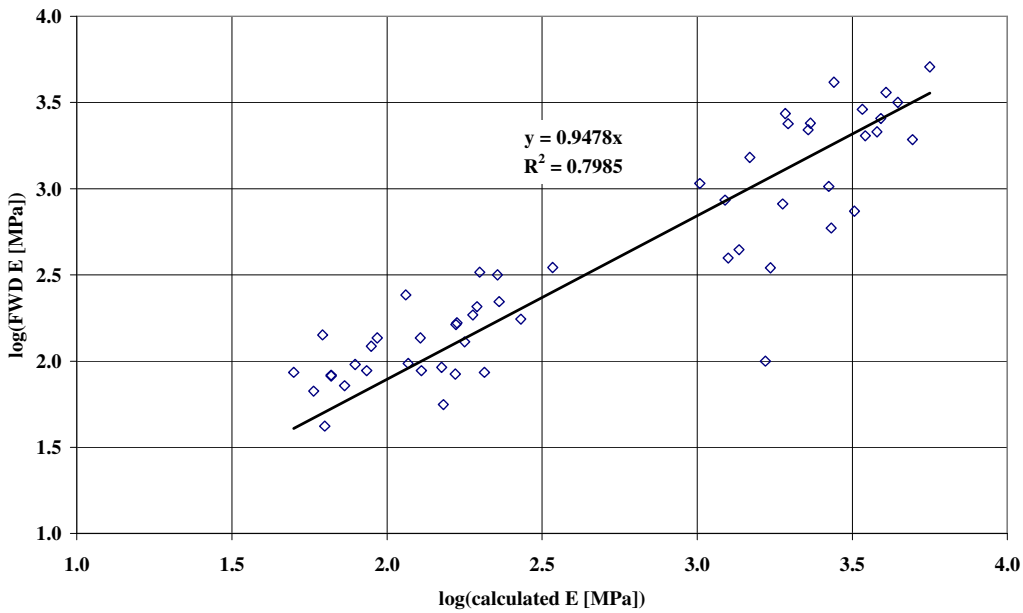

Figure 4.97: Logarithm of terminal moduli, FWD tests versus simulation with *CalME*.

4.12.2 Fatigue of Asphalt Concrete Layers

Figure 4.98 shows the observed cracking (in m/m^2) versus the damage (ω) calculated by *CalME* for the surface layer. Calculated cracking is also shown, as calculated from Equations 4.13 and 4.16, with the assumptions that crack initiation corresponds to 0.5 m/m^2 of cracking and that α = -8 as used in previous calibration studies. The calculations are shown for layer thicknesses of 80 mm, 125 mm, and 170 mm, which correspond roughly to the thickness of the underlying DGAC layer and to the combined asphalt concrete thickness for the sections with thin and thick overlays, respectively.

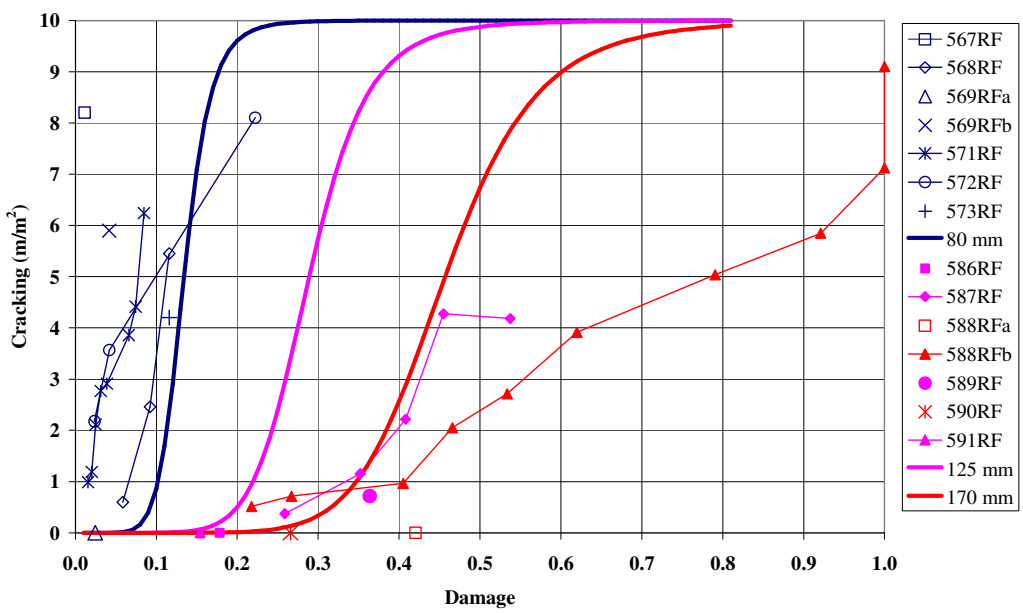

Figure 4.98: Observed cracking versus damage calculated by *CalME*.

The modulus of the DGAC for the original structure from FWD backcalculation was found to be significantly less than the modulus from frequency sweep testing. This difference could be due to early damage of the DGAC layer. If this is the case, then this damage should be added to the damage calculated by *CalME*. This would shift the curves for the original structure toward the right.

A better fit to the measured reflective cracking can be obtained by modifying the parameters in the equations for crack initiation and crack propagation to the values shown in Equations 4.30 and 4.31. Cracking predicted using these equations is compared to the measured cracking in Figure 4.99 and as a function of the observed reflective cracking in Figure 4.100.

$$\omega_{initiation} = \frac{1}{1+\left(\frac{h_{AC}}{350mm}\right)^{-1.9}} \tag{4.30}$$

$$Crm/m^2 = \frac{10}{1+\left(\frac{\omega}{\omega_o}\right)^{-6}} \tag{4.31}$$

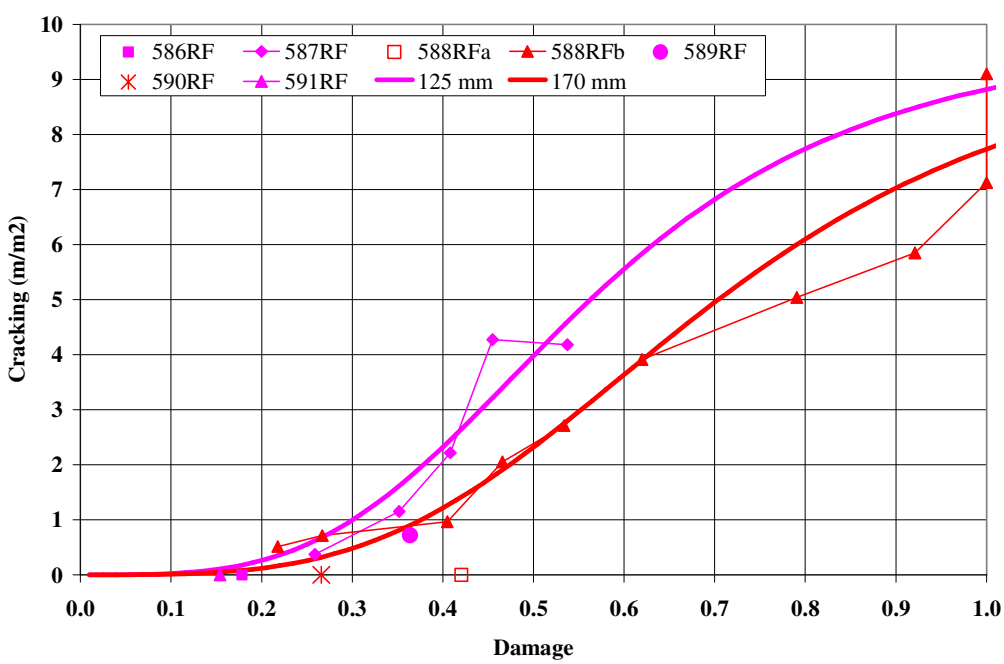

Figure 4.99: Observed reflective cracking versus damage calculated using modified parameters.

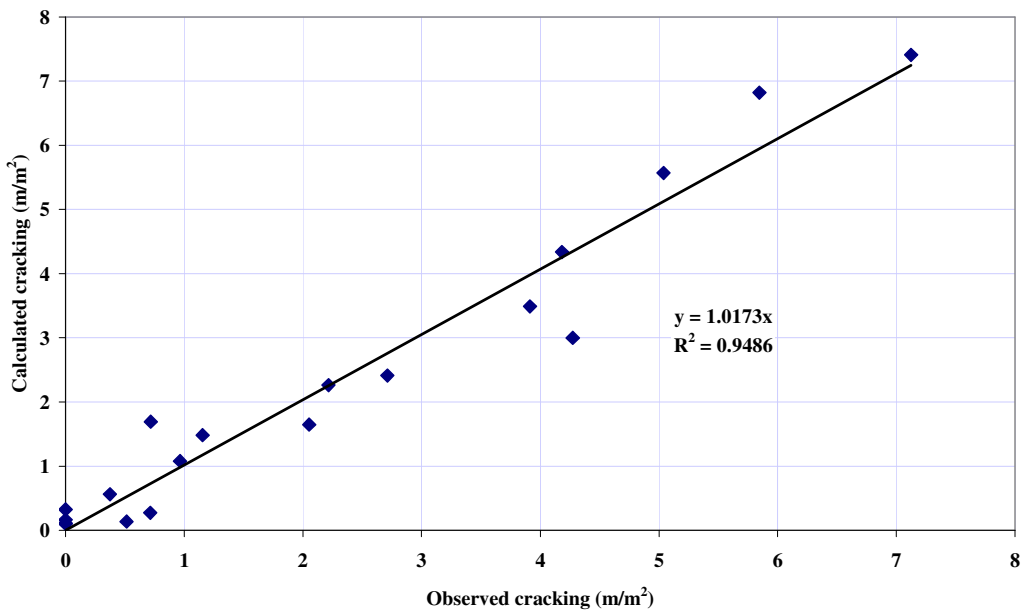

Figure 4.100: Predicted versus observed reflective cracking, using modified parameters.

In cases where the intact modulus of the existing asphalt concrete layer and/or the crack spacing is not known, the cracking of the overlay may still be predicted reasonably well from the fatigue damage calculated for the layer. The observed cracking is shown versus the calculated fatigue damage of the overlay in Figure 4.101. The fatigue damage is calculated based on the strain at the bottom of the original asphalt layer.

A better fit to the measured reflective cracking can once again be obtained by modifying the parameters in the equations for crack initiation and crack propagation to the values shown in Equations 4.32 and 4.33. Notice that crack initiation occurs at a damage of 0.21, independently of the thickness of the asphalt layers. Cracking predicted using these equations is compared to the measured cracking in Figure 4.102 and as a function of the observed reflective cracking in Figure 4.103.

$$\omega_{initiation} = \frac{0.42}{1+\left(\frac{h_{AC}}{250mm}\right)^{0}} \quad \textbf{(4.32)}$$

$$Crm/m^2 = \frac{10}{1+\left(\frac{\omega}{\omega_o}\right)^{-3.8}} \quad \textbf{(4.33)}$$

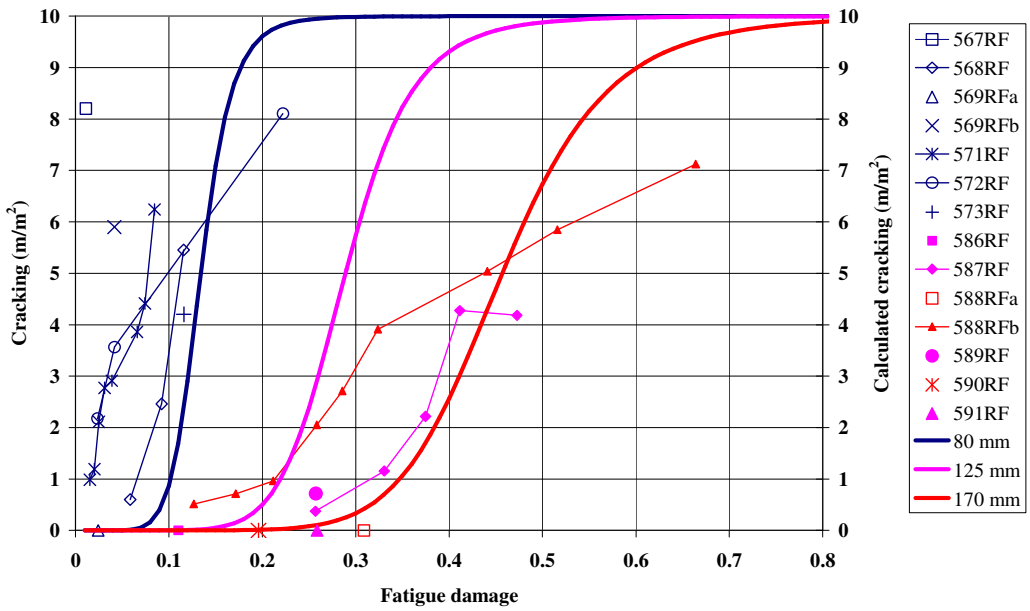

Figure 4.101: Observed cracking versus calculated fatigue damage of overlay.

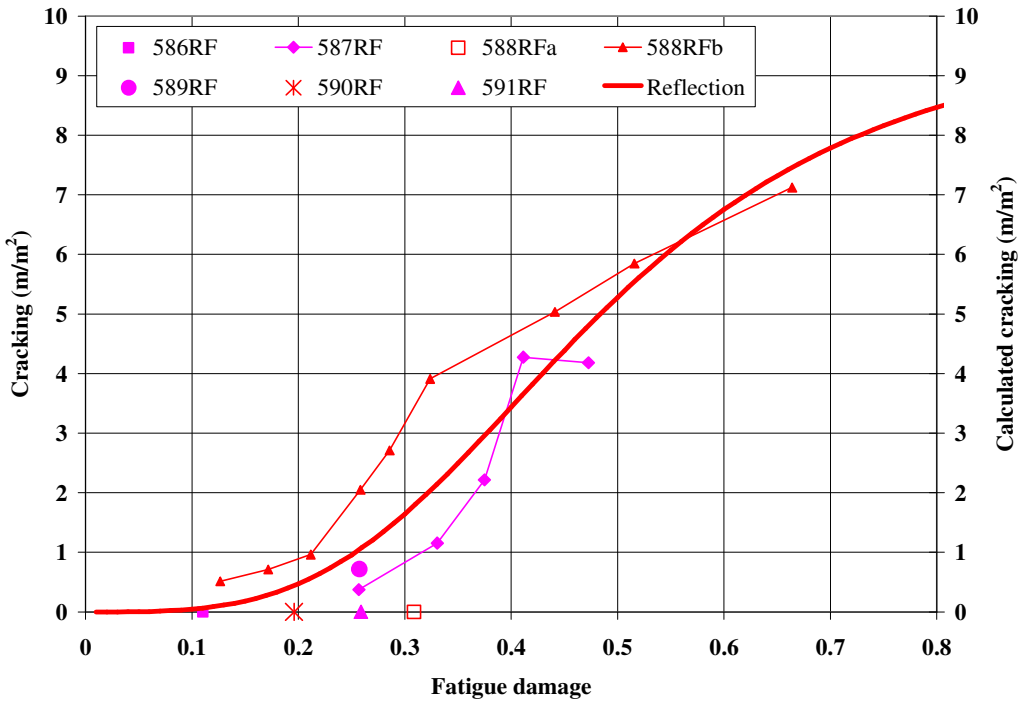

Figure 4.102: Observed cracking versus fatigue damage calculated using modified parameters.

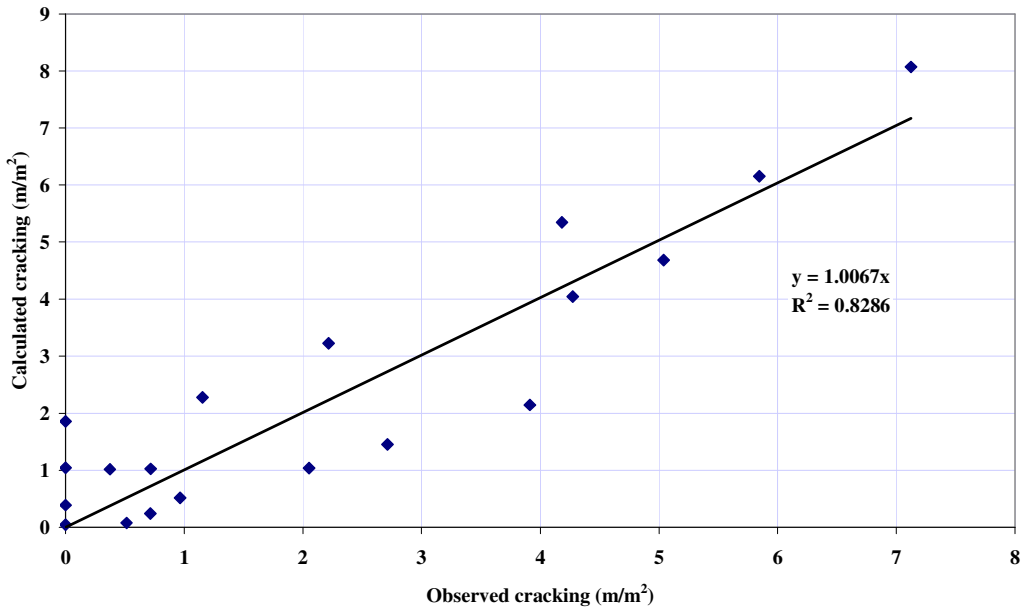

Figure 4.103: Predicted versus observed reflective cracking
(Based on fatigue cracking using modified parameters.)

4.12.3 Permanent Deformation

The terminal overall permanent deformation calculated by *CalME* at the end of each HVS test and the average measured down rut from profile measurements are shown in Table 4.12 and Figure 4.104.

Table 4.12: Overall Permanent Deformation from *CalME* and as Measured

Section		Surface Permanent Deformation (mm)	
Number	**Overlay**	***CalME***	**Profile**
567RF	Underlying DGAC	5.0	11.5
568RF		8.1	10.0
569RFb		7.1	6.8
571RF		6.8	9.7
572RF		10.0	12.9
573RF		8.0	10.1
580RF	MB15-G	10.7	9.5
581RF	RAC-G	9.2	14.0
582RF	AR4000-D	10.3	10.7
583RF	MB4-G	13.2	13.0
584RF	MB4-G	16.1	16.2
585RF	MAC15-G	10.7	12.5
586RF	MB15-G	3.0	3.2
587RF	RAC-G	11.6	12.6
588RFb	AR4000-D	10.8	13.2
589RF	MB4-G	11.0	17.8
590RF	MB4-G	8.1	10.8
591RF	MAC15-G	7.7	5.9

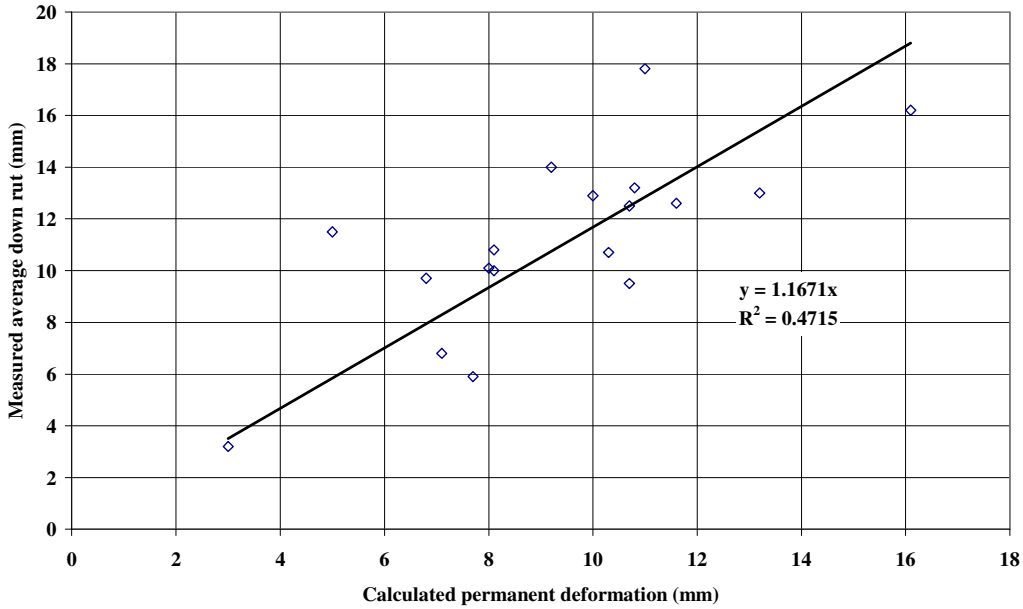

Figure 4.104: Final down rut versus calculated overall permanent deformation.

On average, *CalME* underestimates the overall permanent deformation by about seven percent, but the correlation coefficient is quite low. This should be seen in the light of the very large variation of down rut within some of the HVS sections. A difference of 5 mm to 10 mm between the minimum and the maximum down rut measured within the 6.0-m long test section is not unusual and in one case (589RF) it reached 30 mm. All of the down ruts (mean values) measured during the HVS tests are compared to the calculated values in Figure 4.105.

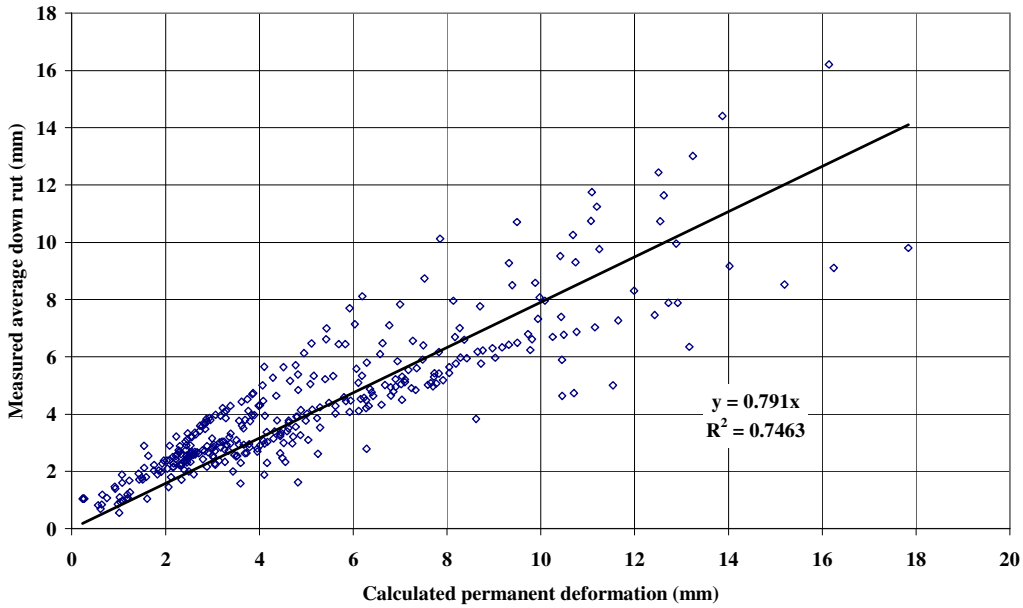

Figure 4.105: Average of all measured down ruts compared to calculated values.

Table 4.13 and Figure 4.106 show the final permanent deformation at the top MDD module as calculated by *CalME* and as measured. Whereas the resilient deflections at the surface (RSD) and at the top MDD module are very similar, this is not the case for the permanent deformation which, in many cases, is mostly in the asphalt concrete layers and therefore not recorded by the MDDs. The MDD sensors were positioned in the base rather than the surface due to space limitations in the relatively thin asphalt layers.

Table 4.13: Final Deformation of Top MDD Module from *CalME* Simulation and as Measured

Section		Permanent Deformation (mm)		
Number	**Overlay**	***CalME***	**Depth**	**MDD**
567RF		0.9	90	4.0
568RF		-	-	-
569RFb	Underlying	1.7	90	1.5
571RF	DGAC	2.0	90	6.3
572RF		-	-	-
573RF		-	-	-
580RF	MB15-G	1.1	122	2.5
581RF	RAC-G	0.8	120	0.6
582RF	AR4000-D	1.0	195	0.8
583RF	MB4-G	1.1	132	0.3
584RF	MB4-G	2.3	158	0.0
585RF	MAC15-G	1.4	122	1.6
586RF	MB15-G	1.0	120-162	2.5
587RF	RAC-G	3.3	132	7.8
588RFb	AR4000-D	-	-	-
589RF	MB4-G	4.1	132	6.7
590RF	MB4-G	3.5	158	1.5
591RF	MAC15-G	2.7	120-125	2.7

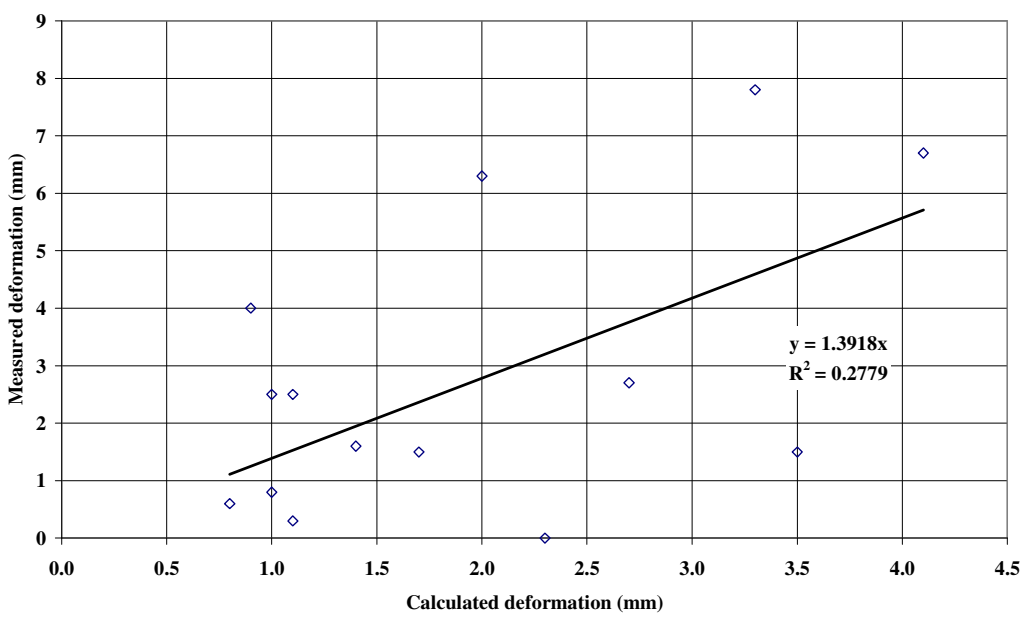

Figure 4.106: Measured final permanent deformation of top MDD versus calculated value.

The permanent deformation of the top MDD comprises the permanent compression of the aggregate base layers and the permanent deformation of the subgrade. The permanent deformation of the subgrade is usually very low, less than 1.0 mm. In two cases, 587RF and 589RF, one of the MDDs recorded final permanent deformations at the subgrade of 2.5 mm and 1.5 mm, respectively. In both cases, however, another MDD recorded a permanent deformation close to zero. The calculated values were 0.8 mm and 1.3 mm, respectively.

An approximate value for the permanent compression of the asphalt concrete layer(s) may be obtained by subtracting the permanent deformation of the top MDD module from the average down rut, although it should be recalled that the first value is from one to three test points and the latter is the average over the whole 6.0-m long test section (except where the section was split into two subsections). In addition the MDDs are not exactly at the asphalt concrete/base interface. The calculated permanent deformation (*dp*) of the individual asphalt concrete layers, together with the measured thickness of the layers (*h*) are shown in Table 4.14 and Figure 4.107.

Table 4.14: Calculated Compression of Asphalt Concrete Layers

Section		Overlay		DGAC	
No	**Overlay**	**Measured Thickness**	**Calculated Compression**	**Measured Thickness**	**Calculated Compression**
567RF	Underlying DGAC	-	-	83	4.0
568RF		-	-	82	5.7
569RFb		-	-	88	5.3
571RF		-	-	79	4.6
572RF		-	-	83	7.3
573RF		-	-	88	5.3
580RF	MB15-G	46	3.9	83	5.7
581RF	RAC-G	48	2.7	82	5.7
582RF	AR4000-D	95	7.9	88	1.2
583RF	MB4-G	49	4.2	79	7.5
584RF	MB4-G	86	5.9	83	7.5
585RF	MAC15-G	46	2.9	88	6.4
586RF	MB15-G	46	0.6	83	1.4
587RF	RAC-G	48	1.4	82	6.7
588RFb	AR4000-D	95	10.7	88	0.2
589RF	MB4-G	49	1.4	79	7.1
590RF	MB4-G	89	3.3	83	1.3
591RF	MAC15-G	46	0.3	77	4.7

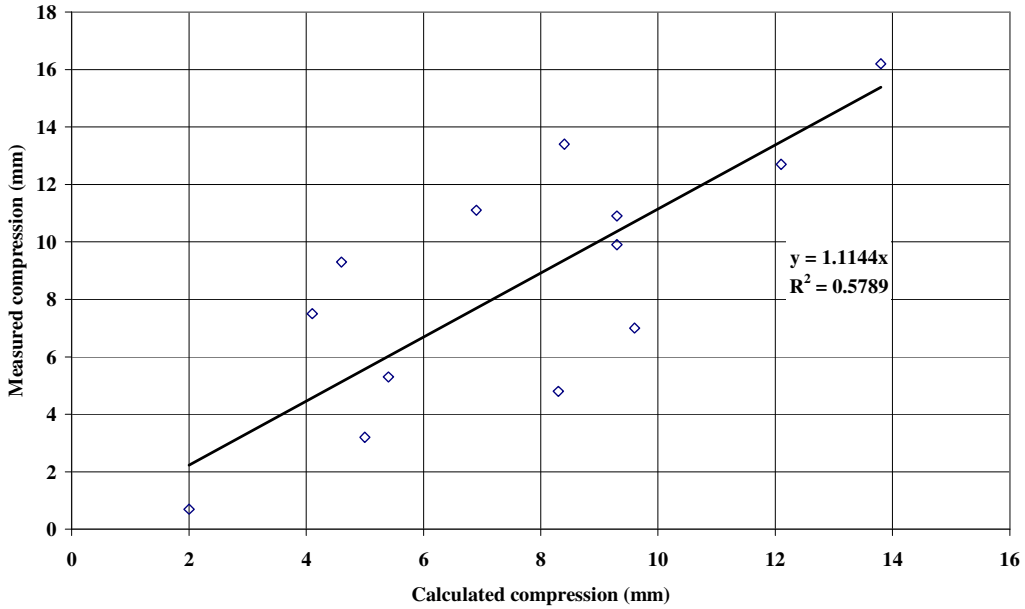

Figure 4.107: Measured final compression of AC from profile and MDD versus calculated value.

4.13. Simulation of Overlaid Sections (Uniform Conditions): Rutting Study

Experience has shown that the HVS testing conditions always have some influence on the performance of a particular section. This influence increases with increasing duration of the test. The rutting study was considered to consist of short duration tests since the overlay was placed on sections that had not been trafficked previously with the HVS. As a consequence, the influence of the test conditions was less pronounced than it was in the fatigue experiment, which had a longer duration and included overlays placed on the cracked underlying layer. For completeness, the simulations were repeated for the rutting experiment using the same underlying structure used for the reflective cracking study in discussed in Section 4.14, with the exception that the modulus of the underlying asphalt was assumed to be 3,200 MPa at 20°C, corresponding to the approximate layer moduli determined from FWD tests. The pavement structure and test conditions for HVS Test 584RF (90-mm MB4-G) was used for the simulation of uniform conditions. Almost 20,000 load repetitions were applied to this section.

The results of the simulations are shown in Figure 4.108.

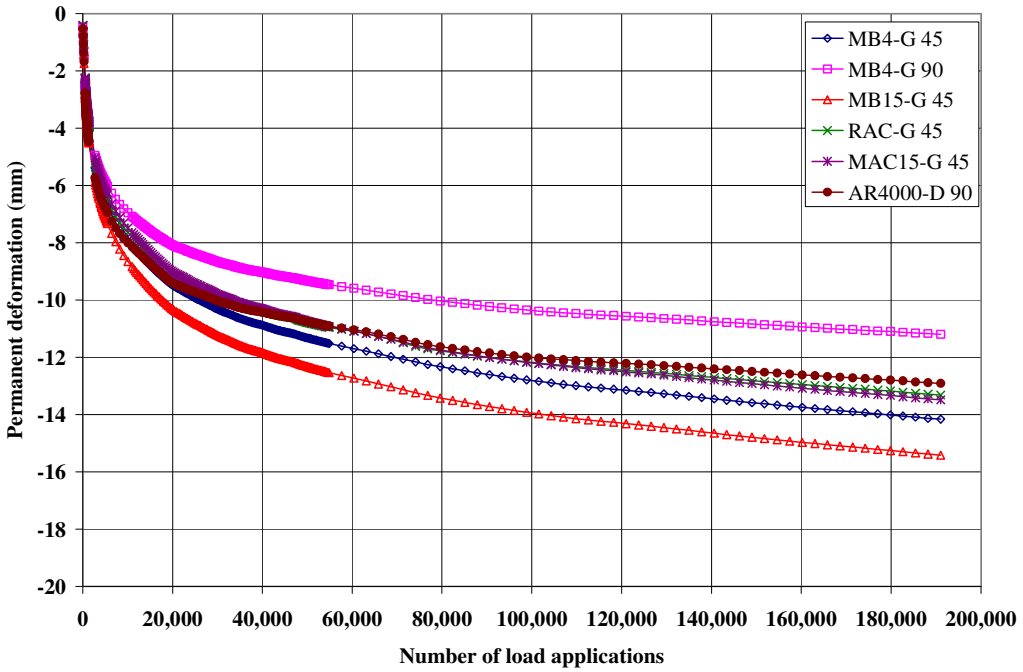

Figure 4.108: Rutting simulation with uniform conditions.

4.14. Simulation of Overlaid Sections (Uniform Conditions): Reflective Cracking Study

Although the original pavement was built to provide a uniform support for the reflective cracking study, the forensic investigation showed that there was some variation over the length of the structure, specifically with regard to layer thickness, composition of the recycled aggregate, and degree of recementation of the aggregate particles. The conditions of the underlying structure, wheel loads, and climate should be identical when ranking the different overlays. The simulations were therefore repeated using uniform conditions. The HVS loading and climate for Section 591RF were used and the underlying structure was substituted with that listed in Table 4.15. The number of load applications was multiplied by 50.

Table 4.15: Underlying Structure for Ranking of Overlays

Layer	Thickness (mm)	Modulus (MPa)
Original DGAC	80	3,581
Aggregate Base	400	400
Subgrade	Infinite	100

An intact modulus of 12,000 MPa with a damage of 0.253 was assumed for the original DGAC. The aggregate base and the subgrade were assumed to have stiffness factors equal to 0.8 and 0.46, respectively, and have nonlinearities of +0.6 and -0.3, respectively.

The damage and cracking was determined at the end of the (simulated) HVS loading, at 458 million ESALs. Cracking was calculated using Equations 4.30 and 4.31. The values, ranked according to the amount of cracking from best to worst, are shown in Table 4.16.

Table 4.16: Ranking of Overlays after Increasing Damage

Layer	Thickness (mm)	Damage	Cracking (m/m^2)	Rank
MAC15-G	45	0.48	3.1	1
MB4-G	45	0.56	5.0	2
MB4-G	90	0.75	5.5	3
MB15-G	45	0.69	6.7	4
RAC-G	45	0.76	7.4	5
AR4000	90	1.00	7.7	6

Fatigue damage is calculated based on the maximum tensile strain at the bottom of the overlay or at the bottom of the original asphalt layer. The maximum value at the beginning of the simulation is at the bottom of the original asphalt, but after a certain amount of damage further fatigue damage can be controlled by the strain at the bottom of the overlay, depending on the thickness and moduli of the layers. The strain at the bottom of a 45-mm thick overlay would typically be very small, and normally less than the strain at the bottom of the original asphalt layer. Therefore, the controlling strain would be at a depth of 125 mm. The opposite may be true for a 90-mm overlay, where the controlling strain would be at a depth of 90 mm. Under these circumstances, the resulting damage will be larger for a 90-mm overlay than for a 45-mm overlay, which explains the higher damage simulated on the 90-mm thick MB4-G overlay compared to the 45-mm MB4-G overlay.

The simulated reflective cracking is shown as a function of the number of loads (in ESALs) in Figure 4.109. The ranking depends to some extent on the number of load applications. The ranking would not change significantly if it was based on the reflective cracking predicted from fatigue damage of the overlay.

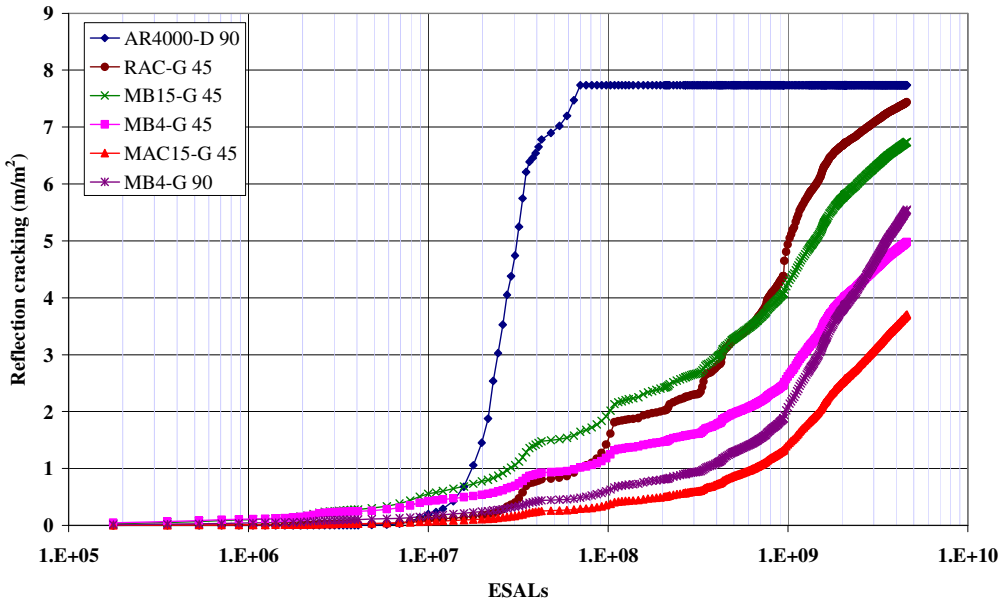

Figure 4.109: Simulated damage for identical testing conditions.

4.15. Extrapolation to Field Conditions and Sensitivity Analyses

In this section, the *CalME* analysis procedure calibrated in the previous sections was used to simulate reflective cracking and rutting performance of the different asphalt concrete overlays under various field conditions. The purpose of this was to evaluate the relative reflective cracking and rutting performance of the mixes (including MB and MAC binders in dense-graded mixes) used in overlays on cracked asphalt concrete under different combinations of climate zone, layer thickness, and traffic speed. Asphalt concrete overlays on portland cement concrete were not evaluated as these models have not been finalized or calibrated for the *CalME* software. This set of simulations provides general guidelines for using the different asphalt concrete mixes investigated in this study, by extrapolating performance observed in the HVS tests to performance in the field. The results provide a preliminary assessment only of expected field performance and include the limitations and assumptions of the modeling.

4.15.1 Methodology

Two groups of simulations were performed in the extrapolation and sensitivity analyses. The mix types, climate conditions, and structure types considered are listed in Table 4.17. Simulations in Group B were limited to a constant 20°C climate condition because laboratory fatigue tests for mixes used in the group were conducted only at this temperature.

Table 4.17: Factors Considered in the Extrapolation and Sensitivity Analyses

Group	Mix types*	Structure	Climate conditions
A	AR4000-D-F RAC-G-F MB4-G-F MB15-G-F MAC15-G-F	AC-over-AC overlay	Central Valley, Desert, and South Coast
B	AR4000-D-L RAC-G-L MB4-D-L MB15-D-L MAC15-D-L MB4-G-L MB15-G-L MAC15-G-L	AC-over-AC overlay	20°C constant
* Mix types are identified by binder type (AR4000, RAC [Asphalt Rubber Binder], MB4, MB15 and MAC15), aggregate gradation type (D for dense graded, and G for gap graded), and mix preparation method (F for field-mix, lab-compact, and L for lab-mix, lab-compact)			

The following additional input parameters were considered:

- Data collected from Weigh-In-Motion (WIM) station No. 057058 located at Pinole, Contra Costa County, California was used for a highway traffic load spectrum. The ESAL over axle ratio for this WIM station was 0.23 according to the load spectrum recorded.
- *CalME* applies axle load directly. The number of axles applied is determined by the number of ESALs (i.e. 80 kN single axle dual wheel) and the ESAL over axle ratio. Traffic was assumed to be evenly distributed over all the months.
- Traffic speed was either 10 km/h or 70 km/hour. Traffic speed affects loading time, which in turn affects asphalt concrete stiffness.
- Air void content was assumed to be six percent for all asphalt concrete mixes.
- No aging was considered.
- Aggregate base and subgrade were characterized in the same way as described previously, but were not subjected to stiffness degradation.
- For the different climate zones considered in Group A simulations, pavement temperatures were assumed to be constant for a 24-hour cycle within each month and there was no year-to-year change. Monthly average temperatures were calculated using BELLS equation (24) with parameters determined from 30 years of Enhanced Integrated Climate Model (EICM) simulations (25).
- The time that pavements are opened to traffic is important for Group A simulations because of the difference between summer and winter climatic conditions, specifically temperature. All of the simulations in this group start in July. Monthly traffic volumes are assumed to be constant.
- Fatigue model parameters were determined by fitting the bending-beam fatigue test results. Rutting (permanent deformation) model parameters were determined by fitting shear (RSST-CH)

test results. Asphalt concrete stiffness master curves were determined by fitting bending beam frequency sweep test results.

- *CalME* provides damage and rutting evolution history as traffic accumulates. Other modes of distresses were not included in the simulations.
- Cracking life of a pavement in this simulation was defined as the time required for surface crack density to reach 2.5 m/m^2. The conversion from damage to surface crack density was obtained by using Equations 4.30 and 4.31, with the assumption that crack initiation corresponds to 0.5 m/m^2 of surface cracking.
- Rutting life of a pavement in this simulation was defined as the time required for total surface rut to reach 12.5 mm. It was assumed that the ratio between downward rut calculated by *CalME* and total rut is 0.7, based on HVS test results.
- It was assumed that the maximum pavement life is 15 years.

It is important to note that the simulations did not include strains induced by temperature gradient or daily and seasonal temperature variations.

4.15.2 Parameters for Different Groups of Simulations

Group A: Asphalt Concrete-over-Asphalt Concrete Overlays with FMLC Mix

Parameters of the underlying pavement structure for this set of simulations are listed in Table 4.18, while variations of different variables considered in the simulations are listed in Table 4.19. This set of simulations essentially represents asphalt concrete overlays placed on extensively cracked old asphalt concrete pavement.

Table 4.18: Common Variables for the Reference Simulation Case

Parameter	Value
Underlying old AC stiffness (MPa)	3,300
Crack spacing (mm)	100
Crack opening (mm)	3
Old DGAC thickness (mm)	150
Aggregate base thickness (mm)	300
Aggregate base stiffness (MPa)	108
Subgrade stiffness (MPa)	67.8

Table 4.19: Variations of variables considered for Group A1

Parameter	Design Points	Number of Levels
Mix type	MB4-G, MB15-G, MAC15-G, RAC-G, AR4000-D	5
Overlay thickness (mm)	45, 60, 90	3
Climate Zones	Desert, Central Valley, South Coast	3
Traffic (TI for 10 years)	10, 11, 14	3
Wheel speed (km/h)	10, 70	2
Total number of simulations		270

Group B: Asphalt Concrete-over-Asphalt Concrete Overlays with LMLC Mix

This set of simulations evaluates reflective cracking performance of different LMLC asphalt concrete overlays over old cracked asphalt concrete pavement. The underlying asphalt concrete pavement structure had the same parameters as listed in Table 4.18. The variations of variables considered are listed in Table 4.20.

Table 4.20: Variations of Variables Considered for Group B1

Variable	Design Points	Number of Levels
Mix Type (LMLC)	MB4-D, MB15-D, MAC15-D, RAC-G, AR4000-D, MB4-G, MB15-G, MAC15-G	8
Overlay thickness (mm) Wheel speed (km/h)	45, 60, 90, 120 10, 70	4 2
Total number of simulations		64

4.16. Simulation Results

Results of initial runs with *CalME* indicated that pavement performance was generally over-estimated in the simulations. An additional scale factor of 0.3 was therefore applied to the pavement life predicted by *CalME* to counter this anomaly. The results reported in the following sections include this adjustment, and the plots and associated rankings should be considered as relative. Final shift factors are being calibrated.

4.16.1 FMLC Mix Reflective Cracking Performance in Different Climate Zones

The average relative reflective cracking life grouped by different factors is shown in Figure 4.110, based on results from Group A. The ranking is similar to that obtained from the HVS simulation results, except that the relative ranking between the RAC-G and MB15-G mixes is reversed. Overall, reflective cracking life increases with increasing traffic speed, increasing overlay thickness, and lower traffic volume. Interestingly, climate zone has very little effect.

Figure 4.110 also indicates that changing the traffic speed from 10 km/h to 70 km/h, was less significant compared to overlay thickness, and traffic volume (TI for 10 years).

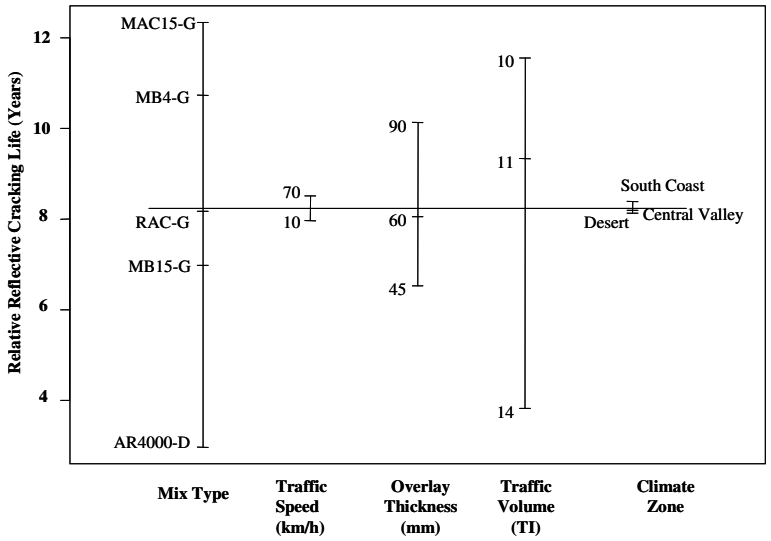

Figure 4.110: Design plot of relative reflective cracking life with FMLC mixes.

The relative reflective cracking performance of the different FMLC mix asphalt concrete overlays in different climate zones is shown in Figure 4.111 in the form of a bar chart. The range of reflective cracking life is also indicated in these charts using range bars (vertical lines with horizontal whiskers) showing minimum and maximum values. The figure shows that all the mixes perform approximately the same in the three different climate zones.

Figure 4.112 shows the relative reflective cracking performance of FMLC mixes in asphalt concrete overlays grouped by overlay thickness. Increasing thickness improves the performance for all mix types.

Figure 4.113 illustrates the relative reflective cracking performance of FMLC mixes in asphalt concrete overlays grouped by Traffic Index (TI) for 10 years. As expected, reflective cracking life decreases as traffic volume increases.

Figure 4.114 shows the relative reflective cracking performance of FMLC mixes in asphalt concrete overlays grouped by highway traffic speed. As expected, reflective cracking life increases as traffic speed increases because of higher stiffnesses in the asphalt concrete mixes related to shorter loading time. However, the difference between the two speeds is not significant.

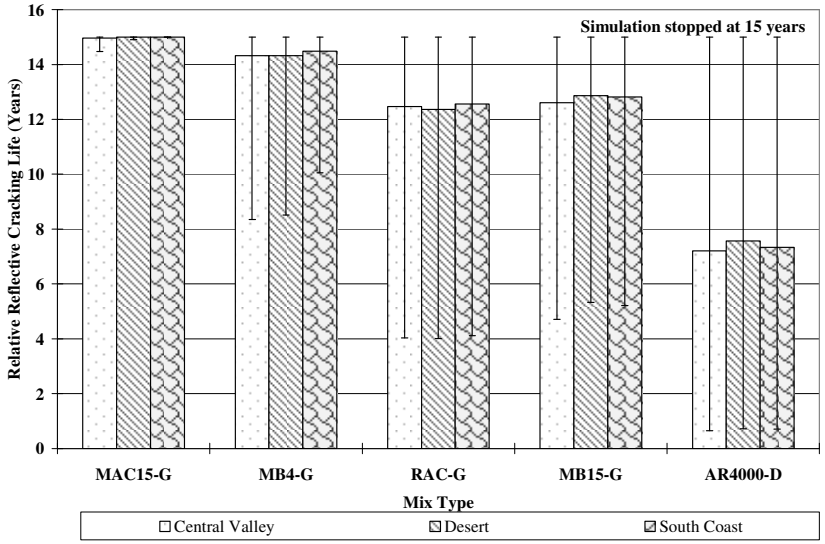

Figure 4.111: Relative reflective cracking performance of FMLC mixes, grouped by climate zone.

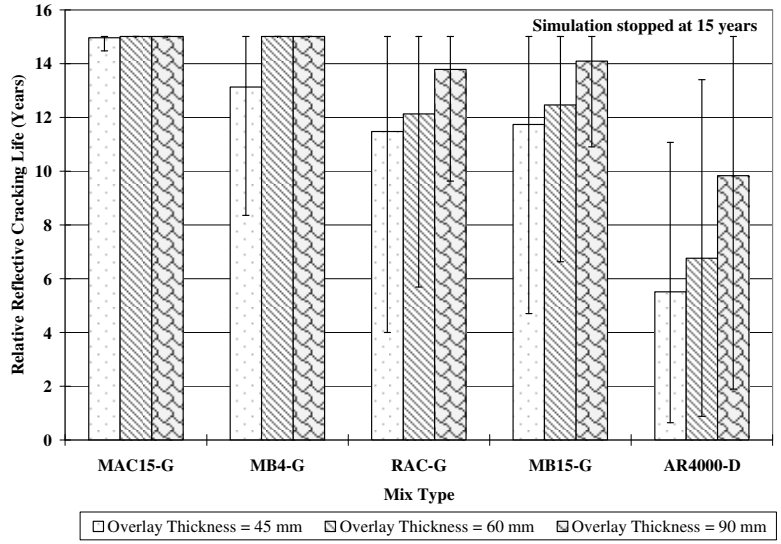

Figure 4.112: Relative reflective cracking performance of FMLC mixes, grouped by thickness.

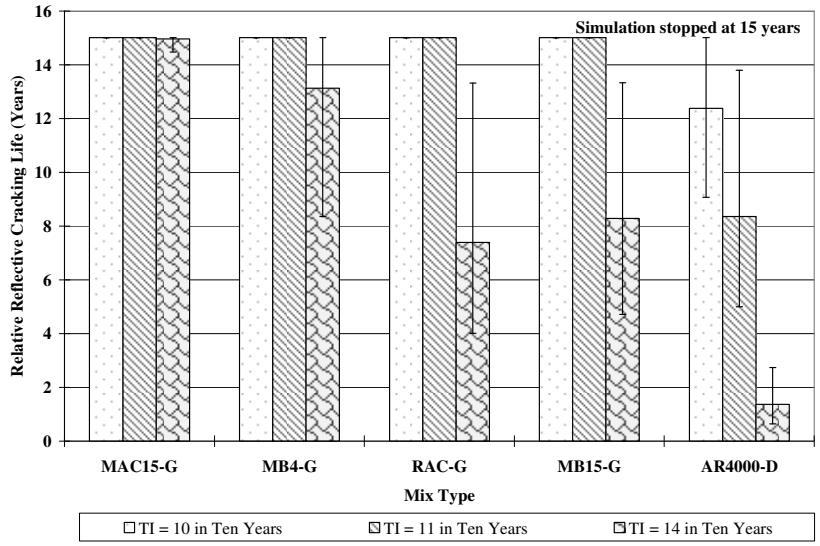

Figure 4.113: Relative reflective cracking performance of FMLC mixes, grouped by TI for 10 years.

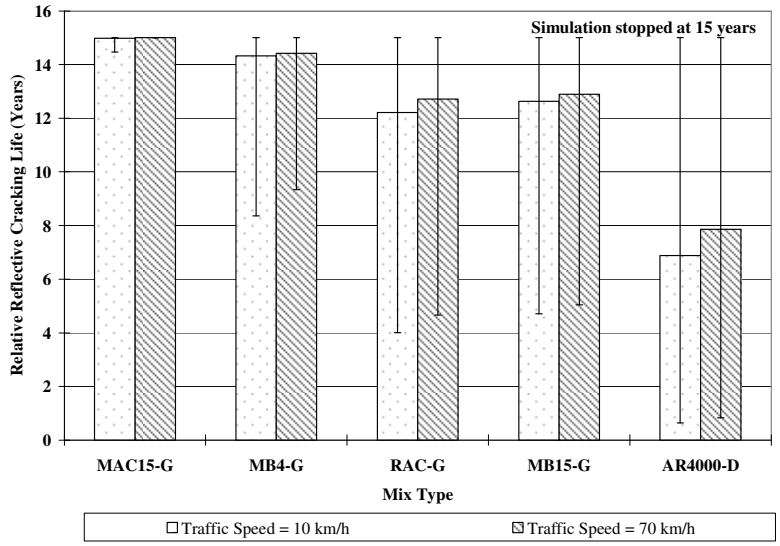

Figure 4.114: Relative reflective cracking performance of FMLC mixes, grouped by traffic speed.

4.16.2 FMLC Mix Rutting Performance in Different Climate Zones

The average relative rutting life grouped by the different factors is shown in Figure 4.115, based on results from Group A. The ranking is significantly different from that obtained from the HVS tests and simulation of the HVS results, discussed earlier in this section. This is attributed to the HVS rutting tests being carried out on overlays over an intact, untrafficked and relatively new underlying asphalt and base layers, compared to this set of simulations, which were carried out using an older, cracked and relatively heavily trafficked underlying layers. Although rutting performance on the HVS fatigue tests was not simulated in this study, observations from the first-level analysis reports indicate that rutting on the fatigue sections was most severe in areas overlying the most densely cracked areas on the underlying DGAC layer.

Overall, rutting life increased with increasing traffic speed, increasing overlay thickness, and lower traffic volume. Climate zone had a larger effect on rutting life than on fatigue life, with shorter rutting life predicted in hotter climates, as expected.

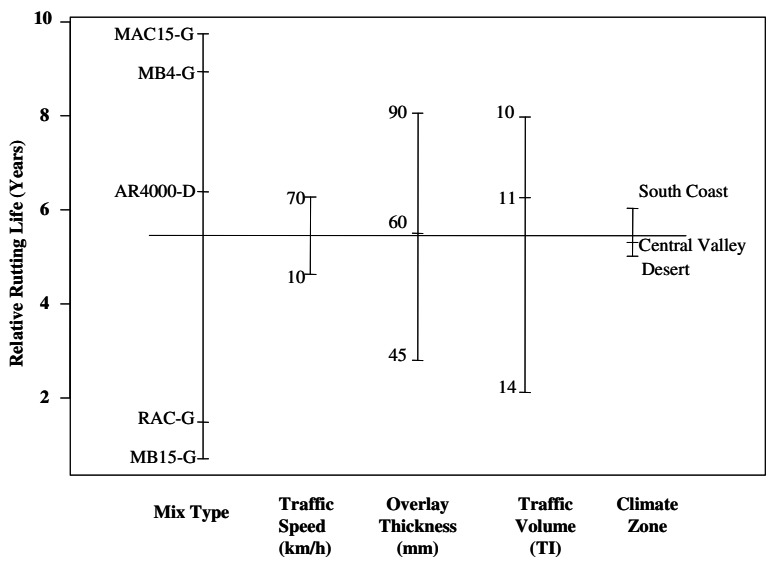

Figure 4.115: Design plot of relative rutting life with FMLC mixes.

The relative rutting performance of different FMLC mix asphalt concrete overlays in different climate zones is shown in Figure 4.116 in the form of a bar chart. Climate zone had a significant effect on the rutting life of the RAC-G and MB15-G mixes, but not have a insignificant influence on the other mixes.

Figure 4.117 shows the relative rutting performance of FMLC mixes in asphalt concrete overlays grouped by overlay thickness. Increasing thickness improved the performance for all mix types. Overall, an increase in thickness from 45 mm to 60 mm was more effective than an increase from 60 mm to 90 mm.

Figure 4.118 illustrates the relative rutting performance of FMLC mixes in asphalt concrete overlays grouped by Traffic Index (TI) for 10 years. As expected, rutting performance decreases as traffic volume increases.

Figure 4.119 shows the relative rutting performance of FMLC mixes in asphalt concrete overlays grouped by highway traffic speed. As expected, rutting performance improves with an increase in traffic speed because of the shorter loading time. This effect was especially significant for the RAC-G and MB15-G mixes.

4.16.3 LMLC Mix Reflective Cracking Performance in Overlays at 20°C

This section presents results from the Group B simulation (i.e., LMLC mix used in asphalt concrete overlays on old asphalt concrete pavements). Note that in this section, mixes using modified binders (including MAC15, MB4, and MB15) were prepared as both dense-graded and gap-graded mixes (11,12), which differs from those mixes used in the Group A simulations, where the modified binders were only used in gap-graded mixes. The average relative reflective cracking life grouped by different factors is shown in Figure 4.120. Overall, reflective cracking life increased with increasing traffic speed and increasing overlay thickness. The effect of overlay thickness (which varied from 45 mm to 120 mm) was more significant than that of traffic speed (which varied from 10 km/h to 70 km/h). The ranking is consistent with the ranking for reflective cracking performance shown in Section 4.16.1. It should be noted that the simulations were only run for a pavement life of 15 years, and that some overlays may not have failed in this time period.

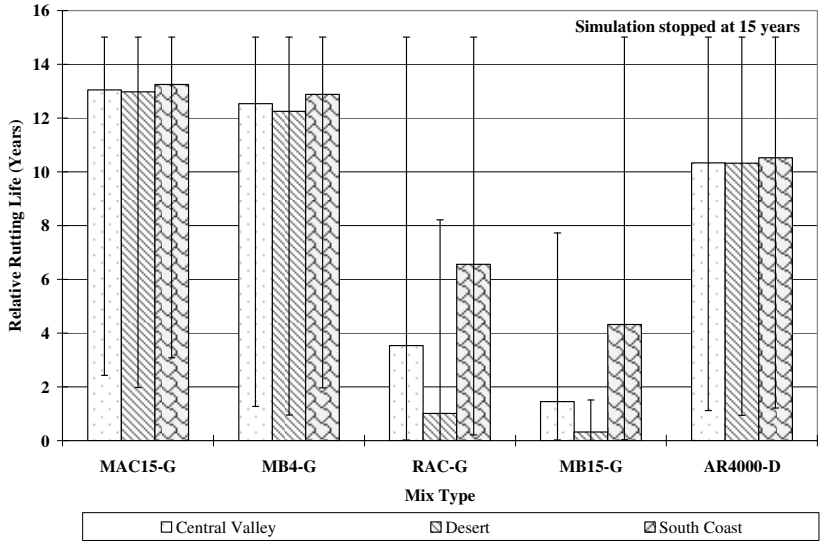

Figure 4.116: Relative rutting performance of FMLC mixes, grouped by climate zone.

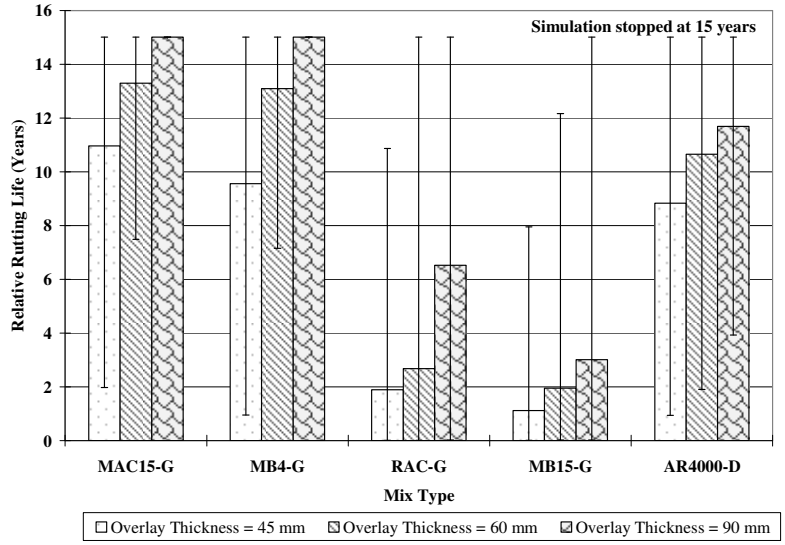

Figure 4.117: Relative rutting performance of FMLC mixes, grouped by overlay thickness.

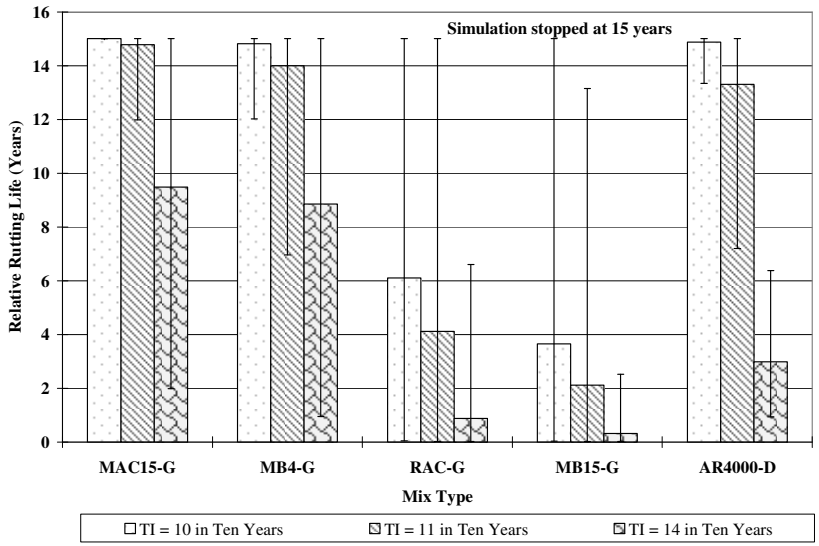

Figure 4.118: Relative rutting performance of FMLC mixes, grouped by TI for 10 years.

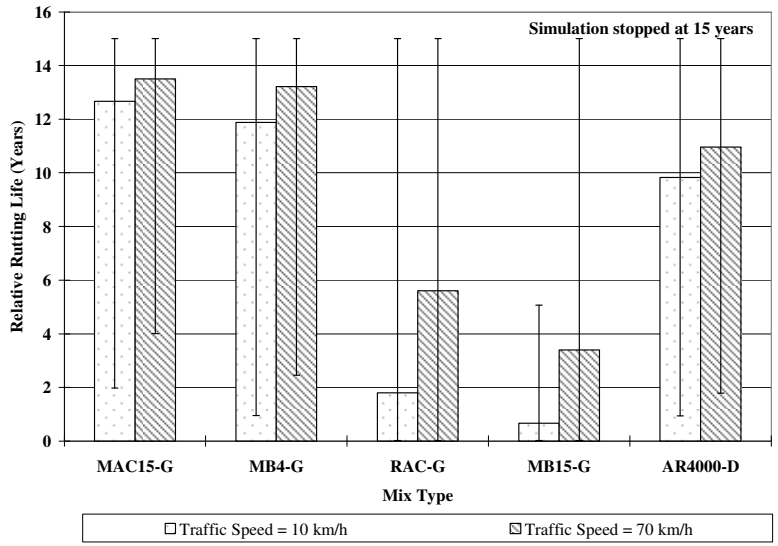

Figure 4.119: Relative rutting performance of FMLC mixes, grouped by traffic speed.

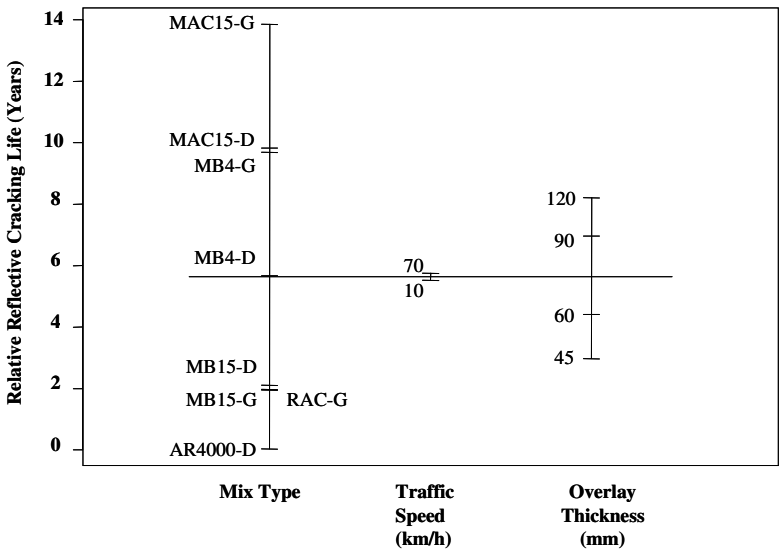

Figure 4.120: Design plot of relative reflective cracking life with LMLC mixes at 20°C.

Figure 4.121 shows the relative reflective cracking performance of LMLC mixes in asphalt concrete overlays at 20°C grouped by overlay thickness. Several observations can be made from the figure:

- As expected, reflective cracking life generally increased with overlay thickness
- For mixes using rubber modified binders (i.e., MB4-D, MB4-G, MB15-D, MB15-G, MAC15-D and MAC15-G), gap-graded mixes generally performed better than dense-graded mixes except the mixes with MB15 binder, the performance of which did not depend on aggregate gradation.
- Mixes with terminal blended rubber modified binders generally performed better than the RAC-G and AR4000-D mixes, except for the mixes with MB15 binder, the performance of which were approximately the same as the RAC-G mix.

Figure 4.122 shows the relative reflective cracking performance of LMLC mixes in asphalt concrete overlays at 20°C grouped by highway traffic speed. As expected, reflective cracking life generally increased with increase in traffic speed because of shorter loading times. However, the difference between the two speeds was not significant.

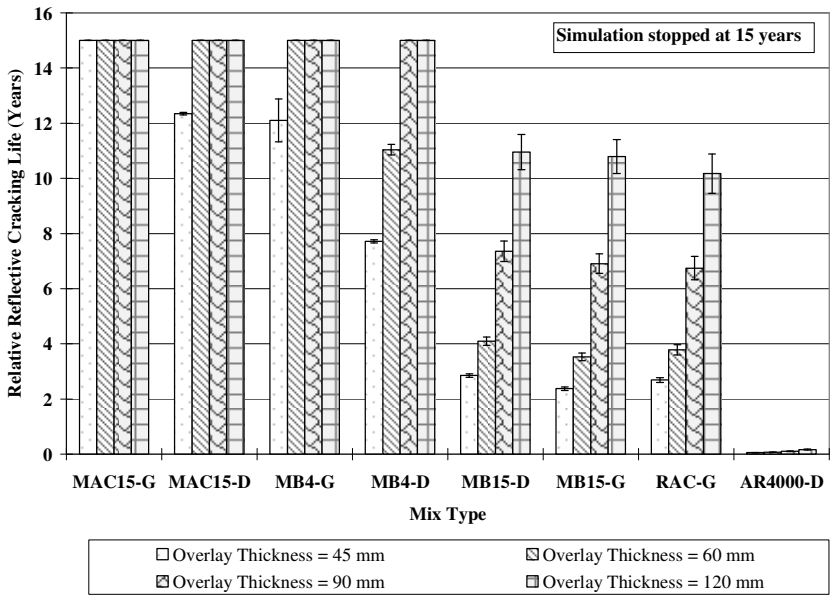

Figure 4.121: Relative reflective cracking performance of LMLC, grouped by overlay thickness

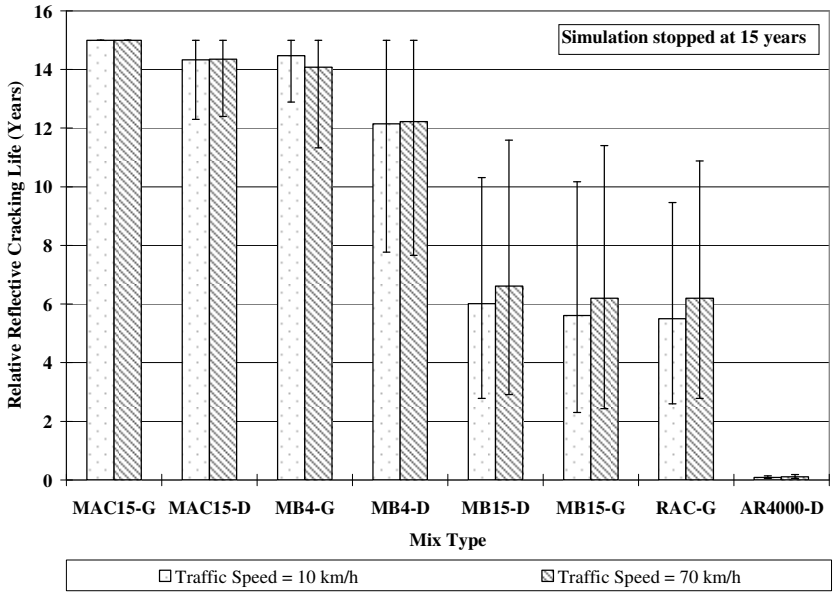

Figure 4.122: Relative reflective cracking performance of LMLC, grouped by traffic speed

4.16.4 LMLC Mix Rutting Performance in Overlays at 20°C

This section presents rutting results from the Group B simulation (i.e., LMLC mix used in asphalt concrete overlays on old asphalt concrete pavements). The average relative rutting life grouped by different factors is shown in Figure 4.123. Overall, rutting life increases with increasing traffic speed and increasing overlay thickness. The effect of overlay thickness (which varied from 45 mm to 120 mm) was more significant than that of traffic speed (which varied from 10 km/h to 70 km/h). An increase in overlay

thickness from 60 mm to 120 mm was more effective than an increase from 45 mm to 60 mm. The relative performance ranking is consistent with that shown in Section 4.16.2 and the reflective cracking performance shown in Section 4.16.3, which implies that mixes with good reflective cracking performance also have good rutting performance. The ranking differs from the observations for FMLC mixes in various climate zones.

The laboratory shear test results for LMLC AR4000-D were identified in the laboratory shear report (12) as not following the same ranking relative to the other LMLC mixes and to the FMLC mixes. The AR4000-D LMLC simulations should therefore be interpreted with some caution.

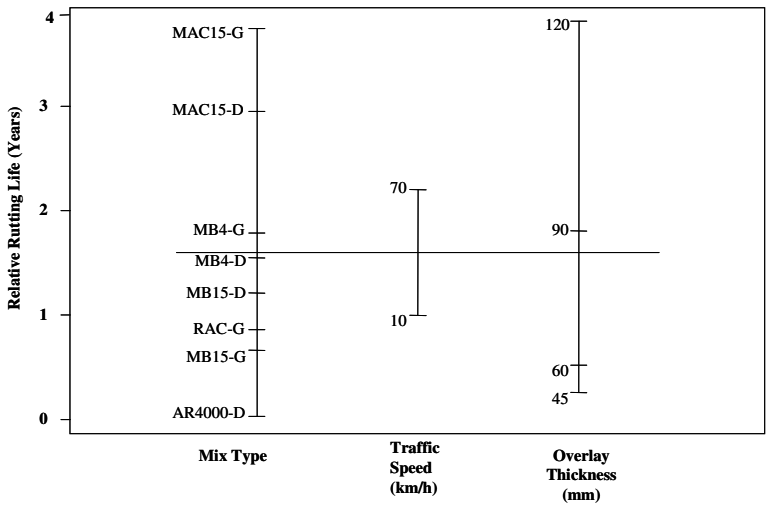

Figure 4.123: Design plot of relative rutting life with LMLC mixes at 20°C

Figure 4.124 shows the relative rutting performance of the LMLC mixes grouped by overlay thickness. Several observations can be made from the figure:

- As expected, rutting life generally increases with overlay thickness
- For mixes using rubber modified binders (i.e., MB4-D, MB4-G, MB15-D, MB15-G, MAC15-D and MAC15-G), the gap-graded mixes generally performed better than the dense-graded mixes, except for the MB15-G mix, which performed worse than the MB15-D mix.
- Mixes with terminal blend rubber modified binders generally performed better than the RAC-G and AR4000-D mixes except for the mixes with MB15 binder, the performance of which was slightly worse than the RAC-G mix.

Figure 4.125 shows the relative rutting performance of the LMLC mixes grouped by highway traffic speed. As expected, rutting life generally increased as traffic speed increased because of the shorter loading time. An increase in traffic speed from 10 km/h to 70 km/h approximately doubled the rutting life.

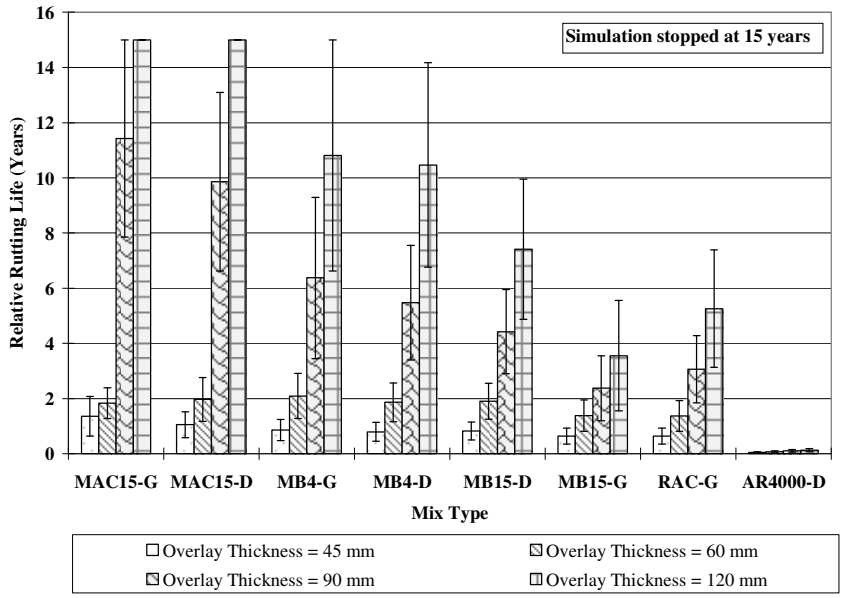

Figure 4.124: Relative rutting performance of LMLC, grouped by overlay thickness

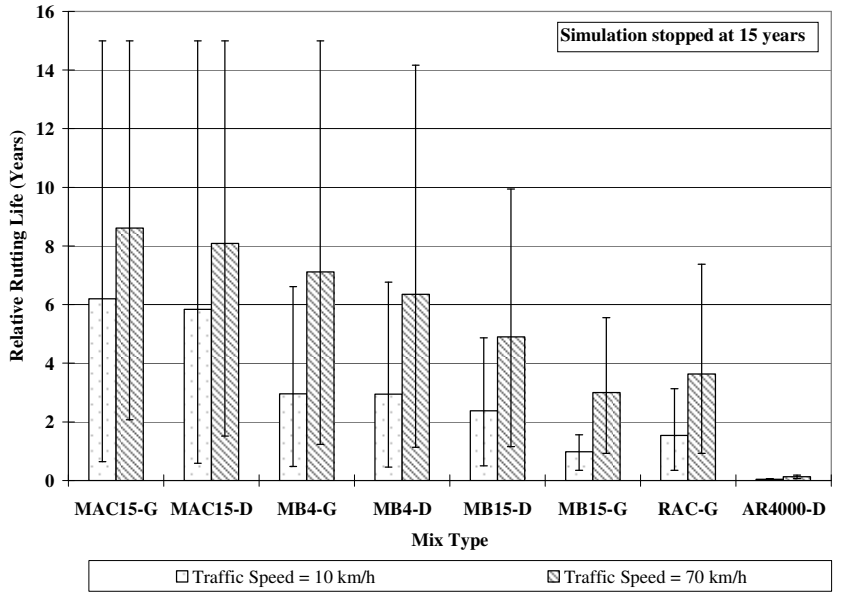

Figure 4.125: Relative rutting performance of LMLC, grouped by traffic speed

5. CONTINUUM DAMAGE MECHANICS SIMULATIONS

5.1. Introduction

This chapter presents simulations of the HVS tests on the test track using non-local continuum damage mechanics (CDM) implemented using a finite element method (FEM). The simulations are divided into three parts:

- Calibration of the simulation procedure using actual in situ conditions of different overlays as model inputs and matching model predictions with observed reflective cracking performance for the HVS cracking tests on the overlaid structure at moderate temperatures;
- Simulation of the reflective cracking performance of the different asphalt concrete overlays observed from the HVS tests using uniform design thicknesses, underlying pavement structures, and temperatures, and
- Simulation of reflective cracking performance for a hypothetical set of typical Caltrans structures and traffic conditions in different climate regions in the state.

The first set of simulations (first-stage) serves as validation of the FEM procedure. The results obtained in the second set of simulations (second-stage) provide objective ranking of different asphalt concrete overlays with respect to reflective cracking performance without the influence of underlying conditions, which varied in the actual HVS tests. The third set (third-stage) of simulations provides extrapolation of the HVS results to field conditions and an understanding of the sensitivity of the predicted performance of the different overlays. These results will be used to prepare recommendations for implementation of the results of this project.

Details of the simulation procedure can be found in Wu 2005 (22). The general methodology and model assumptions are listed below.

- The pavement system was analyzed as a two-dimensional (2-D) plain strain model with considerations accounting for the three-dimensional (3-D) nature of HVS wheel loads.
- Asphalt concrete overlays are assumed to be linear elastic with loading time and temperature-dependent stiffness, and ubjected to damage driven by a measure of strain.
- The underlying cracked asphalt concrete layer is assumed to be linear elastic with stiffness that is independent of loading time and temperature. Cracks are modeled directly with empty spaces in the underlying asphalt concrete layer. The underlying asphalt concrete layer is not subjected to damage because of the extensive existing cracks.

- Aggregate base (AB) and subgrade (SG) are assumed to be linear elastic with stiffness degradation determined by backcalculation from surface deflections measured during the HVS tests using the Road Surface Deflectometer (RSD). Aggregate base and subgrade layers can not sustain tensile strains larger than 0.1 percent, in which case their stiffness along the tensile direction is reduced to 10 percent of the original value.
- Subgrade is assumed to be 6,000 mm deep and is subdivided into two layers: the top 400 mm and the remaining 5,600 mm.

5.2. Development of CDM Model Inputs

5.2.1 Pavement Structure, Environment, and Loading

The CDM simulations require inputs that are related to the HVS test sections with respect to structure (layer thickness and mechanical properties), environment (pavement temperatures), and loading (loading history). These inputs are derived from field measurements (4-9) and laboratory test results (11, 12). A summary of the pavement structure, asphalt concrete air-void contents, pavement temperatures, and load history is provided in Chapter 2. For simulation purposes, an air-void content of 6.0 percent was used for each section.

5.2.2 Underlying DGAC Crack Spacing and Width

In the FEM model, crack spacing is assumed to be constant for each individual simulation. Observations from the test sections (4-9) indicated that the majority of the cracks were transverse. Accordingly, the crack spacing is referred to as the distance between cracks in the longitudinal direction of the section. Each HVS test section was divided into five one-meter subsections with center at Stations 4, 6, 8, 10, and 12 respectively. Crack spacing for each subsection was calculated by counting the number of transverse cracks within a ±0.5 m range from the subsection center. For example, the crack spacing is 1,000/(n-1) mm if n cracks are counted. Table 5.1 lists the number of cracks counted for each subsection of the six HVS test sections prior to placement of the overlays.

Table 5.1: Number of Cracks Counted on the Underlying DGAC Layer

Section		Number of Cracks per Subsection Station Center				
Number	Underlying	4	6	8	10	12
567RF	MB15-G	9	6	9	8	9
568RF	RAC-G	8	9	10	9	9
569RF	AR4000-D	1	0	4/0*	9	7
571RF	MB4-G	4/2*	7	8	9	11
572RF	MB4-G	10	9	9	0/3*	4/2*
573RF	MAC15-G	3/2*	6	7	11	9

* These subsections have significantly different crack densities for the two sides of the subsection center and therefore the crack numbers are counted separately.

As shown in Table 5.1, cracks may exist on one half of the test section only. Based on Table 5.1, crack spacing in the underlying layer was calculated and is shown in Table 5.2.

The cracks on the surface of the underlying DGAC layer were generally small with crack widths of between 1.0 mm and 5.0 mm. Accordingly, crack widths were set at 3.0 mm in the FEM model for this study.

Table 5.2: Crack Spacing at Different Locations on the Underlying DGAC Layer

Section		Crack Spacing (mm) per Subsection Station Center				
No.	**Underlying**	**4**	**6**	**8**	**10**	**12**
567RF	MB15-G	125	200	125	143	125
568RF	RAC-G	143	125	111	125	125
569RF	AR4000-D	1 crack[1]	NC[2]	167/NC[2]	125	167
571RF	MB4-G	167/NC[2]	167	143	125	100
572RF	MB4-G	111	125	125	250/NC[2]	167/NC[2]
573RF	MAC15-G	250/NC[2]	200	167	100	125

1 The crack is placed at the center of the FEM model when there is only one crack.
2 NC = "No Crack." In this instance there are cracks on one half of the model, but no cracks on the other half, or no crack in the whole model.

5.2.3 Backcalculation of Base and Subgrade Moduli

Layer moduli backcalculated from RSD data provided the basis for characterizing the different layers. The following assumptions were made when performing the backcalculation.

- Displacements were calculated based on multilayer elastic theory using *ELSYM5;*
- The subgrade was 6,000 mm (6.0 m) in total thickness, supported by bedrock. The inclusion of bedrock allows the direct use of back-calculated layer moduli in FEM analyses.
- The subgrade was divided into the two sublayers described in Section 5.1 to provide a simple way of accounting for variations in subgrade stiffness with respect to depth.
- All of the layers were assumed to be linear elastic.
- Stiffness for the underlying DGAC layer was assumed to be no more than 30 percent of its original intact stiffness.

Backcalculation results indicated that stiffnesses for the base and the top 400 mm of the subgrade decreased significantly under HVS trafficking. This decrease is described by the following exponential function (Equation 5.1):

$$E(n)=E_0\exp(-\alpha\times n) \quad \textbf{(5.1)}$$

where: E is the stiffness

n is the number of load repetitions, and

Variables E_0 and α are regression constants, representing initial stiffness and rate of stiffness degradation, respectively.

Comparison of average fitted stiffness for aggregate base and subgrade are shown in Figures 5.1 to 5.3. The regression parameters are listed in Tables C.1 through C.6 in Appendix C. Note that aggregate base stiffness underwent sudden changes in some of the HVS test sections and required two sets of equations to describe the degradation. There were also significant differences in the base and subgrade stiffnesses between the six HVS test sections.

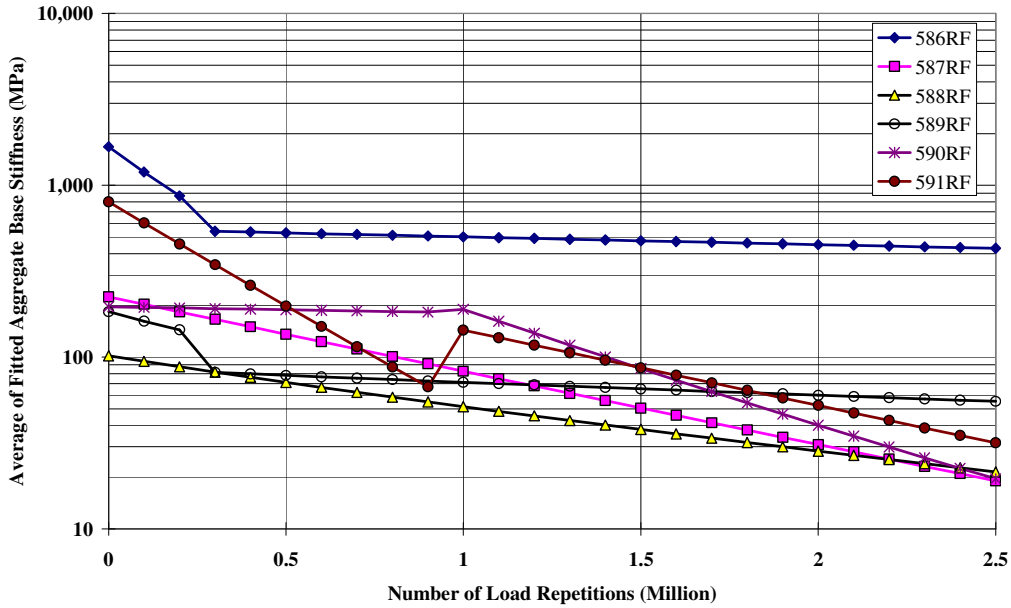

Figure 5.1: Comparison of average fitted aggregate base stiffness for the HVS sections.

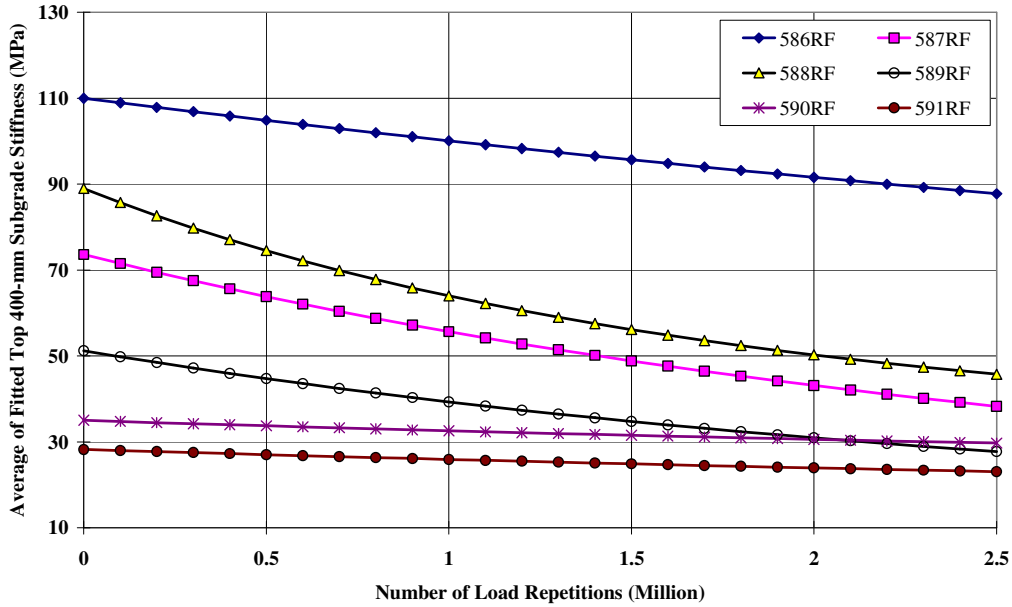

Figure 5.2: Comparison of average fitted upper 400 mm subgrade stiffness for the HVS sections.

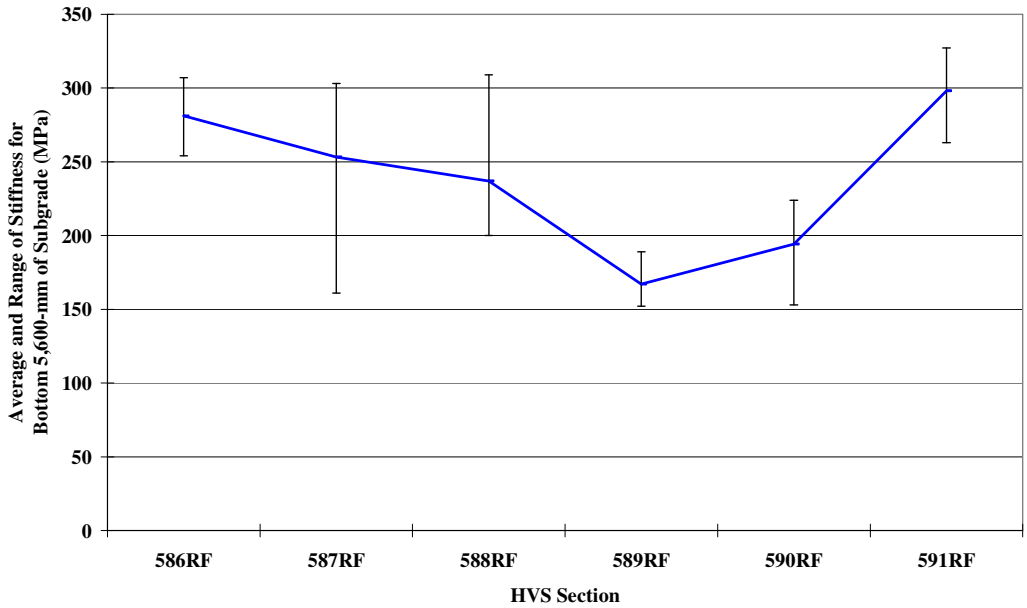

Figure 5.3: Comparison of lower 5,600 mm backcalculated subgrade stiffness for the HVS sections.
(Error bars show range of values for the five subsections.)

5.2.4 Asphalt Layer Characterization

The asphalt concrete overlay was modeled as a linear elastic material with rate- and temperature-dependent stiffness. Stiffness degradation was modeled by the nonlocal continuum damage mechanics model developed by Wu (22). To characterize an asphalt concrete overlay, it is necessary to determine the intact stiffness as well as the parameters that control damage evolution. The intact stiffness is determined based on the in-situ asphalt concrete mix air-void contents, HVS loading time, and pavement temperature using the stiffness master curve constructed from laboratory frequency sweep test data (11). The damage parameters are determined based on fatigue test data using procedures developed by Wu (22).

The underlying DGAC layer was also modeled as linear elastic with rate- and temperature-dependent stiffness. The extensive damage in this layer resulting from the Phase 1 HVS tests had the following implications:

- Stiffness could not be determined directly using master curves developed in flexural beam frequency sweep tests, and
- Little if any additional damage is likely to have occurred to the underlying DGAC during Phase 2 HVS trafficking on the overlays.

Accordingly, it was decided that no stiffness degradation needed to be applied to the underlying DGAC layer during Phase 2 HVS trafficking on the overlays, implying that the layer stiffness could be determined by backcalculation using RSD data collected at the beginning of this phase.

Methodology

The following methodology was followed to determine asphalt concrete layer moduli:

- The overlay asphalt concrete stiffness was calculated using the master curve constructed from laboratory frequency sweep test data. The loading frequency was calculated using the creep speed for HVS wheels during RSD data collection. Loading temperature was taken as the pavement temperature recorded while RSD data were collected. Aging was also accounted for using a simplified procedure.
- With known moduli for the overlay asphalt concrete, the stiffness for the underlying DGAC, aggregate base, and subgrade were backcalculated. The backcalculated results were manually adjusted where necessary to achieve reasonable results.
- The overlay and underlying DGAC layer moduli were both adjusted to account for the difference in loading frequency and pavement temperature between various trafficking conditions and initial RSD data collection conditions.

Details of these steps will be discussed in the following subsections. Since the backcalculated underlying DGAC layer moduli exhibit some variation, the first five sets of RSD data during the HVS test were used to determine the asphalt concrete layer moduli. Each set of RSD data was subjected to the analyses listed above and the final asphalt concrete layer moduli were averaged across the five sets to obtain a final value for use in the FEM simulation.

Step 1: Overlay Asphalt Concrete Moduli when RSD Data Were Collected

Determination of asphalt concrete moduli requires loading time, loading temperature, and aging condition. The loading time is determined by using the following equation (Equation 5.2):

$$t = \frac{L + D \times 2}{V} \tag{5.2}$$

where: L is the length of wheel footprint along the traffic direction,
D is the depth to the middle of the overlay, and
V is the HVS wheel speed while RSD data were collected.

The corresponding loading frequency is calculated as (Equation 5.3):

$$f = \frac{1}{2\pi \times t} \tag{5.3}$$

This equation gives a horizontal stress loading time that is about three times the equivalent loading time in square waveform for vertical compressive stress (26). Typically the ratio between loading time for

horizontal stress and vertical stress is about 1.7 to 4.2 with an average of 3.0 for the ratio of shear moduli between the top two layers ranging from 2.5 to 250. Accordingly, Equations 5.2 and 5.3 provide a good estimate for loading time for horizontal stress.

The length of the wheel footprint along the trafficking direction can be calculated using the following equation (Equation 5.4):

$$L=\frac{F}{2\times p\times W\times C_g} \tag{5.4}$$

where: F is the force applied by the HVS during RSD data collection,

p is the HVS wheel tire pressure,

W is the overall tread width, and

C_g is a correction factor to account for the reduction in contact area due to the grooves in the tire.

For HVS trafficking and data collection, p is 720 kPa, W is 205 mm, and C_g is approximately 0.8 for the tires used. HVS trafficking speed was 9.6 km/h, while the data collection wheel speed was 1.8 km/h. Asphalt concrete layer thicknesses are listed in Figure 2.2. The loading frequencies for different load levels and different wheel speeds can be calculated after combining Equations 5.2, 5.3, and 5.4. These results are listed in Table 5.3.

Table 5.3: Loading Frequencies for Different Load Levels and Section Thickness

Section	Layer	Load Level (kN)*	Trafficking Loading Frequency (Hz)	Data Collection Loading Frequency (Hz)
Half-thickness (45 mm) sections	AC overlay (47 mm)	60	1.45	0.27
		90	1.03	0.19
		80	1.19	0.22
		100	0.97	0.18
	Underlying DGAC (82 mm)	60	1.01	0.19
		90	0.79	0.15
		80	0.87	0.16
		100	0.75	0.14
Full-thickness (90 mm) sections	AC overlay (91 mm)	60	1.26	0.24
		90	0.93	0.17
		80	1.06	0.20
		100	0.88	0.17
	Underlying DGAC (82 mm)	60	0.83	0.16
		90	0.68	0.13
		80	0.74	0.14
		100	0.65	0.12
Average			0.94	0.18
Standard Deviation			0.22	0.05

* Actual average load levels determined with a static scale after testing:
60 kN = 58 kN 90 kN = 86 kN 80 kN = 73 kN 100 kN = 92 kN

According to Table 5.3, the loading frequencies do not show significant differences for different load levels and layers. Therefore, the average loading frequencies, irrespective of the load level, layer thickness, and layer location, were used. Specifically, a loading frequency of 0.94 Hz was used for HVS trafficking and 0.18 Hz for data collection. This simplification leads to a potential error of about ±15 percent in asphalt concrete stiffness for temperatures between 10°C and 20°C, which is considered acceptable given the variation in layer thickness, air-void content, and the simplification from visco-elasticity to linear elasticity.

Based on the laboratory test results (11), aging for some mixes had significant effects on stiffness and needed to be accounted for in the analysis. For the purposes of this study, aging is assumed to follow an exponential pattern (Equation 5.5):

$$R = 1 - \exp(-\alpha \times t) \quad \textbf{(5.5)}$$

where: R is the aging ratio,

t is the time after construction in years, and

α is the rate of aging.

In this study, it was assumed that 90 percent of aging occurs in the first 15 years, thus α was calculated as 0.15. Asphalt concrete stiffness is a function of aging ratio (Equation 5.6):

$$E_{aged} = E_{unaged} + R(E_{\infty} - E_{unaged}) \quad \textbf{(5.6)}$$

where: E_{∞} is the stiffness corresponding to maximum aging.

With long-term oven aging (LTOA — aging of compacted specimens at 85°C for six days) stiffness corresponding to approximately 15 years in the field (27), and E_{unaged} the stiffness for asphalt concrete without LTOA aging, E_{∞} can be calculated as (Equation 5.7):

$$E_{\infty} = \frac{E_{LTOA} - E_{unaged}}{0.90} + E_{unaged} \quad \textbf{(5.7)}$$

While E_{∞} depends on loading time and temperature, R is only a function of years after pavement construction. Aging ratios for asphalt concrete mixes in different HVS test sections as well as the underlying DGAC are listed in Table 5.4, based on flexural stiffness of LTOA specimens for each overlay type.

Pavement temperatures at 50 mm depth during the first five RSD data collections for each HVS section are listed in Table 5.5. Note that temperatures for Sections 589RF and 590RF were interpolated from

manual readings before and after the data collection, while other temperatures were recorded directly through the data acquisition system during data collection.

Table 5.4: Aging Ratio for Different HVS Sections at Start of HVS Trafficking

Section		Start Date	Time After Construction (years)	Aging Ratio
No.	Overlay			
586RF	MB15-G	5/25/2006	2.9	0.36
587RF	RAC-G	3/15/2005	1.8	0.23
588RF	AR4000-D	11/2/2005	2.4	0.30
589RF	MB4-G	6/23/2004	1.0	0.14
590RF	MB4-G	1/13/2004	0.6	0.08
591RF	MAC15-G	1/10/2007	3.6	0.42
Underlying DGAC	-	-	1.8*	0.23

* Counted only to the time when the overlay was placed.

Table 5.5: Pavement Temperatures and Load Repetitions for the First Five RSD Data Collections

Section	1st		2nd		3rd		4th		5th	
	Temp. (°C)	Reps	Temp (°C)	Reps.	Temp (°C)	Reps.	Temp (°C)	Reps.	Temp (°C)	Reps.
586RF	16.7	10	18.3	15,000	18.1	45,000	18.9	77,029	18.4	109,500
587RF	13.3	15,000	13.6	51,733	14.4	106,164	16.5	165,300	17.5	208,896
588RF	16.0	10	15.4	15,000	19.6	41,830	15.0	78,000	12.2	105,000
589RF	21.5	10	22.0	15,000	22.0	45,000	21.0	76,000	21.0	98,176
590RF	20.0	10	20.5	15,000	21.0	30,000	20.0	60,250	20.0	90,000
591RF	20.2	10	19.2	15,000	20.1	45,000	20.5	75,000	19.4	105,000

Using the temperatures listed in Table 5.5 and the master curves for asphalt concrete stiffness (11), with RSD loading frequency of 0.18 Hz and the aging ratio listed in Table 5.4, the overlay layer moduli can be calculated. Results are listed in Table 5.6.

Table 5.6: Overlay Layer Moduli for the First Five RSD Data Collections

Section		Layer Moduli (MPa)				
No.	Overlay	1st	2nd	3rd	4th	5th
586RF	MB15-G	654	499	517	450	491
587RF	RAC-G	3,181	3,071	2,794	2,169	1,920
588RF	AR4000-D	5,195	5,463	3,743	5,646	7,020
589RF	MB4-G	214	201	201	228	228
590RF	MB4-G	250	233	217	250	250
591RF	MAC15-G	752	881	764	718	853

Step 2: Backcalculation of Underlying DGAC Stiffness

After running preliminary analyses using the RSD data, it was found that the backcalculated moduli for the underlying DGAC layer appeared to be unrealistically high even though the RMS of error in the surface deflections was mostly very small. It was therefore necessary to use a threshold for the layer moduli. Since this layer had been subjected to extensive trafficking during Phase 1 and was extensively cracked, it was decided that the layer moduli could not exceed 30 percent of its intact moduli with the aging effect. The final backcalculated layer moduli are listed in Tables C.7 through C.12 in Appendix C. Note that all of the underlying DGAC moduli are set to the maximum threshold for Section 586RF.

The backcalculated layer moduli were adjusted to the reference temperature of 20°C and trafficking loading frequency of 0.94 Hz. This adjustment is based on the master curve obtained from laboratory frequency sweep tests for the original asphalt concrete mix used in the underlying layer. Median values of the adjusted reference stiffness were adopted for use in later simulations. The reference stiffness and the median values are shown in Tables C.13 through C.18 in Appendix C. The median values are summarized in Table 5.7. The only locations where the underlying DGAC was less stiff than 30 percent of its intact stiffness were Stations 8, 10, and 12 on Section 588RF (90 mm DGAC overlay).

Table 5.7: Layer Moduli for Underlying DGAC at 20°C at Trafficking Speed

Section		Reference Trafficking Stiffness (MPa)				
Number	Overlay	4CL	6CL	8CL	10CL	12CL
586RF	MB15-G	1,596	1,596	1,596	1,596	1,596
587RF	RAC-G	1,596	1,596	1,596	1,596	1,596
588RF	AR4000-D	1,596	1,596	1,446	322	262
589RF	MB4-G	1,596	1,596	1,596	1,596	1,596
590RF	MB4-G	1,596	1,596	1,596	1,596	1,596
591RF	MAC15-G	1,596	1,596	1,596	1,596	1,596

Overlay stiffness under traffic loading frequency (i.e., 0.94 Hz) and 20°C are listed in Table 5.8. Note that these values were developed with aging taken into account.

Table 5.8: Layer Moduli for Overlays at 20°C at Trafficking Speed

Section		Reference Trafficking Stiffness (MPa)
Number	Overlay	
586RF	MB15-G	812
587RF	RAC-G	2,526
588RF	AR4000-D	5,669
589RF	MB4-G	596
590RF	MB4-G	574
591RF	MAC15-G	1,606

Step 3: Adjust Asphalt Concrete Moduli to Trafficking Temperature

Asphalt concrete moduli need to be further adjusted to account for actual trafficking temperature. This is accomplished using the master curve for the original asphalt concrete mixes. Average pavement temperatures at 50 mm depth, along with the corresponding standard deviations, are provided in Section 2.5.2 for different stages of testing for each individual HVS test. Since pavement temperature fluctuations are relatively small within each stage, they were assumed to be constant within each individual testing stage. Using the average pavement temperature, the ratio between in-situ asphalt concrete stiffness and the reference values can be calculated. Results are listed in Table 5.9.

Table 5.9: Adjusted Factors for Asphalt Concrete Stiffness

Section		Parameter	Stage 1	Stage 2	Stage 3
Number	Overlay				
586RF	MB15-G	Repetitions (Millions)	0 to 1.0	1.0 to the end	-
		Temperature (°C)	19.6 (1.6)	16.6 (2.8)	-
		Overlay SR[1]	1.07	1.78	-
		Underlying AC SR	1.04	1.33	-
587RF	RAC-G	Repetitions (Millions)	0 to 1.0	1.0 to 1.7	1.7 to the end
		Temperature (°C)	18.5 (1.7)	16.9 (0.6)	18.1 (1.6)
		Overlay SR[1]	1.15	1.33	1.19
		Underlying AC SR	1.14	1.30	1.18
588RF	AR4000-D	Repetitions (Millions)	0 to the end	-	-
		Temperature (°C)	14.3 (1.7)	-	-
		Overlay SR[1]	1.57	-	-
		Underlying AC SR	1.54	-	-
589RF	MB4-G	Repetitions (Millions)	0 to 1.0	1.0 to the end	-
		Temperature (°C)	21.4 (0.8)	15.3 (1.4)	-
		Overlay SR[1]	0.83	2.00	-
		Underlying AC SR	0.87	1.45	-
590RF	MB4-G	Repetitions (Millions)	0 to the end	-	-
		Temperature (°C)	20.7 (1.1)	-	-
		Overlay SR[1]	0.91	-	-
		Underlying AC SR	0.93	-	-
591RF	MAC15-G	Repetitions (Millions)	0 to 1.0	1.0 to the end	-
		Temperature (°C)	20.0	15.0	-
		Overlay SR[1]	1.0	1.38	-
		Underlying AC SR	1.0	1.88	-

[1] SR - Stiffness ratio Note — Standard deviations of temperatures are shown in parentheses.

5.2.5 Damage Evolution Parameters

Damage evolution parameters were identified by simulating the laboratory flexural beam fatigue tests and matching the measured stiffness reduction curves. The laboratory fatigue tests were conducted at 10°C, 20°C, and 30°C with two strain levels (400 and 700 μstrain) at each temperature. The damage evolution parameters for each asphalt concrete mix derived from the laboratory test data are shown in Table 5.10. Parameters for in-situ pavement temperatures were interpolated linearly based on these values. The function that determines stiffness reduction is shown in Equation 5.8 (22):

$$-\log(SR)=\exp(a_0+a_1\bar{\varepsilon})\log^b(N) \quad \textbf{(5.8)}$$

where: SR is the residual stiffness ratio,

$\bar{\varepsilon}$ is the measure of strain that drives damage,

N is the number of load repetitions applied, and

a_0, a_1 and b are parameters that control the rate of stiffness reduction.

Typically, a_0 is negative while a_1 and b are positive. The rate of stiffness reduction increases as each of these parameters increases. Furthermore, a_0 mostly controls the initial damage rate (i.e., higher SR values), while a_1 and b mostly control the damage rate at later stages. Note that the parameters for the MB4-G and MAC15-G mixes are exactly the same at both 20°C and 30°C. It should be noted that the three mixes with

rubber modified binders (i.e., MB4-G, MB15-G, and MAC15-G) have smaller values for a_1 and b but larger values for a_0 compared to the control mixes (i.e., AR4000-D and RAC-G). This indicates faster initial damage rates but slower crack propagation rates for rubber modified binders.

Table 5.10: Damage Evolution Parameters for Different Aspahlt Concrete Overlay Mixes

Mix Type	Temperature (°C)	Damage Evolution Parameter		
		a_0	a_1	b
AR4000-D	10	-11.0	4,500	4.5
	20	-11.2	5,000	4.5
	30	-11.0	4,500	4.5
RAC-G	10	-10.3	3,800	4.0
	20	-9.1	4,000	3.3
	30	-7.6	3,000	2.7
MB4-G	10	-8.8	4,500	2.7
	20	-7.3	2,800	2.4
	30	-6.2	2,500	1.9
MAC15-G	10	-8.8	3,200	3.4
	20	-7.3	2,800	2.4
	30	-6.2	2,500	1.9
MB15-G	10	-9.3	5,000	3.0
	20	-7.6	2,500	2.6
	30	-6.9	2,500	2.3

5.3. Simulation Procedure

The overall procedure for FEM simulation of reflective cracking in asphalt concrete overlays is described in detail in Wu 2005 (22). In summary, the simulation procedure follows the steps below:

1. The intact (undamaged) stiffness of the different asphalt concrete layers is established based on current pavement temperature, and the aggregate base and subgrade stiffness is established based on current accumulated traffic count.
2. The nonlocal strain field is calculated for those parts of the overlay that are close to an underlying crack.
3. The damage induced by ΔN additional HVS trafficking is calculated using the nonlocal strain determined in Step 2. Step size ΔN is determined in an adaptive manner using the current maximum damage rate within the overlay.
4. The damage is applied to the asphalt concrete overlay, which leads to a decrease in stiffness.
5. An element is then removed and the crack propagated once the stiffness at all Gauss points within certain elements have been reduced to one percent of their intact value.
6. Steps 1 through 5 are repeated until cracks reach the surface of the overlay.

Further details about the procedure are described in the following subsections.

5.3.1 FEM Model

The asphalt concrete overlay systems were analyzed with a two-dimensional plane strain model. HVS test sections were 8.0 m long and 1.0 m wide. Most of the cracks in the underlying DGAC were aligned with the transverse direction (See Figure 2.3). Accordingly, the plane modeled by the two-dimensional (2-D) FEM mesh is assumed to be the longitudinal vertical plane of symmetry of the HVS test section. The transverse cracks in the underlying DGAC layer were represented as line cracks in the FEM model, while the longitudinal cracks were not modeled. A typical FEM mesh is shown in Figures 5.4 through 5.6.

In the figures, only cracks near the center of the FEM model are modeled directly. The effect of all the other cracks is assumed to be represented by the reduced stiffness of the underlying asphalt concrete layer.

During early simulations, it was found that cracks would initially propagate horizontally, causing debonding of the overlay from the underlying DGAC layer. Although debonding is likely to occur during HVS trafficking, it is regarded as less important than vertical crack propagation. It was therefore decided to prevent cracks from propagating horizontally at the beginning of each HVS test simulation. This was achieved by preventing damage from accumulating in some areas around the tip of the old crack (Figure 5.6).

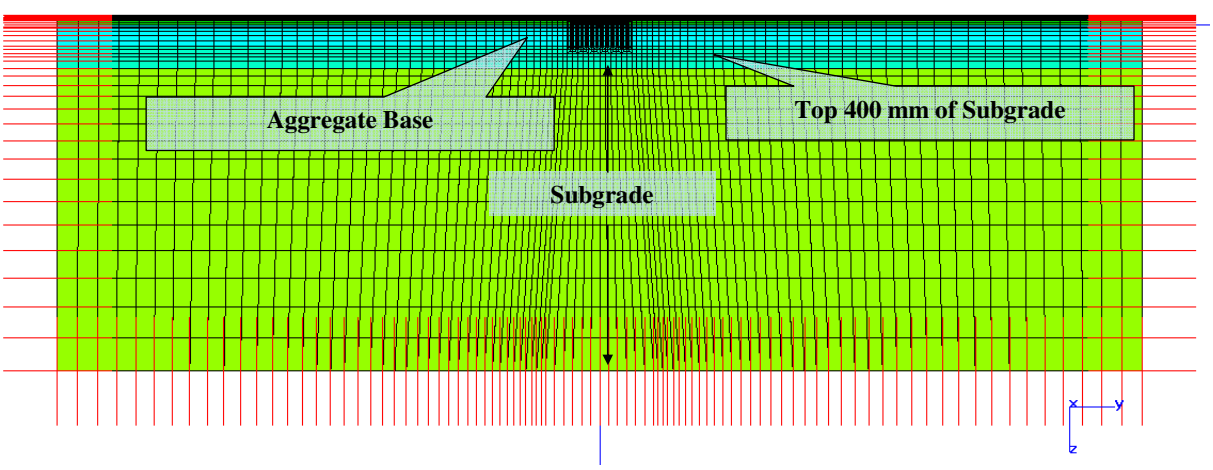

Figure 5.4: Overall FEM mesh for a typical HVS simulation.
(Red lines at the left, right, and bottom boundary indicate confinements in the direction of the lines; colors of the mesh indicate material specifications.)

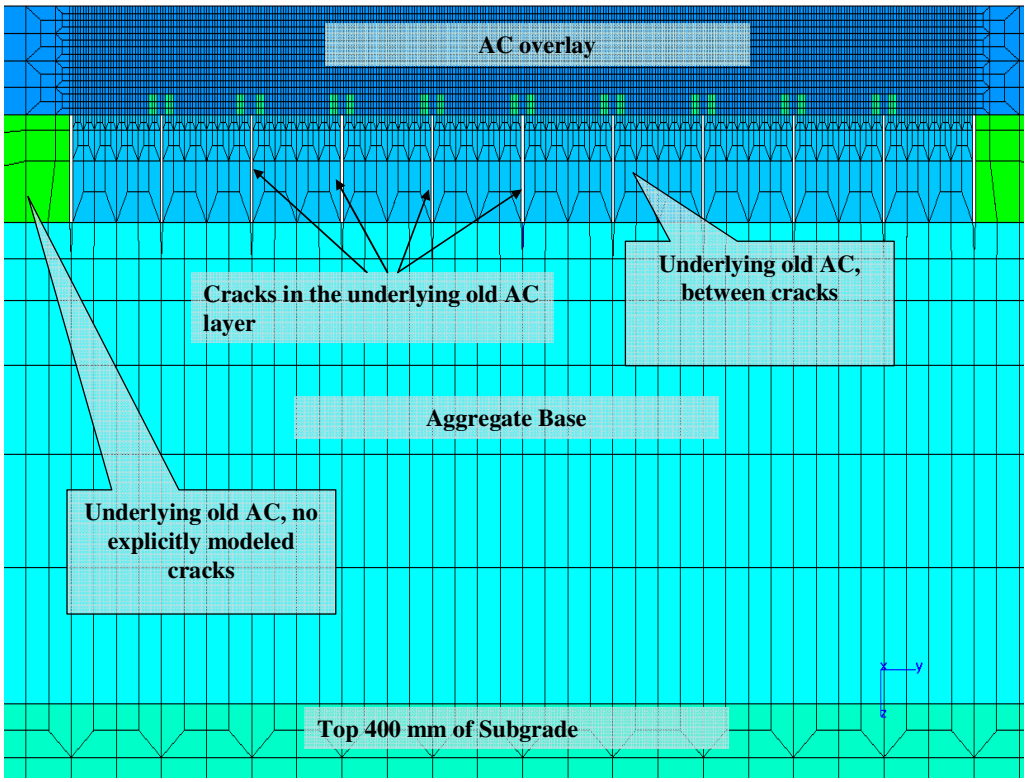

Figure 5.5: Close-up view (1) of the FEM mesh shown in Figure 5.4.
(Note that 11 cracks are modeled directly and the cracks are evenly distributed.)

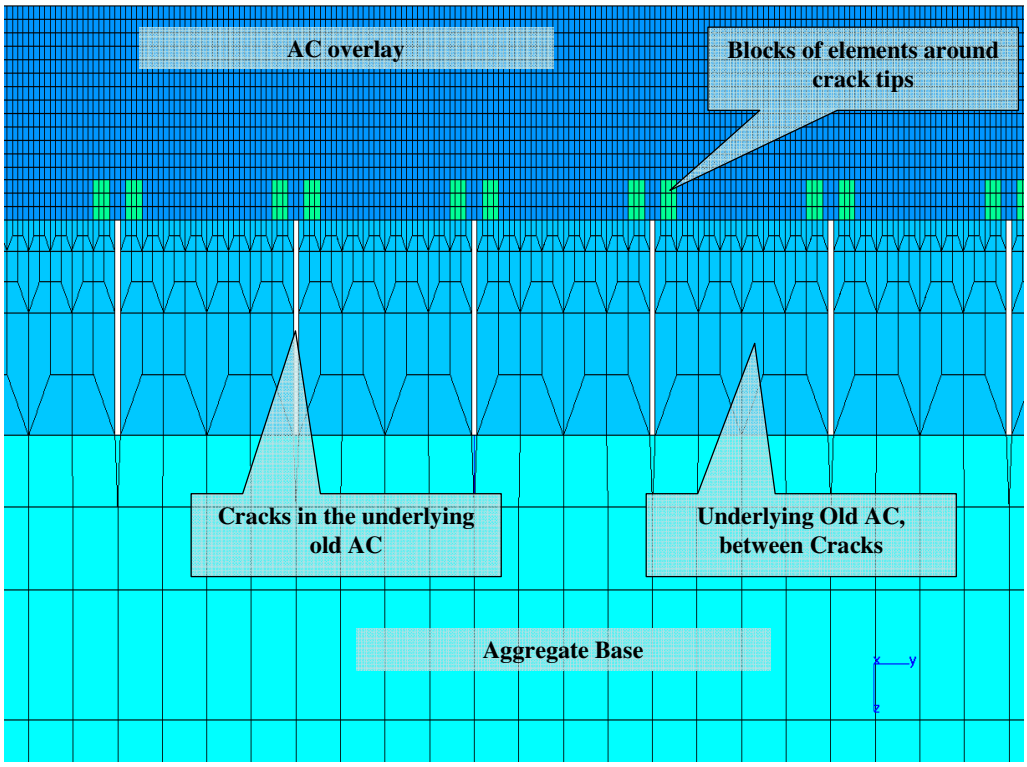

Figure 5.6: Close-up view (1) of the FEM mesh shown in Figure 5.5.
(Green blocks in the overlay around the tip of the underlying cracks indicate areas that are not subjected to damage. These blocks are necessary to force cracks to propagate upward instead of sideways.)

5.3.2 Considerations for FEM Model Use

3-D Loading in a 2-D FEM Model

The 2-D plane strain FEM model used in the simulations is a simplification of the actual HVS test, which is three-dimensional in nature. To render the strain calculated in a 2-D FEM model approximately equal to the actual strain occurring in the overlay during the HVS tests, the load pressure was scaled by a factor. This load pressure scale factor is calculated as the ratio between actual surface deflection measured by the RSD and the calculated surface deflection from 2-D FEM analysis. When measured surface deflections were not available, they were replaced by values calculated using multilayer elastic theory using *ELSYM5* with the underlying cracks ignored. In the HVS simulations for this project, load pressure scale factors were mostly around 0.20. This procedure was shown to work well by Wu (22).

Wander Characterization

During HVS tests, the load wheels wander transversely in 50-mm increments. The change in strain on the longitudinal plane of symmetry during this wander therefore needs to be considered since the 2-D FEM model represents this plane of an HVS test section. Time-consuming 3-D FEM analyses can be used for this assessment. As an alternative, it was decided to determine whether the surface deflections on the longitudinal plane of symmetry change when the HVS wheels wander in the transverse direction. The underlying assumption is that similar surface deflections imply similar strain for a given structure.

Although the observations from the first-level analysis of the HVS tests indicated that surface deflections were significantly higher over cracked areas than over noncracked areas, FEM calculations showed that inclusion of cracks in the underlying asphalt concrete layer alone do not significantly increase surface deflection. In the FEM analyses, the increase in surface deflection was mostly attributed to the weaker supporting layers under the cracked areas rather than just the existence of the cracks. Accordingly, the overlay system could be analyzed using multilayer elastic theory, and it was not necessary to include the cracks when calculating surface deflections.

The dual HVS wheels each have a tread width of 205 mm, and the distance between the centers of the two wheels are 365 mm. The overall width of the dual wheels is thus 570 mm. Considering the HVS test section is 1,000 mm wide, the largest transverse distance between the center of the test section and the center of the HVS wheel set can be calculated as 215 mm. Figure 5.7 illustrates the variation of surface deflection for Section 588RF with respect to the transverse distance between the center of the HVS wheel set and the center of the test section. According to Figure 5.7, the surface deflection on the longitudinal plane of symmetry decreased by a maximum of about six percent (which is insignificant) from the reference value, which corresponds to the case when the HVS wheel set is centered on the test section. This implies that the effect of HVS wheel wander on the longitudinal centerline of the section can be

ignored for Section 588RF. Calculation for other HVS sections yielded similar results and it was decided that the effect of wheel wander could be ignored when simulating reflective cracking on the longitudinal plane of symmetry for all of the HVS tests in the project.

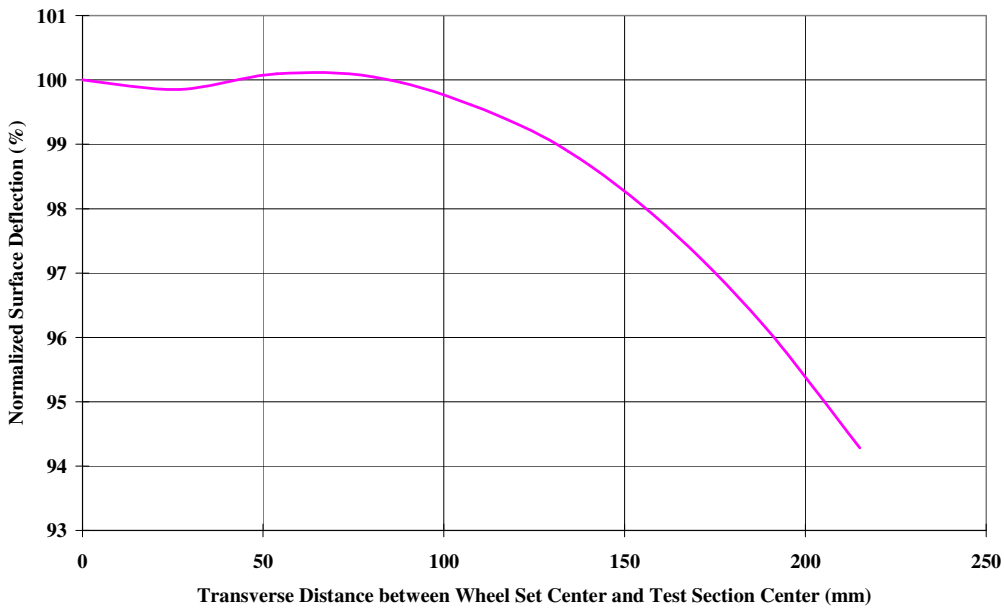

Figure 5.7: Surface deflection corresponding to different transverse HVS wheel locations.
(Surface deflection corresponding to the point when the HVS wheel set was centered in the transverse direction on the test section was used as the reference value for normalization.)

Accounting for Wheel Movements in the Longitudinal Direction

HVS wheels apply a dynamic load on pavement systems. The inertia effect of the dynamic wheel load was ignored because the wheels were moving at relatively constant speeds except when changing direction at the ends of the test section. The speed of the HVS wheels affect the loading time was accounted for as discussed previously.

An additional effect of the moving wheel is that different points in the overlay do not reach maximum strain simultaneously. This implies that fixing wheels at any specific location may lead to an underestimation of the strain field and hence underestimation of the damage rate. The detailed procedure used to account for this effect of moving wheels can be found in Wu 2005 (22). In summary, the maximum strain that any point experiences during a passage of the wheels is used to drive the damage evolution at that point in the FEM simulations.

5.4. First-Stage Simulation Results

This section presents results from the first-stage simulations. As discussed, the main purpose for these simulations is to validate the FEM procedure. The criterion for validation is that reflective cracking life predicted by simulation should match the observed value with reasonable accuracy.

5.4.1 Comparison Between Observed and Predicted Reflective Cracking Life

Reflective cracking life is defined for this study as the time required for cracks to appear on the surface of an overlay. Comparisons of observed and predicted reflective cracking lives for different HVS test sections are listed in Table 5.11. As shown in the table, the predicted (calculated) reflective cracking lives are not exactly the same but the differences between them are mostly within 0.3 million repetitions when they can be calculated. For sections that did not reach the end of their reflective cracking lives in the HVS tests, namely sections 586RF, 589RF, 590RF, and 591RF, the predicted reflective cracking lives are mostly compatible with the observations. Although some of the predictions differ from the observed values by up to 50 percent (e.g., Stations 8, 10, and 12 for Section 588RF), they are still regarded as reasonable because the absolute errors are still relatively small. It is concluded that the simulation procedure generally provides reasonable predictions for reflective cracking lives on asphalt concrete overlays with structures similar to those tested in this project.

Table 5.11: Reflective Cracking Life for Different HVS Sections

Section	Parameter	Reflective Cracking Life (x 1,000,000 Repetitions)				
		Station 4	Station 6	Station 8	Station 10	Station 12
586RF (MB15-G)	Observed	No crack after 2.49 million load repetitions				
	Calculated	No crack after 10.0 million load repetitions				
587RF (RAC-G)	Observed	1.52	1.49	1.55	2.08	2.94
	Calculated	1.52	1.72	1.52	1.82	1.89
588RF (AR4000-D)	Observed	0.51	>1.4	0.51	0.51	0.51
	Calculated	0.48	0.94	0.31	0.21	0.26
589RF (MB4-G)	Observed	No crack after 2.09 million load repetitions				1.6
	Calculated	3.19	4.44	3.59	2.03	1.49
590RF (MB4-G)	Observed	No surface crack after 1.98 million load repetitions				
	Calculated	2.35	2.24	1.84	1.63	1.63
591RF (MAC15-G)	Observed	No surface crack after 2.55 million load repetitions				
	Calculated	2.92	2.77	2.67	3.31	3.03

5.4.2 Crack Propagation History Plots

During simulations of all of the HVS sections except 586RF, cracks initiated from the bottom of the overlay and propagated upward until they reached the surface. In other words, all of the simulated cracks in the HVS sections were bottom-up cracks except 586RF, which had no crack initiation after 10 million load repetitions.

Crack propagation history plots are shown in Figures 5.8 through 5.12 for all the HVS tests. In these figures, the height of the crack tips was plotted against the number of load repetitions. Note that crack height was calculated using the bottom of the overlay as the reference. These figures show that reflective cracking performance can vary significantly even for different locations within the same HVS test section. This variation stems from the fact that the conditions of the underlying layers varied among the different stations within each test section.

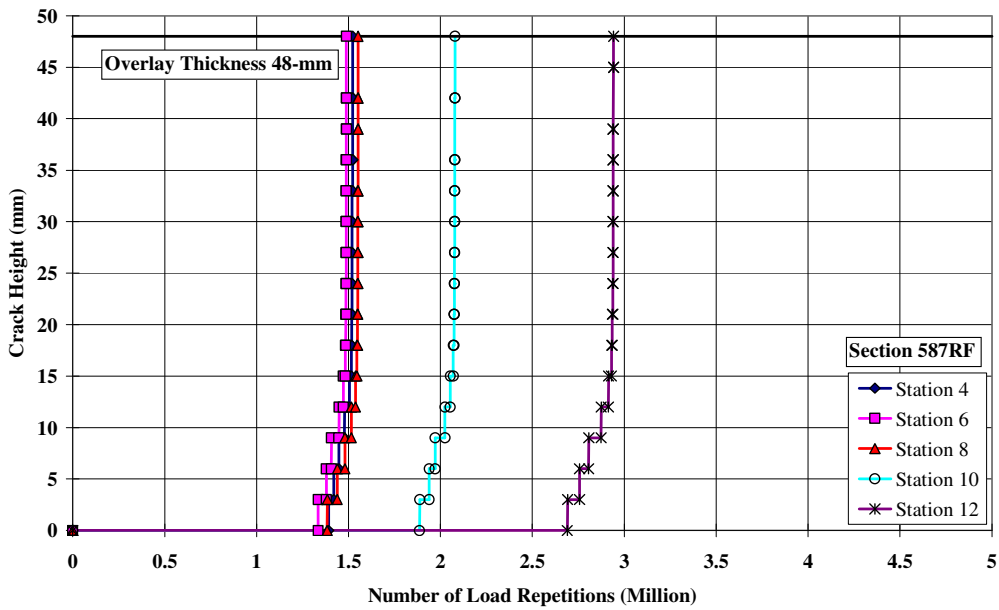

Figure 5.8: Evolution of crack tip height with load repetitions for Section 587RF (RAC-G).

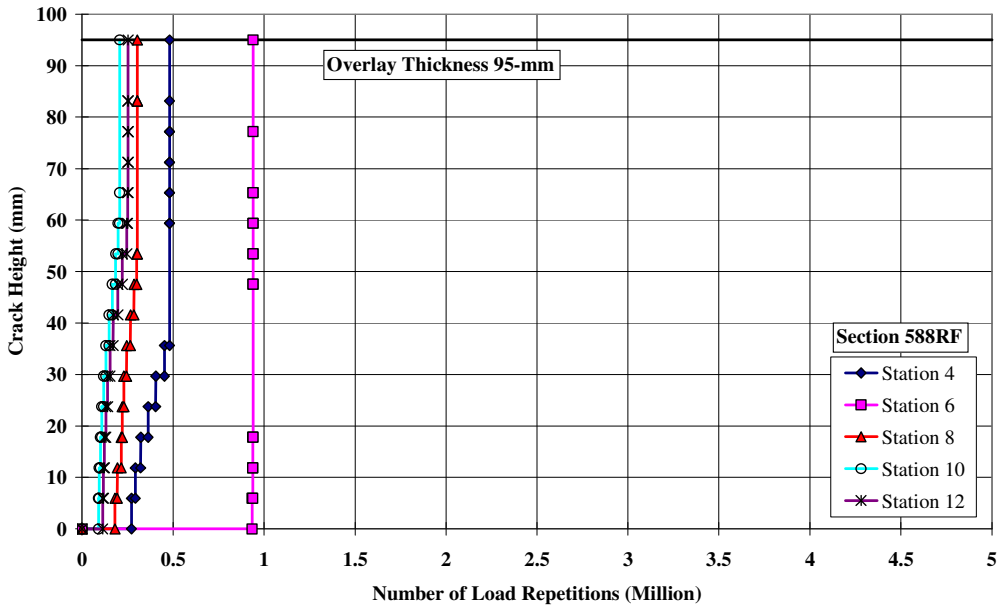

Figure 5.9: Evolution of crack tip height with load repetitions for Section 588RF (AR4000-D).

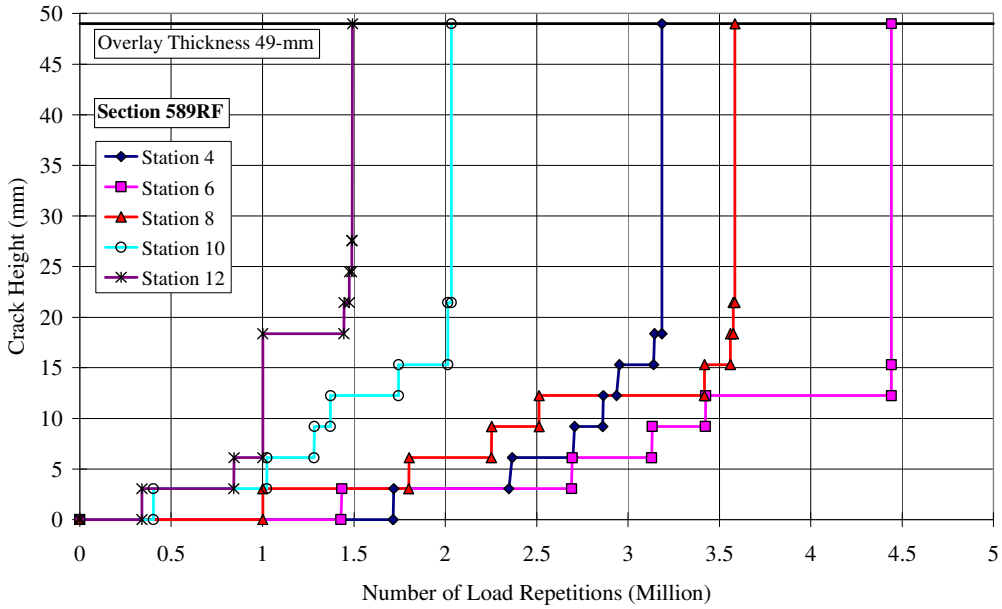

Figure 5.10: Evolution of crack tip height with load repetitions for Section 589RF (45mm MB4-G).

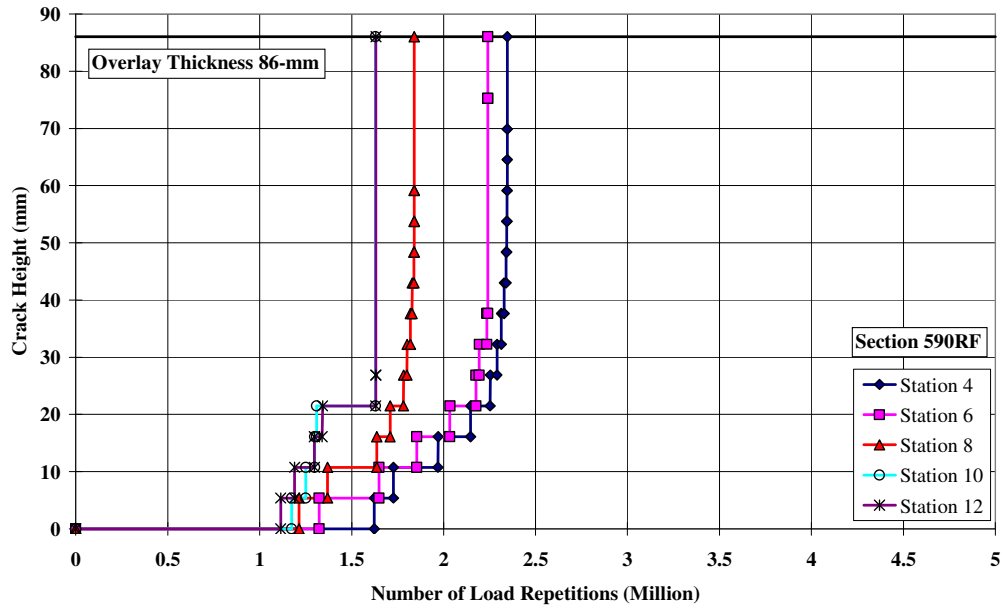

Figure 5.11: Evolution of crack tip height with load repetitions for Section 590RF (90mm MB4-G).

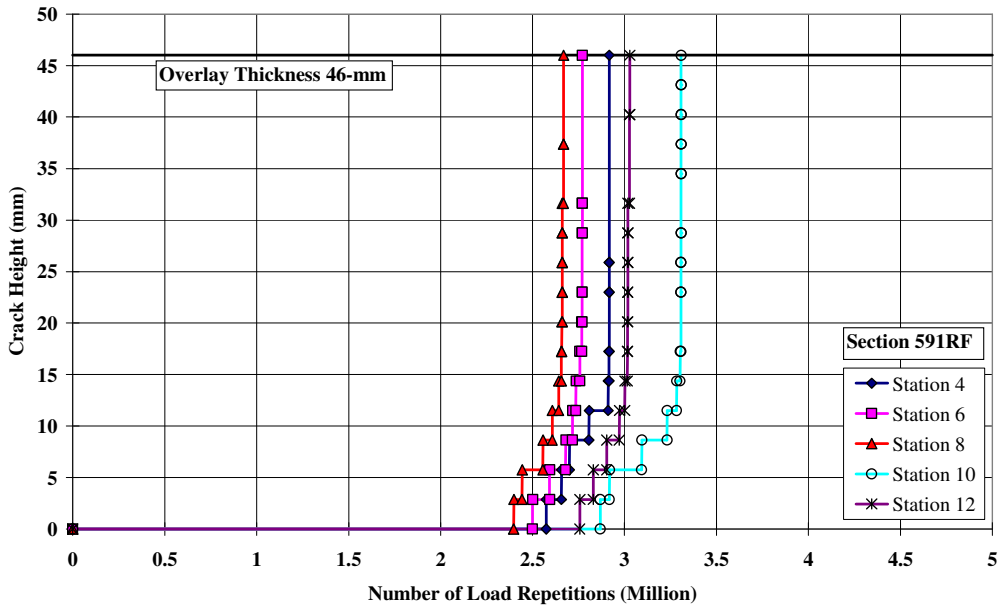

Figure 5.12: Evolution of crack tip height with load repetitions for Section 591RF (MAC15-G).

5.4.3 Summary of Simulation Results

Based on the results presented above, the simulation procedure was found to predict the reflective cracking lives of asphalt concrete overlays in the project with reasonable accuracy. It was also found that the difference in the underlying pavement layers led to significantly different reflective cracking performances within each test section. It is therefore important to account for the effect of underlying layers when comparing the reflective cracking performance of different overlays.

5.5. Second-Stage Simulations and Ranking of Cracking Performance

The procedure validated in the first-stage simulations was used to predict the reflective cracking performance of different asphalt concrete overlays placed on identical underlying layers and with exactly the same temperatures and loading sequences. As discussed in Section 5.1, these analyses are referred to as second-stage simulations and are used to rank the relative performance of the different asphalt concrete overlays used in this study with respect to reflective cracking.

5.5.1 Methodology

In order to rank reflective cracking performance, different overlays were placed on identical underlying structures and their reflective cracking lives calculated using the procedure validated in the first-stage simulations. Different underlying structures were included to determine the sensitivity of the performance

ranking with respect to overlay thickness and aggregate base stiffness. These input variations are summarized in Table 5.12 and all fixed input variables are listed in Table 5.13.

Table 5.12: Variable Inputs Used in Stage 2 Simulations

Input Variable	Variations	Number of Levels
Mix Type	AR4000-D, RAC-G, MB4-G, MB15-G, MAC15-G	5
Overlay Thickness (mm)	45, 90	2
Base Stiffness (MPa)	300, 150, both degraded to 80	2
Total		20

Table 5.13: Fixed Inputs Used in Stage 2 Simulations

Parameter	Value
Loading	As for Section 588RF, but trafficking continues until overlay fails
Pavement temperature	20°C
Mix air-void content	6%
Mix aging	No aging
Mix gradation	DGAC for AR4000, gap-graded AC for all others
Mix preparation method	Field-mixed, lab-compacted (FMLC)
Underlying DGAC stiffness	30% of intact stiffness
Crack spacing	100 mm
Underlying DGAC thickness	90 mm
Aggregate base thickness	400 mm
Stiffness of top 400 mm of subgrade	50 MPa
Stiffness of remaining subgrade	300 MPa

5.5.2 Simulation Results

The effects of overlay thickness on reflective cracking life are shown in Figure 5.13. Increasing the overlay thickness from 45 mm to 90 mm increases the reflective cracking life by between 30 and 70 percent for all the mixes except the AR4000-D, the reflective cracking life of which is essentially the same for both overlay thicknesses. This indicates that the benefits of increasing the overlay thickness from 45 mm to 90 mm are insignificant and cannot be distinguished by the model used.

The effects of aggregate base stiffness are shown in Figure 5.14. As shown, increasing the base stiffness (from 150 MPa to 300 MPa) increases reflective cracking lives significantly for all the asphalt concrete mixes. Improvement ranges from 80 percent increase in life for the AR4000-D mix to 230 percent for the MAC15-G mix.

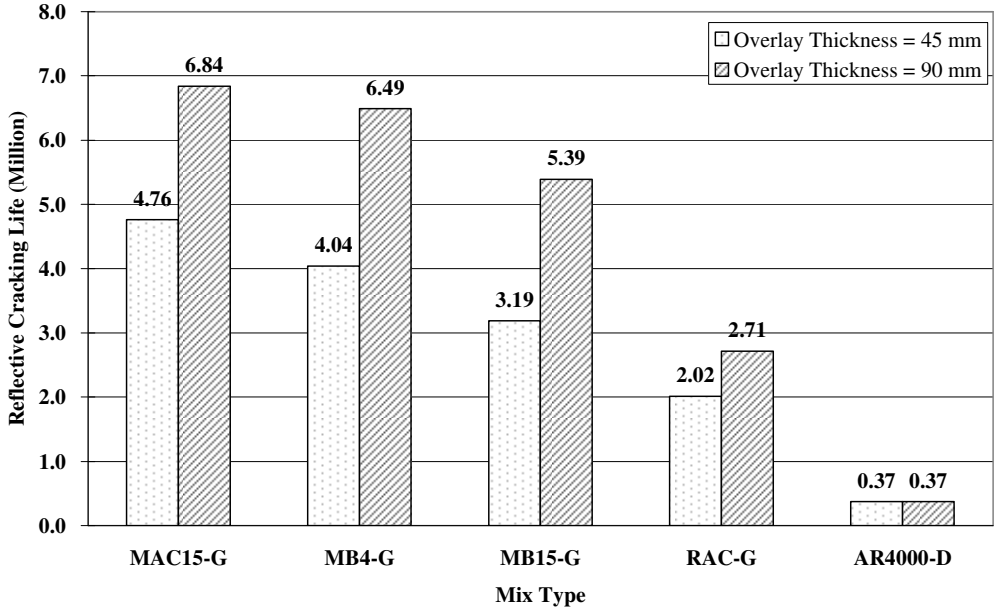

Figure 5.13: Effects of overlay thickness on reflective cracking life for different mixes.

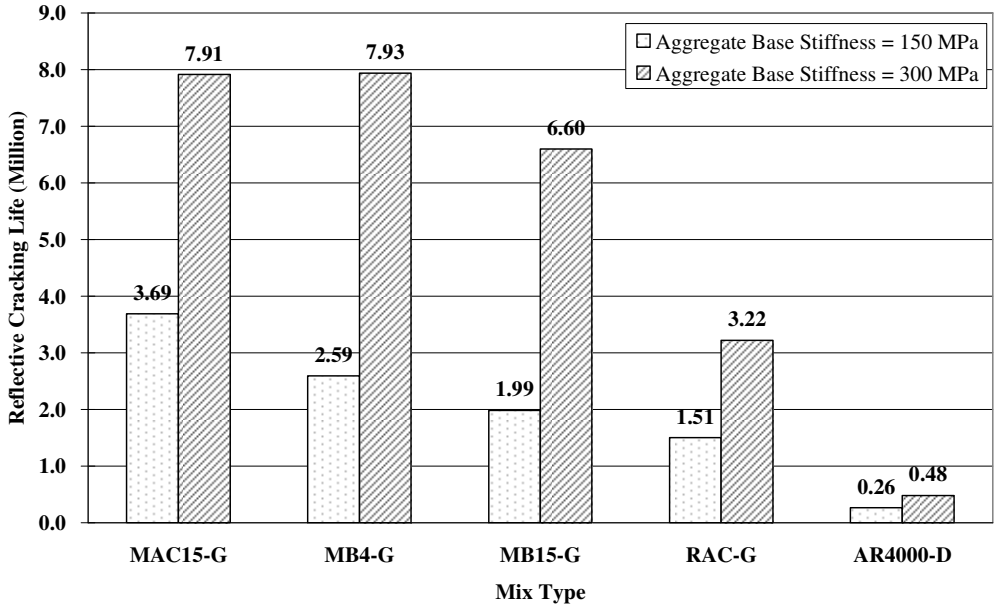

Figure 5.14: Effects of base stiffness on reflective cracking life for different AC mixes.

According to the results shown in Figure 5.13, increasing the asphalt concrete overlay thickness from 45 mm to 90 mm is not as effective in improving reflective cracking performance as increasing the base stiffness from 150 to 300 MPa. The overall ranking of reflective cracking performance is listed in Table 5.14.

Table 5.14: Ranking of Reflective Cracking Performance of Asphalt Concrete Mixes
(based on simulations and uniform conditions)

Performance Ranking (Best to Worst)	Overlay Mix Type	Normalized Reflective Cracking Life
1	MAC15-G	1.00
2	MB4-G	0.91
3	MB15-G	0.74
4	RAC-G	0.41
5	AR4000-D	0.06

5.6. Extrapolation to Field Conditions and Sensitivity Analyses

In this section, the analysis procedure calibrated in the previous sections was used to simulate reflective cracking performances of the different asphalt concrete overlays under various field conditions. The purpose of this is to evaluate the reflective cracking performance of different asphalt concrete mixes, including MB and MAC binders in dense-graded mixes, under different combinations of climate zone, layer thickness, traffic speed, and underlying structure type (cracked asphalt concrete vs. cracked portland cement concrete). This third-stage set of simulations provides general guidelines for using the different asphalt concrete mixes under investigation in this project.

5.6.1 Methodology

Two groups of simulations were performed in the extrapolation and sensitivity analyses. The mix types, climate conditions, and structure types considered are listed in Table 5.15. Mix types are identified by binder type (AR4000, RAC [Asphalt Rubber Binder], MB4, MB15, and MAC15), aggregate gradation type (dense-graded [D], and gap-graded [G]), and mix preparation method (field-mixed, lab-compacted [F], and lab-mixed, lab-compacted [L]). Simulations in Group B were limited to a constant 20°C climate condition because laboratory fatigue tests for mixes used in the group were conducted only at this temperature.

Table 5.15: Factors Considered in the Extrapolation and Sensitivity Analyses

Group	AC Mix Types*	Structure Type	Climate Conditions
A	AR4000-D-F RAC-G-F MB4-G-F MB15-G-F MAC15-G-F	1. AC-over-AC overlay 2. AC-over-PCC overlay	Central Valley, Desert, and South Coast
B	AR4000-D-L RAC-G-L MB4-D-L MB15-D-L MAC15-D-L MB4-G-L MB15-G-L MAC15-G-L	1. AC-over-AC overlay 2. AC-over-PCC overlay	20°C constant

* Mix types identified by binder (AR4000, RAC, MB4, MB15, and MAC15), aggregate gradation (dense-graded [D], and gap-graded [G]), and mix preparation method (field-mixed, lab-compacted [F], and lab-mixed, lab-compacted [L]).

The following additional input parameters were considered:

- Highway traffic was represented by ESAL (i.e., 80 kN single axle dual wheel).
- Traffic speed was either 10 km/h or 70 km/h. Traffic speed affects loading time, which in turn affects asphalt concrete stiffness.
- Damage evolution parameters for asphalt concrete mixes were assumed to be independent of loading time and were only affected by pavement temperature. Accordingly, these parameters were determined by piecewise linear interpolation/extrapolation using pavement temperature as the independent variable.
- Air-void content was assumed to be six percent for all asphalt concrete mixes.
- No aging was considered.
- Aggregate base and subgrade were characterized in the same way as described previously, but were not subjected to stiffness degradation.
- For the different climate zones considered in the Group A simulations, pavement temperatures were assumed to be constant for a 24-hour cycle within each month and there was no year-to-year change. Monthly average temperatures were calculated using BELLS equation (20, 24) with parameters determined from thirty years of Enhanced Integrated Climate Model (EICM) simulations (25).
- The time that pavements are opened to traffic is important for Group A simulations because of the difference between summer and winter climatic conditions, specifically temperature. All of the simulations in this group start in July. Monthly traffic volumes are assumed to be constant.
- The cracking life of a pavement in this simulation was defined as the time required for cracks to appear on the pavement surface. For most of the overlay cases, this is the time required for cracks in the underlying layer to propagate from the bottom to the surface of the overlay. In some cases, simulation results indicate that cracks initiated at the pavement surface (i.e., top-down cracking).
- Cracking simulations were run for 15 years of traffic using a ten-year traffic index (TI) of 15 to calculate the upper limit of traffic for simulations in Group B.

It is important to note that the simulations did not include strains induced by temperature gradient or daily and seasonal temperature variations. Rutting and distresses other than cracking were not included in the simulations.

5.6.2 Parameters for Different Groups of Simulations

<u>Group A1: Asphalt Concrete-over-Asphalt Concrete Overlays with FMLC Mix</u>

Parameters of the underlying pavement structure for this set of simulations are listed in Table 5.16, while variations of different variables considered in the simulations are listed in Table 5.17. This set of

simulations essentially represents asphalt concrete overlays placed on extensively cracked old asphalt concrete pavement.

Table 5.16: Common Variables for the Reference Simulation Case

Parameter	Value
Underlying old AC stiffness (MPa)	3,300
Crack spacing (mm)	100
Crack opening (mm)	3
Old DGAC thickness (mm)	150
Aggregate base thickness (mm)	300
Aggregate base stiffness (MPa)	108
Subgrade stiffness (MPa)	67.8

Table 5.17: Variations of Variables Considered for Group A1

Parameter	Design Points	Number of Levels
Mix type	MB4-G, MB15-G, MAC15-G, RAC-G, AR4000-D	5
Overlay thickness (mm)	45, 60, 90	3
Climate zones	Desert, Central Valley, South Coast	3
Traffic (TI for 10 years)	10, 11, 14	3
Wheel speed (km/h)	10, 70	2
Total number of simulations		270

Group A2: Asphalt Concrete-over-Portland Cement Concrete Overlays with FMLC Mix

This set of simulations considered the same variations of variables as in Group A1 (as listed in Table 5.17), except that the underlying asphalt concrete layer was replaced by a 200-mm thick portland cement concrete layer. Accordingly, the crack spacing was set at 3,500 mm and the crack/joint opening was assumed to be 5.0 mm.

Group B1: Asphalt Concrete-over-Asphalt Concrete Overlays with LMLC Mix

This set of simulations evaluates reflective cracking performance of different LMLC asphalt concrete overlays over old cracked asphalt concrete pavement. The underlying asphalt concrete pavement structure had the same parameters as listed in Table 5.16. The variations of variables considered are listed in Table 5.18.

Table 5.18: Variations of Variables Considered for Group B1

Variable	Design Points	Number of Levels
Mix type (LMLC)	MB4-D, MB15-D, MAC15-D, RAC-G, AR4000-D, MB4-G, MB15-G, MAC15-G	8
Overlay thickness (mm)	45, 60, 90, 120	4
Wheel speed (km/h)	10, 70	2
Total number of simulations		64

Group B2: Asphalt Concrete-over-Portland Cement Concrete Overlays with LMLC Mix

This set of simulations considered the same variations of variables as in Group B1 (as listed in Tables 5.16 and 5.18). In this group, the underlying asphalt concrete layer was replaced with a 200-mm thick portland

cement concrete layer. As with Group A2, the crack spacing was set at 3,500 mm and the crack/joint opening was assumed to be 5.0 mm.

5.7. Simulation Results

Simulation results for the various groups are discussed below. The predicted reflective cracking performance, performance design plots and associated performance rankings should be considered as relative.

5.7.1 FMLC Mix Performance in Different Climate Zones

The average relative reflective cracking life grouped by different factors is shown in the design plots, Figure 5.15 and 5.16. These are based on results from Groups A1 and A2. The type of underlying pavement (i.e., asphalt concrete or portland cement concrete) did not affect the relative ranking of reflective cracking performance of the different asphalt concrete mixes. The rankings were similar to those obtained from the HVS simulation results, except that the relative ranking between the RAC-G and MB15-G mixes was reversed. Overall, reflective cracking life increased with increasing traffic speed, cooler climate, and lower traffic volume. Note that the South Coast is cooler than the Central Valley because this region has approximately the same yearly average temperature, but the South Coast has a smaller yearly temperature variation. Figures 5.15 and 5.16 also indicate that changing the overlay thickness from 45 mm to 90 mm was less significant compared to traffic speed, climate zone, and traffic volume (TI for 10 years).

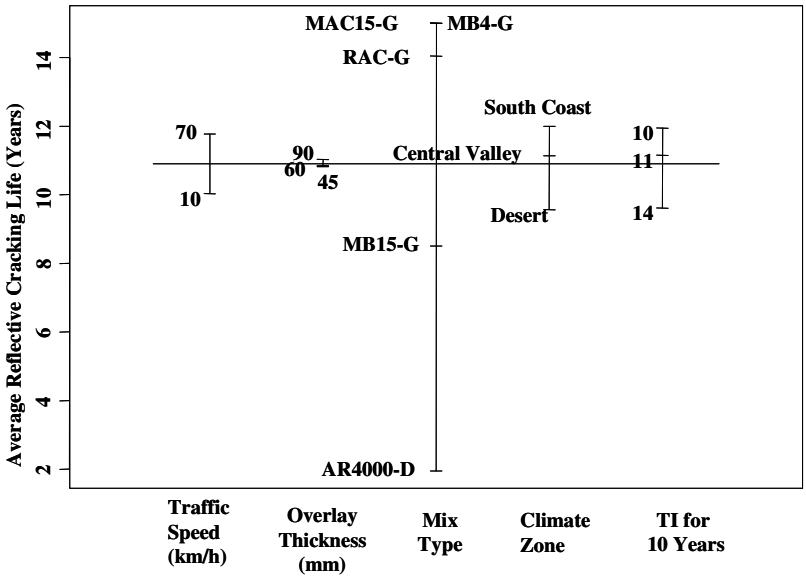

Figure 5.15: Design plot of reflective cracking life for AC-over-AC overlays with FMLC mixes.

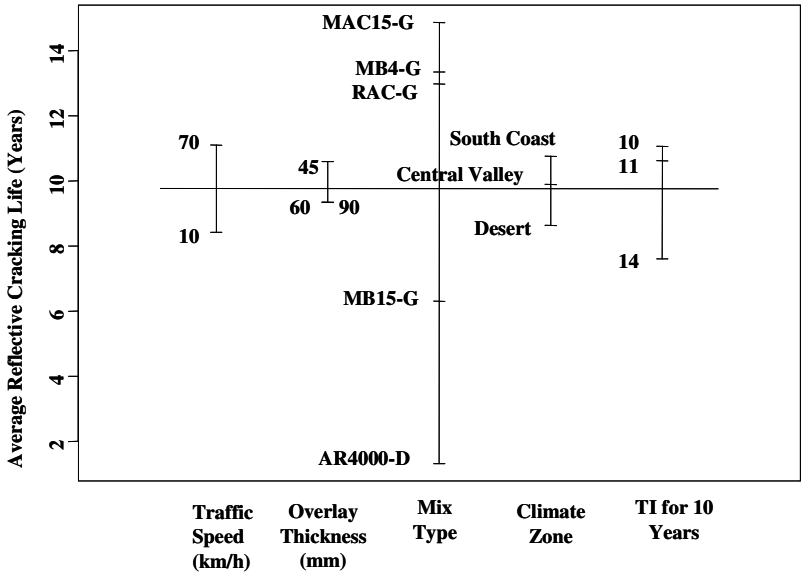

Figure 5.16: Design plot of reflective cracking life for AC-over-PCC overlays with FMLC mixes.

Relative reflective cracking performance of different FMLC-mix asphalt concrete overlays in different climate zones are shown in Figures 5.17 and 5.18 in the form of bar charts. The range of reflective cracking life is also indicated in these charts using range bars (vertical lines and horizontal whiskers) showing minimum and maximum values. The figures show that all the mixes perform approximately the same in the three different climate zones. The only exceptions are the MB15-G and AR4000-D mixes, which show significant decreases in reflective cracking life under desert climate compared to the other two climate zones.

Figures 5.19 and 5.20 show the relative reflective cracking performance of FMLC mixes in asphalt concrete overlays grouped by overlay thickness. Increasing the thickness was not always beneficial for modified binders, although it always improved the performance of the conventional AR4000-D mix. For the simulations, increasing overlay thickness implies a slightly longer loading time, resulting in a less stiff overlay. This could offset the benefit of a longer propagation path for thicker overlays. Adding thickness to low-stiffness mixes, such as those of 90 mm or less used in this factorial, did not change the strain significantly.

Figures 5.21 and 5.22 illustrate the relative reflective cracking performance of FMLC mixes in asphalt concrete overlays grouped by Traffic Index (TI) for 10 years. As expected, reflective cracking life decreased as traffic volume increases.

Figures 5.23 and 5.24 show the relative reflective cracking performance of FMLC mixes in asphalt concrete overlays grouped by highway traffic speed. As expected, reflective cracking life increased as

traffic speed increased because of higher stiffnesses for the asphalt concrete mixes due to shorter loading time. According to the figures, increasing the traffic speed from 10 km/h to 70 km/h approximately doubled the reflective cracking life for the AR4000-D and MB15-G mixes. The reflective cracking life for MB4-G, MAC15-G, and RAC-G were less sensitive to traffic speed.

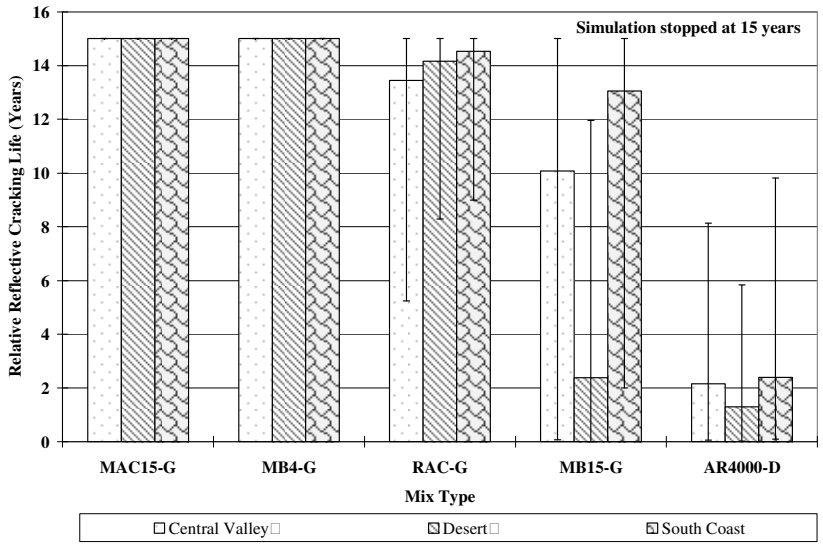

Figure 5.17: Performance of FMLC mixes in AC-over-AC overlays, grouped by climate zone.

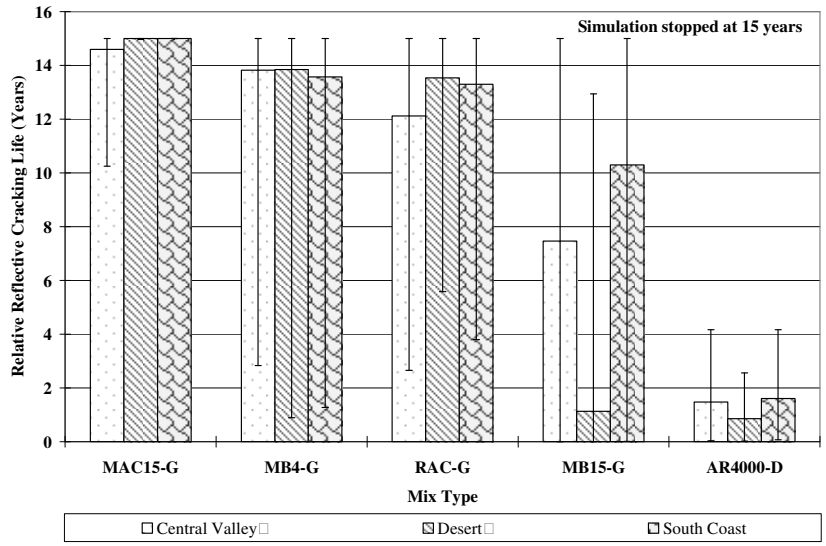

Figure 5.18: Performance of FMLC mixes in AC-over-PCC overlays, grouped by climate zone.

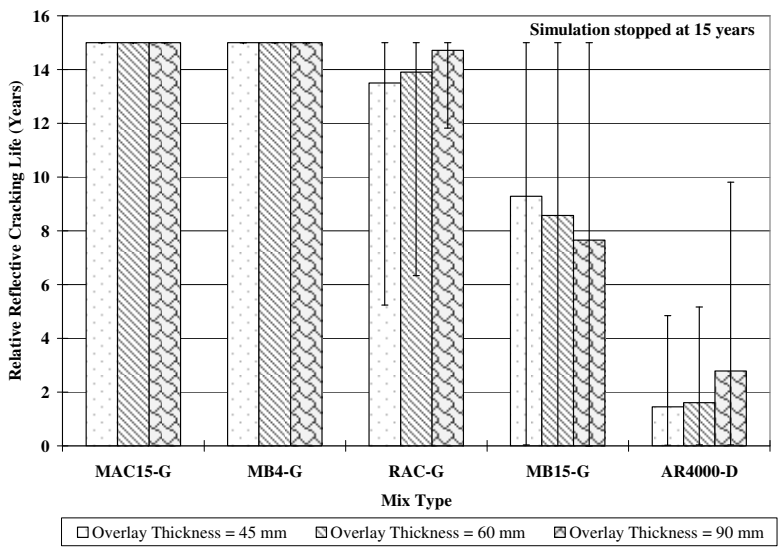

Figure 5.19: Performance of FMLC mixes in AC-over-AC overlays, grouped by overlay thickness.

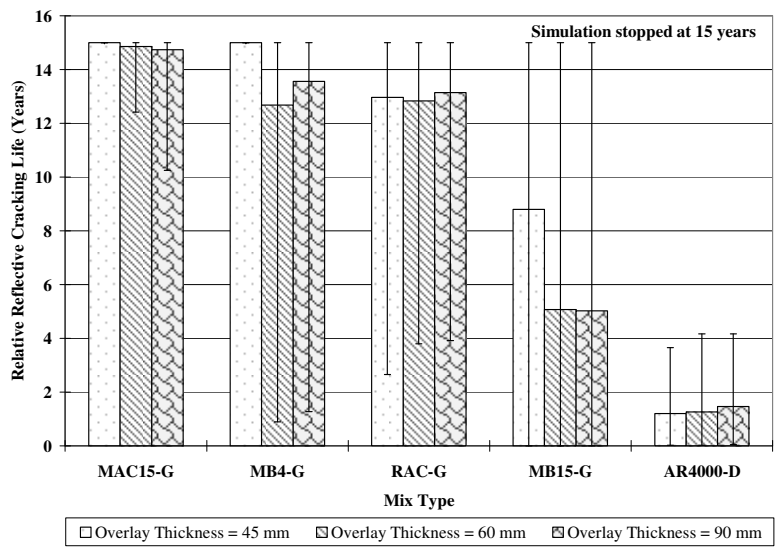

Figure 5.20: Performance of FMLC mixes in AC-over-PCC overlays, grouped by overlay thickness.

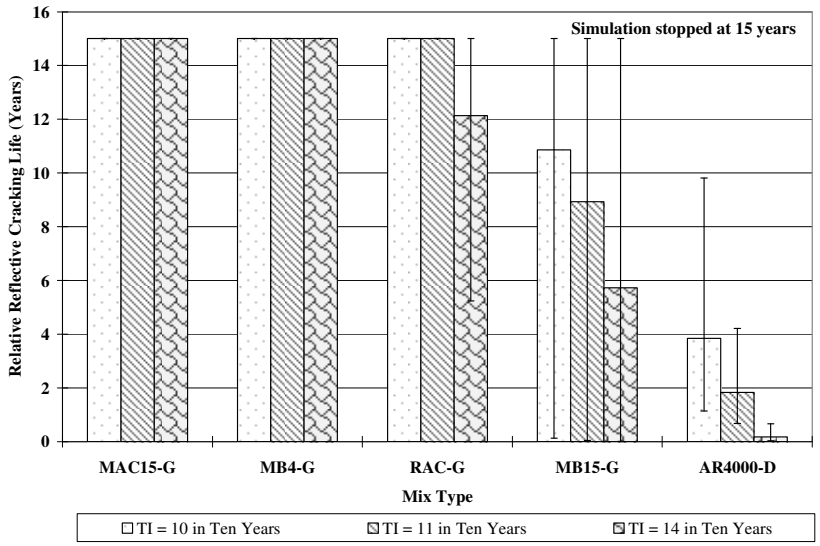

Figure 5.21: Performance of FMLC mixes in AC-over-AC overlays, grouped by TI for 10 years.

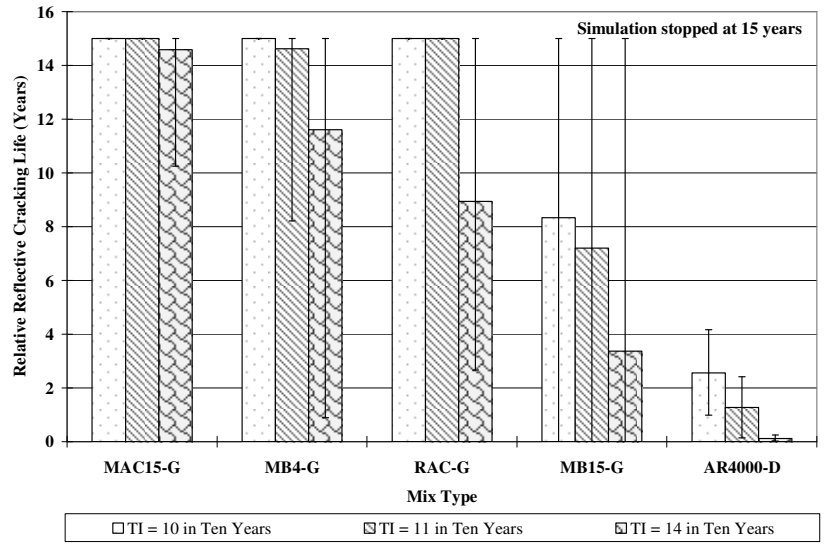

Figure 5.22: Performance of FMLC mixes in AC-over-PCC overlays, grouped by TI for 10 years.

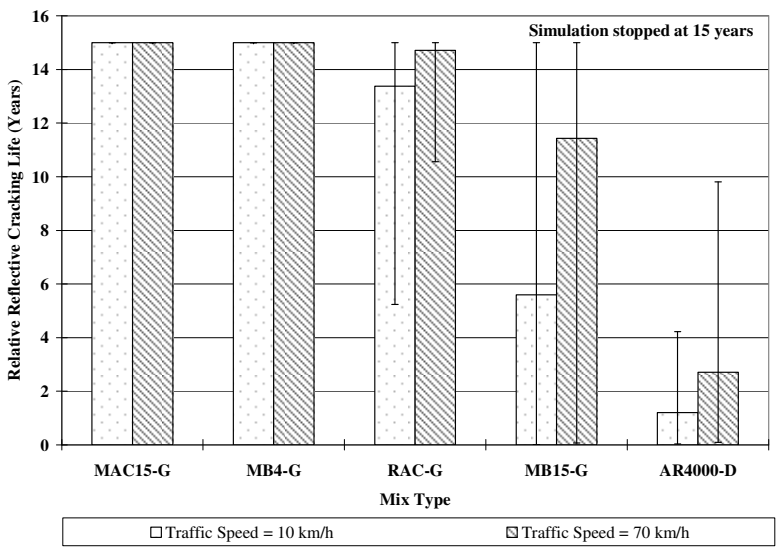

Figure 5.23: Performance of FMLC mixes in AC–over-AC overlays, grouped by traffic speed.

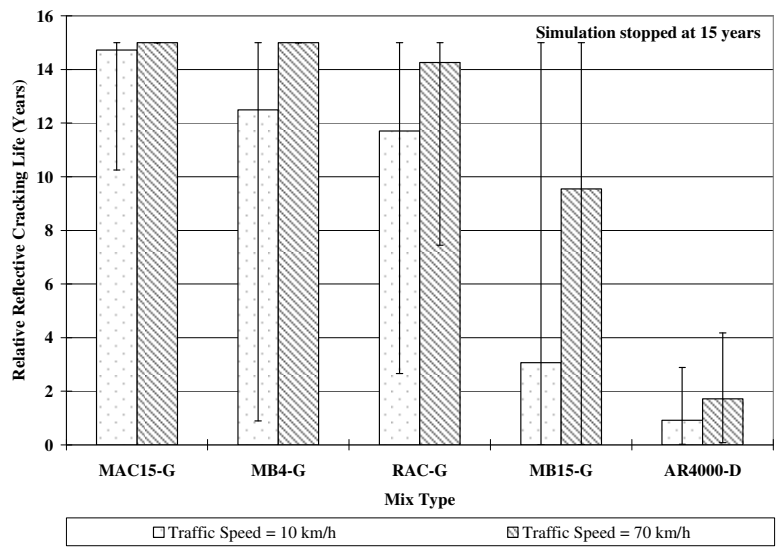

Figure 5.24: Performance of FMLC mixes in AC-over-PCC overlays, grouped by traffic speed.

5.7.2 LMLC Mix Performance in Overlays at 20°C

This section presents results from simulation groups B1 and B2 (i.e., LMLC mix used in asphalt concrete overlays on either asphalt concrete or portland cement concrete pavements). Note that in this section, mixes using modified binders (including MAC15, MB4, and MB15) were prepared with both dense-graded and gap-graded mixes, which differs from those mixes used in simulation Group A, where dense-graded mixes were not used with the modified binders. The average relative reflective cracking life grouped by different factors is shown in the design plots, Figures 5.25 and 5.26. Overall, reflective cracking life increased with increasing traffic speed and increasing overlay thickness. The effect of overlay thickness (which varied from 45 mm to 120 mm) was less significant than that of traffic speed (which varied from 10 km/h to 70 km/h).

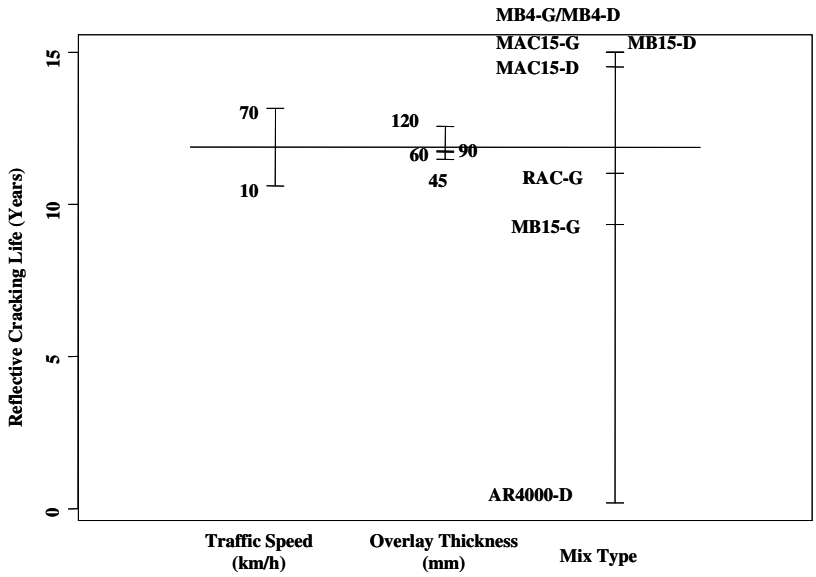

Figure 5.25: Design plot of reflective cracking life for AC-over-AC overlays with LMLC mixes.

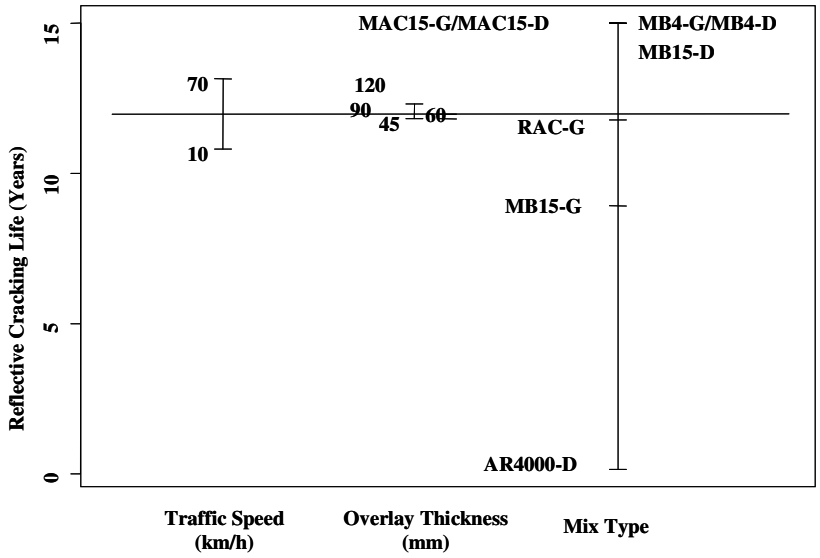

Figure 5.26: Design plot of reflective cracking life for AC-over-PCC overlays with LMLC mixes.

Figures 5.27 and 5.28 illustrate the relative reflective cracking performance of LMLC mixes in asphalt concrete overlays at 20°C grouped by overlay thickness. Several observations can be made based on the two figures:

- As expected, reflective cracking life generally increased with overlay thickness except for the MB15-G overlay. This anomaly is attributed to the MB15-G being significantly softer than the other mixes.
- For mixes using rubber-modified binders (i.e., MB4-D, MB4-G, MB15-D, MB15-G, MAC15-D, and MAC15-G), dense aggregate gradation was beneficial for softer mixes (e.g., MB15), while gap gradation was beneficial for stiffer mixes (e.g., MAC15) with respect to reflective cracking performance.
- Four mixes including MB4-D, MB4-G, MB15-D, and MAC15-D did not fail in reflective cracking after fifteen years of traffic. Mixes with rubber-modified binders generally performed better than the RAC-G and AR4000-D mixes.
- For overlays using the RAC-G mix, a critical thickness exists above which increasing the overlay thickness becomes considerably more effective in increasing reflective cracking life. This critical thickness is between 90 mm and 120 mm.

Figures 5.29 and 5.30 show the relative reflective cracking performance of LMLC mixes in asphalt concrete overlays at 20°C grouped by highway traffic speed. As expected, reflective cracking life increases as traffic speed increases because of the higher stiffness for asphalt concrete mixes related to shorter loading time. According to the figures, increasing the traffic speed from 10 km/h to 70 km/h approximately doubles the reflective cracking life for the AR4000-D and RAC-G mixes, while the reflective cracking life for the MB4-D, MAC15-D, and MB15-D mixes were not sensitive to traffic speed.

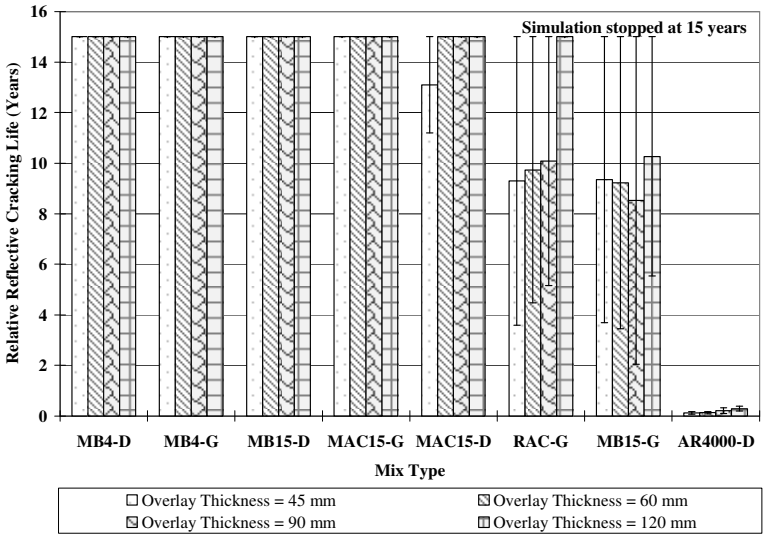

Figure 5.27: Performance of LMLC mixes in AC-over-AC overlays, grouped by overlay thickness.

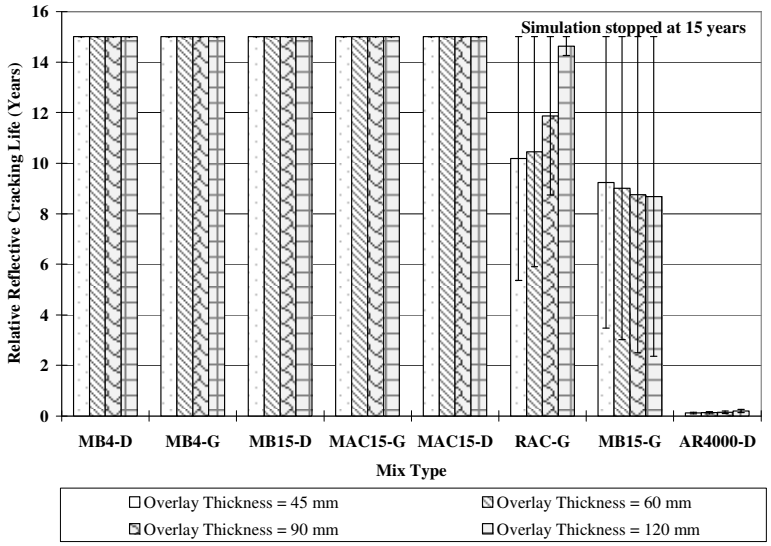

Figure 5.28: Performance of LMLC mixes in AC–over-PCC overlays, grouped by overlay thickness.

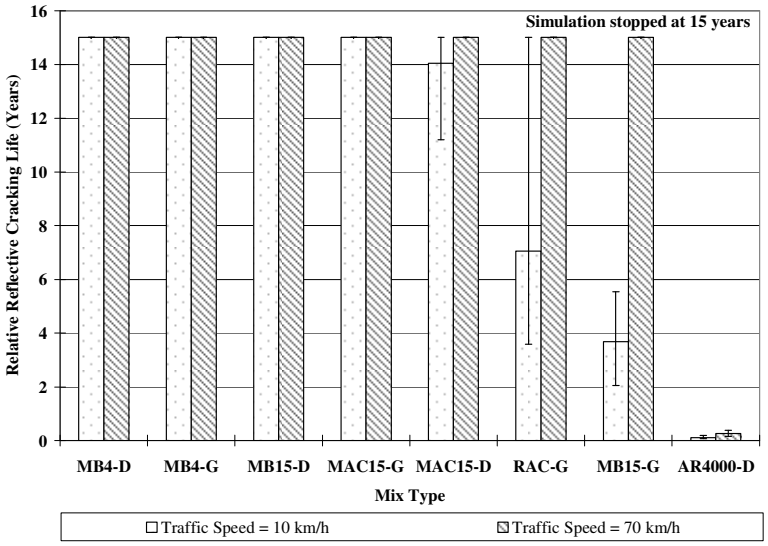

Figure 5.29: Performance of LMLC mixes in AC-over-AC overlays, grouped by traffic speed.

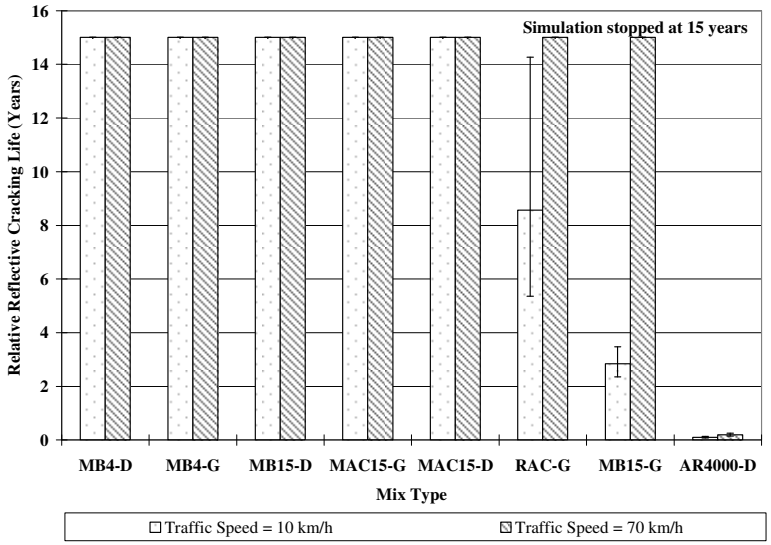

Figure 5.30: Performance of LMLC mixes in AC-over-PCC overlays, grouped by traffic speed.

5.8. Summary and Observations

5.8.1 Simulation of HVS Test Sections

Two kinds of analyses that use different types of simulations were used to re-create the cracking performance of the HVS test sections:

- Simulations used to validate an FEM-simulation procedure based on nonlocal continuum damage mechanics with actual input and performance data collected during HVS tests.
- Simulations used to predict reflective cracking performance of different mixes in asphalt concrete overlays under HVS testing conditions, using a uniform underlying structure, loading, and temperature regime.

The following observations were made based on the results from these simulations:

- The simulation procedure predicts the reflective cracking lives of asphalt concrete overlays in the project with reasonable accuracy. For tests with very short reflective cracking lives, the relative error in life prediction can be as high as 40 to 60 percent. These predictions are still regarded as reasonable because the absolute errors are still within 0.3 million load repetitions.
- Increasing the overlay thickness from 45 mm to 90 mm increases reflective cracking lives by 30 to 70 percent for all the mixes except AR4000-D, for which the reflective cracking life is essentially the same for both overlay thicknesses.
- Increasing aggregate base stiffness from 150 MPa to 300 MPa increases reflective cracking lives between 80 percent and 230 percent.

The overall relative ranking of different mixes used in the project with respect to reflective cracking under HVS testing conditions is, from best to worst:

1. MAC15-G
2. MB4-G
3. MB15-G
4. RAC-G
5. AR4000-D

All the mixes containing rubber modified binders (i.e., MAC15-G, MB4-G, MB15-G, and RAC-G mixes) performed significantly better than the conventional AR4000-D mix.

5.8.2 General Simulations

Simulations were presented for predicting cracking performance of asphalt concrete overlays under various conditions different from those in the HVS tests. These simulations allow extrapolation of mix

performance in HVS tests to performance in the field. However, these results only provide a preliminary assessment of expected field performance, include the many limitations of the modeling, and should be checked with field results. Based on the results of the simulations, the following observations are made:

- For FMLC mixes in asphalt concrete overlays under field climate conditions:
  - The relative ranking with respect to reflective cracking under field conditions is the same as the ranking under HVS test conditions, with the only exception being the RAC-G and MB15-G mixes. RAC-G performed better than MB15-G in the field simulations but worse in the HVS tests.
  - AR4000-D and MB15-G mixes have significantly shorter reflective cracking life under the Desert climate than under South Coast and Central Valley climates. The other mixes do not appear to be sensitive to climate conditions.
  - Reflective cracking life is generally not sensitive to an increase in overlay thickness from 45 mm to 90 mm, and so increasing the overlay thickness from 45 mm to 90 mm will not necessarily result in a longer reflective cracking life.
  - Reflective cracking life decreases as traffic volume increases, but the life decreases at a rate much smaller than the increase in traffic volume.
  - Increasing traffic speed from 10 km/h to 70 km/h approximately doubles the reflective cracking life for AR4000-D and MB15-G mixes. However, the reflective cracking life for MB4-G, MAC15-G, and RAC-G mixes are less sensitive to traffic speed.
- For asphalt concrete overlays using LMLC mixes at 20°C:
  - Overlays with mixes using MB4, MB15, and MAC15 binders generally did not fail in reflective cracking after fifteen years of traffic, with the only exceptions being the MB15-G mixes, and MAC15-D mix.
  - A critical thickness exists below which increasing the overlay thickness does not influence reflective cracking life.
  - The effect of aggregate gradation on reflective cracking life depends on mix stiffness. Dense gradation is better for softer mixes (i.e., MB15), while gap gradation is better for stiffer mixes. For mixes that have adequate stiffness (i.e., MB4), aggregate gradation has no significant effect on reflective cracking performance.

6. CONCLUSIONS AND RECOMMENDATIONS

This report follows a series of seven first-level HVS testing reports, two laboratory reports on shear and fatigue testing, a forensic investigation report, and a report on the backcalculation of deflection measurements, all of which document an investigation undertaken to validate Caltrans overlay strategies for the rehabilitation of cracked asphalt concrete. It presents the findings from a detailed analysis of the laboratory fatigue and shear results, and a series of simulations using *CalME* mechanistic-empirical design software and continuum damage mechanics (CDM) implemented using a finite element method (FEM).

This work was conducted by the University of California Pavement Research Center as part of Partnered Pavement Research Center Strategic Plan Item 4.10: "Development of Improved Rehabilitation Designs for Reflective Cracking." This work was originally requested by the Caltrans/Industry Rubber Asphalt Concrete Task Group (RACTG), to compare the performance of one set of examples of thin overlays of cracked asphalt pavement, containing different types of binders modified with recycled tire rubber. This work, included as Appendix H of the Rubber Modified Binder Pilot Projects Review prepared by the RACTG is part of a more comprehensive work plan prepared by the Task Group that included evaluation of pilot projects and construction and monitoring of field test sections; which was not undertaken by UCPRC.

Five binders were assessed during the study, including MB4, MB4 with minimum 15 percent recycled tire rubber, MAC15TR with minimum 15 percent recycled tire rubber (all terminal blended), asphalt rubber binder (ARB) (field blended), and AR4000 (approximately equivalent to PG64-16). The asphalt rubber and AR4000 binders were included for control purposes.

6.1. Conclusions

The following conclusions are drawn from the results of this study, organized by the study objectives agreed to by the RACTG, and documented in the project work plan at the beginning of the study. All of these conclusions are based on the set of one example of each binder at one binder content, included in the experiment design.

Objective 1: Develop Improved Mechanistic Models of Reflective Cracking

Two sets of mechanistic-empirical models were developed for reflective cracking as part of this study:

- One set of models is based on the use of layer-elastic theory, and has been incorporated into the mechanistic-empirical pavement design and analysis software, *CalME* (final calculations were

made using Version December-2007. Version 1.0 will be delivered to Caltrans in June 2008 when documentation is completed). *CalME* is being developed under the technical supervision of a Caltrans technical working group under the direction of the Division of Design, and is intended to be used as a design and analysis tool by Caltrans engineers and their consultants.

- The second set of models, which does not have a formal name and is not intended as a full-scale design tool by Caltrans, is based on the finite element method and continuum damage mechanics. It is a more sophisticated method that provides greater insight into the crack propagation process and local-versus-global damage (i.e., damage under the wheel versus damage away from the wheel) than does the use of layer-elastic theory. However, it requires faster computation than can currently be accommodated in a design and analysis method to be used in practice. The findings from comparison of the results of modeling individual crack propagation with these models are being used to enhance the models used in *CalME.*

Objective 2: Calibrate and Validate Mechanistic Models

Results from a comprehensive HVS study, during which more than 15 million load repetitions equating to about 400 million Equivalent Standard Axle Loads, and a comprehensive laboratory study, during which about 400 Repeated Simple Shear and Flexural Fatigue Beam tests were completed, were used together with results from other studies to calibrate and verify the models discussed above. Conclusions for this objective include:

- Both mechanistic-empirical models described in Objective 1 were calibrated and validated using the laboratory and HVS data generated in this study, as well as several data sets from other HVS tests and test tracks. The calibrations resulted in models that predicted the performance of the sections in terms of calculated versus measured deflections, changes in stiffnesses, and ranking of reflective cracking performance. The overall approaches were validated when it was shown that use of the same calibrated coefficients across all the different tests sections resulted in a good match between predicted performance and measured performance.
- It was found during calibration that bonding was a significant variable in predicting the actual performance of several HVS test sections where forensic evidence showed that layers had become unbonded. The reason for the debonding is uncertain because a tack coat was applied. This conclusion emphasizes the need for continued use and improvement of effective bonding strategies. It also emphasizes the need for mechanistic-empirical analysis methods to explicitly consider the extent of bonding.
- The methods of characterizing the fatigue damage process in the mechanistic-empirical design models developed in this project were successful in predicting the performance of mixes with modified and rubberized binders. The fatigue damage curve characterization of laboratory data

and the incremental-recursive damage updating approach successfully modeled the significantly better crack propagation resistance of these mixes. In particular, the modified binder mixes tended to have laboratory fatigue damage curves that showed a decreasing rate of damage during propagation, whereas the conventional AR4000 dense-graded mix had an increasing damage rate during the propagation phase. This is a significant improvement over traditional mechanistic-empirical analysis approaches, which tended to under-predict the reflective cracking performance of these mixes.

- A forensic investigation of the HVS rutting tests showed that most of the shear deformation actually occurred in the underlying asphalt concrete layer and not in the overlays, although the ranking of the total HVS rutting followed the laboratory shear deformation resistance test results of the overlay mixes. The mechanistic-empirical models for rutting of the asphalt layers predicted the overall rutting performance ranking of each section, but did not fully capture the distribution of rutting between the overlay and the underlying asphalt layers. It is not clear whether the relative lack of aging and trafficking of the underlying asphalt layers (light car traffic and fewer than five delivery trucks per day at the HVS test site over three years) before placing the overlay influenced this behavior. It is also not clear whether this phenomenon occurs on in-service pavements, where longer loading periods, lighter traffic loads, and more years of age-hardening in the underlying asphalt layers differentiate them from HVS tests. These HVS results and model predictions suggest the need for forensic investigation of several rutted field pavements with thin rubberized and modified binder mixes.

Objective 3: Evaluate the Most Effective Strategies for Reflective Cracking

A more detailed analysis of the laboratory results and a series of simulations with the calibrated mechanistic-empirical models were used to evaluate which strategies had the best reflective cracking performance. Conclusions for this objective include:

- Second-level analysis of the fatigue and shear laboratory test data using three-stage Weibull analysis identified significant differences in the crack initiation and propagation performance, and the shear deformation resistance of the different mixes under various conditions. The performance with respect to fatigue and shear were combined using similar parameters into a single plot. This approach can be used in the future by designers in the consideration of relative risk of fatigue and shear, and in considering the effects of aging and gradation. This is an improvement on past strategies which do not always optimize both shear and fatigue performance aspects for a given application.
- Although the shear test results correlated well with the observed rutting performance under the HVS, the results showed the importance of using mechanistic-empirical analysis to develop

rutting- and cracking-performance estimates that consider the overlay material as well as its interaction with the rest of the pavement structure, instead of using only laboratory data.

- Controlled-deformation fatigue beam testing used in this project was also found to match the reflective cracking of thin overlays for the structures tested by the HVS. However, the ranking of fatigue beam tests and predicted or actual field performance of thicker overlays and/or different pavement structures may differ because of interaction of the overlay with the pavement structure.
- The results of a limited exploratory laboratory experiment (included in the approved work plan) using modified binders in dense-graded mixes indicate that these mixes have lower cracking resistance, higher stiffness, and better rutting resistance compared to mixes with the same binders but using gap-gradation. This suggests that, apart from their use in thin reflective cracking overlays, the modified binders also hold promise for use in thicker structural overlays and new pavements. Mechanistic-empirical simulations for dense-graded modified binder mixes showed superior cracking resistance but poorer rutting resistance than conventional DGAC (now called hot-mix asphalt [HMA]).

Objective 4: Provide Recommendations for Reflective Cracking Overlay Strategies

Findings of the more detailed analysis of the laboratory shear and fatigue results, and the simulations with the calibrated models were used to prepare recommendations for reflective cracking studies. Conclusions for this objective include:

- Overall, the results indicate that the half-thickness modified binder mixes assessed in this study provide better performance than the full-thickness conventional dense-graded asphalt concrete (HMA) with respect to reflective cracking when used as thin overlays on cracked pavement. This is demonstrated by the absence of reflective cracking on the half-thickness modified binder overlays despite their being subjected to over a million more HVS repetitions than that required to crack the full-thickness AR4000-D overlay. The half-thickness RAC-G mix did not perform as well as the modified mixes but it still showed superior reflective cracking performance compared to the full-thickness AR4000-D, confirming results from previous HVS studies performed for Caltrans by the UCPRC.
- The re-analysis of the HVS fatigue test results using uniform underlying conditions, as opposed to the actual underlying conditions (which varied between HVS test sections) used during calibration, showed that the reflective cracking resistance of the modified and rubberized mixes in half-thickness overlays remained significantly better than that of the conventional dense-graded asphalt concrete full-thickness overlay. This was found to be true using both mechanistic-empirical analysis approaches (*CalME* and continuum damage mechanics models).

- Re-analysis of the HVS rutting test results using uniform underlying conditions indicates that there is a faster rutting of the asphalt layers when the modified mixes are used with slow traffic in hot climates. Performance should be assessed in pilot projects before wider use is considered under these conditions.
- Overall, the results indicate that the modified binder mixes (regardless of half or full thickness) assessed in this study have a greater risk of asphalt rutting under slow, heavy loads and hot conditions compared to the full-thickness conventional dense-graded asphalt concrete (HMA) overlay. The modified binder mix designs were performed using the same Hveem Stabilometer procedure used for RAC-G mixes. It is not known to what extent the rutting performance would have been improved, and conversely if the reflective cracking performance would have been effected, by using a different method that selected lower design binder contents.

6.2. Recommendations

Pilot Projects

The following recommendations with regard to the establishment of pilot projects are made based on the conclusions presented above:

- There is sufficient evidence from this study that a number of production-level pilot projects should be constructed using mixes with modified binders.
- Control mixes should be included in the pilot projects.
- Mixes used in the pilot projects should be subjected to laboratory testing and analysis of the type (reduced experiment design) used in this research project. This testing and analysis is needed to identify the range of performance for these mix types, which could not be measured with the one binder example in this study.
- The initial pilot projects with modified binder mixes should not be placed in locations with very hot climates and/or high traffic counts of slow, heavy trucks.
- The pilot projects should be monitored following the Pavement Preservation Study Technical Advisory Guide (PPSTAG [UCPRC-GL-2005-01]).

Testing and Analysis

The following recommendations with regard to the testing and analysis are made based on the conclusions presented above:

- New mixes developed for reflective cracking, with either new gradations or new binders, should be evaluated with the laboratory testing and analysis techniques and the mechanistic-empirical analysis models developed in this study. Based on the available research and performance data,

additional HVS testing is not warranted before constructing and evaluating pilot projects, unless there is uncertainty from the modeling results for these new mixes.

- Laboratory investigation, additional analysis, and HVS validation is recommended to improve mix design procedures for rubberized and modified binder mixes. The mixes used in this study were designed using the Hveem Stabilometer with criteria (e.g., gradation) that were not consistent between mixes with conventional binders and mixes with rubberized and modified binders.
- Additional laboratory and modeling studies and HVS tests are also warranted to better assess the risk of rutting using mixes with these binders in thicker overlays, hot climates, and under slow, heavy loads, and the effects of changes to the mix design on reducing that risk.

7. REFERENCES

1. **Generic experimental design for product/strategy evaluation** — crumb rubber modified materials. 2005. Sacramento, CA: Caltrans.
2. **Reflective Cracking Study: Workplan for the Comparison of MB, RAC-G, and DGAC Mixes Under HVS and Laboratory Testing.** 2003. Davis and Berkeley, CA: University of California Pavement Research Center. (UCPRC-WP-2003-01).
3. BEJARANO, M., Jones, D., Morton, B., and Scheffy, C. 2005. **Reflective Cracking Study: Summary of Construction Activities, Phase 1 HVS Testing, and Overlay Construction**. Davis and Berkeley, CA: University of California Pavement Research Center. (UCPRC-RR-2005-03).
4. JONES, D. Tsai, B.W., and Harvey, J. 2006. **Reflective Cracking Study: First-level Report on HVS Testing on Section 590RF — 90 mm MB4-G Overlay.** Davis and Berkeley, CA: University of California Pavement Research Center. (UCPRC-RR-2006-04).
5. JONES, D., Wu, R., Lea, J., and Harvey, J. 2006. **Reflective Cracking Study: First-level Report on HVS Testing on Section 589RF — 45 mm MB4-G Overlay.** Davis and Berkeley, CA: University of California Pavement Research Center. (UCPRC-RR-2006-05).
6. WU, R., Jones, D., and Harvey, J. 2006. **Reflective Cracking Study: First-level Report on HVS Testing on Section 587RF — 45 mm RAC-G Overlay.** Davis and Berkeley, CA: University of California Pavement Research Center. (UCPRC-RR-2006-06).
7. JONES, D., Wu, R., and Harvey, J. 2006. **Reflective Cracking Study: First-level Report on HVS Testing on Section 588RF — 90 mm DGAC Overlay.** Davis and Berkeley, CA: University of California Pavement Research Center. (UCPRC-RR-2006-07).
8. JONES, D., Wu, R., and Harvey, J. 2006. **Reflective Cracking Study: First-level Report on HVS Testing on Section 586RF — 45 mm MB15-G Overlay.** Davis and Berkeley, CA: University of California Pavement Research Center. (UCPRC-RR-2006-12).
9. JONES, D., Wu, R., and Harvey, J. 2007. **Reflective Cracking Study: First-level Report on HVS Testing on Section 591RF — 45 mm MAC15-G Overlay.** Davis and Berkeley, CA: University of California Pavement Research Center. (UCPRC-RR-2007-04).
10. STEVEN, B., Jones, D., and Harvey, J. 2007. **Reflective Cracking Study: First-level Report on the HVS Rutting Experiment.** Davis and Berkeley, CA: University of California Pavement Research Center. (UCPRC-RR-2007-06).
11. TSAI, B.W., Jones, D., Harvey, J., and Monismith, C. 2006. **Reflective Cracking Study: First-level Report on Laboratory Fatigue Testing.** Davis and Berkeley, CA: University of California Pavement Research Center. (UCPRC-RR-2006-08).

12. GUADA, I., Signore, J., Tsai, B.W., Jones, D., Harvey, J., and Monismith, C. 2006. **Reflective Cracking Study: First-level Report on Laboratory Shear Testing.** Davis and Berkeley, CA: University of California Pavement Research Center. (UCPRC-RR-2006-11).
13. JONES, D., Harvey, J., and Steven, B. 2007. **Reflective Cracking Study: HVS Test Section Forensic Report.** Davis and Berkeley, CA: University of California Pavement Research Center. (UCPRC-RR-2007-05).
14. HARVEY, J., Du Plessis, L., Long, F., Deacon, J., Guada, I., Hung, D., and Scheffy, C. 1997. **CAL/APT Program: Test Results from Accelerated Pavement Test on Pavement Structure Containing Untreated Base – Section 501RF**. Davis and Berkeley, CA: University of California Pavement Research Center. (UCPRC-RR-1997-03 and RTA-65W4845-3).
15. JIANG, R., and Murthy, D.N. 1995. Reliability Modeling Involving Two Weibull Distributions. **Reliability Engineering and System Safety**. Vol. 47. pp. 187-198.
16. TSAI, B.W., Harvey, J., and Monismith, C. 2005. Using the Three-Stage Weibull Equation and Tree-Based Model to Characterize Mix Fatigue Damage Process. **Transportation Research Record, No. 1929.** Washington, D.C.: Transportation Research Board. pp. 227-237.
17. TSAI, B.W., Kannekanti, V.N., and Harvey, J. 2004. The Application of Genetic Algorithm in Asphalt Pavement Design. **Transportation Research Record, No. 1891.** Washington, D.C.: Transportation Research Board. pp. 112-120.
18. BREIMAN, L., Friedman, J.H., Olshen, R.A., and Stone, C.J. 1984. **Classification and Regression Trees.** Belmont, CA: Wadsworth International Group.
19. THOEGERSEN, F., Busch, C. and Henrichsen, A. 2004. **Mechanistic design of semi-rigid pavements - An incremental approach.** Fløng, Denmark: Danish Road Institute. (Report 138).
20. ULLIDTZ, P., Harvey, J., Tsai, B.W., and Monismith, C. 2006. **Calibration of Incremental-Recursive Flexible Damage Models in *CalME* Using HVS Experiments**. Davis and Berkeley, CA: University of California Pavement Research Center. (UCPRC-RR-2005-06).
21. ULLIDTZ, P., Harvey, J., Tsai, B.W., and Monismith, C. 2006. **Calibration of *CalME* models using WesTrack performance data.** Davis and Berkeley, CA: University of California Pavement Research Center. (UCPRC-RR-2006-14).
22. WU, R. 2005. Finite Element Analyses of Reflective Cracking in Asphalt Concrete Overlays. PhD Thesis. University of California, Berkeley.
23. DEACON, J.A., Harvey, J.T., Guarda, I., Popescu, L., and Monismith, C.L. 2002. Analytically based approach to rutting prediction. **Transportation Research Record, TRR-1806.** Washington, DC: Transportation Research Board.

24. LUKANEN, E.O., Stubstad, R. and Briggs, R. 2000. **Temperature Predictions and Adjustment Factors for Asphalt Pavement**. Washington, DC: Federal Highway Administration. (Report FHWA-RD-98-085).

25. ONGEL, A. and Harvey, J. 2004. **Analysis of 30 Years of Pavement Temperatures using the Enhanced Integrated Climate Model (EICM).** Davis and Berkeley, CA: University of California Pavement Research Center. (UCPRC-RR-2004-05).

26. McLEAN, D.B. **Permanent Deformation Characteristics of Asphalt Concrete.** 1975, University of California, Berkeley.

27. BELL, C.A., Wieder, A.J., and Fellin, M.J. 1994. **Laboratory aging of asphalt-aggregate mixtures: field validation.** Washington, DC: Strategic Highway Research Program (SHRP), Transportation Research Board. (SHRP-A-390).

Appendix A

Laboratory Fatigue and Shear Testing

APPENDIX A. LABORATORY FATIGUE AND SHEAR

A.1. Tree Structure for Predicting Initial Stiffness

Section 3.3.2

The entire tree structure for predicting initial stiffness (ln*stif*) can be written as follows [ref2.6]:

```
> print(lnstif.z)
node), split, n, deviance, yval
      * denotes terminal node

  1) root 172 99.92000 7.909
    2) binder:mb15,mb4 72 27.78000 7.338
      4) temp<15.085 12  0.08681 8.349 *
      5) temp>15.085 60 12.98000 7.136
       10) temp<25.1 48  4.14300 7.325
         20) cond:none 40  2.55200 7.257
           40) grad:gg 32  1.72800 7.187
             80) comp:lmlc 8  0.37890 6.987 *
             81) comp:fmlc 24  0.91810 7.254 *
           41) grad:dg 8  0.04766 7.536 *
         21) cond:aging 8  0.48270 7.665 *
       11) temp>25.1 12  0.25570 6.379 *
    3) binder:ar4000,mac15,rac 100 31.70000 8.321
      6) temp<19.915 32  3.89800 8.826
       12) temp<15.215 18  0.78420 8.999 *
       13) temp>15.215 14  1.88100 8.603
         26) binder:mac15,rac 5  0.01484 8.183 *
         27) binder:ar4000 9  0.49220 8.837 *
      7) temp>19.915 68 15.80000 8.083
       14) cond:none 57  9.67400 7.967
         28) binder:mac15 24  2.99000 7.682
           56) temp<20.75 17  1.29100 7.844
            112) temp<19.985 9  0.68090 7.725 *
            113) temp>19.985 8  0.33770 7.978 *
           57) temp>20.75 7  0.17300 7.289 *
         29) binder:ar4000,rac 33  3.33100 8.174
           58) temp<25.11 21  1.44500 8.305
            116) binder:rac 13  0.23190 8.177 *
            117) binder:ar4000 8  0.65880 8.512 *
           59) temp>25.11 12  0.89540 7.944 *
       15) cond:aging 11  1.34200 8.687
         30) temp<20.04 5  0.57380 8.810 *
         31) temp>20.04 6  0.62840 8.584 *
>
```

The first number after the split rule is the number of observations. The second number is the deviance, which is a measure of node heterogeneity used in the tree-growing algorithm. A zero deviance represents a perfectly homogeneous node. The third number is the group mean from the node below. If the number is accompanied by an asterisk (*), it represents the group mean of a leaf.

A.2. Weibull Curves of Modified Binder Fatigue Results

Section 3.4.1

The laboratory fatigue test results and associated Weibull-fitted curves are presented in Tables A.1 to A.9 and Figures A.1 to A.33.

Table A.1: AR4000-D Mixes: Summary of Three-Stage Weibull Fatigue Analysis: Temperature Effect

(FMLC, AV = 6.0±0.5 %, AC=5.0 %).

Specimen Designation	Three-Stage Weibull Fitting										*Nf* (SR=0.5)	*SR@ n_1*	*SR@ n_2*	*Last SR*
	1st Stage		2nd Stage				3rd Stage							
	$ln\alpha_1$	β_1	n_1	γ_1	$ln\alpha_2$	β_2	n_2	γ_2	$ln\alpha_3$	β_3				
G9-DGAC-17B	-7.3913	0.5797			-7.3913	0.5797	9522	-29624	-27.2824	2.3831	51,204		0.883	0.208
G9-DGAC-12B	-6.9888	0.5663			-6.9888	0.5663	7094	-9919	-15.1974	1.3581	45,566		0.868	0.193
G9-DGAC-4A	-9.1281	0.7376			-9.1281	0.7376	11433	-19271	-22.7016	1.9808	58,924		0.897	0.199
G9-DGAC-11B	-16.6465	2.7944	73	49	-7.5633	0.9148	4210	2595	-2.5616	0.3550	2,626	0.991	0.338	0.100
G9-DGAC-17A	-11.3116	1.2391	582	142	-9.1280	0.9371	6489	-2569	-13.1077	1.3374	11,345	0.967	0.670	0.163
G9-DGAC-20B	-18.5197	3.4062	73	59	-5.6908	0.6687	6068	2987	-2.6267	0.3429	2,887	0.978	0.323	0.101
G9-DGAC-8A	-12.4046	1.5549	176	101	-7.2290	0.6637	2226	-4398	-20.3467	2.0688	11,233	0.987	0.885	0.205
G9-DGAC-15A	-10.4340	1.1240	176	70	-7.7944	0.6797	15414	-53754	-35.3873	3.0638	40,131	0.991	0.742	0.103
G9-DGAC-22A	-12.7204	1.7310	98	65	-6.8451	0.5892	6302	-24393	-31.6558	2.8997	24,895	0.984	0.831	0.184
G9-DGAC-13B	-15.6384	2.5704	83	59	-6.6394	0.7425	3422	-11009	-31.1260	3.1864	4,543	0.986	0.573	0.105
G9-DGAC-21B	-13.1053	1.9689	89	55	-6.9452	0.7590	2403	-5981	-25.5344	2.7097	4,853	0.984	0.702	0.119
G9-DGAC-14B	-12.6831	2.0450	67	42	-6.5328	0.7596	1239	-1570	-15.3008	1.7822	2,871	0.983	0.737	0.117
G9-DGAC-15B	-10.3989	1.3180	160	102	-5.6499	0.4775	67633	-229362	-26.8029	2.1000	65,015	0.972	0.502	0.122
G9-DGAC-18B	-10.2257	1.2666	186	121	-5.4746	0.4469	78926	-579336	-50.4472	3.7329	92,330	0.971	0.530	0.121
G9-DGAC-16A	-9.6441	1.1707	170	102	-5.6001	0.4669	27788	-259021	-61.6091	4.8370	61,006	0.963	0.642	0.104
G9-DGAC-14A	-19.2518	3.4331	80	64	-6.0665	0.6763	3192	-4949	-16.4747	1.7603	4,554	0.984	0.586	0.059
G9-DGAC-6A	-14.8531	2.4618	83	61	-5.9777	0.6468	4381	-16002	-30.8457	3.0519	5,748	0.982	0.562	0.072
G9-DGAC-8B	-13.1228	2.0949	97	68	-5.6200	0.6200	3782	-14761	-30.9483	3.0958	4,761	0.972	0.553	0.098

Table A.2: RAC-G Mixes: Summary of Three-Stage Weibull Fatigue Analysis: Temperature Effect

(FMLC, AV = 6.0±0.5 %, AC = 8.0%).

Specimen Designation	Three-Stage Weibull Fitting										*Nf* (SR=0.5)	*SR@ n_1*	*SR@ n_2*	*Last SR*
	1st Stage		2nd Stage				3rd Stage							
	$ln\alpha_1$	β_1	n_1	γ_1	$ln\alpha_2$	β_2	n_2	γ_2	$ln\alpha_3$	β_3				
G9-RACG-6A	-6.4894	0.5003	683	264	-5.0762	0.3068	12381	-54450	-20.9888	1.6919	141,141	0.954	0.890	0.293
G9-RACG-3A	-6.6293	0.4942	2285	794	-5.1643	0.3226	29152	-103994	-19.7272	1.5145	253,404	0.924	0.853	0.160
G9-RACG-5B	-6.7776	0.5209	213	18	-6.4989	0.4768	69481	-367586	-40.1493	3.0002	215,076	0.980	0.735	0.223
G9-RACG-6B	-10.9268	1.4038	103	48	-7.4306	0.7513	1919	-1316	-12.2673	1.2989	8,245	0.987	0.845	0.200
G9-RACG-18B	-12.8237	1.8709	109	73	-6.2428	0.6150	16188	-20618	-15.0528	1.4047	14,459	0.982	0.484	0.136
G9-RACG-4A	-13.6245	1.9788	99	63	-7.0677	0.7095	4051	-1579	-9.8367	1.0018	11,216	0.989	0.740	0.154
G9-RACG-14A	-10.4127	1.2922	174	124	-5.1872	0.3688	256682	-373106	-12.6829	0.9054	453,380	0.977	0.591	0.190
G9-RACG-1B	-12.0754	1.6569	113	81	-5.8482	0.4637	307401	-240576	-10.9152	0.8269	136,983	0.986	0.383	0.124
G9-RACG-12B	-12.0838	1.7050	116	92	-5.1241	0.3596	1179235	-6955028	-39.5713	2.4809	637,582	0.985	0.452	0.159
G9-RACG-16A	-18.7476	3.3561	76	64	-5.5378	0.5326	6830	-9126	-12.9955	1.2560	14,532	0.984	0.655	0.224
G9-RACG-4B	-13.6742	2.1050	129	102	-4.9228	0.4473	58700	-80213	-12.5694	1.0605	27,070	0.971	0.396	0.118
G9-RACG-5A	-10.8201	1.6816	84	60	-4.8956	0.4812	54077	-11466	-6.1275	0.5839	11,755	0.964	0.266	0.075
G9-RACG-16B	-16.4746	2.6997	102	87	-5.0822	0.4014	8606	4130	-3.2226	0.2109	752,449	0.983	0.796	0.368
G9-RACG-19B	-9.9844	1.3278	118	86	-4.8892	0.3576	32563	16445	-2.8937	0.1775	1,562,551	0.969	0.733	0.456
G9-RACG-10B	-11.1698	1.5571	137	105	-4.7583	0.3611	15141	5884	-3.3155	0.2224	538,708*	0.969	0.762	0.604
G9-RACG-13A	-16.8901	3.0085	72	60	-5.2930	0.5058	1973	876	-3.5007	0.2899	46,845	0.982	0.797	0.195
G9-RACG-1A	-21.4416	4.0417	70	61	-5.3785	0.5143	2039	880	-3.6017	0.3014	44,642	0.984	0.803	0.264
G9-RACG-13B	-14.4567	2.3991	83	65	-5.3614	0.5185	1768	840	-3.4345	0.2826	49,882	0.979	0.809	0.311

*: extrapolation

Table A.3: MAC15-G Mixes: Summary of Three-Stage Weibull Fatigue Analysis: Temperature Effect

(FMLC, AV = 6.0±0.5 %, AC = 7.4%).

Specimen Designation	Three-Stage Weibull Fitting										*Nf (SR=0.5)*	*SR@ n_1*	*SR@n_2*	*Last SR*
	1st Stage		2nd Stage				3rd Stage							
	$ln\alpha_1$	β_1	n_1	$ln\alpha_1$	β_1	n_1	$ln\alpha_1$	β_1	n_1	$ln\alpha_1$				
G9-MAC15-25A	-8.8075	0.8782	196	137	-5.2564	0.2653	116775	-3512016	-126.8500	8.2551	932,673	0.989	0.881	0.213
G9-MAC15-2B	-8.8644	0.8401	540	344	-5.1919	0.3056	41949	-320384	-36.0039	2.6610	345,709	0.972	0.877	0.172
G9-MAC15-19A	-7.4499	0.5651	1248	685	-5.0343	0.2547	55306	-891678	-63.0272	4.4162	571,417	0.969	0.895	0.213
G9-MAC15-11A	-8.6200	1.0425	117	58	-5.7761	0.5209	10142	-18387	-16.0925	1.4737	25,360	0.976	0.685	0.146
G9-MAC15-4B	-14.3840	2.0386	140	102	-6.2785	0.5428	6093	-23653	-29.3223	2.6955	23,920	0.984	0.807	0.118
G9-MAC15-15B	-11.8610	1.5878	144	94	-6.1296	0.5519	22390	-88240	-32.4060	2.7382	34,249	0.981	0.584	0.135
G9-MAC15-24B	-7.5699	0.7258	736	482	-4.1693	0.2510			-4.1693	0.2510	4,167,967	0.940		0.492
G9-MAC15-13B	-10.7581	1.2067	408	315	-4.7469	0.2742			-4.7469	0.2742	8,853,486*	0.980		0.593
G9-MAC15-1B	-6.6105	0.5229	5019	3027	-3.7316	0.2075	909525	-20880388	-85.1714	4.9883	3,405,270	0.900	0.675	0.243
G9-MAC15-26A	-10.7974	1.5426	120	90	-4.7488	0.3914	5470	2468	-3.1351	0.2184	331,919	0.968	0.787	0.354
G9-MAC15-9B	-16.1028	2.5990	92	76	-5.6115	0.4533	6992	3153	-3.6801	0.2516	519,505	0.985	0.819	0.414
G9-MAC15-13A	-10.8754	1.5067	141	106	-4.7331	0.3703	8893	3958	-3.1394	0.2080	664,993	0.968	0.778	0.399
G9-MAC15-10A	-11.2715	1.5755	111	87	-4.9037	0.3321			-4.9037	0.3321	2,062,190*	0.976		0.879
G9-MAC15-11B	-9.9011	1.2580	146	108	-4.8174	0.3264	42542	21375	-2.9609	0.1628	8,847,719	0.974	0.788	0.498
G9-MAC15-20B	-8.7973	1.0331	160	109	-4.8653	0.3327	23123	11820	-3.0488	0.1634	15,136,954*	0.976	0.808	0.556
G9-MAC15-1A	-15.0886	2.4561	93	78	-5.0052	0.3900	7452	4615	-2.7251	0.1501	6,982,693*	0.981	0.813	0.568
G9-MAC15-25B	-12.4354	1.8626	108	86	-4.8987	0.3812	17734	11123	-2.4269	0.1428	2,025,612	0.976	0.745	0.440
G9-MAC15-8B	-18.0753	3.1775	76	66	-5.2743	0.4163	10453	6890	-2.5922	0.1428	7,014,195*	0.986	0.801	0.528

*: extrapolation

Table A.4: MB15-G Mixes: Summary of Three-Stage Weibull Fatigue Analysis: Temperature Effect

(FMLC, AV = 6.0±0.5 %, AC = 7.1 %).

Specimen Designation	Three-Stage Weibull Fitting										*Nf (SR=0.5)*	*SR@ n_1*	*SR@n_2*	*Last SR*
	1st Stage		2nd Stage				3rd Stage							
	$ln\alpha_1$	β_1	n_1	$ln\alpha_1$	β_1	n_1	$ln\alpha_1$	β_1	n_1	$ln\alpha_1$				
G9-MB15-20B	-11.1878	1.3403	297	243	-4.5285	0.2436	91577	-26265	-5.4159	0.3142	9,803,239*	0.970	0.856	0.603
G9-MB15-27A	-7.6502	0.7042	602	381	-4.5370	0.2582			-4.5370	0.2582	10,728,429*	0.959		0.564
G9-MB15-23B	-7.8251	0.7349	429	290	-4.5513	0.2391	155681	-71210	-5.9987	0.3492	10,352,525*	0.968	0.845	0.586
G9-MB15-32B	-13.7964	2.0382	122	93	-5.6289	0.4837	15455	-89057	-38.9991	3.2909	38,892	0.981	0.681	0.105
G9-MB15-29B	-10.4837	1.4008	161	112	-5.0214	0.4250	103929	-556167	-36.3237	2.7023	51,073	0.967	0.402	0.104
G9-MB15-9A	-13.2273	1.9064	172	142	-4.5318	0.3294	152366	-1351313	-46.8860	3.2542	292,775	0.973	0.617	0.111
G9-MB15-20A	-9.3707	1.0880	229	143	-5.2744	0.4076	28068	17624	-2.5123	0.1524	1,303,284	0.968	0.718	0.415
G9-MB15-1A	-7.1443	0.6945	620	407	-3.9608	0.2390			-3.9608	0.2390	3,406,799	0.937		0.449
G9-MB15-30B	-6.4002	0.4855	5865	3476	-3.7263	0.1978	913786	-14570430	-56.7054	3.3640	4,191,041	0.907	0.693	0.307
G9-MB15-25B	-8.5214	1.0538	144	86	-5.0115	0.4250	5311	2803	-2.9693	0.2039	355,412	0.964	0.773	0.295
G9-MB15-34A	-10.7151	1.5855	108	84	-4.4174	0.3547	7313	2876	-3.0939	0.2177	286,651	0.960	0.766	0.253
G9-MB15-26A	-5.5864	0.4915	3305	1775	-3.2723	0.2275	1941339	-5953087	-14.6858	0.9261	337,904	0.821	0.372	0.224
G9-MB15-19B	-7.2481	0.7727	236	145	-4.3777	0.2993	145703	62601	-2.7554	0.1708	1,273,806	0.952	0.649	0.414
G9-MB15-5A	-6.0376	0.5743	302	161	-4.0831	0.2677	8747	1797	-3.5751	0.2167	2,760,082	0.936	0.825	0.466
G9-MB15-7A	-5.7718	0.5745	244	152	-3.5930	0.2165			-3.5930	0.2165	3,122,129	0.931		0.479
G9-MB15-12A	-17.8013	3.0372	93	80	-5.1361	0.4286	3925	2034	-3.1890	0.2109	628,905	0.979	0.819	0.346
G9-MB15-26B	-11.8540	1.7966	102	81	-4.6475	0.3627	5760	1638	-3.7037	0.2632	318,278	0.974	0.806	0.374
G9-MB15-33A	-9.3839	1.3041	104	76	-4.4836	0.3477	14811	6285	-2.9673	0.2012	408,079	0.966	0.733	0.317

*: extrapolation

Table A.5: MB4-G Mixes: Summary of Three-Stage Weibull Fatigue Analysis: Temperature Effect

(FMLC, AV = 6.0±0.5 %, AC = 7.2 %).

Specimen Designation	Three-Stage Weibull Fitting										*Nf* (SR=0.5)	*SR@ n_1*	*SR@ n_2*	*Last SR*
	1st Stage		2nd Stage				3rd Stage							
	$ln\alpha_1$	β_1	n_1	$ln\alpha_1$	β_1	n_1	$ln\alpha_1$	β_1	n_1	$ln\alpha_1$				
G9-MB4-13A	-6.2224	0.5398	128	46	-5.1240	0.3452	9233	3877	-3.7018	0.2013	17,664,495*	0.970	0.870	0.587
G9-MB4-17A	-8.3090	0.8359	219	115	-5.6532	0.3978	1411	693	-4.2517	0.2204	35,231,219*	0.976	0.939	0.645
G9-MB4-17B	-8.1086	0.7618	557	337	-4.9150	0.3009	13148	4042	-4.0190	0.2138	27,633,563*	0.958	0.879	0.620
G9-MB4-5B	-9.9012	1.2608	184	127	-4.9138	0.3927	10950	4781	-3.2194	0.2238	372,928	0.964	0.758	0.356
G9-MB4-12B	-12.4703	1.8424	113	85	-5.2487	0.4483	4422	1844	-3.5874	0.2665	186,987	0.976	0.803	0.265
G9-MB4-11A	-8.2500	0.9535	150	81	-5.3392	0.4404	3586	1858	-3.3629	0.2171	1,019,530	0.969	0.842	0.424
G9-MB4-30B	-8.5333	1.0685	95	66	-4.7714	0.3270	17165	8754	-3.0378	0.1609	18,774,076*	0.979	0.823	0.568
G9-MB4-8B	-18.4049	3.2342	75	66	-5.3273	0.3995	6711	3966	-3.1181	0.1651	29,211,530*	0.989	0.863	0.592
G9-MB4-26B	-9.4276	1.1906	118	77	-5.2863	0.4142	27065	20571	-1.9350	0.0997	7,725,081*	0.979	0.710	0.510
G9-MB4-14A	-16.3920	2.8223	87	73	-4.9279	0.4368	13106	8875	-1.9732	0.1418	85,028	0.975	0.650	0.322
G9-MB4-32A	-11.8204	1.7871	105	83	-4.6676	0.3756	11674	7559	-2.2624	0.1334	1,682,779	0.968	0.741	0.458
G9-MB4-7B	-13.9567	2.3397	84	70	-4.6225	0.3883	10581	7008	-2.1066	0.1320	492,375	0.979	0.716	0.405
G9-MB4-20B	-6.0017	0.5124	659	348	-4.0658	0.2421	130434	92481	-1.9596	0.0706	6,241,325,854*	0.934	0.752	0.693
G9-MB4-11B	-8.2955	0.9605	203	140	-4.4366	0.3002	5850	2780	-3.1356	0.1614	26,790,763*	0.947	0.845	0.637
G9-MB4-30A	-20.2508	3.6763	75	67	-5.1205	0.3637	9428	5671	-2.9962	0.1460	66,007,390*	0.986	0.856	0.675
G9-MB4-21B	-11.3179	1.6192	126	97	-4.7545	0.3763	4360	2695	-2.6994	0.1469	9,169,275	0.967	0.825	0.555
G9-MB4-26A	-7.7791	0.9517	178	125	-3.9655	0.2822	51333	38356	-1.5831	0.0715	38,534,397	0.946	0.678	0.550
G9-MB4-25A	-6.9816	0.7886	155	91	-4.3537	0.3249	11419	7242	-2.3198	0.1198	14,971,040	0.949	0.767	0.540

*: extrapolation

Table A.6: Summary of Three-Stage Weibull Fatigue Analysis: Air-Void Content Effect

(FMLC, AV = 9.0±1.0 %).

Specimen Designation	Three-Stage Weibull Fitting										*Nf* (*SR=0.5*)	*SR@ n_1*	*SR@ n_2*	*Last SR*
	1st Stage		2nd Stage				3rd Stage							
	$ln\alpha_1$	β_1	n_1	$ln\alpha_1$	β_1	n_1	$ln\alpha_1$	β_1	n_1	$ln\alpha_1$				
G9-DGAC-12A	-12.9634	1.6469	116	67	-7.8016	0.6869	20863	-78084	-38.5641	3.2682	42,335	0.995	0.681	0.075
G9-DGAC-5A	-11.8966	1.5851	65	37	-7.6138	0.6972	11349	-29514	-27.8450	2.5182	25,461	0.995	0.708	0.075
G9-DGAC-10A	-14.4021	1.9755	108	69	-7.7633	0.7139	6362	-6665	-15.5224	1.4780	22,074	0.993	0.804	0.151
G9-DGAC-3A	-29.3987	6.1907	57	48	-6.5934	1.0000	581	-155	-9.4254	1.3802	566	0.999	0.498	0.229
G9-DGAC-2B	-15.3005	2.4810	90	63	-6.5688	0.7409	924	-658	-11.5927	1.3617	3,262	0.983	0.807	0.125
G9-DGAC-1B	-24.8818	4.7796	65	54	-6.9139	0.8248	634	-309	-10.8531	1.3413	2,202	0.992	0.829	0.194
G9-RACG-22A	-7.8463	0.8225	256	143	-5.0053	0.3636	82561	-202533	-16.6863	1.2576	231,682	0.970	0.659	0.149
G9-RACG-25A	-7.6731	0.7457	895	502	-4.5626	0.3278	1324911	-2610496	-14.7318	0.9739	343,953	0.925	0.381	0.117
G9-RACG-20A	-12.3418	1.7219	112	81	-5.8145	0.4666	156480	-69659	-8.5515	0.6746	125,409	0.987	0.474	0.239
G9-RACG-23A	-10.6935	1.3582	269	182	-5.0475	0.4373	9355	-13294	-11.8857	1.0799	32,123	0.955	0.704	0.156
G9-RACG-20B	-13.6259	2.1971	99	77	-5.0356	0.4859	4318	-11637	-18.6689	1.8282	11,344	0.972	0.685	0.138
G9-RACG-24B	-17.0044	2.9734	83	68	-5.2604	0.5186	13443	-843	-5.6327	0.5540	13,447	0.979	0.510	0.106
GR-MAC15-3A	-11.0551	1.3390	255	219	-4.3185	0.1906	35202	-170597	-16.0404	1.1211	1,011,990	0.976	0.912	0.187
G9-MAC15-1B	-10.5651	1.1977	320	252	-4.7232	0.2529			-4.7232	0.2529	33,987,640*	0.974		0.640
G9-MAC15-18A	-15.8511	2.6133	74	62	-5.6558	0.4220	3007	1226	-4.1949	0.2552	3,324,576	0.989	0.908	0.460
GR-MAC15-4B	-8.5981	0.9961	370	266	-3.9999	0.2785	42926	-398962	-38.5366	2.8854	170,744	0.937	0.703	0.183
G9-MAC15-29B	-11.5413	1.5930	167	129	-4.6812	0.3562	119296	-428789	-22.1670	1.6383	186,137	0.972	0.568	0.083
G9-MAC15-16A	-15.0003	2.4739	92	77	-4.8864	0.3971	90252	-334722	-24.6069	1.8712	103,599	0.979	0.533	0.108
G9-MB15-17B	-10.6529	1.3703	172	137	-4.5831	0.2770			-4.5831	0.2770	4,353,301	0.973		0.487
G9-MB15-2A	-7.4218	0.7670	238	154	-4.4245	0.2707	248133	56151	-3.6116	0.2096	5,049,641	0.959	0.715	0.497
G9-MB15-21A	-17.2016	2.8404	84	71	-5.6746	0.4174	2954	938	-4.5709	0.2920	2,003,311*	0.991	0.912	0.766
G9-MB15-18A	-6.8584	0.7565	215	144	-3.8620	0.2499	338193	-1473295	-19.9771	1.3391	839,731	0.941	0.598	0.304
G9-MB15-16B	-8.8727	1.1428	195	148	-3.8977	0.2738	52555	-161645	-14.6575	1.1189	201,789	0.946	0.674	0.207
G9-MB15-11B	-18.3710	3.2455	97	88	-4.2076	0.3050	1700597	-2786212	-12.1567	0.8046	328,634	0.977	0.359	0.117
G9-MB4-35B	-6.6772	0.7256	135	83	-4.2283	0.2808	49313	30462	-2.2530	0.1075	48,334,981*	0.957	0.746	0.561
G9-MB4-35A	-5.1479	0.4341	326	133	-3.9930	0.2578	26010	12389	-2.6655	0.1357	26,496,683*	0.928	0.772	0.578
G9-MB4-37A	-17.4037	2.8965	92	80	-5.2779	0.3853	8939	4620	-3.3480	0.1878	10,935,169*	0.986	0.854	0.556
G9-MB4-38B	-19.4997	3.5817	80	71	-4.6940	0.4091	2794	1661	-2.6549	0.1702	788,798*	0.978	0.797	0.540
G9-MB4-37B	-6.3980	0.6844	451	310	-3.2705	0.2133	284026	-91646	-4.2178	0.2825	705,515	0.901	0.573	0.459
G9-MB4-38A	-17.2570	3.0261	87	76	-4.6998	0.3947	7646	4837	-2.3368	0.1464	669,923	0.974	0.746	0.412

*: extrapolation

Table A.7: Summary of Three-Stage Weibull Fatigue Analysis: Aging Effect

(FMLC, AV = 6.0±0.5 %, LTOA 6 days).

Specimen Designation	Three-Stage Weibull Fitting										*Nf* (*SR=0.5*)	*SR@ n_1*	*SR@ n_2*	*Last SR*
	1st Stage		2nd Stage				3rd Stage							
	$ln\alpha_1$	β_1	n_1	$ln\alpha_1$	β_1	n_1	$ln\alpha_1$	β_1	n_1	$ln\alpha_1$				
G9-DGAC-9B	-15.2682	2.1274	133	92	-7.3270	0.6623	7353	-24926	-31.4276	2.8885	22,963	0.993	0.778	0.096
G9-DGAC-21A	-15.3597	2.0911	152	100	-7.6755	0.7146	8372	-11486	-18.2072	1.7155	21,445	0.994	0.745	0.123
G9-DGAC-6B	-19.0213	3.3111	72	51	-7.8283	0.9758	833	-806	-16.4723	2.0460	1,860	0.992	0.766	0.108
G9-DGAC-20A	-12.7036	1.8085	160	91	-6.8079	0.7756	943	-1399	-18.1163	2.1320	2,788	0.972	0.807	0.175
G9-RACG-7A	-9.7185	1.2261	164	127	-4.4857	0.2817			-4.4857	0.2817	3,428,264*	0.967		0.827
G9-RACG-17A	-12.6188	1.6118	194	148	-5.5863	0.3808	74201	15354	-4.6400	0.3026	1,334,858	0.984	0.774	0.432
G9-RACG-15B	-32.9579	6.7935	63	58	-5.6892	0.5549	23176	-15540	-9.9304	0.9293	16,223	0.991	0.452	0.180
G9-RACG-15A	-15.6629	2.5904	103	84	-5.0244	0.4659	11223	-29744	-18.8819	1.7136	20,898	0.972	0.611	0.138
GR-MAC15-28A	-9.5881	1.0831	205	148	-5.0244	0.2978	732963	-10418455	-74.5302	4.5311	2,577,541	0.980	0.699	0.154
GR-MAC15-10A	-8.7848	0.9128	364	245	-4.8319	0.2991	532510	-6236044	-60.7088	3.8035	1,611,280	0.967	0.663	0.187
GR-MAC15-5A	-16.3788	2.6649	111	96	-4.8259	0.3646	310677	-2526053	-49.6887	3.3297	243,046	0.979	0.503	0.121
GR-MAC15-9B	-10.6640	1.4127	189	137	-4.7902	0.3881	76150	-540109	-42.3705	3.1461	96,394	0.963	0.542	0.108
G9-MB15-33B	-13.1692	1.9716	112	90	-5.0913	0.3945	16571	9565	-2.7457	0.1677	1,492,524	0.979	0.756	0.424
G9-MB15-7B	-18.2994	3.1155	84	71	-5.6906	0.4708	19009	12492	-2.4765	0.1620	474,502	0.991	0.716	0.351
G9-MB15-10A	-12.3337	1.8786	104	77	-5.1702	0.4759	13411	8868	-2.0158	0.1621	35,099	0.974	0.602	0.194
G9-MB15-27B	-14.5360	2.3307	112	92	-4.7651	0.4095	8383	4352	-2.7231	0.1991	153,375	0.972	0.720	0.311
G9-MB4-22A	-10.7575	1.4115	168	130	-4.6945	0.3213	9459	4721	-3.1383	0.1632	30,661,062*	0.973	0.845	0.645
G9-MB4-18A	-10.7552	1.4795	134	106	-4.5591	0.3142	16012	7945	-2.9531	0.1593	11,997,565*	0.971	0.813	0.605
G9-MB4-25B	-12.9007	2.0211	115	96	-4.3302	0.3447	6801	3860	-2.5008	0.1512	1,534,331	0.964	0.768	0.504
G9-MB4-7A	-8.8188	1.0780	316	241	-3.7179	0.2557	7672	2567	-2.9384	0.1756	2,343,174	0.933	0.790	0.453

*: extrapolation

Table A.8: Summary of Three-Stage Weibull Fatigue Analysis: Compaction Effect

(LMLC, AV = 6.0±0.5 %, gap-graded).

Specimen Designation	Three-Stage Weibull Fitting										*Nf* (*SR=0.5*)	*SR@ n_1*	*SR@ n_2*	*Last SR*
	1st Stage		2nd Stage				3rd Stage							
	$ln\alpha_1$	β_1	n_1	$ln\alpha_1$	β_1	n_1	$ln\alpha_1$	β_1	n_1	$ln\alpha_1$				
G9L-RACG-4A1	-11.5843	1.6896	97	75	-5.0110	0.3758	4908	1658	-3.8668	0.2527	1,171,604*	0.980	0.850	0.554
G9L-RACG-6A2	-8.8652	1.1058	147	105	-4.5414	0.3188	696204	-1258575	-13.2205	0.8952	520,228	0.969	0.474	0.175
G9L-RACG-6A1	-18.8596	3.3463	88	77	-4.9409	0.4373	25471	-25715	-10.0633	0.8814	36,322	0.979	0.555	0.118
G9L-RACG-3A1	-10.8677	1.5267	156	122	-4.3467	0.3370	1235507	-640427	-26.5564	1.9312	151,182	0.962	0.516	0.119
G9L-MAC15G-3A2	-10.8187	1.4290	188	172	-3.6814	0.1240	117315	-114549	-5.2663	0.2454	1,860,333,570*	0.969	0.909	0.822
G9L-MAC15G-2A1	-8.9773	0.9779	214	167	-4.5605	0.2155	247279	-80289	-5.5124	0.2857	96,539,623*	0.968	0.851	0.736
G9L-MAC15G-3A1	-12.7144	1.9693	104	87	-4.5301	0.3368	1009	444	-3.5395	0.2065	2,979,048*	0.969	0.898	0.713
G9L-MAC15G-5A2	-5.6789	0.5119	1109	684	-3.2774	0.1962	874185	-7113194	-29.1092	1.7942	2,322,056	0.889	0.587	0.205
G9L-MB15G-1A1	-7.5782	0.8211	300	206	-4.0638	0.2572			-4.0638	0.2572	1,896,344*	0.948		0.585
G9L-MB15G-6A1	-6.6966	0.6844	299	206	-3.7650	0.2137			-3.7650	0.2137	8,815,565*	0.942		0.544
G9L-MB15G-2A1	-6.2318	0.6332	447	269	-3.6756	0.2523	96361	-88494	-6.6675	0.4854	370,451	0.905	0.631	0.160
G9L-MB15G-6A2	-6.9701	0.7191	579	388	-3.6453	0.2378	959935	-4006339	-19.3447	1.2307	1,046,590	0.919	0.505	0.257
G9L-MB4G-2A1	-8.1806	0.9077	493	362	-3.7278	0.2412	34994	19941	-2.2152	0.1048	53,953,532*	0.927	0.741	0.568
G9L-MB4G-1A1	-6.5403	0.5630	982	440	-4.6181	0.3108	18126	9832	-2.8934	0.1458	40,412,562*	0.934	0.822	0.617
G9L-MB4G-3A1	-14.3438	2.3632	106	91	-4.2401	0.3381	6617	3742	-2.4565	0.1490	1,348,690	0.969	0.762	0.389
G9L-MB4G-4B1	-10.2427	1.4249	156	119	-4.2872	0.3422	13696	8650	-2.1154	0.1272	996,318	0.952	0.712	0.470

*: extrapolation

Table A.9: Summary of Three-Stage Weibull Fatigue Analysis: Gradation Effect

(LMLC, AV = 6.0±0.5 %, dense-graded).

Specimen Designation	Three-Stage Weibull Fitting										*Nf (SR=0.5)*	*SR@n 1*	*SR@n 2*	*Last SR*
	1st Stage		2nd Stage				3rd Stage							
	$ln\alpha_1$	β_1	n_1	$ln\alpha_1$	β_1	n_1	$ln\alpha_1$	β_1	n_1	$ln\alpha_1$				
G9L-DGAC6-5A2	-13.2989	1.9101	130	102	-5.3834	0.4146	8408	-19610	-15.9648	1.3987	51,896	0.983	0.822	0.104
G9L-DGAC6-2B2	-13.3243	1.9780	81	53	-6.8720	0.6739	2186	-1832	-12.2421	1.2696	9,680	0.989	0.836	0.232
G9L-DGAC6-4B2	-13.2275	2.1034	111	82	-5.1775	0.5519	2550	-8935	-24.8769	2.5683	5,313	0.961	0.652	0.125
G9L-DGAC6-6B2	-11.8682	1.6405	202	139	-5.2898	0.5132	4043	-31313	-49.7134	4.6469	10,187	0.962	0.693	0.154
G9L-MAC15D6-1C1	-15.8786	2.5712	100	86	-4.9687	0.3551	406709	-2377560	-36.4653	2.4316	738,408	0.985	0.562	0.135
G9L-MAC15D6-4D1	-9.6909	1.1645	234	178	-4.4759	0.2821	661881	-12347285	-91.5547	5.5466	1,564,754	0.968	0.613	0.192
G9L-MAC15D6-1C2	-16.0424	2.7169	104	92	-4.2433	0.3273	8311	-74483	-38.6245	3.2966	37,569	0.969	0.757	0.152
G9L-MAC15D6-3C2	-18.5822	3.3801	75	64	-5.1260	0.4761	11403	-14174	-11.5805	1.0739	20,082	0.983	0.612	0.121
G9L-MB15D6-4B1	-10.1906	1.4133	128	98	-4.4473	0.3284	15530	6421	-3.0476	0.1938	1,130,268*	0.967	0.765	0.530
G9L-MB15D6-5A2	-19.1381	3.3617	86	76	-5.0593	0.3890	5349	2652	-3.2977	0.1990	2,713,330	0.984	0.843	0.471
G9L-MB15D6-5A1	-18.7323	3.3053	97	85	-4.6030	0.4019	5240	2870	-2.6036	0.1848	187,478	0.969	0.750	0.353
G9L-MB15D6-1A2	-11.6478	1.7074	140	106	-4.6577	0.4113	4445	2485	-2.6217	0.1858	193,472	0.954	0.747	0.262
G9L-MB4D6-9A1	-7.8054	0.9379	173	114	-4.2686	0.3181	9487	5218	-2.5707	0.1449	4,446,984	0.948	0.777	0.498
G9L-MB4D6-9A2	-9.4453	1.2204	157	115	-4.5083	0.3295	17900	10199	-2.5605	0.1427	5,029,498*	0.967	0.764	0.503
G9L-MB4D6-6B1	-23.4457	4.5422	72	64	-5.1004	0.5096	1608	913	-2.8586	0.2292	48,541	0.983	0.778	0.345
G9L-MB4D6-6B2	-18.0508	3.2630	84	73	-4.5678	0.4098	4666	2528	-2.5750	0.1908	102,211	0.973	0.730	0.344

*: extrapolation

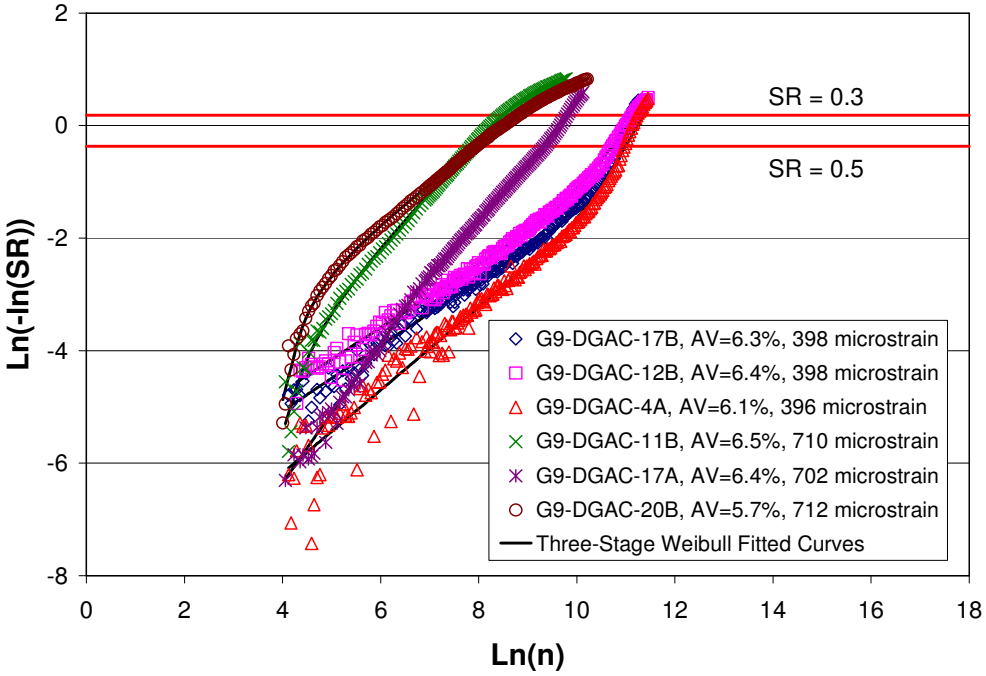

Figure A.1: AR4000-D Fatigue Test Three-stage Weibull curves: Temperature effect at 10°C.
(Binder content = 5.0%; field-mixed, lab-compacted; AV = 6 ± 0.5 %)

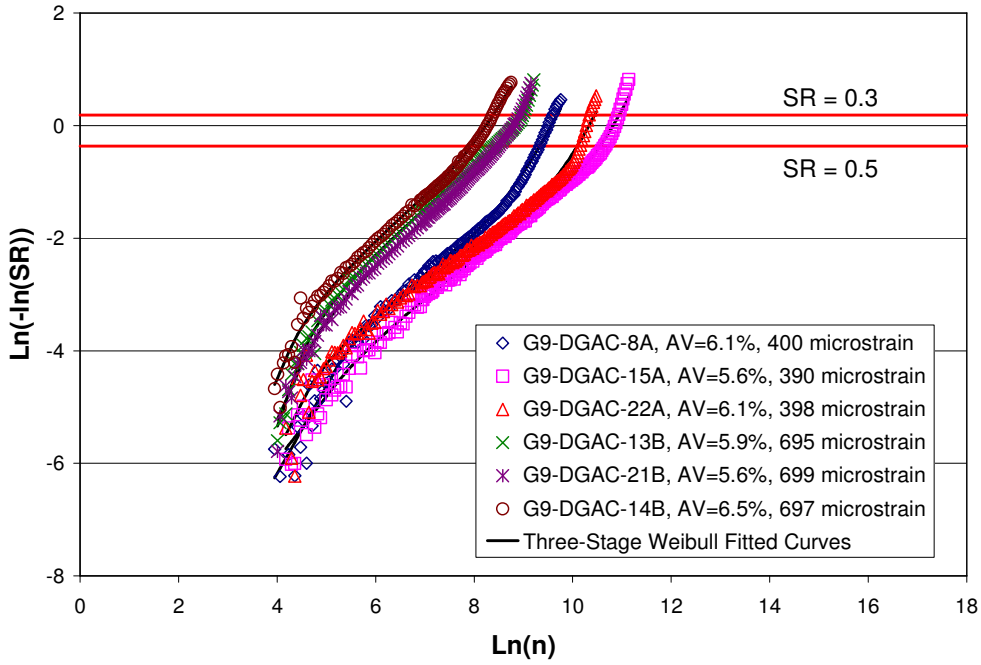

Figure A.2: AR4000-D Fatigue Test Three-stage Weibull curves: Temperature effect at 20°C.
(Binder content = 5.0%; field-mixed, lab-compacted; AV = 6 ± 0.5 %)

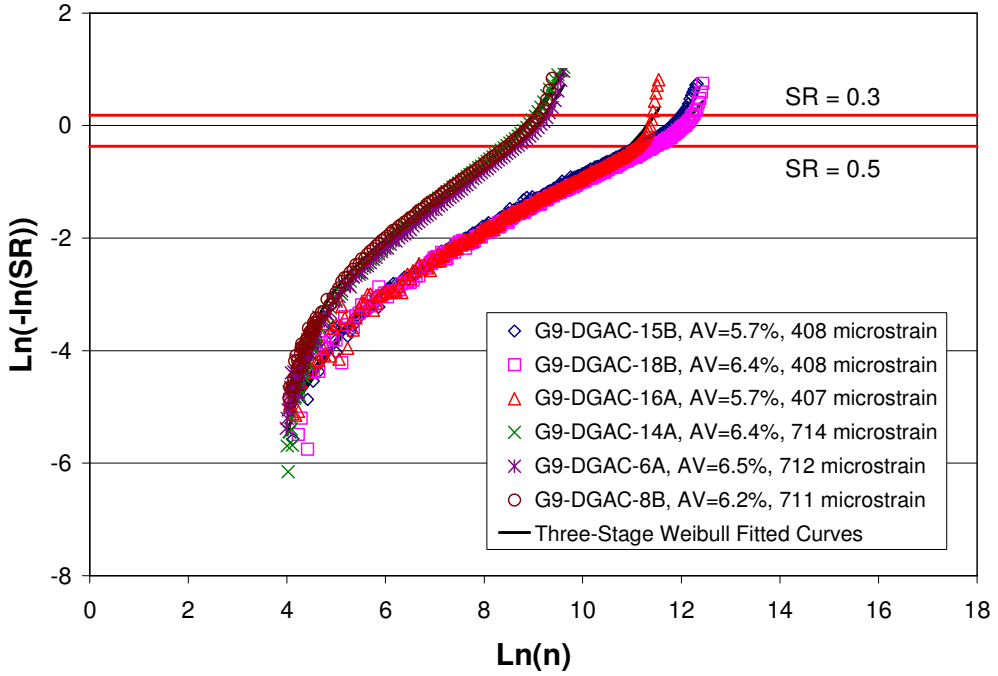

Figure A.3: AR4000-D Fatigue Test Three-stage Weibull curves: Temperature effect at 30°C.
(Binder content = 5.0%; field-mixed, lab-compacted; AV = 6 ± 0.5 %)

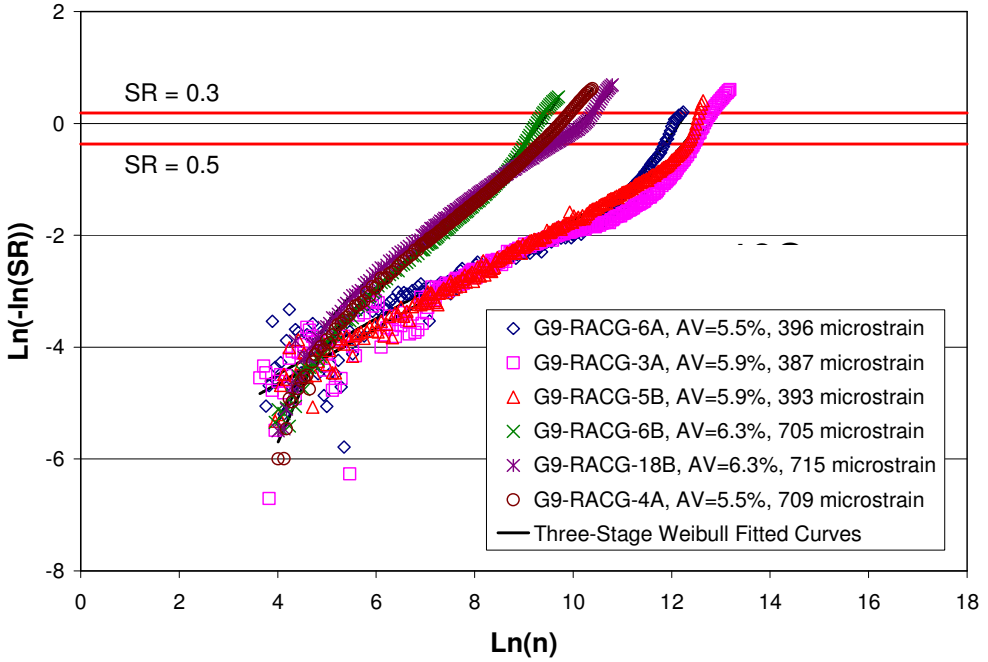

Figure A.4: RAC-G Fatigue Test Three-stage Weibull curves: Temperature effect at 10°C.
(Binder content = 6.3%; field-mixed, lab-compacted; AV = 6 ± 0.5 %)

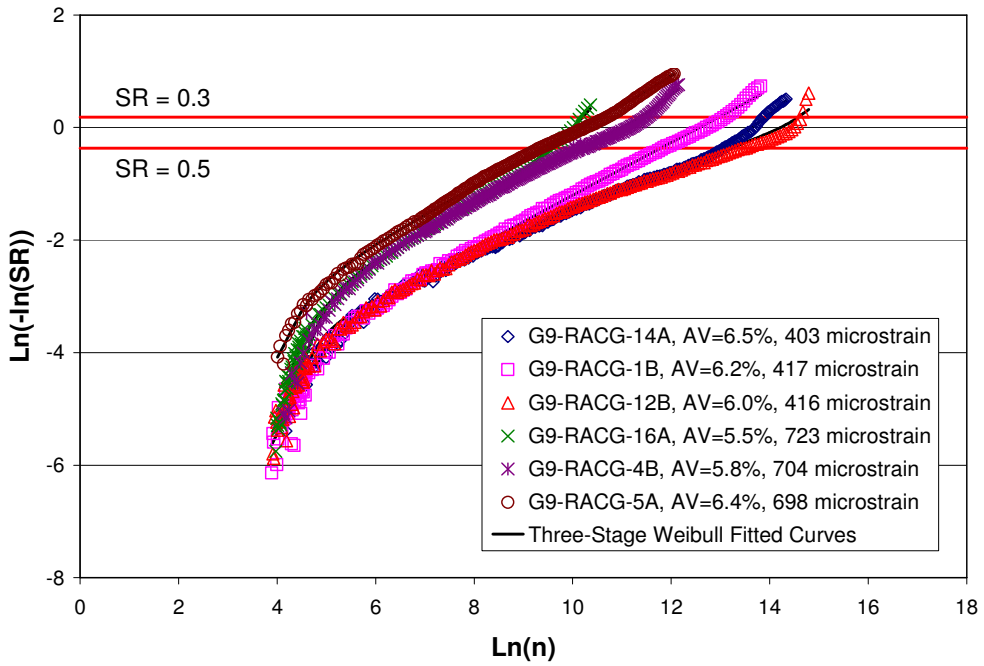

Figure A.5: RAC-G Fatigue Test Three-stage Weibull curves: Temperature effect at 20°C.
(Binder content = 8.0%; field-mixed lab-compacted; AV = 6 ± 0.5 %)

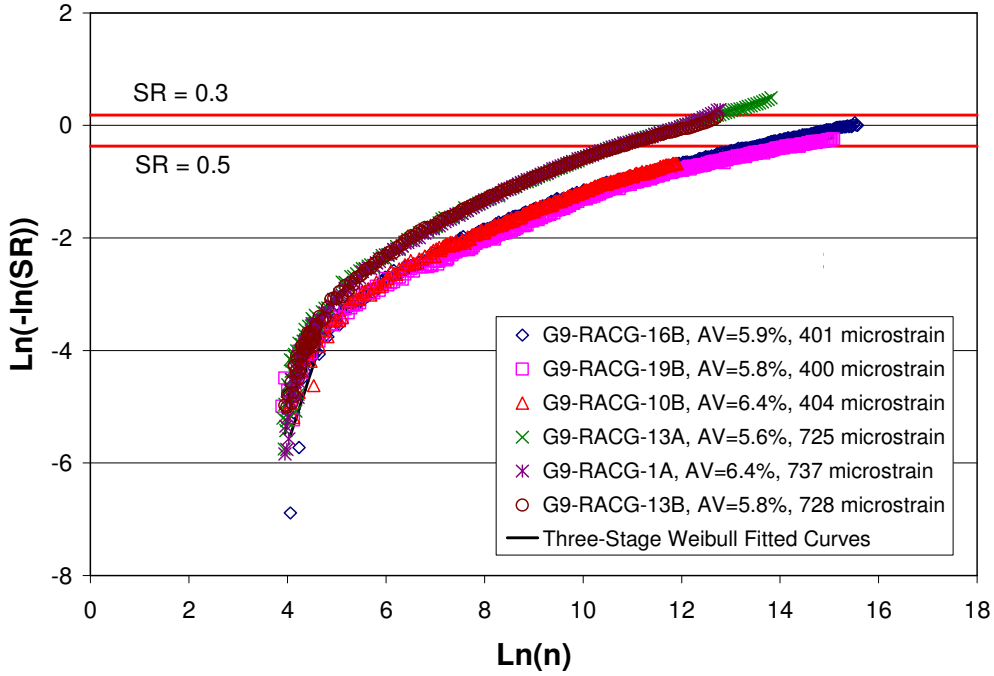

Figure A.6: RAC-G Fatigue Test Three-stage Weibull curves: Temperature effect at 30°C.
(Binder content = 8.0%; field-mixed, lab-compacted; AV = 6 ± 0.5 %)

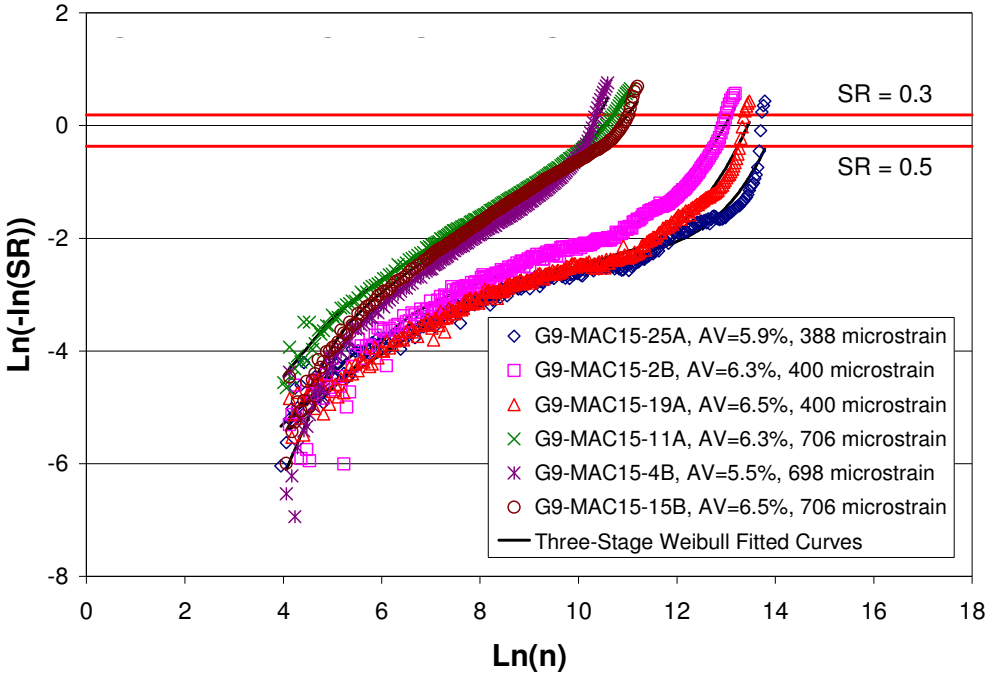

Figure A.7: MAC15-G Fatigue Test Three-stage Weibull curves: Temperature effect at 10°C.
(Binder content = 7.4%; field-mixed, lab-compacted; AV = 6 ± 0.5 %)

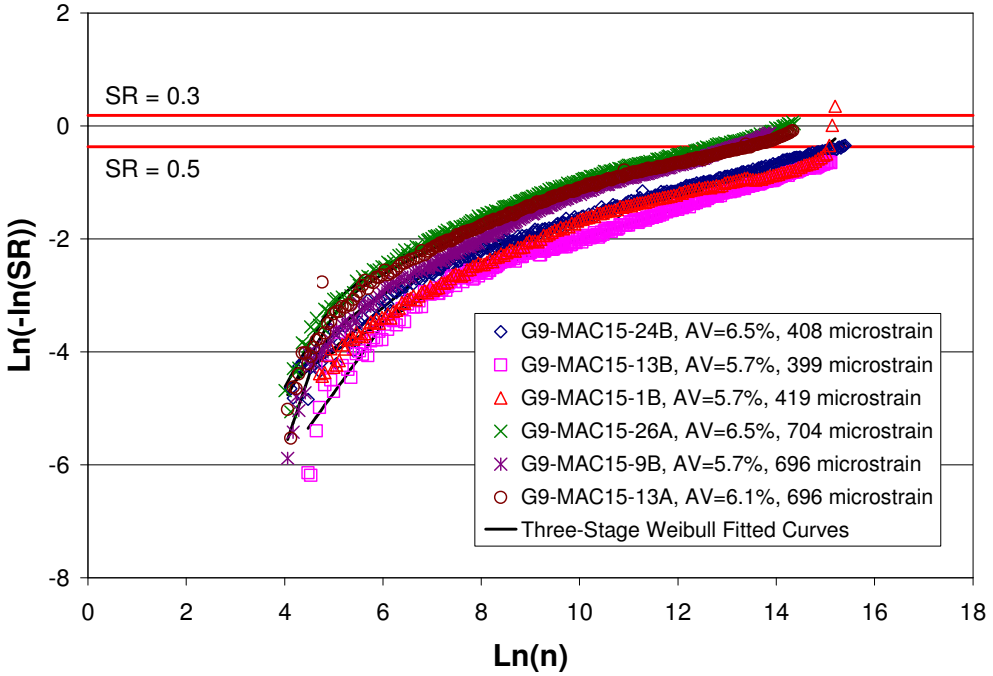

Figure A.8: MAC15-G Fatigue Test Three-stage Weibull curves: Temperature effect at 20°C.
(Binder content = 7.4%; field-mixed, lab-compacted; AV = 6 ± 0.5 %)

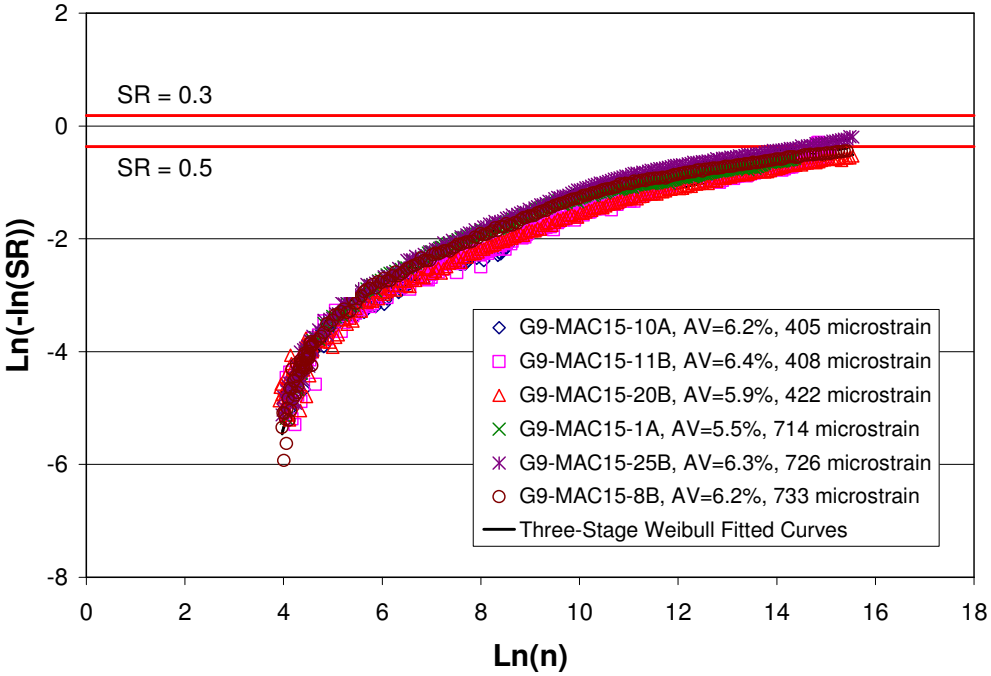

Figure A.9: MAC15-G Fatigue Test Three-stage Weibull curves: Temperature effect at 30°C.
(Binder content = 7.4%; field-mixed, lab-compacted; AV = 6 ± 0.5 %)

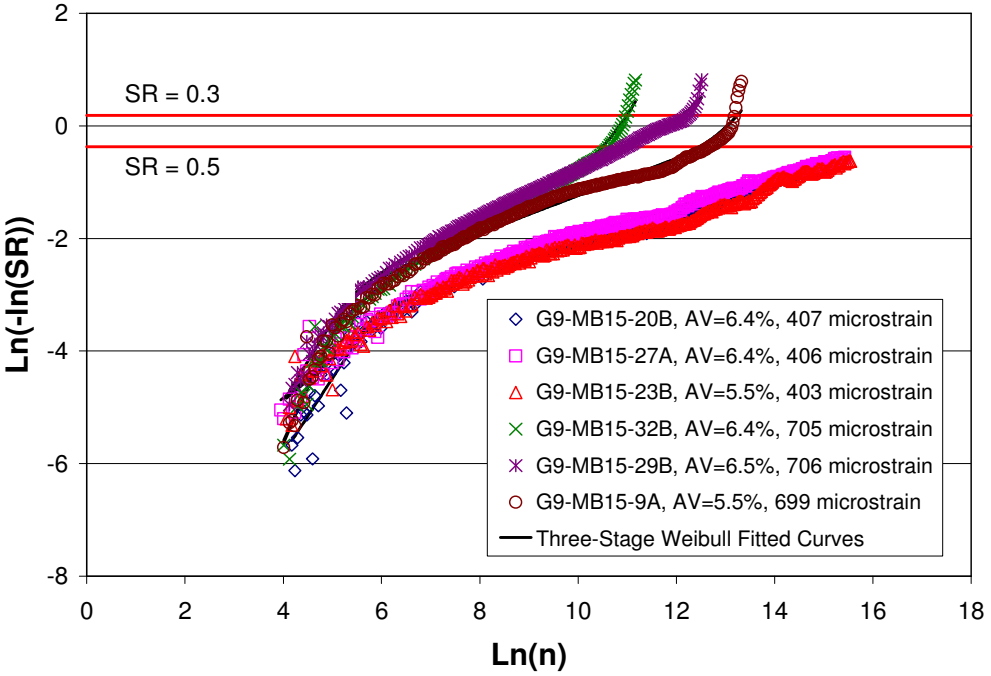

Figure A.10: MB15-G Fatigue Test Three-stage Weibull curves: Temperature effect at 10°C.
(Binder content = 7.1%; field-mixed, lab-compacted; AV = 6 ± 0.5 %)

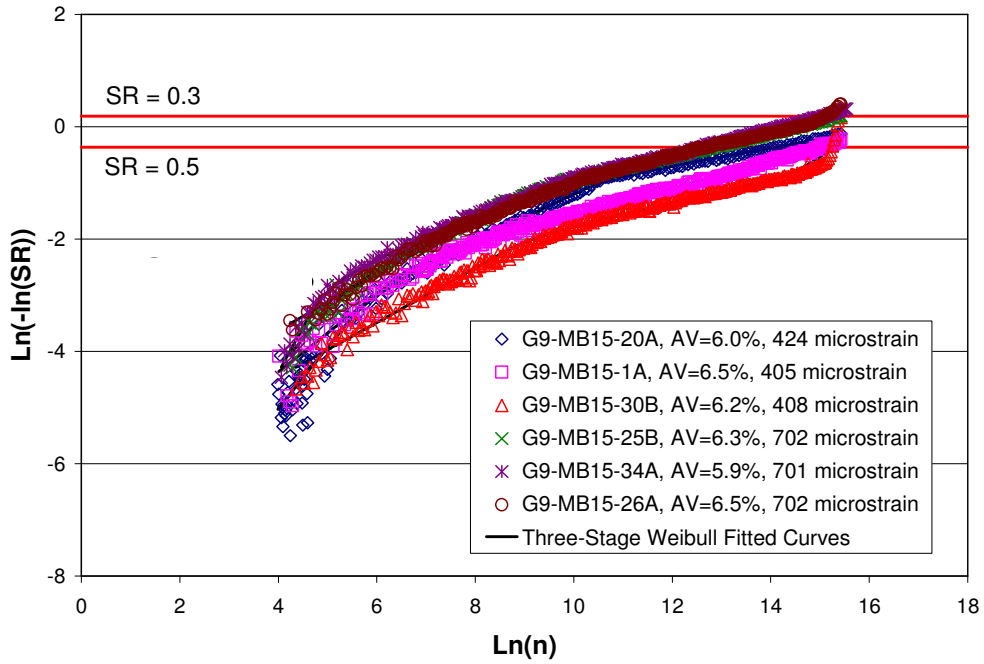

Figure A.11: MB15-G Fatigue Test Three-stage Weibull curves: Temperature effect at 20°C.
(Binder content = 7.1%; field-mixed, lab-compacted; AV = 6 ± 0.5 %)

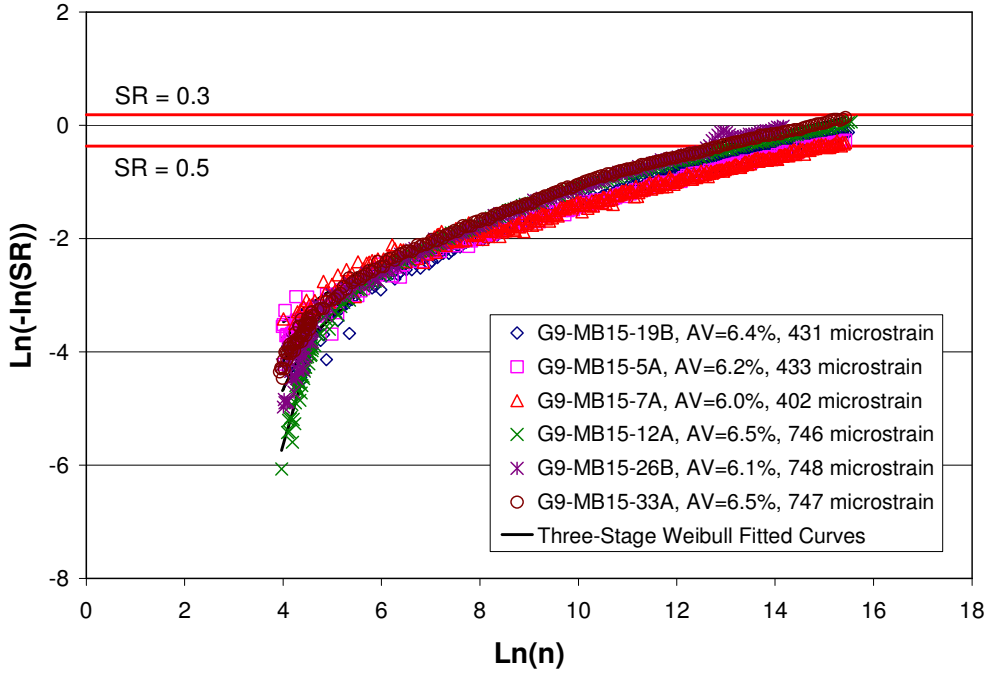

Figure A.12: MB15-G Fatigue Test Three-stage Weibull curves: Temperature effect at 30°C.
(Binder content = 7.1%; field-mixed, lab-compacted; AV = 6 ± 0.5 %)

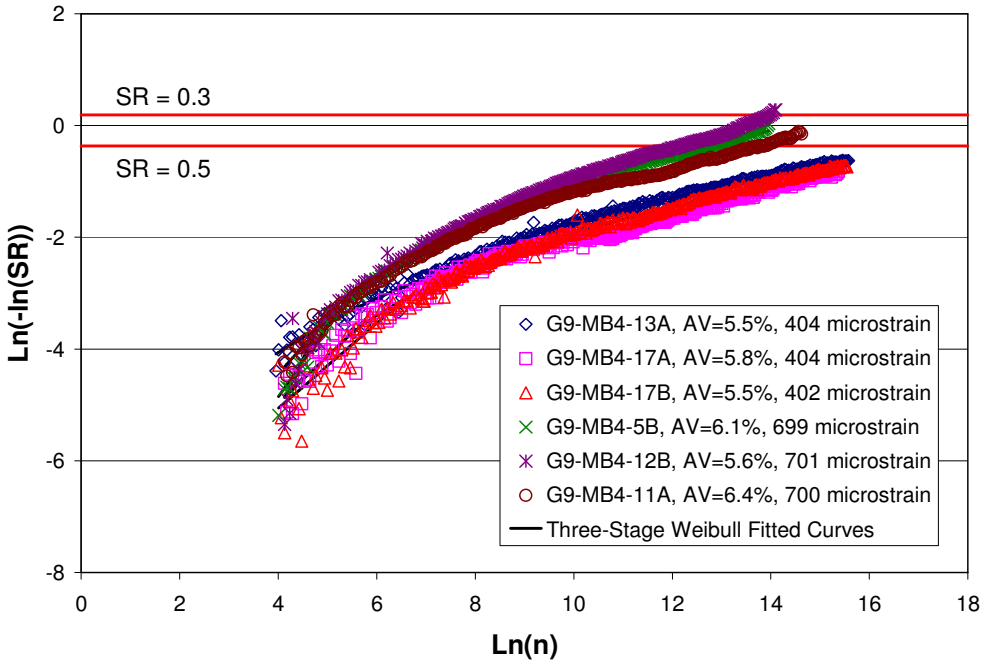

Figure A.13: MB4-G Fatigue Test Three-stage Weibull curves: Temperature effect at 10°C.
(Binder content = 7.2%; field-mixed, lab-compacted; AV = 6 ± 0.5 %)

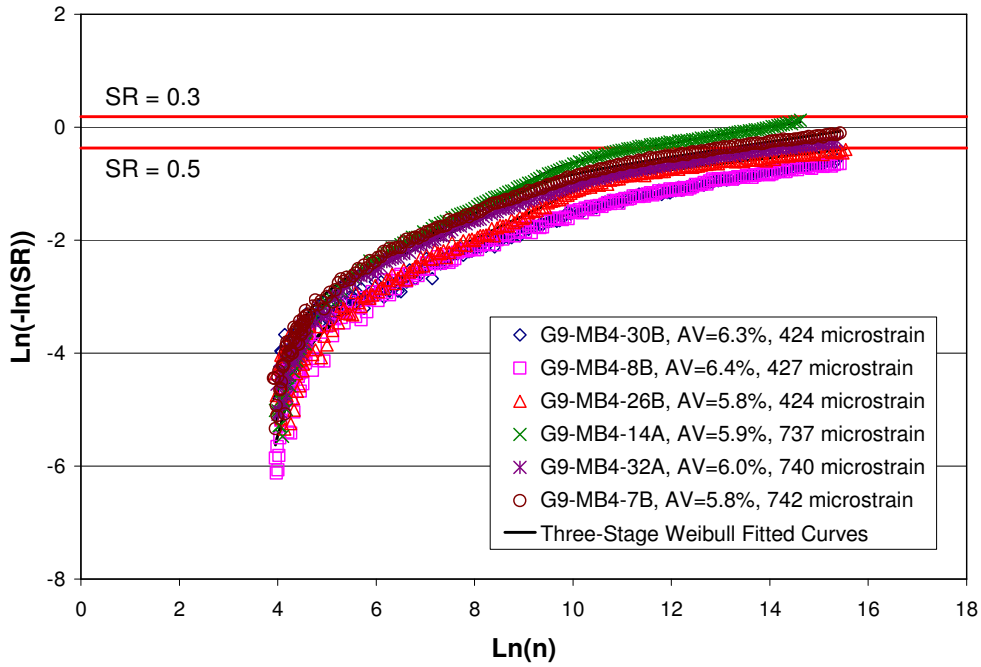

Figure A.14: MB4-G Fatigue Test Three-stage Weibull curves: Temperature effect at 20°C.
(Binder content = 7.2%; field-mixed, lab-compacted; AV = 6 ± 0.5 %)

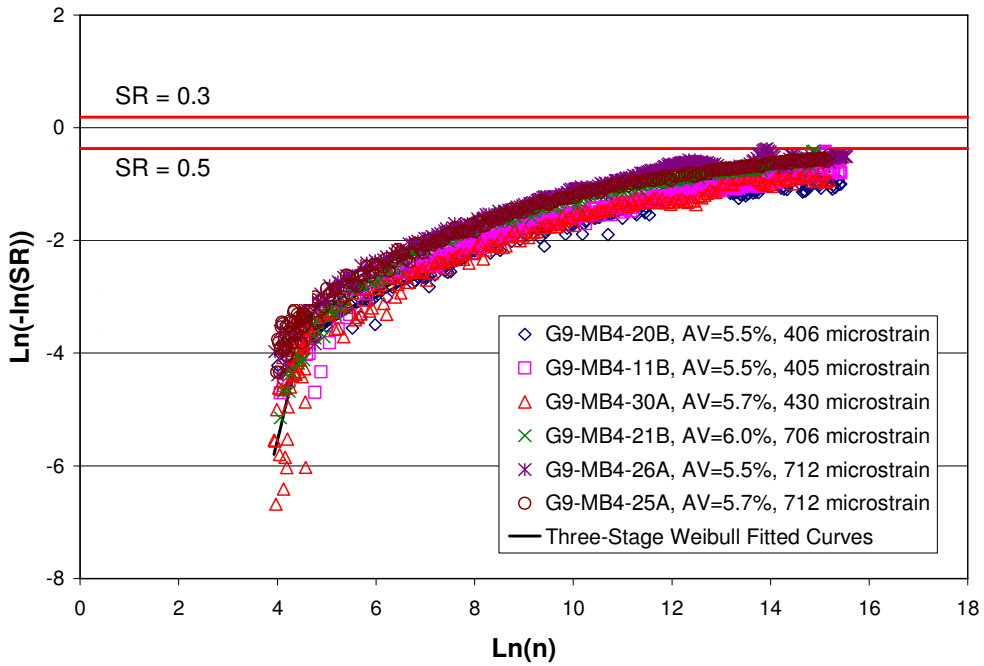

Figure A.15: MB4-G Fatigue Test Three-stage Weibull curves: Temperature effect at 30°C.
(Binder content = 7.2%; field-mixed, lab-compacted; AV = 6 ± 0.5 %)

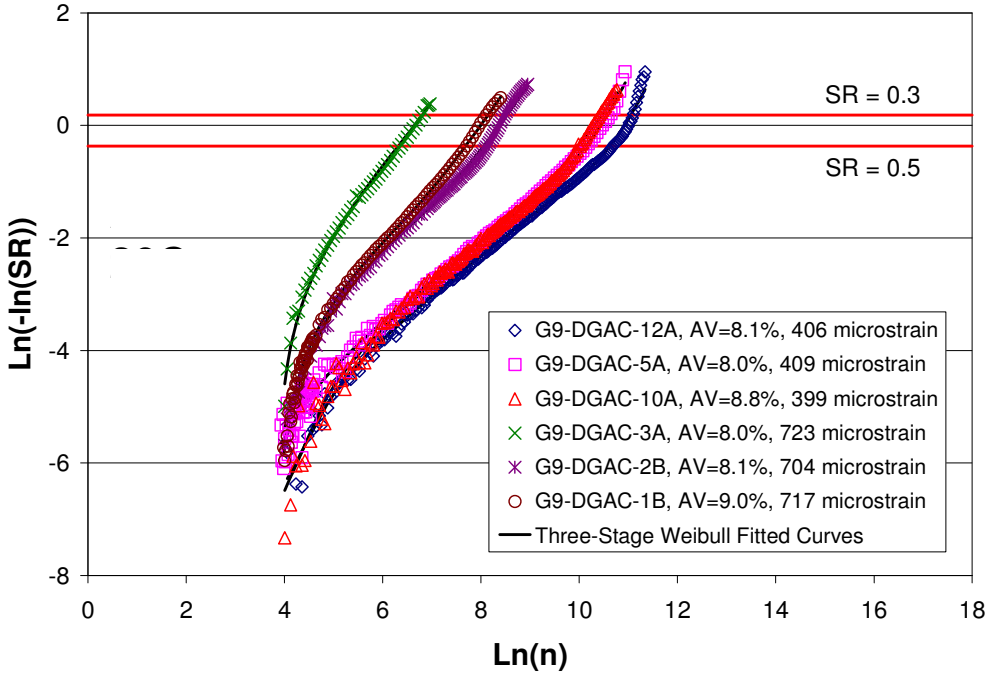

Figure A.16: AR4000-D Fatigue Test Three-stage Weibull curves: Air-void content effect at 20°C.
(Binder content = 5.0%; field-mixed, lab-compacted; AV = 9 ± 1.0 %)

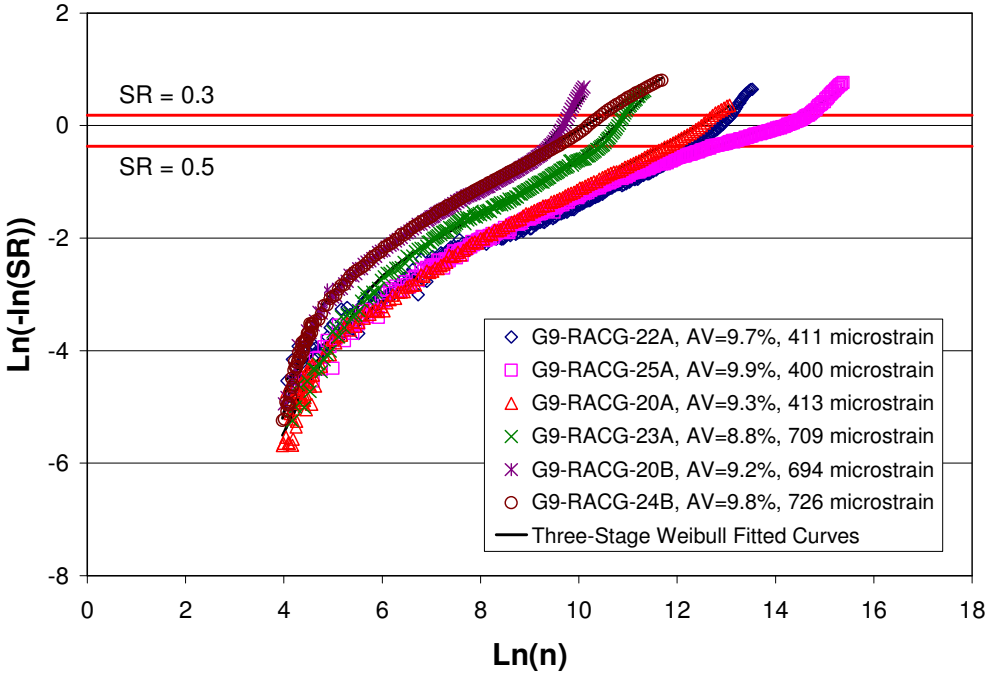

Figure A.17: RAC-G Fatigue Test Three-stage Weibull curves: Air-void content effect at 20°C.
(Binder content = 8.0%; field-mixed, lab-compacted; AV = 9 ± 1.0 %)

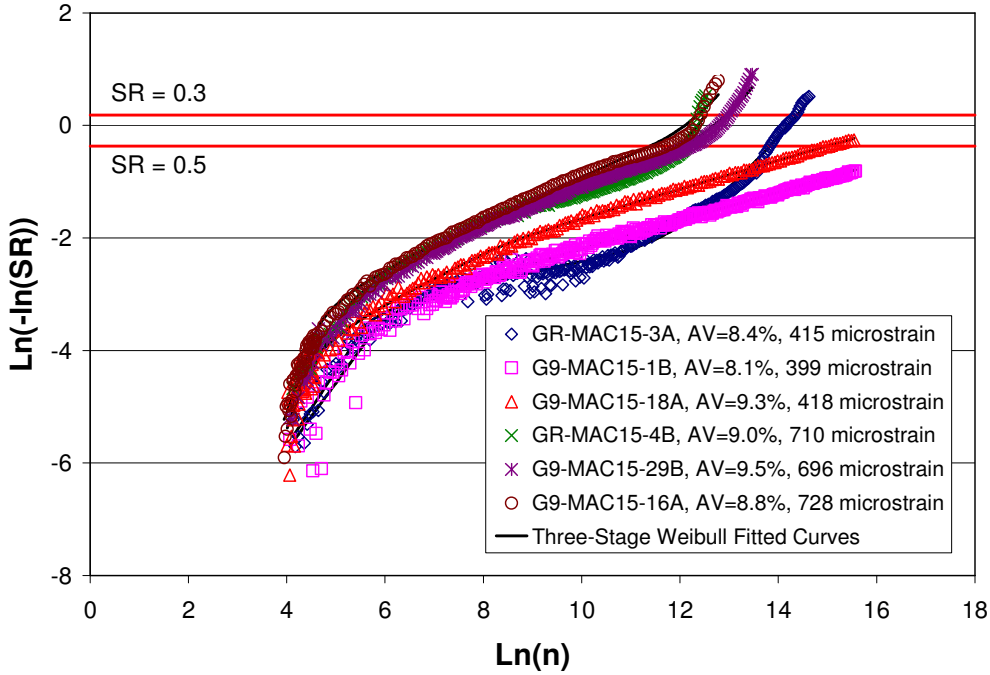

Figure A.18: MAC15-G Fatigue Test Three-stage Weibull curves: Air-void content effect at 20°C.
(Binder content = 7.4%; field-mixed, lab-compacted; AV = 9 ± 1.0 %)

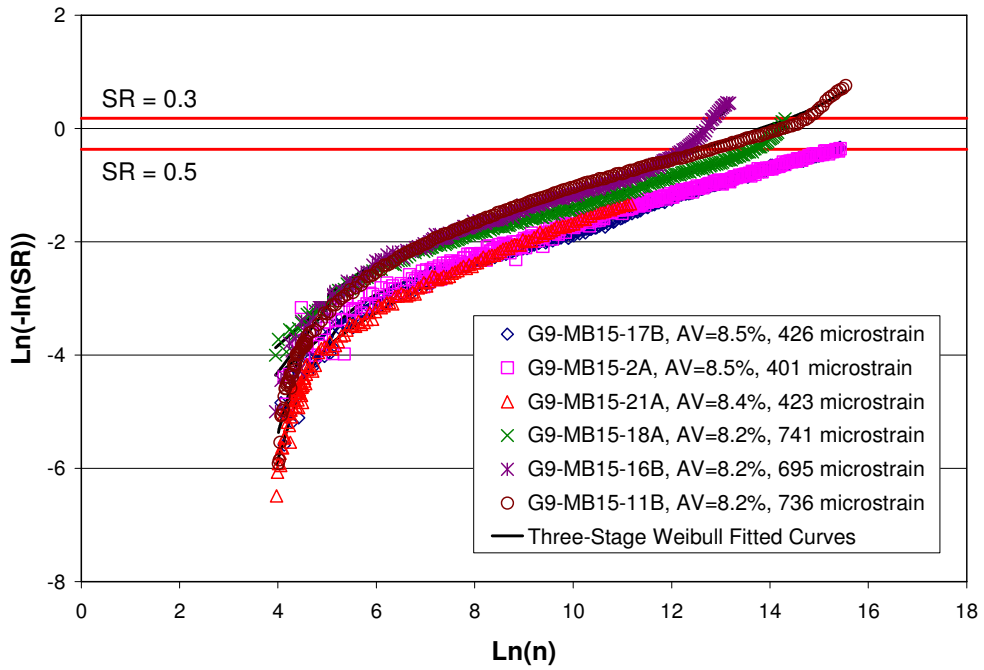

Figure A.19: MB15-G Fatigue Test Three-stage Weibull curves: Air-void content effect at 20°C.
(Binder content = 7.1%; field-mixed, lab-compacted; AV = 9 ± 1.0 %)

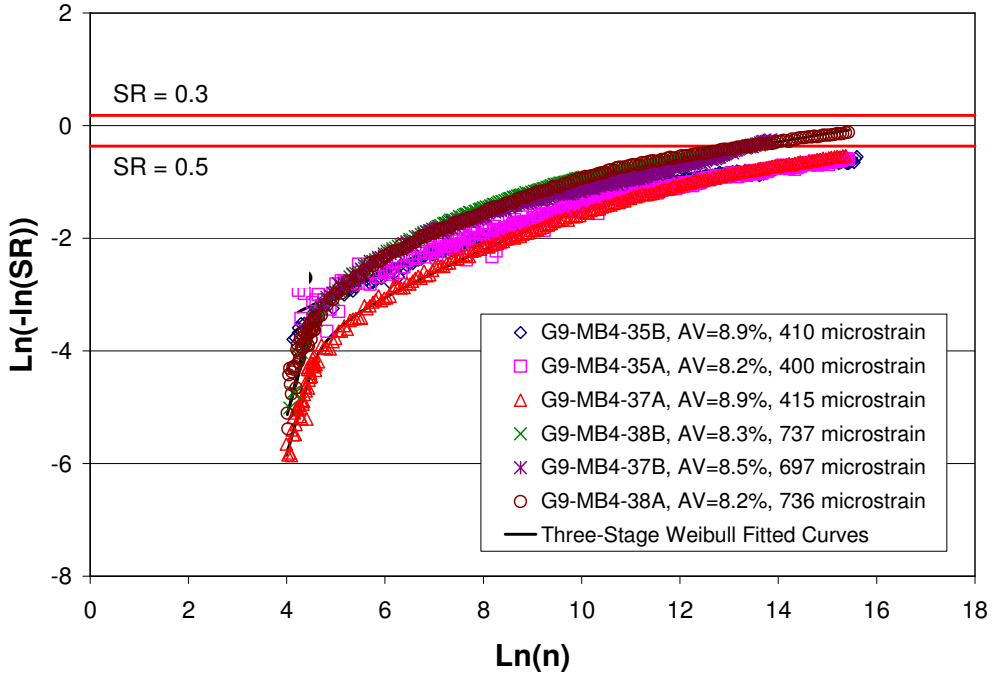

Figure A.20: MB4-G Fatigue Test Three-stage Weibull curves: Air-void content effect at 20°C.
(Binder content = 7.2%; field-mixed, lab-compacted; AV = 9 ± 1.0 %)

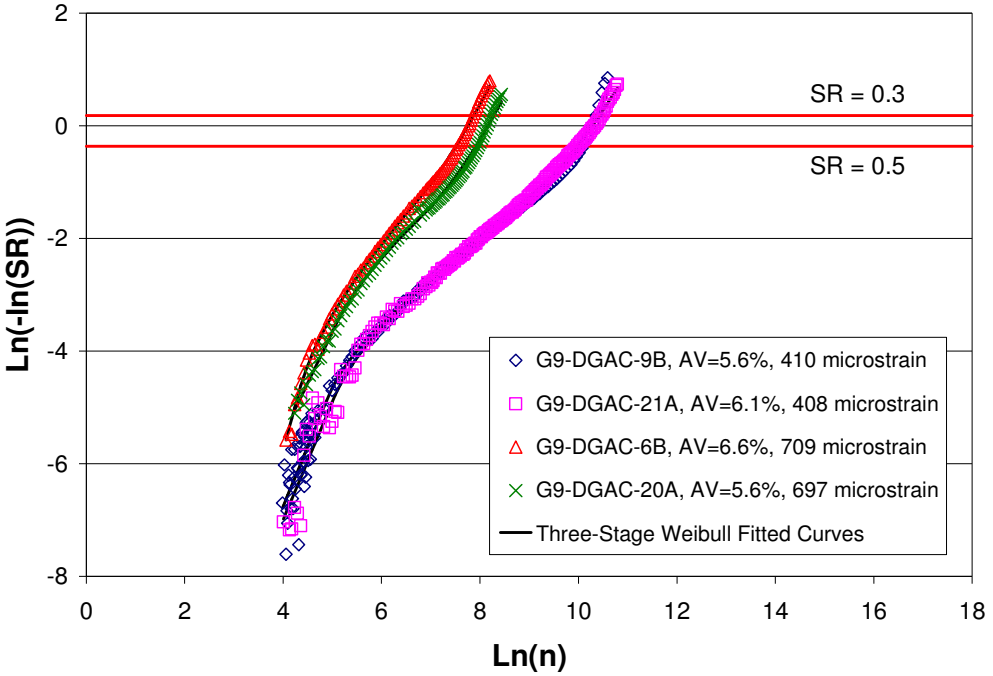

Figure A.21: AR4000-D Fatigue Test Three-stage Weibull curves: Aging effect at 20°C.
(Binder content = 5.0%; field-mixed, lab-compacted; AV = 6 ± 0.5 %, LTOA = 6 days)

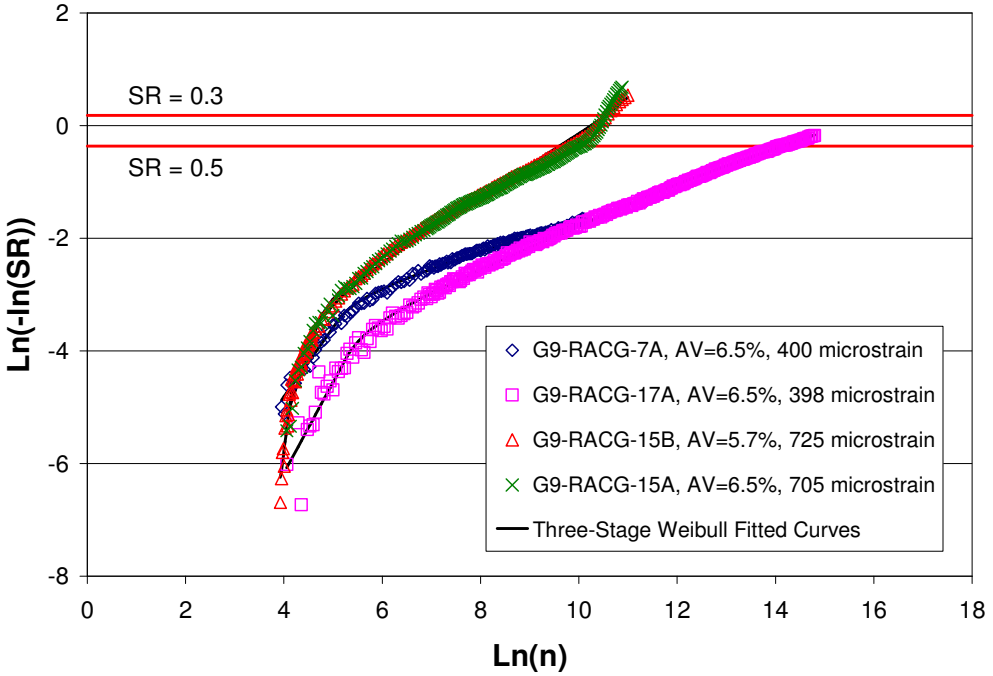

Figure A.22: RAC-G Fatigue Test Three-stage Weibull curves: Aging effect at 20°C.
(Binder content = 8.0%; field-mixed, lab-compacted; AV = 6 ± 0.5 %, LTOA = 6 days)

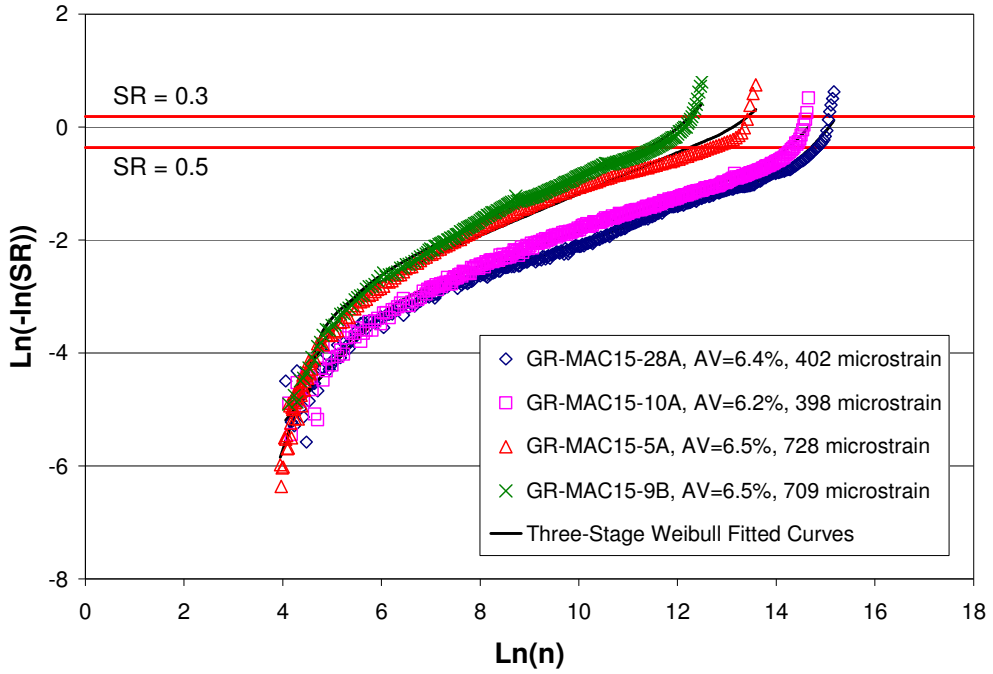

Figure A.23: MAC15-G Fatigue Test Three-stage Weibull curves: Aging effect at 20°C.
(Binder content = 7.4%; field-mixed, lab-compacted; AV = 6 ± 0.5 %, LTOA = 6 days)

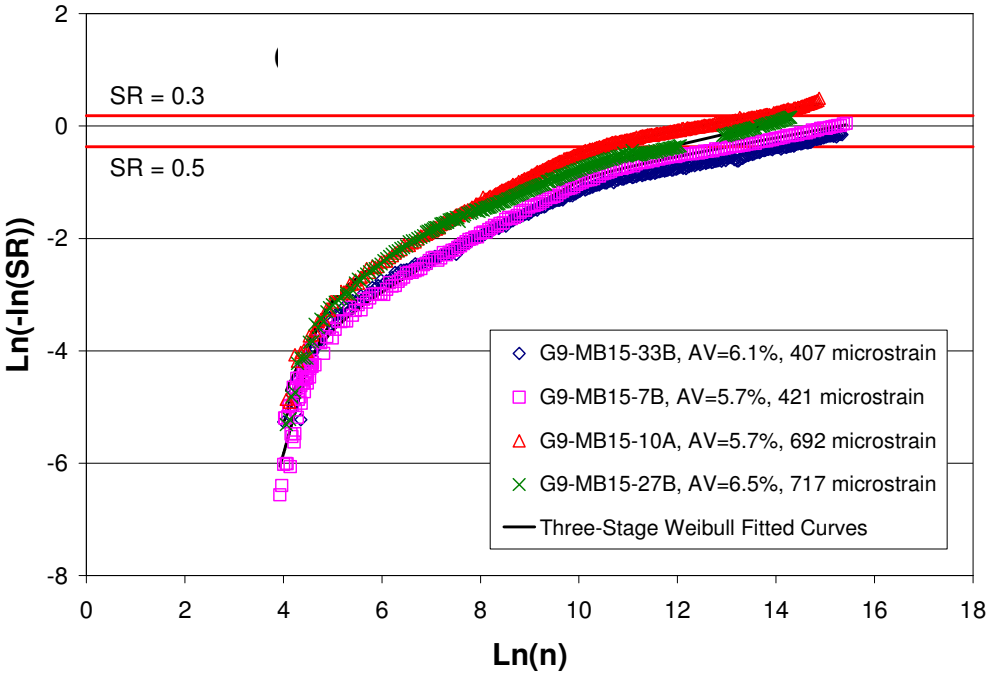

Figure A.24: MB15-G Fatigue Test Three-stage Weibull curves: Aging effect at 20°C.
(Binder content = 7.1%; field-mixed, lab-compacted; AV = 6 ± 0.5 %, LTOA = 6 days)

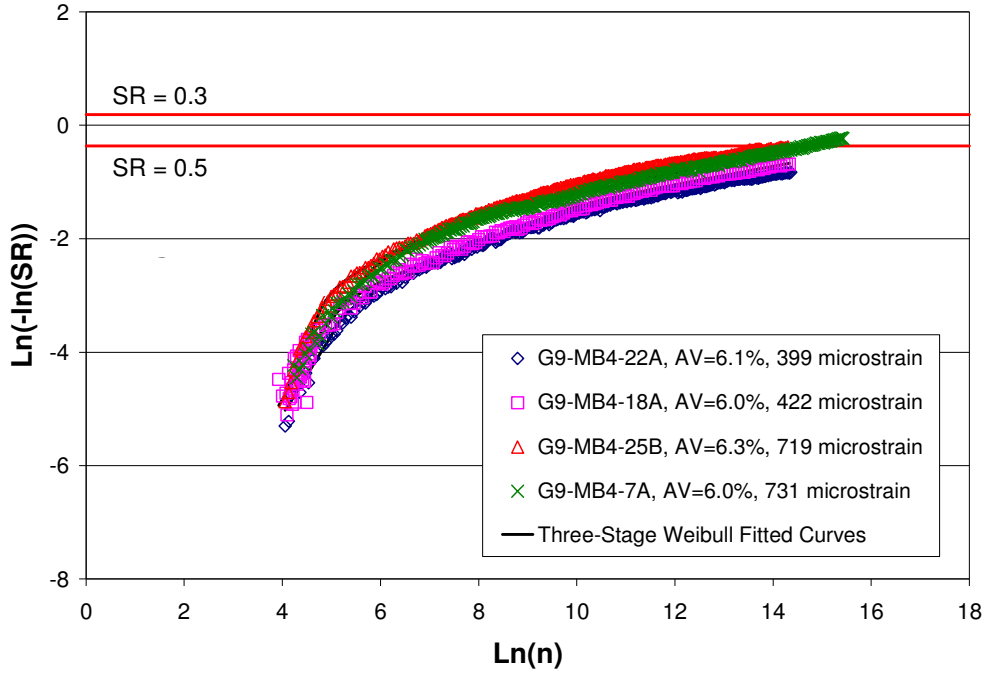

Figure A.25: MB4-G Fatigue Test Three-stage Weibull curves: Aging effect at 20°C.
(Binder content = 7.2%; field-mixed, lab-compacted; AV = 6 ± 0.5 %, LTOA = 6 days)

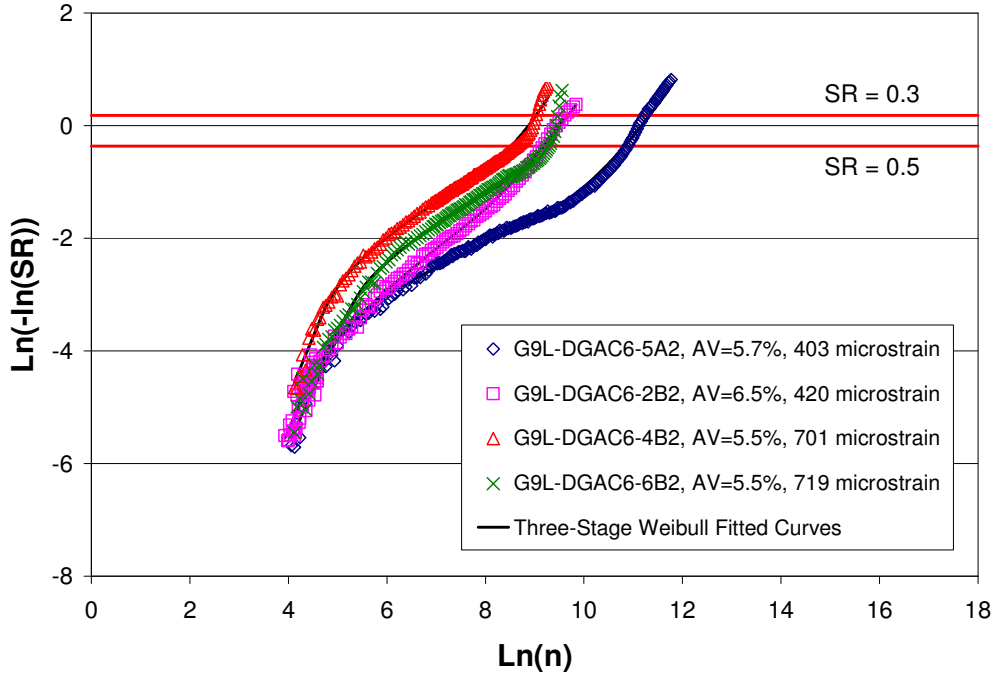

Figure A.26: AR4000-D Fatigue Test Three-stage Weibull curves: Compaction effect at 20°C.
(Binder content = 5.0%; lab-mixed, lab-compacted; AV = 6 ± 0.5 %)

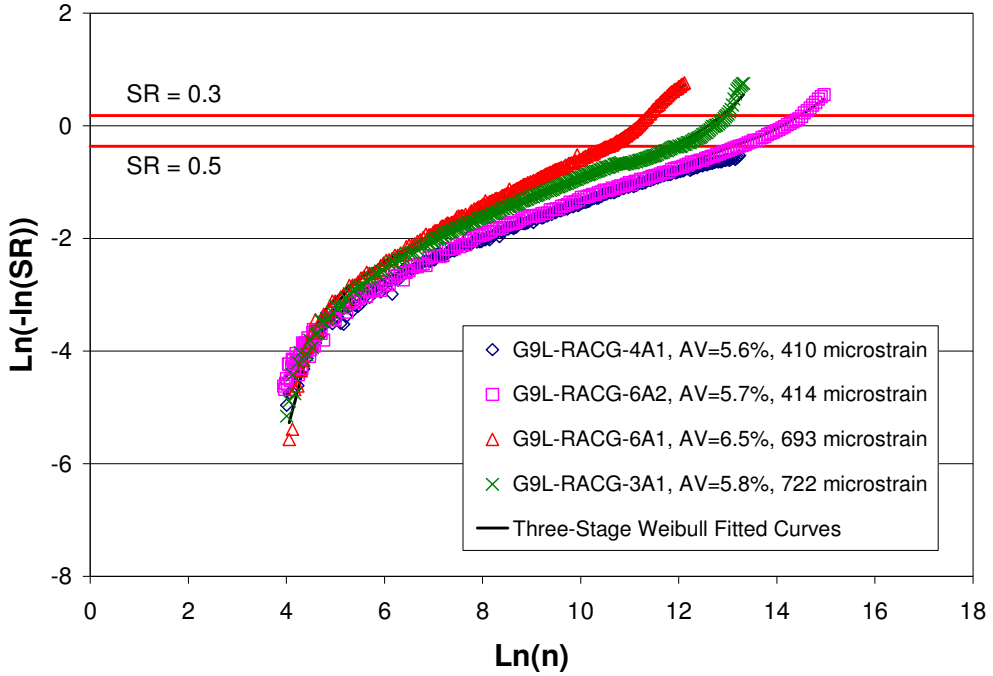

Figure A.27: RAC-G Fatigue Test Three-stage Weibull curves: Compaction effect at 20°C.
(Binder content = 8.0%; lab-mixed, lab-compacted; AV = 6 ± 0.5 %)

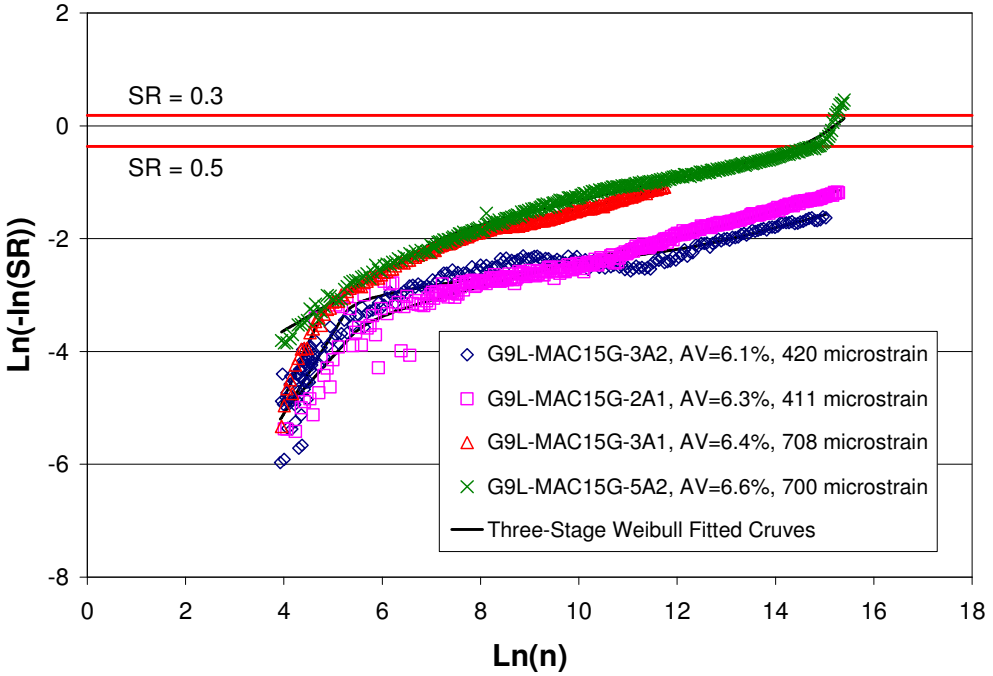

Figure A.28: MAC15-G Fatigue Test Three-stage Weibull curves: Compaction effect at 20°C.
(Binder content = 7.4%; lab-mixed, lab-compacted; AV = 6 ± 0.5 %)

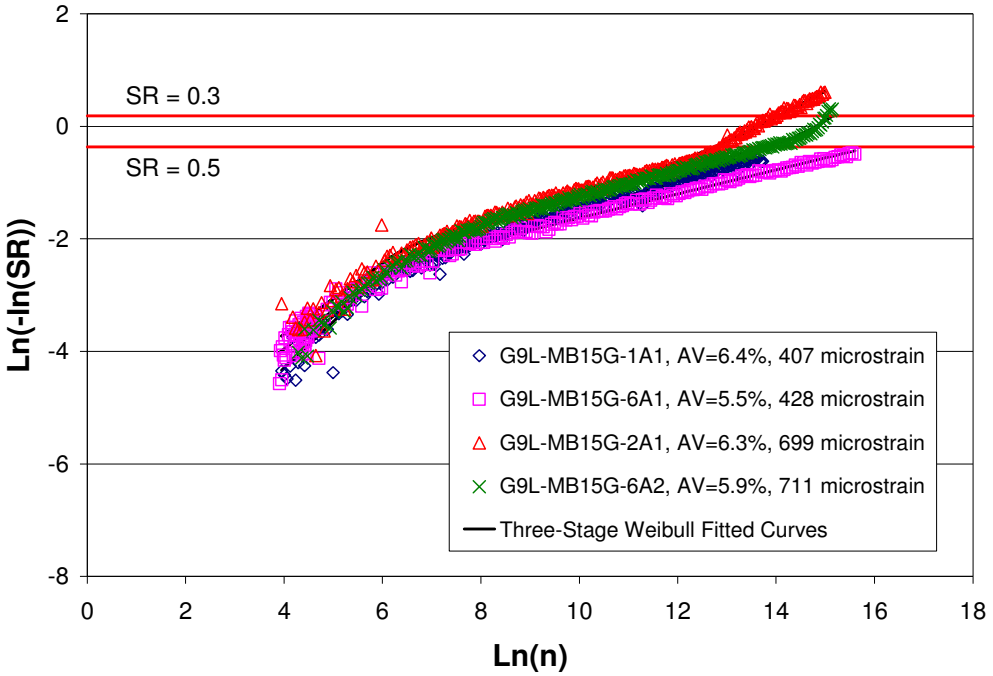

Figure A.29: MB15-G Fatigue Test Three-stage Weibull curves: Compaction effect at 20°C.
(Binder content = 7.1%; lab-mixed, lab-compacted; AV = 6 ± 0.5 %)

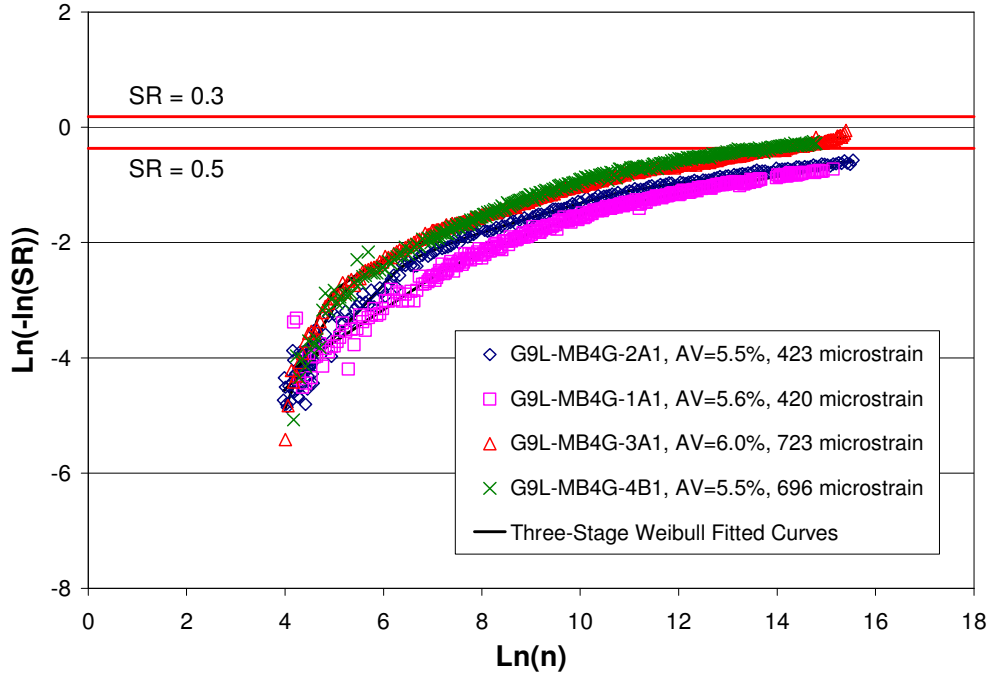

Figure A.30: MB4-G Fatigue Test Three-stage Weibull curves: Compaction effects at 20°C.
(Binder content = 7.2%; lab-mixed, lab-compacted; AV = 6 ± 0.5 %)

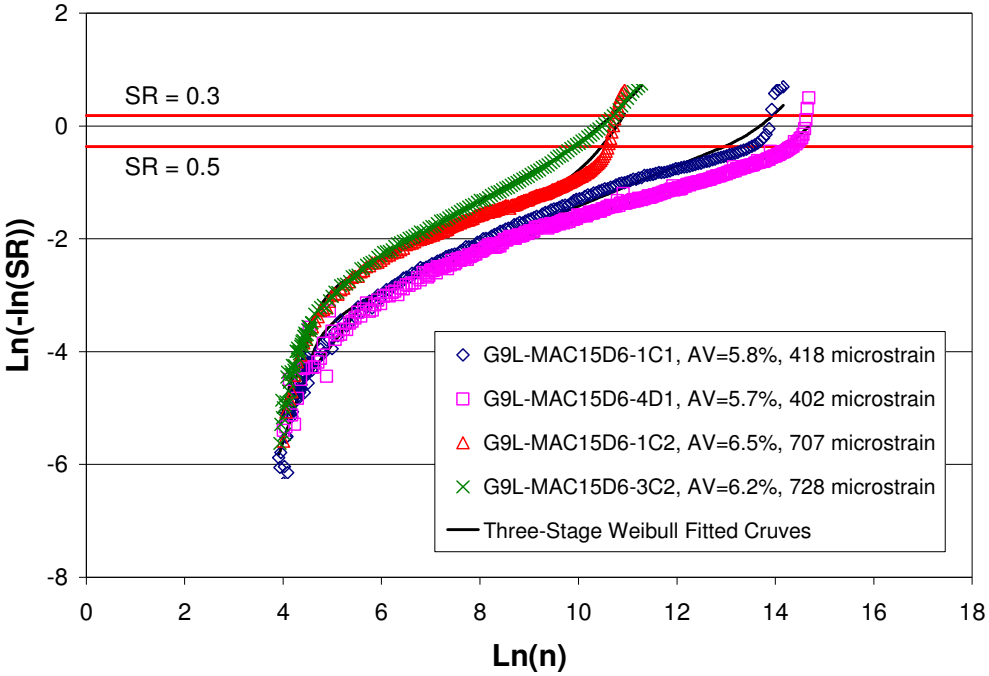

Figure A.31: MAC15-D Fatigue Test Three-stage Weibull curves: Gradation effect at 20°C.
(Binder content = 6.0%; lab-mixed, lab-compacted; AV = 6 ± 0.5 %; dense-graded)

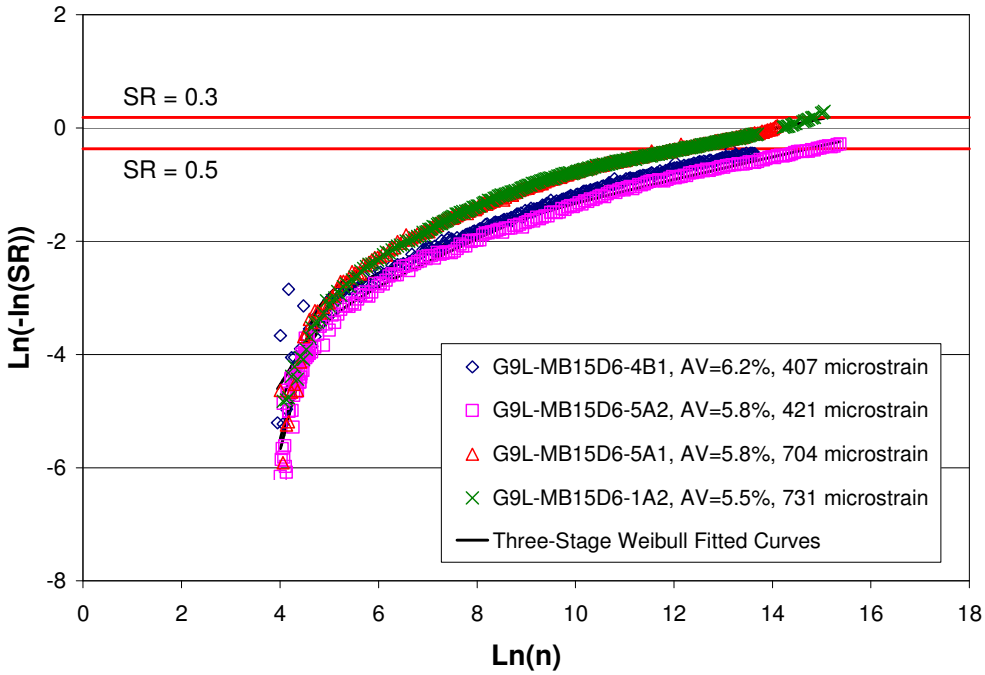

Figure A.32: MB15-D Fatigue Test Three-stage Weibull curves: Gradation effect at 20°C.
(Binder content = 6.0%; lab-mixed, lab-compacted; AV = 6 ± 0.5 %; dense-graded)

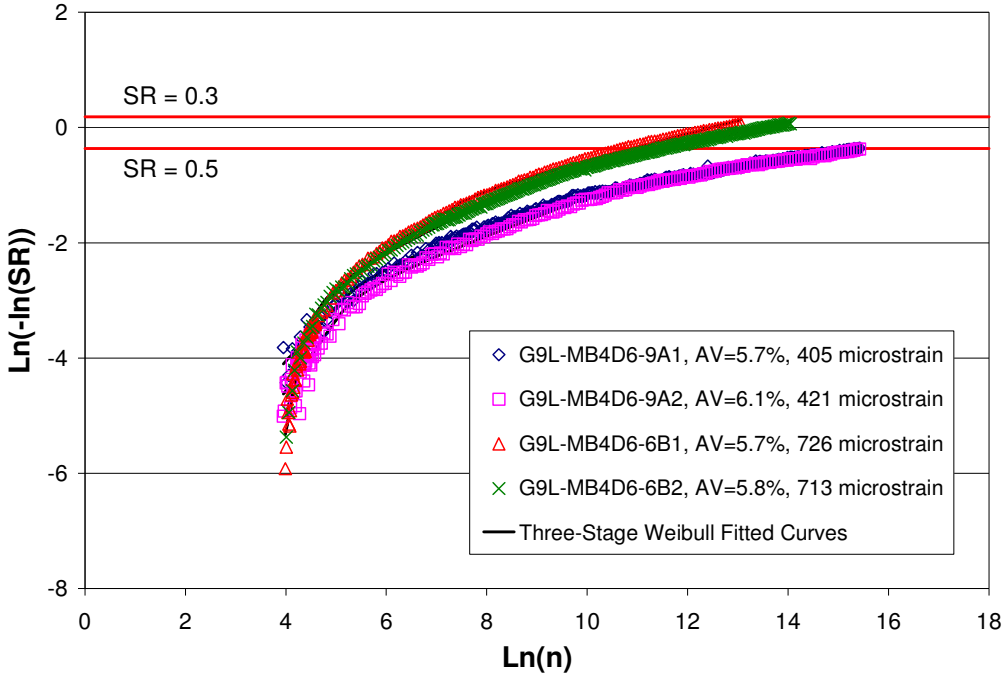

Figure A.33: MB4-D Fatigue Test Three-stage Weibull curves: Gradation effect at 20°C.
(Binder content = 6.3%; lab-mixed, lab-compacted; AV = 6 ± 0.5 %; dense-graded)

A.3. Pruned Dendograms for Laboratory Fatigue Results

Section 3.4.2

Pruned dendrograms for laboratory fatigue results are presented in Figure A.34.

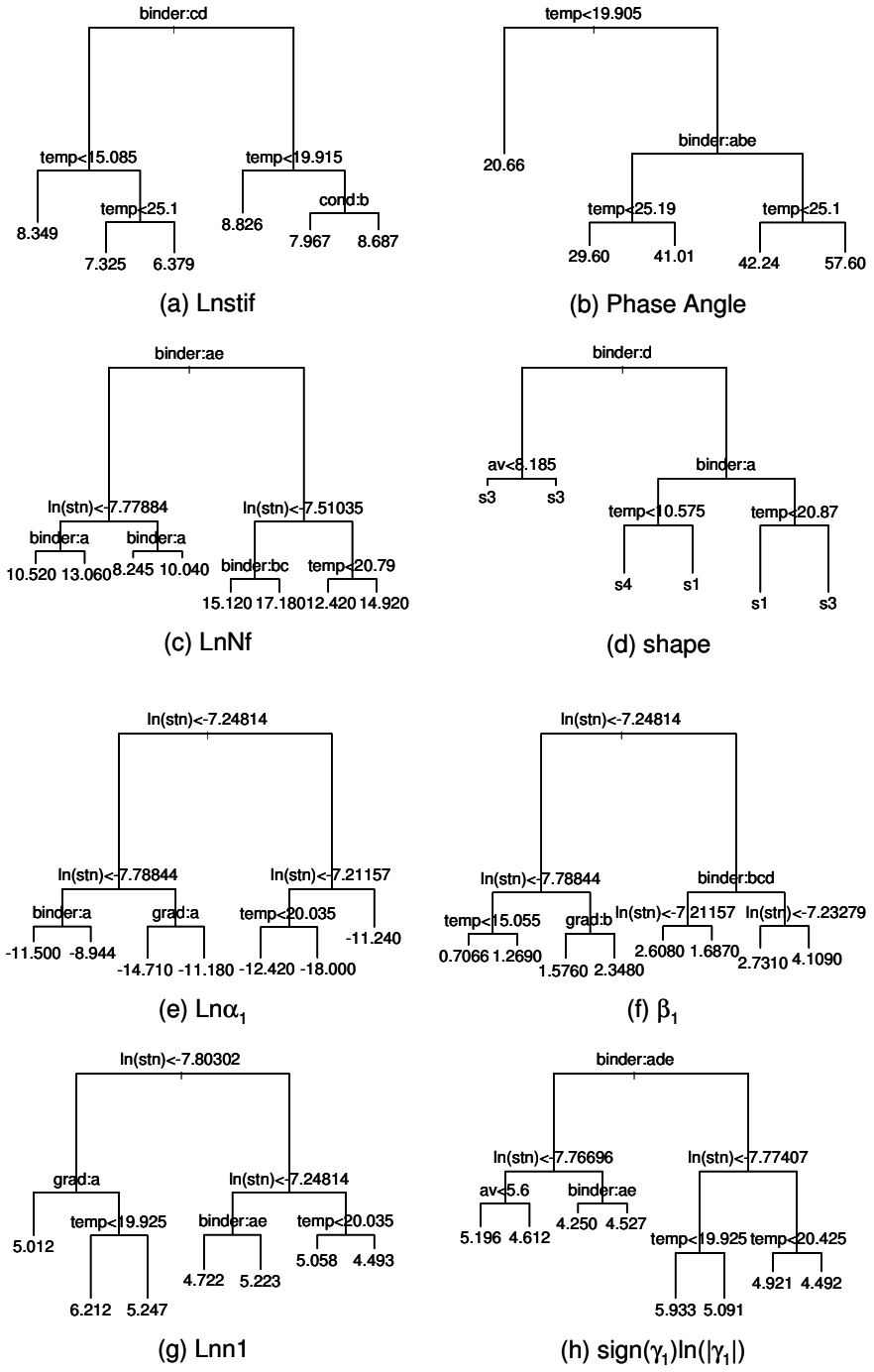

Figure A.34: Pruned dendrograms of fatigue three-stage Weibull parameters.

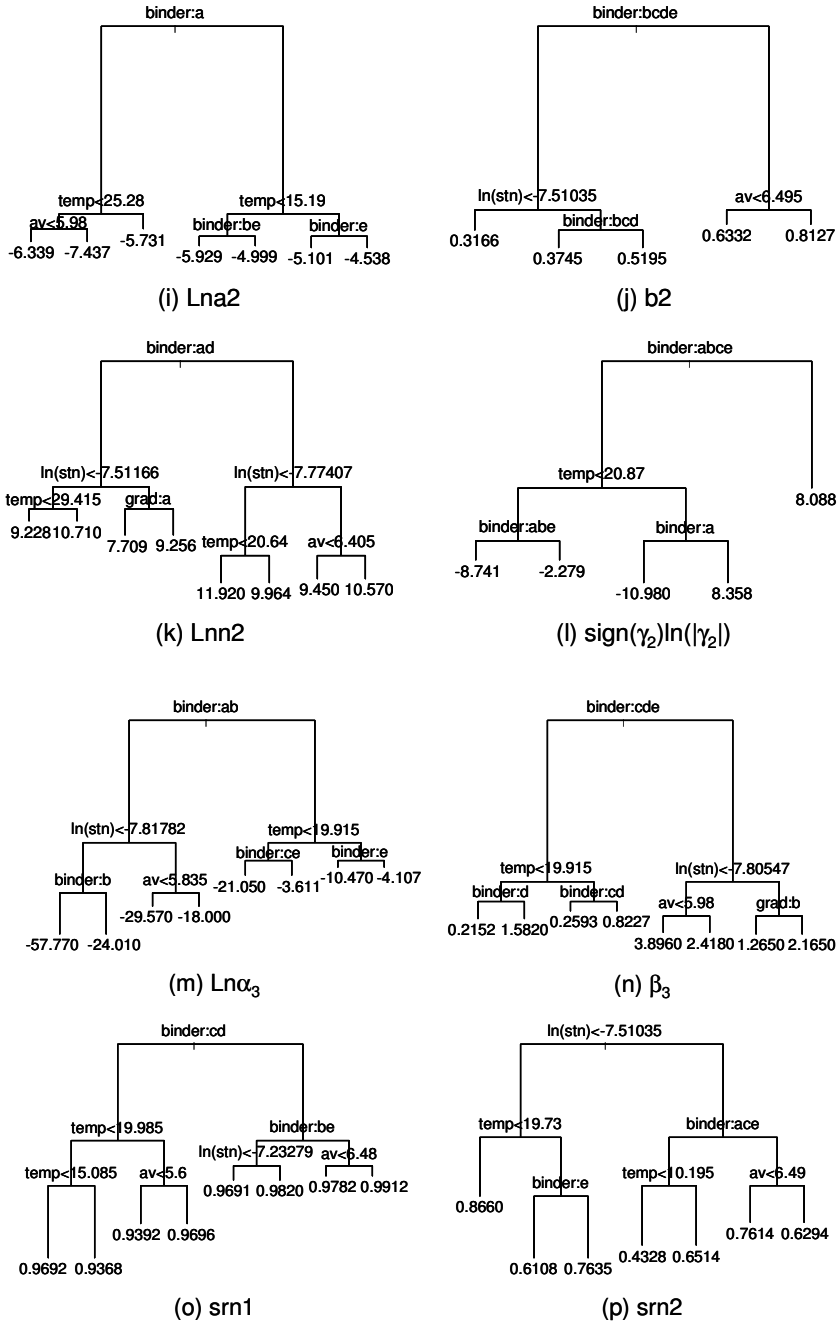

Figure A.34: Pruned dendrograms of fatigue three-stage Weibull parameters (continued).

A.4. Weibull Curves of Modified Binder Shear Results

Section 3.5.1

The laboratory fatigue test results and associated Weibull-fitted curves are presented in Tables A.10 to A.18 and Figures A.35 to A.67.

Table A.10: AR4000-D Mixes: Summary of Three-Stage Weibull Shear Analysis: Temperature Effect

(FMLC, AV = 6.0±0.5 %, AC=5.0 %).

Specimen ID	Three-Stage Weibull Fitting										PSS@ n_1	PSS@ n_2	Last PSS
	1st Stage		2nd Stage				3rd Stage						
	$ln\alpha_1$	β_1	n_1	γ_1	$ln\alpha_2$	β_2	n_2	γ_2	$ln\alpha_3$	β_3			
DGAC-6-6-1-7045	2.07783	-0.08672	25.99	11.68	1.92233	-0.04773	3524.66	2502.04	1.62892	-0.01390	0.00240	0.00959	0.01188
DGAC-6-14-3-7045	2.12037	-0.09394	37.86	17.98	1.92651	-0.04934	176.94	29.47	1.90500	-0.04577	0.00271	0.00476	0.01507
DGAC-6-15-2-7045	2.09796	-0.10615	33.96	12.38	1.93103	-0.06747	286.90	108.79	1.77902	-0.04378	0.00365	0.00892	0.02266
DGAC-6-10-2-7055	1.97095	-0.07514	31.52	14.03	1.83100	-0.04170	1972.33	-570.47	1.93948	-0.05414	0.00389	0.01060	0.01858
DGAC-6-10-3-7055	2.02233	-0.09671	12.09	5.02	1.89184	-0.05653	313.31	-41.35	1.94969	-0.06503	0.00261	0.00824	0.02716
DGAC-6-11-1-7055	1.92577	-0.07425	48.96	12.32	1.83697	-0.05557			1.83697	-0.05557	0.00583		0.02857
DGAC-6-14-1-10045	2.08628	-0.09215	11.88	4.37	1.97558	-0.05822	220.66	68.53	1.86831	-0.04095	0.00162	0.00508	0.01396
DGAC-6-14-2-10045	2.06349	-0.08553	54.67	27.86	1.85920	-0.04194	6169.52	-606.86	1.90156	-0.04628	0.00369	0.01160	0.01591
DGAC-6-15-3-10045	2.17851	-0.09314	3.33	-0.60	2.21716	-0.11003	1509.74	268.93	2.05565	-0.09040	0.00083	0.01641	0.04277
DGAC-6-16-1-10045	2.09875	-0.10159	30.32	12.53	1.92371	-0.05961	156.53	49.35	1.83488	-0.04437	0.00311	0.00617	0.01878
DGAC-6-16-3-10045	2.10957	-0.09562	20.30	7.69	1.97226	-0.05940	118.52	34.35	1.89256	-0.04511	0.00205	0.00436	0.01544
DGAC-6-8-1-10055	1.98033	-0.09575	15.08	4.76	1.87335	-0.06549	759.54	-210.58	2.01830	-0.08418	0.00373	0.01469	0.04234
DGAC-6-8-2-10055	2.00861	-0.10358	6.62	2.37	1.90908	-0.06651	295.58	-21.05	1.94477	-0.07182	0.00219	0.00977	0.03473
DGAC-6-8-3-10055	1.98825	-0.12743	2.66	1.04	1.90129	-0.07775	1021.23	-1288.70	2.72606	-0.17603	0.00160	0.02040	0.06721
DGAC-6-10-1-13045	2.09302	-0.11312	10.97	3.68	1.97138	-0.07516	63.99	18.95	1.87698	-0.05613	0.00205	0.00513	0.02532
DGAC-6-11-2-13045	2.00964	-0.12280	22.89	10.76	1.78753	-0.06505	854.00	-97.28	1.85253	-0.07339	0.00617	0.02113	0.04246
DGAC-6-11-3-13045	2.06635	-0.10499	58.38	25.65	1.84471	-0.05887			1.84471	-0.05887	0.00564		0.03176
DGAC-6-4-1-13055	1.92457	-0.12512	6.55	2.59	1.79348	-0.07563	590.42	-375.13	2.16501	-0.12423	0.00448	0.02453	0.06285
DGAC-6-6-2-13055	1.91485	-0.10743	4.57	1.47	1.83429	-0.07300	811.44	-752.02	2.38173	-0.14091	0.00310	0.02153	0.05012
DGAC-6-6-3-13055	2.00260	-0.13055	5.86	2.84	1.84596	-0.06722	1412.27	-834.95	2.18569	-0.10718	0.00285	0.02041	0.03942

Table A.11: RAC-G Mixes: Summary of Three-Stage Weibull Shear Analysis: Temperature Effect

(FMLC, AV = 6.0±0.5 %, AC=8.0 %).

Specimen ID	Three-Stage Weibull Fitting										PSS@ n_1	PSS@ n_2	Last PSS
	1st Stage		2nd Stage				3rd Stage						
	$ln\alpha_1$	β_1	n_1	γ_1	$ln\alpha_2$	β_2	n_2	γ_2	$ln\alpha_3$	β_3			
RACG-6-10-3-7045	2.12060	-0.09740	2.61	-0.37	2.14872	-0.11128	430.89	202.04	1.79445	-0.05905	0.00052	0.01253	0.03747
RACG-6-13-1-7045	2.25687	-0.12136	38.82	16.80	2.02568	-0.06884	2247.09	1190.62	1.72197	-0.03261	0.00235	0.01155	0.01803
RACG-6-16-1-7045	2.10689	-0.09287	78.77	37.60	1.88182	-0.04854	1491.39	667.46	1.71306	-0.02751	0.00417	0.00987	0.01513
RACG-6-21-2-7045	2.02640	-0.08210	1.92	-0.61	2.07341	-0.10823	252.08	164.69	1.64198	-0.03743	0.00080	0.01226	0.02981
RACG-6-22-3-7045	2.09375	-0.11036	87.28	16.60	1.98107	-0.08937	1364.28	752.61	1.59732	-0.04056	0.00718	0.02188	0.03805
RACG-6-9-3-7045	2.15579	-0.09626	131.85	45.61	1.96651	-0.06296	1355.25	661.81	1.73269	-0.03334	0.00449	0.01056	0.01783
RACG-6-13-2-7055	2.04088	-0.11202	79.92	30.24	1.82209	-0.06964	330.24	134.78	1.66422	-0.04537	0.00893	0.01562	0.03673
RACG-6-16-2-7055	1.88481	-0.11962	39.54	19.79	1.62315	-0.05975	512.97	207.55	1.46438	-0.03700	0.01427	0.03024	0.05166
RACG-6-18-1-7055	1.92561	-0.09947	49.51	21.62	1.72398	-0.05603	294.99	87.50	1.63648	-0.04253	0.00949	0.01677	0.03650
RACG-6-20-2-7055	1.97511	-0.10135	88.39	47.51	1.69479	-0.04687	2193.80	-1620.61	2.02214	-0.08330	0.01018	0.02249	0.04148
RACG-6-22-1-7055	1.94147	-0.13121	26.39	12.20	1.69922	-0.07056	225.87	131.47	1.46246	-0.03117	0.01055	0.02330	0.04311
RACG-6-19-1-10045	2.03820	-0.11292	49.00	21.57	1.80807	-0.06321	405.78	178.76	1.63452	-0.03735	0.00707	0.01522	0.03021
RACG-6-6-1-10045	2.02960	-0.12190	166.82	17.88	1.95042	-0.10883	664.56	364.67	1.53392	-0.05047	0.01728	0.03063	0.06249
RACG-6-6-2-10045	2.02691	-0.07830	2.67	-1.62	2.13319	-0.12577	996.16	410.81	1.73483	-0.07378	0.00091	0.02871	0.06487
RACG-6-17-3-10055	1.88507	-0.10916	35.95	21.38	1.61260	-0.04425	4624.73	-2456.40	1.84280	-0.06807	0.01147	0.03161	0.04477
RACG-6-18-2-10055	1.81897	-0.11893	37.30	20.88	1.53510	-0.05236	6295.30	-2273.36	1.72481	-0.07151	0.01787	0.05293	0.06881
RACG-6-22-2-10055	1.91366	-0.12284	89.95	49.97	1.56234	-0.05460	3406.51	-3503.91	2.11282	-0.11240	0.01978	0.04702	0.07819
RACG-6-17-1-13045	1.98926	-0.11482	30.57	13.81	1.77404	-0.06295	540.70	181.71	1.63187	-0.04289	0.00711	0.01871	0.03683
RACG-6-20-1-13045	2.05948	-0.11294	109.21	49.62	1.78134	-0.06163	3592.63	-272.82	1.83303	-0.06723	0.00972	0.02768	0.04397
RACG-6-20-2-13045	2.03648	-0.13811	110.09	58.21	1.64422	-0.06509	5003.46	-1314.34	1.81825	-0.08315	0.01776	0.05096	0.06862
RACG-6-21-3-13045	2.01614	-0.12597	57.37	20.27	1.80039	-0.08146	464.14	255.87	1.50792	-0.03822	0.01093	0.02493	0.04544
RACG-6-17-2-13055	1.90499	-0.11698	45.16	27.80	1.58764	-0.04497	2221.59	-3043.36	2.16652	-0.10794	0.01333	0.03152	0.05715
RACG-6-18-3-13055	1.82604	-0.14209	12.84	5.92	1.61140	-0.07656	57.27	17.34	1.52935	-0.05953	0.01324	0.02466	0.06525
RACG-6-19-3-13055	1.86650	-0.10364	11.68	4.60	1.73463	-0.06279	2644.92	-2708.99	2.33311	-0.12733	0.00664	0.03178	0.05813

Table A.12: MAC15-G Mixes: Summary of Three-Stage Weibull Shear Analysis: Temperature Effect

(FMLC, AV = 6.0±0.5 %, AC=7.4 %).

Specimen ID	Three-Stage Weibull Fitting										PSS@ n_1	PSS@ n_2	Last PSS
	1st Stage		2nd Stage				3rd Stage						
	$ln\alpha_1$	β_1	n_1	γ_1	$ln\alpha_2$	β_2	n_2	γ_2	$ln\alpha_3$	β_3			
MAC15-6-13-3-7045	2.05019	-0.08775	39.94	15.35	1.89966	-0.05403	346.18	163.30	1.74177	-0.02987	0.00361	0.00753	0.01499
MAC15-6-1-3-7045	2.10499	-0.07748	32.87	5.46	2.04835	-0.06462	354.59	148.88	1.87277	-0.03807	0.00189	0.00490	0.01224
MAC15-6-15-3-7045	2.09238	-0.09793	63.96	23.80	1.91225	-0.06149	539.81	287.02	1.69482	-0.03013	0.00454	0.00989	0.01825
MAC15-6-9-3-7045	2.09297	-0.09014	46.17	15.40	1.95338	-0.06007	994.61	518.36	1.71983	-0.02922	0.00320	0.00936	0.01585
MAC15-6-10-1-7055	1.87824	-0.08799	21.07	10.15	1.71907	-0.04560	2905.76	-1042.11	1.87044	-0.06218	0.00672	0.02068	0.03267
MAC15-6-10-3-7055	1.86010	-0.08422	29.23	14.06	1.69465	-0.04369	4832.03	-2137.08	1.88341	-0.06320	0.00779	0.02328	0.03302
MAC15-6-11-2-7055	1.80831	-0.10352	17.02	8.92	1.61796	-0.04927	61.48	16.43	1.58353	-0.04223	0.01052	0.01577	0.04061
MAC15-6-11-3-10045	1.87036	-0.10211	19.74	7.76	1.71962	-0.06195	55.72	14.88	1.67559	-0.05276	0.00829	0.01236	0.04218
MAC15-6-15-2-10045	1.96152	-0.10411	110.55	68.70	1.61882	-0.03941	10628.28	-15759.93	2.25639	-0.09849	0.01239	0.02995	0.03676
MAC15-6-9-1-10045	2.01999	-0.09320	28.16	10.88	1.87180	-0.05717	537.66	179.46	1.74215	-0.03888	0.00397	0.01056	0.02160
MAC15-6-2-3-10055	1.77658	-0.12140	7.49	3.06	1.63907	-0.07182	540.60	-350.80	1.99657	-0.11911	0.00993	0.03757	0.07740
MAC15-6-6-3-10055	1.85157	-0.11908	10.55	4.24	1.70229	-0.07124	46.71	14.93	1.61963	-0.05331	0.00805	0.01501	0.04820
MAC15-6-7-2-10055	1.82163	-0.11659	27.50	12.77	1.60316	-0.06244	124.88	45.50	1.50187	-0.04421	0.01492	0.02451	0.05046
MAC15-6-11-1-13045	1.85223	-0.14621	4.60	2.10	1.70158	-0.07927	1958.66	-3471.48	2.99269	-0.21999	0.00628	0.04946	0.07798
MAC15-6-8-1-13045	1.99301	-0.10000	20.38	5.66	1.88576	-0.07222	197.09	78.55	1.71984	-0.04472	0.00437	0.01094	0.02955
MAC15-6-8-3-13045	1.96697	-0.09875	32.53	9.39	1.84385	-0.07026	303.40	118.29	1.67546	-0.04424	0.00626	0.01438	0.03391
MAC15-6-1-3-13055	1.72221	-0.11833	23.26	8.74	1.54757	-0.07389	362.12	-406.94	2.18261	-0.16081	0.02051	0.04761	0.07766
MAC15-6-2-1-13055	1.81810	-0.14945	3.81	1.59	1.68760	-0.08707	57.99	-42.43	2.05114	-0.15505	0.00653	0.02234	0.05838
MAC15-6-7-3-13055	1.84948	-0.10995	29.43	14.67	1.62602	-0.05513	3568.44	-1109.94	1.78861	-0.07258	0.01238	0.03937	0.05921

Table A.13: MB15-G Mixes: Summary of Three-Stage Weibull Shear Analysis: Temperature Effect

(FMLC, AV = 6.0±0.5 %, AC=7.1 %).

Specimen ID	Three-Stage Weibull Fitting										PSS@ n_1	PSS@ n_2	Last PSS
	1st Stage		2nd Stage				3rd Stage						
	$ln\alpha_1$	β_1	n_1	γ_1	$ln\alpha_2$	β_2	n_2	γ_2	$ln\alpha_3$	β_3			
MB15-6-6-1-7045	1.86269	-0.10396	33.55	18.00	1.62973	-0.04819	2388.66	-1157.14	1.84440	-0.07208	0.01128	0.02991	0.04978
MB15-6-6-3-7045	1.84280	-0.10754	33.13	18.27	1.59647	-0.04822	4776.12	-1229.92	1.71776	-0.06086	0.01296	0.03768	0.05183
MB15-6-9-1-7045	1.86223	-0.08652	17.49	4.53	1.77883	-0.06409	797.61	-327.89	1.99002	-0.09096	0.00655	0.02107	0.05713
MB15-6-2-2-7055	1.84158	-0.10327	21.57	7.90	1.69559	-0.06546			1.69559	-0.06546	0.01008		0.03994
MB15-6-10-3-7055	1.85522	-0.12345	14.43	6.52	1.66564	-0.06767	500.85	-200.24	1.87475	-0.09597	0.00981	0.03093	0.05969
MB15-6-2-3-7055	1.76889	-0.08111	45.46	26.67	1.55765	-0.03353	2973.01	-1239.00	1.68983	-0.04793	0.01332	0.02623	0.03011
MB15-6-3-1-7055	1.86321	-0.09811	12.66	6.48	1.70147	-0.04792	2164.78	-1531.69	2.00781	-0.08207	0.00649	0.02254	0.04143
MB15-6-4-3-7055	1.80476	-0.08037	9.44	4.52	1.69105	-0.04188			1.69105	-0.04188	0.00626		0.01465
MB15-6-5-2-7055	1.86158	-0.13083	3.23	1.54	1.74422	-0.06858	1369.62	-860.95	2.11107	-0.11181	0.00403	0.03068	0.07352
MB15-6-7-1-7055	1.82267	-0.06512	34.21	17.51	1.68218	-0.03180	1215.44	-218.70	1.73347	-0.03807	0.00731	0.01375	0.01919
MB15-6-10-1-10045	1.86347	-0.11767	17.28	6.32	1.70683	-0.07462	853.98	-876.26	2.33938	-0.15232	0.00990	0.03592	0.07901
MB15-6-11-1-10045	1.83624	-0.08237	80.73	31.24	1.67157	-0.05049	5688.19	-7704.35	2.37123	-0.11954	0.01245	0.03241	0.04938
MB15-6-9-3-10045	1.91803	-0.15419	3.46	1.75	1.76784	-0.07647	779.56	-1275.74	2.80017	-0.20206	0.00367	0.02953	0.08737
MB15-6-10-2-10055	1.79830	-0.14031	5.61	2.59	1.63985	-0.07553	278.83	-455.79	2.54085	-0.20087	0.00878	0.03454	0.08570
MB15-6-11-3-10055	1.82462	-0.11749	3.83	1.50	1.72722	-0.07142	429.71	-334.11	2.14015	-0.12740	0.00520	0.02593	0.05657
MB15-6-8-3-10055	1.72636	-0.08153	17.10	-3.44	1.79092	-0.09794	825.03	-311.09	2.07774	-0.13431	0.01167	0.04458	0.06476
MB15-6-2-1-13045	1.86448	-0.14311	10.81	4.49	1.67808	-0.08367	355.45	-507.44	2.57845	-0.20572	0.01006	0.03778	0.08634
MB15-6-6-2-13045	1.83885	-0.13231	9.97	3.98	1.67690	-0.07949	368.17	-450.96	2.40741	-0.17878	0.00961	0.03535	0.08696
MB15-6-8-2-13045	1.86083	-0.12652	11.06	4.92	1.68414	-0.07021	531.44	-811.82	2.53434	-0.17911	0.00863	0.03133	0.08645
MB15-6-11-2-13055	1.77230	-0.10744	5.38	1.62	1.69113	-0.07514	220.80	-308.77	2.42484	-0.18156	0.00736	0.02714	0.07091
MB15-6-5-3-13055	1.79370	-0.20654	1.51	0.77	1.67796	-0.10059	62.98	-74.90	2.36082	-0.22295	0.00316	0.02944	0.08839
MB15-6-7-2-13055	1.79756	-0.16520	2.46	1.40	1.65270	-0.07073	276.60	-303.41	2.20393	-0.14907	0.00533	0.03009	0.06111

Table A.14: MB4-G Mixes: Summary of Three-Stage Weibull Shear Analysis: Temperature Effect

(FMLC, AV = 6.0±0.5 %, AC=7.2 %).

Specimen ID	Three-Stage Weibull Fitting										PSS@ n_1	PSS@ n_2	Last PSS
	1st Stage		2nd Stage				3rd Stage						
	$ln\alpha_1$	β_1	n_1	γ_1	$ln\alpha_2$	β_2	n_2	γ_2	$ln\alpha_3$	β_3			
MB4-6-1-4-7045	1.96680	-0.08167	39.37	14.19	1.83531	-0.05223	2896.36	-262.39	1.88049	-0.05724	0.00499	0.01602	0.02626
MB4-6-5-3-7045	1.95913	-0.08054	20.47	5.99	1.86818	-0.05695	690.00	195.09	1.75206	-0.04121	0.00383	0.01143	0.02263
MB4-6-7-2-7045	1.94564	-0.08863	16.93	6.70	1.81945	-0.05356	2230.97	458.56	1.72590	-0.04268	0.00428	0.01675	0.02641
MB4-6-15-1-7055	1.86874	-0.08906	25.92	7.36	1.76511	-0.06376	2375.30	-81.15	1.78606	-0.06615	0.00780	0.02840	0.04061
MB4-6-16-1-7055	1.88686	-0.09882	6.77	2.00	1.80677	-0.06967	735.79	-64.64	1.85512	-0.07600	0.00412	0.02108	0.05387
MB4-6-2-1-7055	1.84961	-0.08479	46.66	18.31	1.69608	-0.05152	3152.18	-2768.66	2.12681	-0.09733	0.01006	0.02785	0.04787
MB4-6-1-2-10045	1.90424	-0.09018	24.41	10.13	1.75637	-0.05276	627.60	-27.47	1.78032	-0.05597	0.00640	0.01626	0.03575
MB4-6-2-3-10045	1.93319	-0.11905	3.70	1.30	1.84530	-0.07737	34.48	6.77	1.78894	-0.06461	0.00275	0.00800	0.04020
MB4-6-5-1-10045	1.91552	-0.09279	32.12	6.38	1.83515	-0.07437	510.44	-36.03	1.88060	-0.08062	0.00724	0.01946	0.04460
MB4-6-12-1-10055	1.83042	-0.09531	23.75	4.82	1.75187	-0.07596	722.41	-162.63	1.88807	-0.09368	0.00996	0.03030	0.06099
MB4-6-12-3-10055	1.81193	-0.09826	21.14	5.93	1.70449	-0.07068	272.86	-12.32	1.73649	-0.07551	0.01073	0.02461	0.04566
MB4-6-7-3-10055	1.81932	-0.10692	1.15	0.17	1.80276	-0.09129			1.80276	-0.09129	0.00202		0.02352
MB4-6-3-3-13045	1.93453	-0.14174	2.39	0.82	1.85326	-0.09323	1605.76	-960.81	2.33554	-0.14909	0.00216	0.04071	0.07672
MB4-6-4-2-13045	1.84003	-0.10664	18.96	5.45	1.72415	-0.07600	49.22	11.18	1.67725	-0.06605	0.00985	0.01484	0.05294
MB4-6-7-1-13045	1.90861	-0.10026	23.25	6.37	1.79887	-0.07279	237.81	-31.71	1.87698	-0.08476	0.00724	0.01724	0.04979
MB4-6-3-1-13055	1.77252	-0.11537	13.85	-1.90	1.83111	-0.13123	221.90	-49.29	2.01199	-0.15902	0.01299	0.04601	0.07845
MB4-6-3-2-13055	1.82920	-0.14448	3.00	1.20	1.72128	-0.08658	51.16	-30.34	2.00426	-0.14125	0.00500	0.01866	0.06204
MB4-6-5-2-13055	1.78774	-0.09895	3.02	-0.41	1.81688	-0.11238	263.33	-161.27	2.28516	-0.18092	0.00486	0.03759	0.07795

Table A.15: Summary Of Three-Stage Weibull Shear Analysis for all Mixes: Air-Void Content Effect

(FMLC, AV = 9.0±1.0 %).

Specimen ID	Three-Stage Weibull Fitting										PSS@ n_1	PSS@ n_2	Last PSS
	1st Stage		2nd Stage				3rd Stage						
	$ln\alpha_1$	β_1	n_1	γ_1	$ln\alpha_2$	β_2	n_2	γ_2	$ln\alpha_3$	β_3			
DGAC-69-3-2-7045	2.10193	-0.08787	43.21	17.56	1.94023	-0.05216	11767.82	1255.13	1.88356	-0.04666	0.00278	0.01404	0.01398
DGAC-69-3-3-7045	2.08693	-0.08689	36.17	14.14	1.93878	-0.05292	1157.61	341.52	1.81935	-0.03777	0.00273	0.00828	0.01502
DGAC-69-1-1-7055	1.94379	-0.10291	4.57	1.45	1.86731	-0.07023	611.93	-157.00	2.00465	-0.08846	0.00258	0.01604	0.04047
DGAC-69-1-3-7055	1.91575	-0.08812	36.76	-1.64	1.93397	-0.09206	588.73	-553.60	2.60073	-0.17813	0.00708	0.02163	0.07631
RACG-69-1-2-7045	2.07920	-0.10972	52.19	15.28	1.92525	-0.07759	367.27	153.83	1.72265	-0.04705	0.00561	0.01277	0.03118
RACG-69-2-2-7045	2.05827	-0.12003	53.72	12.84	1.91899	-0.09133	522.77	193.14	1.69192	-0.05904	0.00777	0.02098	0.04255
RACG-6-1-3-7055	1.84666	-0.09857	38.54	16.59	1.66013	-0.05615	3880.25	-811.62	1.77279	-0.06819	0.01189	0.03652	0.05450
RACG-69-1-1-7055	1.97976	-0.13655	5.60	2.18	1.84702	-0.08338	54.50	15.75	1.74288	-0.06175	0.00331	0.01043	0.03946
RACG-69-2-3-7055	1.90721	-0.11546	35.38	11.54	1.74214	-0.07779	88.13	32.72	1.63059	-0.05628	0.01143	0.01702	0.05668
MAC15-9-3-2-7045	2.04373	-0.11584	53.95	13.83	1.89983	-0.08616	725.87	266.06	1.67504	-0.05564	0.00770	0.02228	0.04148
MAC15-9-8-2-7045	2.04790	-0.12338	145.86	30.21	1.89788	-0.09782	999.07	569.82	1.48796	-0.04334	0.01510	0.03292	0.05153
MAC15-9-4-1-7055	1.92801	-0.12673	31.35	10.73	1.74374	-0.08338	161.81	64.92	1.56991	-0.05348	0.01169	0.02311	0.06295
MAC15-9-7-1-7055	1.88867	-0.12344	36.54	15.83	1.65655	-0.06998	127.21	46.44	1.54960	-0.05074	0.01443	0.02291	0.04040
MB15-9-15-1-7045	1.89247	-0.10766	49.25	23.50	1.65574	-0.05629			1.65574	-0.05629	0.01268		0.04545
MB15-9-15-2-7045	1.91120	-0.11300	31.78	14.81	1.69120	-0.06034	6450.80	-16578.96	3.33066	-0.21590	0.01030	0.04087	0.06573
MB15-9-13-2-7055	1.80994	-0.10559	66.27	17.22	1.67139	-0.07816			1.67139	-0.07816	0.01969		0.04963
MB15-9-13-3-7055	1.84415	-0.11502	17.42	6.38	1.69049	-0.07288	534.84	-161.27	1.86192	-0.09601	0.01042	0.03239	0.05631
MB15-9-14-2-7055	2.08444	-0.09350	33.74	-16.52	2.30098	-0.13927	774.89	102.92	2.14137	-0.11825	0.00309	0.01983	0.02827
MB4-9-19-2-7045	1.96002	-0.08967	12.72	4.34	1.85752	-0.05907	768.70	195.99	1.74642	-0.04426	0.00344	0.01308	0.02594
MB4-9-20-1-7045	1.88643	-0.09424	53.63	14.06	1.76692	-0.06953			1.76692	-0.06953	0.01073		0.05101
MB4-69-1-3-7055	1.91351	-0.08762	104.33	-13.42	1.97784	-0.09889	687.83	-578.99	2.60615	-0.17865	0.01104	0.02299	0.07631
MB4-9-17-1-7055	1.83668	-0.12149	8.50	3.06	1.70830	-0.07772	58.50	8.64	1.66948	-0.06990	0.00779	0.01761	0.05360
MB4-9-18-3-7055	1.88378	-0.10343	25.90	4.23	1.81335	-0.08653	301.02	-45.63	1.91180	-0.10106	0.00916	0.02360	0.05609
MB4-9-19-1-7055	1.89379	-0.08996	39.91	8.38	1.80738	-0.07106	188.90	-57.40	1.97206	-0.09696	0.00852	0.01485	0.05111

Table A.16: Summary Of Three-Stage Weibull Shear Analysis for All Mixes: Aging Effect

(FMLC, AV = 6.0±0.5 %).

Specimen ID	Three-Stage Weibull Fitting										PSS@ n_1	PSS@ n_2	Last PSS
	1st Stage		2nd Stage				3rd Stage						
	$ln\alpha_1$	β_1	n_1	γ_1	$ln\alpha_2$	β_2	n_2	γ_2	$ln\alpha_3$	β_3			
DGAC-6-21-1-LT-7045	2.22527	-0.10805	54.70	25.91	1.98398	-0.05688	1242.54	594.12	1.77620	-0.03031	0.00250	0.00771	0.01299
DGAC-6-21-3-LT-7045	2.24137	-0.09707	41.92	14.52	2.08879	-0.06345	795.77	388.71	1.86482	-0.03306	0.00146	0.00495	0.01008
DGAC-6-18-3-LT-7055	2.09168	-0.10165	18.38	6.24	1.96331	-0.06712	570.43	144.92	1.84451	-0.05062	0.00240	0.00940	0.02302
DGAC-6-19-1-LT-7055	2.05909	-0.08807	56.95	22.91	1.88881	-0.05265	3125.05	-737.39	2.00692	-0.06555	0.00406	0.01316	0.02302
RACG-6-8-2-LT-7045	1.97227	-0.14212	64.26	14.64	1.80915	-0.10975	186.91	79.91	1.56256	-0.06817	0.01881	0.03095	0.04986
RACG-6-13-1-LT-7045	2.25711	-0.12142	39.11	17.00	2.02446	-0.06864	2301.25	1225.51	1.71926	-0.03233	0.00236	0.01162	0.01803
RACG-6-13-2-LT-7055	2.03984	-0.11167	98.57	44.31	1.77270	-0.06148	413.04	141.99	1.66255	-0.04519	0.00991	0.01666	0.03673
RACG-6-16-3-LT-7055	2.13523	-0.11185	110.90	14.30	2.05390	-0.09743	947.18	424.10	1.72962	-0.05463	0.00678	0.01807	0.04004
MAC15-6-1-2-LT-7045	1.95189	-0.10683	102.76	45.94	1.69565	-0.05907	1318.97	-318.73	1.83577	-0.07600	0.01347	0.02811	0.05716
MAC15-6-2-1-LT-7045	2.05815	-0.11035	100.63	35.37	1.84828	-0.07156	1021.44	418.31	1.63517	-0.04377	0.00897	0.02052	0.03775
MAC15-6-5-1-LT-7055	2.03075	-0.11615	83.24	16.58	1.90782	-0.09302	263.24	93.95	1.72308	-0.06384	0.01050	0.01757	0.04822
MAC15-6-5-2-LT-7055	1.97708	-0.11570	63.70	18.69	1.80762	-0.08174	561.42	249.03	1.56319	-0.04705	0.01155	0.02589	0.04614
MB15-6-12-2-LT-7045	1.97307	-0.07816	28.79	7.48	1.88748	-0.05786	896.92	-42.66	1.91298	-0.06112	0.00395	0.01176	0.02731
MB15-6-12-3-LT-7045	1.92824	-0.10273	29.27	13.78	1.73036	-0.05437	1104.30	337.11	1.60414	-0.03825	0.00764	0.02093	0.03462
MB15-6-12-1-LT-7055	1.90157	-0.10445	17.39	8.25	1.72472	-0.05489	3160.23	-1032.13	1.89150	-0.07301	0.00675	0.02717	0.03932
MB15-6-2-2-LT-7055	1.84158	-0.10327	21.57	7.90	1.69559	-0.06546			1.69559	-0.06546	0.01008		0.03994
MB4-6-10-1-LT-7045	1.97095	-0.08686	100.49	42.84	1.77253	-0.04983	2079.92	-250.23	1.83481	-0.05700	0.00800	0.01790	0.03077
MB4-6-9-3-LT-7045	1.98196	-0.09029	33.75	10.64	1.85840	-0.06183	355.73	122.91	1.72442	-0.04172	0.00507	0.01148	0.02593
MB4-6-10-2-LT-7055	1.88148	-0.08790	34.94	12.52	1.74455	-0.05641	248.43	76.20	1.64842	-0.04118	0.00817	0.01488	0.03335
MB4-6-10-3-LT-7055	1.89874	-0.08683	63.36	29.06	1.70464	-0.04700	4327.25	-2886.59	2.01222	-0.07888	0.00945	0.02441	0.03716

Table A.17: Summary Of Three-Stage Weibull Shear Analysis for All Mixes: Compaction Effect

(FMLC & LMLC, AV = 6.0±0.5 %).

Specimen ID	Three-Stage Weibull Fitting										PSS@ n_1	PSS@ n_2	Last PSS
	1st Stage		2nd Stage				3rd Stage						
	$ln\alpha_1$	β_1	n_1	γ_1	$ln\alpha_2$	β_2	n_2	γ_2	$ln\alpha_3$	β_3			
DGAC-FD-01-TL-7045	1.99266	-0.09922	25.03	10.77	1.82335	-0.05651	205.34	70.99	1.71670	-0.03902	0.00481	0.01006	0.02434
DGAC-FD-02-TL-7045	1.99445	-0.09018	66.24	24.94	1.82552	-0.05623	2956.02	-1901.89	2.16768	-0.09319	0.00646	0.01898	0.03619
DGAC-FD-05-TL-7045	2.05947	-0.11635	91.01	-12.65	2.14967	-0.13252	1442.77	241.57	1.96009	-0.10937	0.00912	0.03871	0.06856
DGAC-LM-6-2-1-7045	2.00752	-0.14707	2.36	0.57	1.94668	-0.11190	83.42	34.01	1.71264	-0.06673	0.00139	0.01389	0.04211
DGAC-LM-6-2-2-7045	1.97667	-0.11662	50.65	17.64	1.78475	-0.07601	1658.38	-159.28	1.85404	-0.08420	0.01037	0.03352	0.05251
DGAC-LM-6-2-3-7045	1.99372	-0.11191	25.26	8.67	1.83873	-0.07349	735.07	175.53	1.71274	-0.05661	0.00595	0.02052	0.04459
RAC-LM-6-1-1-7045	2.03454	-0.12370	56.34	23.88	1.78389	-0.07127	1565.83	784.23	1.50136	-0.03613	0.00954	0.02888	0.04438
RAC-LM-6-1-2-7045	2.01383	-0.11624	43.04	15.45	1.82376	-0.07452	486.02	181.47	1.64096	-0.04823	0.00787	0.01984	0.04320
RAC-LM-6-2-3-7045	2.09959	-0.10262	117.28	66.92	1.78337	-0.04407	3505.13	-2204.45	2.05756	-0.07319	0.00645	0.01571	0.02577
MAC15-LM-6-1-1-7045	1.94733	-0.16074	3.50	2.19	1.76208	-0.05996	75.36	30.88	1.64303	-0.03645	0.00329	0.01101	0.02869
MAC15-LM-6-1-2-7045	1.92486	-0.09208	7.51	2.37	1.84232	-0.06300	41.98	14.19	1.75752	-0.04421	0.00337	0.00670	0.01674
MAC15-LM-6-1-3-7045	1.90967	-0.08141	17.21	7.24	1.78643	-0.04715	185.84	79.62	1.67277	-0.02804	0.00471	0.00926	0.01865
MAC15-LM-6-3-2-7045	1.92286	-0.10004	30.13	13.03	1.74340	-0.05679	349.82	151.92	1.58936	-0.03337	0.00766	0.01638	0.03079
MB15-LM-6-2-2-7045	1.96899	-0.17450	4.06	2.43	1.75886	-0.07010	891.24	-115.03	1.83161	-0.07936	0.00367	0.02704	0.05298
MB15-LM-6-2-3-7045	1.83641	-0.11695	9.14	4.86	1.65713	-0.05470			1.65713	-0.05470	0.00783		0.03379
MB4-FD-24-TL-7045	1.86093	-0.10918	26.60	11.64	1.66886	-0.06140	373.17	188.78	1.47055	-0.03132	0.01105	0.02463	0.04238
MB4-FD-25-TL-7045	1.85612	-0.10466	30.49	14.75	1.64744	-0.05404	262.35	79.84	1.55698	-0.03984	0.01132	0.02120	0.04311
MB4-FD-26-TL-7045	1.83511	-0.11283	17.68	8.91	1.63254	-0.05597	204.67	111.83	1.45745	-0.02654	0.01064	0.02198	0.03848
MB4-LM-6-1-2-7045	1.92920	-0.10896	32.50	9.96	1.78530	-0.07557	199.90	81.89	1.61280	-0.04695	0.00895	0.01785	0.04194
MB4-LM-6-1-3-7045	1.93836	-0.09795	43.00	17.15	1.76144	-0.05888	564.49	235.97	1.59499	-0.03534	0.00813	0.01789	0.03062
MB4-LM-6-2-3-7045	1.90411	-0.08925	92.15	57.59	1.61895	-0.03347			1.61895	-0.03347	0.01101		0.02786

Table A.18: Summary of Three-Stage Weibull Shear Analysis for MB Mixes: Gradation Effect

(LMLC, AV = 6.0±0.5 %).

Specimen ID	Three-Stage Weibull Fitting										*PSS@ n_1*	*PSS@ n_2*	*Last PSS*
	1st Stage		2nd Stage				3rd Stage						
	$ln\alpha_1$	β_1	n_1	γ_1	$ln\alpha_2$	β_2	n_2	γ_2	$ln\alpha_3$	β_3			
MB4-DG-6-1-3-7045	1.96737	-0.09200	20.84	4.87	1.88326	-0.07048	2216.00	-2831.71	2.71238	-0.16089	0.00441	0.02224	0.06061
MB4-DG-6-3-1-7045	1.97151	-0.09408	41.00	11.57	1.85051	-0.06753	327.32	-41.16	1.92759	-0.07881	0.00634	0.01338	0.04687
MB4-DG-6-3-3-7045	1.99104	-0.08987	22.92	6.27	1.89315	-0.06528	6380.35	-3657.10	2.26849	-0.10280	0.00395	0.02374	0.03669
MB15-DG-6-1-1-7045	1.97542	-0.08811	11.79	4.26	1.87169	-0.05629	192.65	-1.70	1.88282	-0.05807	0.00301	0.00791	0.02692
MB15-DG-6-1-3-7045	1.95996	-0.09159	9.40	2.48	1.88508	-0.06739	1751.55	-963.60	2.20902	-0.10461	0.00308	0.01864	0.04530
MB15-DG-6-2-1-7045	1.93680	-0.10719	3.19	1.06	1.86668	-0.07164	2118.19	-1863.75	2.43503	-0.13475	0.00223	0.02392	0.04833
MAC15-DG-6-1-1-7045	2.04508	-0.08134	90.62	44.40	1.83754	-0.04149			1.83754	-0.04149	0.00464		0.01656
MAC15-DG-6-2-1-7045	2.14975	-0.08851	97.07	29.99	2.00200	-0.06116	1348.80	624.45	1.78379	-0.03359	0.00326	0.00837	0.01451
MAC15-DG-6-2-3-7045	2.12429	-0.09406	78.42	27.15	1.95611	-0.06150	1093.80	533.14	1.73192	-0.03232	0.00387	0.00989	0.01708

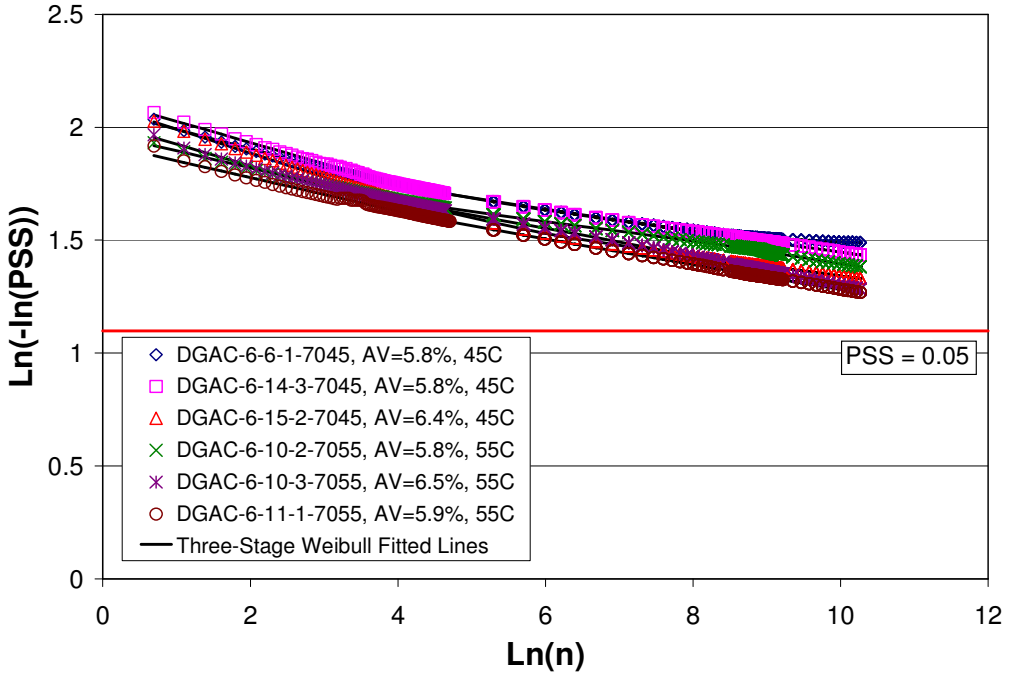

Figure A.35: AR4000-D shear test Three-stage Weibull curves: Temperature effect at 70 kPa.
(Binder content = 5.0%; field-mixed, lab-compacted; AV = 6 ± 0.5 %)

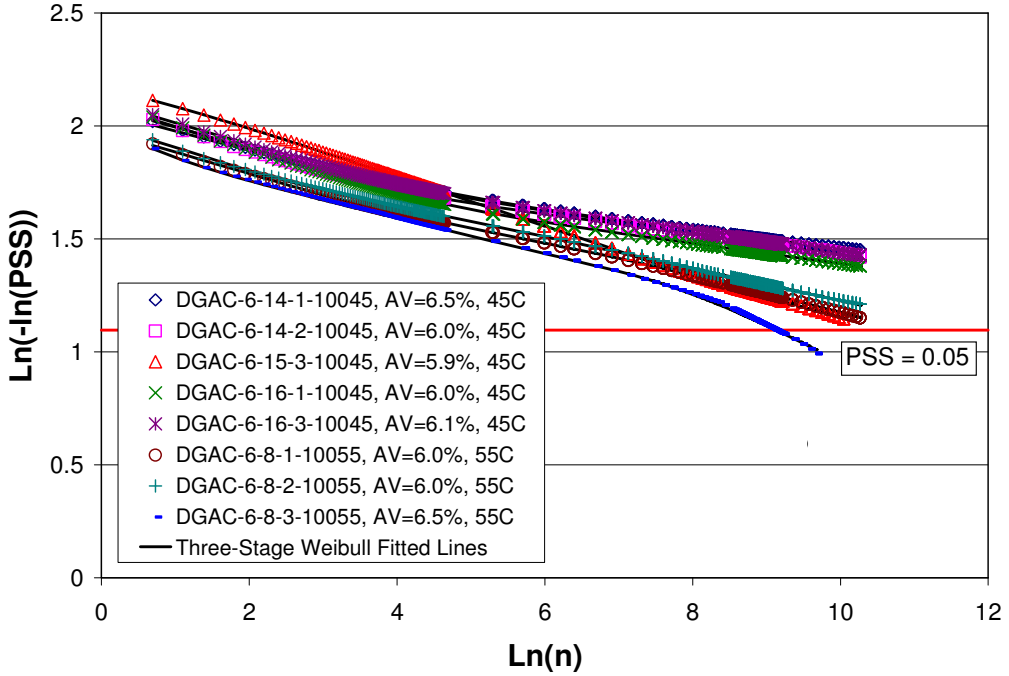

Figure A.36: AR4000-D shear test Three-stage Weibull curves: Temperature effect at 100 kPa.
(Binder content = 5.0%; field-mixed, lab-compacted; AV = 6 ± 0.5 %)

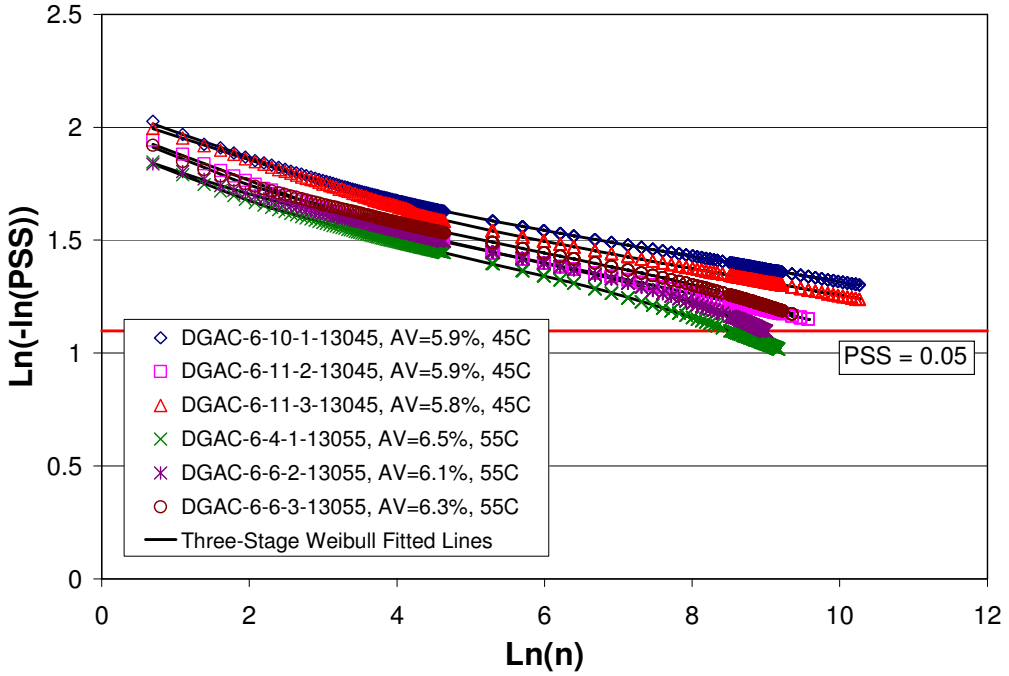

Figure A.37: AR4000-D shear test Three-stage Weibull curves: Temperature effect at 130 kPa.
(Binder content = 5.0%; field-mixed, lab-compacted; AV = 6 ± 0.5 %)

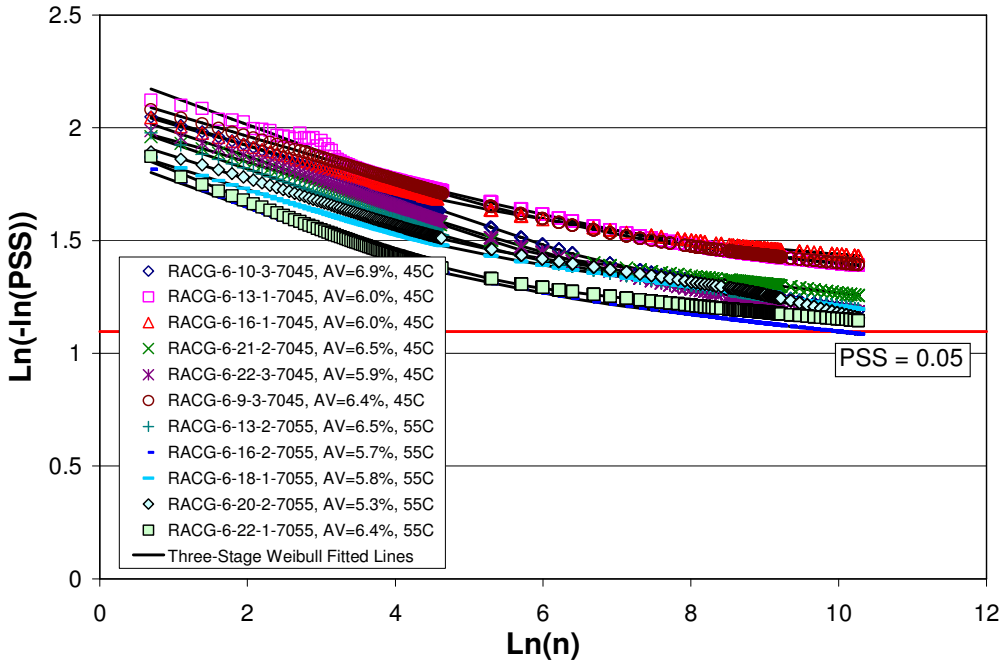

Figure A.38: RAC-G shear test Three-stage Weibull curves: Temperature effect at 70 kPa.
(Binder content = 8.0%; field-mixed, lab-compacted; AV = 6 ± 0.5 %)

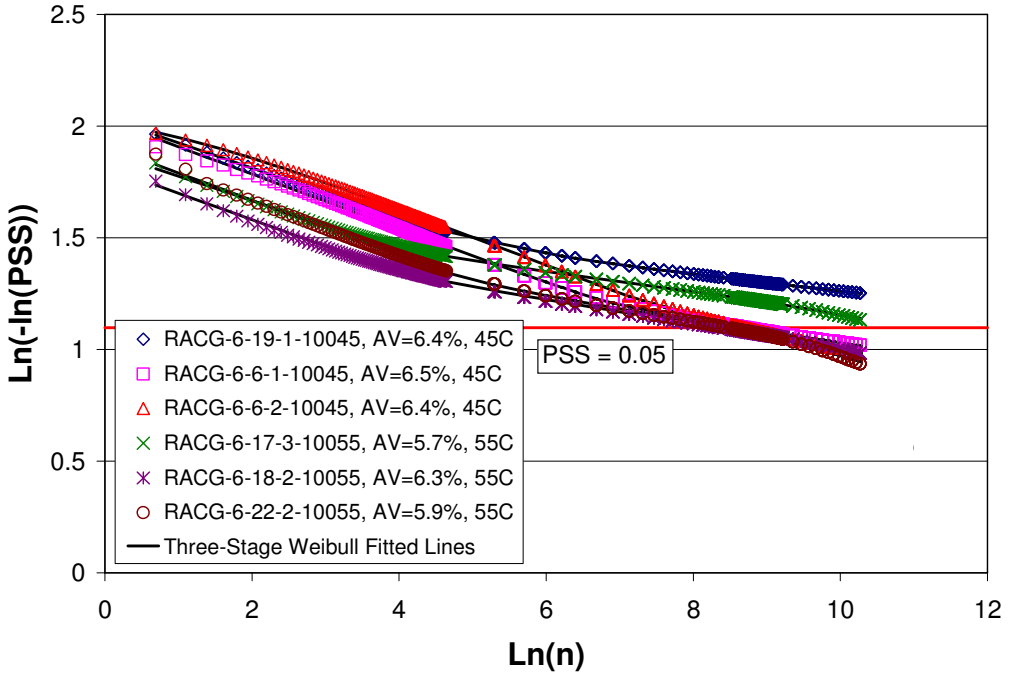

Figure A.39: RAC-G shear test Three-stage Weibull curves: Temperature effect at 100 kPa.
(Binder content = 8.0%; field-mixed, lab-compacted; AV = 6 ± 0.5 %)

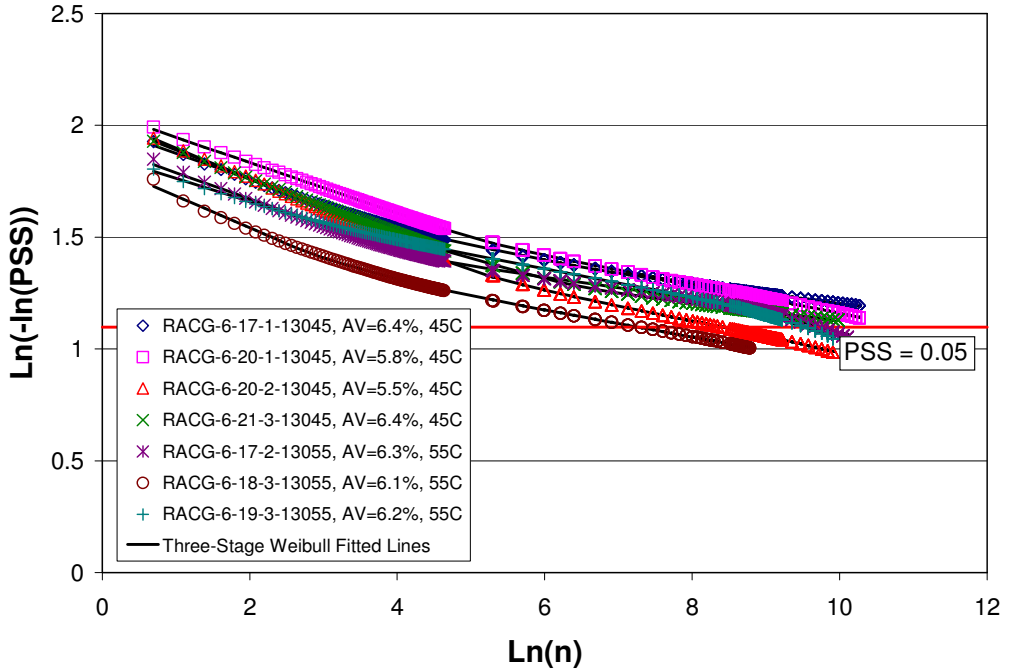

Figure A.40: RAC-G shear test Three-stage Weibull curves: Temperature effect at 130 kPa.
(Binder content = 8.0%; field-mixed, lab-compacted; AV = 6 ± 0.5 %)

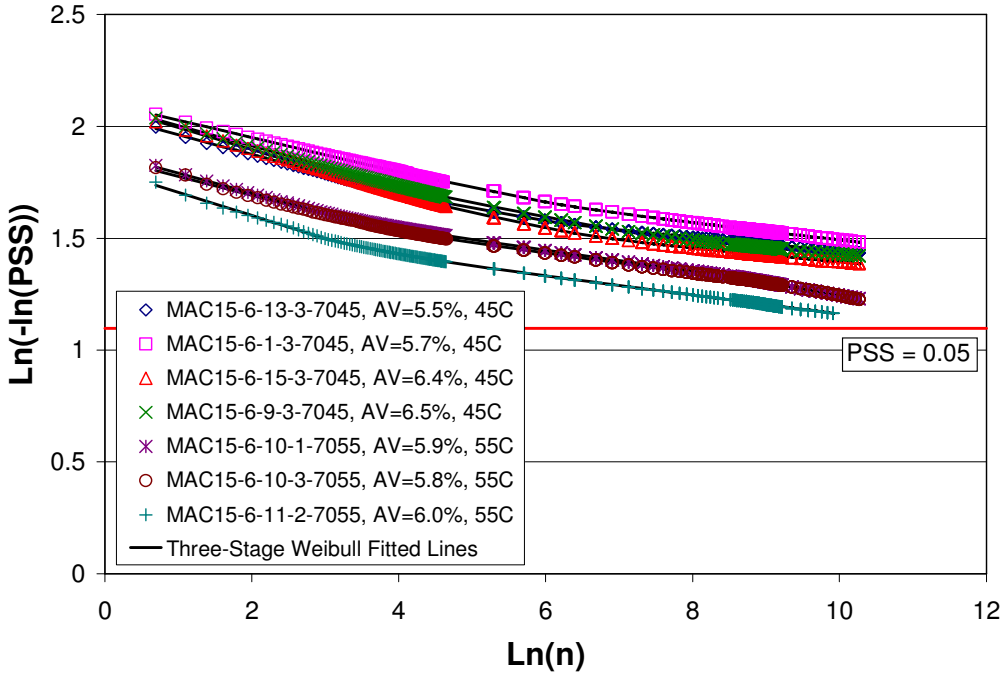

Figure A.41: MAC15-G shear test Three-stage Weibull curves: Temperature effect at 70 kPa.
(Binder content = 7.4%; field-mixed, lab-compacted; AV = 6 ± 0.5 %)

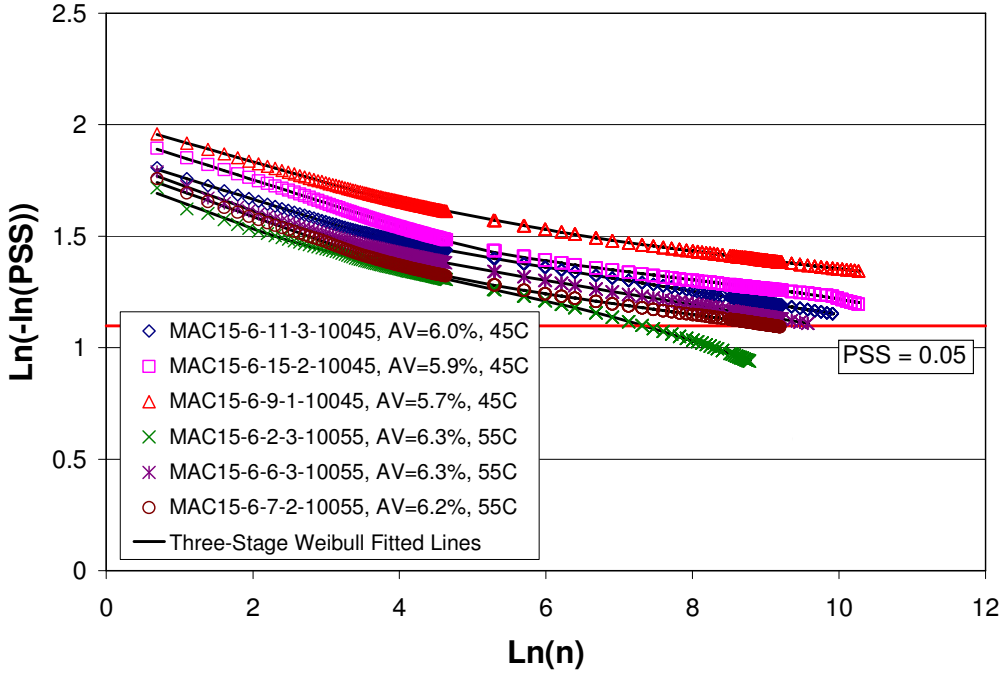

Figure A.42: MAC15-G shear test Three-stage Weibull curves: Temperature effect at 100 kPa.
(Binder content = 7.4%; field-mixed, lab-compacted; AV = 6 ± 0.5 %)

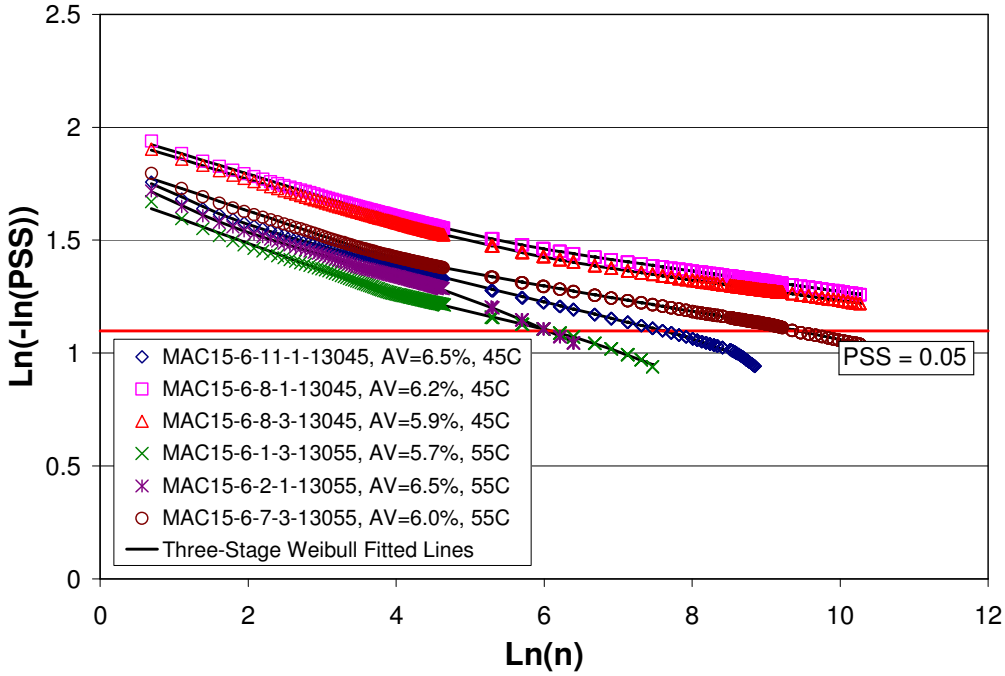

Figure A.43: MAC15-G shear test Three-stage Weibull curves: Temperature effect at 130 kPa.
(Binder content = 7.4%; field-mixed, lab-compacted; AV = 6 ± 0.5 %)

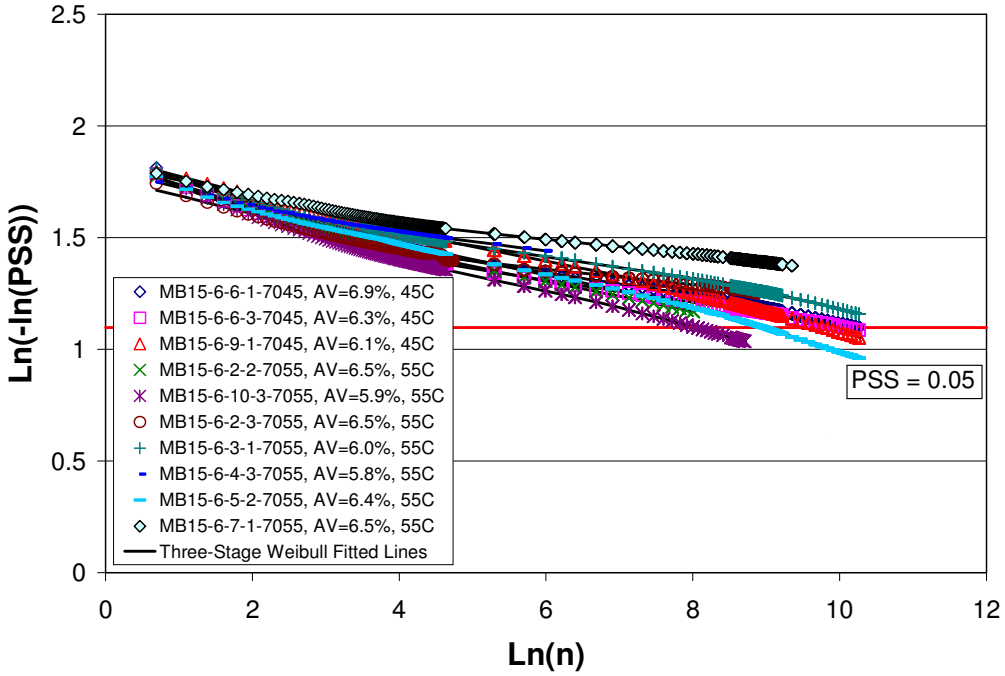

Figure A.44: MB15-G shear test Three-stage Weibull curves: Temperature effect at 70 kPa.
(Binder content = 7.1%; field-mixed, lab-compacted; AV = 6 ± 0.5 %)

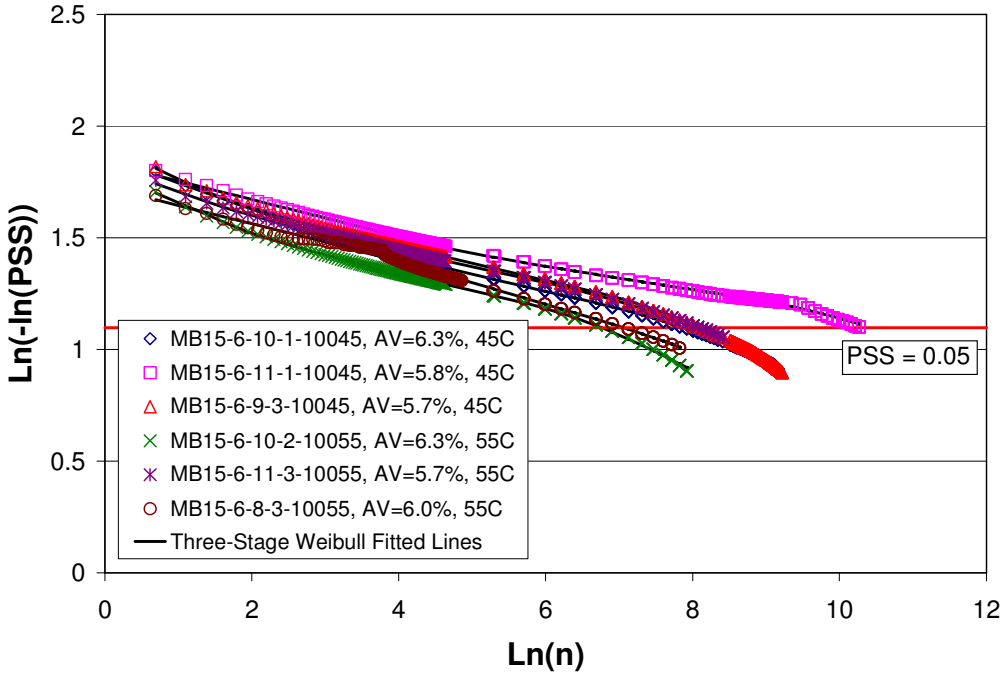

Figure A.45: MB15-G shear test Three-stage Weibull curves: Temperature effect at 100 kPa.
(Binder content = 7.1%; field-mixed, lab-compacted; AV = 6 ± 0.5 %)

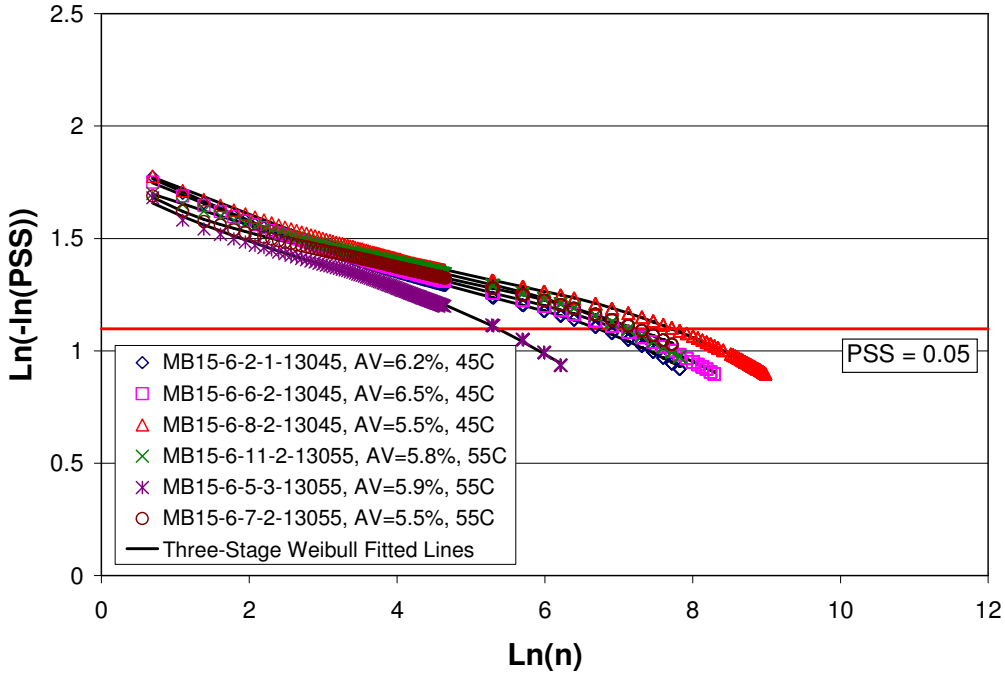

Figure A.46: MB15-G shear test Three-stage Weibull curves: Temperature effects at 130 kPa.
(Binder content = 7.1%; field-mixed, lab-compacted; AV = 6 ± 0.5 %)

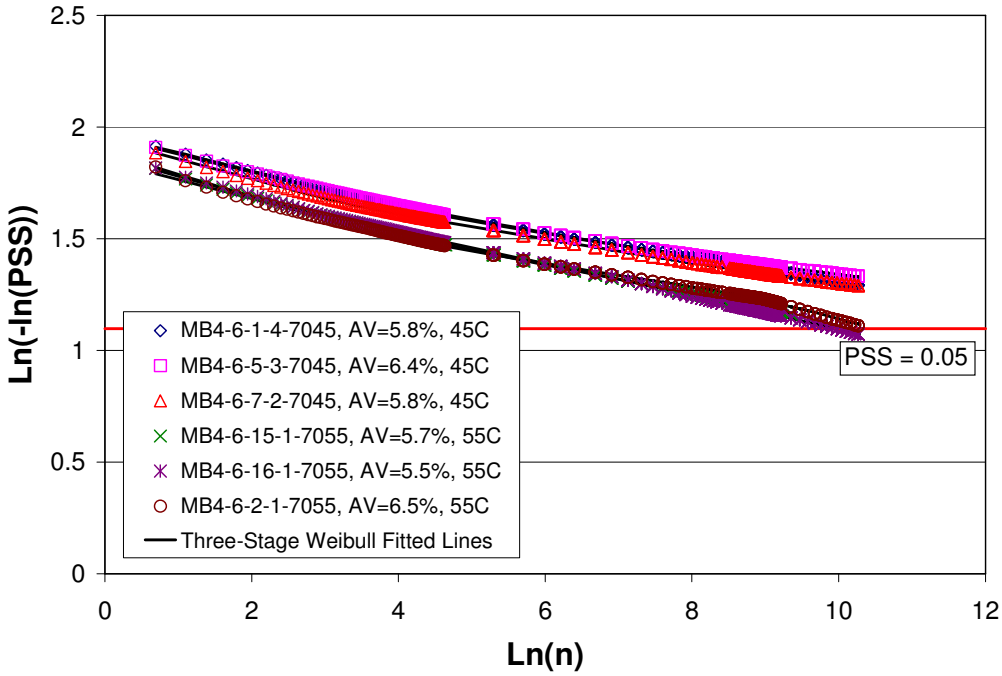

Figure A.47: MB4-G shear test Three-stage Weibull curves: Temperature effect at 70 kPa.
(Binder content = 7.2%; field-mixed, lab-compacted; AV = 6 ± 0.5 %)

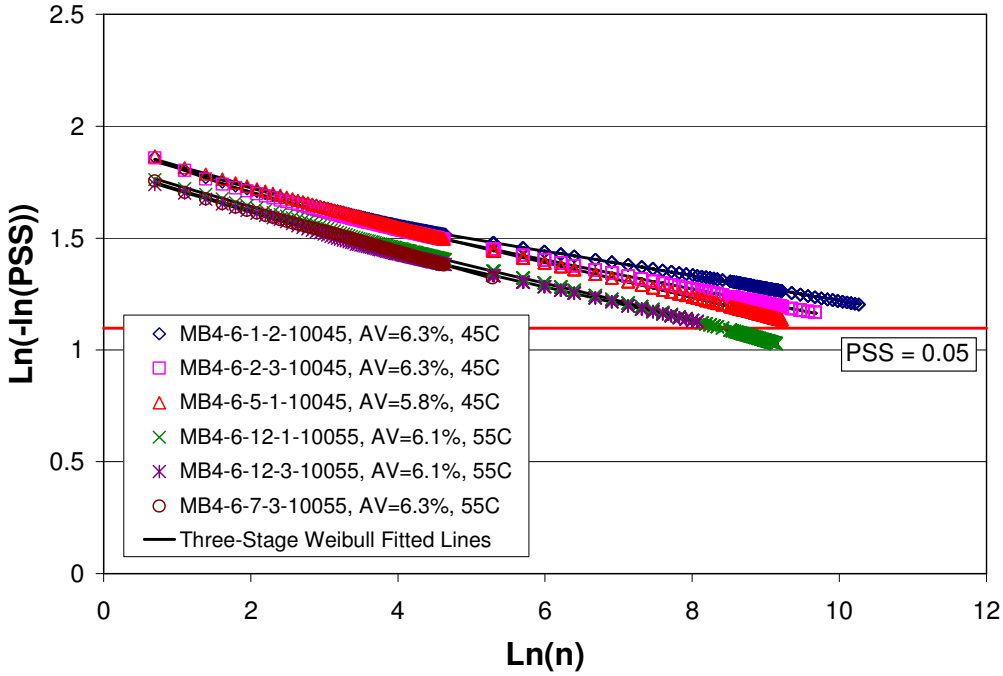

Figure A.48: MB4-G shear test Three-stage Weibull curves: Temperature effect at 100 kPa.
(Binder content = 7.2%; field-mixed, lab-compacted; AV = 6 ± 0.5 %)

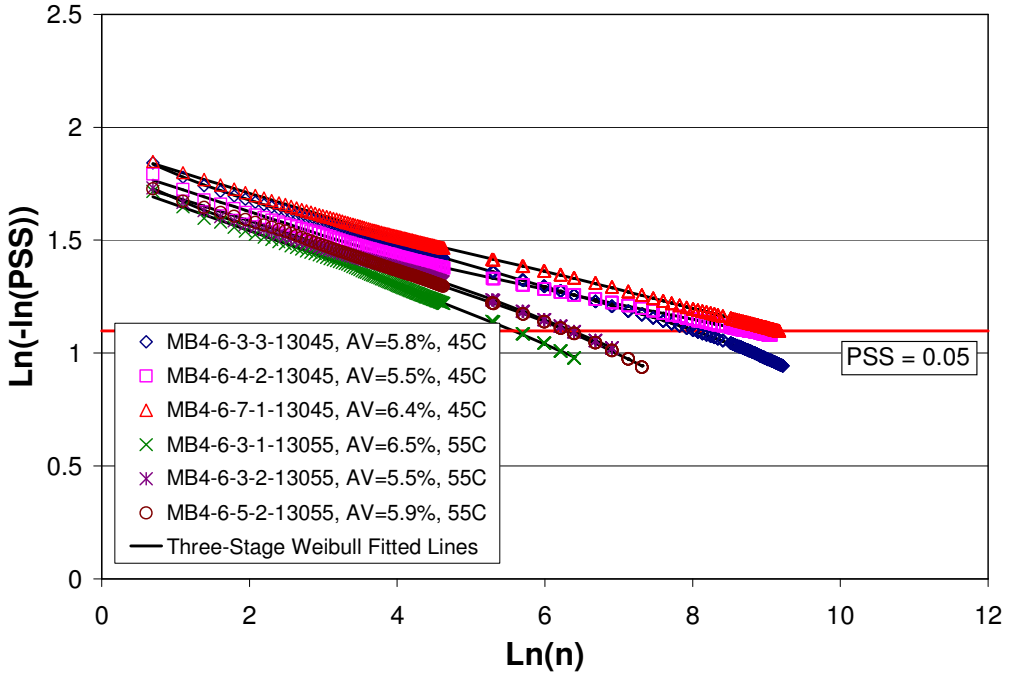

Figure A.49: MB4-G shear test Three-stage Weibull curves: Temperature effect at 130 kPa.
(Binder content = 7.2%; field-mixed, lab-compacted; AV = 6 ± 0.5 %)

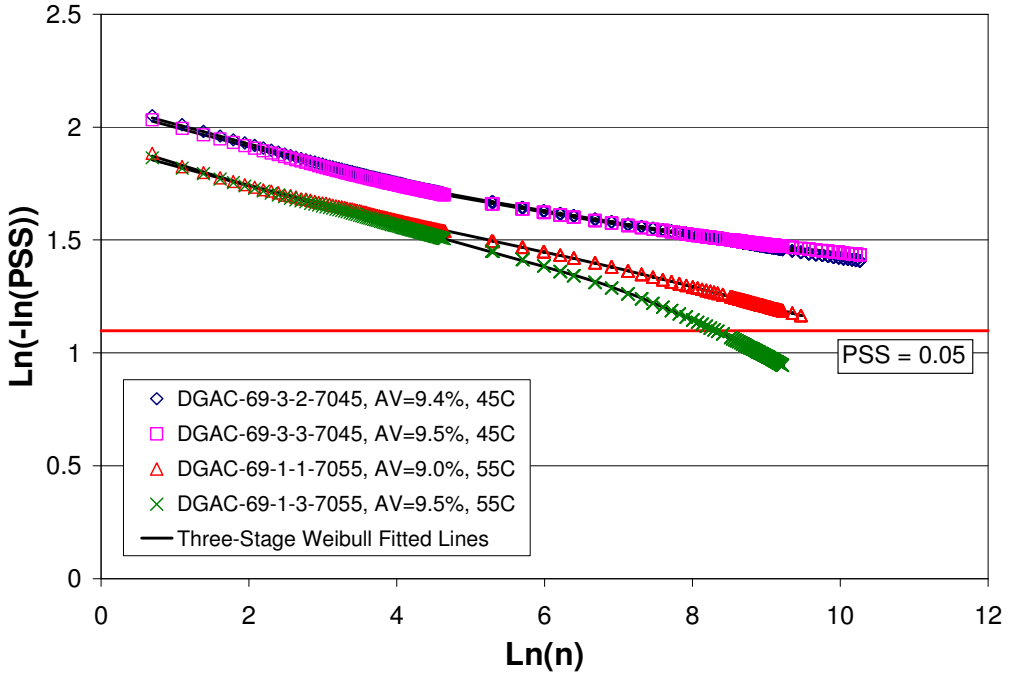

Figure A.50: AR4000-D Shear test Three-stage Weibull curves: Air-void content effect at 70 kPa.
(Binder content = 5.0%; field-mixed, lab-compacted; AV = 9 ± 1.0 %)

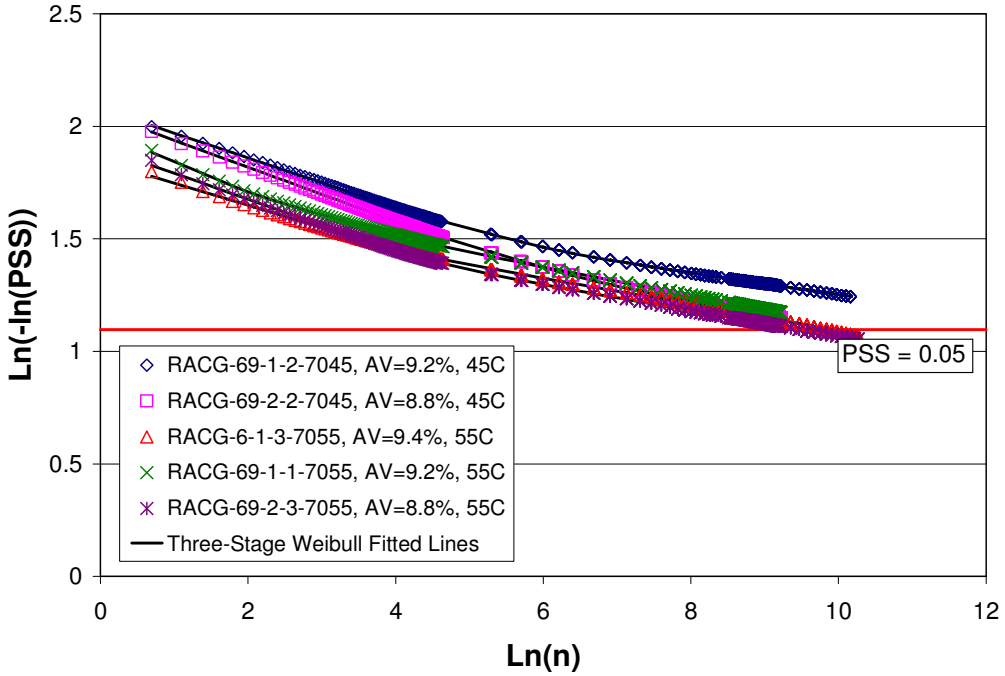

Figure A.51: RAC-G shear test Three-stage Weibull curves: Air-void content effect at 70 kPa.
(Binder content = 8.0%; field-mixed, lab-compacted; AV = 9 ± 1.0 %)

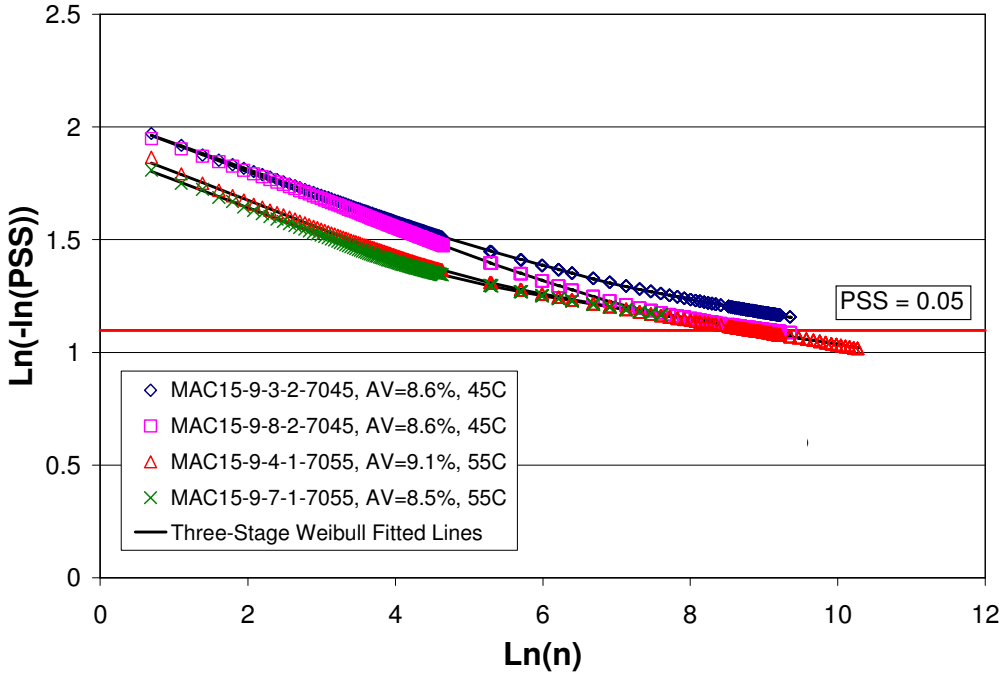

Figure A.52: MAC15-G shear test Three-stage Weibull curves: Air-void content effect at 70 kPa.
(Binder content = 7.4%; field-mixed, lab-compacted; AV = 9 ± 1.0 %)

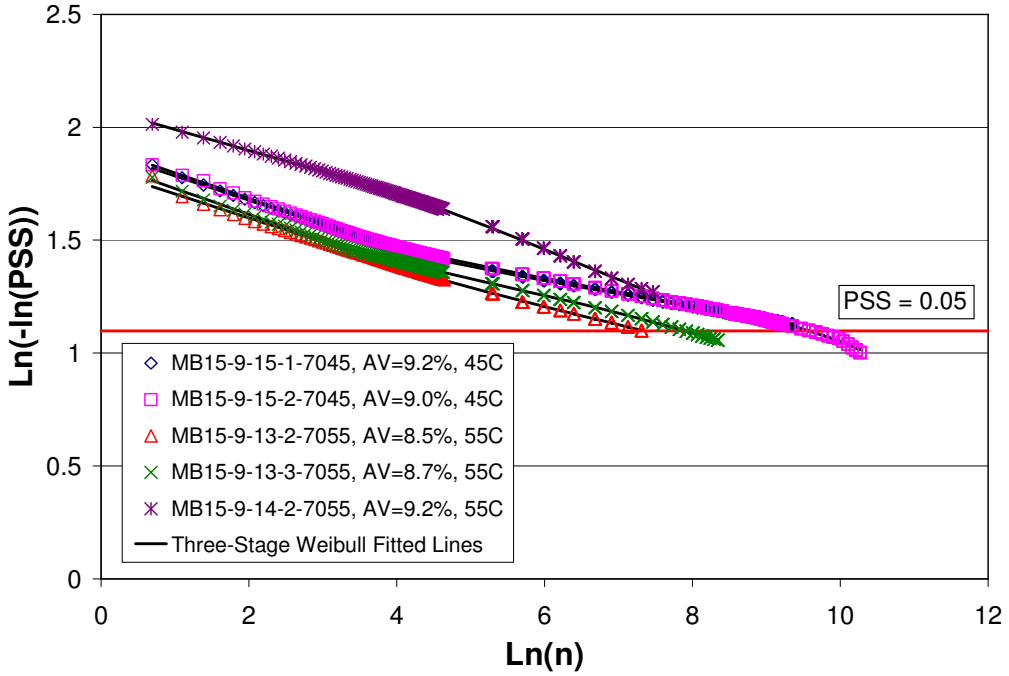

Figure A.53: MB15-G shear test Three-stage Weibull curves: Air-void content effect at 70 kPa.
(Binder content = 7.1%; field-mixed, lab-compacted; AV = 9 ± 1.0 %)

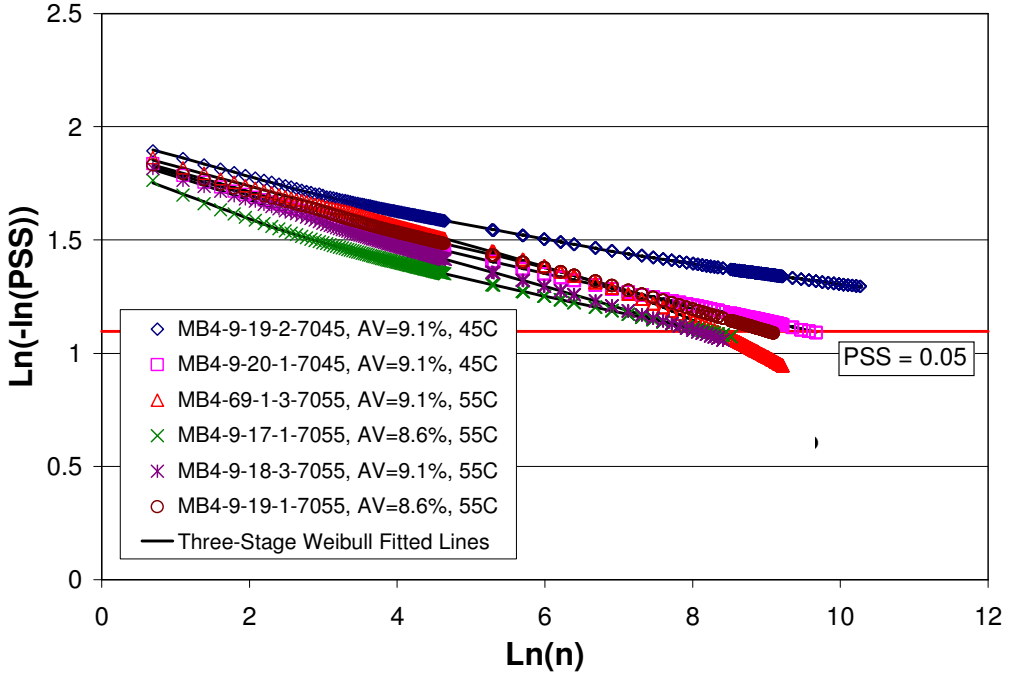

Figure A.54: MB4-G shear test Three-stage Weibull curves: Air-void content effect at 70 kPa.
(Binder content = 7.2%; field-mixed, lab-compacted; AV = 9 ± 1.0 %)

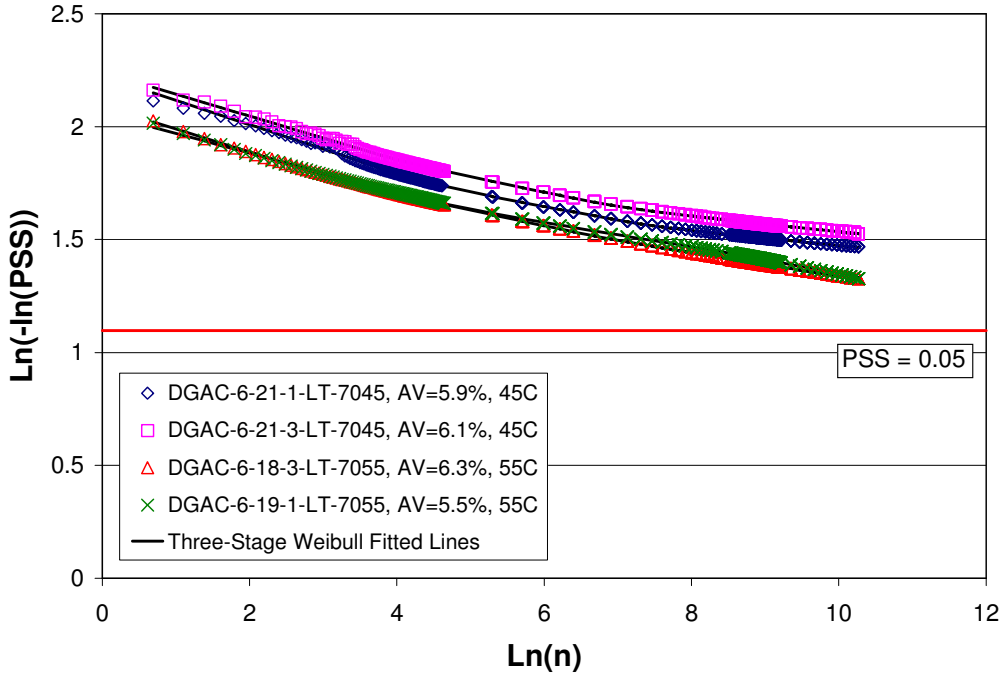

Figure A.55: AR4000-D shear test Three-stage Weibull curves: Aging effect at 70 kPa.
(Binder content = 5.0%; field-mixed, lab-compacted; AV = 6 ± 0.5 %, LTOA = 6 days)

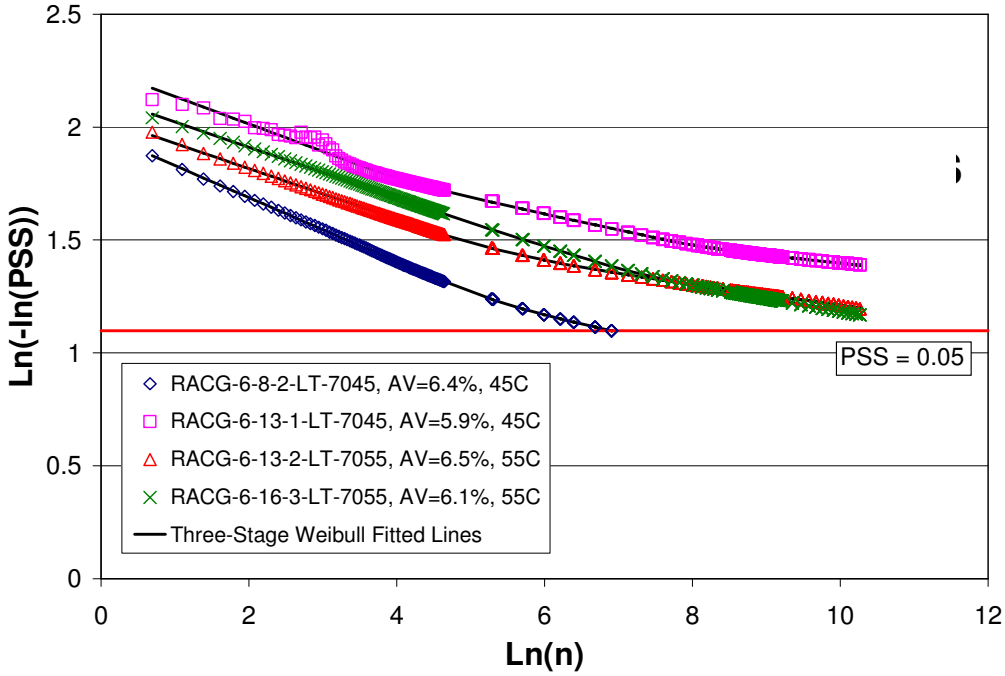

Figure A.56: RAC-G shear test Three-stage Weibull curves: Aging effect at 70 kPa.
(Binder content = 8.0%; field-mixed, lab-compacted; AV = 6 ± 0.5 %, LTOA = 6 days)

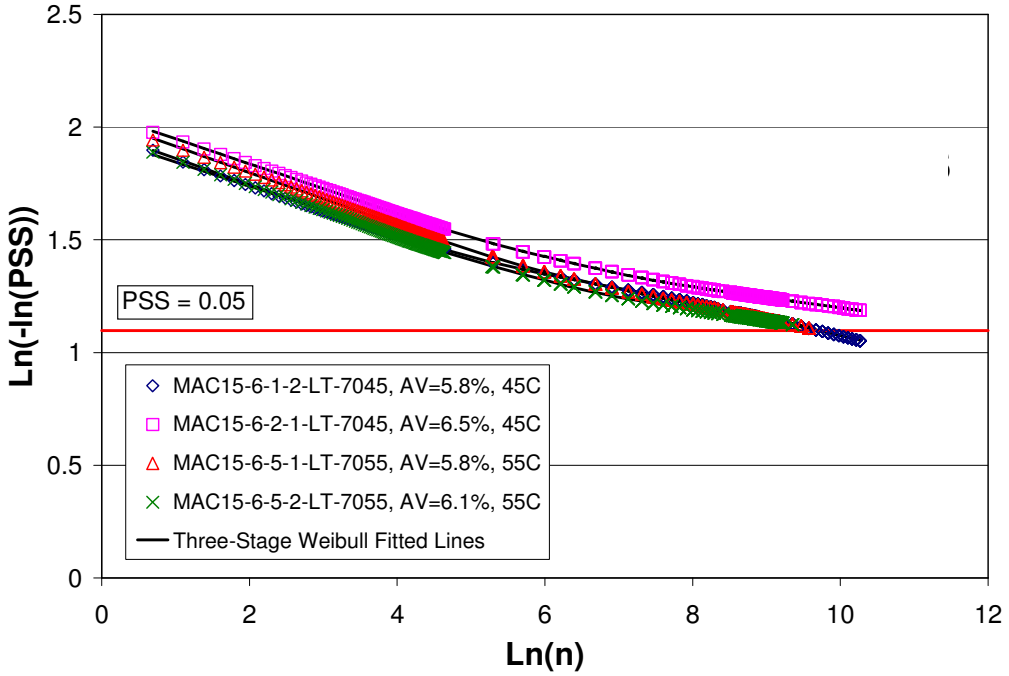

Figure A.57: MAC15-G shear test Three-stage Weibull curves: Aging effect at 70 kPa.
(Binder content = 7.4%; field-mixed, lab-compacted; AV = 6 ± 0.5 %, LTOA = 6 days)

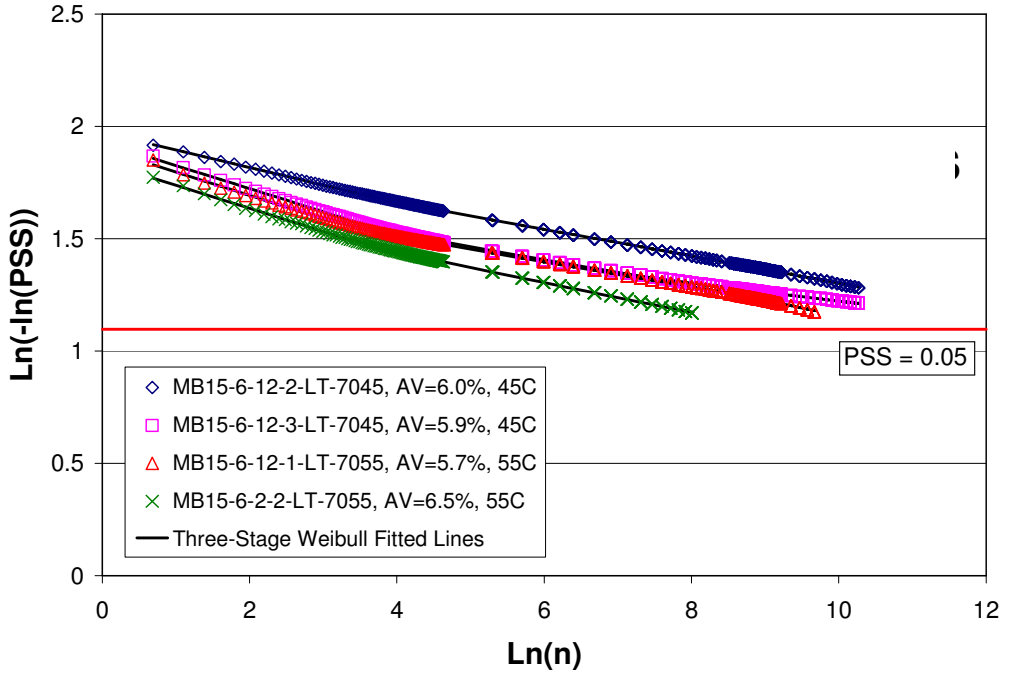

Figure A.58: MB15-G shear test Three-stage Weibull curves: Aging effect 70 kPa.
(Binder content = 7.1%; field-mixed, lab-compacted; AV = 6 ± 0.5 %, LTOA = 6 days)

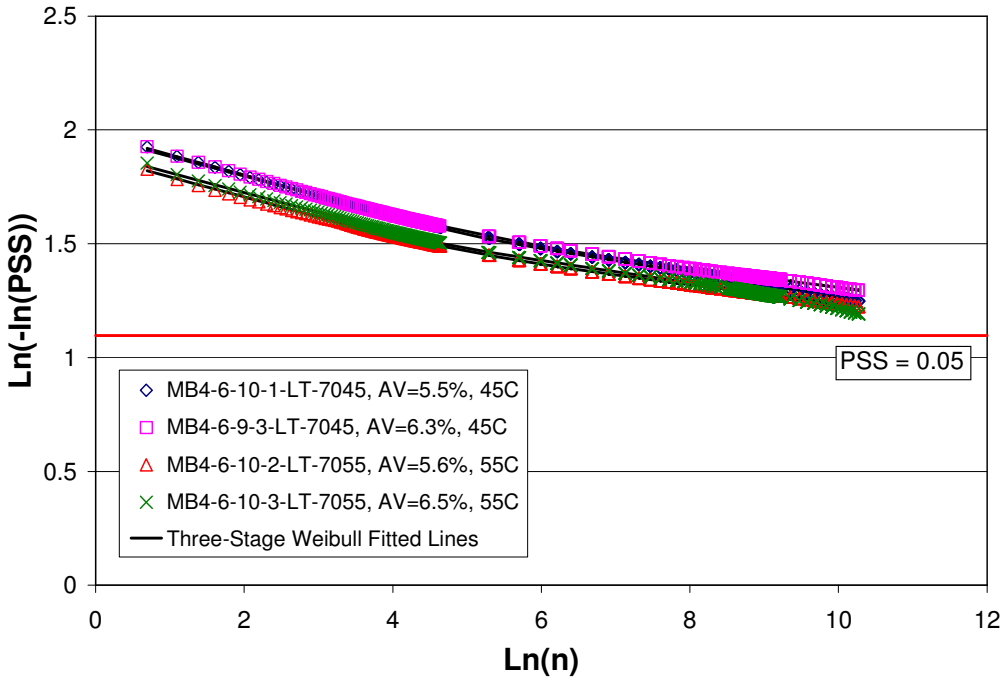

Figure A.59: MB4-G shear test Three-stage Weibull curves: Aging effect at 70 kPa.
(Binder content = 7.2%; field-mixed, lab-compacted; AV = 6 ± 0.5 %, LTOA = 6 days)

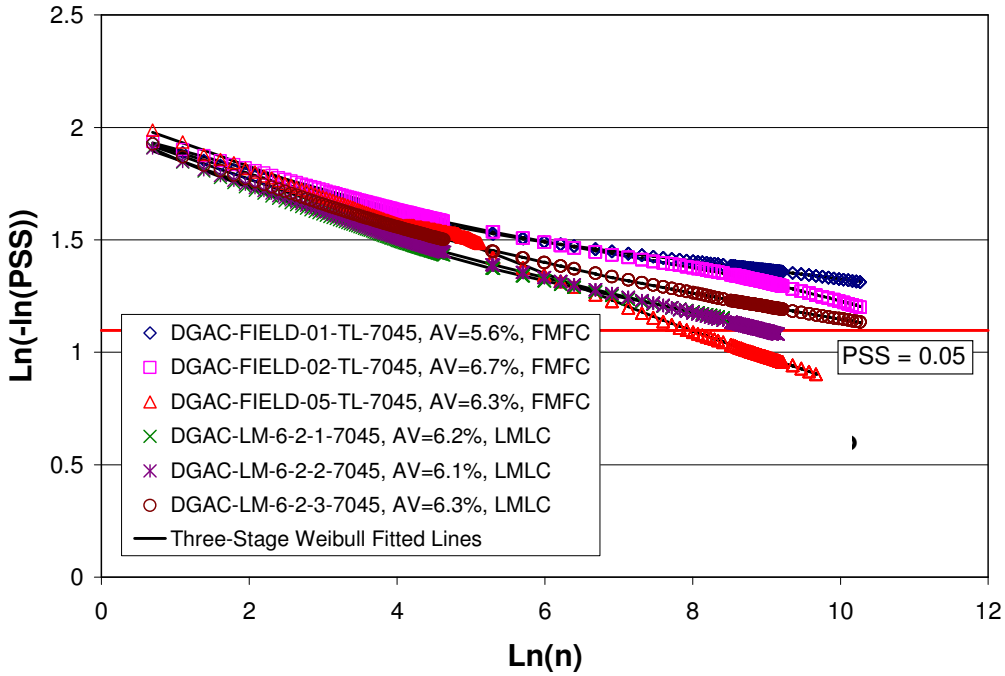

Figure A.60: AR4000-D shear test Three-stage Weibull curves: Compaction effect at 70 kPa.
(Binder content = 5.0%; field-mixed, field-compacted/lab-mixed lab-compacted; AV = 6 ± 0.5%, temp = 45 C)

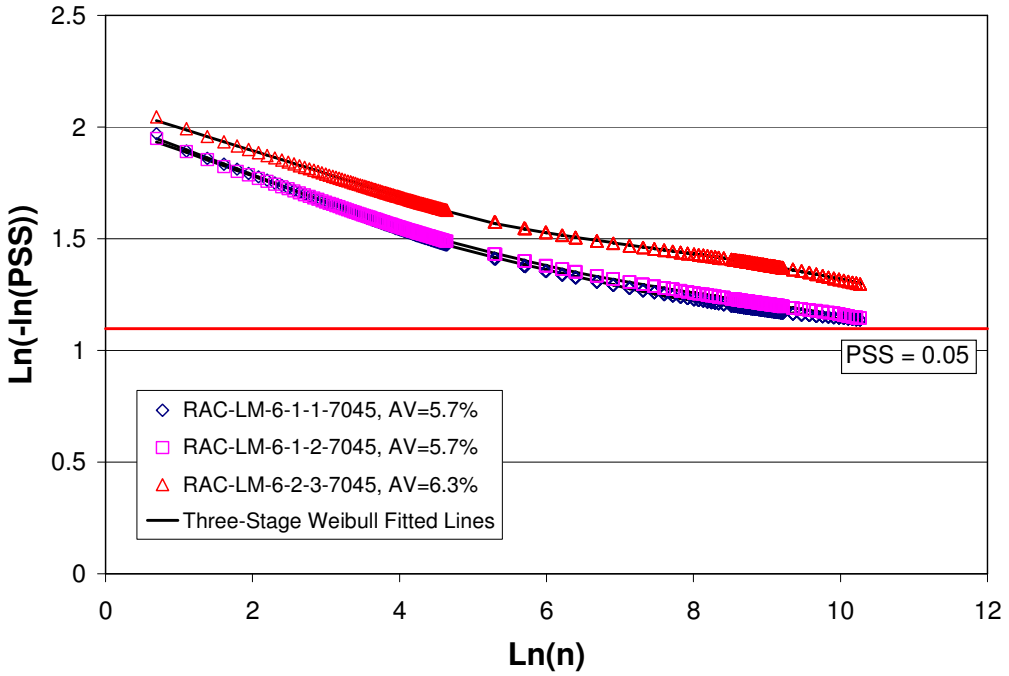

Figure A.61: RAC-G shear test Three-stage Weibull curves: Compaction effect at 70 kPa.
(Binder content = 8.0%; lab-mixed, lab-compacted; AV = 6 ± 0.5 %, temp = 45°C)

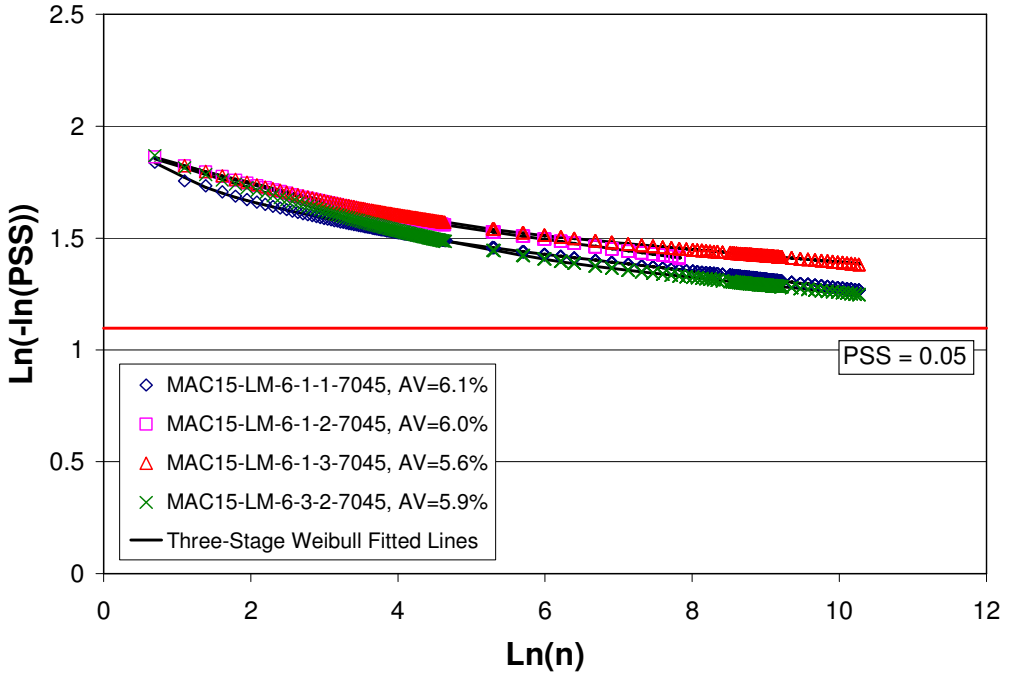

Figure A.62: MAC15-G shear test Three-stage Weibull curves: Compaction effect at 70 kPa.
(Binder content = 7.4%; lab-mixed, lab-compacted; AV = 6 ± 0.5 %, temp = 45°C)

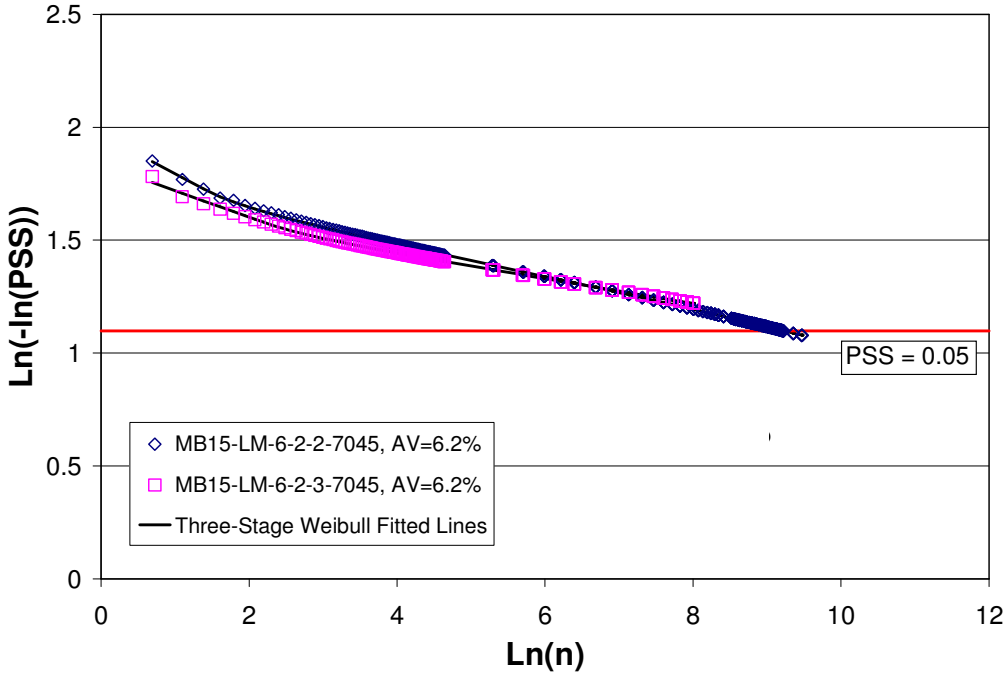

Figure A.63: MB15-G shear test Three-stage Weibull curves: Compaction effect at 70 kPa.
(Binder content = 7.1%; lab-mixed, lab-compacted; AV = 6 ± 0.5 %, temp = 45°C)

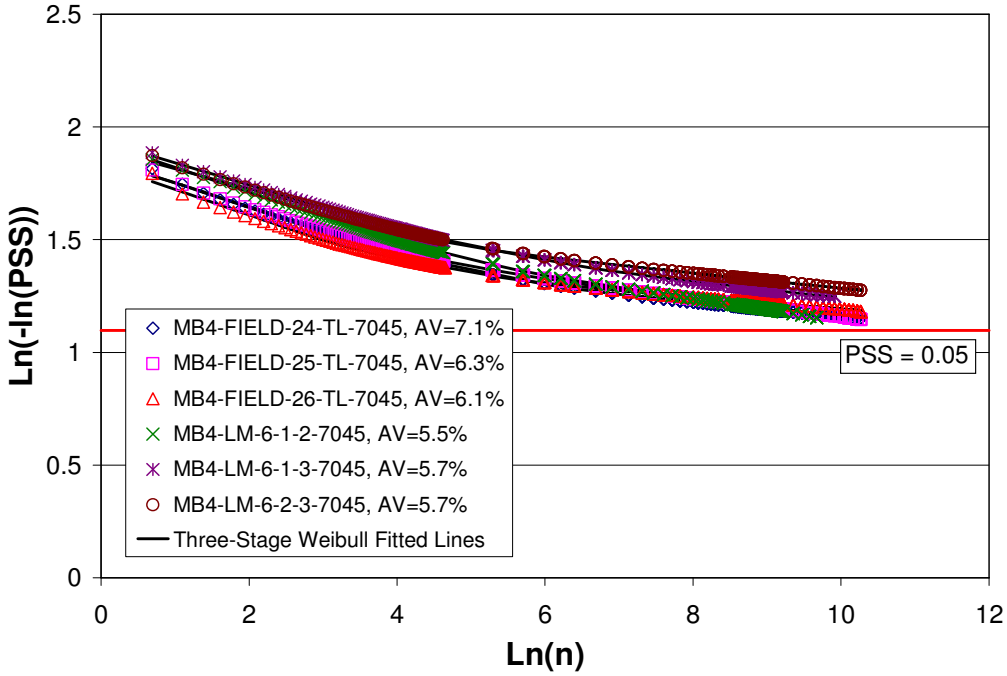

Figure A.64: MB4-G shear test Three-stage Weibull curves: Compaction effect at 70 kPa.
(Binder content = 7.2%; field-mixed, field-compacted/lab-mixed lab-compacted; AV = 6 ± 0.5 %, temp = 45°C)

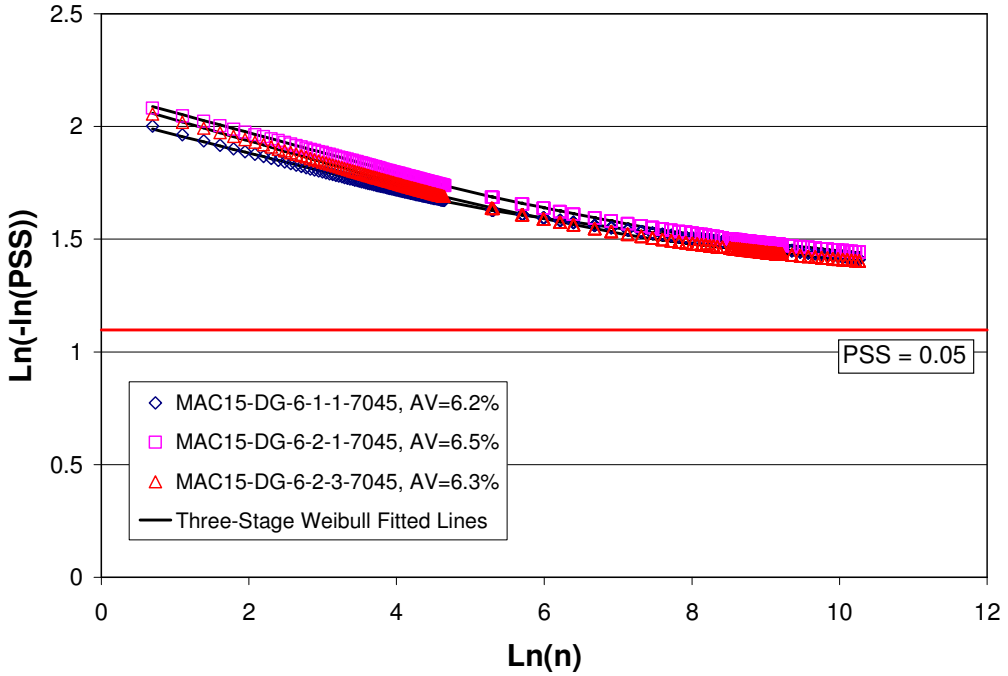

Figure A.65: MAC15-D shear test Three-stage Weibull curves: Gradation effect at 70 kPa.
(Binder content = 6.0%; lab-mixed, lab-compacted; AV = 6 ± 0.5 %; dense-graded, temp = 45°C)

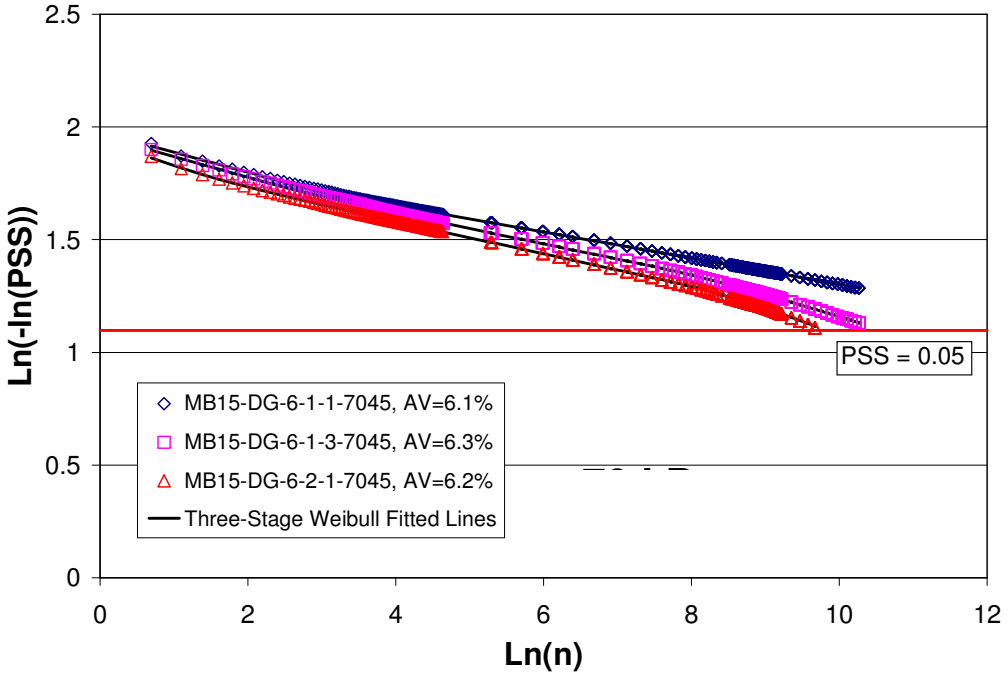

Figure A.66: MB15-D shear test Three-stage Weibull curves: Gradation effect at 70 kPa.
(Binder content = 6.0%; lab-mixed, lab-compacted; AV = 6 ± 0.5 %; dense-graded, temp = 45°C))

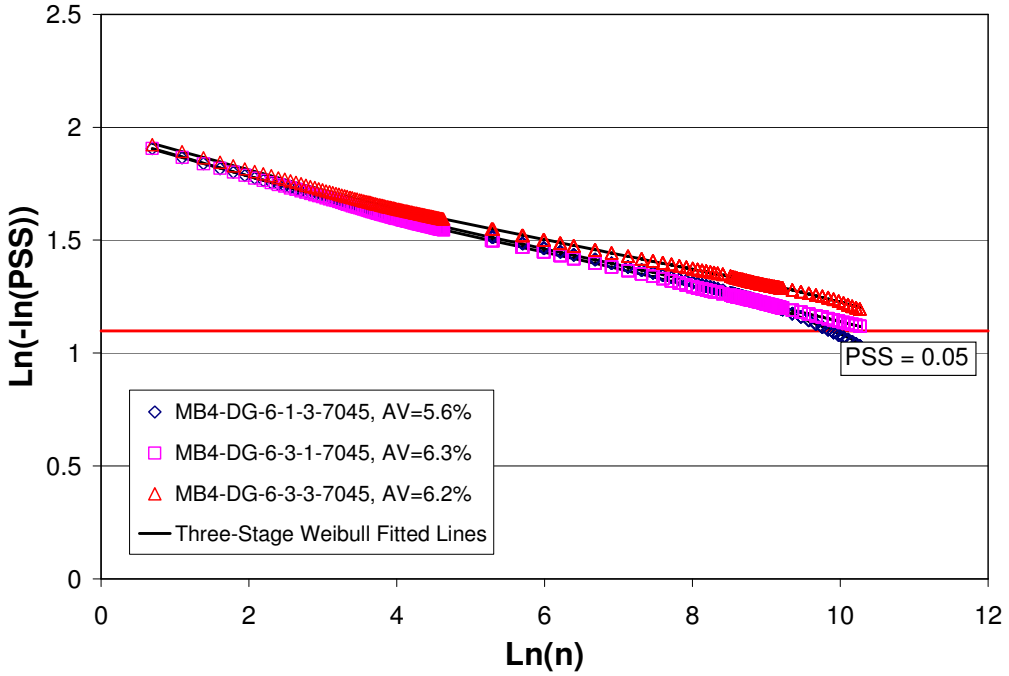

Figure A.67: MB4-D shear test Three-stage Weibull curves: Gradation effect at 70 kPa.
(Binder content = 6.3%; lab-mixed, lab-compacted; AV = 6 ± 0.5 %; dense-graded)

A.5. Pruned Dendograms for Laboratory Shear Results

Section 3.5.2

Pruned dendrograms for laboratory shear results are presented in Figure A.68.

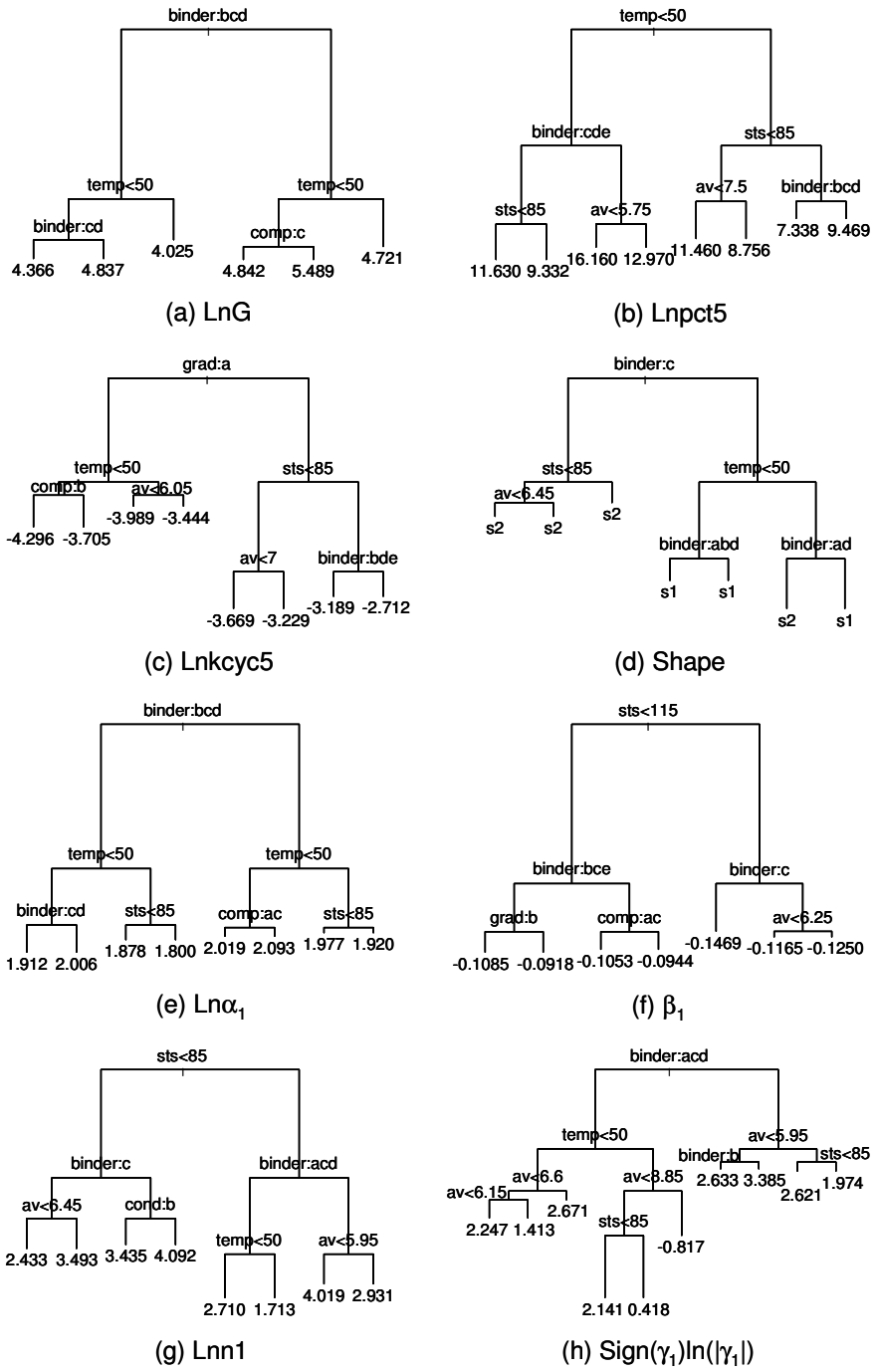

Figure A.68: Pruned dendrograms of shear three-stage Weibull parameters.

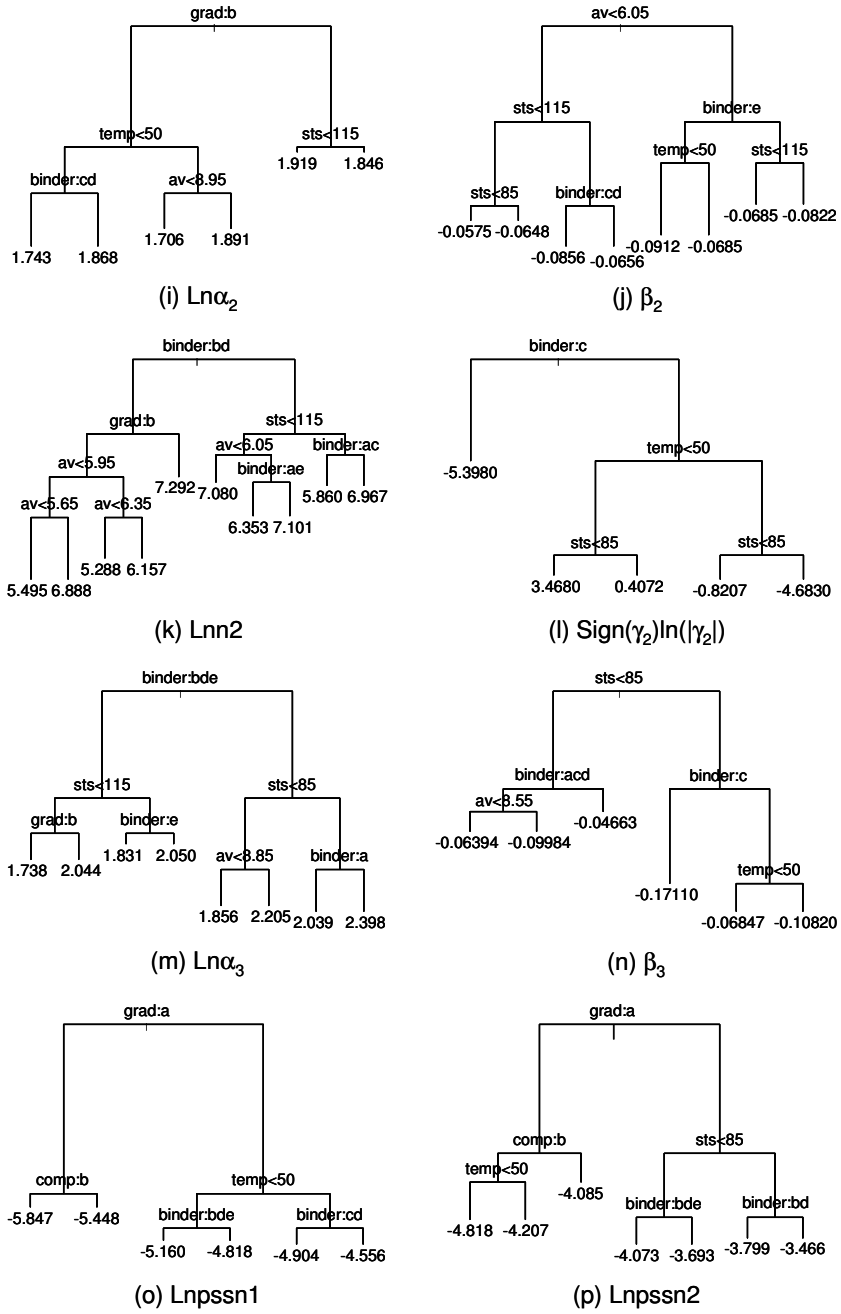

Figure A.68: Pruned dendrograms of shear three-stage Weibull parameters (continued).

A.6. Fatigue and Shear Equations from Temperature Effect Data

Section 3.6.2

Figures A.69 to A.73 and Figures A.74 to A.78 illustrate the fitting results using the laboratory two-stage Weibull fatigue and shear integrated equations for AR4000-D, MAC15-G, MB15-G, MB4-G, and RAC-G mixes respectively (grey lines are the fitted lines).

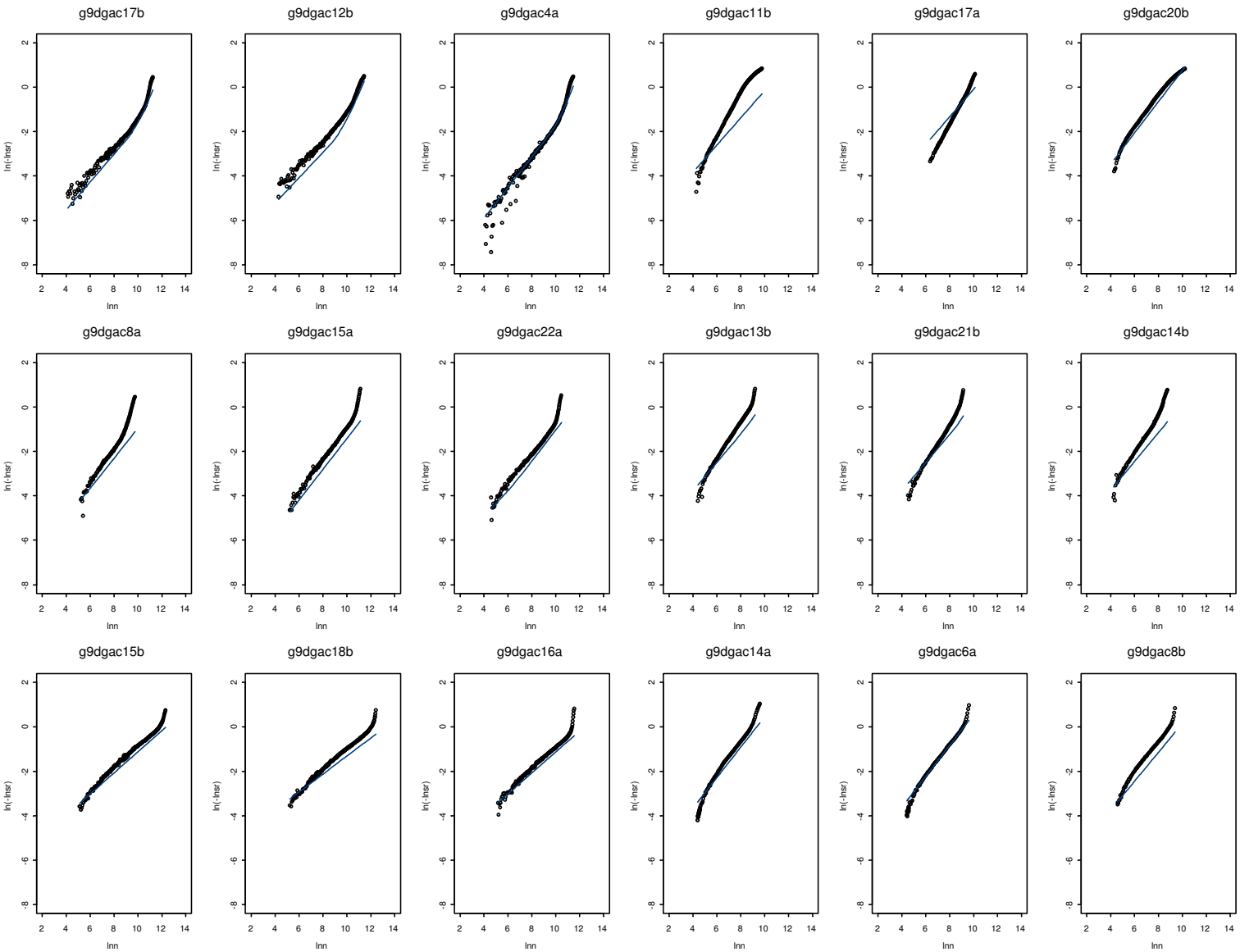

Figure A.69: Fatigue fitting results for AR4000-D mixes (temperature effect data).

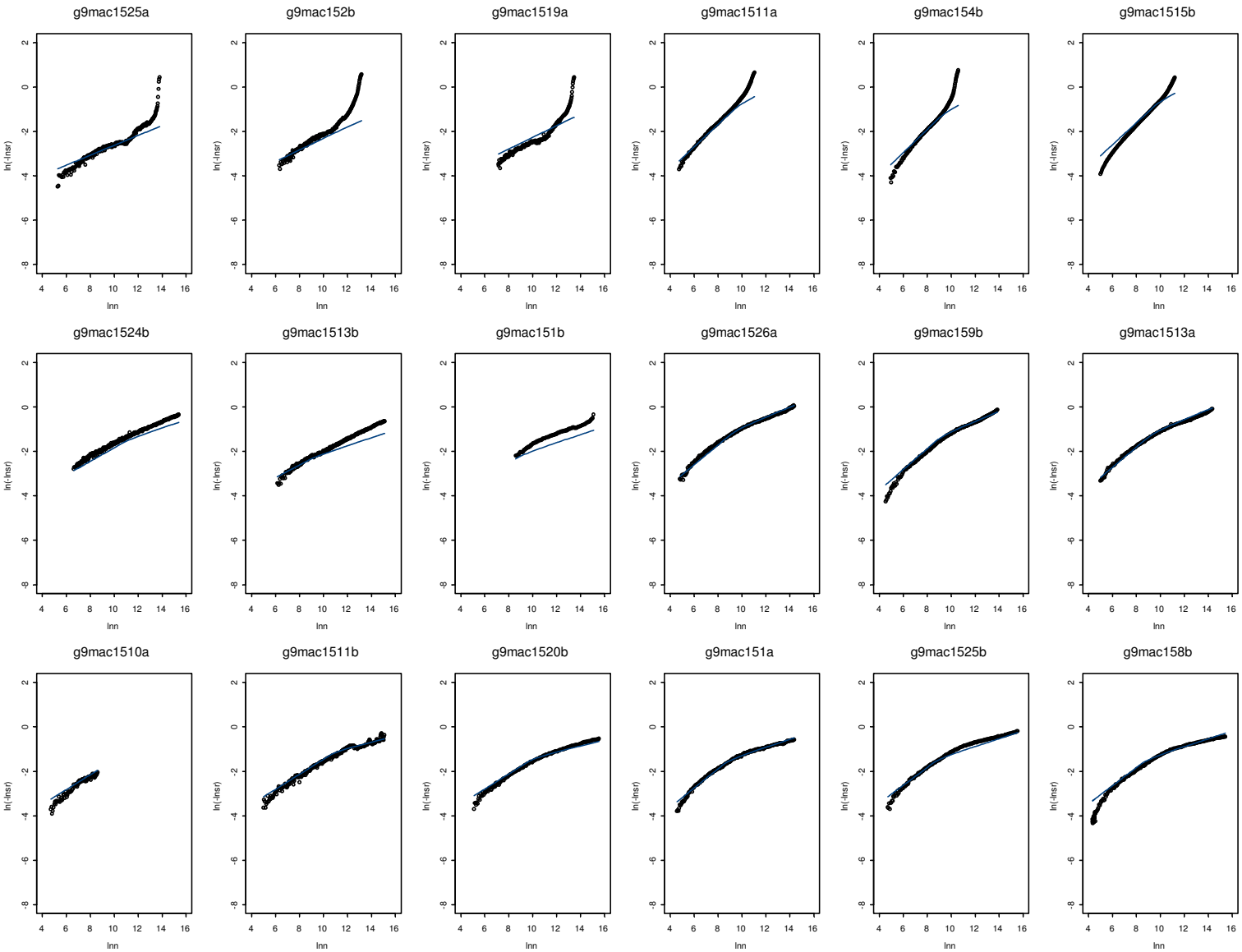

Figure A.70: Fatigue fitting results for MAC15-G mixes (temperature effect data).

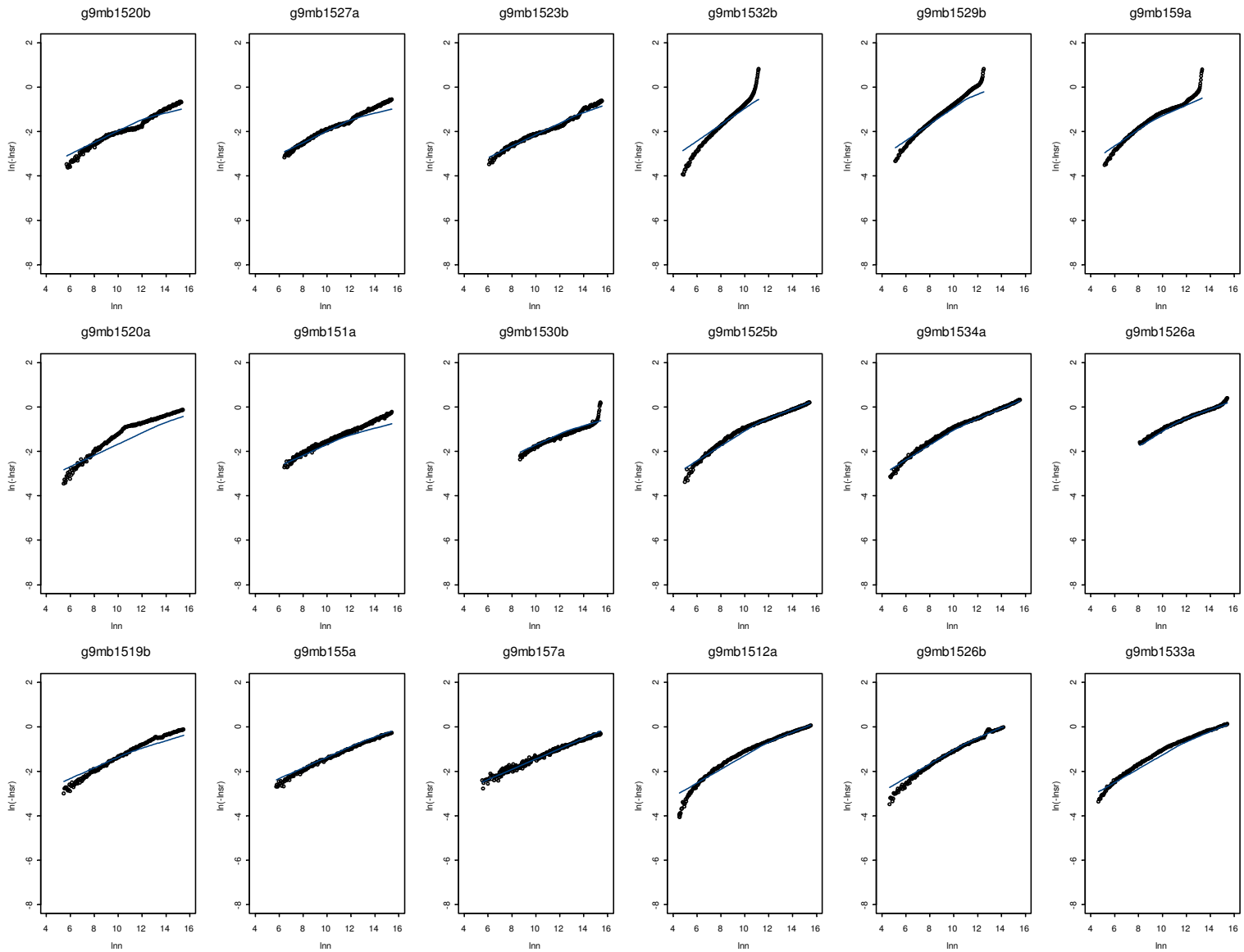

Figure A.71: Fatigue fitting results for MB15-G mixes (temperature effect data).

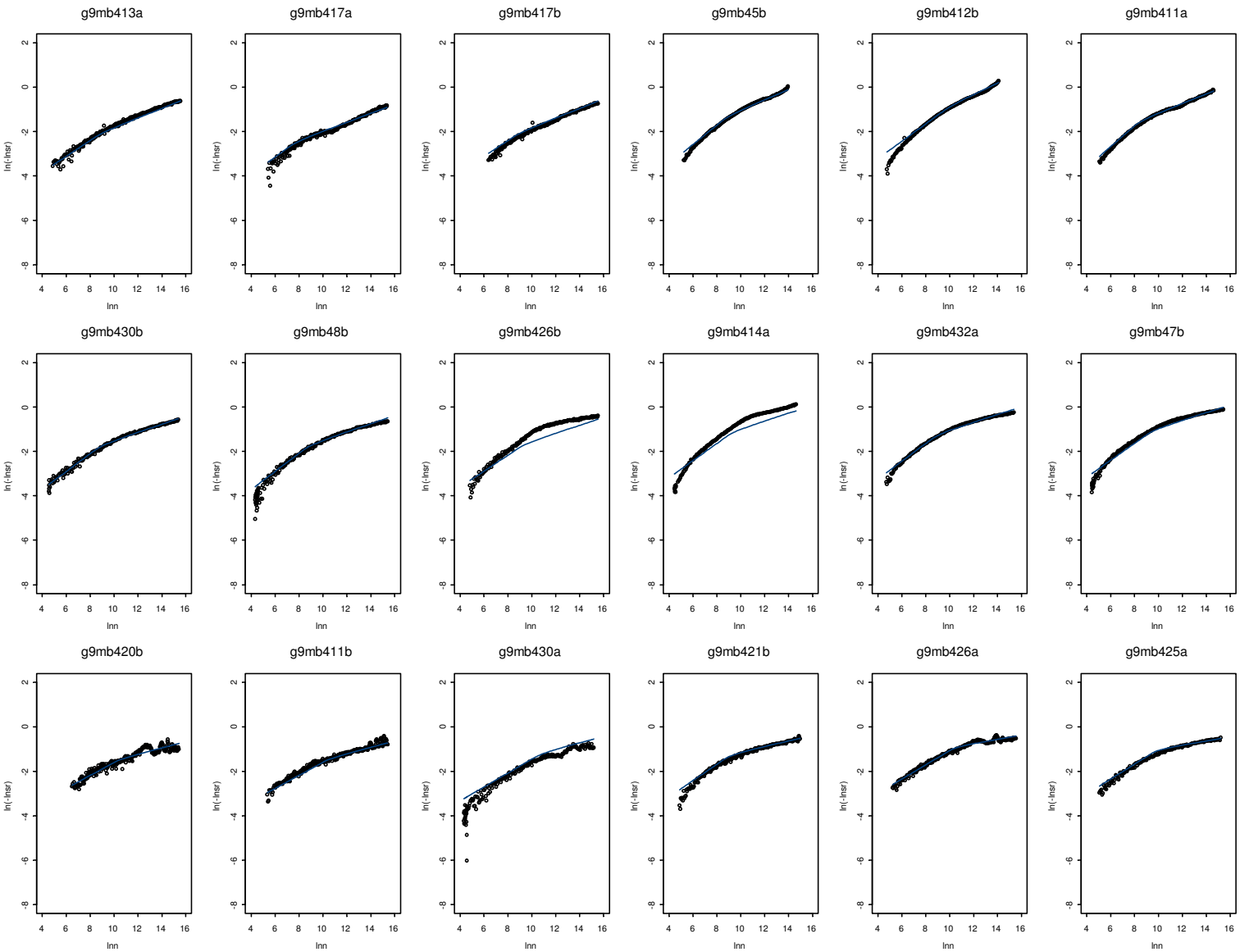

Figure A.72: Fatigue fitting results for MB4-G mixes (temperature effect data).

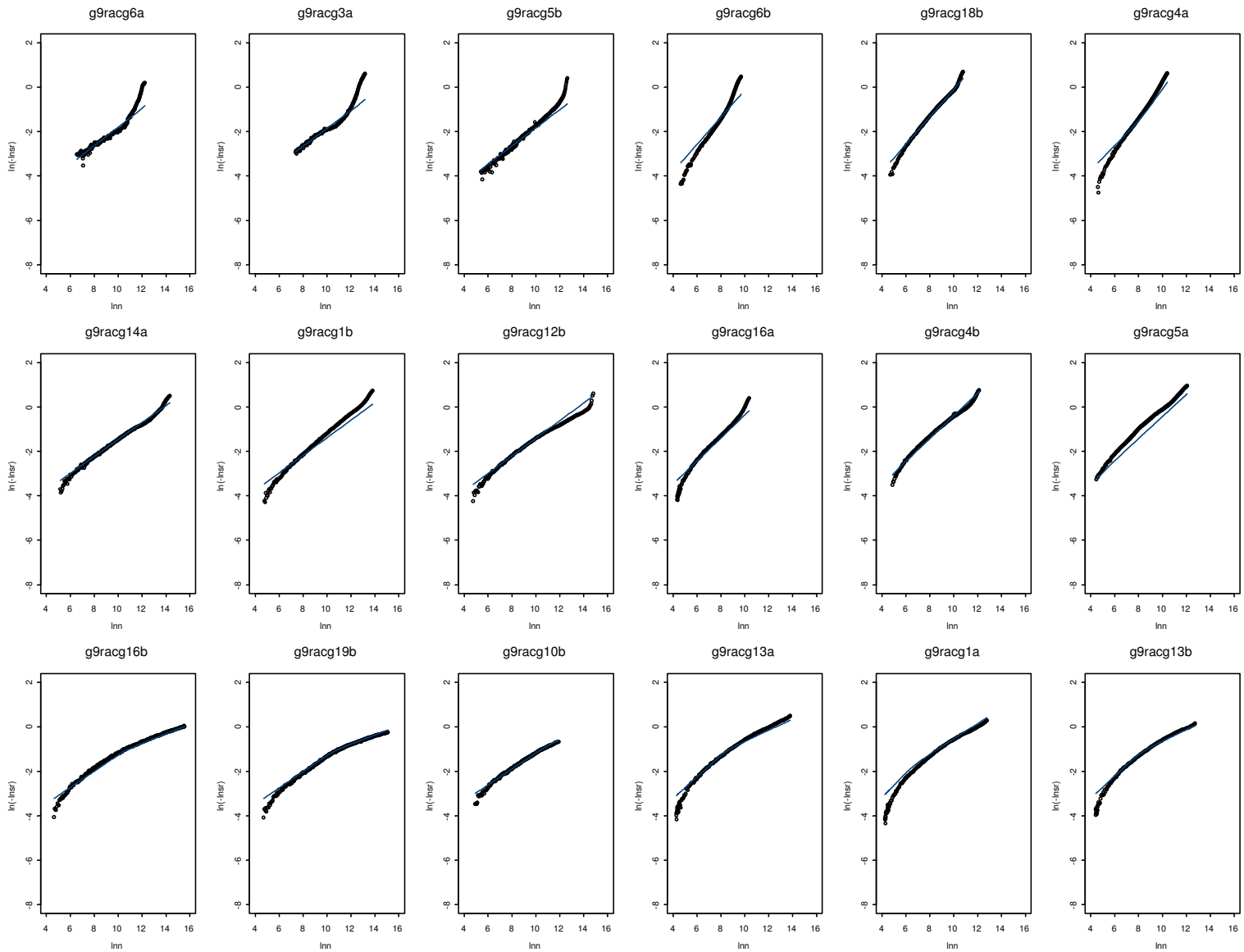

Figure A.73: Fatigue fitting results for RAC-G mixes (temperature effect data).

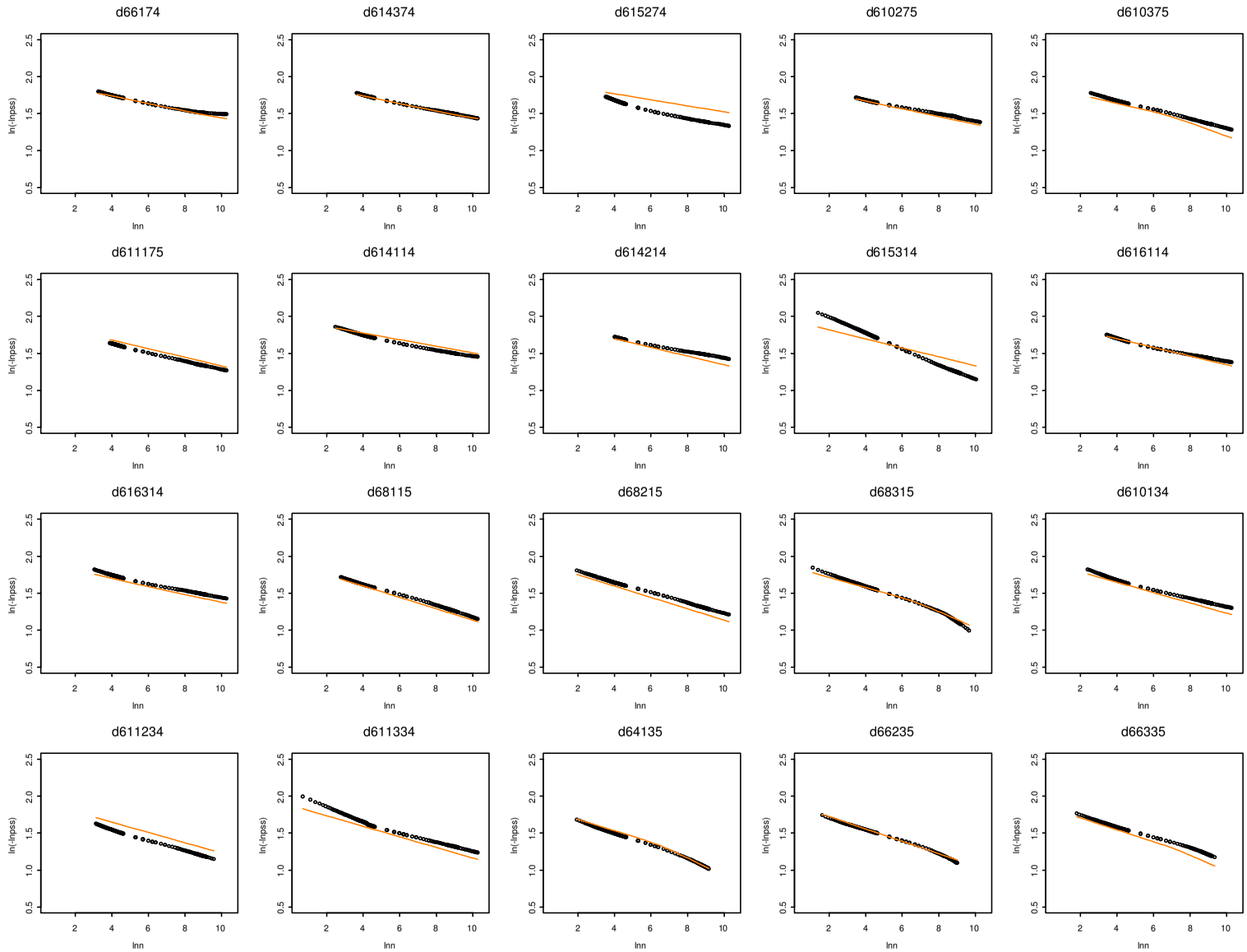

Figure A.74: Shear fitting results for AR4000-D mixes (temperature effect data).

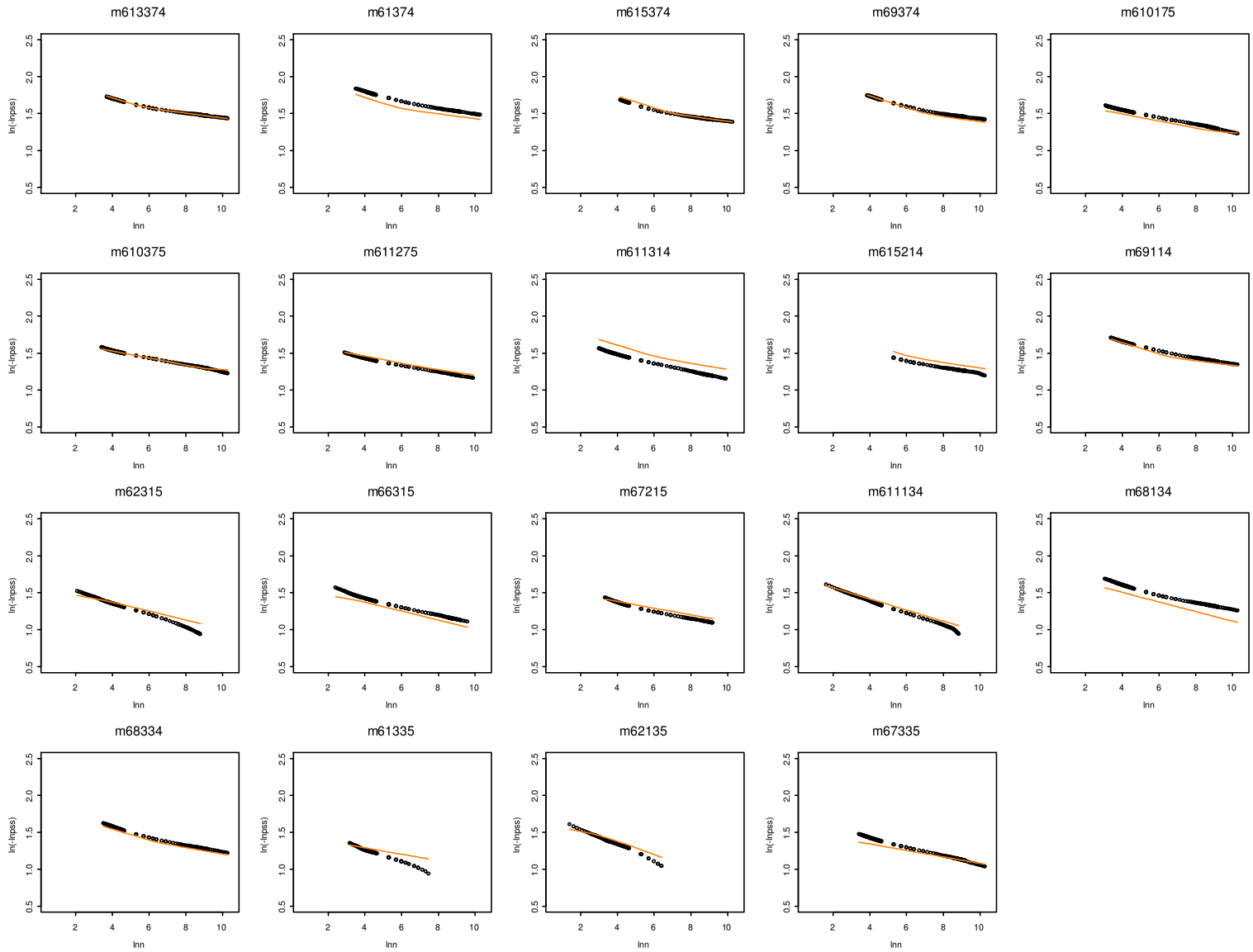

Figure A.75: Shear fitting results for MAC15-G mixes (temperature effect data).

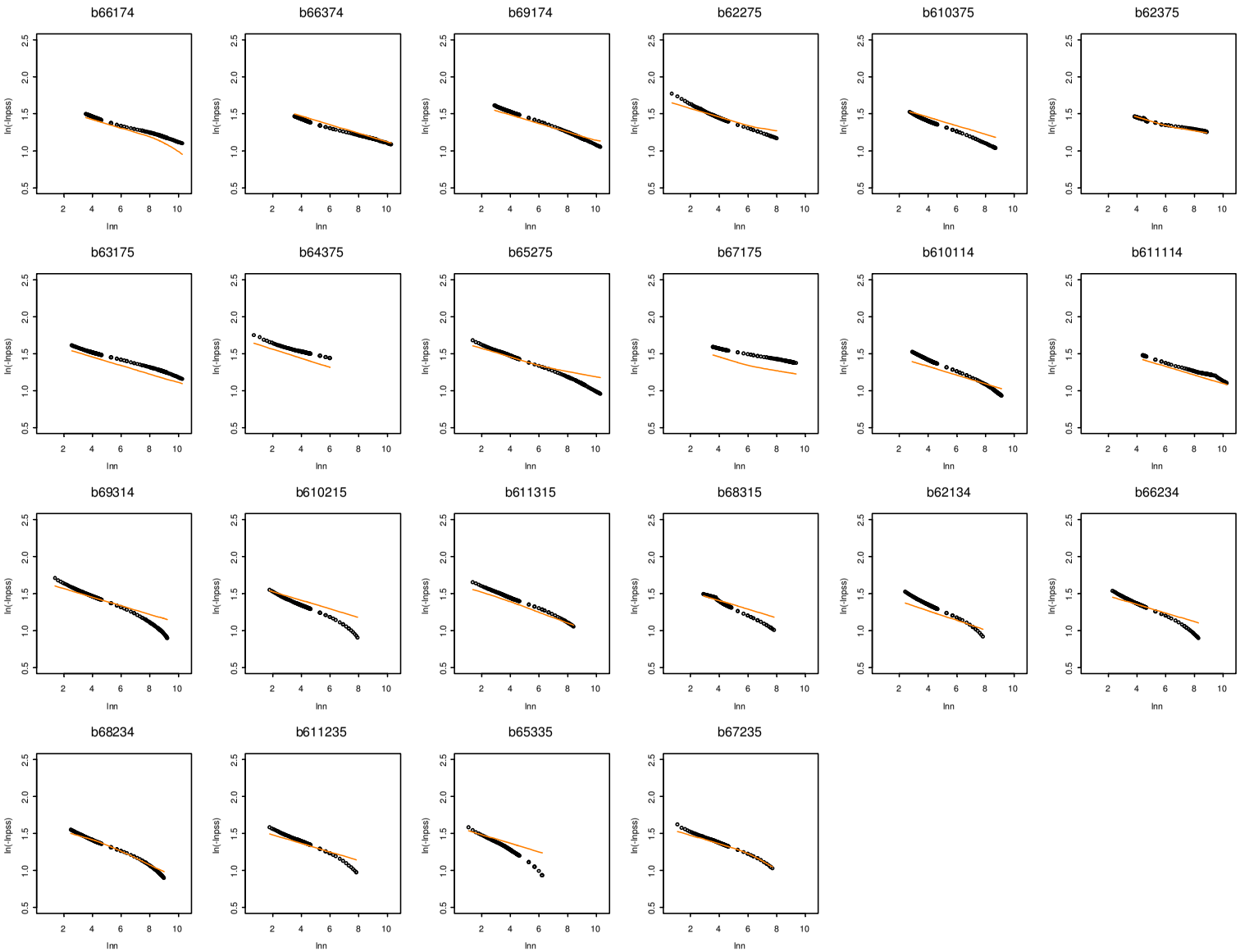

Figure A.76: Shear fitting results for MB15-G mixes (temperature effect data).

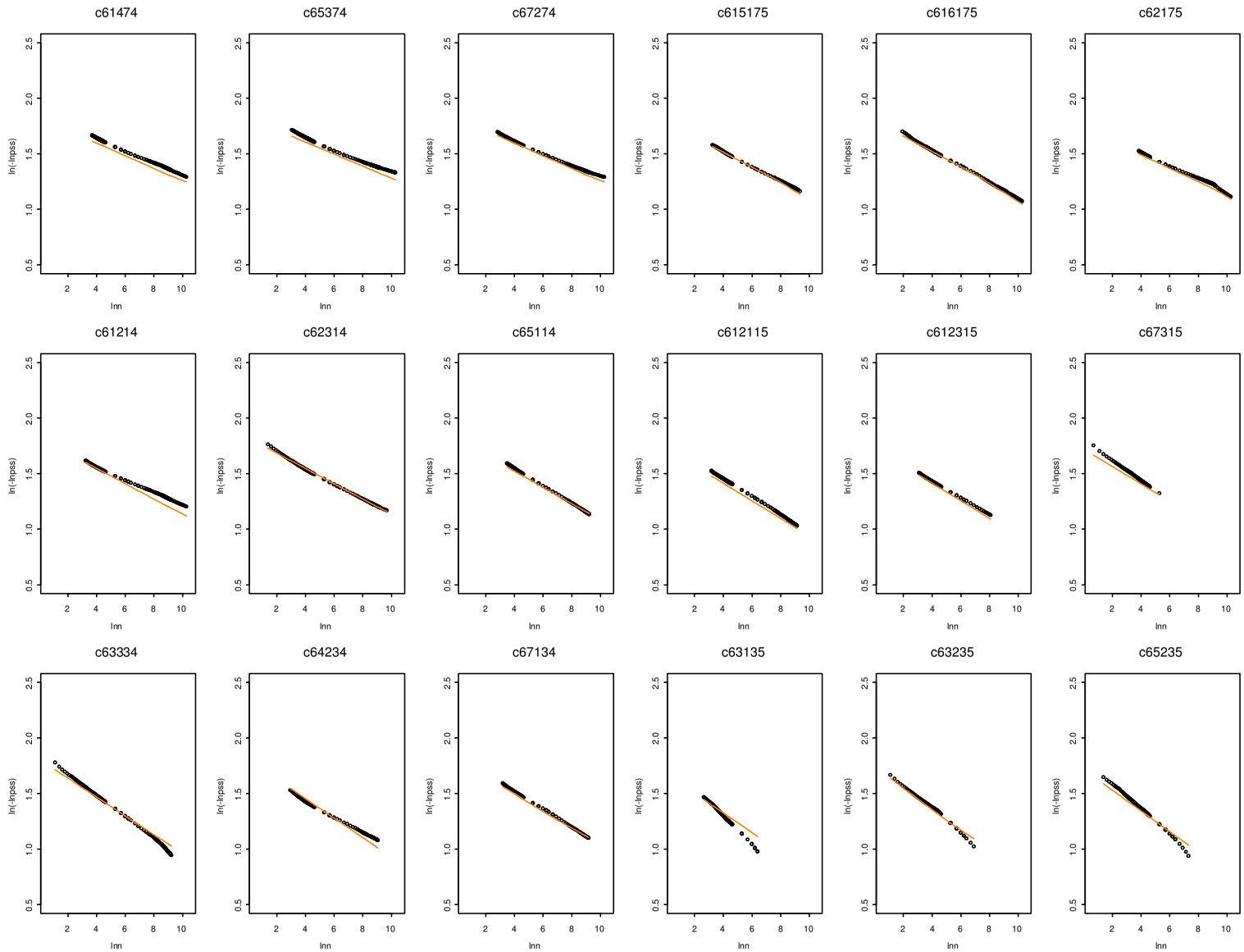

Figure A.77: Shear fitting results for MB4-G mixes (temperature effect data).

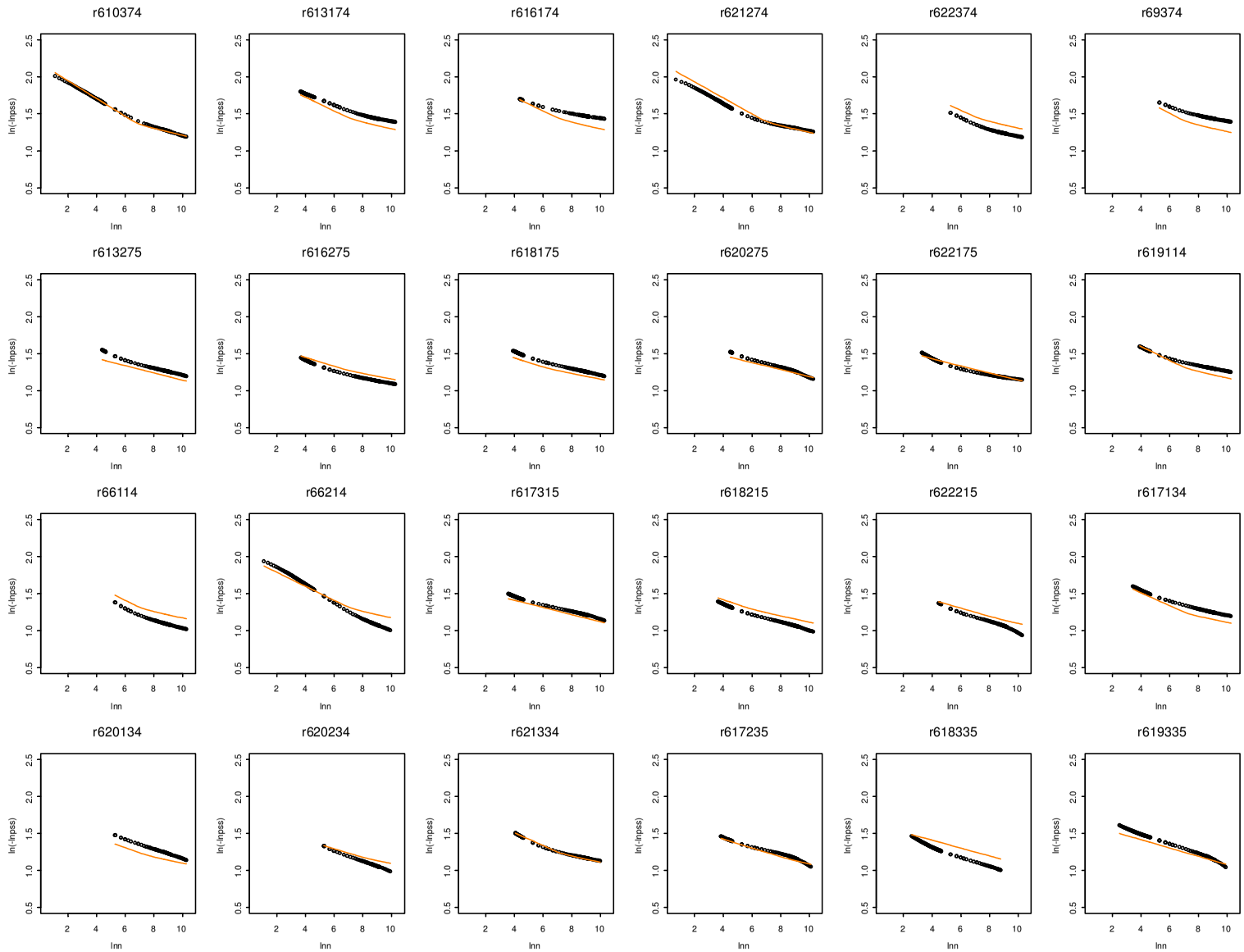

Figure A.78: Shear fitting results for RAC-G mixes (temperature effect data).

A.7. Fatigue and Shear Equations from Gradation Effect Data

Section 3.6.3

Figures A.79 to A.81 (fatigue) and Figures A.82 to A.84 (shear) illustrate the regression fitting results of Stages II and III for the MB4-D, MB15-D and MAC15-D mixes.

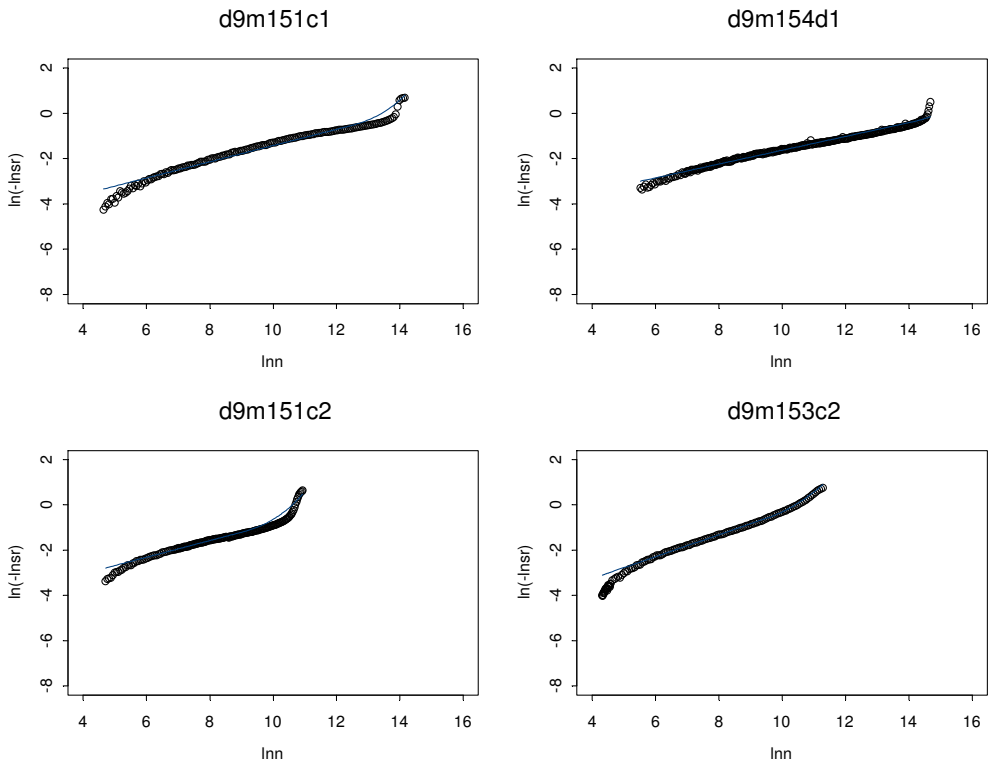

Figure A.79: Fatigue fitting results for MAC15-D mixes (gradation effect data).

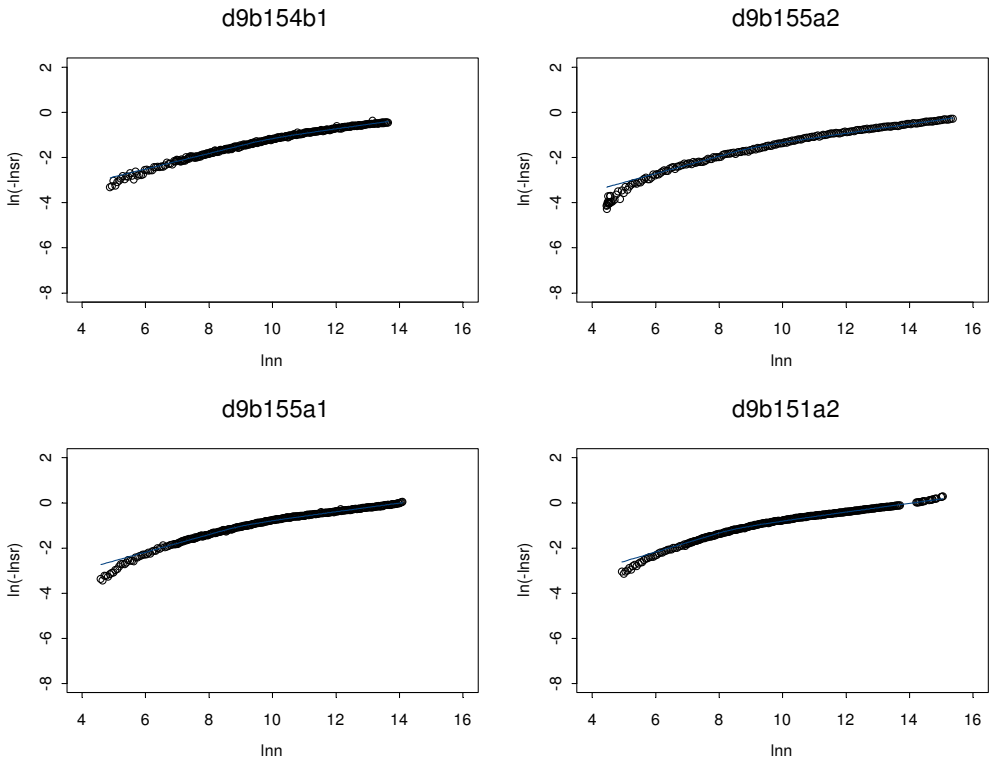

Figure A.80: Fatigue fitting results for MB15-D mixes (gradation effect data).

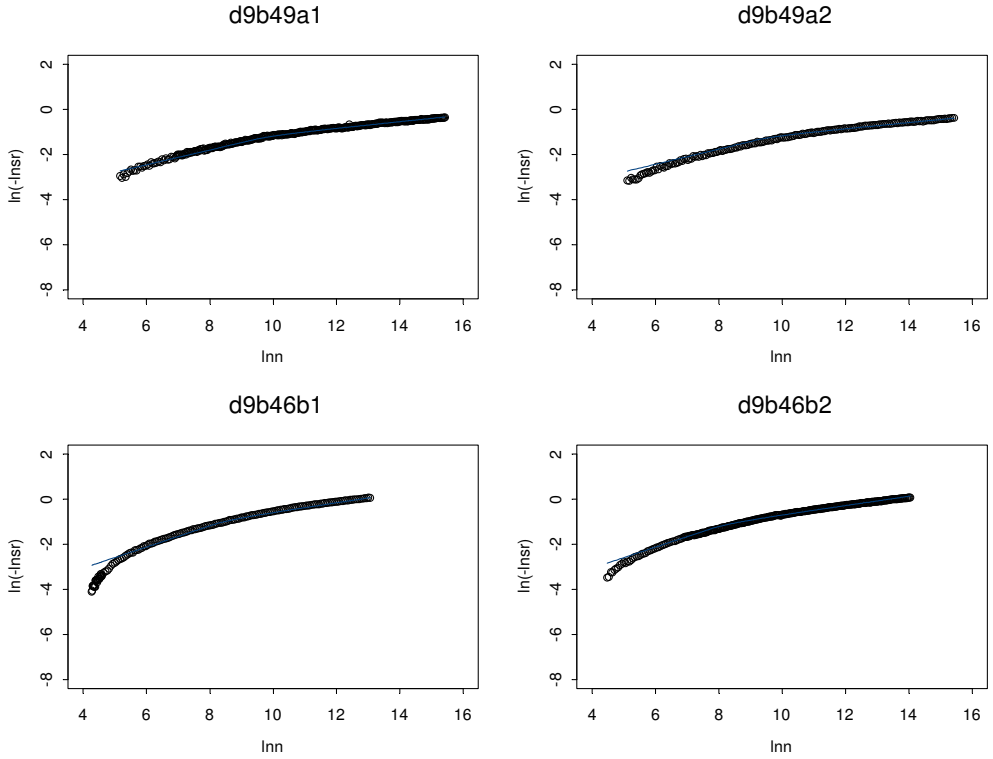

Figure A.81: Fatigue fitting results for MB4-D mixes (gradation effect data).

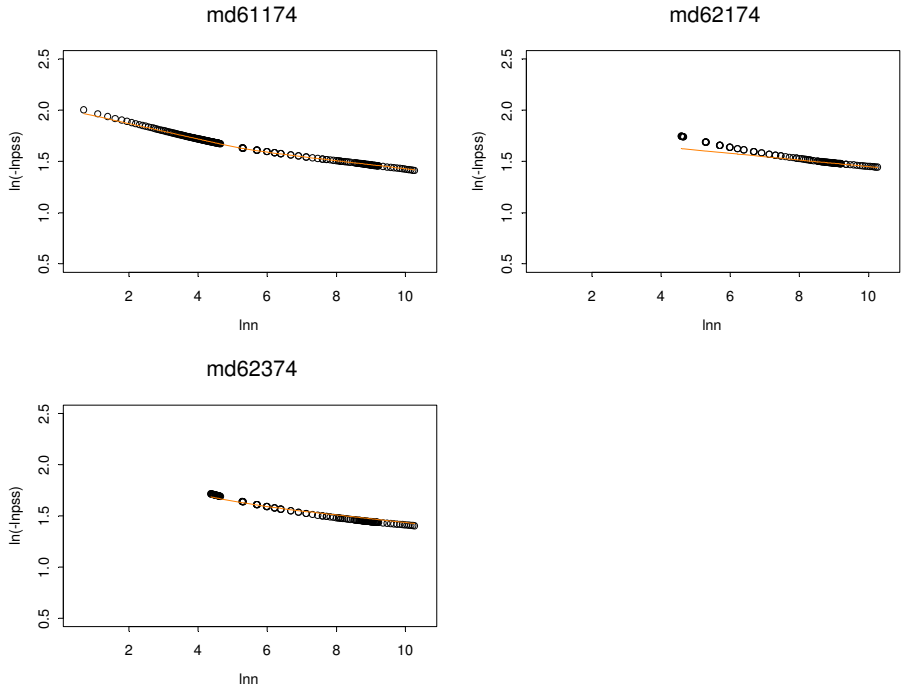

Figure A.82: Shear fitting results for MAC15-D mixes (gradation effect data).

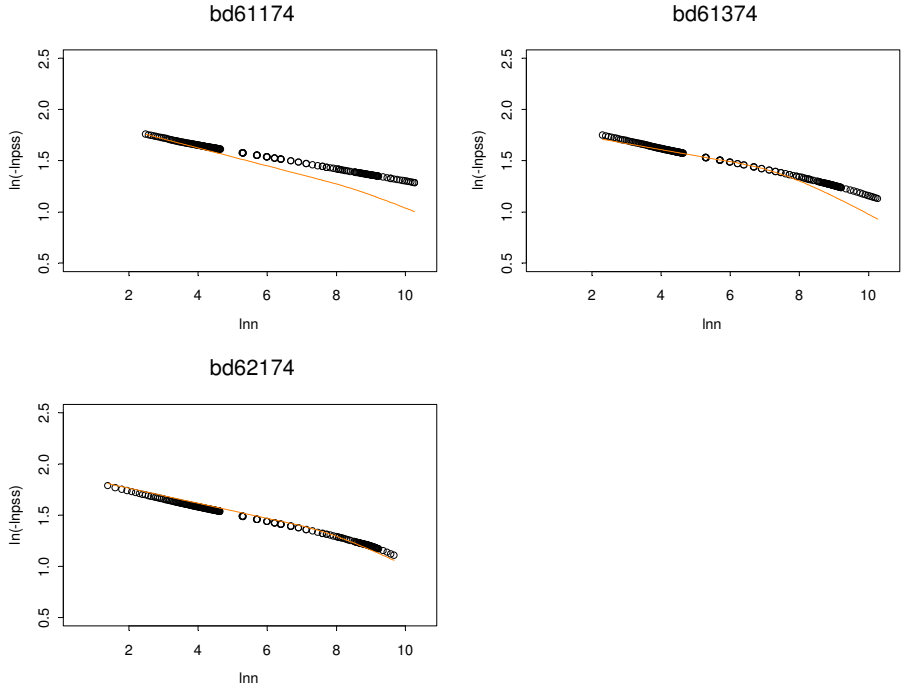

Figure A.83: Shear fitting results for MB15-D mixes (gradation effect data).

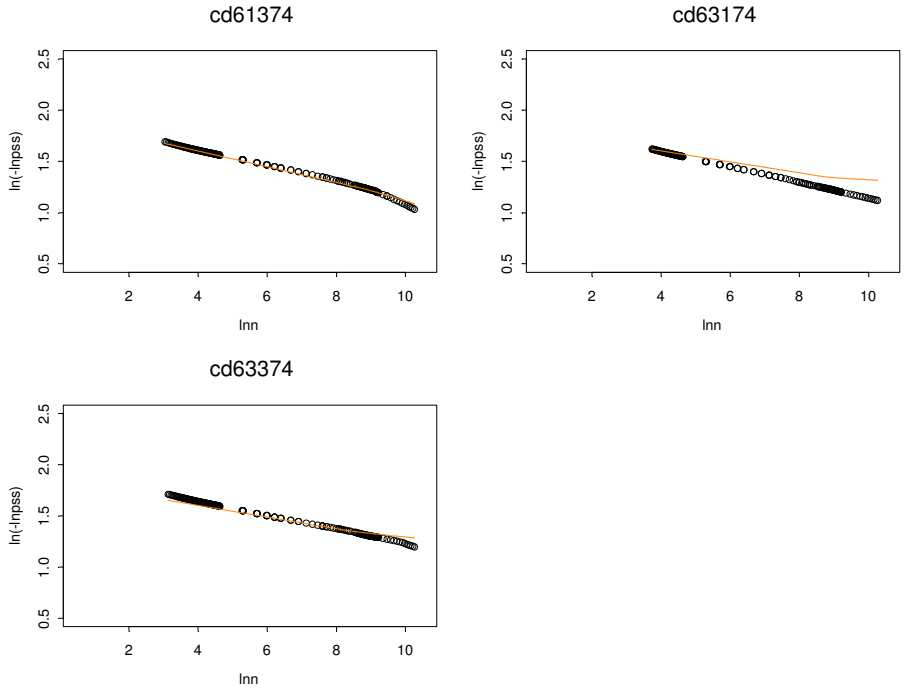

Figure A.84: Shear fitting results for MB4-D mixes (gradation effect data).

Appendix B

Mechanistic Empirical Performance Simulations

APPENDIX B. M.E. PERFORMANCE SIMULATIONS

B.1. Simulation of Overlaid Sections: Rutting Study

Section 4.10.1

The temperatures in the upper 100 mm of the pavement are shown in Figures B.1 through B.6, as a function of the number of load applications. The number in the legend indicates the depth of the thermocouple.

Section 4.10.2

The resilient deflections measured with the MDD are shown in Figures B.7 through B.27. The measured values have a legend "M" followed by the depth of the MDD module in mm or, for the compression of the AB layers, by the depths of the first and second MDD module. All comparisons are at a wheel load of 60 kN.

Section 4.10.4

The permanent deformation at the upper MDD, the permanent compression of the aggregate base layers, and the permanent deformation of the subgrade are shown as functions of the number of load applications in Figures B.28 through B.45 for those sections with useable MDD results. The same legend-convention is used as for the resilient deflections. The figures indicate that the permanent deformation in the base was less than 1.0 mm and in the subgrade less than 0.1 mm.

B.2. Simulation of Overlaid Sections (Actual Conditions): Reflective Cracking Study

Section 4.11.1

The measured and calculated RSD response as a function of the number of load applications is shown in Figures B.46 through B.52. The first value shown (RSD) is the measured value and the second ("Calc.") is the value calculated by *CalME*. The RSD deflections were measured at a number of locations within the test section, whereas the calculated values assume the section to be perfectly uniform. All of the comparisons are at a wheel load of 60 kN.

Section 4.11.2

The measured surface deflection, resilient compression of the AB layers, and deflection of the subgrade are compared to values calculated by *CalME* in Figures B.53 through B.69 in Appendix B on those HVS

sections with useable MDD results. The measured values have a legend "M" followed by the depth of the MDD module in mm or, for the compression of the AB layers, by the depths of the first and second MDD module. All comparisons are at a wheel load of 60 kN.

Section 4.11.5

The permanent deformation at the upper MDD, the permanent compression of the aggregate base layers and the permanent deformation of the subgrade are shown as functions of the number of load applications in Figures B.70 through B.87 in Appendix B, for those sections with useable MDD results. The same legend-convention is used as for the resilient deflections.

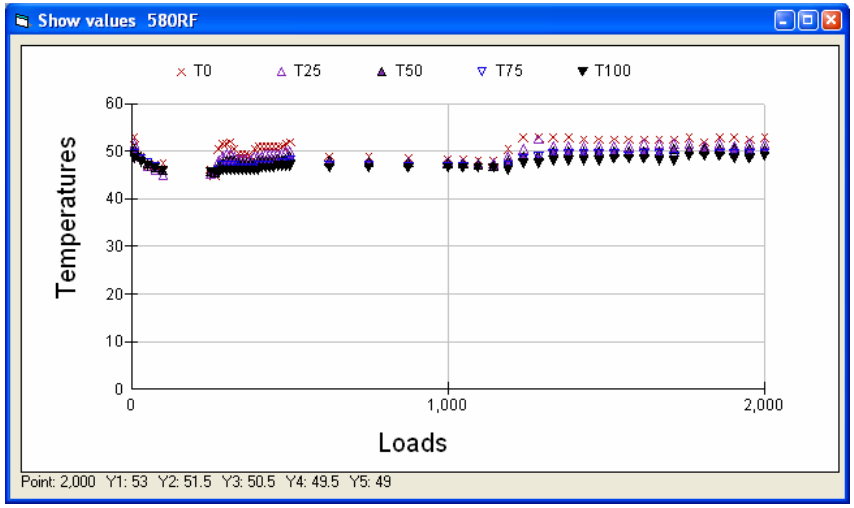

Figure B.1: 580RF, pavement temperatures at various depths.

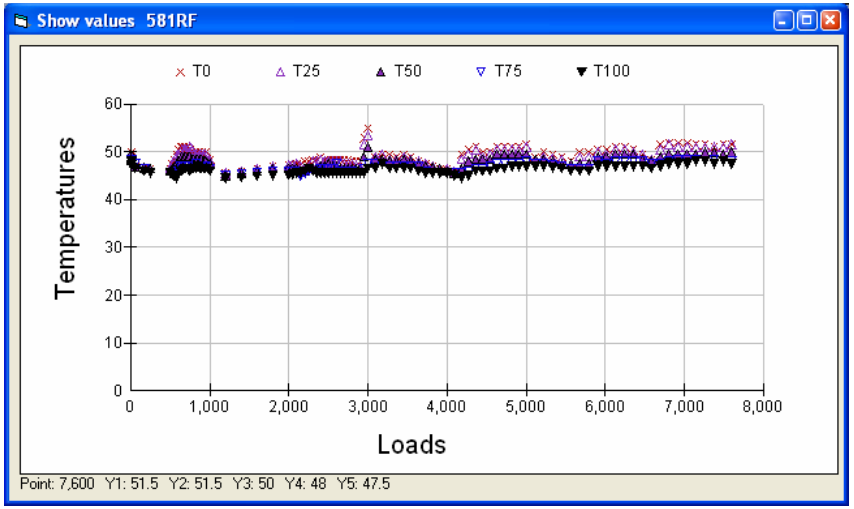

Figure B.2: 581RF, pavement temperatures at various depths.

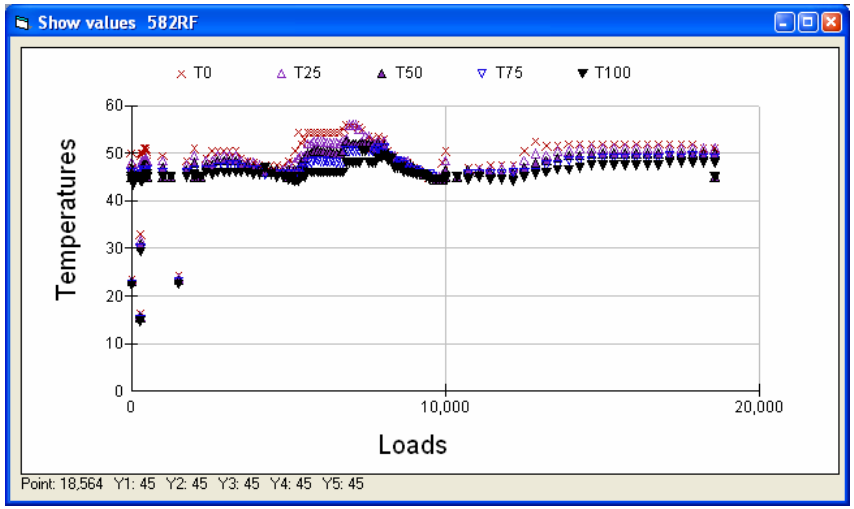

Figure B.3: 582RF, pavement temperatures at various depths.

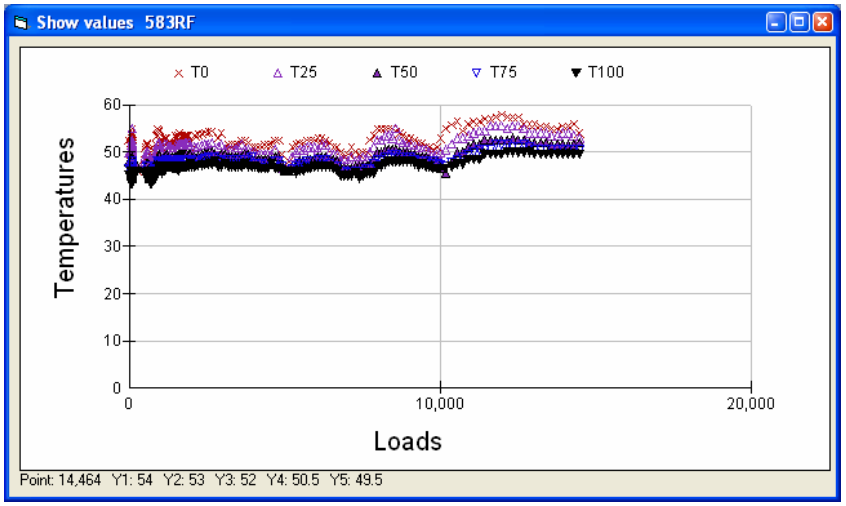

Figure B.4: 583RF, pavement temperatures at various depths.

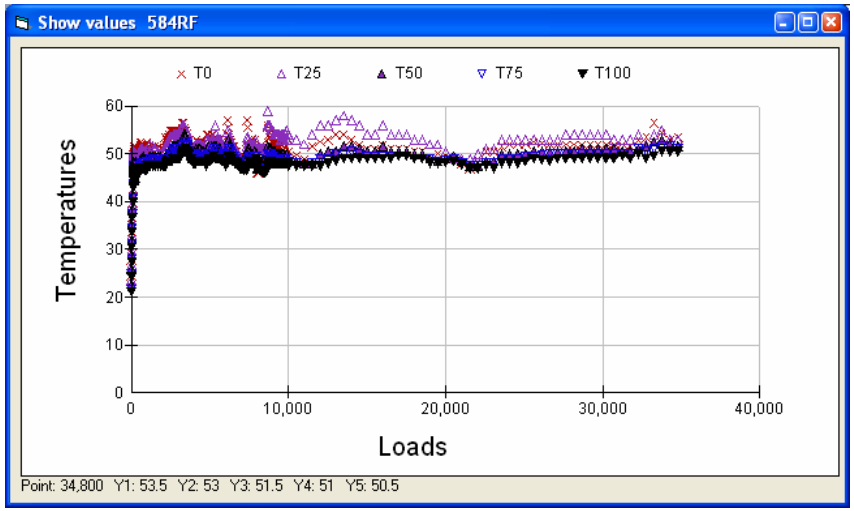

Figure B.5: 584RF, pavement temperatures at various depths.

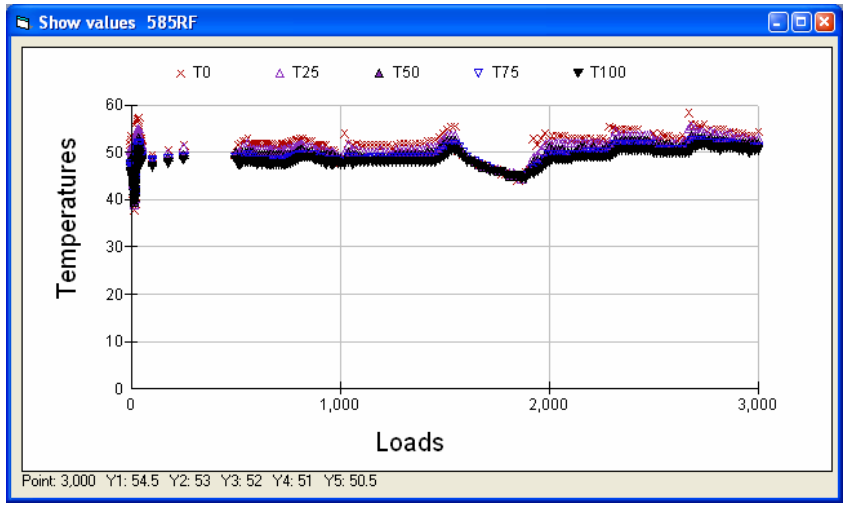

Figure B.6: 585RF, pavement temperatures at various depths.

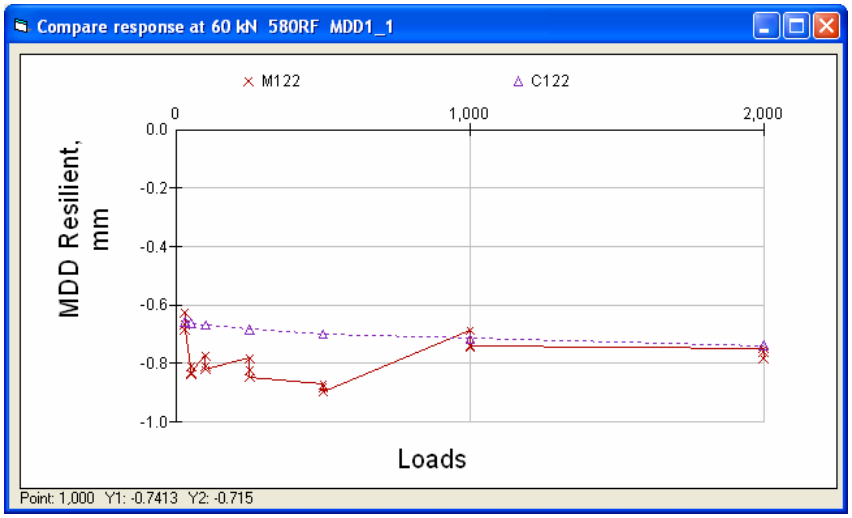

Figure B.7: 580RF, measured and calculated deflection of upper MDD.

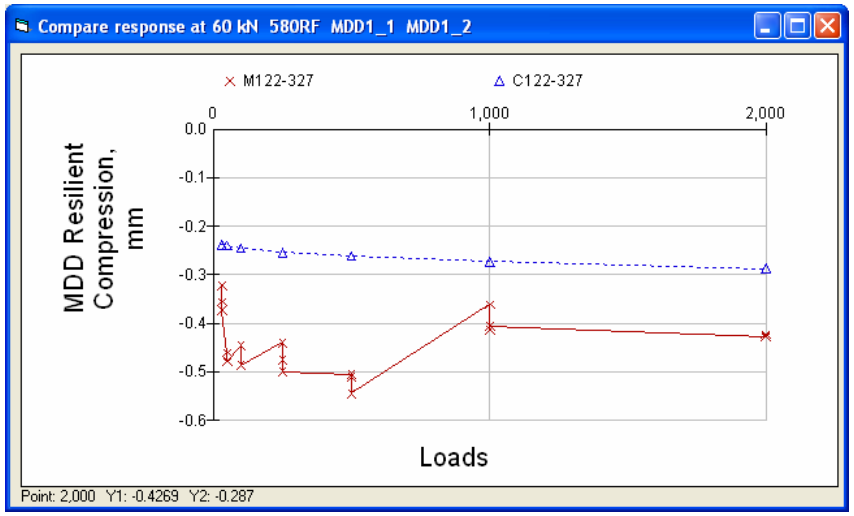

Figure B.8: 580RF, measured and calculated resilient compression of upper AB layers.

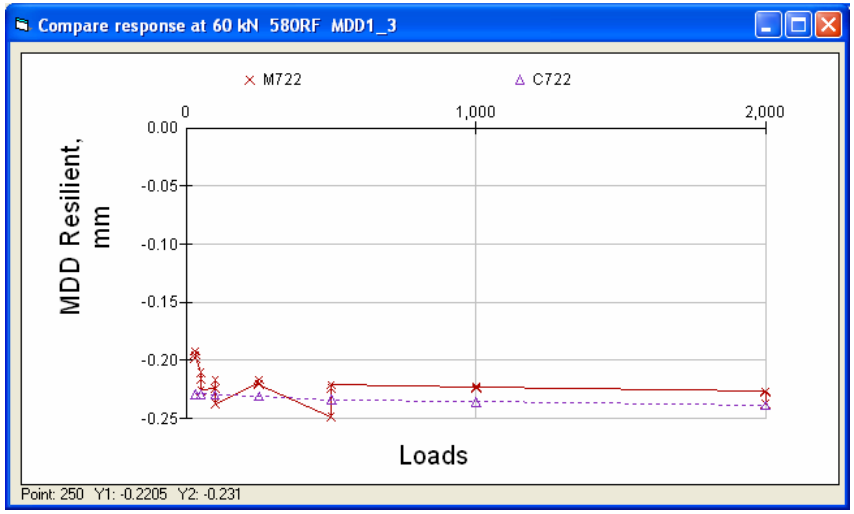

Figure B.9: 580RF, measured (MDD) and calculated deflection at lower subgrade.

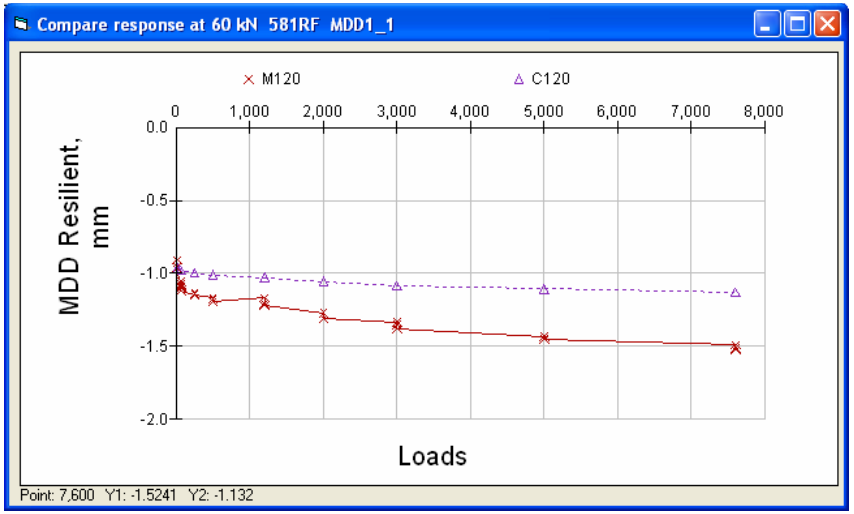

Figure B.10: 581RF, measured and calculated deflection at top MDD.

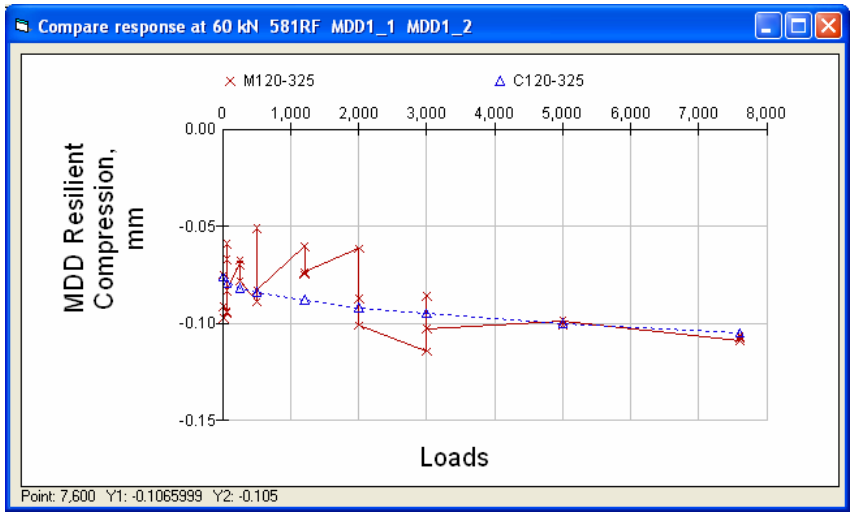

Figure B.11: 581RF, measured and calculated resilient compression of upper AB layers.

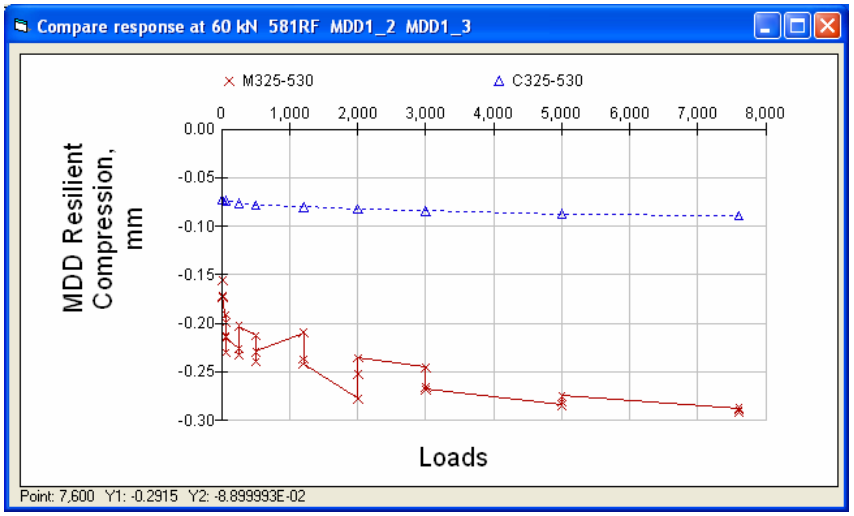

Figure B.12: 581RF, measured and calculated resilient compression of lower AB plus upper subgrade.

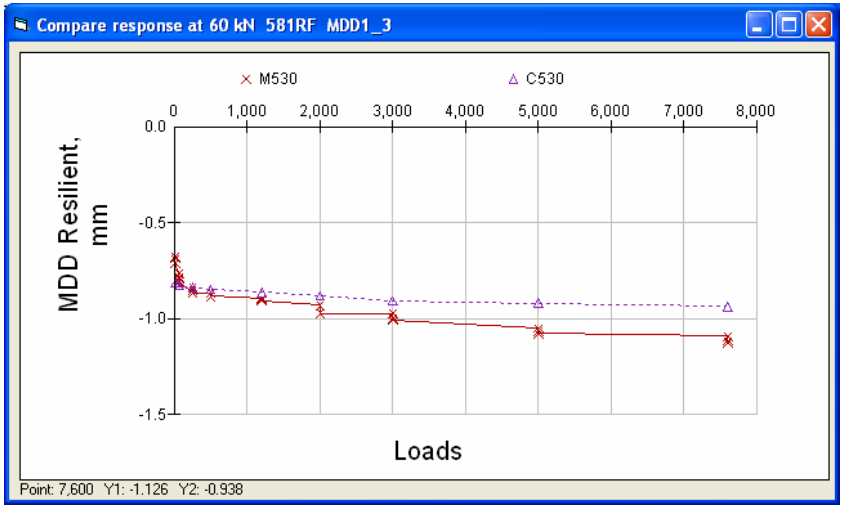

Figure B.13: 581RF, measured (MDD) and calculated deflection of subgrade.

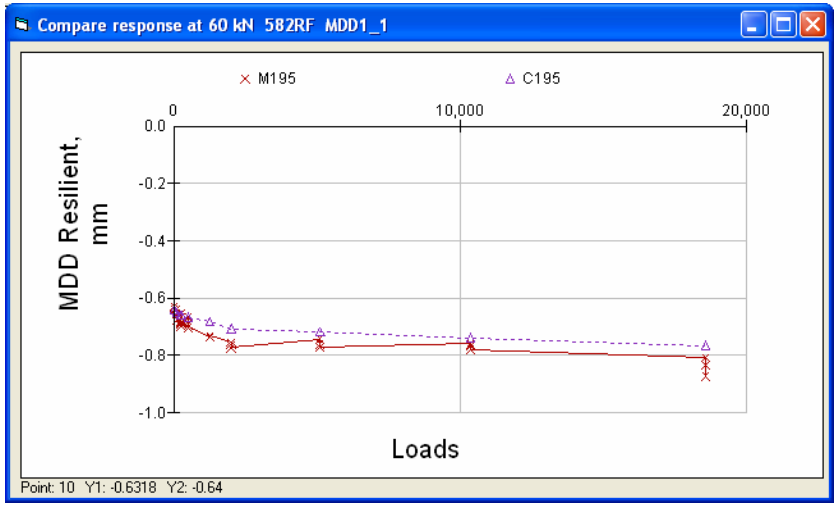

Figure B.14: 582RF, measured and calculated deflection at upper MDD.

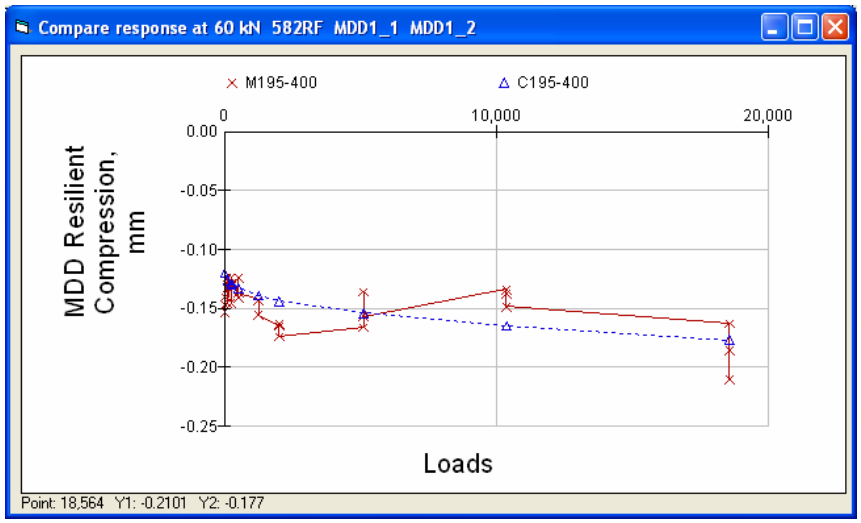

Figure B.15: 582RF, measured and calculated resilient compression of upper AB layers.

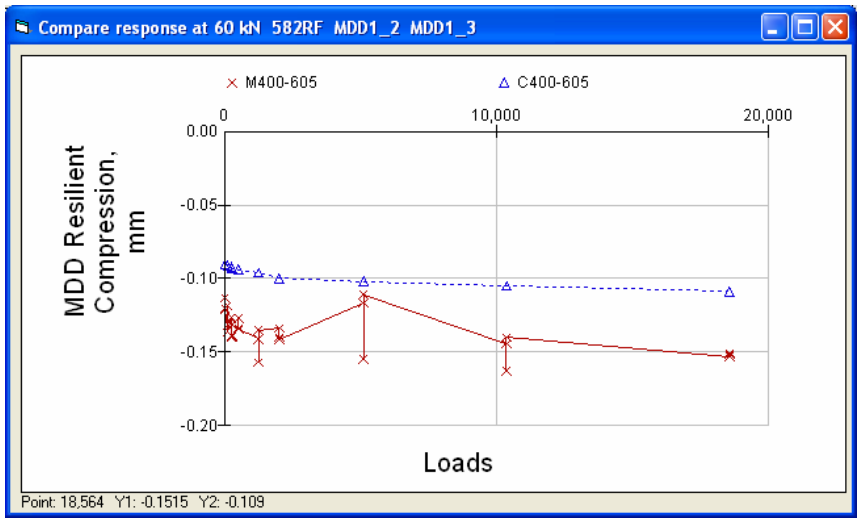

Figure B.16: 582RF, measured and calculated resilient compression of lower AB layers.

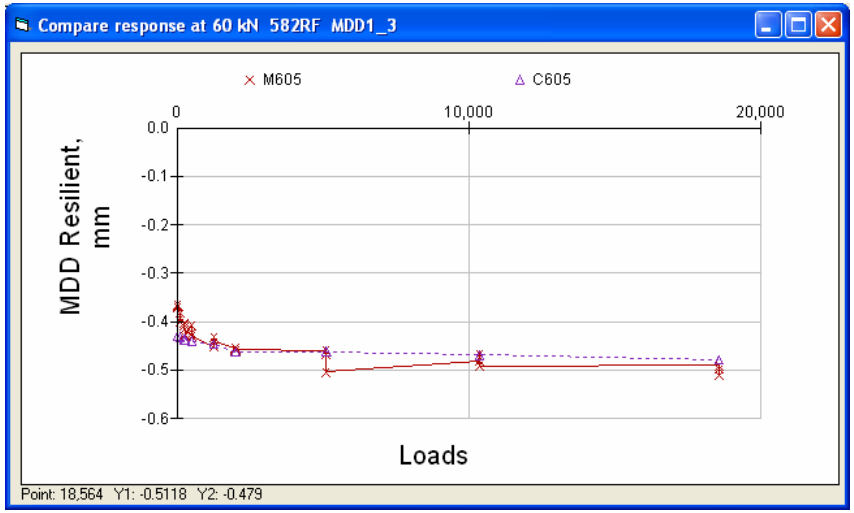

Figure B.17: 582RF, measured (MDD) and calculated deflection of subgrade.

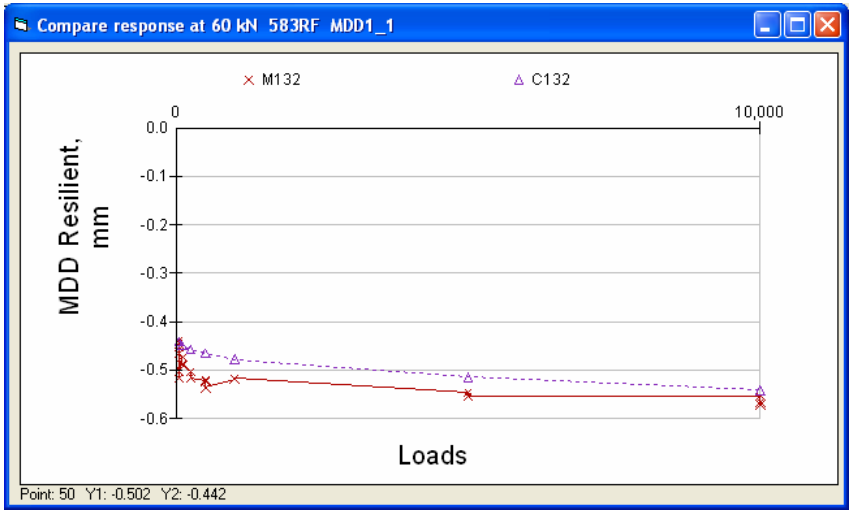

Figure B.18: 583RF, measured and calculated deflection at upper MDD.

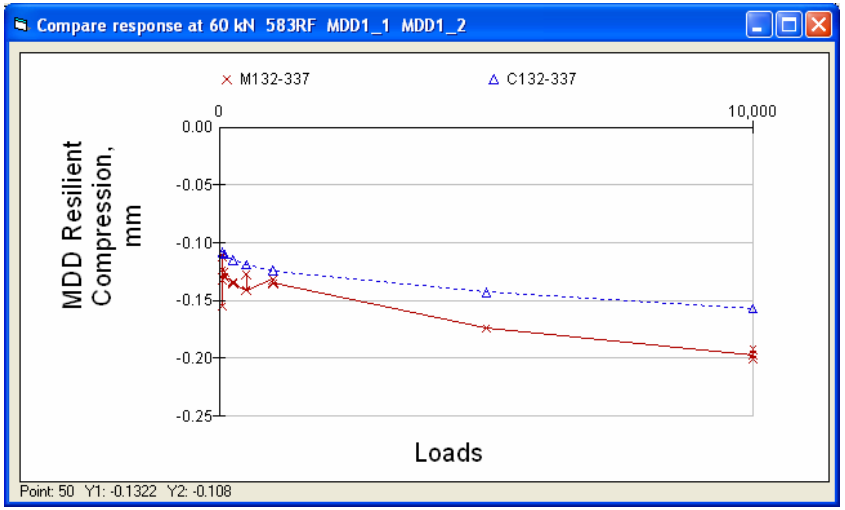

Figure B.19: 583RF, measured and calculated resilient compression of upper AB layers.

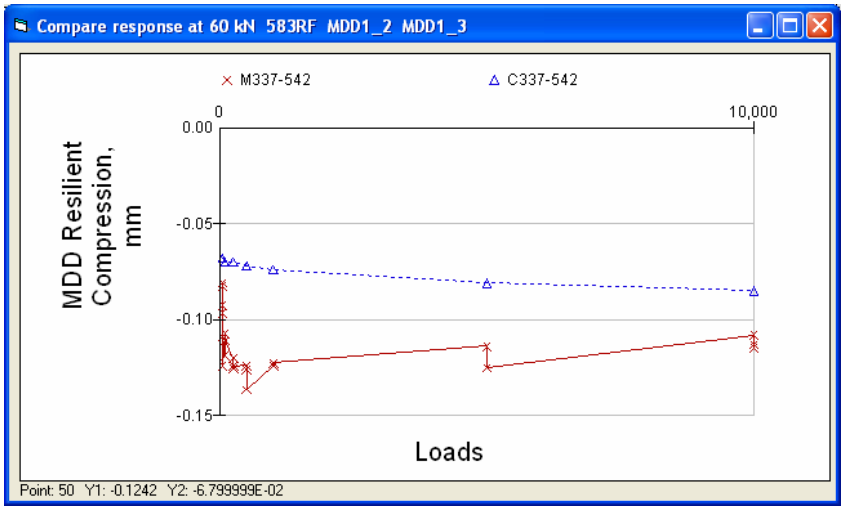

Figure B.20: 583RF, measured and calculated resilient compression of lower AB layers.

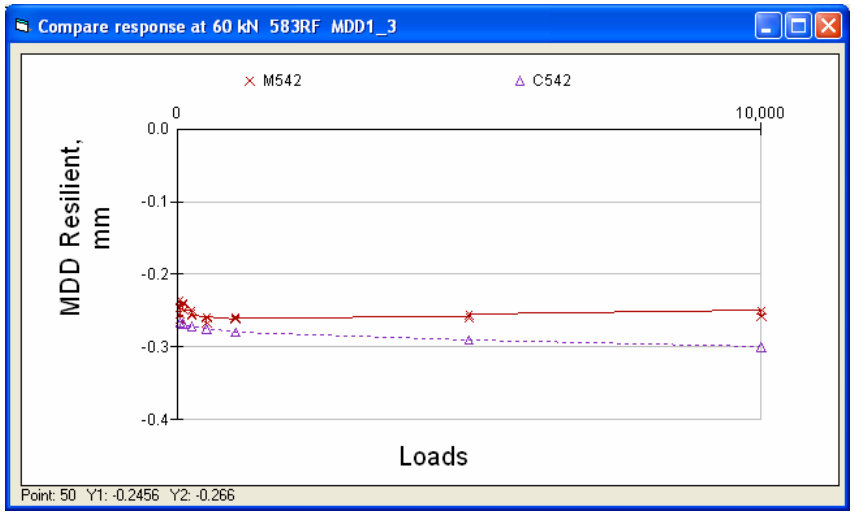

Figure B.21: 583RF, measured (MDD) and calculated deflection of subgrade.

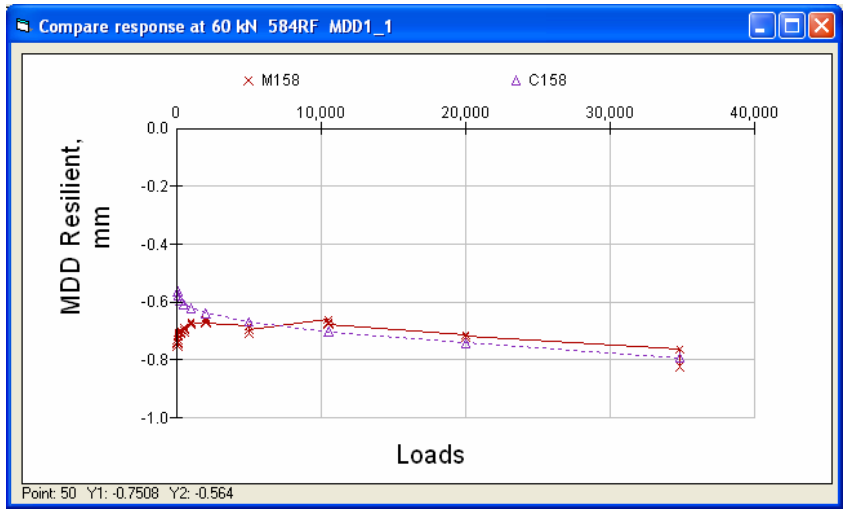

Figure B.22: 584RF, measured and calculated deflection at upper MDD.

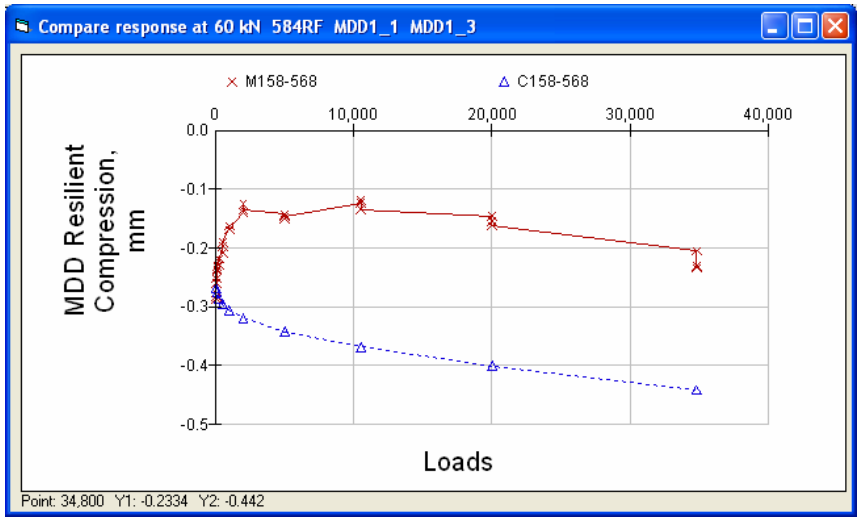

Figure B.23: 584RF, measured and calculated resilient compression of AB layers plus upper subgrade.

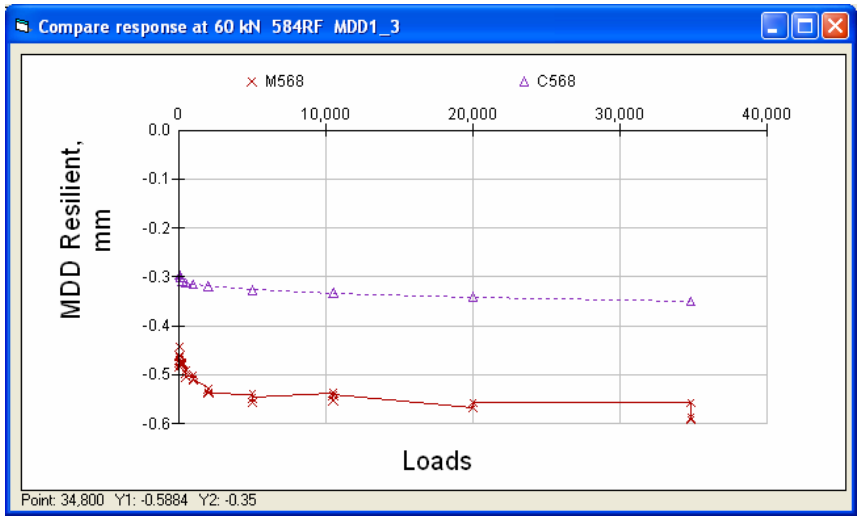

Figure B.24: 584RF, measured (MDD) and calculated deflection of subgrade.

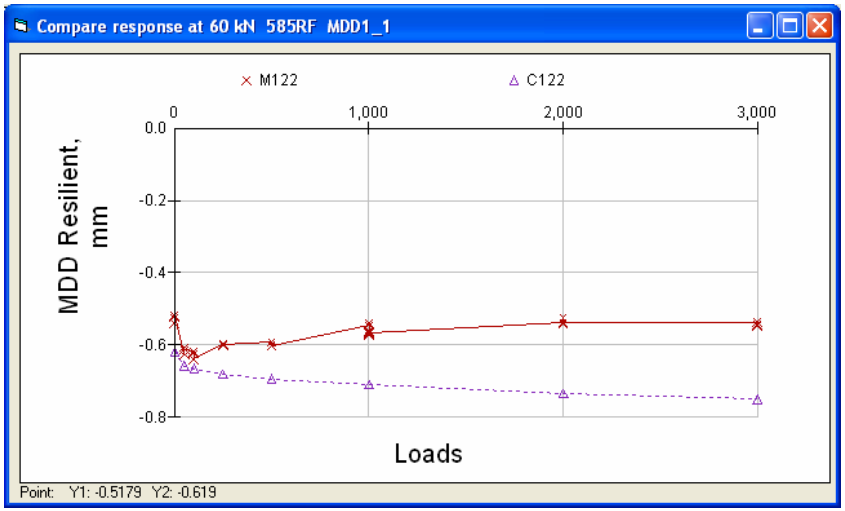

Figure B.25: 585RF, measured and calculated deflection at upper MDD.

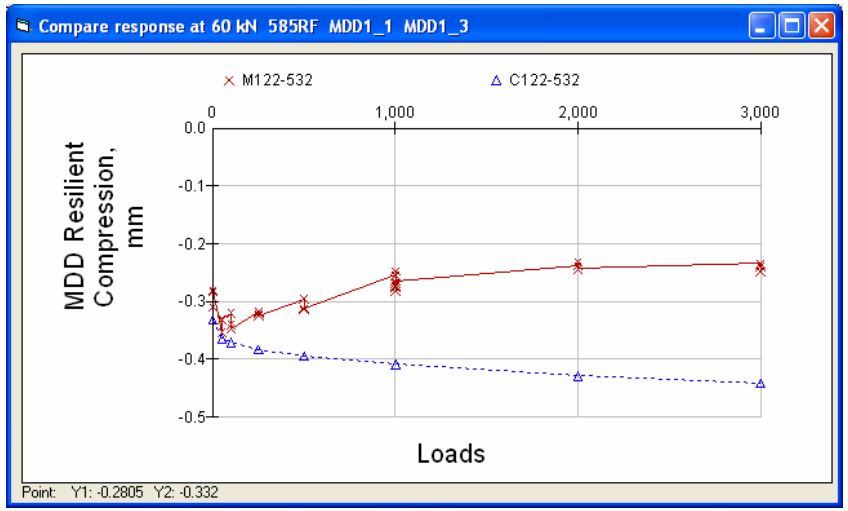

Figure B.26: 585RF, measured and calculated resilient compression of AB layers plus upper subgrade.

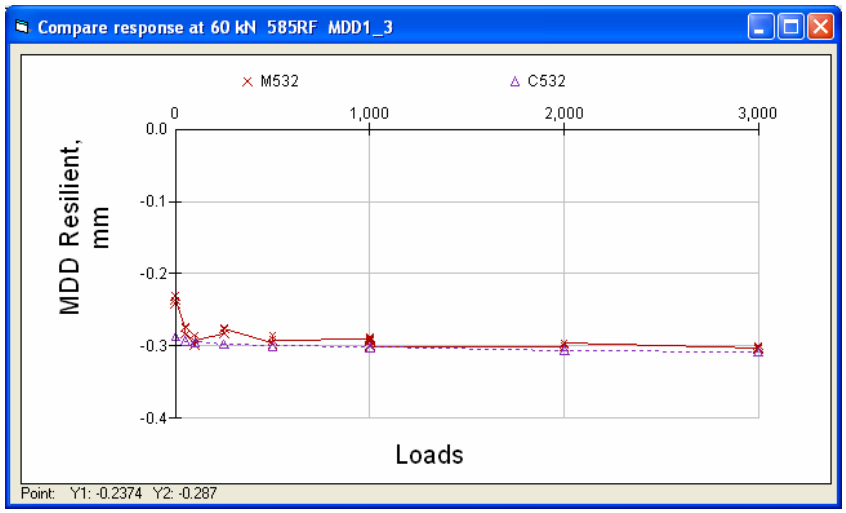

Figure B.27: 585RF, measured (MDD) and calculated deflection of subgrade.

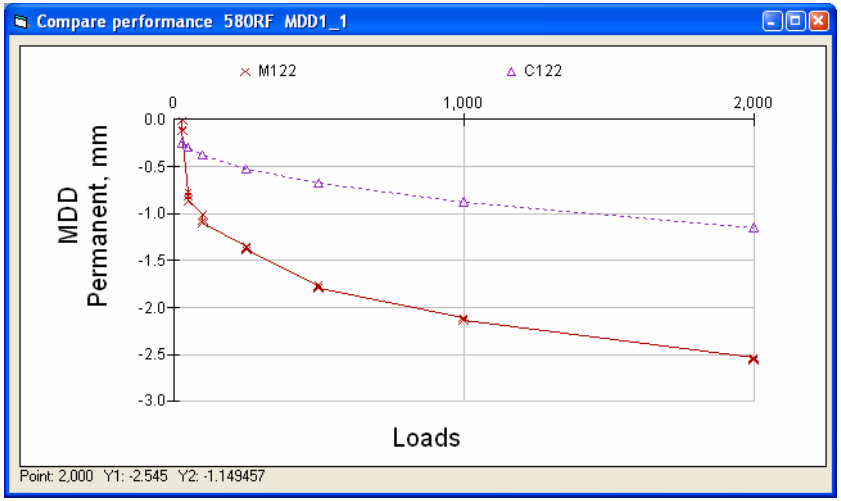

Figure B.28: 580RF, measured and calculated permanent deformation of upper MDD.

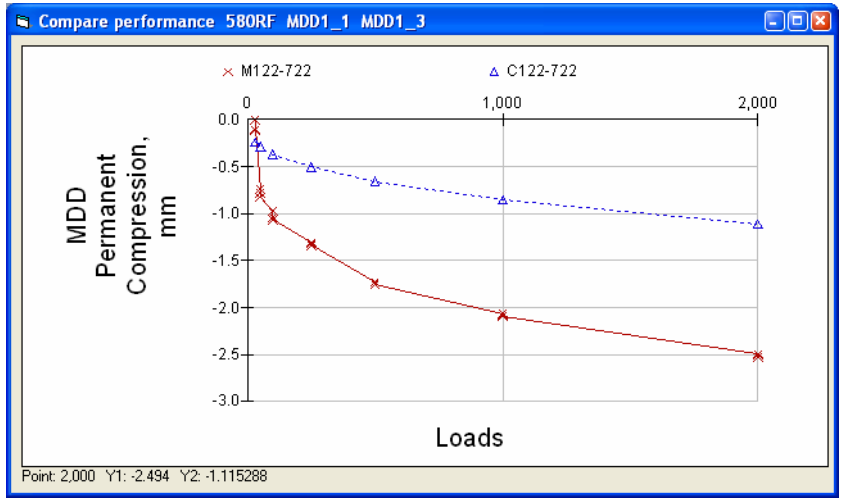

Figure B.29: 580RF, measured and calculated permanent compression of AB layers.

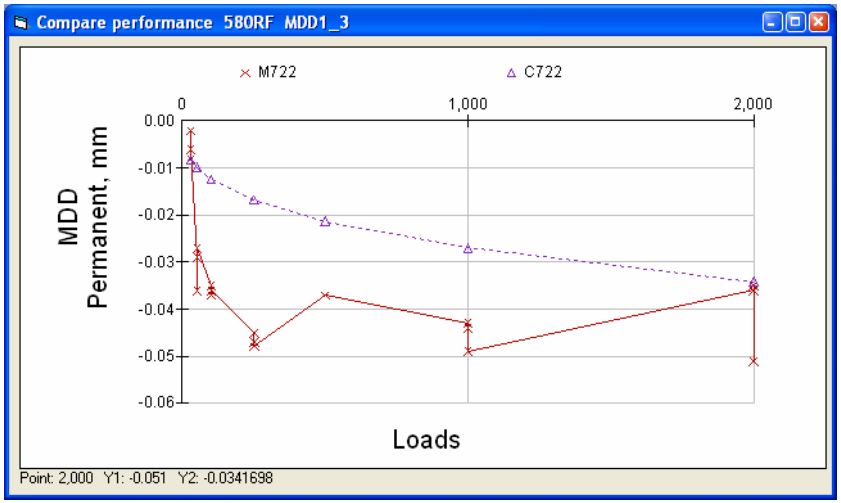

Figure B.30: 580RF, measured and calculated permanent deformation in subgrade.

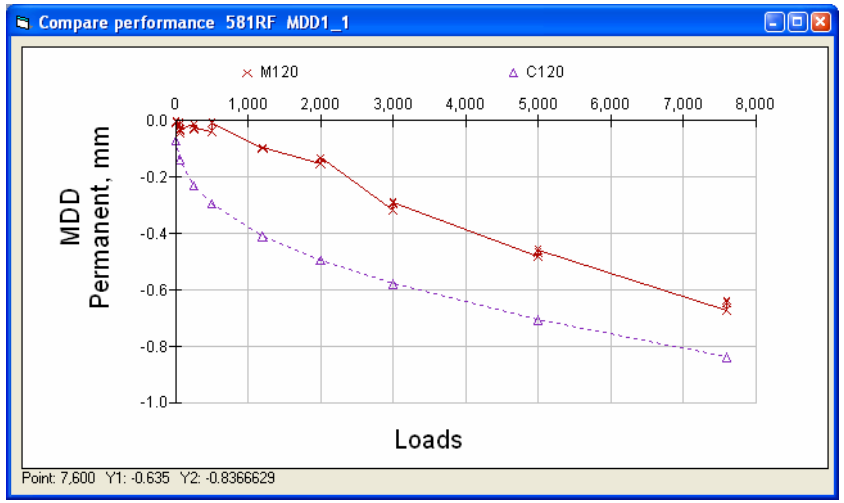

Figure B.31: 581RF, measured and calculated permanent deformation at upper MDD.

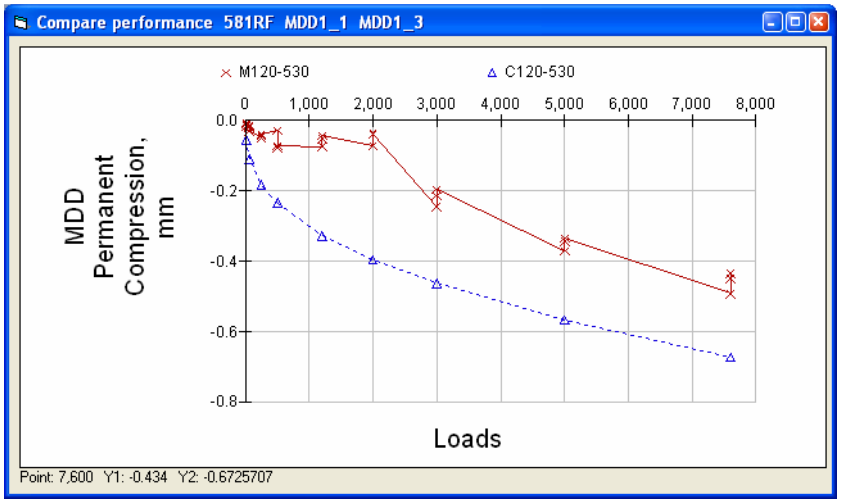

Figure B.32: 581RF, measured and calculated permanent compression of AB layers.

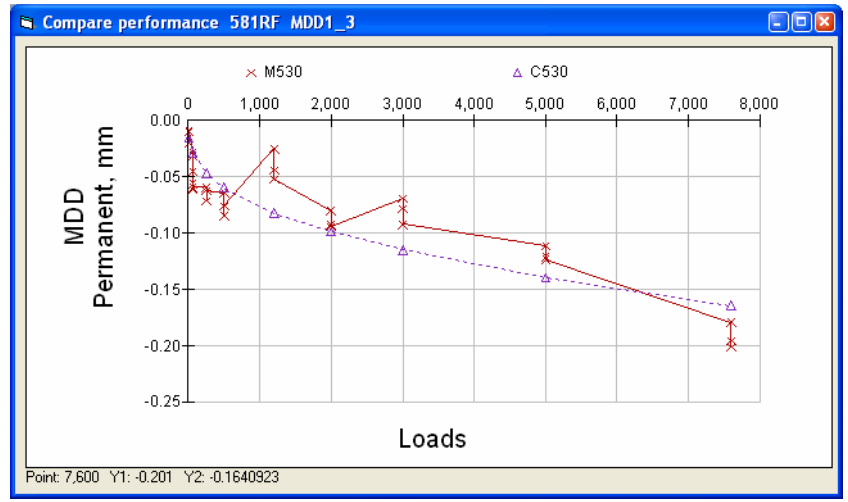

Figure B.33: 581RF, measured and calculated permanent deformation of subgrade.

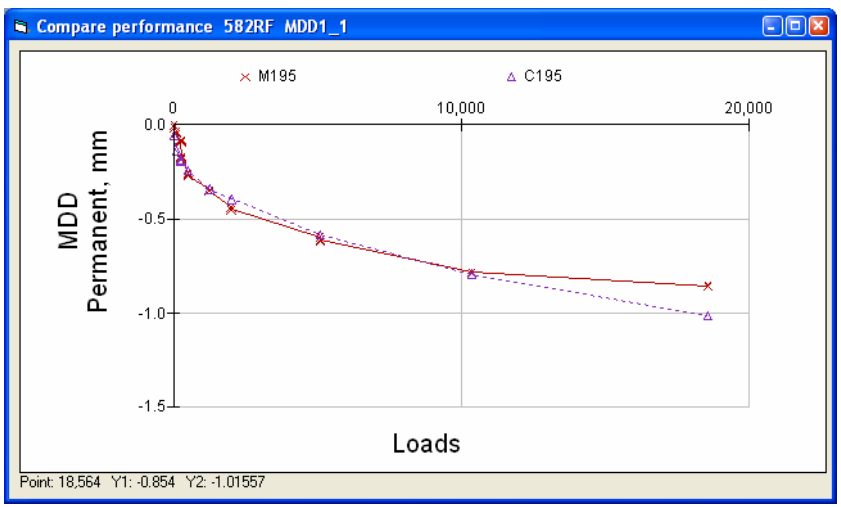

Figure B.34: 582RF, measured and calculated permanent deformation at upper MDD.

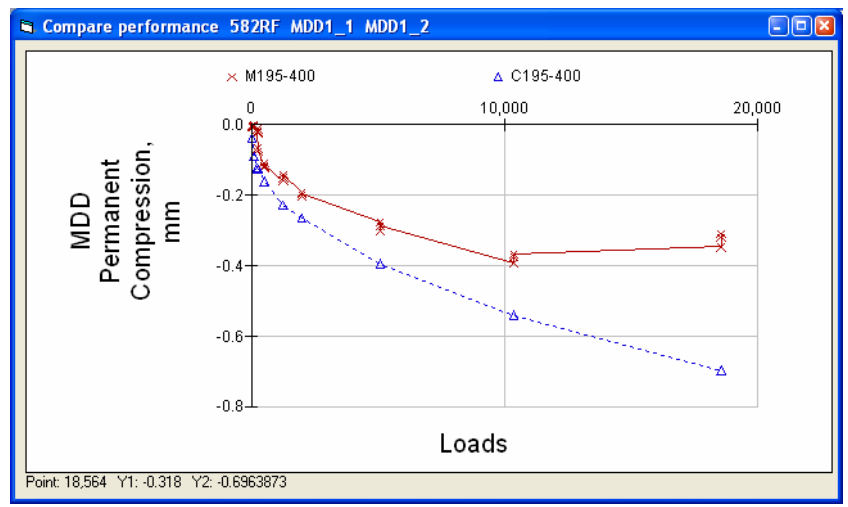

Figure B.35: 582RF, measured and calculated permanent compression of AB layers.

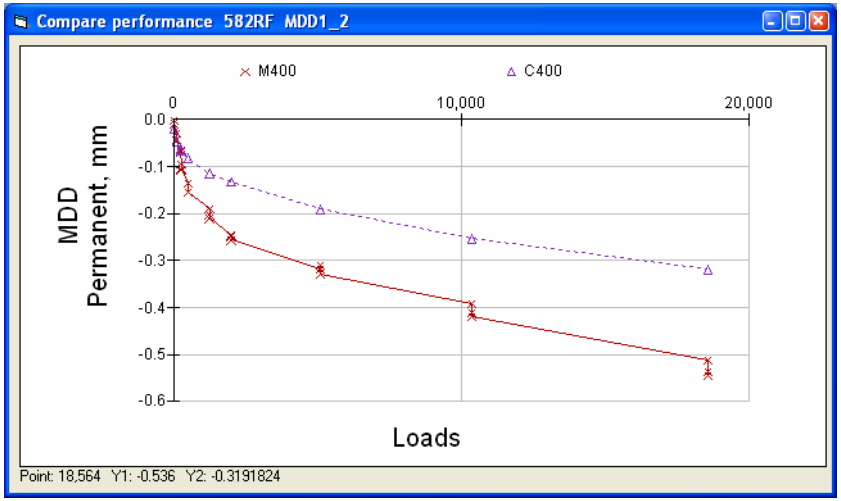

Figure B.36: 582RF, measured and calculated permanent deformation at subgrade.

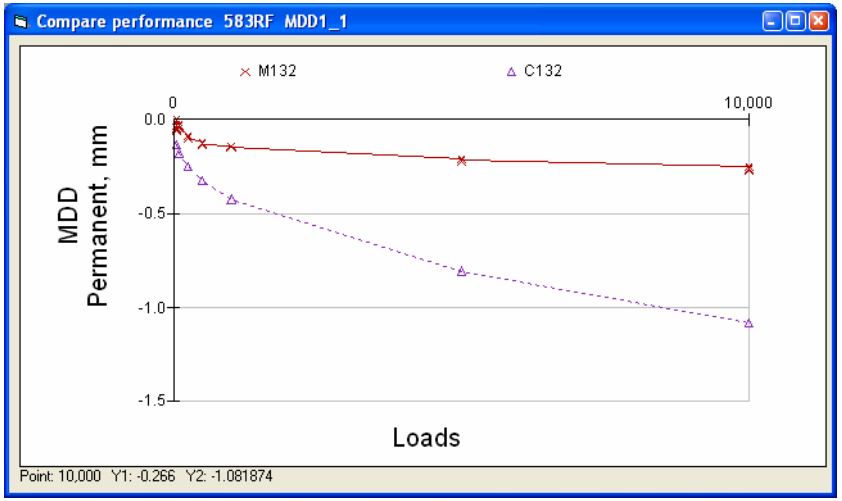

Figure B.37: 583RF, measured and calculated permanent deformation at upper MDD.

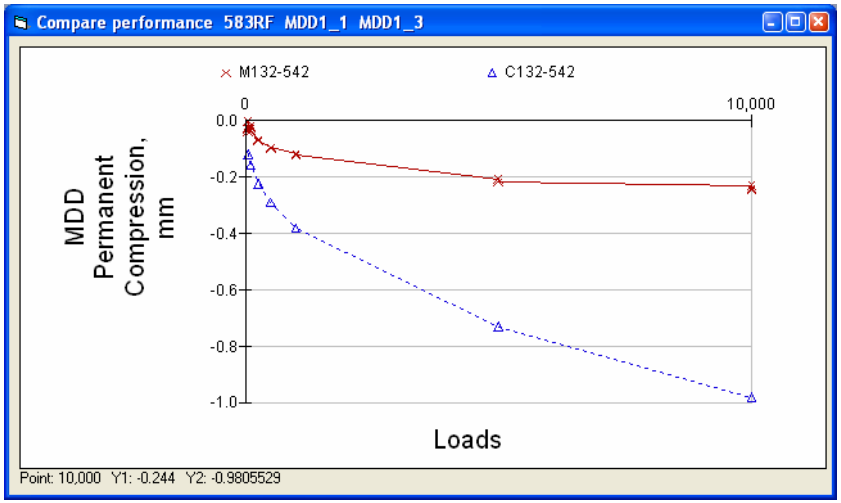

Figure B.38: 583RF, measured and calculated permanent deformation of AB layers.

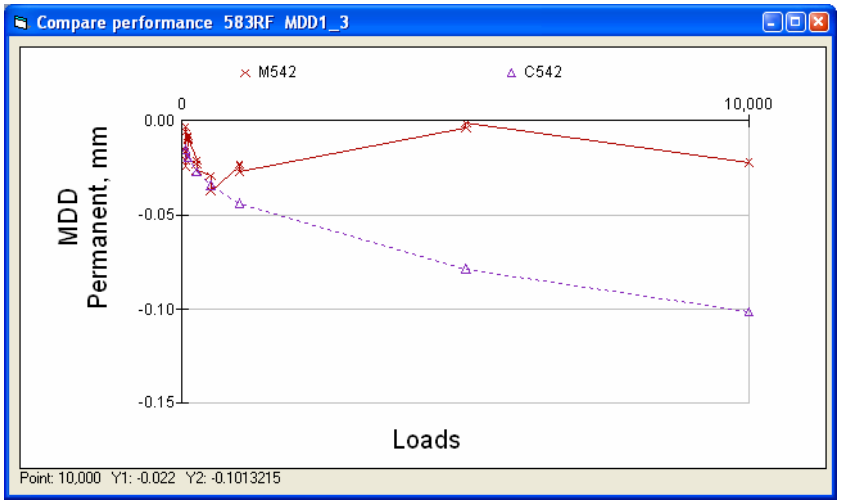

Figure B.39: 583RF, measured and calculated permanent deformation of subgrade.

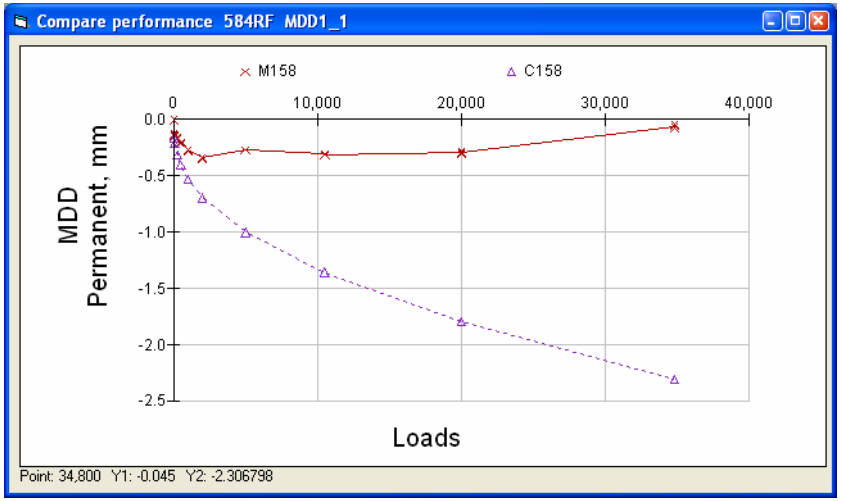

Figure B.40: 584RF, measured and calculated permanent deformation at upper MDD.

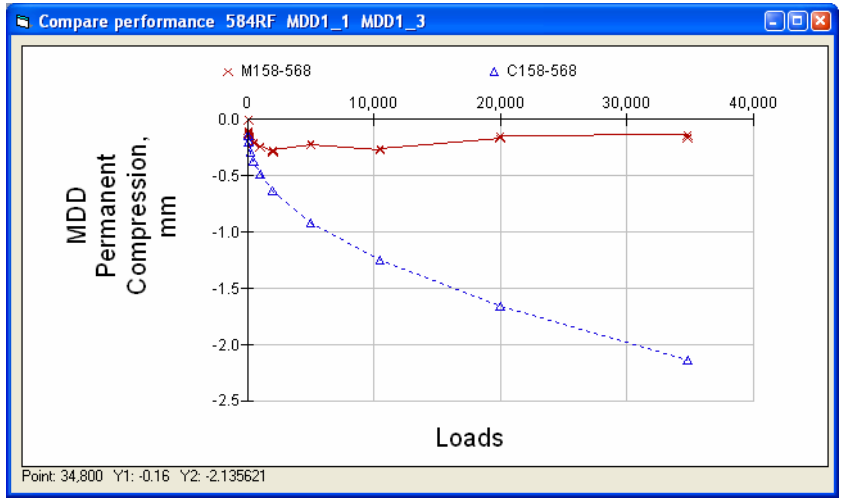

Figure B.41: 584RF, measured and calculated permanent deformation of AB layers.

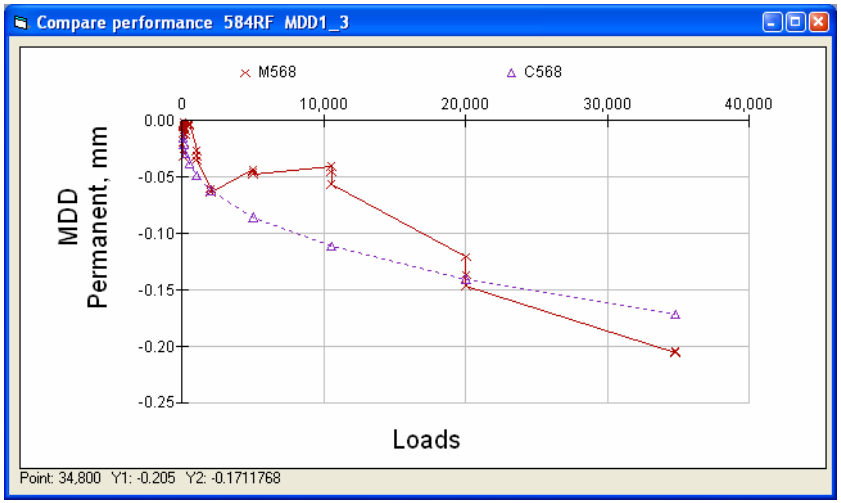

Figure B.42: 584RF, measured and calculated permanent deformation at subgrade.

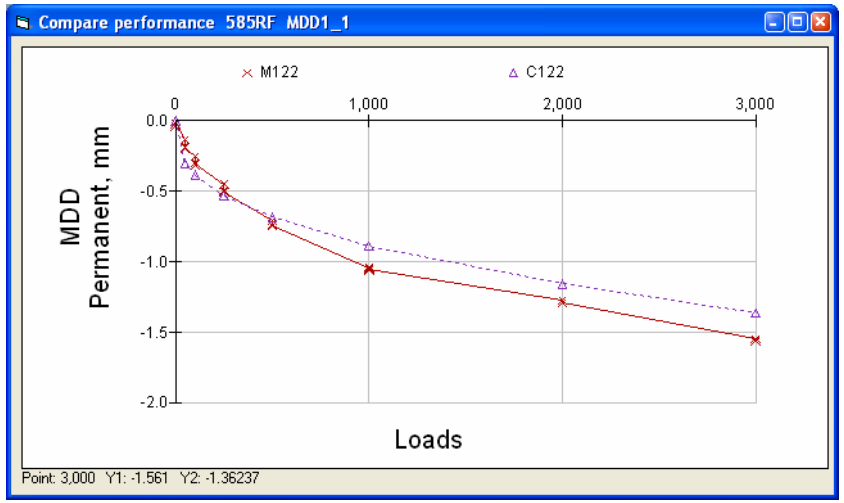

Figure B.43: 585RF, measured and calculated permanent deformation at top MDD.

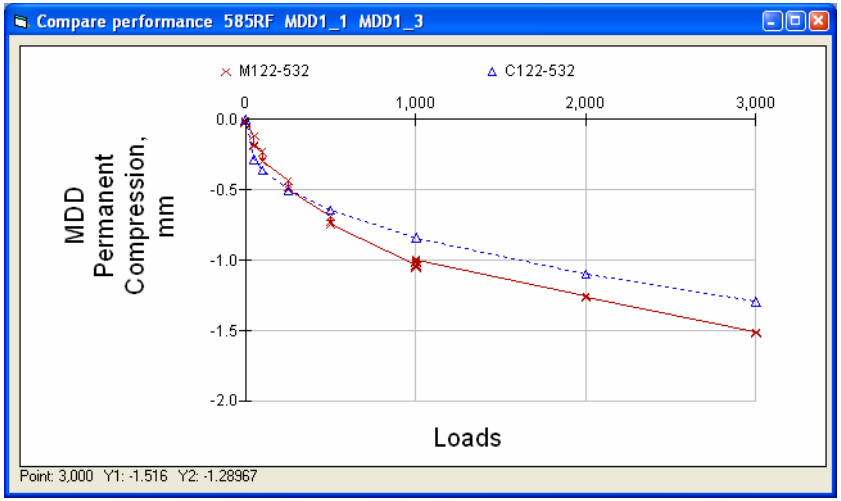

Figure B.44: 585RF, measured and calculated permanent compression of AB layers.

Figure B.45: 585RF, measured and calculated permanent deformation at subgrade.

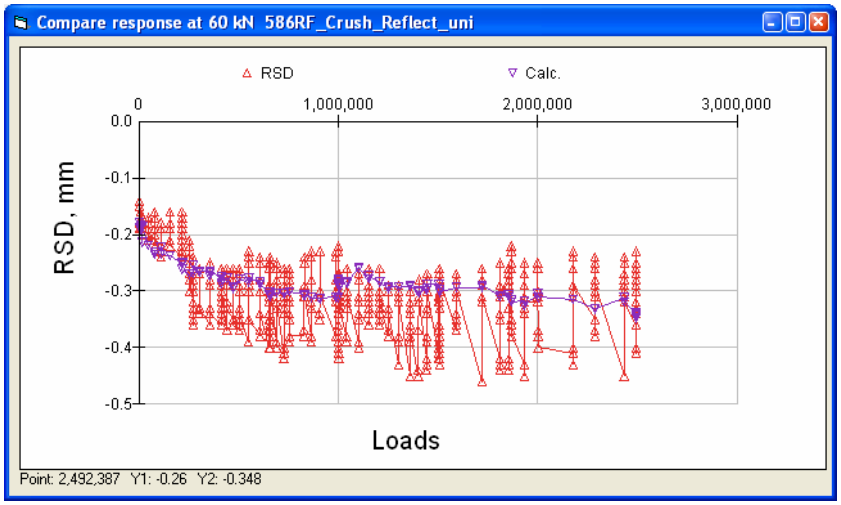

Figure B.46: 586RF, measured (RSD) and calculated surface deflection.

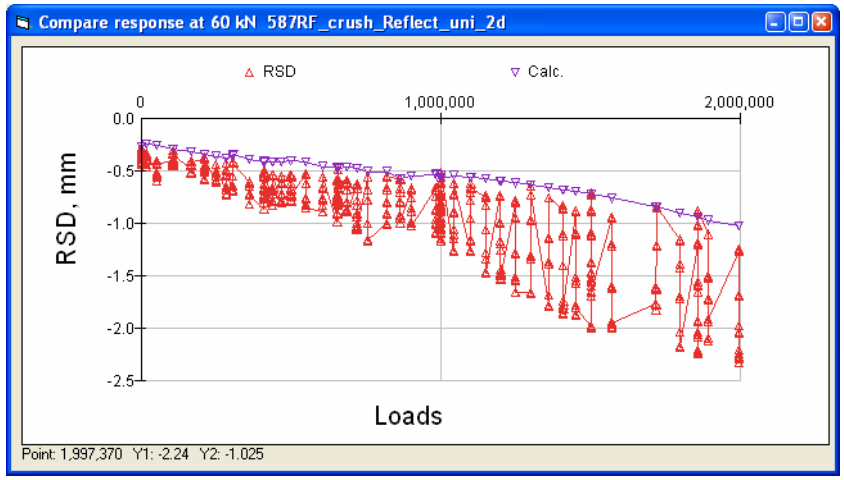

Figure B.47: 587RF, measured (RSD) and calculated surface deflection.

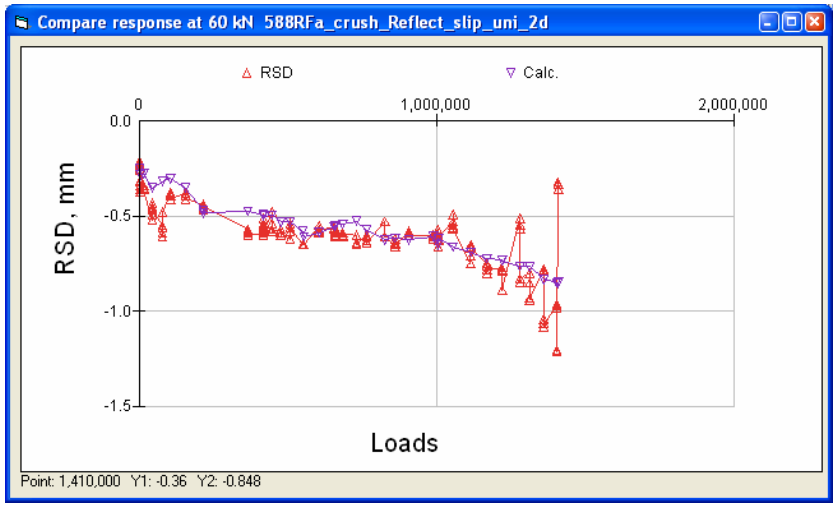

Figure B.48: 588RFa, measured (RSD) and calculated surface deflection.

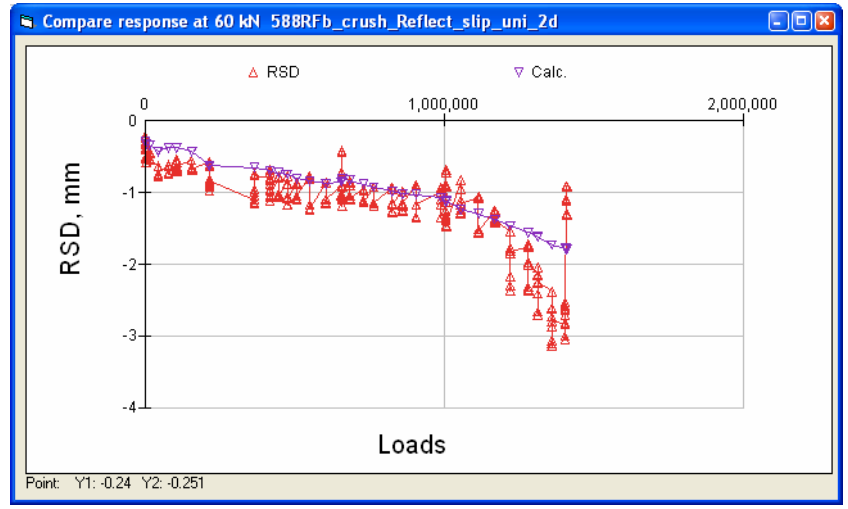

Figure B.49: 588RFb, measured (RSD) and calculated surface deflection.

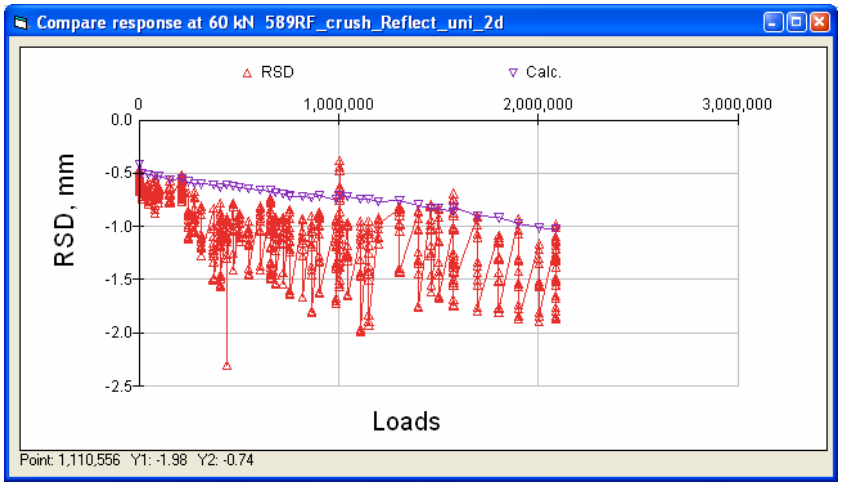

Figure B.50: 589RF, measured (RSD) and calculated surface deflection.

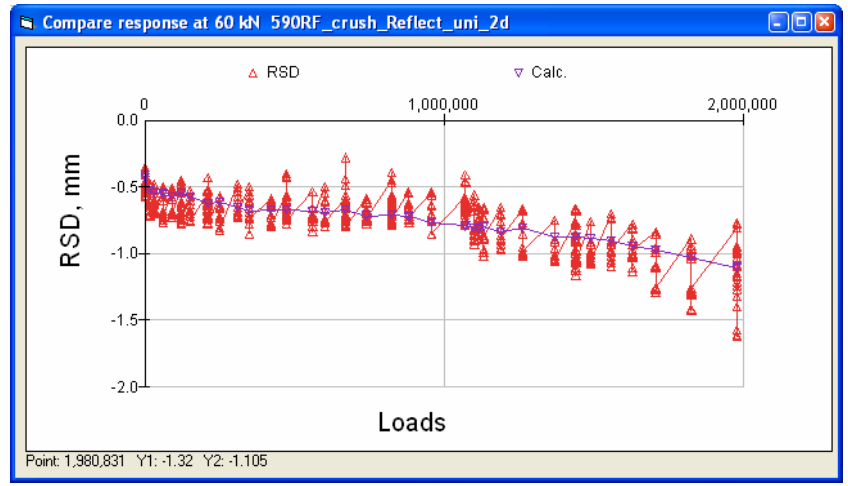

Figure B.51: 590RF, measured (RSD) and calculated surface deflection.

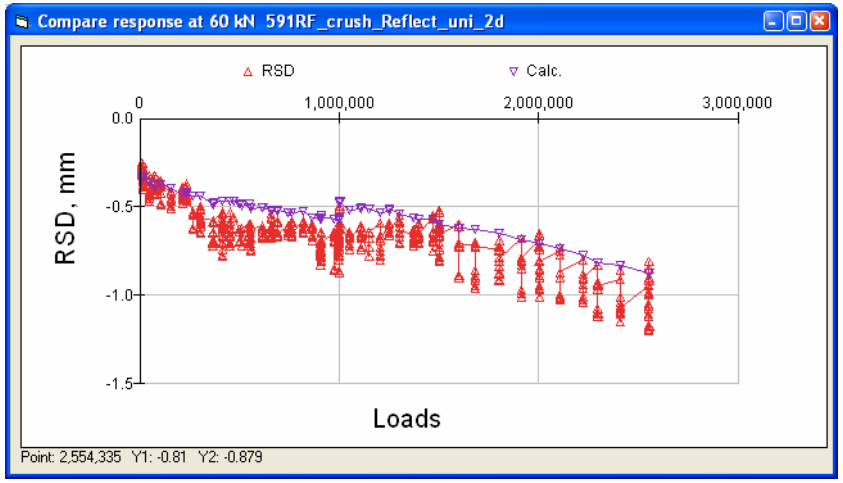

Figure B.52: 591RF, measured (RSD) and calculated surface deflection.

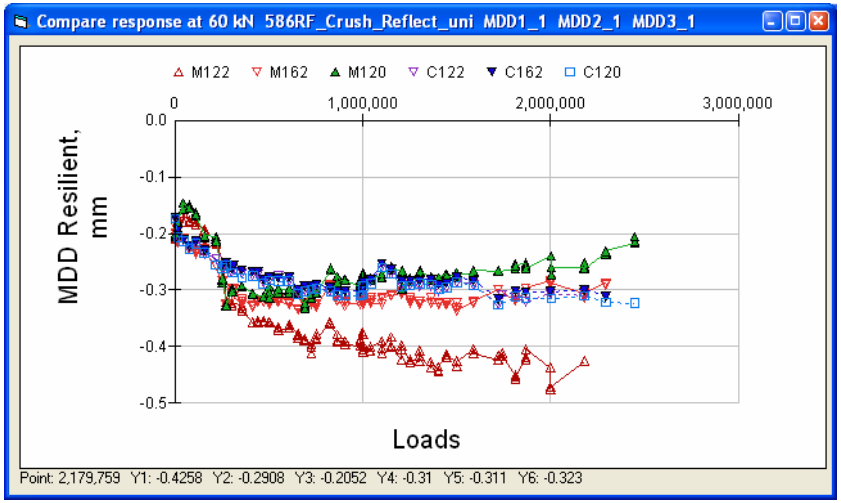

Figure B.53: 586RF, measured and calculated deflection of top MDD.

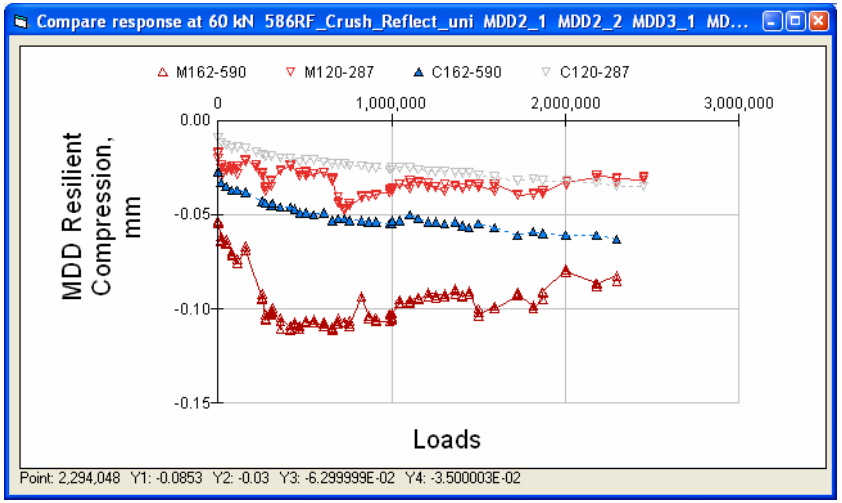

Figure B.54: 586RF, measured (MDD) and calculated resilient compression of AB layers.

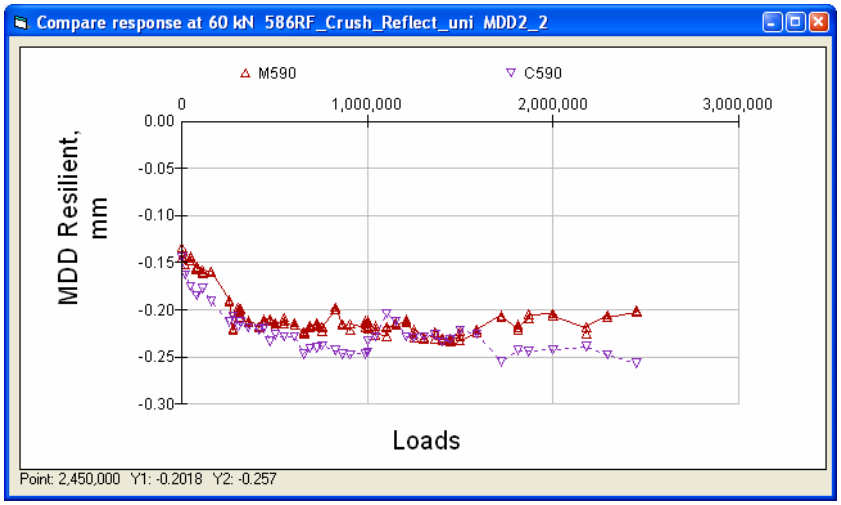

Figure B.55: 586RF, measured (MDD) and calculated deflection at top of subgrade.

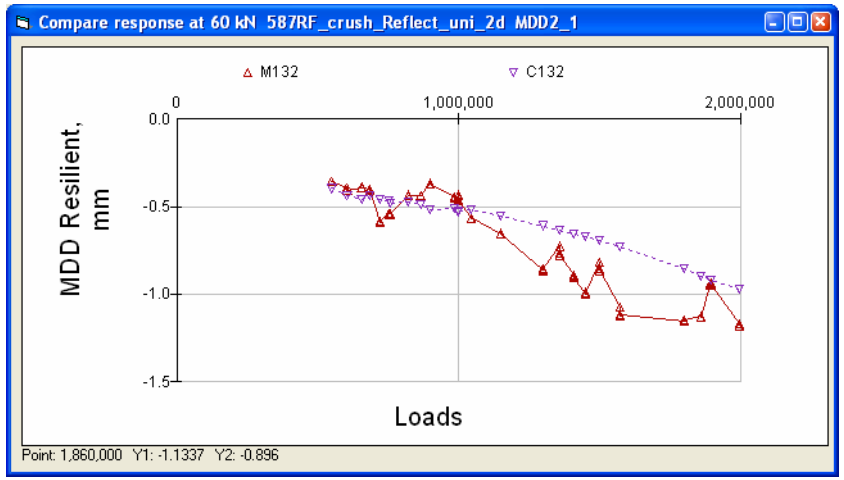

Figure B.56: 587RF, measured and calculated deflection at top MDD.

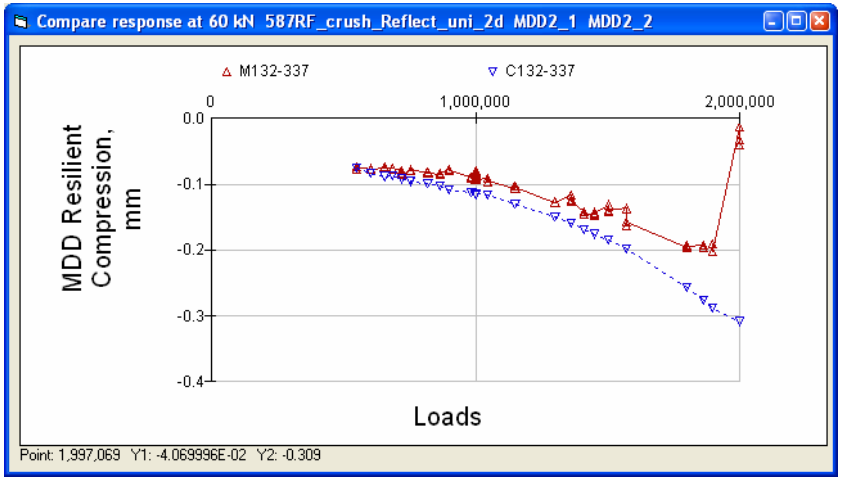

Figure B.57: 587RF, measured (MDD) and calculated resilient compression of upper AB layers.

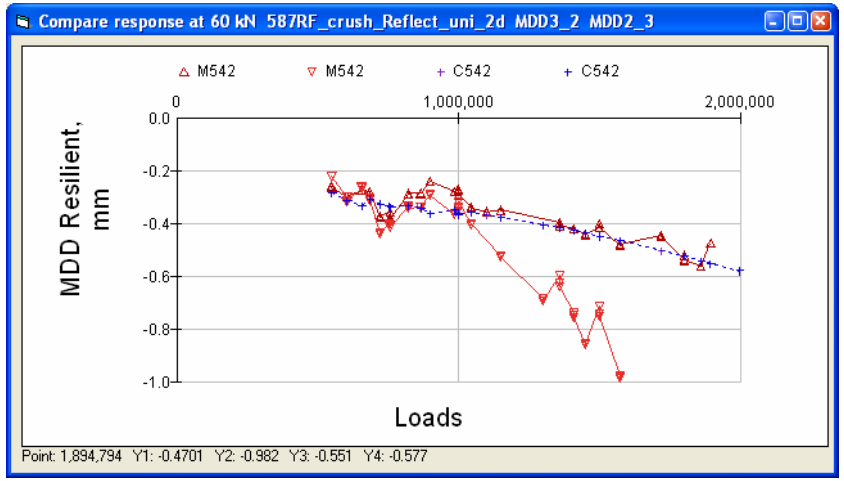

Figure B.58: 587RF, measured (MDD) and calculated deflection of subgrade.

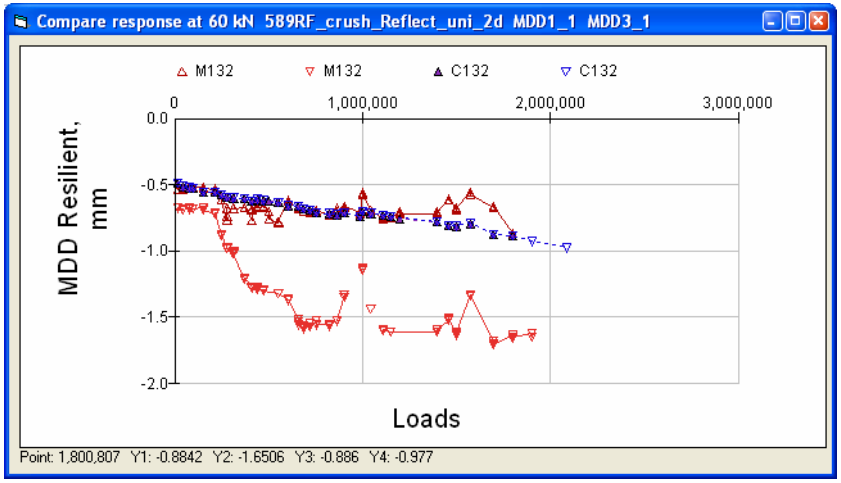

Figure B.59: 589RF, measured and calculated deflection of top MDDs.

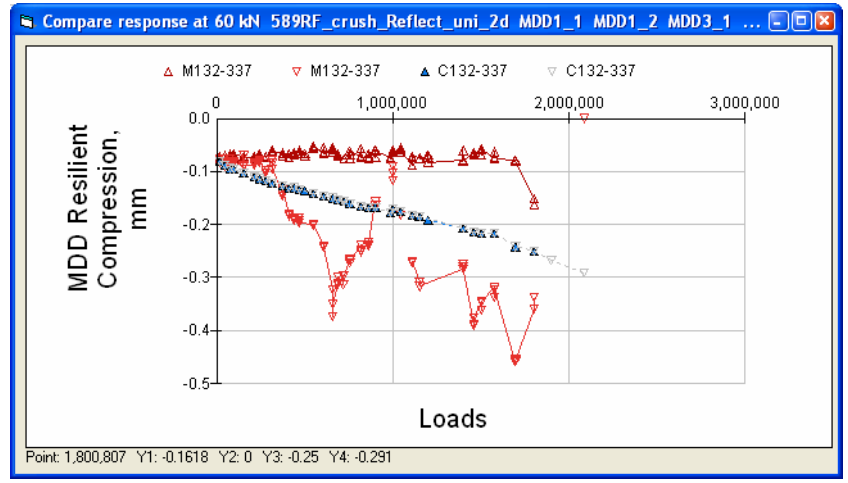

Figure B.60: 589RF, measured (MDD) and calculated resilient compression of the upper AB layers.

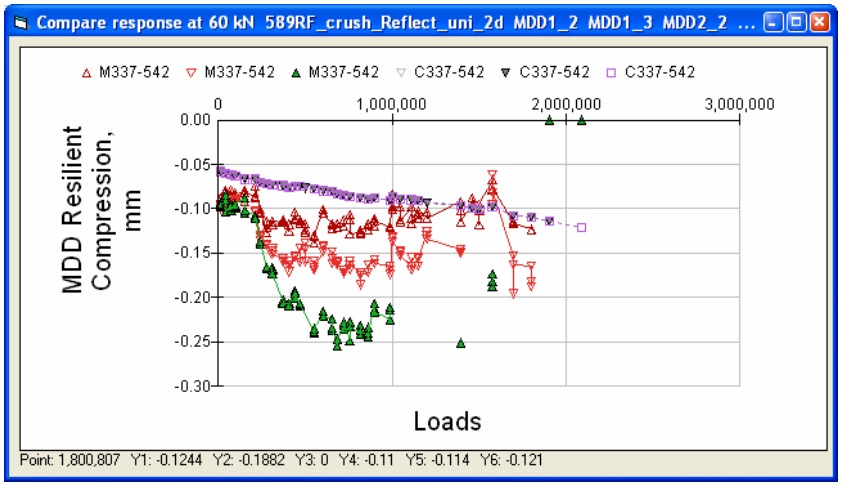

Figure B.61: 589RF, measured (MDD) and calculated resilient compression of the lower AB layers.

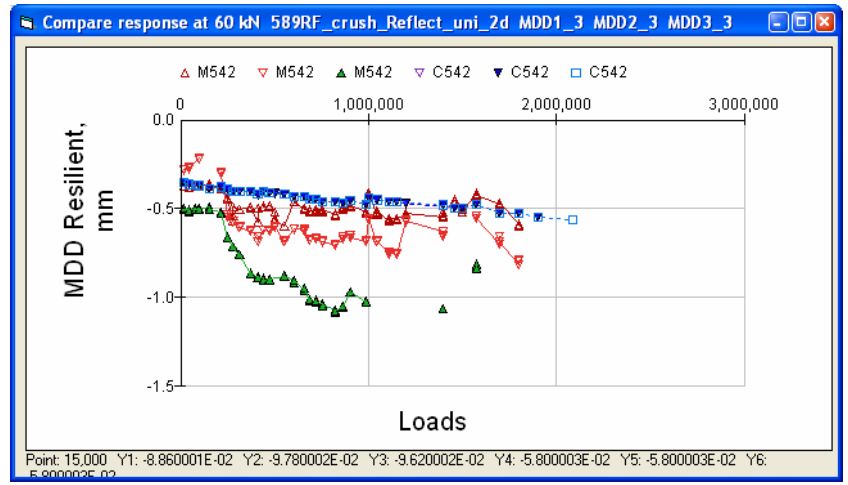

Figure B.62: 589RF, measured (MDD) and calculated deflection near top of subgrade.

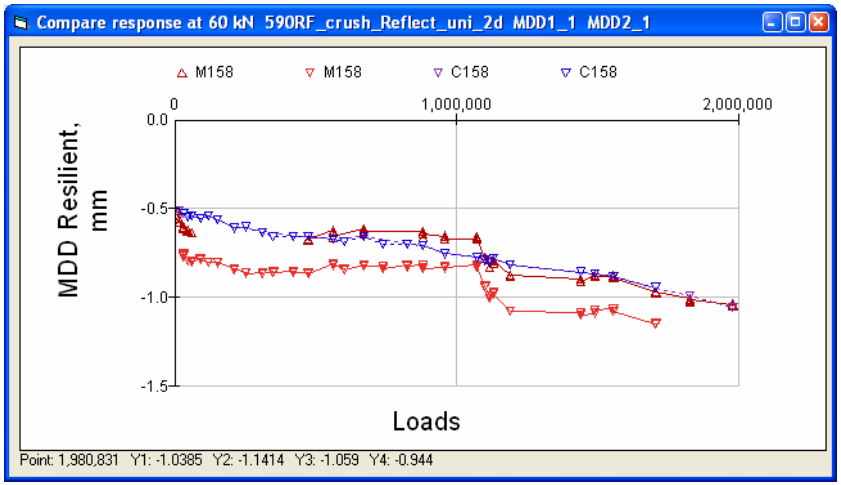

Figure B.63: 590RF, measured and calculated deflection of top MDD.

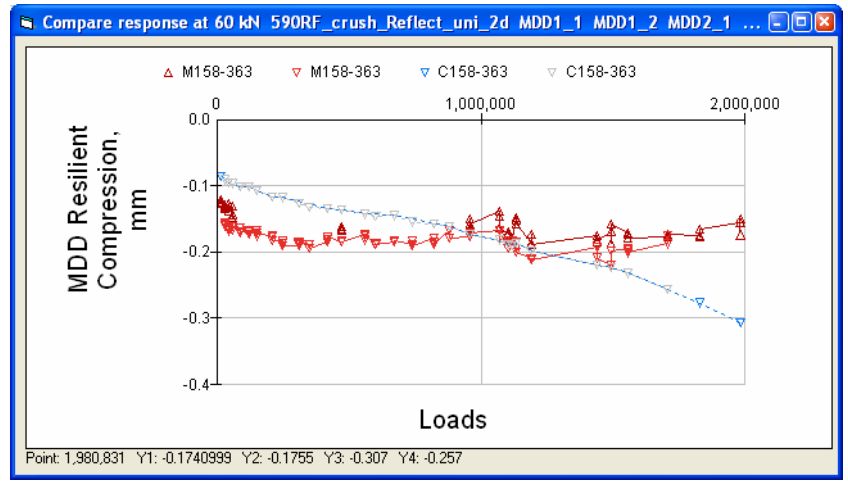

Figure B.64: 590RF, measured (MDD) and calculated resilient compression of upper AB layers.

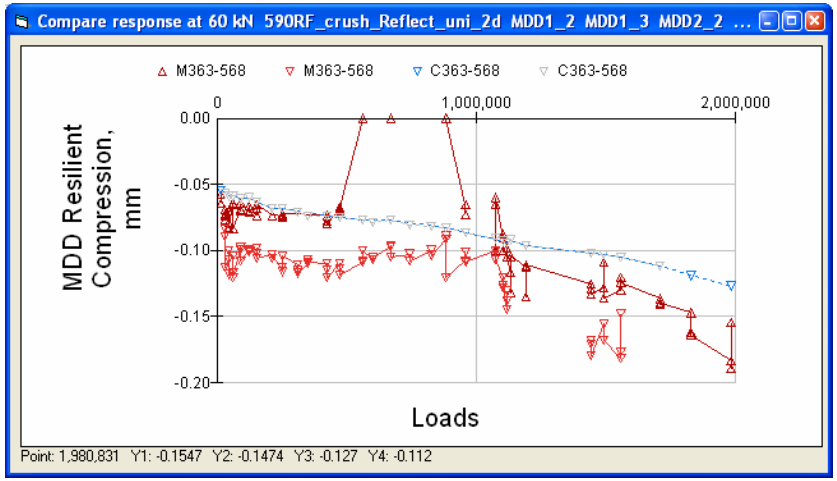

Figure B.65: 590RF, measured (MDD) and calculated resilient compression of lower AB layers.

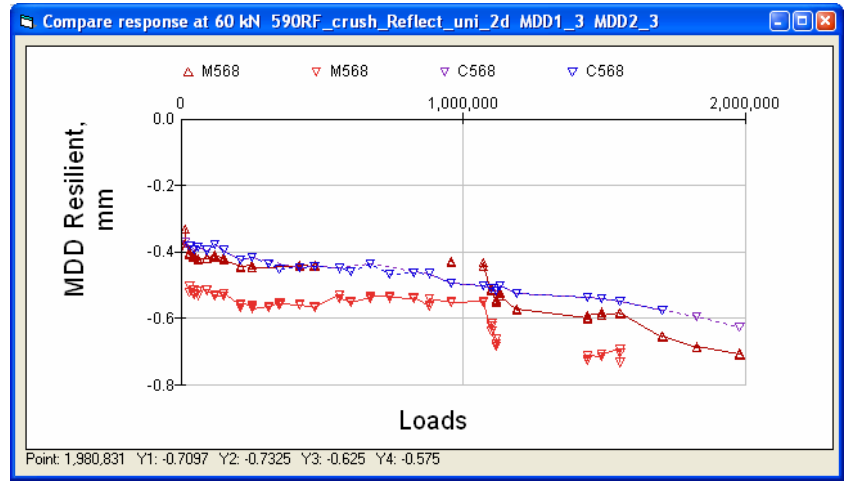

Figure B.66: 590RF, measured (MDD) and calculated deflection of subgrade.

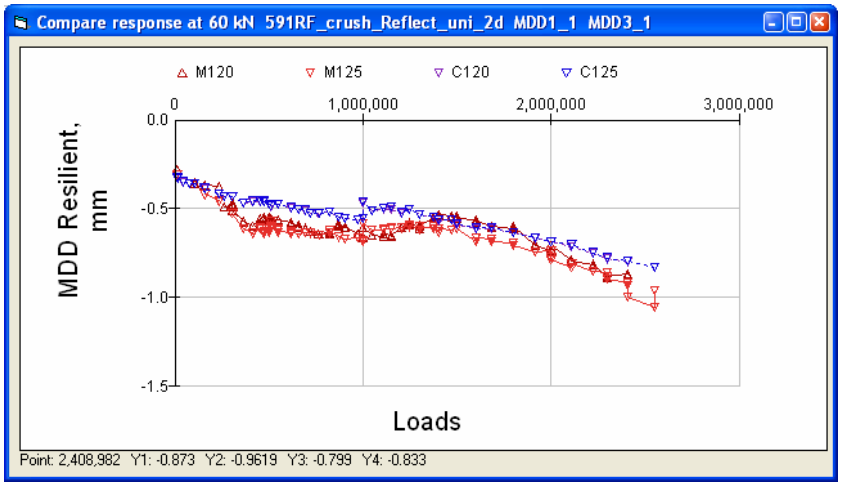

Figure B.67: 591RF, measured and calculated deflection of top MDD.

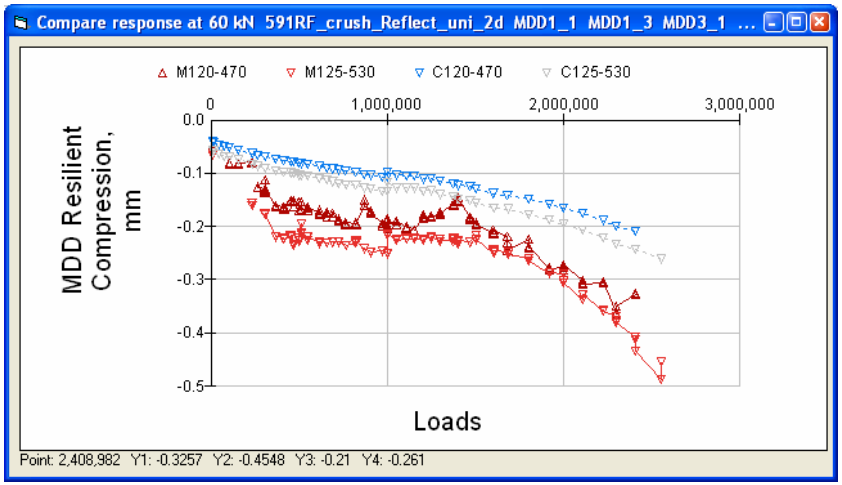

Figure B.68: 591RF, measured (MDD) and calculated resilient compression of AB layers.

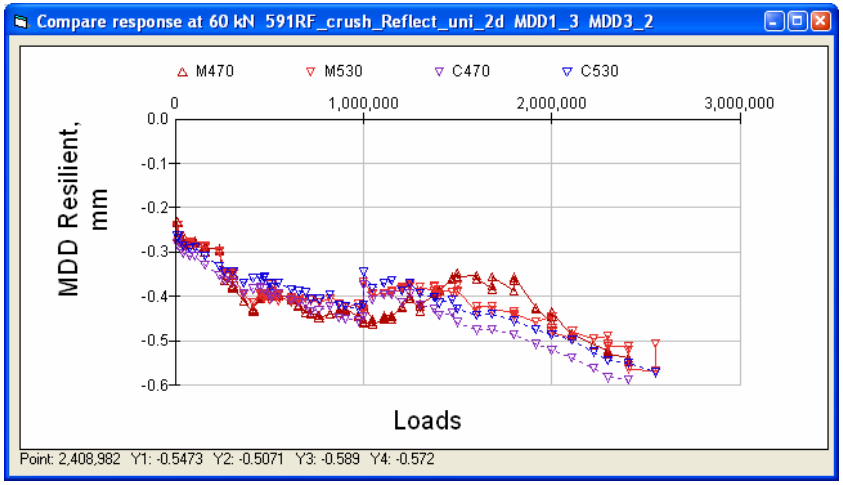

Figure B.69: 591RF, measured (MDD) and calculated deflection of subgrade.

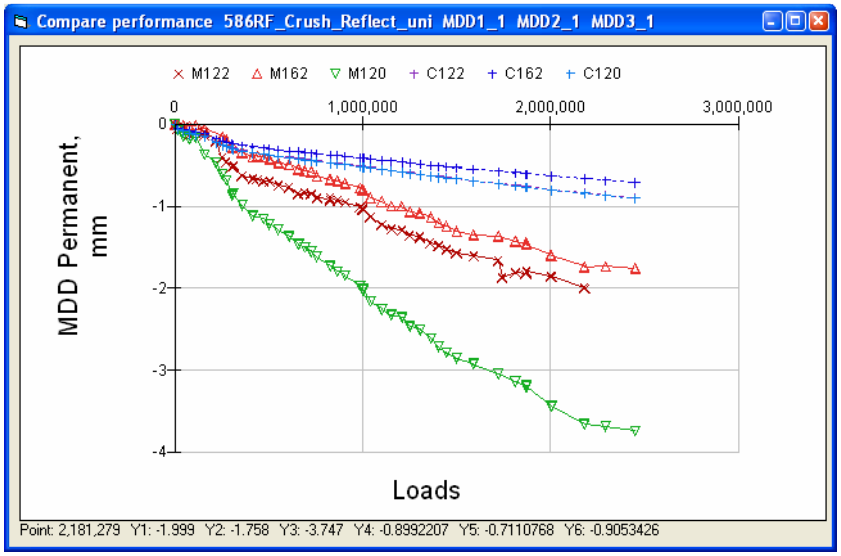

Figure B.70: 586RF, measured and calculated permanent deformation at top MDDs.

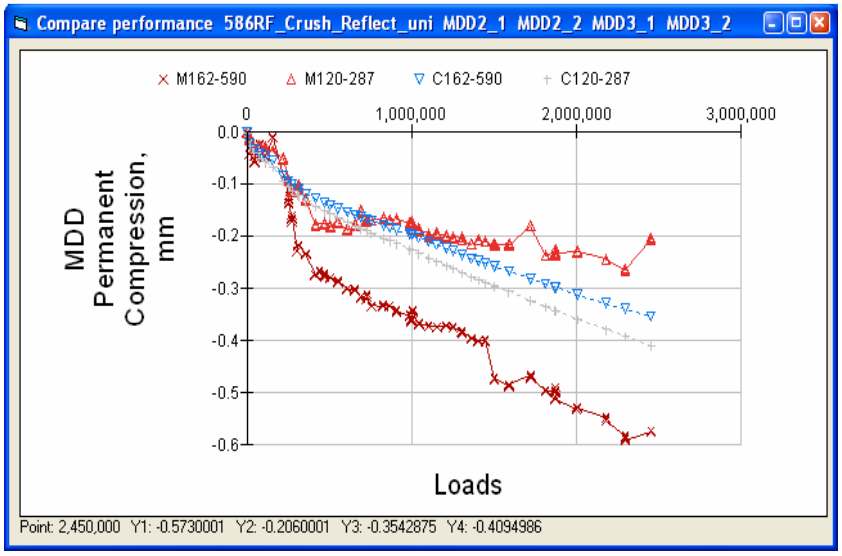

Figure B.71: 586RF, measured (MDD) and calculated permanent deformation of AB layers.

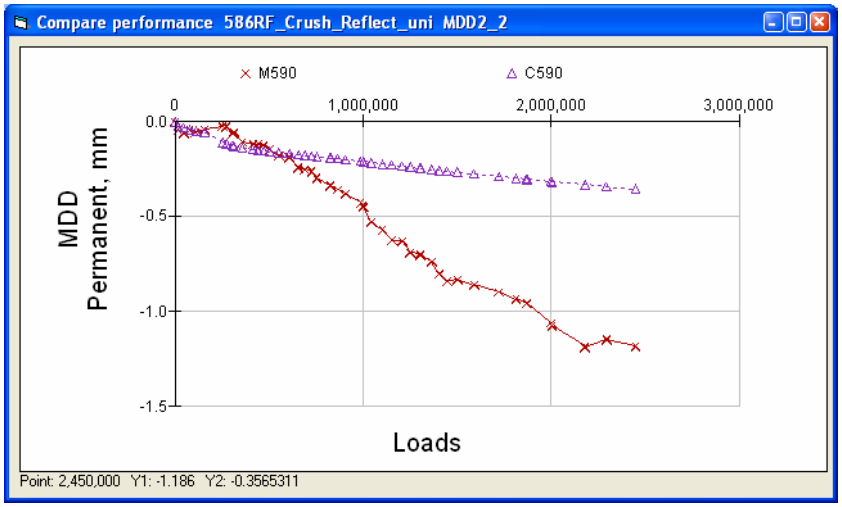

Figure B.72: 586RF, measured (MDD) and calculated permanent deformation of subgrade.

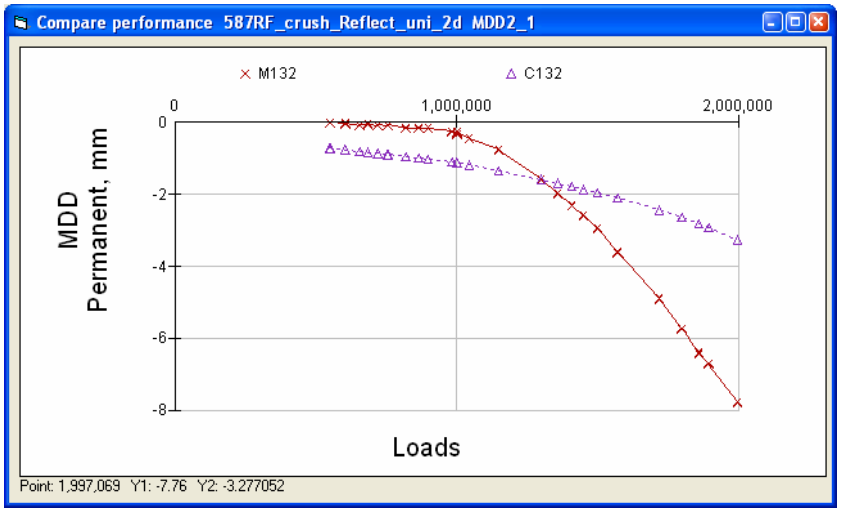

Figure B.73: 587RF, permanent deformation at top MDD.

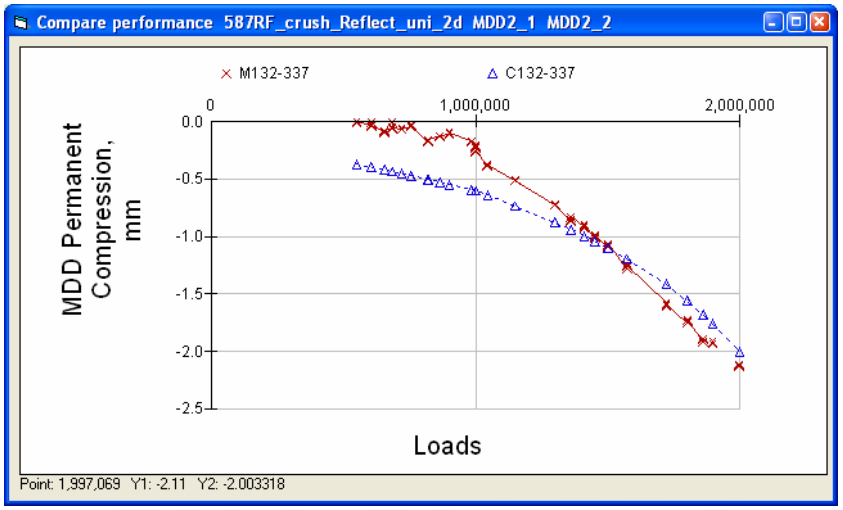

Figure B.74: 587RF, measured (MDD) and calculated permanent compression of top AB layers.

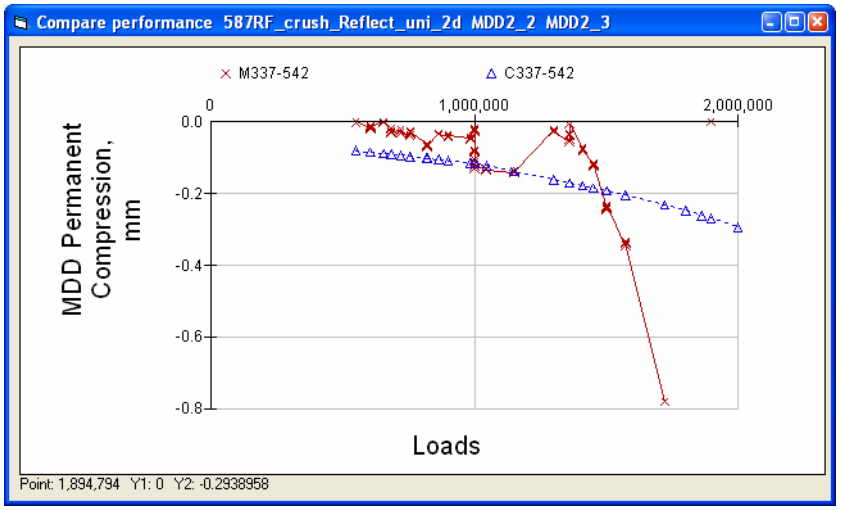

Figure B.75: 587RF, measured (MDD) and calculated permanent compression of bottom AB layers.

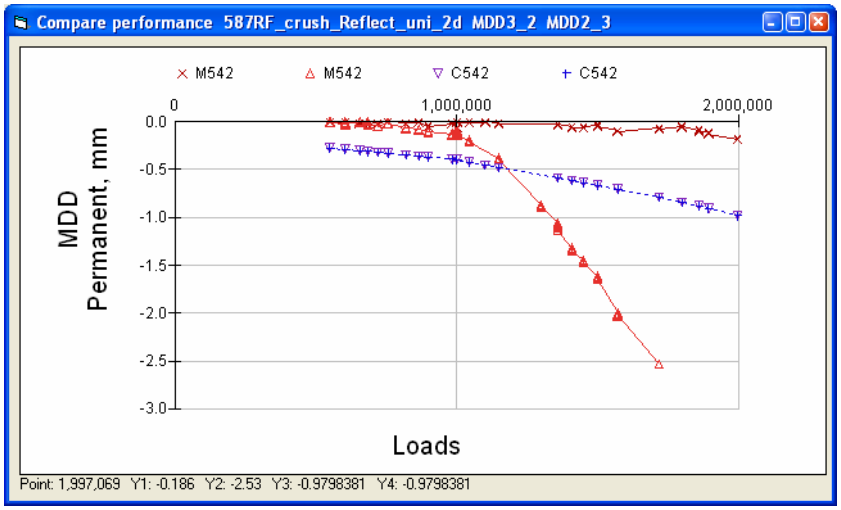

Figure B.76: 587RF, measured (MDD) and calculated permanent deformation of subgrade.

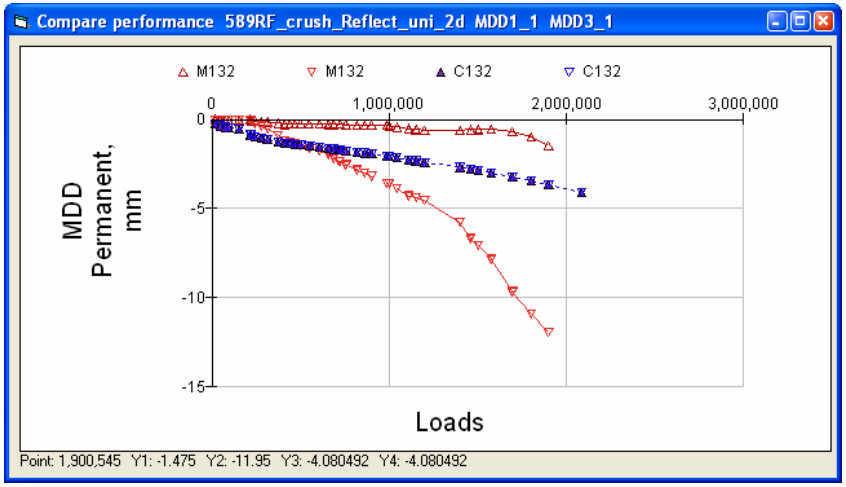

Figure B.77: 589RF, measured and calculated permanent deformation at top MDDs.

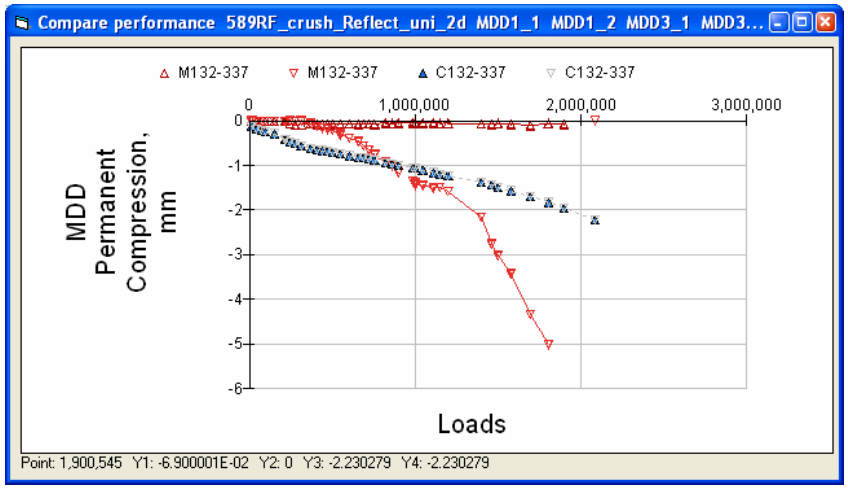

Figure B.78: 589RF, measured (MDD) and calculated permanent compression of upper AB layers.

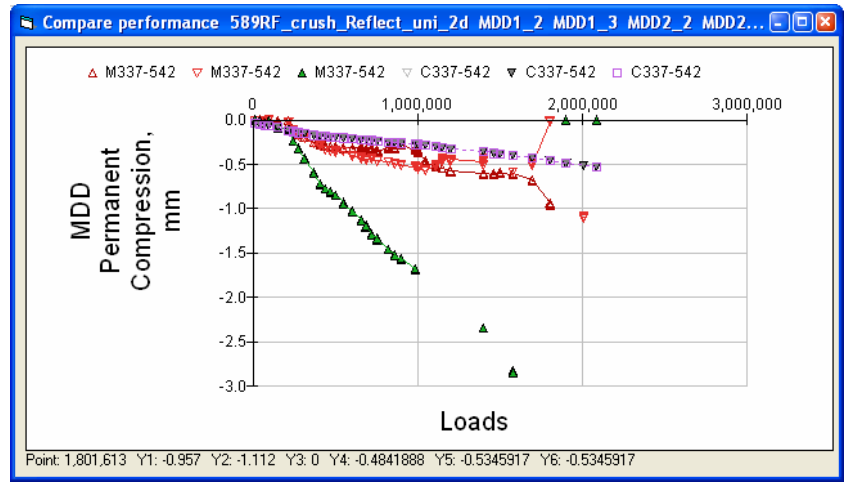

Figure B.79: 589RF, measured (MDD) and calculated permanent compression of lower AB layers.

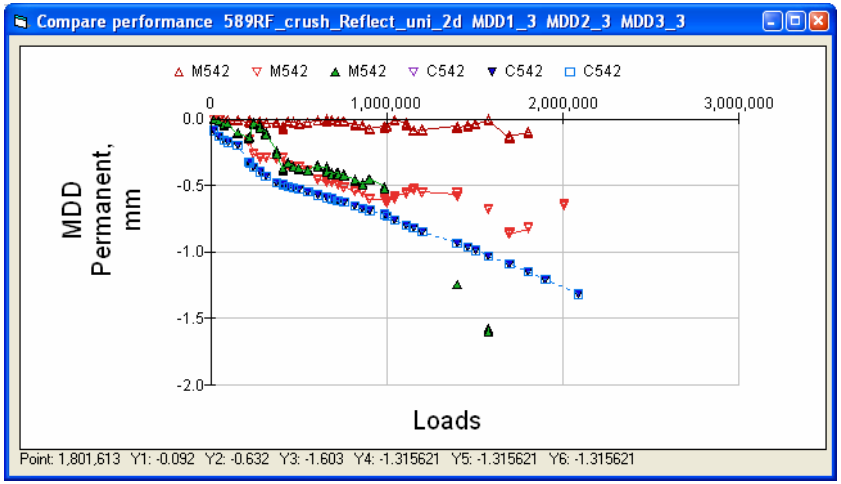

Figure B.80: 589RF, measured (MDD) and calculated permanent deformation of subgrade.

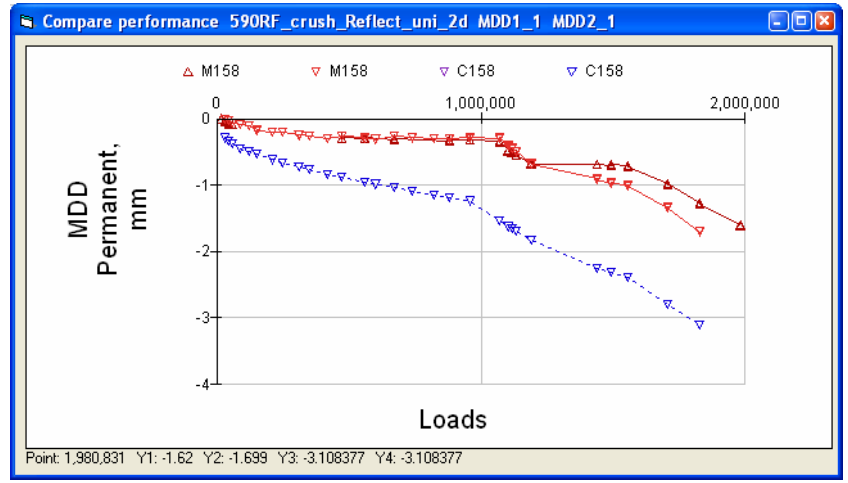

Figure B.81: 590RF, measured and calculated permanent deformation at upper MDDs.

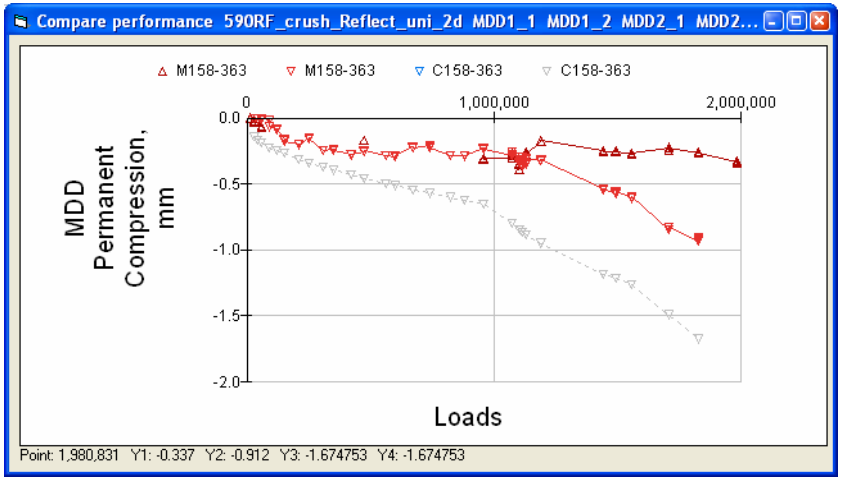

Figure B.82: 590RF, measured (MDD) and calculated permanent compression of upper AB layers.

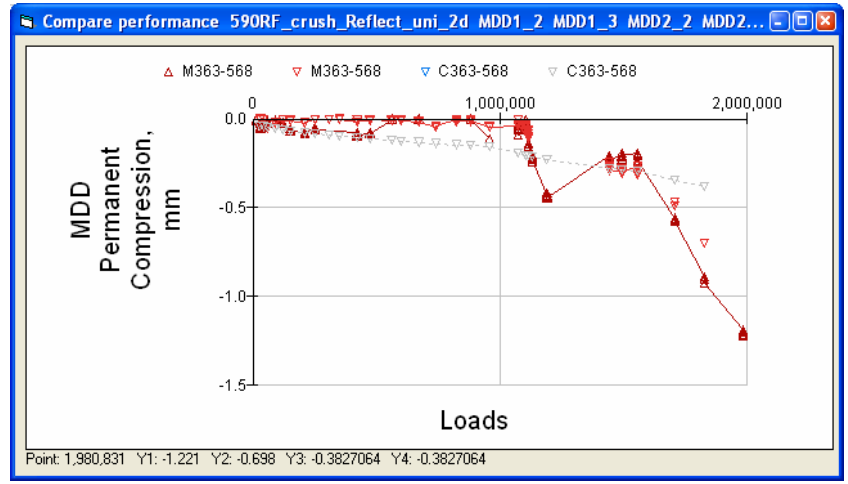

Figure B.83: 590RF, measured (MDD) and calculated permanent deformation of lower AB layers.

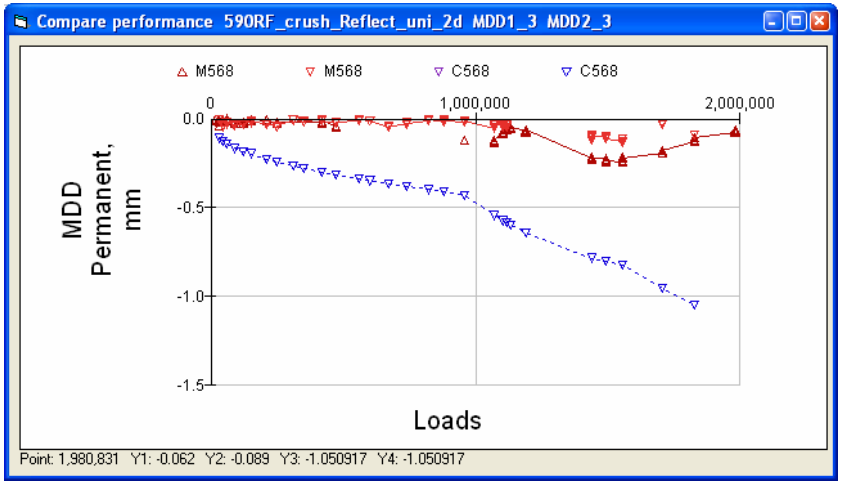

Figure B.84: 590RF, measured (MDD) and calculated permanent deformation of subgrade.

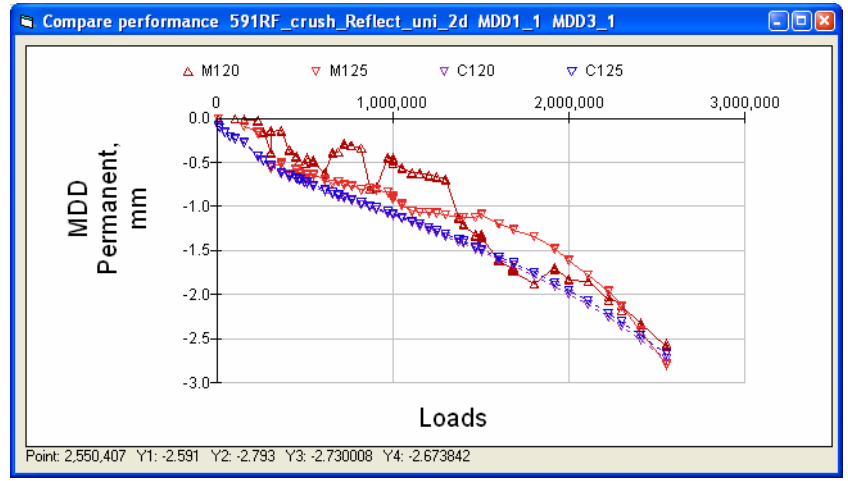

Figure B.85: 591RF, measured and calculated permanent deformation at upper MDDs

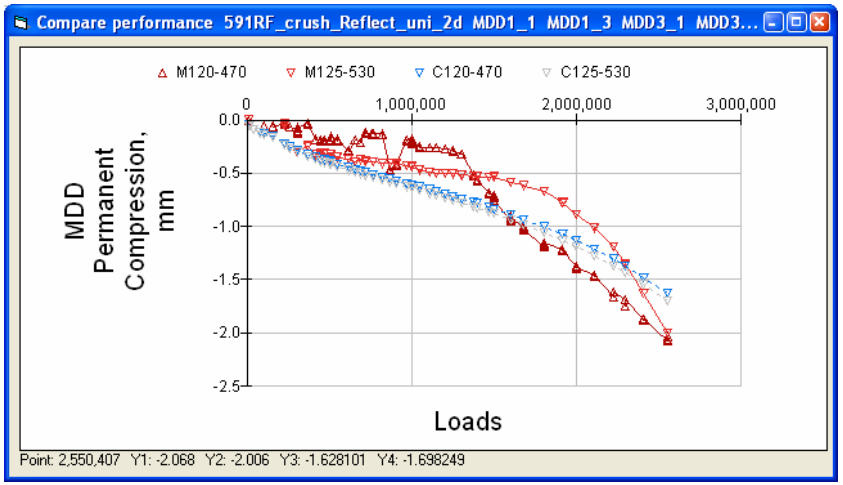

Figure B.86: 591RF, measured (MDD) and calculated permanent compression of aggregate base

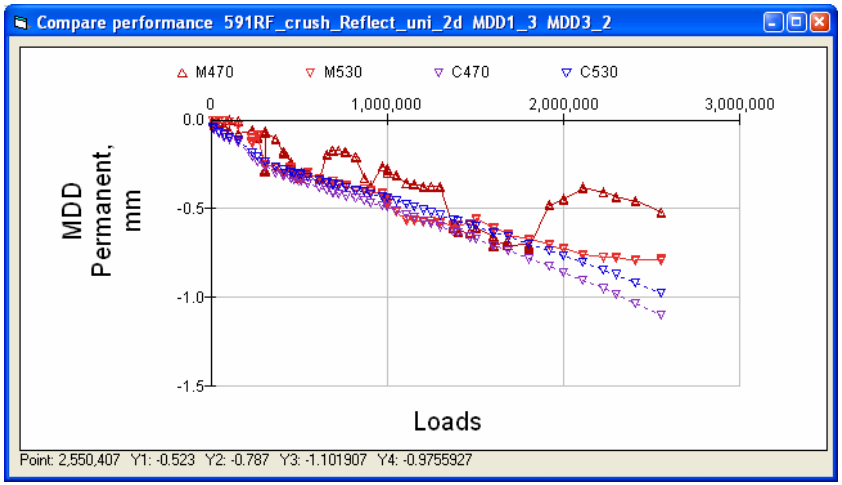

Figure B.87: 591RF, measured (MDD) and calculated permanent deformation of subgrade

Appendix C

Continuum Damage Mechanics Simulations

APPENDIX C. CONTINUUM DAMAGE MECHANICS SIMULATIONS

C.1. Regression Parameters for Base and Subgrade Stiffness Degradation

Tables C.1 through C.6 present regression parameters for stiffness degradation in the aggregate base (AB) and subgrade (SG). These parameters were determined by regression analysis using the backcalculated layer moduli listed in Section 5.1.

Table C.1: 586RF: Stiffness Degradation Parameters for Aggregate Base and Subgrade

Station	Aggregate Base				Top 400 mm of Subgrade		Remaining Subgrade
	Before 215,000 Rep		After 215,000 Rep				
	E_{01}	α_1	E_{02}	α_2	E_0	α	E
4	1232	2.47E-6	402	1.78E-7	112	1.90E-7	254
6	1920	2.01E-6	610	1.85E-7	100	1.00E-7	267
8	1167	6.69E-6	525	2.78E-8	109	2.33E-8	290
10	2456	3.86E-6	799	1.10E-7	129	1.51E-7	307
12	1613	3.12E-6	453	3.95E-8	100	0	287

Table C.2: 587RF: Stiffness Degradation Parameters for Aggregate Base and Subgrade

Station	Aggregate Base		Top 400 mm of Subgrade		Remaining Subgrade
	E_0	α	E_0	α	E
4	200	1.08E-6	60	5.28E-7	250
6	197	1.17E-6	64	2.88E-7	276
8	170	1.02E-6	83	1.32E-7	303
10	247	1.00E-6	66	1.06E-7	276
12	306	0.84E-6	95	4.14E-7	161

Table C.3: 588RF: Stiffness Degradation Parameters for Aggregate Base and Subgrade

Station	Aggregate Base		Top 400 mm of Subgrade		Remaining Subgrade
	E_0	α	E_0	α	E
4	146	5.33E-7	75	6.81E-8	205
6	152	5.14E-7	77	4.56E-7	207
8	95	1.52E-6	82	1.33E-7	264
10	49	4.28E-7	150	7.89E-7	200
12	66	8.63E-7	61	0	309

Table C.4: 589RF: Stiffness Degradation Parameters for Aggregate Base and Subgrade

Station	Aggregate Base				Top 400 mm of Subgrade		Remaining Subgrade
	Before 215,000 Rep		After 215,000 Rep				
	E_{01}	α_1	E_{02}	α_2	E_0	α	E
4	265	2.30E-6	133	2.09E-7	39	1.62E-7	189
6	166	1.34E-6	94	1.31E-7	60	2.91E-7	152
8	152	0	70	0	56	4.25E-7	175
10	147	0	75	2.55E-7	58	4.02E-7	161
12	188	1.92E-6	59	4.33E-7	43	0	158

* Subgrade is assumed to be less than 250 MPa when taking average, but less than 400 MPa when doing backcalculation

Table C.5: 590RF: Stiffness Degradation Parameters for Aggregate Base and Subgrade

Station	Aggregate Base				Top 400 mm of Subgrade		Remaining Subgrade
	Before 1 Million		After 1 Million				
	E_{01}	α_1	E_{02}	α_2	E_0	α	E
4	259	1.87E-7	1474	1.65E-6	38	1.28E-7	223
6	219	1.47E-7	457	9.42E-7	34	2.57E-7	224
8	179	0	1220	1.91E-6	34	0	191
10	159	0	946	1.88E-6	38	0	153
12	165	0	945	1.76E-6	31	0	180

Table C.6: 591RF: Stiffness Degradation Parameters for Aggregate Base and Subgrade

Station	Aggregate Base				Top 400 mm of Subgrade		Remaining Subgrade
	Before 1 Million		After 1 Million				
	E_{01}	α_1	E_{02}	α_2	E_0	α	E
4	807	2.26E-6	449	9.44E-7	30	2.05E-7	279
6	656	2.84E-6	348	9.96E-7	30	6.92E-8	263
8	857	3.27E-6	386	1.12E-6	25	0	298
10	939	3.24E-6	378	1.00E-6	27	0	327
12	744	2.44E-6	415	1.02E-6	29	1.48E-7	323

C.2. Backcalculated Initial Stiffness for Underlying Asphalt Concrete Layer

Tables C.7 through C.12 list the backcalculated stiffness for the underlying AC layer at different stations (i.e., 4, 6, 8, 10, and 12) along the centerline (CL) of the HVS test sections, using the first five sets of RSD data at the beginning of each HVS test.

Table C.7: 586RF: Backcalculated Underlying DGAC Layer Moduli

Stage	Layer Moduli (MPa)				
	4CL	6CL	8CL	10CL	12CL
1st	1395	1395	1395	1395	1395
2nd	1204	1204	1204	1204	1204
3rd	1228	1228	1228	1228	1228
4th	1133	1133	1133	1133	1133
5th	1192	1192	1192	1192	1192

Table C.8: 587RF: Backcalculated Underlying DGAC Layer Moduli

Stage	Layer Moduli (MPa)				
	4CL	6CL	8CL	10CL	12CL
1st	1805	1805	1339	1805	1805
2nd	1769	1500	1769	1746	1380
3rd	1146	1229	1673	1673	1673
4th	1322	1420	1420	1420	1420
5th	1299	1299	1106	1299	1299

Table C.9: 588RF: Backcalculated Underlying DGAC Layer Moduli

Stage	Layer Moduli (MPa)				
	4CL	6CL	8CL	10CL	12CL
1st	1480	1480	1480	1480	1480
2nd	1472	1552	1406	729	255
3rd	1052	1052	1048	212	200
4th	916	738	380	200	200
5th	1936	1936	892	200	200

Table C.10: 589RF: Backcalculated Underlying DGAC Layer Moduli

Stage	Layer Moduli (MPa)				
	4CL	6CL	8CL	10CL	12CL
1st	838	774	838	838	838
2nd	784	721	784	784	784
3rd	784	784	761	784	784
4th	893	893	893	893	893
5th	893	893	893	893	893

Table C.11: 590RF: Backcalculated Underlying DGAC Layer Moduli

Stage	Layer Moduli (MPa)				
	4CL	6CL	8CL	10CL	12CL
1st	1006	1006	1006	1006	858
2nd	949	949	949	949	890
3rd	893	893	893	893	893
4th	1006	1006	1006	1006	1006
5th	1006	1006	1006	1006	1006

Table C.12: 591RF: Backcalculated Underlying DGAC Layer Moduli

Stage	Layer Moduli (MPa)				
	4CL	6CL	8CL	10CL	12CL
1st	983	983	983	983	983
2nd	1098	1098	1098	1098	1098
3rd	994	994	994	994	994
4th	949	949	949	949	949
5th	1075	1075	1075	1075	1075

Tables C.13 through C.18 in this section present the layer moduli for the underlying DGAC layer under trafficking conditions at 20°C. The last column in each table lists the ratios used to adjust for the effect of temperature. RSD data were collected at varying temperatures and these ratios were applied to the backcalculated asphalt concrete moduli to convert them into 20°C moduli.

Table C.13: 586RF: Trafficking Layer Moduli for Underlying DGAC at 20°C

Stage	Layer Moduli (MPa)					
	4CL	6CL	8CL	10CL	12CL	Ratio
1st	1596	1596	1596	1596	1596	1.14
2nd	1596	1596	1596	1596	1596	1.33
3rd	1596	1596	1596	1596	1596	1.30
4th	1596	1596	1596	1596	1596	1.41
5th	1596	1596	1596	1596	1596	1.34
Median	1596	1596	1596	1596	1596	-

Table C.14: 587RF: Trafficking Layer Moduli for Underlying DGAC at 20°C

Stage	Layer Moduli (MPa)					
	4CL	6CL	8CL	10CL	12CL	Ratio
1st	1596	1596	1184	1596	1596	0.88
2nd	1596	1353	1596	1575	1245	0.90
3rd	1093	1172	1596	1596	1596	0.95
4th	1486	1597	1597	1597	1597	1.12
5th	1596	1596	1358	1596	1596	1.23
Median	1596	1596	1596	1596	1596	-

Table C.15: 588RF: Trafficking Layer Moduli for Underlying DGAC at 20°C

Stage	Layer Moduli (MPa)					
	4CL	6CL	8CL	10CL	12CL	Ratio
1st	1596	1596	1596	1596	1596	1.08
2nd	1513	1596	1446	749	262	1.03
3rd	1596	1596	1590	322	303	1.52
4th	913	736	379	199	199	1.00
5th	1596	1596	735	165	165	0.82
Median	1596	1596	1446	322	262	-

Table C.16: 589RF: Trafficking Layer Moduli for Underlying DGAC at 20°C

Stage	Layer Moduli (MPa)					
	4CL	6CL	8CL	10CL	12CL	Ratio
1st	1596	1474	1596	1596	1596	1.90
2nd	1596	1468	1596	1596	1596	2.04
3rd	1596	1596	1549	1596	1596	2.04
4th	1596	1596	1596	1596	1596	1.79
5th	1596	1596	1596	1596	1596	1.79
Median	1596	1596	1596	1596	1596	-

Table C.17: 590RF: Trafficking Layer Moduli for Underlying DGAC at 20°C

Stage	Layer Moduli (MPa)					
	4CL	6CL	8CL	10CL	12CL	Ratio
1st	1596	1596	1596	1596	1361	1.59
2nd	1596	1596	1596	1596	1497	1.68
3rd	1596	1596	1596	1596	1596	1.79
4th	1596	1596	1596	1596	1596	1.59
5th	1596	1596	1596	1596	1596	1.59
Median	1596	1596	1596	1596	1596	-

Table C.18: 591RF: Trafficking Layer Moduli for Underlying DGAC at 20°C

Stage	Layer Moduli (MPa)					
	4CL	6CL	8CL	10CL	12CL	Ratio
1st	1596	1596	1596	1596	1596	1.62
2nd	1596	1596	1596	1596	1596	1.45
3rd	1596	1596	1596	1596	1596	1.61
4th	1596	1596	1596	1596	1596	1.68
5th	1596	1596	1596	1596	1596	1.48
Median	1596	1596	1596	1596	1596	-